

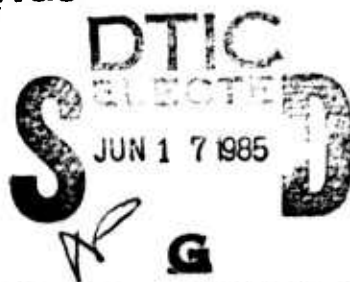
AD-A155 423

---

**SOLID LUBRICATED ROLLING ELEMENT BEARINGS  
SEMIANNUAL STATUS REPORT NO. 3**

(Reporting Period: 1 August 1979 – 31 January 1980)

15 FEBRUARY 1980

APPROVED FOR PUBLIC RELEASE  
DISTRIBUTION IS UNLIMITED (A)

Sponsored by:

Defense Advanced Research Projects Agency (DoD)  
DARPA Order No. 3576

Monitored by AFW, L/MLBT Under Contract No. F33615-78-C-5196

Submitted by:

Hughes Aircraft Company  
Technology Support Division  
Culver City, CA 90230

DTIC FILE COPY

85 06 13 015

Bm

SOLID LUBRICATED ROLLING ELEMENT BEARINGS  
SEMIANNUAL STATUS REPORT NO. 3

(Reporting Period: 1 August 1979 - 31 January 1980)

Michael N. Gardos

Sponsored by:

Defense Advanced Research Projects Agency (DoD)  
DARPA Order No. 3576

Monitored by AFWAL/MLBT Under Contract No. F33615-78-C-5196

Submitted by:

Hughes Aircraft Company  
Technology Support Division  
Culver City, CA 90230

Approved:

  
R. H. Johnson, Manager  
Materials Technology  
Department

Accession For	
NTIS GRA&I	<input checked="" type="checkbox"/>
DTIC TAB	<input type="checkbox"/>
Unannounced	<input type="checkbox"/>
Justification	
By _____	
Distribution/	
Availability Codes	
Dist	Avail and/or Special
A/1	



**BEST  
AVAILABLE COPY**

## FOREWORD

This report was prepared by Hughes Aircraft Company under DARPA Order No. 3576, AFWAL Contract No. F33615-78-C-5196, effective starting date 1 August 1978, under the title of "Solid Lubricated Rolling Element Bearings". The work was administrated under the technical direction of the Fluids, Lubricants and Elastomers Branch, Non-Metallic Materials Division of the Air Force Wright Aeronautical Laboratories Materials Laboratory, with Mr. B. D. McConnell acting as Project Engineer.

The Program Manager and General Principal Investigator is Mr. Michael N. Gardos, (213) 391-0711, Extension 4532. The Principal Investigators of (1) the Type II (turbine) bearing work and (2) the in-house wear equation and high temperature solid lubricant/ceramics interaction studies are Messrs. C. R. Meeks and J. J. Bohner, respectively. They both contributed to the preparation of the summary presented herein.

This report covers work conducted between 1 August 1979 and 31 January 1980 and is the third Semiannual Progress Report on this contract.



## TABLE OF CONTENTS

SECTION	Page
I. INTRODUCTION . . . . .	1
II. PROGRAM HISTORY . . . . .	2
III. ACCOMPLISHMENTS TO DATE . . . . .	5
A. Current Program Plan . . . . .	5
B. Technical Achievements . . . . .	7
1. Bearing Surface Integrity and Solid Lubricants Research . . . . .	7
(a) Bearing Surface Machining Studies . . . . .	7
(b) Bearing Surface Stabilization with Hardcoats . . . . .	12
(c) Intercalated Dichalcogenides for Wide Temperature Range Use . . . . .	28
(d) Fundamentals of the Westinghouse Compact . . . . .	28
(e) Solid Lubricant Deposition Studies . . . . .	31
(f) Shear Strength of Solid Lubricants at High Loads . . . . .	43
(g) Wear Equations for Self-lubricating Composites . . . . .	43
(h) Bearing Simulation Test Equipment . . . . .	45
2. Gyro (Type I) Bearing Research . . . . .	46
(a) Baseline Studies (Oil Lubricated) . . . . .	46
(b) Baseline Studies ( $\text{MoS}_2$ Lubricated) . . . . .	47
(c) Preparation of Improved Gyro Bearing Retainer Stocks . . . . .	48
3. Turbine Engine (Type II) Bearing Research . . . . .	56
(a) Baseline Studies (Westinghouse Compact Lubricated) . . . . .	56
(b) Polymeric Self-lubricating Retainers for $500^{\circ}\text{F}$ Operation . . . . .	56
(c) The Solid Lubricated ( $500^{\circ}\text{F}$ ) Turbine Engine Bearing Precursor . . . . .	65
(d) Thermal Mapping of the WRC F-107 Cruise Missile Engine by the SKF TRANSIM Computer Diagnostic Method . . . . .	66
(e) PLR - A Concept for Solid Lubrication of $1000^{\circ}\text{F}$ + Rolling Element Bearings . . . . .	67
(f) Retainers for $1000^{\circ}\text{F}$ + Solid Lubricated Rolling Element Bearings . . . . .	72
IV. CONCLUSIONS AND FUTURE WORK . . . . .	74

TABLE OF CONTENTS (Continued)

SECTION	Page
<b>REFERENCES</b> .....	<b>76</b>
<b>APPENDIX A</b> - Baginski, W. A., "Development of Solid Lubricated Gyro Bearings," R&D Status Report No. 13, Document No. 404413, Hughes P.O. 04-493431-FS5, Litton Guidance and Control Systems, Woodland Hills, California, January 1980 .....	A-1
<b>APPENDIX B</b> - Weglein, R. D. to Gardos, M. N., "Acoustic Microscopy of Gyro Bearing Balls," Hughes Technical Internal Correspondence 7621.30/162, 4 January 1980.....	B-1
<b>APPENDIX C</b> - Demeo, D. A. to Gardos, M. N., "Diamond Turning," Hughes Interdepartmental Correspondence 7621.30/169, 18 January 1980 .....	C-1
<b>APPENDIX D</b> - Ramalingam, S. and Winer, W. O., "Reactive Sputtering of TiN and Solid Lubricants and Shear Strength Testing of Solid Lubricants," Progress Report No. 1, Hughes P.O. 04-406163-FS5, Georgia Institute of Technology, Atlanta, Georgia, 16 January 1980.....	D-1
<b>APPENDIX E</b> - Jamison, W. E., "Solid Lubricant Research," Semi-annual Report, Hughes P.O. 04-406148-FS5, Triboro-Materials Development Corporation, Evergreen, Colorado, 15 January 1980 .....	E-1
<b>APPENDIX F</b> - Pietrokowsky, P. to Gardos, M. N., "Characterization of the Westinghouse Compact," Hughes Technical Internal Correspondence 7621.31/57, 1 February 1980 .....	F-1
<b>APPENDIX G</b> - Christy, R. I. to Gardos, M. N., "Solid Lubricant Sputtering Progress and Plans for DARPA/Hughes S. L. R. E. B. Program," Hughes Interdepartmental Correspondence 4142.20/721, January 22, 1980 ..	G-1
<b>APPENDIX H</b> - Gardos, M. N., "Theory and Practice of Self-Lubricated, Oscillatory Bearing Operation for High Vacuum Applications - Part I; Selection of the Self-Lubricating Composite Retainer Material", paper accepted for presentation and publication at the ASME-ASLE Int. Conf.; Aug. 18-21, 1980, St. Francis Hotel, San Francisco, California .....	H-1

TABLE OF CONTENTS (Continued)

SECTION	Page
APPENDIX I - Meeks, C. R., "Theory and Practice of Self-Lubricated, Oscillatory Bearing Operation for High Vacuum Applications - Part II; Accelerated Life Tests and Analysis of Bearings," paper accepted for presentation and publication at the ASME-ASLE Int. Conf.; Aug. 18-21, 1980, St. Francis Hotel, San Francisco, California . . . . .	I-1
APPENDIX J - Gupta, P. K. and Eusepi, M., "Apparatus and Technique Development for Solid Lubricated Bearing," Monthly Progress Report, Hughes P.O. 04-493436-FS5, Mechanical Technology, Inc., Latham, New York, 15 January 1980 . . . . .	J-1
APPENDIX K - Bohner, J. J. to Gardos, M. N., "Initial Investigation into the Chemical Compatibility at High Temperatures Between Ceramics and Solid Lubricants," Hughes Technical Internal Correspondence 7621.14/47, 22 January 1980 . . . . .	K-1
APPENDIX L Program Schedule (Separate Attachment) . . . . .	L-1
APPENDIX M Performance and Cost Report (Separate Attachment) . . . . .	M-1

## LIST OF FIGURES

Figure	Page
1. The current program network . . . . .	6
2. A recommended first phase of a MANTECH bearing machining study (hardcoat machining preferred) . . . . .	11
3. A recommended second phase of a MANTECH bearing machining study . . . . .	11
4. TMI TiC sputtered 52100 gyro bearing inner race ball path (as received), at various SEM magnifications . . . . .	14
5. TMI TiC sputtered 52100 gyro bearing outer race ball path (as received), at various SEM magnifications . . . . .	15
6. TMI TiC sputtered 52100 gyro bearing balls (as received), at various SEM magnifications . . . . .	16
7. TMI TiC/MoS <sub>2</sub> sputtered 52100 gyro bearing inner and outer race ball paths (as received), at various SEM magnifications and EDX scrutiny . . . . .	17
8. TMI TiC/MoS <sub>2</sub> sputtered 52100 gyro bearing balls (as received), at various SEM magnifications . . . . .	18
9. TMI TiC/MoS <sub>2</sub> sputtered 52100 gyro bearing inner race ball path (MoS <sub>2</sub> removed with Oakite 126 HD), at various SEM magnifications and EDX scrutiny . . . . .	19
10. TMI TiC/MoS <sub>2</sub> sputtered 52100 gyro bearing inner race ball path (MoS <sub>2</sub> removed with Oakite 126 HD), at various SEM magnifications and EDX scrutiny . . . . .	20
11. TMI TiC/MoS <sub>2</sub> sputtered 52100 gyro bearing outer race ball path (MoS <sub>2</sub> removed with Oakite 126 HD), at 800X SEM magnification and EDX scrutiny . . . . .	21
12. TMI TiC/MoS <sub>2</sub> sputtered 52100 gyro bearing balls (MoS <sub>2</sub> removed with Oakite 126 HD), at various SEM magnifications . . . . .	22
13. Typical flux distribution from a DC magnetron target (Reference 4) . . . . .	23
14. Overall top view of a 5-station, 15 gyro component, planetary rotating sputtering fixture of TMI for TiC/MoS <sub>2</sub> -Sb <sub>2</sub> O <sub>3</sub> coating of hemispherical gas (gyro) bearings (Reference 4) . . . . .	24
15. Bottom view of multiple drive mechanism for planetary rotation of individual stations (also see Figure 14); from Reference 4 . . . . .	25

LIST OF FIGURES (Continued)

Figure		Page
16.	Current Hughes fixturing method for production type RF planar sputtering of small angular contact bearing components .....	33
17.	Bare and TiN-sputtered 52100 steel and variously machined, bare phenolic retainer traction specimens for MoS <sub>2</sub> sputtering at Hughes and traction studies at MTI .....	34
18.	Thickness control of thin MoS <sub>2</sub> films on MTI traction discs by fringes of equal chromatic order .....	35
19.	Dead-weight load versus Hertzian stress correlation of the Hughes rolling thrust bearing attachment of the Faville No. 6 friction and wear tester .....	37
20.	SEM photomicrographs at 450X and 4500X magnifications and EDX spectra of NYE-CARB®-coated copper specimen after thermal cycling .....	40
21.	The hardness of electroless nickel platings as a function of phosphorus content and heat treatment time at 400°C (Reference 27) .....	41
22.	The improved preparation process of the Hughes 2D carbon/polyimide gyro bearing retainer stock.....	50
23.	Improved, expanding silicone rubber plug-prepared Hughes 2D carbon/polyimide gyro bearing retainer stock .....	51
24.	Integrity of improved CCA-3/Thermid 600 gyro retainer tube edge .....	51
25.	Quality control sections of the improved Thornel 300/Thermid 600 gyro retainer tube stock .....	52
26.	Edge and side (OD) integrity of improved, as-molded and machined, CCA-3/Thermid 600 gyro retainer tube stock at various SEM magnifications .....	53
27.	Typical edge integrity of improved, as-molded, Thornel 300/Thermid 600 gyro retainer tube stock at 26X SEM magnification.....	54
28.	HIP of gyro retainer tube stock at FMI .....	55
29.	PERT schedule; MTI development of solid lubricated bearings .....	59

## LIST OF FIGURES (Continued)

Figure		Page
30.	The preparation process of the Hughes 3D cylindrical carbon-graphite weave/Thermid 600 turbine bearing retainer stock for 500°F use . . . . .	61
31.	Unacceptable and promising short (1 in.) moldings of 3D cylindrical Thorne 300 weave/Thermid 600 turbine bearing retainer tube stock . . . . .	62
32.	Edge and side (OD) integrity of as-molded and machined, 3D cylindrical, short Thorne 300 weave/Thermid 600 turbine bearing retainer tube stock at various SEM magnifications . . . . .	63
33.	Unacceptable, long (3 in.) moldings of 3D cylindrical Thorne 300 weave/Thermid 600 turbine bearing retainer tube stock . . . . .	64
34.	The PLR solid lubrication concept for high temperature rolling element bearing applications . . . . .	68
35.	Hot hardness of selected high temperature bearing alloys after a 30 minute soak at the indicated temperatures (Reference 3) . . . . .	71

## LIST OF TABLES

Table		Page
1.	Thermid 600/advanced solid lubricant additives screening blends weight loss on postcure (Reference 12) . . . . .	29
2.	Advanced solid lubricant additives weight loss on air-aging at 316°C (600°F); (Reference 12). . . . .	29
3.	Change in weight of specimens of WSe <sub>2</sub> and self-lubricating sintered material - WSe <sub>2</sub> + 25 Wt. % Ga/In due to oxidation by dry air (Reference 13). . . . .	30
4.	MoS <sub>2</sub> -sputtered gyro bearing baseline and MTI traction specimens . . . . .	36
5.	Weight percent chemical composition of selected high temperature bearing alloys (Reference 3) . . . . .	71

## I. INTRODUCTION

The DARPA/Hughes Solid Lubricated Rolling Element Bearing Program deals with the development of advanced dry-lubricated bearings for cruise missile gyro and turbine engine application, keeping the latter in the focal point of the main research effort. → (top 74)

The test philosophy, as well as the accomplishments prior to this reporting period were thoroughly described in References 1 and 2 and supplemented by verbal presentations at the most recent Program Design Review held on October 11-13, 1979, in Dayton, Ohio, under Joint Hughes-AFWAL/MLBT sponsorship.

As established in the previous semiannual report (Reference 2), the main text here again represents a summary of all work during this reporting period. All pertinent Hughes and subcontractor reports under discussion are attached as Appendices for more thorough scrutiny by the reader and to give proper credit to all contributors.

Note that the bulk of the experimental effort for this two year feasibility study was started at the onset of the second half of the program (November, 1979), when F Y'80 funds were received.

## II. PROGRAM HISTORY

A chronological sequence of significant program events is presented below, representing highlights of the current reporting period.

August '79: The Second Semiannual Report was mailed to everyone on the report distribution list. A Hughes/Litton meeting was arranged to discuss acoustic microscopy of gyro bearing ball surfaces.

September '79: The Swiss CVD CrC-TiC hardcoated balls ran successfully in 52100 gyro bearings, in the oil lubricated condition at loads up to five times of that normally applied. Independent Hughes and Litton SEM/EDX examination of unused, TiC and TiC/MoS<sub>2</sub> sputtered (by TMI, Santa Barbara, California), 52100 Litton baseline gyro bearing balls and races indicated unacceptably poor adhesion of the DC magnetron sputtered hardcoat. FMI (Biddeford, Maine) completed 4 each 3D cylindrical carbon/graphite weave turbine retainer practice preforms for preliminary testing. All preparations were completed for the October 1979 Design Review (DR).

October '79: Three-day DR held in Dayton, Ohio. Over 40 guests and participants attended 20 formal presentations by Hughes and its subcontractors, by Naval Research Laboratory (NRL) scientists and by selected potential Hughes subcontractors who wanted to demonstrate that they had something significant to offer. The latter were invited by the Hughes program manager to give their special presentations. Hughes/AFWAL-MLBT/SKF/WRC technical discussions were held at Williams Research Corporation (WRC), Walled Lake, Michigan to lay the ground work for computer thermal modeling of the F-107 cruise missile engine and its mainshaft bearings. Hughes in-house work on high temperature ceramic/solid lubricant interactions started. Based on difficulties with their TiC/MoS<sub>2</sub> DC magnetron sputtering gyro baseline work, TMI declined further participation in the program. A Hughes/Litton technical meeting was held to coordinate Westinghouse compact identification and high temperature solid lubricant/ceramic research applicable to the high temperature turbine engine bearing efforts.

November '79: Hughes/Litton/Georgia Institute of Technology (GIT) technical meeting was held at GIT (Atlanta, Georgia) to finalize the Statement of Work (SOW) with respect to reactive sputtering of the TiN hardcoat, DC magnetron (mini-gun) sputtering of experimental solid lubricant

November '79:  
(Continued)

combinations and shear strength testing of solid lubricants. A Hughes/NRL technical conference was held to define the type and number of specimen coupons required for Rutherford backscattering (RB) and x-ray photoelectron spectroscopy (XPS) surface analytical work on solid lubricants. Also discussed was high pressure diamond cell x-ray diffractometry of solid lubricants, with early emphasis on the identification of the Ga/In/WSe<sub>2</sub> Westinghouse compact materials parameters. The Hughes program manager visited DARPA/AFSC (Washington, D. C.) for a program executive committee meeting. Litton completed letter type reports to those West European and U.S. bearing manufacturers who provided specially machined gyro and turbine bearing specimens free of charge to our program, describing the degree of surface damage of each sample. Litton accepted the additional task of investigating the Westinghouse compact's fundamentals, with the participation of Mr. W. Baginski. The FY '80 funds were received from AFML on 15 November 1979.

December '79:

All FY '80 funds were forwarded to the Hughes subcontractors. Twenty five additional F-107 No. 3 turbine engine bearing specimens were ordered from Barden. Barden also agreed to machine similar bearings from experimental stock to be prepared by hot isostatic pressing (HIP) of rapid solidification rate (RSR) M-50 powder. Three heats of this powder will be provided by Pratt & Whitney, through arrangements with Mr. A. M. Adair of AFWAL/MLLM. Estimated delivery of the powder is in February '80. Hughes generated x-ray diffraction data on the Westinghouse compact and acoustic microscopy data on gyro bearing balls. A schedule problem developed with LSRH/RMB (Switzerland) due to the forecasted delay in delivery of C<sub>x</sub>C-TiC CVD hardcoated gyro bearings races to the fall of 1980. Hughes and Litton personnel made arrangements for a January '80 on-site meeting with the respective Swiss firms to remedy this situation.

January '80:

The Hughes program manager and the AFWAL/MLBT project engineer presented the technical thrust of the FY '81/82 follow-on effort to the DARPA program manager and AFSC representatives at a Wright-Patterson AFB presentation. The Hughes program manager also gave a presentation on suggestions for the possible forthcoming AFWAL MANTECH bearing machining study, based on the data gathered by the DARPA/Hughes Solid Lubricated Rolling Element Bearing Program. GIT and California State University, Northridge (CSUN) were issued purchase orders and thus

January '80:  
(Continued)

formally joined the program team. RFQ's were sent to WRC and SKF for the cooperative F-107 cruise missile engine computer modeling work, anticipating a February '80 start. The recently appointed Type II (turbine) bearing Hughes principal investigator (Mr. C. R. Meeks) took his first survey trip to MTI and SKF, also delivering all MoS<sub>2</sub> sputtered traction specimens to MTI for their evaluation. Hughes successfully prepared the first concentric 3D (cylindrical) carbon fiber weave reinforced polyimide retainer stock for the 500°F turbine engine bearing. The Hughes/Litton trip to Switzerland did not succeed in improving the CVD CrC-TiC coated and final machined gyro bearing race delivery before September 1980 (possible delivery of 30 to 50 sets only out of the 120 were promised), due to RMB's large backlog.

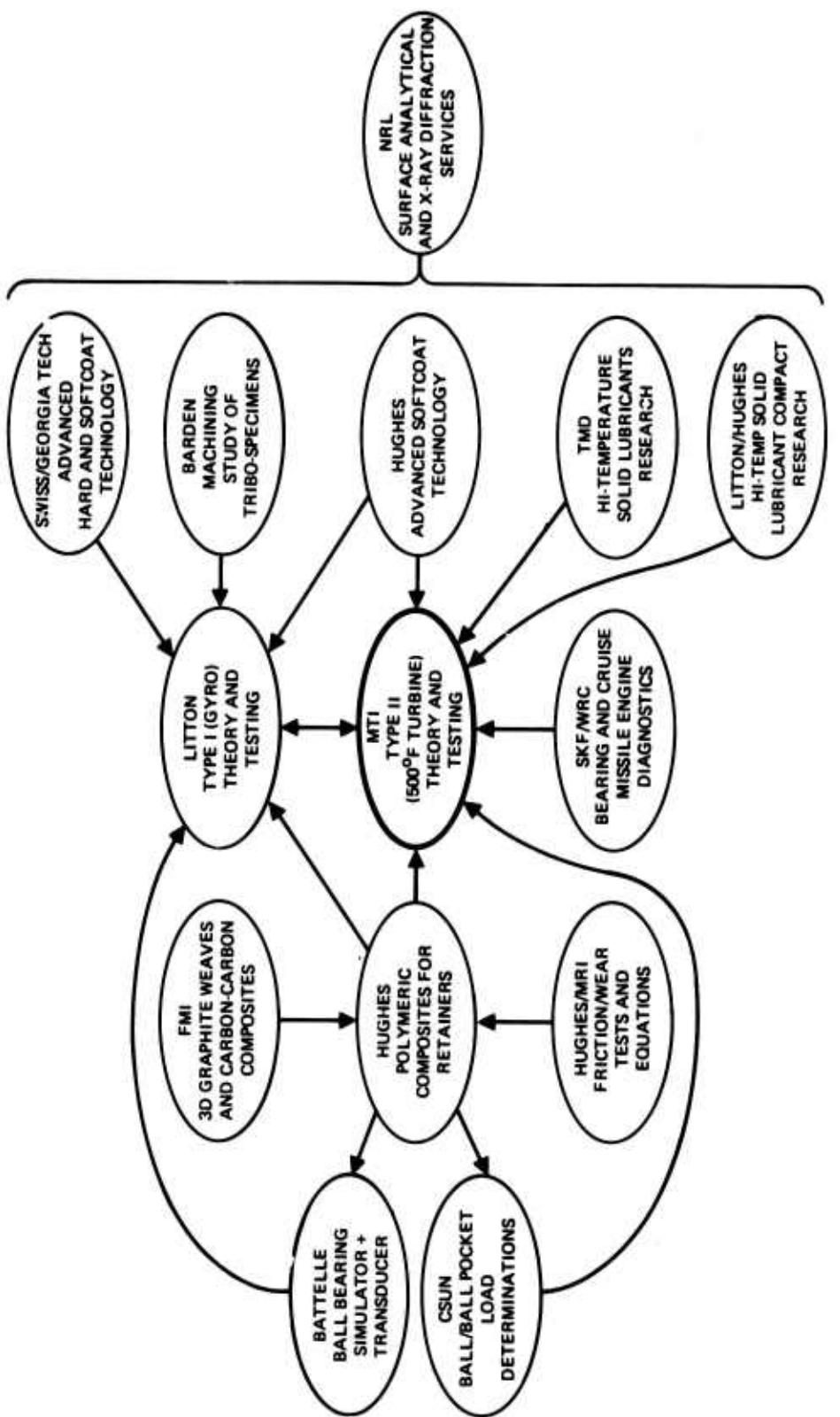
### III. ACCOMPLISHMENTS TO DATE

#### A. Current Program Plan

The current program network is shown in Figure 1, indicating some changes from the previous network presented in Reference 2.

The major changes are as follows:

1. TMI was dropped from the program, while GIT and WRC were added to the program team.
2. SKF's computer modeling task was expanded to include nodal temperature prognosis of the F-107 cruise missile engine bearings, aided by additional data from the engine manufacturer (WRC).
3. FMI's tasks were expanded into research quantity preparation of SiC-coated carbon/carbon composites for use as 1000°F+ turbine engine retainer stock and into other improved polymeric gyro and turbine bearing retainer tube stock fabrication work.
4. Hughes teamed with Litton and NRL to establish the materials and related tribological fundamentals of the Westinghouse compact and thus lay the groundwork for the synthesis of better 1000°F+ self-lubricating materials.
5. Hughes started its own wear equation development on polymeric self-lubricating composites to complement the MRI effort.
6. Hughes also started theoretical and practical work in establishing likely high temperature, oxidative degradation reactions between selected high temperature (1000°F+) solid lubricants and various stocks of hot-pressed silicon nitride ( $\text{Si}_3\text{N}_4$ ) normally used for bearing fabrication.



FEBRUARY 1980

Figure 1. The current program network.

## B. Technical Achievements

### 1. Bearing Surface Integrity and Solid Lubricants Research

(a) Bearing Surface Machining Studies - Previously reported work (References 1 and 2) indicated that the adherence of solid lubricant layers to conventionally machined, steel rolling element bearing surfaces is highly dependent on a reasonably damage-free ball and race finish. Unfortunately, present ball and race machining techniques leave the rolling contact surfaces in a seriously damaged condition. Such poorly prepared surfaces lead to early failure of even oil/grease lubricated precision bearings and are deemed unacceptable for solid lubricated bearings.

In order to complete the survey originally described in References 1 and 2, additional rolling element bearing surfaces of both gyro and turbine engine bearings were scrutinized by the Litton developed layer etch/SEM method. The samples were forwarded to us by several W. European and U.S. bearing manufacturers, representing routinely and specially fabricated balls and races. The evaluation of these samples is presented in Appendix A herein.

The data indicate poor understanding or total disregard for the surface integrity requirements of the machined bearings by most bearing manufacturers. Occasionally, good quality surfaces are produced, either accidentally or with some intent. However, it seems that the inherent nature of grinding and lapping is such that not all damage can be eliminated. It can only be minimized by the appropriate identification and incorporation of the many influencing (ideal) variables. This latter task is enormously complex, because none of the (ideal) feed rate/wheel type and speed/machining fluid/alloy type parameters applicable to a given bearing size and design can be singled out as one of overriding influence. Moreover, a given set of these heavily interacting variables considered ideal for one bearing size and alloy cannot be transferred across-the-board to a different size or metal stock.

Nevertheless, the data indicate a glimmer of hope that relatively damage-free surfaces can be attained, but only at the cost of abandoning the currently employed machining practices dictated by the need for high production rates and commercially profitable operation. One of the main culprits is the rough grinding cut, forced to remove an excessive amount of stock in order to speed up the machining process. Feed rates that are too high tend to dull the wheel prematurely. A continued effort of rapid stock removal with a dull wheel generates most of the initial surface damage, which can only be "remedied" by a prolonged finishing operation. The latter is the only avenue for providing visually and geometrically acceptable surfaces, because the excessive rough machining damage cannot be eliminated by the final integrity cut alone. Prolonged polishing, however, adds its own characteristic damage to the surfaces. Unfortunately, both this new and the previously inflicted metallurgical damage is hidden below a high surface finish produced by a smear (Beilby) layer.

The damage mechanisms may be summarized as follows:

- Dull wheels of the high feed rate rough grinding process overstress the bearing surface by ploughing instead of cutting and imparts the initial surface and subsurface damage on the raceways.
- Prolonged final polishing of races and rough ground balls cause decarburization of the martensitic matrix and preferential precipitation of subsurface carbides. The soft, carbon-poor matrix forms a good surface finish producing smear layer which hides the now multi-faceted damage regions below.
- The bearing surface damage is aggravated by the poor homogeneity of even the best commercially available (e.g., vacuum induction melted-vacuum arc remelted [VIM-VAR]) bearing stocks, mainly in terms of uneven particle size and density of the carbide precipitates in the martensitic matrix. The superimposed heat-to-heat variations in the microstructure of a given alloy further increases the likelihood of unpredictably poor surface and subsurface metallurgy.

Clearly, our program is confronted with the most difficult task of providing acceptable bearing surfaces for solid lubricants that are not yet obtainable in a reproducible manner from bearing manufacturers. As shown in Appendix A and by a forthcoming discussion, we intend to solve this problem (at least in the case of the feasibility study gyro bearings) through the incorporation of the Swiss CVD CrC-TiC hardcoat process. This process generates a refractory hard metal coating of a single-phase solid solution with satisfactory adherence, ductility, hardness and wear resistance. In addition, this coating is machinable to extremely close tolerances and surface finishes with far greater ease than any of the bearing alloys currently used. This ease of machining is the result of the inherent crystal structure and fragmentation characteristics of the hardcoat.

The unfortunate shortcoming of this CVD technique is the high deposition and re-quenching temperatures (approximately 1000°C) that tend to distort the anisotropic, wrought stocks of the commercially available bearing steels. Data from Switzerland indicate that of 100 each ABEC 9 440C races (~15 mm dia.) only 10 remain ABEC 9 (20 to 30 ABEC 7 and 20 to 30 ABEC 5) after coating and the final quench/temper cycle. 52100 steel bearings are oil-quenchable, therefore their deformation could be even more severe. In our case, this distortion causes an estimated 90 percent attrition in the 440C gyro bearing races used in this program and implies virtual unusability for larger bearings (e.g., turbine bearings). Yet, the CVD hardcoat process tends to heal some of the bearing surface machining damage and provides an ideal, corrosion resistant, hard substrate for both oil and solid lubricated rolling element bearings.

Not being able to wait for the results of an extensive bearing machining program that is now being planned by the US Air Force for the near future, this immediate problem is being addressed in the following manner:

- We are simultaneously pursuing solid lubricated bearing work with acceptably in-round CVD CrC-TiC hardcoated 440C gyro bearing races and balls, and with reactively sputtered TiN-coated bearings of the same size (see forthcoming discussion). The latter process is applied to final-machined bearing surfaces and requires no finishing operation after coating. However, TiN sputtering is not expected to yield the high adhesion of the hardcoat provided by CVD. Nevertheless, pursuit of the latter is a reasonable backup process, because it can be applied both to small and large size (e.g., turbine) bearings without suffering dimensional distortion due to lower deposition temperatures.

- We are trying to identify fabrication processes and alloy types that can yield more isotropic bearing stocks by concentrating on powder metallurgically prepared (i.e., hot isostatically pressed [HIP]) versions of rapid solidification rate (RSR) M-50 (the turbine engine specimen alloy) and similar materials previously examined by others (see Reference 3). The latter will include selected crucible powder metallurgically (CPM) prepared stock by the Crucible Steel Division of Colt Industries. With respect to more isotropic bearing race stocks, AFWAL/MLLM arranged for three heats of RSR M-50, to be HIP-ed into 2 inch diameter, approximately 1 or 2 ft. long billet or similar diameter "hockey pucks" for further experimental machining by Barden and eventual CVD coating by LSRH. To establish a baseline for distortion, the outer and the split inner races of one commercially available M-50, F-107 No. 3 bearing (the turbine engine bearing specimen of this program, now machined by Barden) is being measured for roundness by MTI and will be sent to LSRH for CVD coating. Post measurements both after coating and after the re-quenching and tempering steps will give us some idea on the degree of total distortion. Similar future work with the machined RSR-HIP P/M stock will hopefully indicate reduced distortion, keeping the roundness within acceptable tolerances. Elimination of large carbide precipitates in the improved stock may also, in certain cases, increase the fatigue resistance by reducing the number of inclusions that can act as subsurface stress risers for fatigue crack formation.

In the light of the above discussion, any forthcoming MANTECH machining study that is now being considered by AFWAL/MLLM should be started immediately, following the general guidelines given below:

- Learn to finish the CVD CrC-TiC hardcoated gyro bearings and for now, live with the high attrition rate due to distortion. The overall cost per bearing will still be less expensive than that of the bare steel version, because only a small number of steel bearings of a given lot meet the extremely close tolerance requirements of high quality gyros. There is no question that learning CVD hardcoat finishing procedures appears to offer the best short-term solution.

- Learn to machine conventional bearing steel rolling element bearing surfaces by identifying the ideal fabrication variables attainable with currently used grinders, lapping machines and machining fluids. This step is extremely complex, time consuming and expensive, but technically feasible. The machining activity must be willing to isolate their best grinding and lapping machines in a controlled laboratory environment to do the above listed steps satisfactorily.

- Aid either or both of these steps by investigating hardcoated cutting tools that provide better service life and performance than bare tool steels or cobalt-bonded WC and by developing improved grinding wheels. The latter should consist of the increased use of sharp synthetic diamond and diamond-like abrasive particles properly aligned on the wheel OD to form ideal rake angles and the utilization of solid lubricant pigments in the wheel binder for more orderly stock removal.

- Conceive improved bearing steel stock fabrication techniques by RSR-HIP P/M methods, combining them with the suggestions listed above. This step is needed for nearly every aspect of improvements. Continuation of the work described in Reference 3 should be accelerated immediately, incorporating not only P/M bearing ball but race stock preparation also.

The recommended MANTECH study should be completed in two phases, as shown in Figures 2 and 3.

Laying the research groundwork for such a study is not part of the contractual requirements of the DARPA/Hughes program. Nevertheless, the problems described here are very much of concern to us and the successful development of solid lubricated bearings would be immeasurably helped by the preparation of improved bearing alloys and an immediate start of bearing machining research activities. Clearly, such extended activities are beyond the scope of our present program.

The DARPA/Hughes Solid Lubricated Rolling Element Bearing Program would like to retain some ties with any forthcoming bearing machining study, preferably in the role of a technical consultant, providing guidance for quality control (QC). At this time, the Litton-developed layer etch/SEM technique is the only QC technique available for bearing surface integrity examination. In order to develop other, less expensive, less time-consuming non-destructive techniques, Hughes conducted some preliminary research on the use of acoustic microscopy (AM) for non-destructive evaluation (NDE) of 52100 gyro bearing ball surfaces (see Appendix B).

As-lapped and metallographically cross-sectioned and polished layers of randomly selected balls were examined both in the acoustic material signature (AMS) mode\* and in the imaging mode. There were significant differences between the Rayleigh velocity and acoustic

---

\*AMS launches and detects Rayleigh waves coherently.

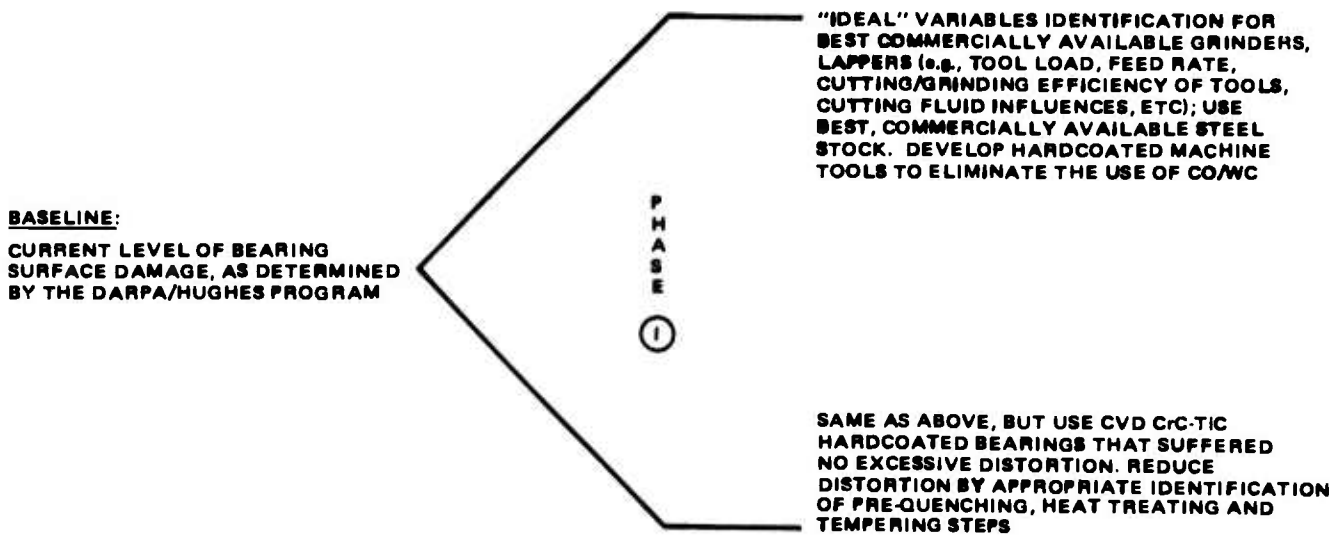


Figure 2. A recommended first phase of a MANTECH bearing machining study (hardcoat machining preferred).

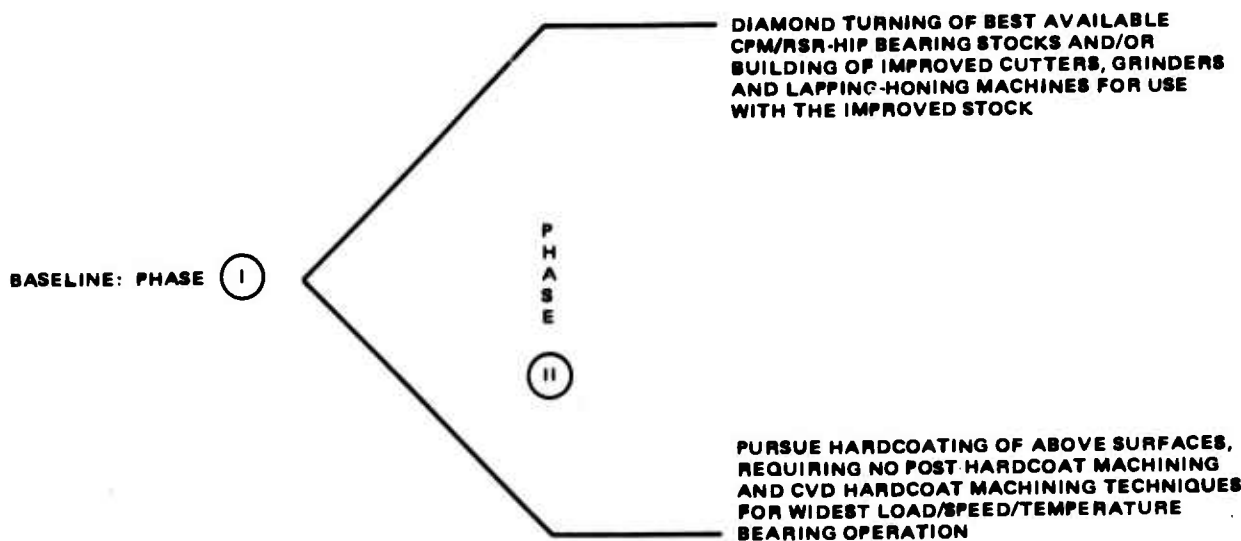


Figure 3. A recommended second phase of a MANTECH bearing machining study.

attenuation of the two surfaces. Also, acoustic depth profiling to determine various degrees of grain (carbide) distribution appears possible. In view of the fact that both concave (race) and convex (ball) surfaces may be inspected, AM could be developed as a potential, low cost NDE technique for the simultaneous QC of bearing surface integrity and bearing stock isotropy. It is felt that along with the use of the layer etch/SEM procedure, AM or similar NDE techniques should be developed to a point of routine QC.

As recommended in Figure 3, the development of improved, more homogeneous, RSR-HIP P/M bearing stocks could lead to the use of advanced machining techniques such as single point diamond turning. This process provides surface and subsurface damage-free parts, mostly for one-step fabrication of optical (metal mirror) - quality surfaces. As shown by the brief Hughes survey in Appendix C, the machining of steel by this process has not met with any success to date, mainly due to the large carbide inclusions and the diamond tool wear thereof and other chemical tool wear effects. This area could be made more promising by the use of virtually inclusion-free, isotropic bearing steels.

(b) Bearing Surface Stabilization with Hardcoats - As previously described above and in References 1 and 2, a properly applied CVD hardcoat will not only yield an ideal surface stock for final, high precision bearing surface finishing, but will stabilize the surface both chemically and physically. Chemical stabilization means corrosion protection for at least 10+ years (or more), while physical stabilization is manifested by the ability of the hardcoat to serve as an ideal underlay for both liquid and solid lubricant layers.

The success of our program will lie in resolving a current dilemma: the CVD process provides the necessary hardcoat for gyro bearings but is not yet usable for larger turbine bearings fabricated from conventional bearing steels, while back-up hardcoating techniques (e.g., reactive sputtering) are estimated to provide reasonable adhesion to machining damage-free surfaces only. Unfortunately, we are not yet capable of attaining such alloy bearing surfaces with any repeatability or reproducibility. Moreover, non-reactive (i.e., ion) sputtering itself has been suspect of not being able to provide the high adhesion needed for cyclic Hertzian stresses of up to and even beyond 250 Kpsi, under any circumstances (see References 1 and 2).

As a first step in resolving the ability of one well-established hardcoat to adhere to 52100 steel rolling element surfaces, several Litton gyro ball bearings were DC magnetron (ion) sputtered at TMI with an approximately 1200 Å thick TiC layer by a patented process originally developed for beryllium gas bearing applications (see References 1, 2 and 4). Some of these Litton bearings (i.e., balls, races and retainers) were also top-coated at TMI with thin (approximately 1000 Å) layers of also DC magnetron sputtered MoS<sub>2</sub>. The TiC/MoS<sub>2</sub> layers were to comprise the solid lubricant hardcoat/softcoat system for the planned Litton baseline bearing tests..

However, as shown in Appendix A, the TiC hardcoat delaminated even from the freshly sputtered bearing surfaces. A Litton layer etch examination of the TiC-coated surfaces revealed both a damaged 52100 steel underlay and the poor adhesion of the TiC to that damaged substrate. Due to the seriousness of this failure, Hughes performed parallel SEM/EDX scrutiny of both the TiC and the TiC/MoS<sub>2</sub> surfaces by the following procedure:

- Out of the twenty-one each total bearings TMI was to coat originally, the first batch of seven were TiC coated, and a few of those were sputtered with MoS<sub>2</sub>. Hughes randomly selected one previously unexamined TiC and two TiC/MoS<sub>2</sub> sputtered bearings from this lot. The TiC-coated balls, inner and outer races of one bearing and the TiC/MoS<sub>2</sub> equivalent of another were examined at various SEM magnifications, with the incorporation of occasional EDX analyses.

- The second TiC/MoS<sub>2</sub> bearing components underwent an MoS<sub>2</sub> stripping operation, normally used at Hughes to remove sputtered MoS<sub>2</sub> from metallic bearing surfaces (Reference 5). This process entails an ~1.5 hour soak in hot (~190°F) Oakite 126 HD alkaline cleaning solution, followed by rubbing and agitation in the same. After a triple distilled water rinse and a final wash of anhydrous ethanol, the parts were blown dry with clean, filtered nitrogen gas and were subjected to the SEM/EDX examination.

The photomicrographs and the occasional EDX spectra are presented in Figures 4 through 12. Figures 4, 5, and 6 represent TiC-sputtered inner and outer race ball paths as well as ball surfaces in the as-received conditions.

The data indicate the following:

- The adhesion of TiC is better on the inner than on the outer race but unacceptable anywhere, on an absolute scale. The inner race coating may have suffered circumferential cracking during the coating process: "scratch" marks did not originally exist on the bare race surfaces prior to sputtering. The outer race ball path contains micro-blisters and morphologically different TiC phases. Some of the micro-blisters were purposely broken with a fine stylus.

- Not only the race, but the ball surfaces suffered peeling of the TiC.

The photomicrographs in Figures 7 and 8 show that a topcoat of MoS<sub>2</sub> seems effective in hiding any possible delamination of the TiC undercoat. The presence of small TiC particles on top of the MoS<sub>2</sub> coating is unexpected, because these bearings were kept in their original packages until examination and could not have been contaminated by the SEM/EDX analytical activity. Those small particles could have only come from the TMI sputtering chamber which was apparently used for both the TiC and the MoS<sub>2</sub> processes.

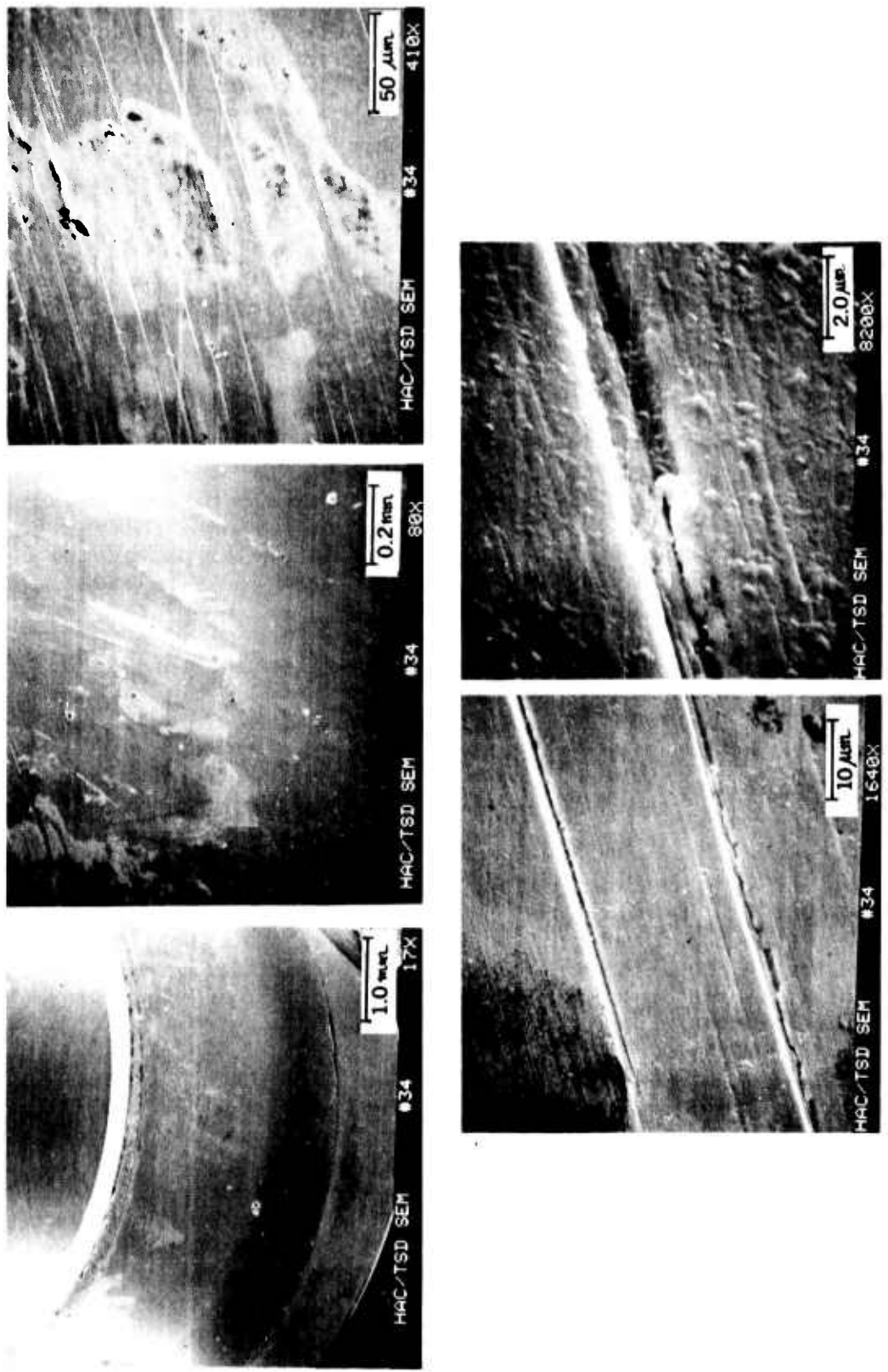


Figure 4. TMI TiC sputtered 52100 gyro bearing inner race ball path (as received), at various SEM magnifications.

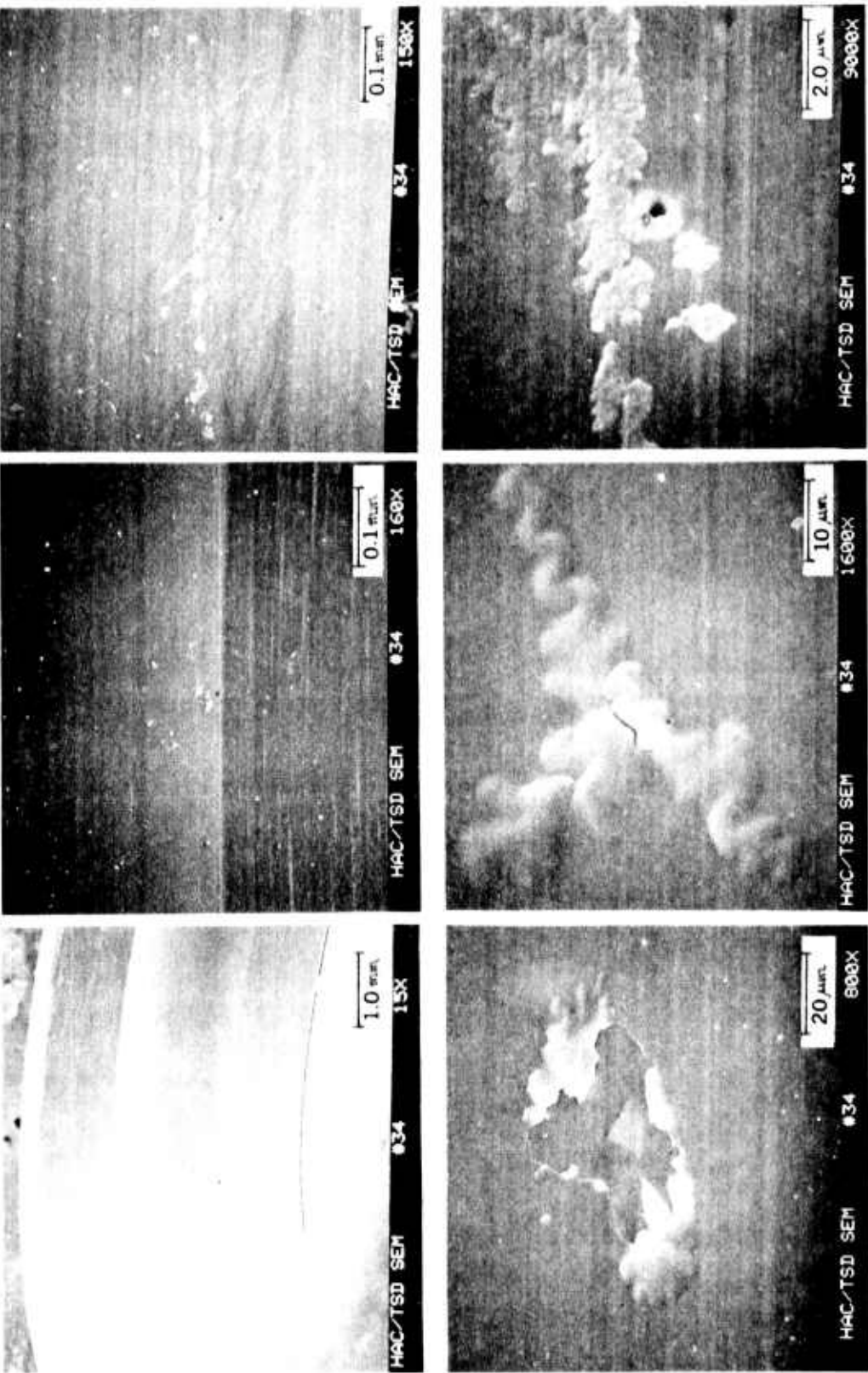


Figure 5. TMI TiC sputtered 52100 gyro bearing outer race ball path (as received), at various SEM magnifications.

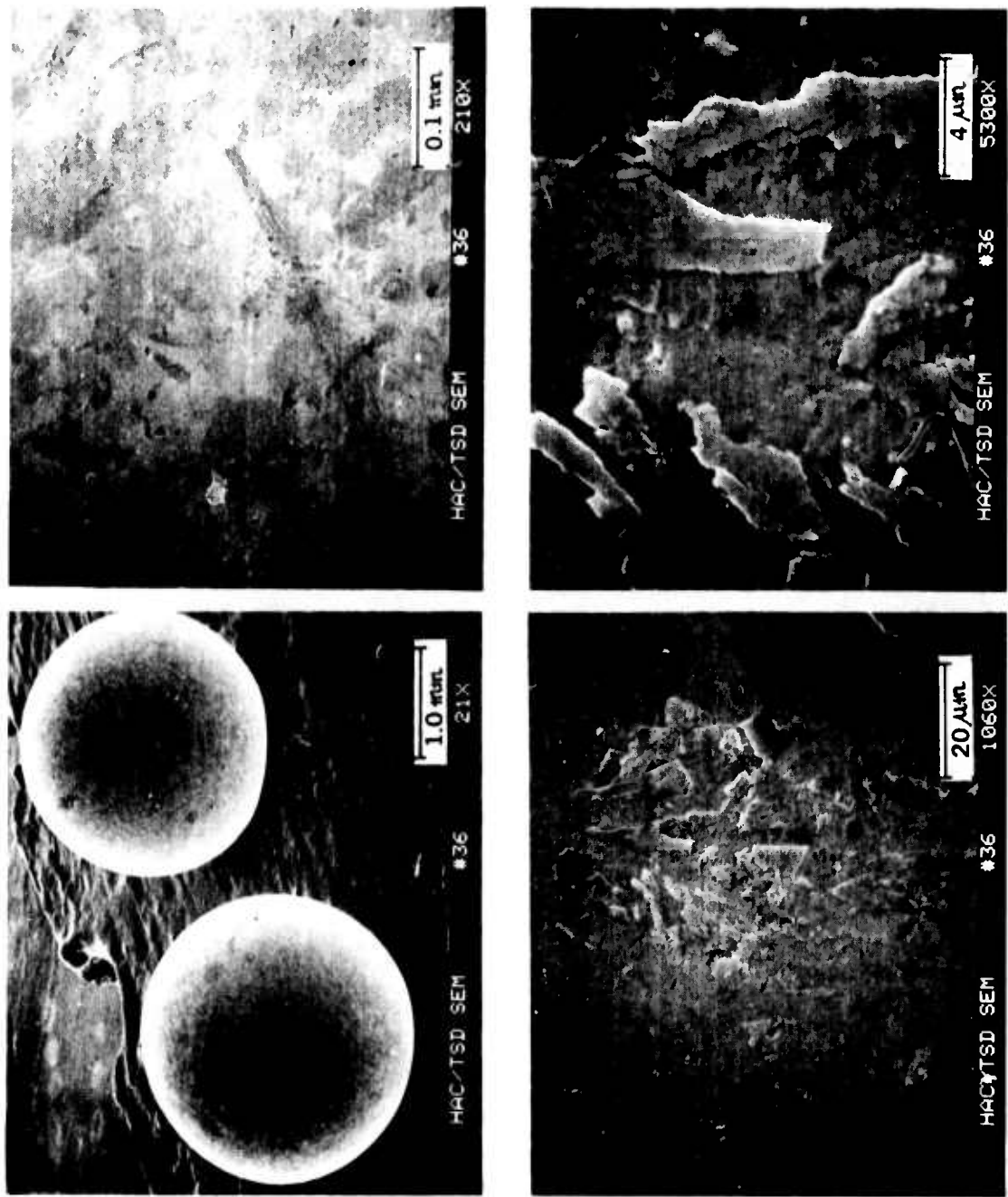


Figure 6. TMI TiC sputtered 52100 gyro bearing balls (as received), at various SEM magnifications.

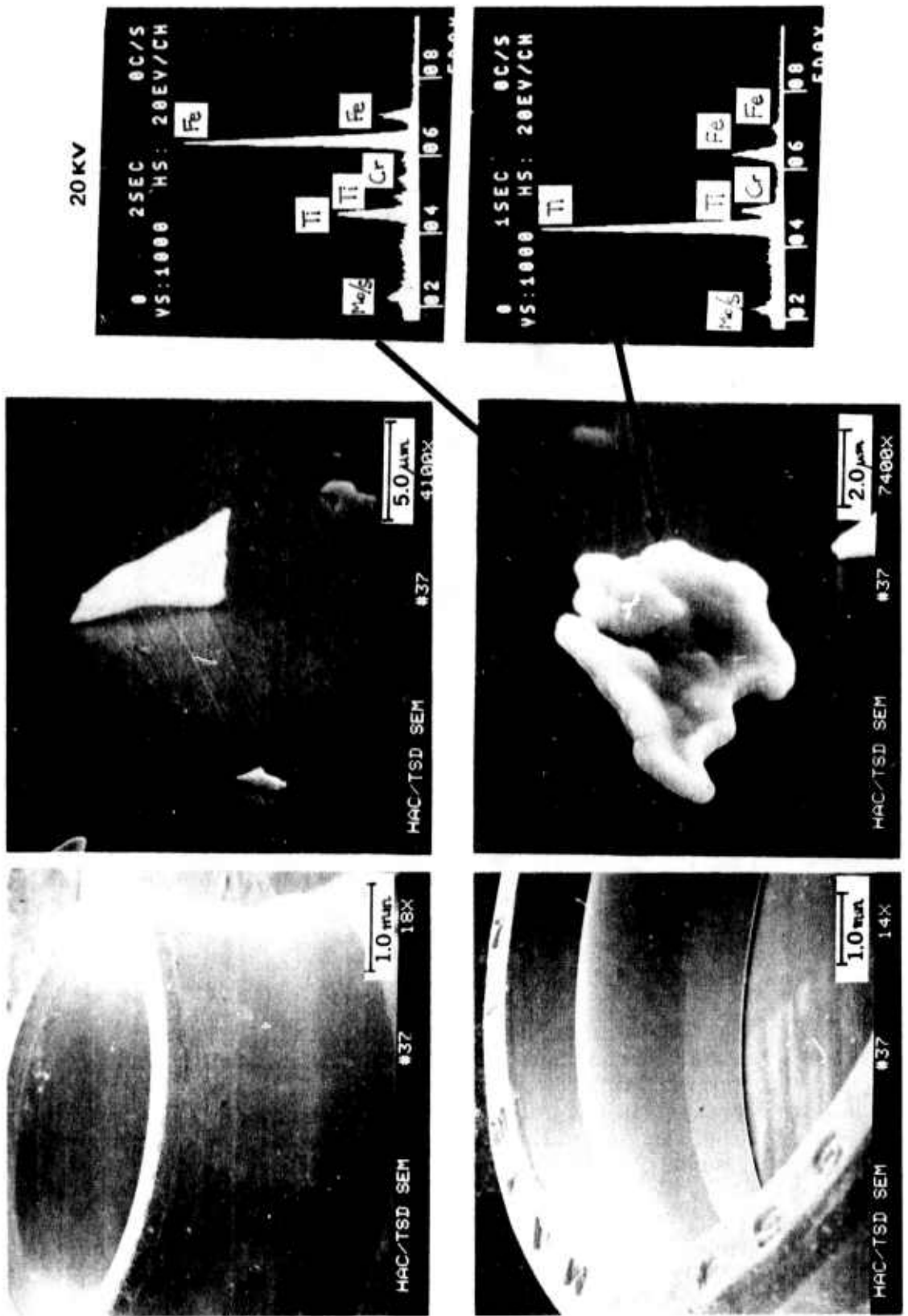
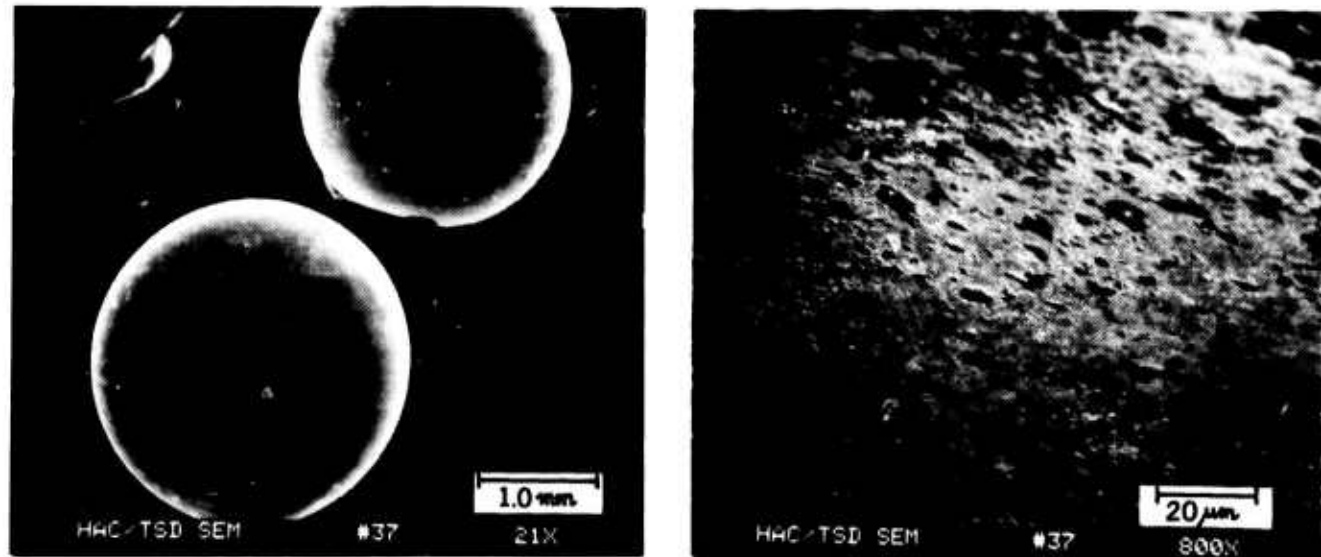


Figure 7. TMI TiC/MoS<sub>2</sub> sputtered 52100 gyro bearing inner and outer race paths (as received) at various SEM magnifications and EDX scrutiny.



**Figure 8.** TMI TiC/MoS<sub>2</sub> sputtered 52100 gyro bearing balls (as received), at various SEM magnifications.

On backbleed of dry nitrogen, argon or air into that chamber after completion of the MoS<sub>2</sub> process, small, loosely adhering, residual particles of TiC may have become dislodged from the inner chamber walls or parts of the fixtures and landed on the top of the MoS<sub>2</sub> coating.

While the appearance of the MoS<sub>2</sub> layers on the races is smooth and acceptable, the ball surfaces are unusually grainy.

Examining the appearance of the TiC layer after removing the MoS<sub>2</sub> topcoat "camouflage" in Figures 9 through 12 confirm the previously observed, poor adherence of the hardcoat. It is suspected that the action of the alkaline cleaner is not unlike that of the etching solution of the Litton layer etch technique in that both processes induce a certain amount of coating stress relief, enhancing the delamination process.

When these figures are compared to the ones in Figures 4, 5 and 6, a pattern is found to emerge. This pattern yields invaluable information with respect to unique fixturing problems arising from sputtering inner and outer race, as well as ball geometries.

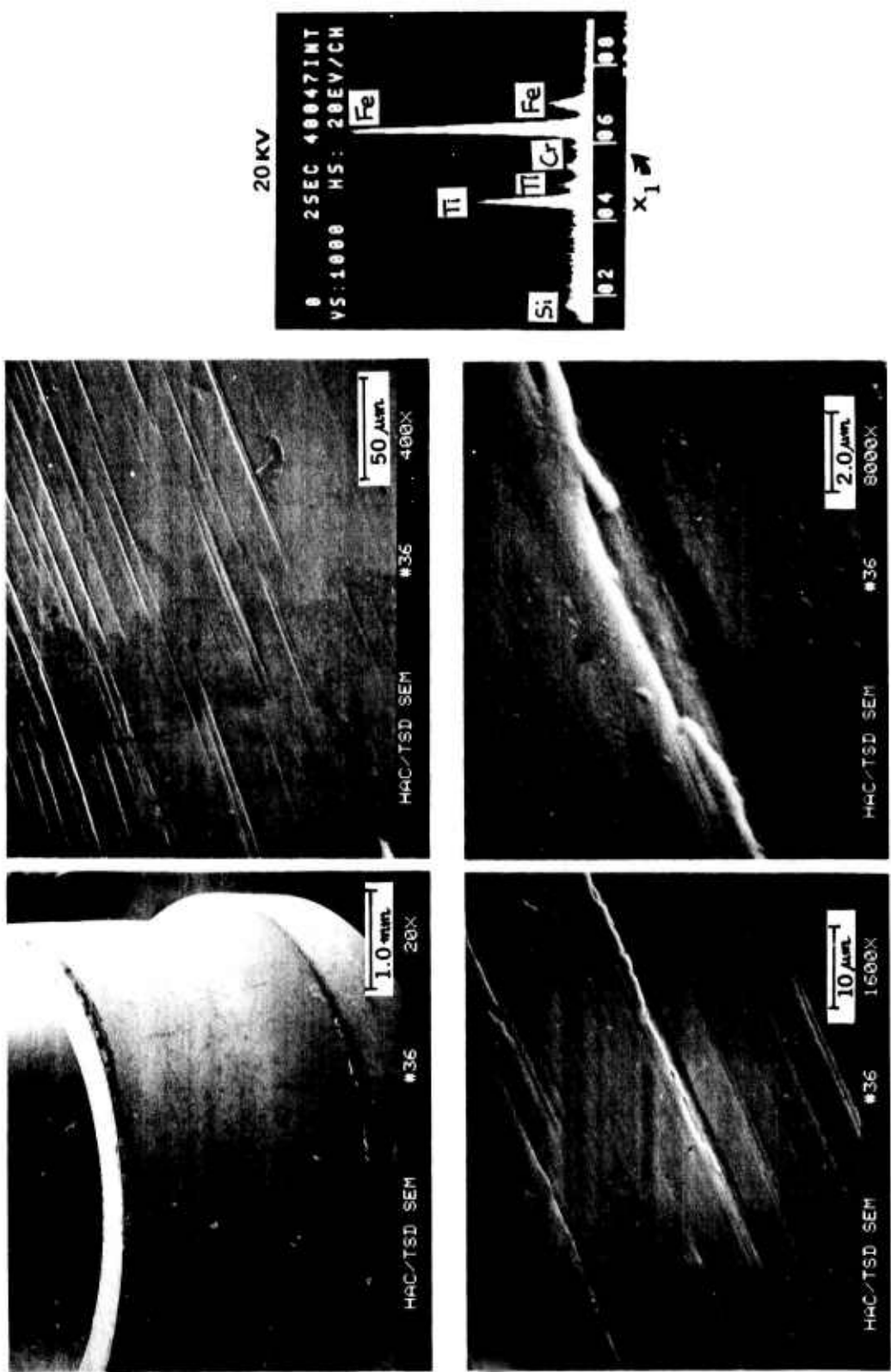


Figure 9. TMI TiC/MoS<sub>2</sub> sputtered 52100 gyro bearing inner race ball path (MoS<sub>2</sub> removed with Oakite 126 HD), at various SEM magnifications and EDX scrutiny.

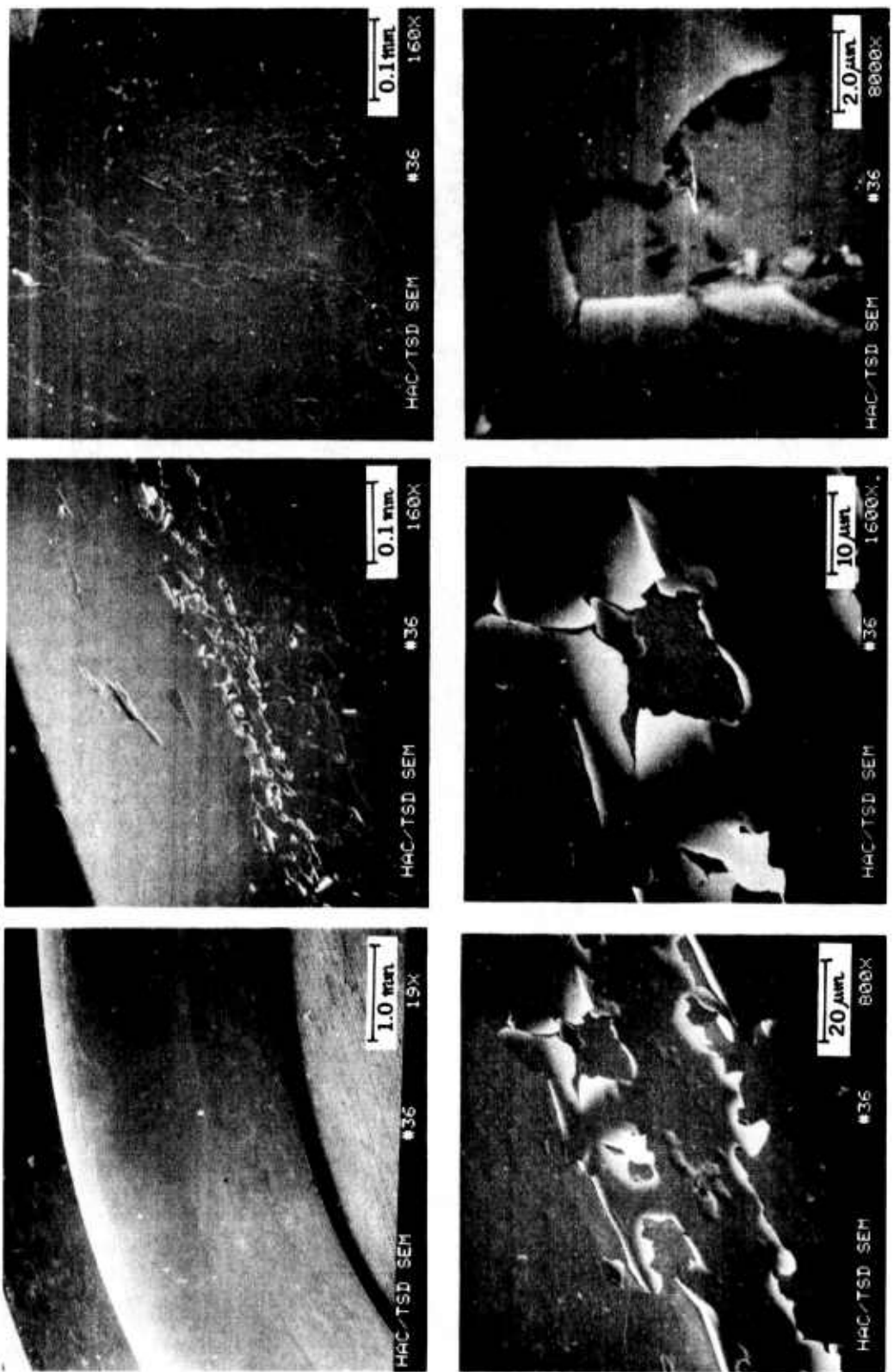


Figure 10. TMI TiC/MoS<sub>2</sub> sputtered 52100 gyro bearing inner race ball path (MoS<sub>2</sub> removed with Oakite 126 HD), at various SEM magnifications and EDX scrutiny.

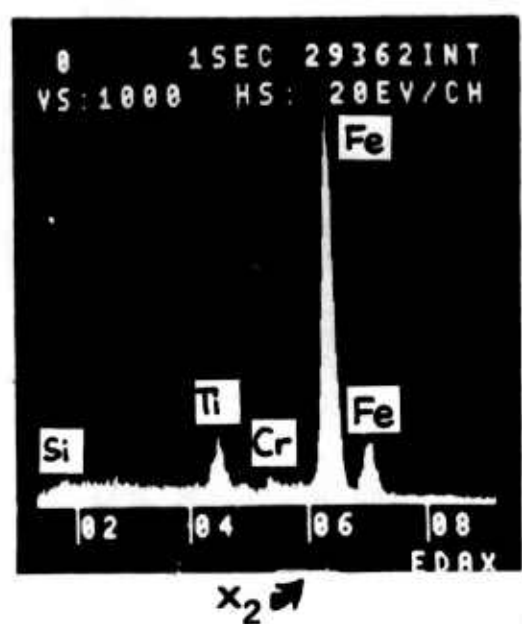
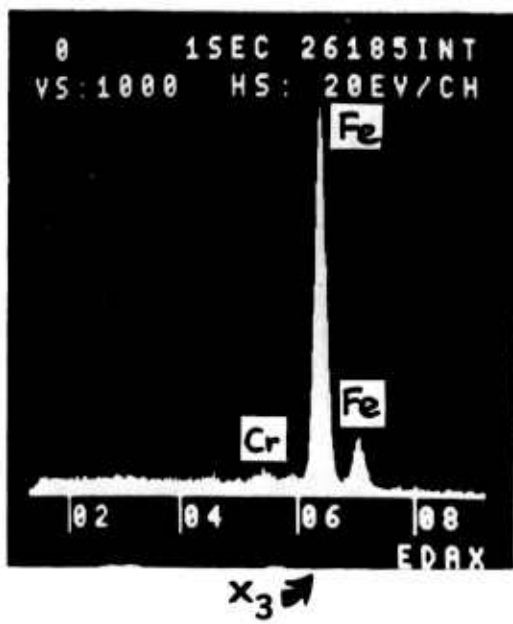
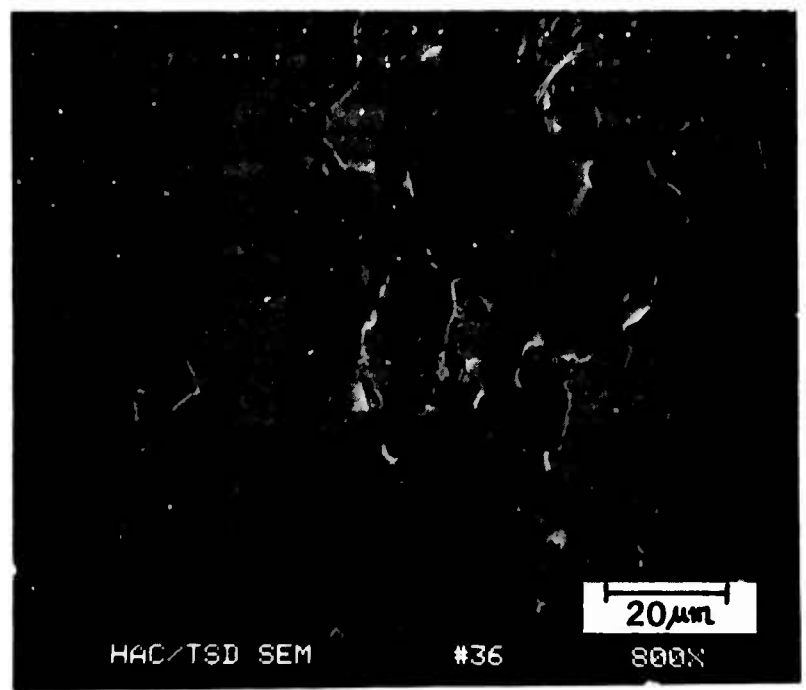


Figure 11. TMI TiC/MoS<sub>2</sub> sputtered 52100 gyro bearing outer race ball path (MoS<sub>2</sub> removed with Oakite 126 HD), at 800X SEM magnification and EDX scrutiny.

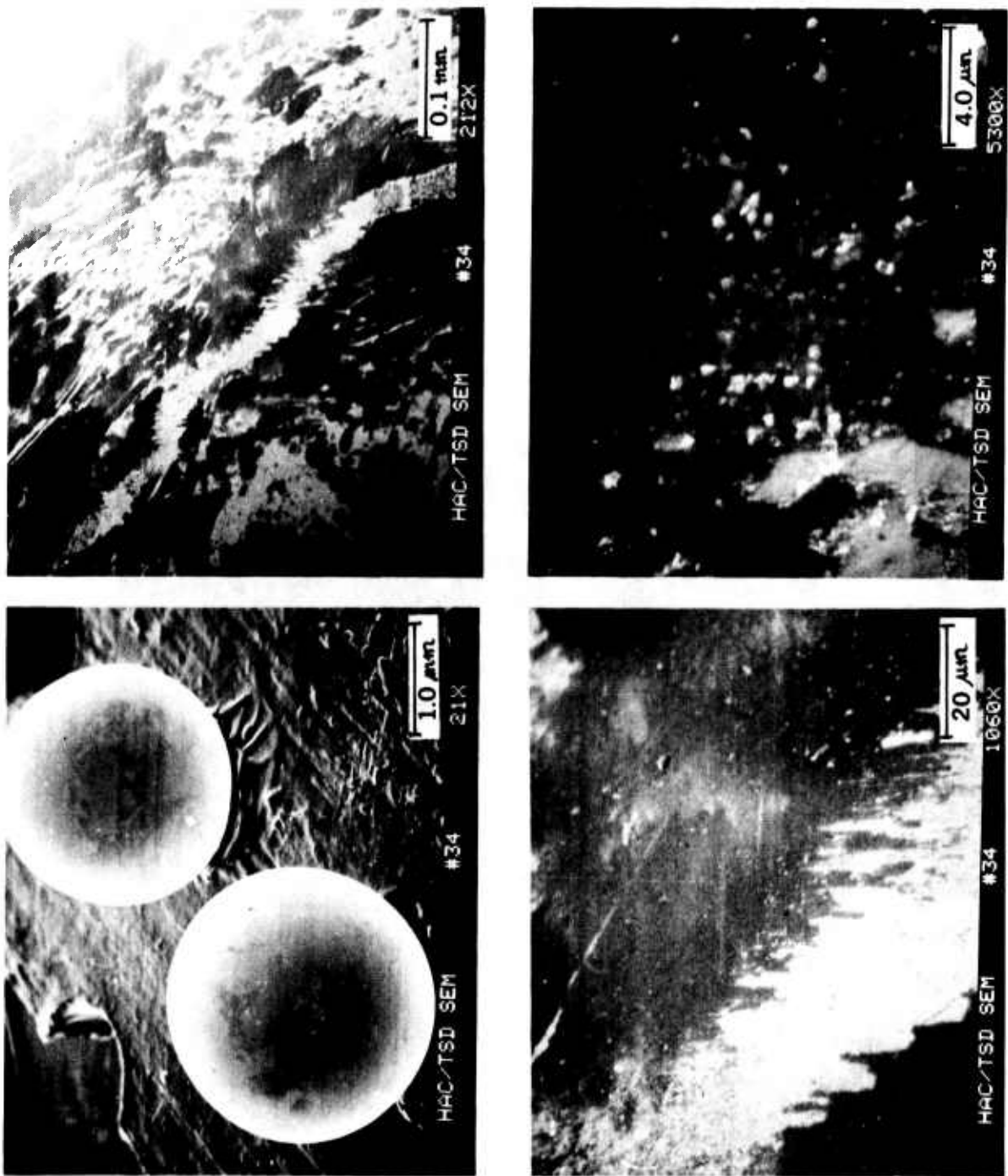


Figure 12. TMI TiC/MoS<sub>2</sub> sputtered 52100 gyro bearing balls (MoS<sub>2</sub> removed with Oakite 126 HD), at various SEM magnifications.

It was previously demonstrated in Reference 2 that a near normal incidence of the flux emanating from the target yields the best adhesion and longest wear life of  $\text{MoS}_2$ , under sliding conditions. Therefore, accessibility of critical sliding or rolling surfaces to a near normal incidence of incoming sputtered species is imperative. Fixturing of the particular substrate (i.e., races or balls) must therefore, be designed to attain this condition. However, one must not lose sight of the fact that not only the ball paths, but all other, less critical surfaces must be hardcoated for corrosion protection. Designing a fixture which exposes all bearing surfaces to a near normal flux is not possible at this time. This may necessitate a second coating cycle, with different fixturing.

The examination of the typical flux distribution from a DC magnetron target from TMI's report (Figure 13, taken from Reference 4) and the type of gas bearing fixturing TMI probably used for the gyro bearings (see Figures 14 and 15) indicate that their planetary rotating fixture system was correctly conceived. Therefore, the poor adhesion of TiC can come about only by:

- Inherent inability of the TMI Ronelus process TiC to adhere to 52100 bearing surfaces which contain machining damage;

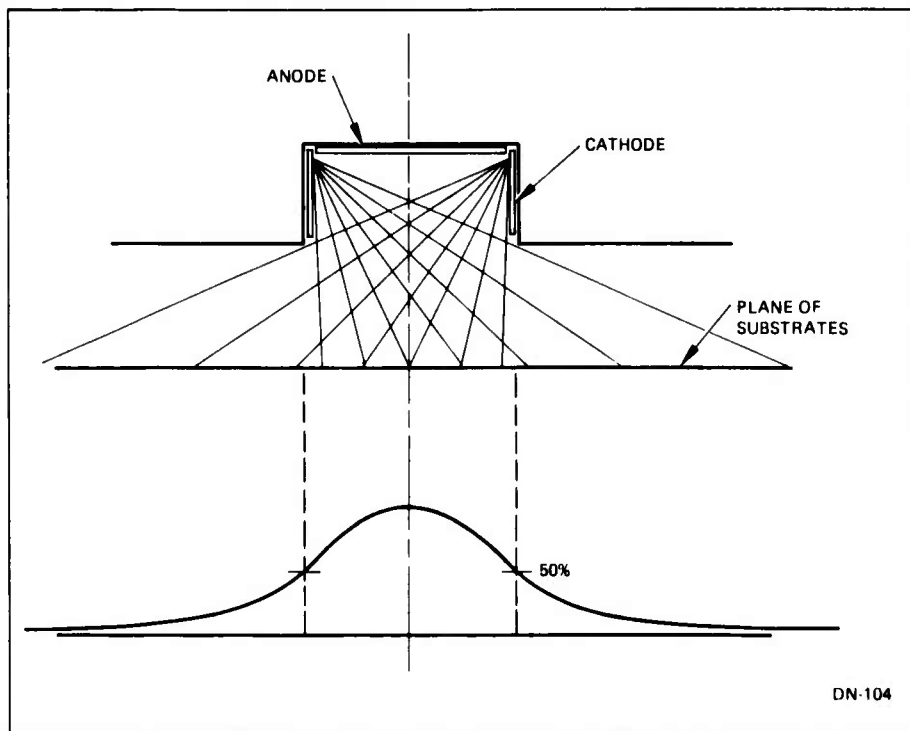


Figure 13. Typical flux distribution from a DC magnetron target (Reference 4).

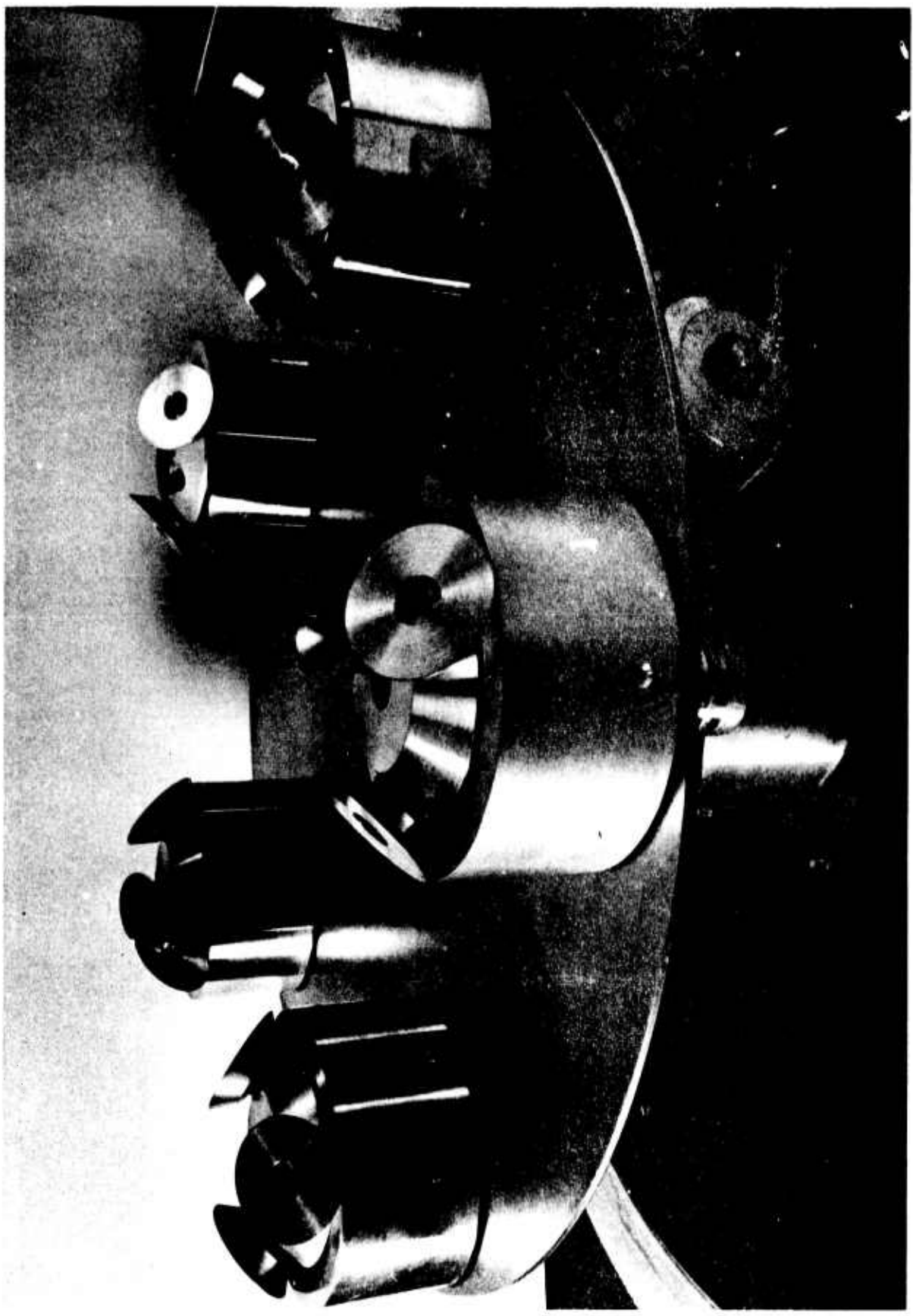


Figure 14. Overall top view of a 5-station, 15 gyro component, planetary rotating sputtering fixture of TMI for  $\text{TiC}/\text{MoS}_2/\text{Sb}_2\text{O}_3$  coating of hemispherical gas (gyro) bearings (Reference 4).

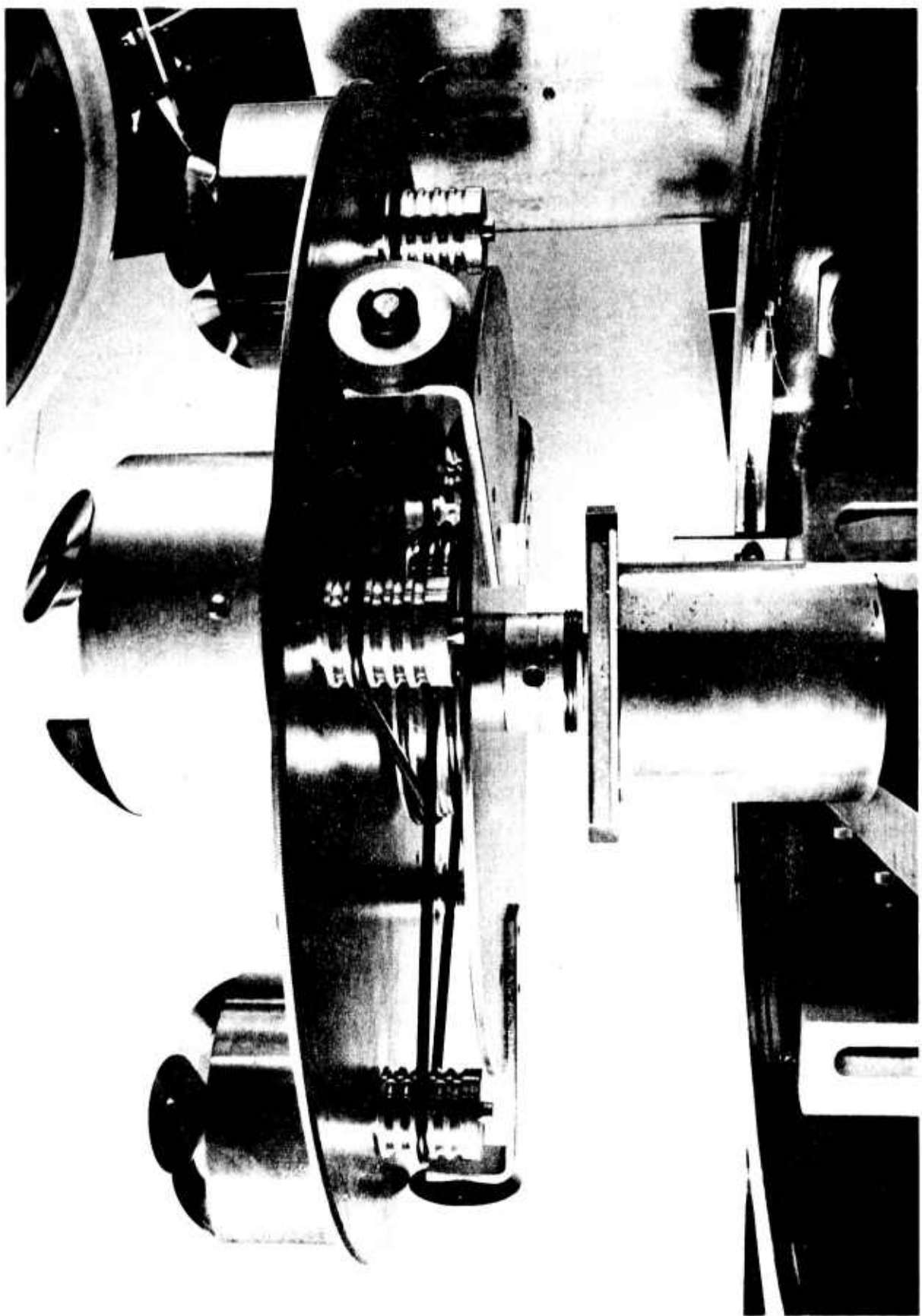


Figure 15. Bottom view of multiple drive mechanism for planetary rotation of individual stations (also see Figure 14); from Reference 4.

- The geometrically inherent problem arising from coating outer races, where the ball path is significantly more shielded from a normal flux than the more accessible OD of the inner race; and
- A similar problem of correct ball fixturing for maximum adhesion and least pick up of extraneous sputtered particles from the rotating dishlike fixture.

Since TMI recently circulated a product information letter among the government as well as the industrial tribological community about the Romelus hardcoating process and its successful use on rolling element bearing surfaces, the poor adhesion of TiC was unexpected. It should be noted, however, that we predicted ion-sputtering to be the least likely hardcoat process which can yield the adhesion needed to withstand high Hertzian stresses (see References 1 and 2). Our prediction was confirmed by tests run under separate sponsorship on TMI TiC/MoS<sub>2</sub> - Sb<sub>2</sub>O<sub>3</sub> sputtered missile hydraulic actuator roller bearings (Reference 6).

On hearing the results on the first seven Litton gyro specimens, TMI declined to complete sputtering of the remainder of the bearings. This firm was therefore dropped from the program team and the use of the ion-sputtered TiC/MoS<sub>2</sub> layer system for the Litton liquid/solid lubricated baselines was abandoned. Instead, (as described under paragraphs III. B. 1(e) and III. B. 2(b) later in this report) Litton switched to CVD CrC-TiC coated 440C and cemented carbide balls running against bare 52100 races for the oil and solid lubricated baseline studies. According to the revised Litton program plan (see Reference 2), the above combination would have been upgraded in the near future (in May or June, 1980) by the delivery and incorporation of CVD CrC-TiC hardcoated 440C gyro bearing races as well.

Unfortunately, a problem developed with LSRH (Switzerland), due to their proposed delivery of all CVD hardcoated gyro bearing races no sooner than December, 1980. This delivery date would be way beyond any acceptably extended deadline. Our intelligence indicated that the delay can be attributed to (a) current RMB (the Swiss bearing manufacturer that will finish the coated races) work overload and (b) delays in completing the P.O. (negotiations with LSRH were started on 13 March 1979, and finished on 7 December 1979) due to the unusual volume of paperwork required from a foreign subcontractor on a U.S. government contract. Note, for example, that the Hughes Subcontract Administrator spent three months justifying the Swiss CVD technique's uniqueness for bearing use through a required survey of the U.S. bearing industry, itself ignorant of the process.

To obtain a partial delivery in May/June 1980, Mr. Baginski of Litton and Mr. Danzl (the Hughes Subcontract Administrator) travelled to LSRH/RMB in January 1980. A partial hardcoated race delivery is deemed to be an absolute technical necessity under any conceivable variation of the program plan. In spite of this effort, a delivery of only 30 to 50 race

sets could be accelerated to September 1980 with a slight likelihood of earlier completion, provided a previously scheduled bearing order by some other customer is cancelled. This late delivery will force the extension of the feasibility study portion of the Litton solid lubricated gyro bearing work into FY '81.

Since our program identified reactive sputtering as the next best hardcoat process to the CVD CrC-TiC, GIT was brought on-board immediately, due to their recent successes with reactively sputtered TiN on sliding (e.g., cutting tool) and rolling element bearing surfaces, as demonstrated by their presentation at the October 1979 DR, Dayton, Ohio. The use of reactively sputtered TiN could be made more cost effective than CVD by the inherent reduction of distortion and the elimination of the re-quenching step — the deposition temperatures are 500°C or less. It follows that this process is applicable to small and large bearings alike, even if the components are fabricated from conventional steel stocks.

Although it is recognized that TiN exhibits, at best, marginal thermal stability at 1000°F even with proper adhesion, this hardcoat is deemed fully acceptable for at least gyro bearing operation. We also believe that a well-applied TiN is presently useful for proving a hardcoat/softcoat system's operability in the 500°F (intermediate) turbine engine bearings.

It is noteworthy that Battelle, Geneva (Switzerland) is also pursuing DC-magnetron reactive TiN sputtering of tribological surfaces at this time (Reference 7).

The first GIT progress report is attached here as Appendix D. Their Statement of Work (SOW) specifies (a) research to obtain reactively sputtered TiN with the best possible adhesion to 52100 steel gyro and M-50 turbine bearing components, (b) sputtering of research quantities of experimental solid lubricants by the use of mini-magnetron gun targets and (c) shear strength testing of thin solid lubricant layers and pellets (in bulk form), at high stresses. Appendix D also deals with TiN sputtering of traction specimens for MTI (see forthcoming discussion in paragraphs III. B. 1(e) and III. B. 2(b) herein), using the current (yet unrefined) TiN coating process which was shown promising on hardened 52100 steel balls at Hertzian stresses up to 190 kpsi, under nearly pure rolling conditions. These preliminary tests indicated that a TiN film tends to survive high stress conditions, but only in thicknesses less than 1.0 μm. This, of course, negates the necessity of remachining the TiN coating to obtain a final finished bearing part, because the relatively thin hardcoat faithfully follows the surface roughness of the metal substrate.

Appendix D also contains initial design estimates for improved ball fixturing, which would assure a sputtering flux as near to normal incidence as practicable. Essentially, a thick perforated mask is inserted between a dynamic (rocking) ball container (basket) and the target. Ideal close packing of the holes and selection of the hole aspect ratio are

intended to assure the best possible adhesion of hard, as well as softcoats on bearing balls. Hughes sputtering technologists recently reviewed this design and found that a few changes are needed to satisfy certain energy considerations. The suggestions were communicated to GIT and will constitute the basis for Hughes ball fixturing preparation also. Design and construction of the race fixtures (probably similar to those shown in Figures 14 and 15) will also be done, aided by the work and information cited in References 4, 8 and the recent theoretical model and computational algorithm in Reference 9.

(c) Intercalated Dichalcogenides for Wide Temperature Range Use

- Dr. Jamison of TMD theorized in Reference 1 that certain high thermal stability dichalcogenides which are poor lubricants could be transformed into better ones through c-axis lattice expansion by intercalation (i.e., a large c/a ratio implies a lamellar nature of crystallites). In Appendix E herein, Jamison completed the preliminary thermodynamic calculations that will lead to the selection of the starting materials and assessed likely intercalants and the anticipated thermal stability of the intercalated dichalcogenides. Based on these calculations and predictions, intercalation of  $TaS_2$  and  $TiS_2$  will be attempted with Cu, Ge and Al first.

Since the electronic state of the candidate materials is an accurate footprint of the degree of intercalation with an electron donor or a substitutional alloying atom of different valence, a high vacuum, contact potential apparatus will be constructed to measure this value (see Appendix E, Figure 2), complementing any x-ray diffraction and Auger-XPS techniques. It was suggested that the contact potential measurements be confirmed by a contactless method, developed by Zeller, et al, mainly to measure the electrical properties of similar intercalation compounds (Reference 10).

A simple Timken-type friction and wear tester will be utilized to initially determine the degree of solid lubricant performance by the intercalated powders. Latter, attempts will be made to deposit the experimental lubricants by DC-magnetron sputtering (see paragraph III. B. 1. (e) for further discussion on this matter) onto other friction, wear and bearing specimens.

(d) Fundamentals of the Westinghouse Compact - As

previously described in References 1, 2, 11 and 12, the Ga/In/ $WSe_2$  Westinghouse compact is currently the best high temperature ( $1000^{\circ}F$ ) self-lubricating compact material either in its bulk form as a bearing retainer, or as a pulverized additive in polymeric self-lubricating composites. Its outstanding thermal stability is indicated by the data in Tables 1 and 2 and was recently confirmed by Russian investigators (see Table 3, taken from Reference 13), at test temperatures up to  $800^{\circ}C$ , in a thermogravimetric analysis mode. Thermal stability data under tribocatalytic action has never been reported. Neither have any data been published anywhere with respect to fundamental materials parameters and their role in the high temperature lubricating and transfer film formation characteristics of the Westinghouse compact, despite the fact that this material is over 13 years old (see References 14 and 15). We believe that the analysis of the compact can lead to important answers for building an even more thermally stable, lower wear rate, high temperature solid lubricant.

TABLE 1

**THERMID 600/ADVANCED SOLID LUBRICANT ADDITIVES  
SCREENING BLENDS WEIGHT LOSS ON POSTCURE  
(Reference 12).**

Additive in Resin/Additive Composite	Weight Loss (%)	Molding Appearance
Soft Molalloy *	1.75	Severe Blistering
Hard Molalloy *	1.42	Some Blistering
Westinghouse Compact	1.02	Very Few Cracks

\*MoS<sub>2</sub> - containing, self-lubricating compact.

TABLE 2

**ADVANCED SOLID LUBRICANT ADDITIVES WEIGHT LOSS  
ON AIR-AGING AT 316°C (600°F); (Reference 12).**

Additive	Percent Weight Loss After		
	100 hours	200 hours	300 hours
Soft Molalloy *	1.60	3.38	6.54
Hard Molalloy *	0.78	1.34	3.13
Westinghouse Compact	0.68	1.36	2.90

\*MoS<sub>2</sub> - containing, self-lubricating compact.

TABLE 3

CHANGE IN WEIGHT OF SPECIMENS OF WSe<sub>2</sub> AND SELF-LUBRICATING SINTERED MATERIAL - WSe<sub>2</sub> + 25 Wt. % Ga/In DUE TO OXIDATION BY DRY AIR (Reference 13).

Material	Weight Change (g/cm <sup>2</sup> ) at Temperature °C <sup>(1)</sup>			
	500	600	700	800
WSe <sub>2</sub>	0.5	0.8	0.9	1.0
WSe <sub>2</sub> + 25 Wt. % Ga/In	0.18 × 10 <sup>-3</sup>	0.22 × 10 <sup>-3</sup>	0.55 × 10 <sup>-3</sup>	1.16 × 10 <sup>-3</sup>

<sup>(1)</sup>Dew Point 30°C, Exposure at Test Temperature 2 Hours, Air Flow Rate 0.66 liter/minute.

Such analytical work was started in FY '80 and is being conducted by the following cooperative effort:

- A Hughes metallurgical and x-ray diffraction specialist already completed identification work that is unique both in terms of the apparatus used and the findings (see Appendix F). Calculations based on unusually sharp diffractograms of the Westinghouse compact and specially prepared model compounds offer deep insights to the composition of this material. The most important part of the data includes evidence of more than one lamellar constituent (with large c/a ratios). These data and the continuation of work with several additional model compounds will guide similar research, about to be started by Litton (see Appendix A).

- The above efforts will be closely coordinated with NRL, whose XPS/RB capabilities for determination of phase stoichiometry will be complemented by high pressure, diamond anvil cell x-ray diffraction work. Past work by Dr. Skelton of NRL in determining the polymorphism and crystal structures of InSb at elevated temperature and pressure (Reference 16) readily lends itself to similar examination of the Westinghouse and other, more improved compacts under Hertzian stress-like pressures and at high temperatures. Dr. Skelton has already received a pulverized sample of the Ga/In/WSe<sub>2</sub> compact and will also perform x-ray diffraction measurements on synthesized model compounds.

The combined efforts are directed towards the identification of materials properties and connecting them with the unique transfer film formation and fragmentation characteristics of the compact under high loads and temperatures (References 6 and 17). Also, in view of the multiphase nature of the Ga/In/WSe<sub>2</sub> material, the tribo-oxidative

degradation of each phase will be examined to find the vulnerable component(s). Identification of the weak spots will be followed either with oxidation inhibition of the degradation-prone phases or by designing more oxidation resistant phases which exhibit desirable crystal structures at elevated temperatures and pressures. Note that certain solids show an unusually anisotropic behavior of compression; for example, the c/a in hexagonal  $V_2O_3$  increases with increasing pressure (Reference 18).

All of the above work will be coordinated closely with Dr. Jamison's efforts on intercalated dichalcogenides for maximum utilization and cross-referencing of information.

(e) Solid Lubricant Deposition Studies - Successful use of solid lubricants in wide temperature range rolling element bearings depends not only on the synthesis of better lubricants, but also on the ability to deposit them in thin, controlled layers. It has been established that physical vapor deposition by argon ion sputtering may not provide adequate adhesion of hardcoats on rolling element bearing surfaces but is ideal for coating these surfaces with thin, low shear strength films of solid lubricants.

Therefore, this program is pursuing two approaches:

(1) Sputtering/fixturing parameters versus ideal stoichiometry and crystal structure are being established for the Hughes, RF planar target-sputtered  $MoS_2$  (the baseline solid lubricant). The work to date and future plans along these lines are presented in Appendix G.

(2) Similar correlations are being established for the Westinghouse compact and other experimental solid lubricants at GIT, using a mini-DC magnetron target similar to the commercially available one described in Reference 2 (also see Reference 19). Among its desirable properties, the 1.5 in. OD, 1.0 in. ID, 0.25 in. thick target ring will yield over 60 percent of sputterable material (cathode utilization of a planar magnetron is less than half of this value), lending itself well to cost-effective deposition of experimental materials available only in limited quantities.

• Hughes  $MoS_2$  deposition studies: Since the Hughes  $MoS_2$  study is aimed at correlating Faville No. 6 sliding and rolling element test specimen wear lives with stoichiometry and crystal structure of the  $MoS_2$  films, the 10 inch diameter RF planar target is an acceptable vehicle, because of the planar nature of the sliding discs and the thrust bearing races (see Reference 2). This enormously simplifies correct fixturing of the parts on the substrate table. Bearing balls, however, need to be fixtured in an improved manner per previous discussions, in close cooperation with GIT.

As an initial step, the best Hughes MoS<sub>2</sub> film to date (see Reference 2 and Appendix G) was sputtered first on Faville No. 6 specimens, then on the bare 52100 races, hardcoated balls and phenolic retainers of a few Litton gyro bearings, representing the new, solid lubricated baseline. The bearing parts were placed on an available rotating substrate fixture that moves all of the sputtered components around in a circle under the target, similar to the manner depicted in Figure 16. This is by no means an ideal fixturing method that can assure the best possible adhesion of MoS<sub>2</sub> to the bearing components: the shallow angle of the MoS<sub>2</sub> flux reaching the inner and outer race ball paths from the parallel, planar target is clearly less than desirable. Still, this fixture represents a currently available one with a long history of successful utilization; its use is reasonable for a realistic baseline. Upgraded fixturing techniques will provide better adhesion and correspondingly better performance of future MoS<sub>2</sub> and other solid lubricant films.

The gyro bearings were sputtered in two lots: the races and the retainers in one, the balls in another. Each lot was accompanied by a thin, 0.5 in.<sup>2</sup> piece of stainless steel foil, serving both as a thickness control specimen and as an XPS coupon. A similarly sized silicon chip, with a 1  $\mu\text{m}$  thick layer of amorphous carbon deposited on one side was also MoS<sub>2</sub> sputtered for the backscattering (RB) studies. The RB samples were specially prepared for our program by Dr. Larry Anderson and Mr. Howard Dunlop of the Hughes Malibu Research Laboratories.

Next, the same MoS<sub>2</sub> film was sputtered on various Hughes-fabricated, 52100 steel traction discs, MTI-supplied inner races and balls and MTI-machined Litton phenolic and Hughes carbon weave reinforced polyimide retainer samples (see Figure 17). All of these samples are slated for the immediately forthcoming MTI traction studies.

The steel discs, the inner races and the ring-type retainer samples were suspended on a rotating mandrel whose axis was parallel with the target plane, in the middle of the target region. The retainer "sticks" were sputtered on both ends in two separate runs, while resting on the substrate table in the stationary mode. In view of the even film thickness distribution attainable by the use of the large, planar RF target (see Reference 20), the MoS<sub>2</sub> thickness was closely controllable. Besides the normally used quartz crystal microbalance control technique, the thickness was measured by two other simultaneous processes. By masking a traction disc (used strictly for thickness control) with the preweighed stainless steel foil square, this coupon collects the film during the rotation of the disc for gravimetric determination of the layer thickness and allows the development of coating steps at the mask lines. As previously demonstrated in References 8 and 21, the thickness of thin, optically transparent solid lubricant layers can also be measured by counting the interference fringes of equal chromatic order at the coating steps (see Figure 18). One disc with

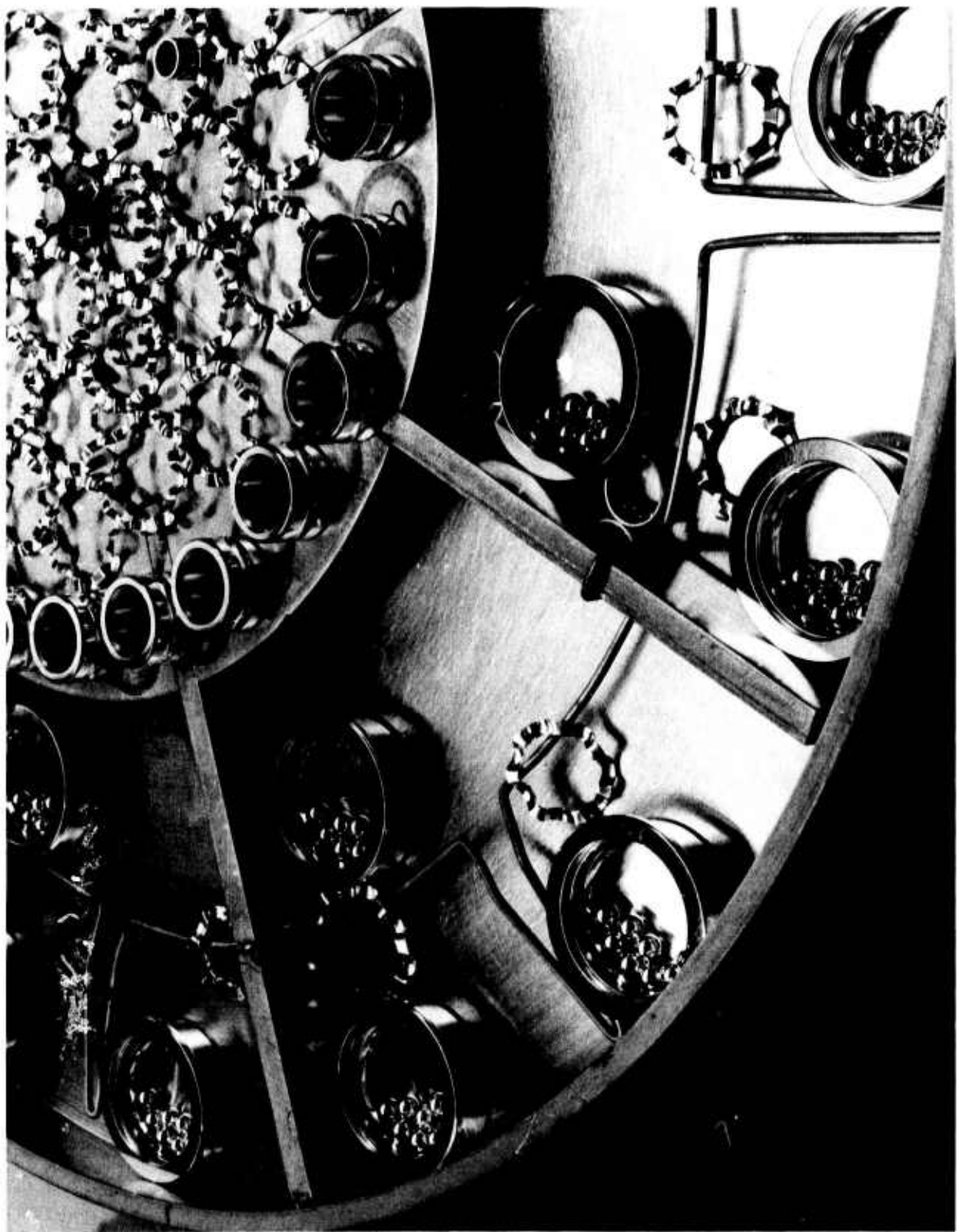


Figure 16. Current Hughes fixturing method for production type, RF planar sputtering of small angular contact bearing components.

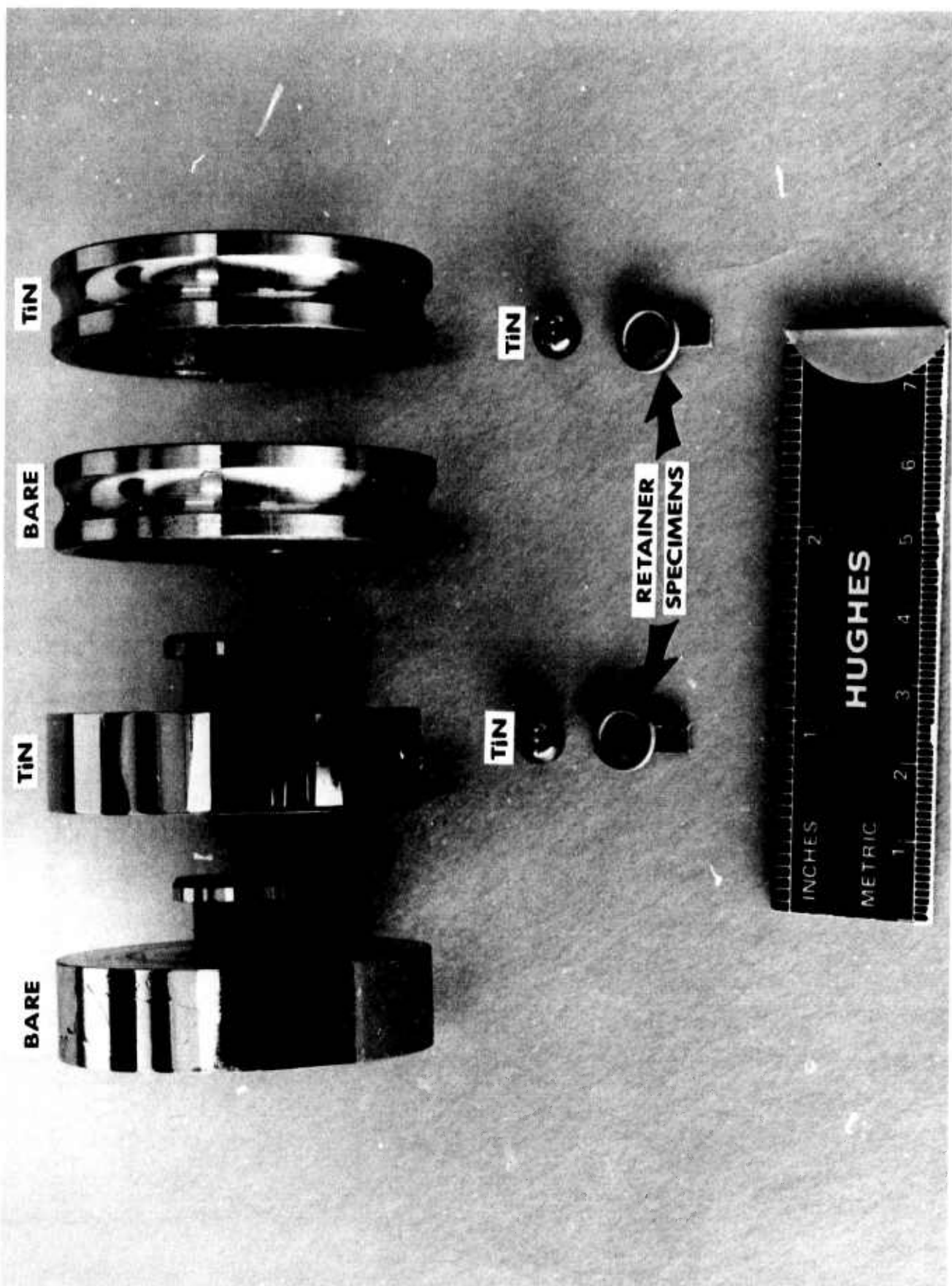


Figure 17. Bare and TiN-sputtered 52100 steel and variously machined, bare phenolic retainer traction specimens for  $\text{MoS}_2$  sputtering at Hughes and traction studies at MTI.



Figure 18. Thickness control of thin  $\text{MoS}_2$  films on MTI traction discs by fringes of equal chromatic order.

successively masked areas on its OD can therefore be used for up to 3 to 4 fringe orders before this technique becomes unusable due to the increased opacity of the coating and increased overlapping of the successive chromatic orders. As an elegant side benefit, by (1) future determination of the stoichiometry, density and crystal structure of the sputtered  $\text{MoS}_2$  coatings, (2) back calculation with the weight gain of the stainless steel coupons and (3) the use of established optical formulas, the (heretofore unpublished) refractive index of  $\text{MoS}_2$  can be determined. This value can now be estimated only from the refractive indices of other chalcogenides of current optical interest ( $n_{\text{MoS}_2} \approx 2.5$ ).

The number of  $\text{MoS}_2$  lots, film thicknesses and the respective XPS/RB samples are correlated with the gyro/traction specimens in Table 4. The XPS/RB specimens were mailed to NRL on 25 January 1980. It is anticipated that at least some of the results and the Westinghouse x-ray diffraction data will be published by NRL in their next progress report to DARPA.

Note that the wear life and friction/traction of any sputtered hardcoat and/or solid lubricant film is highly dependent on not only the speed, load, test environment and specimen configuration of the particular test machine, but on the surface condition of the tribo-specimens prior to the deposition process. For example, the loads of both the Faville No. 6 thrust (rolling)

TABLE 4  
 $\text{MoS}_2$ -SPUTTERED GYRO BEARING BASELINE  
 AND MTI TRACTION SPECIMENS.

Bearing Specimen Type <sup>(1)</sup>	$\text{MoS}_2$ Lot No.	$\text{MoS}_2$ Film <sup>(2)</sup> Thickness ( $\text{\AA}$ )	XPS/RB Specimen Set No.
Gyro bearing balls and races (3 sets)	1	400	1a
Phenolic gyro bearing retainers (3 ea)	2	1200 <sup>(3)</sup>	1b
Bare and TiN-sputtered 52100 traction discs (2 x 2 = 4 total)	3	1200	2
Bare and TiN-sputtered 52100 traction inner races (2 x 2 = 4 total)	4	1200	3
TiN-sputtered 52100 traction balls <sup>(4)</sup> (~40 ea)	5	1200	4
Litton phenolic and Hughes polyimide retainer traction stick ends (2 x 12 ea = 24 total; axial tube lay)	6	1200	5
Litton phenolic and Hughes polyimide retainer traction ring OD-s (2x12 ea = 24 total; circumferential tube lay)	7	1200	6

(1) For appearance of MTI traction specimens, see Figure 17.  
 (2) Coating thickness tolerance is  $\pm 25\%$ .  
 (3) Estimated thickness in ball pockets. More everywhere else.  
 (4) Balls did not rotate during TiN or  $\text{MoS}_2$  sputtering. Intended  $\text{MoS}_2$  thickness on ball apex only.

bearing and the MTI traction rig can attain realistic Hertzian stresses equal to at least those of the gyro bearing (see Figure 19).

However, machining smear on the steel flats or thrust bearing specimen surfaces is seldom controllable: as shown in Appendix A, none of the commercially feasible machining steps that Barden could incorporate for the fabrication of the Faville No. 6 sliding flats provided damage-free surfaces. In fact, all of the different machining sequences resulted in a heavily damaged surface state. If, despite such extensive efforts the results are so disappointing, one can imagine the poor surface integrity of commercially available, off-the-shelf specimens. For this reason, all purchased, as well as specially machined friction/traction test surfaces will undergo a final diamond paper polishing sequence here at Hughes, followed by layer etch/SEM. This step will at least provide test surfaces of approximately the same level of damage. We may possibly learn to improve the final integrity of the bearing surfaces by hand polishing, even if only in experimental quantities.

The MTI traction discs and inner races (see Figure 17) were prepared at Hughes accordingly. Prior to TiN and/or MoS<sub>2</sub> sputtering the rusty, pitted 52100 inner races (the only available parts MTI was able to send us for further work) were vapor degreased in Freon TF and then soaked for five minutes in a saturated solution of oxalic acid, at 200°F, to remove the rust. The bearings were thoroughly rinsed in deionized water,

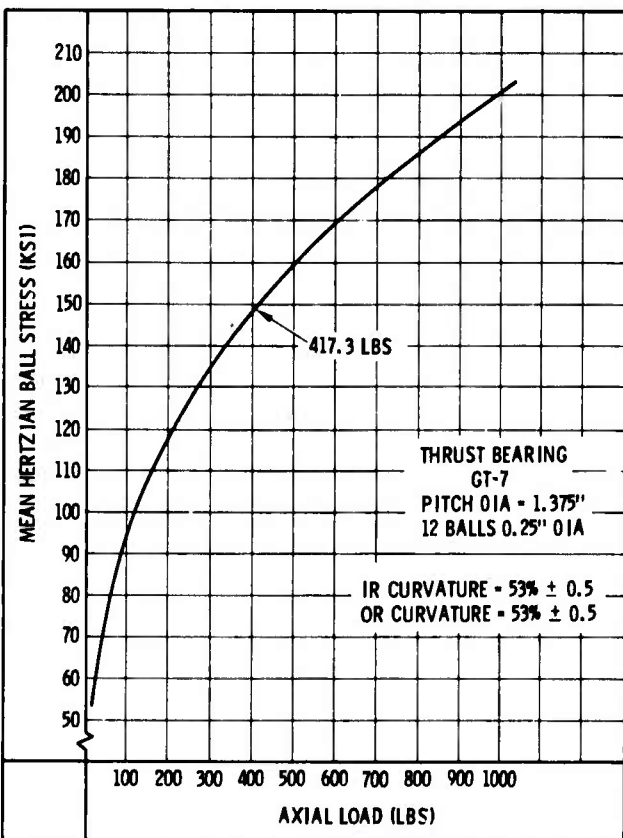


Figure 19. Dead-weight load versus Hertzian stress correlation of the Hughes rolling thrust bearing attachment of the Faville No. 6 friction and wear tester.

dried, then polished on the raceways at the Hughes Culver City Optical Laboratory, using a spinning mandrel and hand-held portions of  $3 \mu\text{m}$  diamond paper.

The 52100 steel discs were ground to better than  $16 \mu\text{in}$ . CLA finish on the OD, then sent to the Optical Lab for polishing. In this case, the OD of the discs were finished with four, successively finer grades of diamond paper ( $30 \mu\text{m}$ ,  $15 \mu\text{m}$ ,  $9 \mu\text{m}$ , and  $3 \mu\text{m}$  particle size diamond) and a final finishing step of polishing with a  $0.3 \mu\text{m}$  alumina/water slurry fed to a hand-held felt pad to remove a few unexpected scratches left behind by the last paper.

All polished discs and races were rinsed in deionized water and dried immediately, followed by spraying the polished and rust-susceptible 52100 surfaces with a peelable, transparent, protective coating. The optical schlieren visible on the OD of the bare steel specimens in Figure 17 is caused by this protective layer.

Extra discs, as well as all other friction and wear test specimens and the acoustic microscopy samples will all undergo the layer etch/SEM examination and the friction/wear data will be interpreted in light of the realistic surface damage conditions.

• GIT Solid Lubricant Deposition Studies: This portion of the work will involve sputtering experimental solid lubricant materials, mostly in the multiphase form. These solid lubricants will be samples of (a) the Ga/In/WSe<sub>2</sub> Westinghouse compact, (b) intercalated dichalcogenides produced by Dr. Warren Jamison of TMD and (c) selected samples of solid lubricant pigments (commercially or experimentally available) cosputtered with selected metallic or metalloid materials (e.g., Ni<sub>3</sub>P), which can act as high temperature, wear and corrosion resistant, ductile binders for the solid lubricant pigments. These composite layers will receive extra attention, because of the "Principle of Layered Redundancy" (PLR) concept this writer developed especially for high load, high temperature bearings (to be further discussed here in paragraph III. B. 3. (e)).

Essentially, for the top solid lubricant film of a PLR layer system, we intend to find binders that are compatible with high temperature alloy and ceramic surfaces and which can provide protection to both the bearing surface and the "encapsulated" lubricant pigment from hot corrosion. This binder must be able to allow metered release of the solid lubricant onto the very top of the rolling surfaces for simultaneous lubrication and tribo-oxidative degradation.

Such bonded films are exemplified by thick layer composite analogs e.g., the Ni<sub>3</sub>P\*-SiC (NYE-CARB<sup>®</sup>) plating process (Reference 22), by Tsuya's solid lubricant pigment-containing metal composites and composite platings (References 23 and 24) and by similar Russian coatings (Reference 25).

\*Electroless nickel

A sample of the NYE-CARB® plating, deposited on copper and scratched with a diamond stylus is depicted in Figure 20. Encapsulation of the SiC particles is complete and the high unit load of the stylus tip smeared/compacted the coating to a compressed film. Close examination of the encapsulated particles exposed on the smeared surface show the retention of homogeneity and implies a favorable scenario if solid lubricant pigments are substituted in the place of SiC.

Similarly small particles of a lamellar solid lubricant would have a tendency to smear, in an even thinner layer, on the very top of the Ni<sub>3</sub>P-bound, sputtered coating. The desired low ball/race traction may be attained with this ultra thin, low shear strength cover layer, without having to utilize an all-solid lubricant film as thick as the entire Ni<sub>3</sub>P-lubricant composite film. It is obvious that the thermo-oxidative and tribocatalytic degradation of an equivalently thick, all-solid lubricant layer would be greater than that of the composite film, provided that the binder itself is thermally and oxidatively stable and won't soften excessively at high temperatures.

At temperatures in excess of 750°F (399°C), electroless nickel (Ni<sub>3</sub>P) softens and loses its effective binding ability. Softening comes about from the destruction of the fine, lamellar microstructure by recrystallization and coarsening of the nickel particles. Heating Ni<sub>3</sub>P to 932°F (500°C) results in a drop in the hardness value from 1100 DPHN to 845 DPHN (Reference 26).

During proper heat treatment at 750°F, the hardness of electroless nickel is dependent on the phosphorus concentration and the heat treating steps. The data in Figure 21 (taken from Reference 27) complement similar, previous information in Reference 28, indicating the realistic high temperature limitations of these alloys.

Superimposed is the oxidation characteristics of both the binder and the lubricant pigment. In the case of Ni-P alloys, the oxide film grows only above 280°C (536°F) and is a two-phase mixture of NiO and P<sub>2</sub>O<sub>5</sub> (Reference 29).

Usability of this or similar composites in very thin, sputtered layers depends mainly on three factors:

- (1) The composite film must be sputtered in the right binder and pigment stoichiometry, in the correct pigment/binder ratio and in the homogeneity comparable to that of the target.
- (2) The hardness and ductility of the binder must not degrade at the use temperatures.
- (3) The binder must have high thermo-oxidative stability and no (or beneficial) reactivity with either the pigment or the substrate (hardcoated steels or ceramics) at those temperatures.

#### PARTICLES

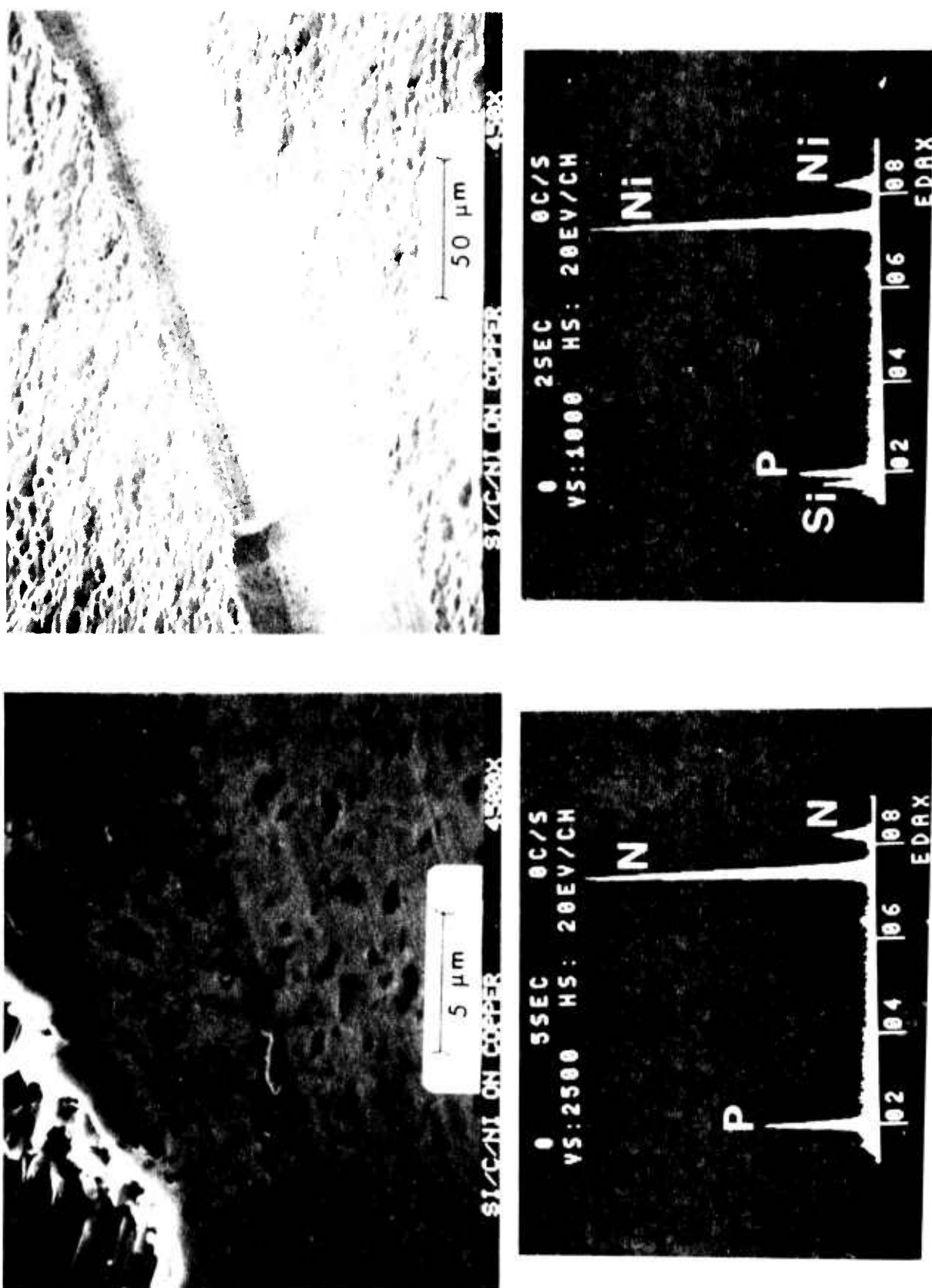


Figure 20. SEM photomicrographs at 450X and 4500X magnifications and EDX spectra of NY-E-CARB<sup>®</sup> coated copper specimen after thermal cycling.

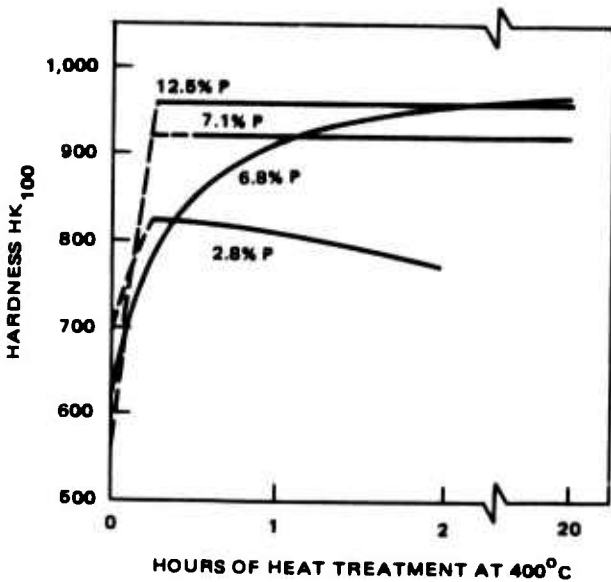


Figure 21. The hardness of electroless nickel platings as a function of phosphorus content and heat treatment time at 400°C (Reference 27).

With respect to the first point, a Ni<sub>3</sub>P-MoS<sub>2</sub> sputtered composite tribological coating is now available commercially (Reference 2). It is suspected, however, that due to the lower atomic weight of phosphorus, the Ni<sub>3</sub>P portion of the target would be depleted in one of the constituents by preferential sputtering. As discussed by Olson and coworkers (Reference 30), the amount of enrichment of the lighter species normal to the target surface decreases quite rapidly with increasing ion energy. This fact indicates a real need for extensive surface analysis of the sputtered composite coatings, correlating sputtering parameters and fixturing with both target and substrate stoichiometry and crystal structure. The above problems also apply to sputtering the Ga/In/WSe<sub>2</sub> Westinghouse compact.

Where the stoichiometry of a multiphase target is not precisely known (e.g., in the case of the Westinghouse compact now), GIT's quality control work shall be based on straight comparison of the chemistry and physics of the bulk target and its sputtered, thin film form. This comparison at GIT shall consist of x-ray diffraction, scanning and transmission electron microscopy, as well as friction and wear tests. Initially, GIT will not be required to reproduce the exact chemistry and physics of the bulk in the thin film form, but will be asked to coat RB and XPS coupons (previously

described) for NRL scrutiny and surface analytical examination. GIT will subsequently utilize these data for improved, more stoichiometric sputtering. The results of the currently started research program by Hughes/Litton/TMD dealing with the identification of the Westinghouse compact phases shall be made available to GIT as soon as possible. This information, along with statistical matrices of selected sputtering parameters controlled by the previously described friction and wear tests on bare and TiN sputtered Faville No. 6 flats and rolling element bearing specimens as well as by coupon-type quality control tests will be used in providing the best sputtered compact/composite films.

The sputtering fixtures designed and used during the hardcoat sputtering portion of GIT's work should be fully usable here also.

Since it is possible to control the stoichiometry of the sputtered coating by appropriately adjusting that of the target (e.g., through the use of preferentially supersaturated, sequential or checkerboard targets), the DC-magnetron mini-gun research targets can be fabricated accordingly. Preparation will be either by powder pressing and sintering or by inert gas atmosphere or vacuum induction melting. Moreover, multi-phase sputtered films may be made more homogeneous in-situ by occasional backspattering to the coated substrate during the process: Eltoukhy and Greene (Reference 31) discovered that the crystal growth and interlayer diffusion of compositionally modulated sputtered InSb/GaSb superlattices can be controlled by the sputtering pressure and ion-bombardment enhanced diffusion during film growth.

Second, the Ni-P binder system may be acceptable for the 500°F turbine bearings, but must be replaced for use at higher temperatures. We are considering Co-P alloys (Reference 32) or even better,  $(Fe, Co, Ni)_3V$  alloys (Reference 33). The latter is from a family of long range ordered alloys of a ductile, cubic structure with  $T_C > 900^\circ C$ , achieving a tensile elongation in excess of 30 percent at room temperature, because of ordering. The combination of excellent strength and adequate ductility makes these new type of alloys attractive not only for high-temperature structural application, but as co-sputtered binders for solid lubricant pigments as well.

Third, the thermo/tribooxidative stability and controlled reactivity of these binders with hardcoats and ceramic surfaces at 1000°F + temperatures may be predicted in a first order manner, but must also be checked. This will be further discussed in paragraph III. B. 3. (e) later in this report.

---

\* $T_C$  = critical temperature

(f) Shear Strength of Solid Lubricants at High Loads -

The successful operation of a solid lubricated bearing is a function of sufficiently low traction values provided by the solid lubricant layer for the ball/race, ball/retainer and retainer/race interfaces. Any computer diagnostic method for the prediction of bearing behavior will need a substitution of accurate traction values to yield reasonable prognosis. The previously described MTI traction measurements on MoS<sub>2</sub> films comprise only the first, cursory step to provide such data with some reliability.

More fundamental work has been recently started by GIT through the use of shear strength equipment and measurement technique described in Reference 34.

The shear strength of up to five solid lubricant candidates, including but not limited to MoS<sub>2</sub>, the sputtered Ga/In/WSe<sub>2</sub> and other sputtered, thin layers of experimental solid lubricants will be measured as a function of temperature to 120°C and pressure to 160 ksi, using existing GIT equipment. The method of measurement will be the coaxial shear of a hollow, cylindrical specimen subjected to hydrostatic pressure. The samples (approximately 5 mm long by 5 mm OD and 2 mm ID) will be cut from 52100 and M-50 steel stocks and sputtered with controlled layers of Hughes-applied MoS<sub>2</sub> and GIT-applied solid lubricants. MoS<sub>2</sub> sputtering of the specimens shall be performed by Hughes, using GIT-supplied shear specimens.

In utilizing an available shear strength test rig originally designed for measuring the limiting shear strength of fluid lubricants, every effort will be made to mitigate or eliminate contamination of the mating solid lubricated surfaces by the pressurizing fluid. If mitigation proves to be marginal or inadequate, either a neutral pressurizing fluid will be selected to find a medium which has the least effect on solid lubricant shear strength data, or the test machine design will be changed.

The experimental friction (traction) of other coated friction and wear specimens from MTI and GIT/Hughes will be compared with those predicted from the more fundamental shear strength measurements.

We foresee the comparison of shear strength values not only with experimental friction/traction measurements but with theoretical calculations of preferred inter-layer binding energy of lamellar solids also (see Reference 35).

(g) Wear Equations for Self-lubricating Composites -

As previously described in References 1 and 2, computer diagnostics of self-lubricated bearings must incorporate the composite ball pocket wear and the resulting transfer film formation values as a function of operating time and bearing design.

Ideally, the wear of polymer or all-polymeric self-lubricating composite retainers should be predictable on the basis of viscoelasticity fundamentals and energy expenditures alone. Unfortunately, efforts along these lines are meager, painting an even more dismal picture for an "equation of state" that can provide precise wear prognosis of solid filler-reinforced, self-lubricating composites, or multiphase, powder-metallurgically prepared compacts.

In lieu of such fundamentals, the practicing technologist must turn to empirical wear equations and their usability through understanding of the precise ball/ball pocket and ball/race interactions in a rolling element bearing. A blueprint for such a cooperative effort is about to be provided by Gardos and Meeks, in a two-part paper (see Appendices H and I), accepted for presentation and publication at the 1980 International ASME-ASLE Lubrication Conference, to be held in August 1980, in San Francisco.

In view of these promising results, MRI has been conducting 316°C (600°F), oscillatory wear equation work on high temperature, self-lubricating composites recently developed at Hughes (References 11 and 12). During discussions at the October 1979 DR it was a consensus that MRI's wear equation development resulted in a formula that described high temperature self-lubricating composite wear with good accuracy, yet provided no insight into wear behavior as a function of materials parameters. It appeared that the wear equation proposed by this writer at the Preliminary Design Review ( $\Delta W = K P^a V^b t^c$ , also see Appendix H) seemed more acceptable to both the statisticians and the materials scientists. This seemed especially true in light of the paper attached here (Appendix H), dealing with factorial wear equations of glass-reinforced PTFE/MoS<sub>2</sub> composites and filler-related effects influencing quantizable wear behavior.

However, in the high load/high speed region, the MRI equation describes wear of the high load/temperature composite more accurately than the Hughes-proposed equation, probably due both to the somewhat erratic behavior of the material in that regime and to an apparently better curve-fitting with the MRI version. The decision must therefore be made as to which equation type is more useful to the computer technologist. For now, both approaches are being pursued. Accordingly, an in-house Hughes program was started to complete additional room ambient temperature wear equations with other PTFE-based composites. The equations will further enrich or modify this writer's hypothesis on the usefulness of regression analysis-developed, factorial wear formulas for tailoring self-lubricating composites for specific applications. The additional Hughes wear equation development will be concluded before the 1980 Critical Design Review (CDR) to provide an alternative approach to solving the retainer wear predictability problem in self-lubricated rolling element bearings.

The outcome of the experimental results will guide the future development of wear equations in the double transfer (i.e., ball/roller-bearing-like) mode, for the ball bearing simulator and the ball/ball pocket load predictability portions of this program.

(h) Bearing Simulation Test Equipment - As previously described in References 1 and 2, this task is aimed at investigating the behavior of materials under ball bearing-like operation by generating semi-empirical values such as hardcoat adhesion versus dynamic Hertzian stresses, ball/ball pocket traction and load under various Hertzian stress/speed conditions, etc.

The Battelle-designed ball bearing simulator is now under construction. The operation of the "brass board" model was successfully demonstrated at the Dayton DR.

The California State University, Northridge (CSUN) effort, under the direction of Dr. Lester Nypand has been recently started to determine the likely ball/ball pocket loads observed in solid lubricated turbine engine bearings. This work will begin with ambient temperature tests to show the usefulness of an existing rig, to be redesigned from the liquid to the solid lubricated mode. The measured ball/ball pocket loads will be directly substitutable into the empirical retainer wear equations described above, completing the loop of wear and film formation characteristics predictability of self-lubricating composite/compact retainers operating in solid lubricated turbine bearings.

## 2. Gyro (Type I) Bearing Research

Solid lubricated gyro bearings provide the initial vehicle of materials and design research toward the general development of wide temperature range, dry lubricated rolling element bearings. A significant spinoff is the development of a rugged, reliable bearing for high performance, high reliability inertial measuring systems.

The hardcoat/softcoat lubricant layer system especially lends itself for use in the heading reference units of air and ground vehicles, where corrosion, shock, vibration and wide temperature range environments proved especially troublesome. Solid lubricated gyros could be used not only in the cruise missile, but in helicopters and land combat vehicles also.

Original plans for the gyro baseline tests included examination of the TMI (ion-sputtered) TiC both in the conventional, oil lubricated mode and in the MoS<sub>2</sub> - sputtered condition, both representing off-the-shelf methods of bearing lubrication. As previously described, failure of the TiC and TiC/MoS<sub>2</sub> to adhere properly to the 52100 gyro races, coupled with the projected late delivery of the CVD CrC-TiC coated races forced alteration of the initial plans.

The new baseline tests are also divided into two parts: liquid lubrication of 52100 bearings containing the CVD coated 440C and cobalt bonded WC balls and comparison of the results with the wide Litton data base on conventional 52100 gyro bearings, and solid lubrication of the same components with currently available, sputtered MoS<sub>2</sub> films.

(a) Baseline Studies (Oil Lubricated) - As described in Appendix A, the performance of the hardcoated balls is singularly outstanding. Not only did Litton prove the excellent adhesion of the CVD CrC-TiC to the 440C substrate at loads up to 5 times of those normally used in gyro bearings, but also showed that the bare 52100 races work well in tandem with these improved balls, even at high bearing loads.

This load carrying ability combined with a lack of increased surface damage and torque during long term operation have the following important implications:

- Fluid lubricated gyros may be immediately upgraded by the simple incorporation of hardcoated balls. These balls can be CVD coated and lapped by well-established methods: it is amazing that Saphirwerk's routine polishing techniques are able to provide the extraordinary surface finish and in-round geometry due to the presence of the hardcoat. On the basis of these preliminary results (communicated to Saphirwerk and LITEF during the January 1980 Litton/Hughes/LITEF trip to Switzerland), Saphirwerk discontinued the production of polished metal balls and switched to the manufacturing of ceramic and hardcoated steel balls only. LITEF has also made plans to incorporate hardcoated balls in some of their high performance gyro bearings. Since balls can be coated and finished

satisfactorily in 30 to 40,000 ball lots, parts availability should not be a problem. Saphirwerk U.S.A. should be encouraged to expand its present sales activity in this country to a manufacturing operation also, thereby providing an excellent subcontractor candidate for any forthcoming MANTECH bearing component machining study.

• The incorporation of hardcoated races into fluid lubricated gyros can only further improve bearing performance.

• If the distortion problems could be alleviated by the use of acceptable P/M turbine bearing ball and race stocks and the CVD hardcoat proves to be adherent at the much higher turbine temperatures and bearing loads, hardcoating oil-lubricated cruise missile bearings will also constitute an immediate design upgrade. Moreover, if the reactively sputtered TiN is proven to be equally acceptable, an upgrade could be made even more imminent due to the immediate usability of off-the-shelf cruise missile (M-50) bearings. It is our understanding that the current bearings operate very close to their design limit and incorporation of the hardcoated components would shift the cruise missile bearings' operational envelope into the safe zone.

At the time of this writing, gyro bearing life tests with the hardcoated balls exceeded 1000 hours of testing time, at three-times the normally used bearing loads (i.e., at 6 lbs. load), running at 22,500 rpm. The life tests are continuing with no detectable inconsistencies.

b. Baseline Studies (MoS<sub>2</sub> Lubricated) - The complex interdisciplinary nature of the DARPA/Hughes program is exemplified by this portion of the work, consisting of Litton tests (see Appendix A) with balls coated by LSRH and finished by Saphirwerk, bearing parts sputtered with MoS<sub>2</sub> at Hughes and MoS<sub>2</sub> film QC by NRL. The test results are scrutinized by an MTI computer program, aided by MoS<sub>2</sub>-coated traction specimens fabricated at Hughes, sputtered at GIT and Hughes and tested at MTI.

As previously described in this report, three 52100 race/phenolic retainer-containing bearings, one with CVD CrC-TiC hardcoated 440C balls and two containing CVD CrC-TiC hardcoated Co/WC balls of two different sizes (leading to different contact angles) were sputtered with the Hughes MoS<sub>2</sub> baseline coating. Low and high speed tests are immediately forthcoming at Litton.

The initial questions to be answered are concerned with MoS<sub>2</sub> adhesion to the various components, MoS<sub>2</sub> film thickness, retainer behavior in a solid lubricated condition and general bearing behavior. We suspect that the high surface finish and chemically inert nature of the CrC-TiC coating may not be as immediately desirable for solid lubrication as it is for the liquid lubricated counterpart. It is possible that not only the presence of hardcoat on the balls and/or races, the relative hardness of the

coats on these specific sites, the thickness and nature of the solid lubricant films on these sites, but the purposeful roughening of the hardcoat(s) prior to solid lubricant sputtering will be one of the important controlling factors. Note that the possibility of changing the bearing design has not been taken into consideration yet: the feasibility study is starting with solid lubrication of gyro bearings originally designed for liquid lubrication.

Simultaneous with the above work, MTI is now starting the MoS<sub>2</sub> traction measurements, as well as the DREB computer simulation studies based on these measurements. The Litton solid lubricated gyro bearing data to be generated will eventually be incorporated into the computer program.

(c) Preparation of Improved Gyro Bearing Retainer

Stocks - The solid lubricated baseline Litton gyro bearing will be operating with the MoS<sub>2</sub>-sputtered porous phenolic retainer normally used in the liquid lubricated bearing. As described in References 1 and 2, this selection is not unreasonable, but only in the sense of comparing one available material for the two modes. The hardness and heat resistance of the paper-reinforced, porous phenolic are considered marginal, if not inadequate, for solid lubricated use, at least by this writer.

Among other tailorable properties, the low traction values needed between the ball/ball pocket and retainer/race contact are highly dependent on the hardness and thermal/dimensional stability of the solid lubricated retainer. The analogy of the hardcoat/softcoat combination is directly translatable to the concept of a hard retainer material/softcoat system. Moreover, none of the solid lubricants can provide the same cooling capacity as the heat transfer yielded by the circulating liquid lubricant in the oil-operated gyro bearing. It follows that the solid lubricated gyros will work hotter, magnifying any marginal suitability of phenolic retainers for solid lubricated operation.

Based on recent Hughes research on high load, high temperature self-lubricating composites (References 11 and 12), the initial efforts to provide better retainer stocks were described in References 1 and 2.

These alternative stocks consist of 13 mm OD, 6 mm ID tubes wrapped from preps prepared from Thermid 600 polyimide resin impregnated, two-dimensional (2D) weaves of carbon and graphite cloth, pressed and cured by a special process. Efforts to date resulted in tubes with reasonably predictable fiber lay and promising, but yet unacceptable reinforcement weave configuration.

It was found that porosity in the tube wall was caused by two factors. First, wrapping a dry and brittle prepreg with no tack and drape around a 0.25 inch steel mandrel resulted in loss of resin through flaking and spalling. Second, the silicone rubber expandable plug, threaded through the "green" prepreg tube was permitted to expand both radially and linearly in the mold. However, only the radial expansion is the worker; the

other is in fact a parasite, robbing the curing composite tube's wall from the maximum pressure the rubber plug could exert radially, if it were restrained axially.

The processing steps were therefore altered, as shown in Figure 22.

The first major change was the substitution of fine, stainless steel wire for the mylar shrink tape, to hold the "green" prepreg tube consolidated during subsequent processing (Figure 22A). The wound, but now resin-depleted tube was then re-impregnated by dip coating with Thermid 600/n-methyl pyrrolidone (NMP) varnish, in three successive dip-dry cycles (see Figure 22B). The fully resin-saturated prepreg tube was removed from the steel wrapping mandrel and threaded with the expanding rubber plug, as before (Figure 22C). To prevent longitudinal expansion of the rubber plug and thereby force its maximum radial effect, aluminum gate stops were inserted at the inlet and the outlet of the mold (Figure 22D).

As shown in Figure 23, the resultant composite tubes were sufficiently pore-free to permit machining of one tube section to gyro retainer dimensions (Figure 23A) from the as-molded precursors (Figures 23B and C).

Low magnification photomicrographic examination of the gyro retainer tube (Figure 23A) edge in Figure 24 confirms the pore-free nature and good integrity of the tube, save for a small crack induced by machining. Figure 24 also indicates that due to the spiral wrap nature of the preparation process, perfect concentricity of the reinforcing weave is inherently prevented. Nevertheless, the characteristic wrinkling of both the CCA-3 and Thorne 300 2D weaves in the resin-rich, melting and curing tube wall during molding (see Figure 25) can be ignored, if the wrinkled, outer portion can be machined away. The fact that the ends of the tube tend to wrinkle less and remain more concentrically spiral than the middle is probably caused by the uneven expansion of the silicone plug in the heated mold and its inability to move and distribute the expansion force isotropically along the tube length. All indications are that shorter tubes in shorter molds will meet with less wrinkling and concentricity problems.

If the wrinkling can be eliminated, the wall integrity of both the thin CCA-3/Thermid 600 and the thick Thorne 300/Thermid 600 tubes is sufficiently pore-free to provide working retainers, as indicated by the SEM photographs in Figures 26 and 27. Note that the white areas in the photo depict resin-rich regions due to electron charging.

The best tubes, reinforced with carbon (Thorne 300) and graphite (HMS) weaves, with or without selected lubricant additives will comprise the specimen lots of gyro retainer-like hoops for comparison with those fabricated from the Litton phenolic baseline materials. Flat-pressed moldings of the same materials will serve as ASTM-type test specimen stocks. Actual gyro retainers machined from the best candidates will receive full scale bearing testing at Litton, in the solid lubricated mode.

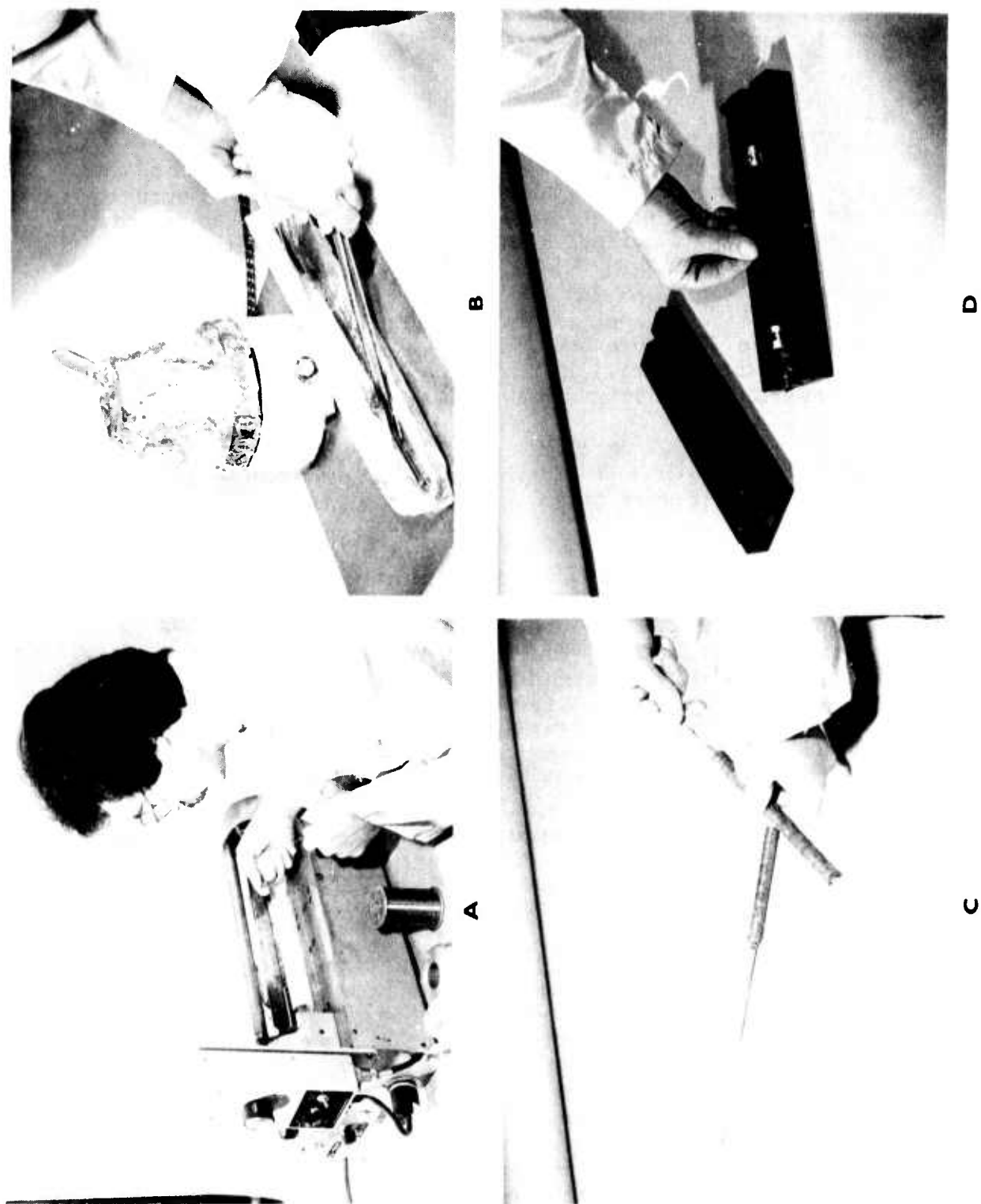


Figure 22. The improved preparation process of the Hughes 2D carbon/polyimide gyro bearing retainer stock.



Figure 23. Improved, expanding silicone rubber plug-prepared Hughes 2D carbon/polyimide gyro bearing retainer stock.

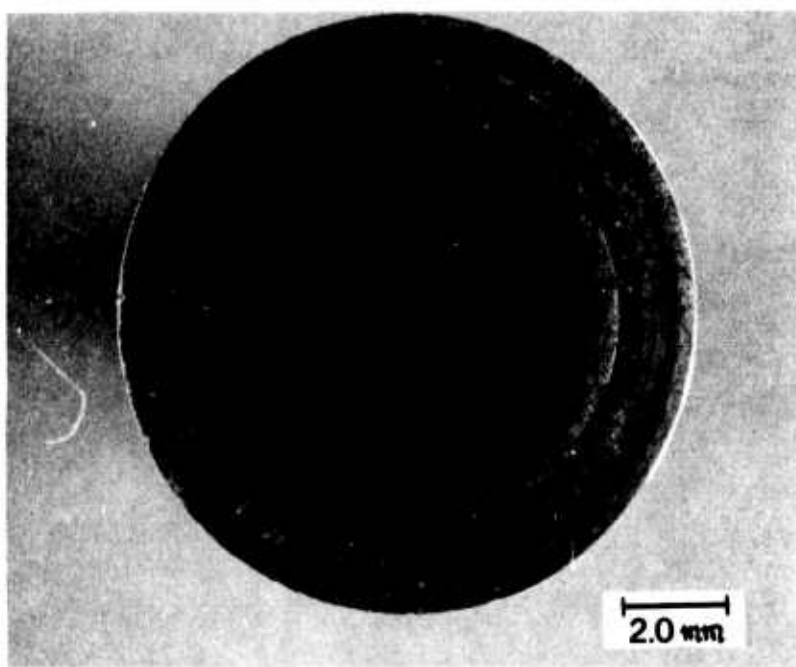


Figure 24. Integrity of improved CCA-3/Thermid 600 gyro retainer tube edge.

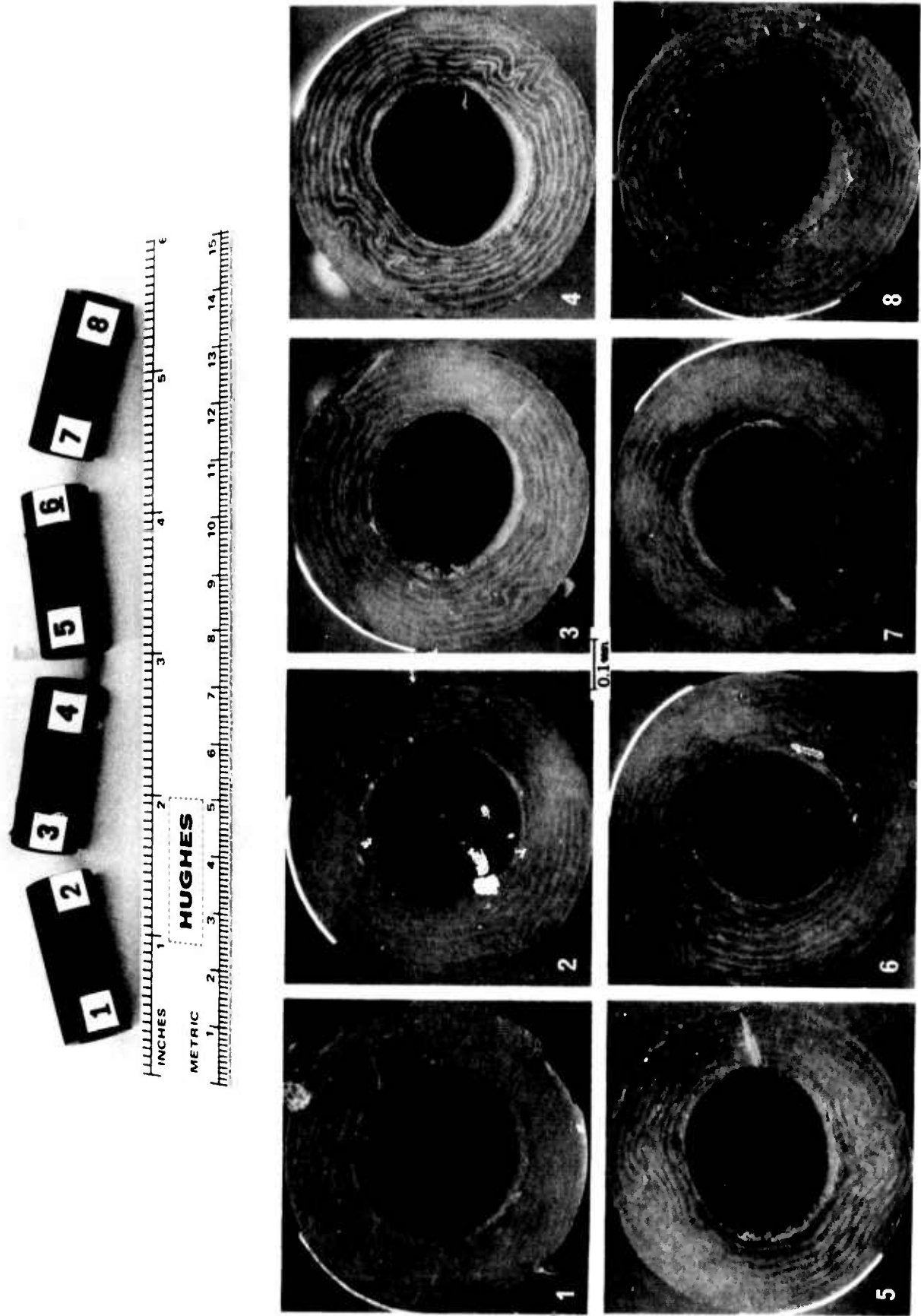


Figure 25. Quality control sections of the improved Thornel 3000/Thermid 600 gyro retainer tube stock.

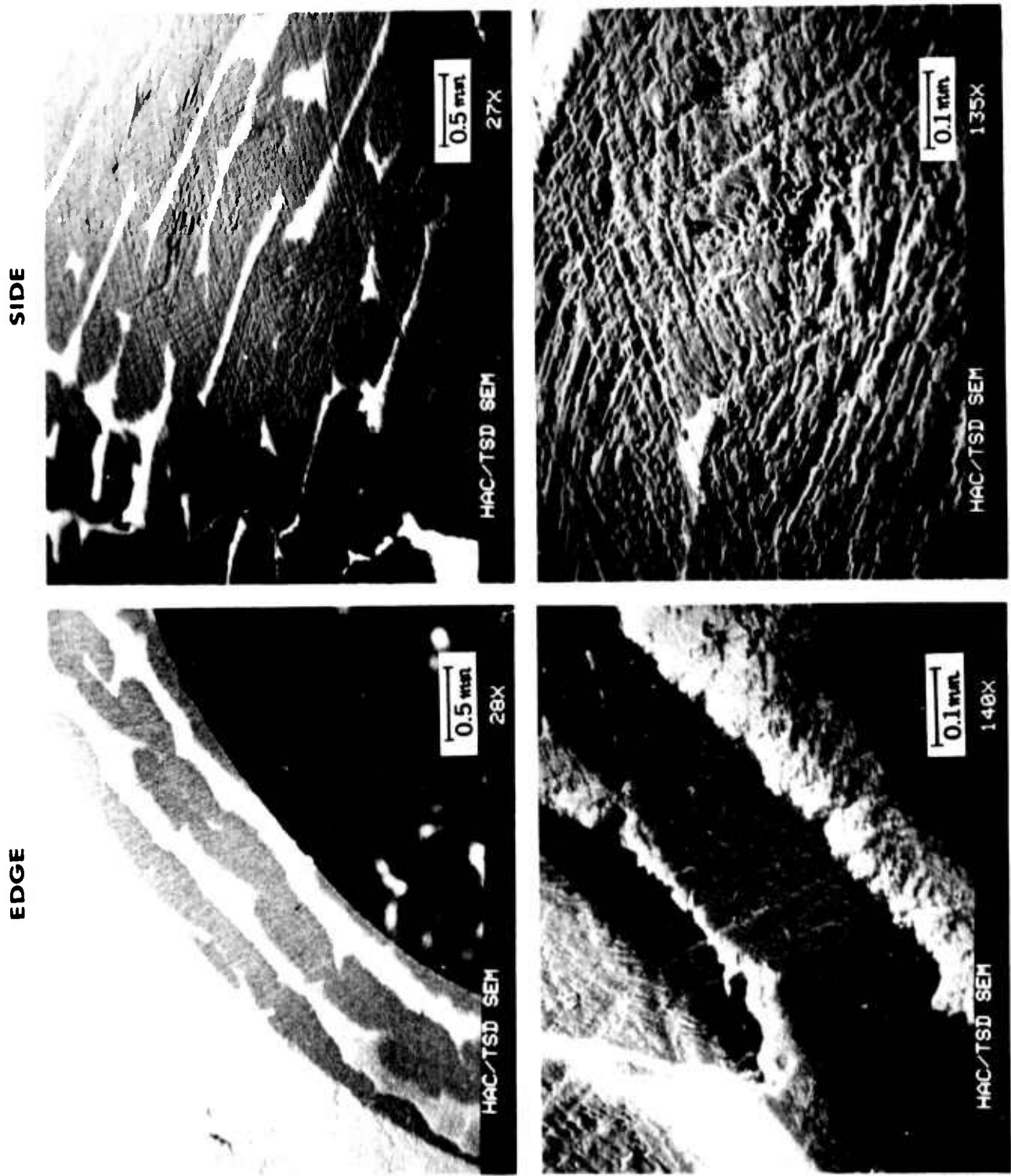


Figure 26. Edge and side (OD) integrity of improved, as-molded and machined, CCA-3/Thermid 600 gyro retainer tube stock at various SEM magnifications.

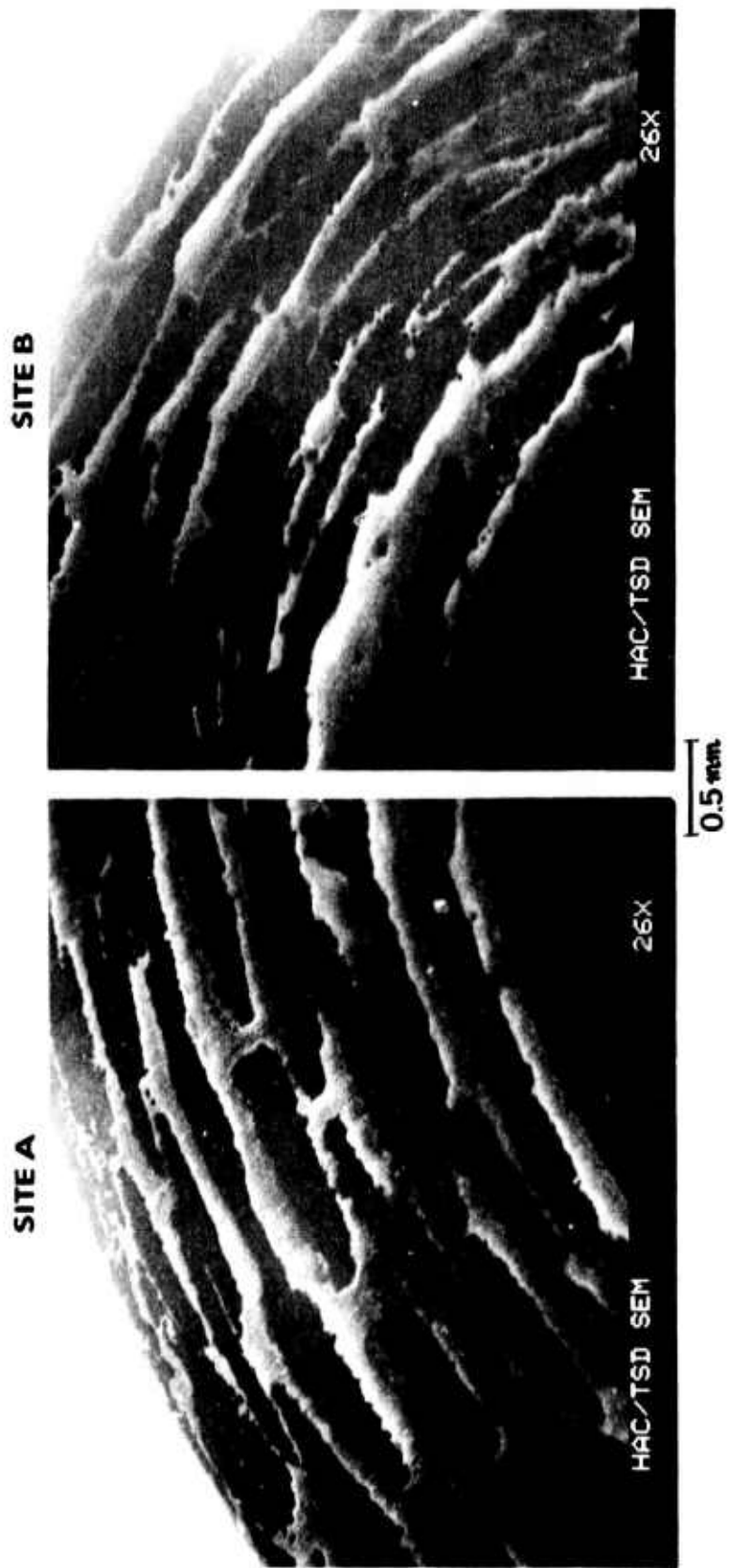


Figure 27. Typical edge integrity of improved, as-molded, Thermel 300/  
Thermid 600 gyro retainer tube stock at 26X SEM magnification.

Note that we are seeking even further improvements in gyro retainer preparation methods through HIP of the Hughes-prepared "green" prepreg tubes, at FMI (see Figure 28). Also, as guided by the promising results with the turbine bearing composite retainer (see forthcoming paragraph III. B. 3. (b)), we are contemplating the preparation of very fine, 3D cylindrical weaves of carbon/graphite reinforcement at FMI for the gyro retainer tubes also, starting in FY '81. This reinforcement geometry would provide the best isotropic skeleton to the gyro retainers, just as it has done for the turbine engine bearing equivalent.

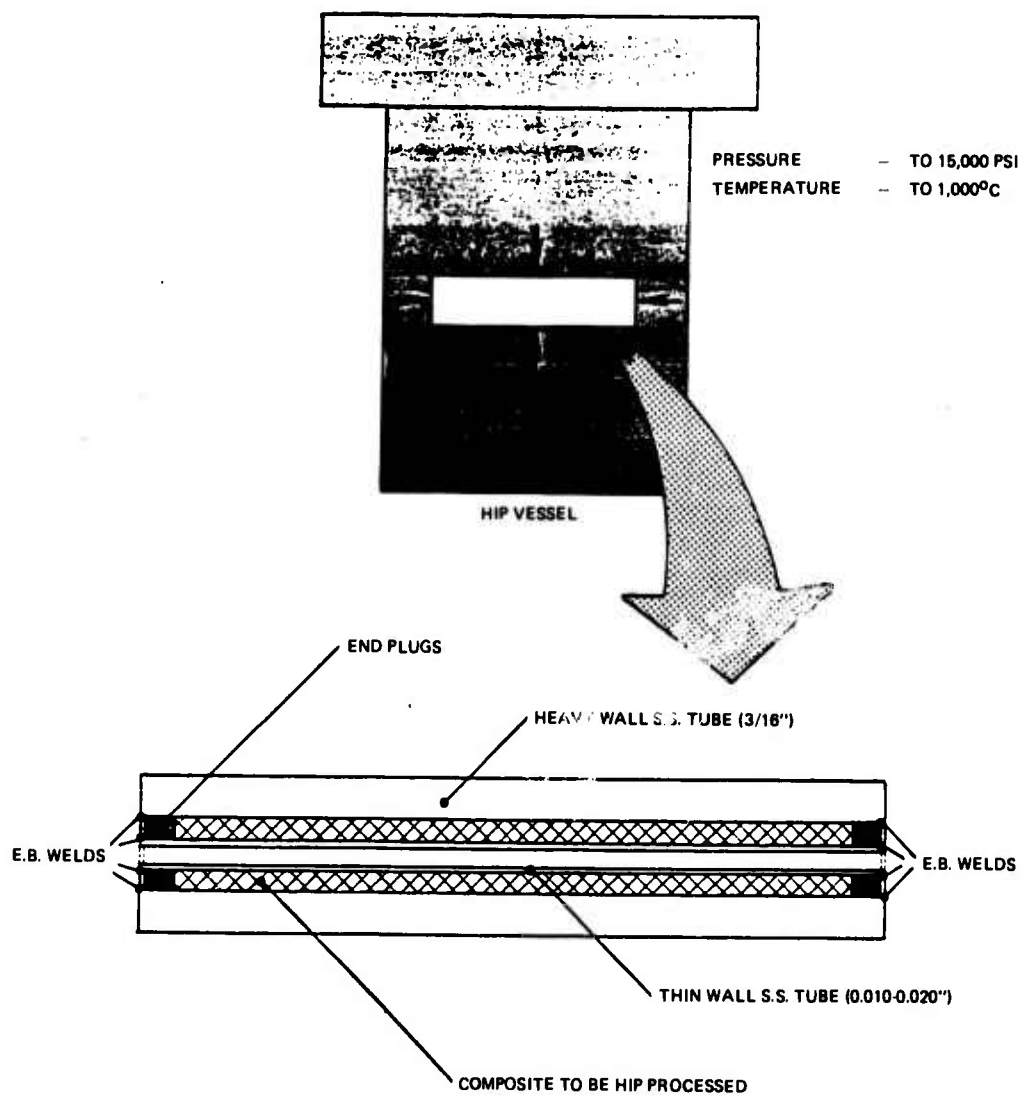


Figure 28. HIP of gyro retainer tube stock at FMI.

### 3. Turbine Engine (Type II) Bearing Research

During a January 1980 visit to MTI, Mr. C. R. Meeks of Hughes helped establish the nodes for a PERT chart that prescribes MTI's forthcoming activities. This diagram is given in Figure 29. MTI's tasks, along with SKF's computer diagnostics work and the ancillary activities (also refer back to Figure 1) comprise the major technical thrust of the DARPA/Hughes Solid Lubricated Rolling Element Bearing Program.

#### (a) Baseline Studies (Westinghouse Compact Lubricated) -

MTI purchased 10 each of the M-50, F-107, No. 3 bearings from Barden, for use as the baseline turbine engine specimens. A design study was started to evaluate the feasibility of building a Westinghouse compact-containing, self-lubricating separator for the baseline bearing, either with compact ball pocket inserts in a metal (e.g., titanium) retainer, or as a complete ring reinforced by a metal shroud. (For other recent efforts along these lines, see References 36 and 37). Samples of the compact large enough for the inserts were forwarded to MTI during the first part of December 1979 and even larger discs will be made available to them in February or March, 1980 for the alternative configuration. The various likely designs are being evaluated for machinability, ease of assembly and dynamic stability (i.e., balance, guiding surface interactions, etc.).

Other primary activities consisted of test rig modifications for the bearing tests and rotor dynamics analysis of the several possible configurations of the rig design (Appendix J).

All concepts which were considered employed a two-bearing support shaft with a quill extension enclosed in a semi-sealed environmental enclosure. Ball bearing type support bearings were compared with hydrodynamic oil bearings for stiffness, damping, and life. A pivoted shoe, hydrodynamic oil bearing that has been used successfully in other MTI tests was selected and incorporated into the bearing tester design.

A multi-stage thermal shield on the rotor minimizes heat flow from the environmental enclosure to the support bearings.

The blueline engineering drawings of the final design are too bulky to be presented here; they are available for inspection at MTI or at Hughes.

The test apparatus will be fabricated and debugged during the next report period.

#### (b) Polymeric Self-Lubricating Retainers for 500°F

Operation - There is little doubt that an elevated temperature rolling element bearing will operate for any extended period of time only if equipped with a self-lubricating retainer. The PLR concept previously mentioned and thoroughly described in the upcoming paragraph III. B. 3.(e) can only retard failure of a bearing. Extended bearing life is basically dependent on the

strength, thermo-oxidative and wear/transfer film formation characteristics of the retainer composite or compact, provided the bearing ball/race material and the retainer shroud (if any) remains structurally sound.

Parallel with the development of composite tubes for gyro retainers, similar but larger diameter tubes were prepared from 3D cylindrical weaves-reinforced Thermid 600, as previously described in References 1 and 2. FMI forwarded several of those test preforms to Hughes, for the determination of the best impregnation/mold/cure steps. These steps are now basically established, as depicted in Figure 30.

Either a preweighed and premeasured Thorne 300 (carbon) or Thorne 50 (graphite) practice weave preform (1.45 inch diameter, 0.80 inch wall thickness, 3 inch long) was pulled over a tight-fitting, perforated, hollow aluminum mandrel as shown in Figure 30A. Next, the assembly was repeatedly dipped/dried using a premeasured amount of hot Thermid 600/NMP varnish, until all of the resin was absorbed by the preform (Figure 30B and 30C). The impregnated preform was final dried for 80 minutes at 350°F, followed by cooling and reweighing for the determination of fiber/resin content. The "green" prepreg was transferred to another tight fitting aluminum mandrel containing a 0.75 inch diameter, 2000 W heating element and the entire assembly was vacuum bagged, as shown in Figure 30D. Evacuation of the 0.002 inch thick Kapton bag was followed by leak checking, transfer of the bag into an autoclave and the connection of all heater and thermocouple wires. The autoclave was pressurized to 100 psig and the heater was turned on to attain a 500°F temperature of the mandrel as soon as possible. This temperature and the pressure were held for one hour.

The first attempt of pressing and curing a one inch long prepreg segment with the above procedure resulted in failure due to an incorrectly registering thermocouple. The porous, overheated and burnt molding is shown in Figure 31A. The molding in Figure 31B was processed similarly, with two thermocouples controlling the heating cycle, assisted by the autoclave heaters. The final moldings exhibited a wrinkled appearance around the OD, but had excellent concentricity. One acceptable ring was machined to a 1.555 in. OD, 1.383 in. ID hoop, as depicted in Figure 31C.

SEM photomicrographs of the hoop in Figure 31C are given in Figure 32. The outstanding concentricity and symmetry of the composite hoop is readily visible. The porosity, however, is still higher than desired.

An attempt to mold 3 inch long prepreg tubes in a similar manner indicated the same wrinkling on the OD and porosity previously noted with the one inch long counterpart (Figure 33A and 33B). Furthermore, an apparent weave movement during molding reduced the concentricity of the tube along the axis, as shown in Figure 33C. Removal of

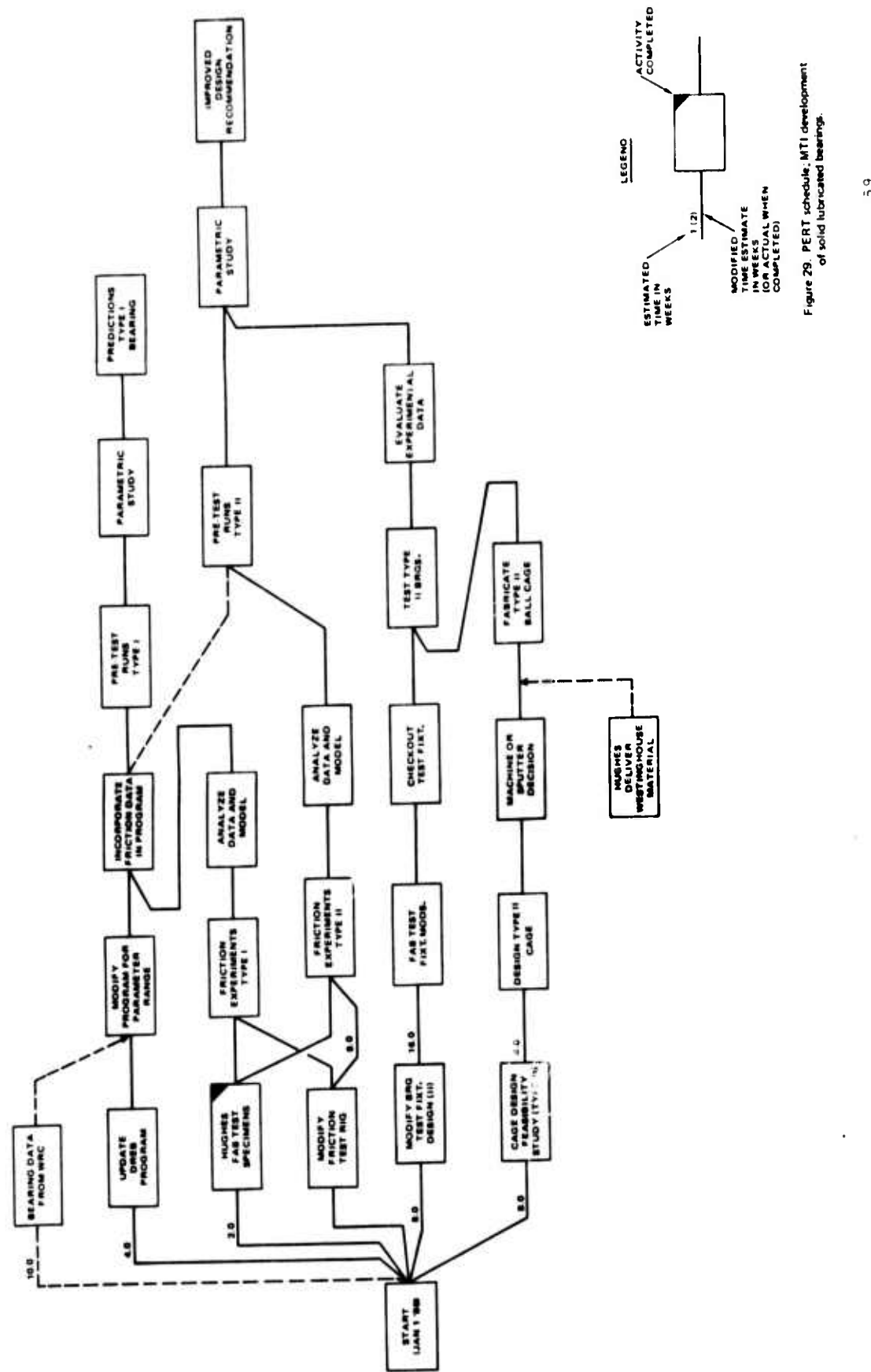
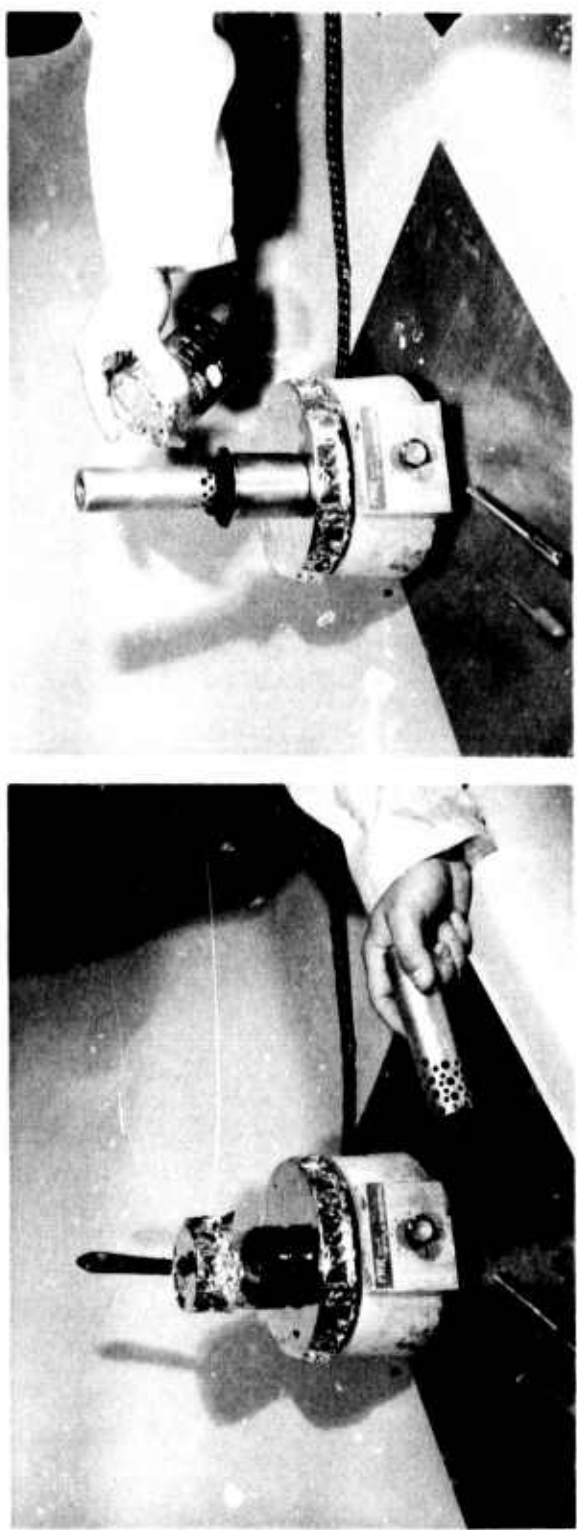
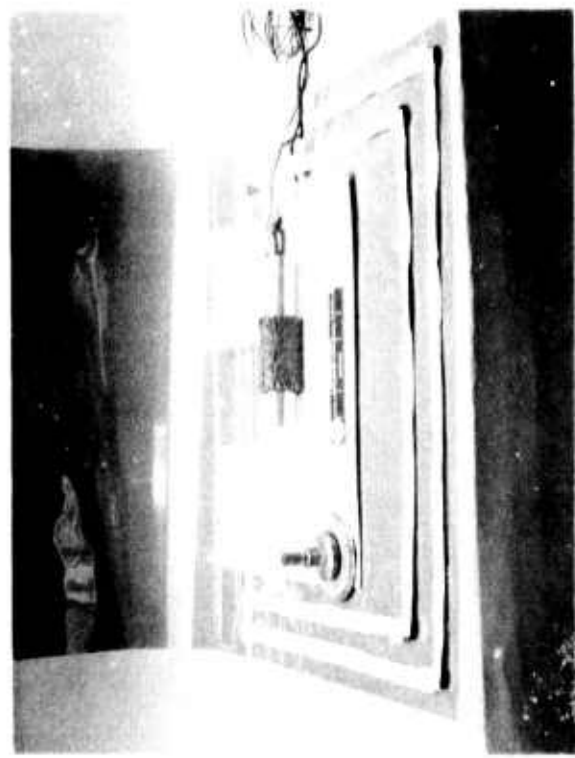


Figure 29. PERT schedule, NTI development of solid lubricated bearing.



A



B



C

D

Figure 30. The preparation process of the Hughes 3D cylindrical carbon-graphite weave/Thermid 600 turbine bearing retainer stock for 500°F use.

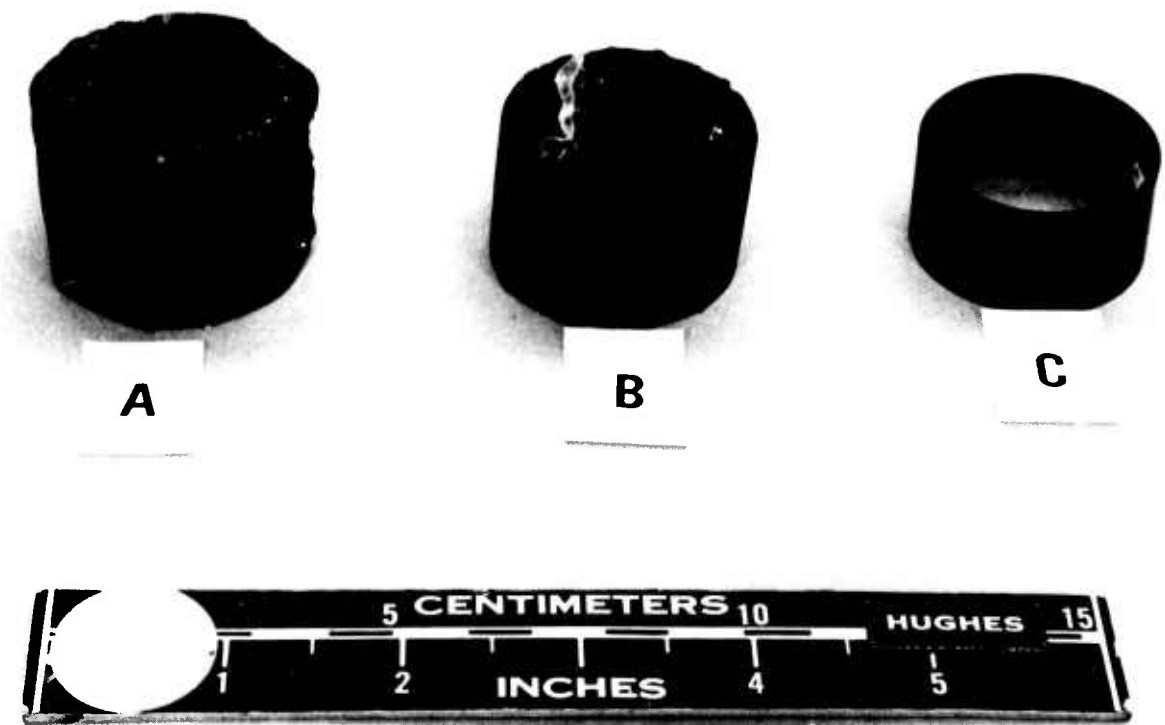


Figure 31. Unacceptable and promising short (1 in.) moldings of 3D cylindrical Thorne 300 weave/Thermid 600 turbine bearing retainer tube stock.

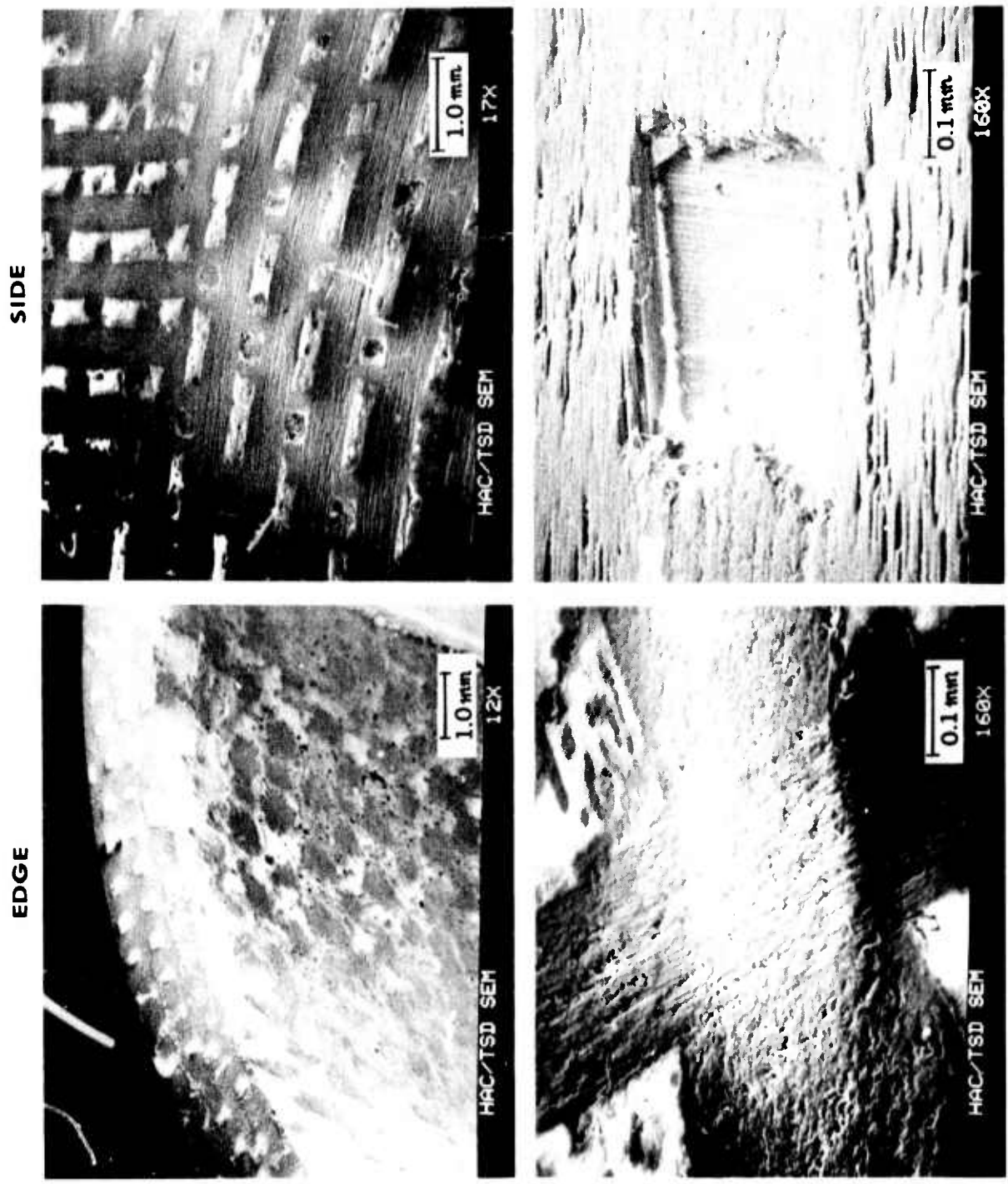


Figure 32. Edge and side (OD) integrity of as-molded and machined, 3D cylindrical, short Thorne 300 weave/Thermid 600 turbine bearing retainer tube stock at various SEM magnifications.

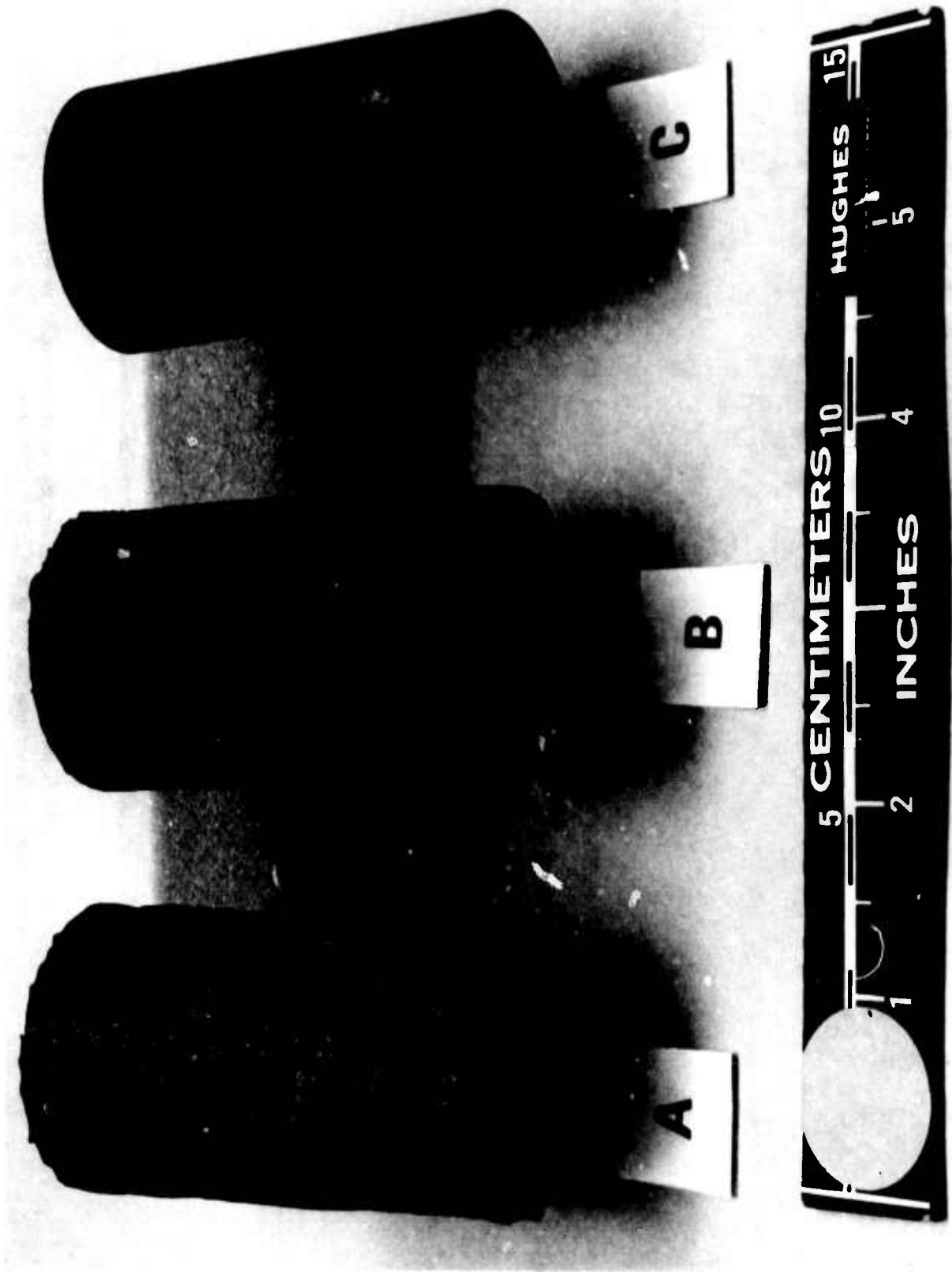


Figure 33. Unacceptable, long (3 inch) moldings of 3D cylindrical Thormel 300 weave/Thermid 600 turbine bearing retainer tube stock.

all wrinkles from the OD left the machined tubes undersized, as compared with the dimensions of the F-107, No. 3 bearing retainer ( $1.632 \pm 0.003$  in. OD;  $1.472 \pm 0.0005$  in. ID). Any redesign of the final, 12 inch long FMI preforms, either in terms of larger diameter preforms or axial/radial yarn size compensation to bring the machined tubes to the desired dimensions will depend on a forthcoming FMI/Hughes technical conference to assess the above results. Possible methods of porosity reduction will also be discussed.

The undersized tubes will be subjected to a variety of structural integrity tests to compare their properties with metal baseline retainer stocks (e.g., titanium) of the same diameter.

It is interesting to note the parallel behavior of wrapped 2D gyro preprints and 3D weave reinforced turbine preprints in that shorter preforms yield more isotropic tubes. The similarity probably lies in the similarity of preparation procedures.

While the production of retainer stock in research quantities is not influenced by the relatively low yield of the current process, manufacturing technology production requires further thinking. A lot will depend on the success or failure of HIP-ing of the gyro retainer stock: if the process seems promising, the turbine retainer preprints could also be manufactured by the same method, in far larger yields.

Eventual incorporation of solid lubricant additives into the resin matrix will be a routine matter, as previously worked out in References 11 and 12. Additionally,  $600^{\circ}\text{F}$  friction and wear tests are now being completed by MRI (Kansas City, Missouri) on model compounds to more completely assess the high speed/load capability of advanced reinforcement weaves and additives. Also, FMI is going to prepare 3D flat weaves of Thorne 50 and Thorne 300 by using the weave parameters of the 3D cylindrical retainer preforms. The flat weaves shall be pressed into plate-like composite molds. Again, these molded blanks will lend themselves to the kind of structural integrity evaluation (e.g., ASTM-type tests) the retainer hoops are incapable of offering due to their unusual shape.

(c) The Solid Lubricated ( $500^{\circ}\text{F}$ ) Turbine Engine Bearing Precursor - This portion of the work concerns itself not so much with the ability to operate a  $500^{\circ}\text{F}$  turbine engine bearing for extended periods of time, but with the capability of correlating computer diagnostic predictions with actual bearing behavior.

A most important undertaking is the proper instrumentation of the MTI bearing tester for the measurement of the parameters that enable one to check the input/output data of the computer programs. This is an extremely difficult task for elevated temperature bearings due to the thermal limitations of electronic sensors other than thermocouples or thermistors (e.g., proximity sensors). To circumvent this problem, certain design tricks may have to be incorporated.

Construction and shakedown of the MTI tester will be preceded by certain preliminary computer predictions on solid lubricated bearing behavior. Because of a lack of test information on traction, slip and friction of the candidate bearing surfaces, it was decided to use a preliminary parametric analysis approach for the SKF SHABERTH predictions. The program is being modified to permit insertion of various values of friction and slip interaction of balls, raceways and separator. Using this parametric approach, the resulting Type II bearing temperatures vs. friction parameters can be estimated.

This will aid in establishing property boundaries for the materials development and inject early realism into the thermal survivability requirements for bearing materials and lubricants. Additionally, it is hoped that this preliminary analysis will aid in determining if auxiliary bearing cooling is required and to establish quantitative guidelines for heat transfer system design.

All of the above information will help define a method for determining a solid lubricated bearing survivability window in terms of lubricant/bearing material properties and characteristic traction/wear behavior. A need for specific experimental data will also be defined to enhance the credibility of simulation results. Clearly, the initial MTI traction tests are only a first step in acquiring such data. In view of the reasonable thermal stability of MoS<sub>2</sub> at 500°F, a self-lubricating (resin/graphite/MoS<sub>2</sub>) retainer-operated bearing, containing sputtered TiN/MoS<sub>2</sub> on the balls and the races is an excellent candidate for the 500°F turbine engine bearing precursor. The baseline bearing is automatically a candidate.

The MTI DREB program will undergo similar modifications and exercises, helped by the immediately forthcoming traction tests.

(d) Thermal Mapping of the WRC F-107 Cruise Missile Engine by the SKF TRANSIM Computer Diagnostic Method - As previously mentioned, SKF will analyze drawings for the F-107 engine and catalogue the data needed for a complete material and detailed spatial description of the load. The data will be supplied by WRC, under contract to Hughes.

First, SKF will develop a nodal network representation of the load support assembly as well as the relevant thermomechanical environment and prepare the information gathered for TRANSIM INPUT. The OUTPUT data will be compared to the results of the WRC instrumented engine tests.

Next, TRANSIM will be executed for idle, 75 percent maximum, 90 percent maximum and 100 percent maximum engine power settings at sea level, static and standard day conditions, followed by a similar set starting with 135°F hot-soaked engine initial condition. One thermal transient analysis will also be performed where the initial condition will be represented by an idling engine, comprising the steady state start for subsequent, 5 minute interval increases in operating power from idle to 75 percent to 90 percent to 100 percent maximum.

Clearly, the above exercises are aimed toward the examination of individual load supports (i.e., bearings) which may reveal marginal operating characteristics. These potential trouble spots will be examined in more detail by other available SKF computer programs as well.

Guidance to circumventing these obstacles will be offered by "what if?" and "why not?" software experiments to determine the effect of a heat pipe cooled inner race and change in the bypass air supply on shifting load support performance from the unacceptable to the marginal and finally to the safe zone.

All of the above work will be applicable both to the existing F-107 engine and to the advanced versions now on drawing boards. Note that in the advanced engines, temperatures of 1000° to 1500°F are being forecasted for bearings near the hot section, due to the increased turbine inlet temperatures. In that environment only high temperature solid lubricants and very few high temperature alloy or ceramic bearings can survive: fluid or grease lubrication will be out of the question.

(e) PLR - A Concept for Solid Lubrication of 1000°F + Rolling Element Bearings - There is little doubt that the cruise missile engine of the 1990's will operate with solid lubricated rolling element bearings. In order for our program to be responsive to the missile design and development calendar, a solid lubricated engine should be operational on a test stand by 1985, with bearings rotating predictably and reliably at speeds of 60,000 rpm, at temperatures up to 1000°F, for at least 10 hours.

A carefully planned, solid lubricant/bearing design effort must therefore be conducted, with well-defined, intermediate milestones. We believe, however, that in order to meet these milestones, more advanced concepts of high temperature bearing lubrication must be developed beyond the relatively simple ones presented elsewhere, or even in our previous reports.

Based on the research conducted so far in our program, this writer is now prepared to propose the "Principle of Layered Redundancy" (PLR) lubrication concept for both metallic and ceramic bearing surfaces. The PLR is applicable under the following conditions:

- As long as there is enough power to run a cruise missile engine bearing on the shaft and the bearing structural integrity is adequate, barring excessive shaft vibrations, the engine will operate and the cruise missile will fly.

- The bearings operate at elevated temperatures, in a full air-flow environment.

- Any failure of the bearing must occur on the solid lubricated sliding/rolling interfaces by wear attrition alone. The alloy or ceramic bearing material will not exhibit subsurface failures that result in large fatigue spalls and destruction of the balls or races; the retainer will keep its structural integrity throughout the lifetime of the bearing.

- Regardless of bearing design manipulations (e.g., heat pipe shafts, airflow adjustment through the bearing), any changes in traction values due to the differences in the coefficients of friction of the developing PLR lubricating layers can be accounted for by the bearing design.

The PLR is an extension of the softcoat-on-hardcoat concept, as indicated in Figure 34. Each layer provides sufficiently low traction values to allow high speed turning of the bearing with adequate stability and, in turn, physically/chemically protects its immediate substrate. Upon tribocatalytic exhaustion of the low shear strength softcoat, the degradation products of the underlying hardcoat itself will act as antiseize agents, alone or in conjunction with any remainder of the soft topcoat. Similar exhaustion of the hardcoat will be followed by the "last line of defense": glaze development of the substrate metal alloy or ceramic, under the given high temperature, oxidative environment. Each successive layer is less capable of providing the initial, low traction values of the low shear-strength solid lubricant top layer, but will prevent seizure of the rolling element bearing surfaces.

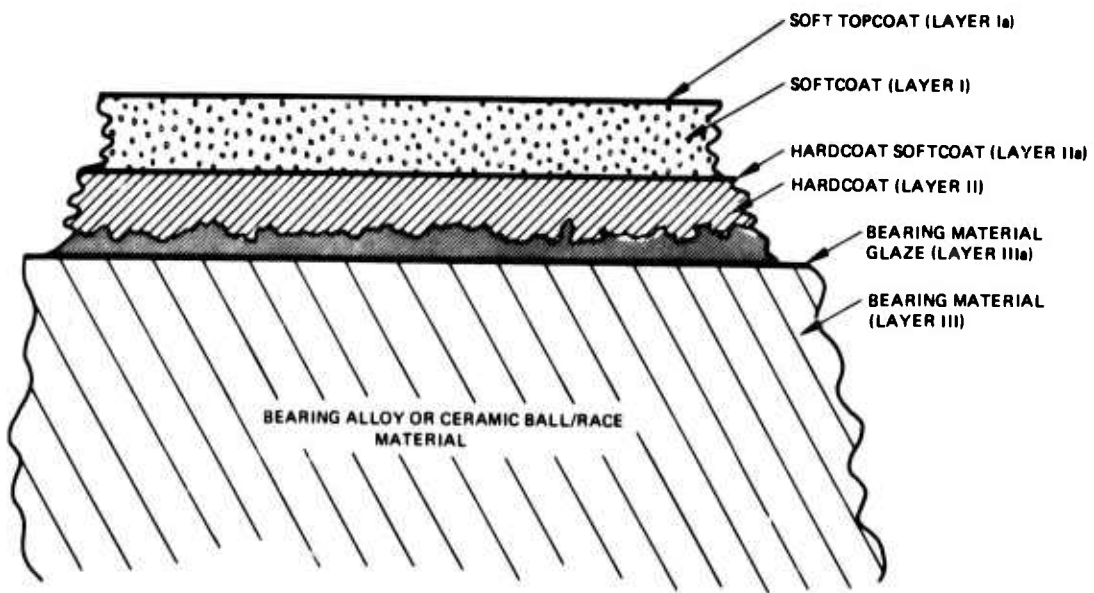


Figure 34. The PLR solid lubrication concept for high temperature rolling element bearing applications.

The PLR concept is also applicable for the bearing retainer/ball or retainer/race sliding surfaces in terms of the mechanism itself (e.g., in the case of the "benign" retainer, when it is lubricated but itself is not self-lubricative), or through the use of a self-lubricating retainer, which retards the tribo-oxidative degradation of the hardcoat and assures low traction by continually enriching the soft topcoat.

A hypothetical scenario may be developed by suggesting possible materials combinations and utilizing Figure 34 herein.

Let us assume that Layer I is a sputtered composite softcoat, containing the Westinghouse compact or a successfully intercalated dichalcogenide co-deposited with a  $(\text{Fe}, \text{Co}, \text{Ni})_3\text{V}$  (Reference 33) alloy binder. As established by this writer in Reference 12, preferential accumulation of thermally stable solid lubricant pigment(s) on the worn surface of a self-lubricating composite does occur due to the normal wear mechanism. The very thin (probably less than 500Å) Layer Ia is either purposely established by sputtering pure Westinghouse compact (or another solid lubricant) on the top of Layer I, or it will naturally develop during the first few revolutions of the bearing. Either of the two forms of Layer Ia will provide the lowest traction values attainable.

Any further degradation in bearing performance will depend on the tribo-oxidative wear life of the composite layer. It is possible that the oxidation products of the binder itself will act synergistically with the chemically stable solid lubricant. As previously shown in Reference 38, certain nickel-base alloys show a predictable and very reproducible reduction in sliding friction above a certain transition temperature. This change can be correlated with the formation of a stable, adherent, thermally softened oxide layer or glaze on the load bearing areas during sliding.

Upon exhaustion of portions of Layer I (it is unreasonable to assume that all parts of Layer I will be depleted uniformly), tribocatalytic exposure of the hardcoat (Layer II) will commence. By assuming the presence of a CVD CrC-TiC hardcoat, the TiC-rich top layer will oxidize into  $\text{TiO}_2$ , which in itself has been used as a solid lubricant with a low coefficient of friction (Reference 39). In fact, Wu (Reference 40) used checkerboard arrays of  $\text{TiO}_2$  reservoirs in a TiC matrix to produce wear lives over that obtained from steel coated with either  $\text{TiO}_2$  or TiC alone. Wu and Greene (Reference 41) recently showed that reactively sputtered  $\text{TiO}_2$  on the top of TiC exhibited a coefficient of friction of  $0.25 \pm 0.03$  in a pin-on-disc experiment (probably at room temperature) where the rider was a 6.35 mm dia, 52100 steel rider. The above information may be coupled with the fact that Green and Zilko (Reference 42) could increase the adhesion of argon ion (bias) sputtered TiC to steel by mixing oxygen, at very small partial pressures, with the argon sputtering gas during the initial stages of TiC deposition. A complex interfacial region exhibiting high adhesion was produced with chemically graded layers of Fe (substrate),  $\text{FeTiO}_3$ ,  $\text{TiO}_2$  and TiC. (A similar trick was utilized by NASA Lewis technologists through

initial increase in the nitrogen content of the N<sub>2</sub> + Ar reactive sputtering atmosphere, thereby developing a mixed iron-titanium nitride interface region prior to the deposition of the sputtered TiC, see Reference 43). The point is that on the imaginary inversion of the TiO<sub>2</sub>/TiC layers, a reasonably adherent TiO<sub>2</sub> film that forms gradually on the surface of the oxidatively degrading, TiC-rich top layer of the CVD CrC-TiC solid solution could aid the remainder of the softcoat by participating in the formation of a conglomerate lubricant coating. Such a "macadam road"-like thin film, consisting of well-blended and finely crushed solid lubricant particles and bearing ball/race wear debris can successfully lubricate rolling element bearings both at ambient temperatures (see Appendices H and I) and at elevated temperatures (Reference 6), for prolonged periods of time.

Thermal degradation of reactively sputtered or CVD TiN may also provide a similar mechanism. However, depletion of any hardcoat (Layer II) must be by gradual microfatigue and abrasive wear. Any sudden delamination of the entire layer will stop an orderly PLR process.

Thermo-oxidative wear of the CVD CrC-TiC layer will be altered in the CrC-rich region. The reduction in TiO<sub>2</sub> formation and increase in the oxides of chromium will reduce ball and race wear but will also increase traction. This increase should be monotonic to the hardcoat attrition limit of Layer IIIa.

Let us now assume, that the bearing alloy (Layer III) was a relatively high chromium content, P/M alloy, as shown in Table 5. Even a chromium content of 4 percent by wt. may be sufficient for the CVD CrC-TiC's adhesion (440C contains approximately 11 percent by wt. chromium). Also, the data in Figure 35 indicate reasonable substrate strength of both M-50 and the EX 00007, and outstanding strength of T-15, at 1000°F. The T-15 alloy itself has already been used for the fabrication of rolling elements, operating as X-ray target bearings at 1000°F, at ~150 ksi Hertzian stresses (Reference 44). Glaze development of Cr-containing alloys will undoubtedly consist of the hard, corrosion resistant, thin layers of chrome oxides (Layer IIIa). It is believed that unless there remains a sufficient amount of PLR layer debris acting as a residual solid lubricant, bearing surface failure at this point is imminent.

The above scenario is presented to show that proper design of the PLR layers could retard bearing surface failure throughout the relatively short lifetime of a 1000°F + solid lubricated cruise missile bearing. Obviously, not all possible tribochemical interactions can be accounted for *a priori* by this hypothesis. Also, the substitution of a ceramic (i. e., Si<sub>3</sub>N<sub>4</sub>) for a high temperature bearing alloy will drastically change the required chemistry of the PLR layers.

TABLE 5.  
WEIGHT PERCENT CHEMICAL COMPOSITION OF SELECTED  
HIGH TEMPERATURE ALLOYS (Reference 3).

	C	Cr	Mo	V	W	Co	Cb	Si	Mn
00007	1.1	14.0	2.0	1.0	----	---	0.3	0.3	0.4
T-15	1.6	4.0	---	5.0	12.0	5.0	---	0.3	0.3
M-50	0.8	4.0	4.2	1.0	----	---	---	0.2	0.2

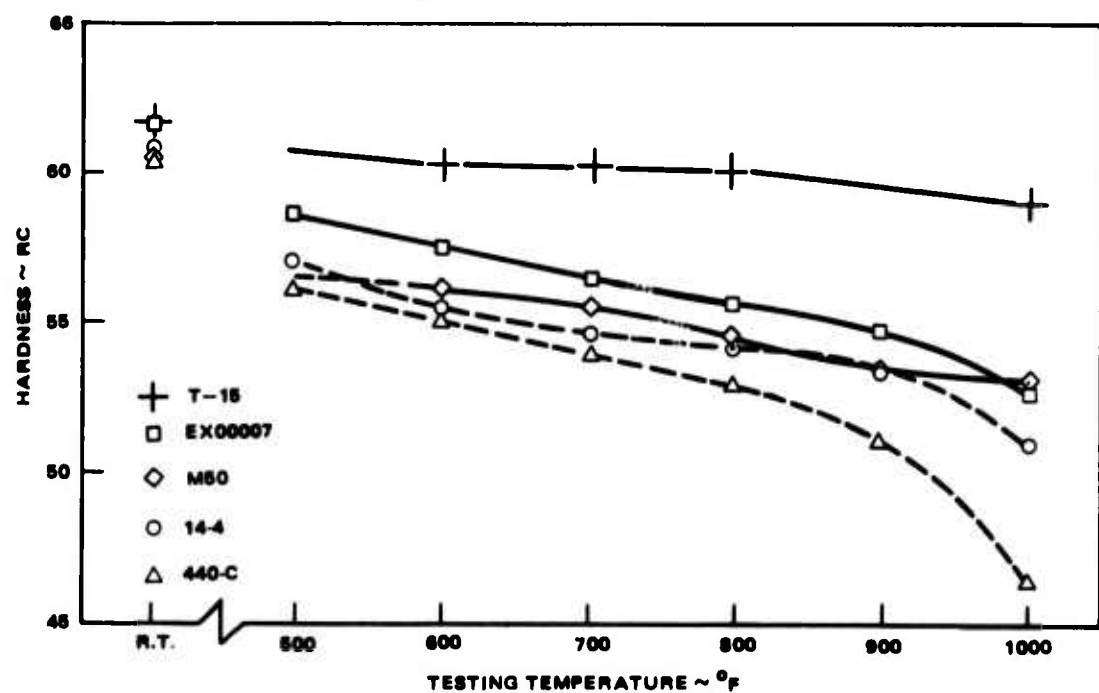


Figure 35. Hot hardness of selected high temperature bearing alloys after a 30 minute soak at the indicated temperatures (Reference 3).

To provide some idea of a similar scenario for silicon nitride bearings, Hughes began an investigation into the chemical compatibility at high temperatures between various available forms of hot pressed  $\text{Si}_3\text{N}_4$  and likely solid lubricants (Appendix K). The collected information shows that the chemistry of the sintering aid used makes a great deal of difference in the oxidation resistance of  $\text{Si}_3\text{N}_4$ . Furthermore, reduction of the impurity content and flaws on the surfaces by CVD of pure  $\text{Si}_3\text{N}_4$  on the top of the machined, hot-pressed silicon nitride improved oxidation resistance by an order of magnitude. A combination CVD of  $\text{Si}_3\text{N}_4$ , followed by TiN could provide a reasonable hardcoat underlay for any solid lubricant topcoat, because we suspect that the surface of the as-machined, hot-pressed  $\text{Si}_3\text{N}_4$  would be sensitive to certain solid lubricants (e.g.,  $\text{CaF}_2/\text{BaF}_2$ ). As further proof of the inert nature of pure  $\text{Si}_3\text{N}_4$ , through recent silicon nitride encapsulation of gallium arsenide by low energy ion beam sputtering, layers having mechanical stability to above  $900^\circ\text{C}$  ( $1652^\circ\text{F}$ ) were formed (Reference 45).

Due to the current lack of hard data, a PLR scenario is more difficult to formulate for a ceramic ( $\text{Si}_3\text{N}_4$ ) bearing substrate. Only small pieces of the puzzle are available today. For example, we know that oil shut-off tests after steady state operation of 35 mm M-50 bearings with hot-pressed silicon nitride balls led to bearing failure in 90 seconds. All M-50 bearings with steel balls failed in 45 seconds (Reference 46). Therefore, dependence on a IIIa layer alone (consisting of  $\text{SiO}_2$  formed in a full flow of air) as a "last line of defense" seems inadvisable.

Our forthcoming experimental study will concentrate on the evaluation of both the Norton Noralide NC 132 and the West-German equivalent material. In spite of SKF's current concentration on the US - made material for MANTECH machining of F-107 cruise missile engine bearing balls, rollers and races (for the most recent report, see Reference 47), we believe that the Annasnid d (AD-H) deserves greater scrutiny than it has received to date in this country. Finished AD-H balls from Saphirwerk, Switzerland and AD-H blanks have been procured for future comparison with balls fabricated by SKF and similar blanks of NC 132. We have reasons to believe that the AD-H material may exhibit more desirable properties than the U.S. version, for both solid and liquid lubricated rolling element bearing applications.

(f) Retainers for  $1000^\circ\text{F}$  + Solid Lubricated Rolling Element Bearings - The PLR concept will work best through the replenishment of the composite softcoat from self-lubricating compact ball pockets. Considering the relatively small size of the F-107 No. 3 bearing, it is unlikely that an advanced, high temperature compact will be strong enough to serve both as the structural member and the lubricant reservoir in a retainer. In other words, dimensionally stable, high specific strength retainer shrouds must be used in conjunction with compact ball pocket inserts or compressively contained compact rings.

As an extension of the ideas utilized in developing polymeric, self-lubricating composite retainers for 500°F service, we foresee the use of carbon-carbon (C/C) composite as the structural member of high temperature (1000°F+) rolling element bearing retainers. Oxidation stability of the C/C will be increased by the formation of SiC on the retainer surfaces (Reference 48).

FMI will prepare 3D C/C cylindrical preforms by weaving the preforms to the dimensions of the F-107 No. 3 bearing retainer from Thornel 50 and Thornel 300. These preforms will be fully densified by the best available methods, then fabricated to near-dimensions of the retainer. Machining will be followed by the deposition of silicon carbide oxidation barrier on all surfaces. The over or undersize of the retainer OD, ID and the ball pocket diameters will depend on the deposition characteristics of two coating techniques:

- CVD of a discrete SiC layer (5  $\mu$ m nominal);
- Surface conversion of the C/C substrate to SiC by silane vapor/solid phase reaction (5  $\mu$ m nominal SiC "skin").

The most desirable process is the one providing a gradual rather than an abrupt transition between the two materials of differing coefficients of thermal expansion. The gradation will reduce the stress concentration between the substrate and the SiC coating in the same manner as that of the CVD CrC - TiC layer/440C steel interdiffusion layer does.

Any distortion of a SiC-coated, C/C near-shape retainer due to the respective coating processes and the thermal behavior of the C/C composites themselves will be measured. Thickness of the residual SiC layers on the final-machined retainer surfaces will be determined by metallographic sectioning.

The SiC layer is intended to act both as an oxidation barrier and as a hardcoat substrate for subsequent solid lubrication. The PLR concept may be applicable here if we learn to tailor the hardcoat chemically, as previously described. Mostly, however, the SiC-coated C/C retainers will be compared to similar ones fabricated from other, high specific strength, high temperature alloys (e.g., Ti6Al4V) as likely shrouds for self-lubricated bearings.

#### IV. CONCLUSIONS AND FUTURE WORK

*(cont'd p 1)*  
The most significant accomplishments to date may be summarized as follows:

- 1) We established the theoretical and practical basis of and demonstrated the need for immediate bearing surface integrity studies and the need for improved, more homogeneous bearing steels.
- 2) In spite of the lack of experimental data, based solely on literature information and the understanding of tribology fundamentals, we were asked to predict success or failure for ion-sputtered versus chemical vapor deposited (CVD) hardcoats for high Hertzian stress, rolling element bearing use. We predicted failure for the former and success for the latter. After having defended our position against severe criticism, Litton and Hughes developed experimental data, proving our original contentions. AISI 52100 steel gyro bearings (oil lubricated) were operated with the Swiss CVDCrC-TiC coated 440C balls at several times the normally used bearing load, with outstanding gyro performance. Moreover, the excellent, high precision geometry of the hardcoated balls and the outstanding adhesion and surface finish of the CVD hardcoat show great promise not only for the forthcoming, solid lubricated bearing tests but also for the immediate upgrading of conventional, oil lubricated bearing technology by the use of hardcoated bearings. On the other hand, ion-sputtered TiC thin films delaminated from gyro bearing surfaces immediately after coating, due to fundamental and general processing problems.
- 3) We identified reactive sputtering of selected hardcoats (e.g., TiN) as the next best hardcoating process to CVD in terms of adhesion. It was further stated that reactive sputtering of selected hardcoats could be made cost effective to eliminate the overtempering problem of the CVD process and the resultant attrition due to bearing distortion. Room temperature, rolling element bearing-like work by Georgia Institute of Technology (GIT) tribologists did indeed show that less than 1  $\mu$ m thick, reactively sputtered TiN film remained adherent on a 52100, oil lubricated steel ball for over one million revolutions, at Hertzian stresses over 180 kpsi.
4. In spite of the fact that the feasibility study here heavily emphasizes an operational, solid lubricated gyro bearing and will only have time to briefly look at the possibility of building a predictably operating, 5000°F turbine engine bearing-like specimen, we recognized the need of proper preparation for designing a real (1000°F+) turbine engine bearing. The theoretical portion of this problem began to be solved by bringing Williams Research Corporation, SKF, Hughes and AFWAL technologists together for thermal modeling of the bearing sections of, first, the existing F107 cruise missile engine, then the

advanced version(s) now on the drawing boards. Practical work has started by identifying the fundamentals of the Westinghouse compact, initiating research into synthesis, characterization and deposition of high temperature lubricants and formulating a hypothesis (the PLR concept) for the mechanism of high temperature bearing operation.

Clearly, this report now completes the blueprint of the work ahead, some of which we would have liked to see completed already. However, notwithstanding the good technical cooperation with team members, funding transfer inertia leads to delays in subcontracting due mainly to the unreasonable amount of paperwork required. This is inherent in the current, government dictated procurement process and needs to be changed.

We must have more control over hardcoating activities, substantiating our previously forecasted need for a central CVD/sputtering/ion-plating laboratory. All forthcoming program efforts, both during the remainder of this fiscal year and the follow-on portion, must be closely correlated with current plans for improved versions of the cruise missile engine and with related technologies. Bearing hardcoating science is an integral part of the design upgrade.

Finally, it must be stated here in the strongest possible terms that we are continually feeling the pressure of technical need before the fundamentals governing the solution of that need are determined. The area of advanced tribology we have recently begun to explore has been neglected for so long that the temptation for demanding short-term breakthroughs is almost overwhelming. In spite of this, it is this program manager's intention to strike a reasonable balance between an orderly, scientific approach to the solution of long-standing problems and acceleration of work to produce useful hardware as soon as practicable.

## REFERENCES

1. Gardos, M. N., "Solid Lubricated Rolling Element Bearings-Semianual Status Report No. 1", DARPA Order No. 3576, AFWAL Contract No. F33615-78-C-5196, Hughes Aircraft Company Report No. FR-79-76-595, 15 February 1979.
2. Gardos, M. N., "Solid Lubricated Rolling Element Bearings-Semiannual Status Report No. 2," DARPA Order No. 3576, AFWAL Contract No. F33615-78-C-5196, Hughes Aircraft Company Report No. FR-79-76-1041, 15 August 1979.
3. Brown, P. F. and Potts, J. R., "Evaluation of Powder Processed Turbine Engine Ball Bearings", AFAPL-TR-77-26, United Technologies Corporation, Pratt & Whitney Aircraft Group, West Palm Beach, Florida, 30 June 1977.
4. Riegert, R. P., "Sputtered Coatings for Gas Bearing Applications", AFML-TR-78-192, Technology of Materials, Incorporated, Santa Barbara, California, December 1978.
5. Hughes Process (HP) 7-31, "Radio Frequency Sputtering of Molybdenum Disulfide to Metallic Bearing Surfaces".
6. Gardos, M. N. and Bohner, J. J., "Self-Lubricating Composite Bearing Materials-Part II: Corrosion Preventive Solid Lubrication of the ASALM Missile Hydraulic Actuator Bearings", AFML-TR-4091, Part II (Final Report), Hughes Aircraft Company, Culver City, California, October 1979.
7. Zega, B., and Talmor, Y., "Information Note on the Battelle Geneva High-Rate Physical Deposition Method and Resulting Coating", Battelle Memorial Institute, Geneva, Switzerland, 1978 (also see MCIC Current Awareness Bulletin, Issue No. 66, Sept. 28, 1979, p. 4).
8. Gardos, M. N., "Quality Control of Sputtered MoS<sub>2</sub> Films", Lub. Eng., 32, 436 (1976).
9. Yao, S. K., "Theoretical Model of Thin Film Deposition Profile with Shadow Effect", J. Appl. Phys., 50, 3390 (1979).
10. Zeller, C. et al, "Contactless Technique for the Measurement of Electrical Resistivity in Anisotropic Materials", Rev. Sci. Instrum., 50, 602, (1979).
11. Gardos, M. N. and Castillo, A. A., "Self-Lubricating Composite Bearing Materials," AFML-TR-77-69, Interim Summary Report, Contract No. F33615-76-C-5082, Hughes Aircraft Company, May 1977.

12. Gardos, M. N. and Castillo, A. A., "Self-Lubricating Composite Bearing Materials - Part I: Development of a High Load, High Temperature, Self-Lubricating Composite", AFML-TR-4091, Part I, (Final Report), Hughes Aircraft Company, August 1979.
13. Kiparisov, S. S. et al Moskovskii Institut Stali i Splavov (Moscow Institute of Steels and Alloys) Moscow, U.S.S.R. "Investigation of the Structure and Properties of a WSe<sub>2</sub>-Based Self-Lubricating Material", Poroshkovaia Metallurgiia (Powder Metallurgy), 185, (N.), 5, 88 (1978).
14. Boes, D. J., "Unique Solid Lubricating Materials for High Temperature-Air Applications", ASLE Trans. 10, 19 (1967).
15. Boes, D. J. and Chamberlain, B., "Chemical Interactions Involved in the Formation of Oxidation-Resistant Solid Lubricant Composites", ASLE Trans. 11, 131 (1968).
16. Yu, S. C., Spain, I. L. and Skelton, E. F., "Polymorphism and the Crystal Structures of InSb at Elevated Temperature and Pressure," J. Appl. Phys. 49, 4741 (1978).
17. Jones, J. R. and Gardos, M. N., "Transfer Film Formation by Lubricative Composites", Proc. 2nd Int. Conf. on Solid Lubrication, 24-27 August, 1971, Denver, Colorado, ASLE SP-3, pp. 185-197.
18. Sato, Y. and Akimoto, S., "Hydrostatic Compression of Four Corundum-type Compounds:  $\alpha$ -Al<sub>2</sub>O<sub>3</sub>, V<sub>2</sub>O<sub>3</sub>, C<sub>2</sub>O<sub>3</sub> and  $\alpha$ -Fe<sub>2</sub>O<sub>3</sub>", J. Appl. Phys., 50, 5285 (1979).
19. Clarke, P., "The Research S-Gun", Semiconductor International, June 1979.
20. Lamont, L. T., "Thickness Uniformity - Thin Film Notebook, Chapter 20", Varian Vacuum Views, May, 1973.
21. Gardos, M. N., and Preston, D. F., "A Ball Bearing Simulator - A Tool for Accelerated Testing of Self-Lubricated Bearings", ASLE Trans., 20, 133 (1977).
22. Hubbell, F. N., "Chemically Deposited Composites - A New Generation of Electroless Coatings", Plating and Surface Finishing, 65, 58 (1978).
23. Tsuya, Y. et al "A Study of Some Metal - Base Self-Lubricating Composites Containing Tungsten Disulfide", Lub. Eng., 29, 498 (1973).
24. Tsuya, Y. et al "Codeposited Composite Metal-Graphite Fluoride Platings", ASLE Trans., 17, 229 (1974).

25. Borodin, I. N., "Self-lubricating Nickel Coatings Containing Oxides, Carbides and Borides", Poroshkovaya Metallurgiya (Powder Metallurgy), No. 2 (194), 51 (1979).
26. Grewal, M. S. et al "Amorphous to Crystalline Transformation in Bulk Electroless Nickel by Differential Scanning Calorimetry," Thermochemica Acta, 14, 25 (1976).
27. Anon., "Hardness of Electroless Nickel/Phosphorous Coatings", U. S. Army Material Development and Readiness Command Manufacturing Technology Note NTN-78/0397, ST4, 161-172, (Filing Code: 71E-007), March 1978.
28. Graham, A. H. et al "The Structure and Mechanical Properties of Electroless Nickel", J. Electrochem. Soc., 112, 401 (1965).
29. Gupta, K. et al "Oxidation Characteristics of Some Nickel Alloy Films in Air and Water Vapor", J. Electrochem. Soc.: Solid State Science and Technology, p. 118, January 1974.
30. Olson, R. R., "Mass Effects of Angular Distribution of Sputtered Atoms", J. Appl. Phys. 50, 3678 (1979).
31. Eltoukhy, A. N. and Greene, J. E., "Compositional Modulated Sputtered InSb/GaSb Superlattices: Crystal Growth and Interlayer Diffusion", J. Appl. Phys., 50, 505 (1979).
32. Brenner, A. et al, "Electrodeposition of Alloys of Phosphorus with Nickel and Cobalt", J. Res. of NBS, 44, 109 (1950).
33. Liu, C. T. and Inouye, H., "Control of Ordered Structure and Ductility of (Fe, Co, Ni)<sub>3</sub>V Alloys", Met. Trans. A., 10A, 1515 (1979).
34. Bair, S. and Winer, W. O., "Shear Strength Measurements of Lubricants at High Pressure", ASME J. Lub. Tech. 101, 251 (1979).
35. Ward, W. and Phillips, J. M., "Calculated Lamellar Binding, I: Van der Waals Bonding in Talc and Pyrophyllite", Surface Sci., 25, 379 (1971).
36. Dayton, R. D., and Sheets, M. A., "Evaluation of Grooved Solid Lubricated Bearings", AFAPL-TR-75-76, February 1976.
37. Boes, D. J., "Development of Light Weight Solid Lubricated Bearing Retainers," AFAPL-TR-78-72, Westinghouse R & D Center, Pittsburgh, Pennsylvania, September 1978.
38. Lin, D. S. et al, "The Effects of Elevated Ambient Temperatures on the Friction and Wear Behavior of Some Commercial Nickel Base Alloys", ASLE Trans., 17, 29 (1974).  
A

39. Wu, L. C. et al, in "Wear of Materials", edited by W. A. Glaser, K. C. Ludema and S. K. Rhee (ASME, New York, 1977).
40. Wu, L. C., Ph.D. Thesis, University of Illinois, 1979.
41. Wu, L. C. and Greene, J. E., Mechanisms of the Reactive and Chemical-Sputter Deposition of  $TiO_2$  from Ti and TiC Targets in Mixed Ar + O<sub>2</sub> Discharges", J. Appl. Phys., 50, 4966 (1979).
42. Greene, J. E. and Zilko, J. L., "The Nature of the Transition Region Formed Between DC-Biased, RF-Sputtered TiC Films and Steel Substrates", Surf. Sci., 72, 109 (1978).
43. Brainard, W. A. et al, "Adherence of Sputtered Titanium Carbides," NASA TM 79117, 1979.
44. Personal Communications with Mr. J. J. Murphy, The Barden Corporation, Danbury, Connecticut, 26 December 1979.
45. Bradley, L. E. and Sites, J. R., "Silicon Nitride Layers on Gallium Arsenide by Low Energy Ion Beam Sputtering", Report SF-14 (AD A061652), Colorado State University, Fort Collins, Colorado, Contract No. N00014-76-C-0976, 1 October 1978.
46. Grace, W., "Survivability of Silicon Nitride Bearing", PWA-FR-11012, Pratt and Whitney Aircraft Group, West Palm Beach, Florida, Contract N00140-77-C-0974, December 1978.
47. Scilingo, A. A., "Manufacturing Methods for Ceramic Bearings," Sixth Quarterly Report (15 August 1979 through 15 November 1979), Report No. R-358-7-6, SKF Technology Services; SKF Industries, Inc., King of Prussia, Pennsylvania, Contract F 33615-78-C-5010, November 15, 1979.
48. Paxton, R. R. et al, "Performance of Siliconized Graphite as a Mating Face in Mechanical Seals", Lub. Eng., 33, 650 (1977).

## APPENDIX A

BAGINSKI, W. A.  
"DEVELOPMENT OF SOLID LUBRICATED GYRO BEARINGS"  
R&D Status Report No 13, Document No. 404413,  
Hughes P.O 04-493431-F35,  
Litton Guidance and Control Systems,  
Woodland Hills, California,  
January 1980.

**DEVELOPMENT OF SOLID LUBRICATED GYRO BEARINGS**

**SEMI-ANNUAL REPORT,**

**STATUS REPORT NO. 13**

**Prepared for**

**Hughes Aircraft Company**

**Under**

**Customer Contract No. 04-493**

**Prime Contract No. F33615-78-C-5196**

**Prepared by:**

Willi A. Baginski  
Willi A. Baginski



**LITTON GUIDANCE & CONTROL SYSTEMS**  
5500 Canoga Avenue, Woodland Hills, California 91365

TABLE OF CONTENT

Paragraph	Title	Page
1.	BACKGROUND . . . . .	A-1
2.	CONCLUSIONS. . . . .	A-4
3.	SURFACE ANALYSIS OF BEARING SURFACES MACHINED BY MANUFACTURERES IN THIS COUNTRY AND ABROAD . . .	A-6
	A. INTRODUCTION . . . . .	A-6
	B. EVALUATION OF THE SURFACE INTEGRITY OF INSTRUMENT INSTRUMENT BEARING RACES AND BALLS MACHINED BY MANUFACTURER A . . . . .	A-8
	C. EVALUATION OF THE SURFACE INTEGRITY OF INSTRUMENT BEARING BALLS MACHINED BY MANUFACTURER B . . . . .	A-12
	D. EVALUATION OF THE SURFACE INTEGRITY OF TURBINE BEARINGS, RACES, BALLS AND ROLLERS MACHINED BY MANUFACTURER C . . . . .	A-13
	E. RESULTS OF THE SURFACE INTEGRITY EVALUATION OF AN M50 STEEL CYLINDRICAL ROLLER BEARING OUTER RING BY FINISHING PORTIONS OF THE STANDARD MACHINED RING BY A VARIETY OF POLISHING METHODS. . . . .	A-15
	F. EVALUATION OF THE SURFACE INTEGRITY OF A WILLIAMS RESEARCH CORPORATION TURBINE BEARING (M50-STEEL) BARDEN PART NO. M1906GX14, MACHINED BY MANUFACTURER E. . . . .	A-16
4.	METALLURIGICAL CHARACTERIZATION AND PRELIMINARY HIGH SPEED AND LIFE TESTING OF CrC-TiC COATED 440C STEEL AND TiC COATED CEMENTED TUNGSTEN CARBIDE BALLS IN BALL BEARINGS WITH UNCOATED 52100 STEEL RACES . . . . .	A-17
	A. BALL GEOMETRY. . . . .	A-18
	B. HIGH SPEED AND LIFE TEST RESULTS OF R-3 INSTRUMENT BALL BEARINGS WITH HARD METAL COATED BALLS AND UNCOATED RACES. . . . .	A-20
5.	BASELINE PROPERTY STUDY OF INSTRUMENT BALL BEARINGS COATED WITH TITANIUM CARBIDE IN COMBINATION WITH AN OVERLAY OF THE LAYER- LATTICE MOLYBDENUM DISULFIDE BY APPLYING THE DUPLEX COATING BY COLD SPUTTERING . . . . .	A-23
6.	PHASE III DEVELOPMENT PROGRAM: CHARACTERIZATION OF THE WESTINGHOUSE SOLID LUBRICANT WSe <sub>2</sub> -Ga+In FOR THE DEVELOPMENT OF ADVANCED SOLID LUBRICANTS FOR INSTRUMENT AND TURBINE BEARINGS . . . . .	A-26

## LIST OF ILLUSTRATIONS

Figure	Title	Page
22	Race 1 Unetched 3000X . . . . .	A-31
23	Race 1 Layer Etched 3000X . . . . .	A-31
24	Race 2 Unetched 1000X . . . . .	A-31
25	Race 2 Layer Etched 3000X . . . . .	A-31
26	Unetched Race No. 3 1000X . . . . .	A-32
27	Layer Etched Race No. 3 3000X . . . . .	A-32
28	Second Layer Etch Race No. 3 3000X . . . . .	A-32
29	Unetched Race No. 4 1000X . . . . .	A-33
30	First Layer Etch Race No. 4 3000X . . . . .	A-33
31	Second Layer Etch Race No. 4 3000X . . . . .	A-33
32	Unetched Race No. 5 1000X . . . . .	A-34
33	First Layer Etch Race No. 5 1000X . . . . .	A-34
34	Race No. 6 Unetched 3000X . . . . .	A-35
35	Race No. 6 First Layer Etch 1000X . . . . .	A-35
36	Race No. 6 Magnification of 35 - Notice Micro-Cracks 3000X . . . . .	A-35
37	Grade 3 Ball 3000X . . . . .	A-36
38	Grade 3 Ball First Layer Etch 1000X . . . . .	A-36
39	Grade 3 Ball Second Layer Etch 1000X . . . . .	A-36
40	Grade 3 Ball 3000X . . . . .	A-37
41	Grade 4 Ball First Layer Etch 1000X . . . . .	A-37
42	Grade 3 Ball Second Layer Etch 1000X . . . . .	A-37
43	Grade 10 Ball 3000X . . . . .	A-38
44	Grade 10 Ball First Layer Etch 1000X . . . . .	A-38
45	Grade 10 Ball Magnification of Figure 41 3000X . . . . .	A-38
43	Unetched Manufactured 2 Group 1 Balls 1000X . .	A-39
44	First Layer Etch 3000X . . . . .	A-39
45	Second Layer Etch Group 1 Balls 3000X . . . . .	A-39

**LIST OF ILLUSTRATIONS (cont)**

<b>Figure</b>	<b>Title</b>	<b>Page</b>
46	Unetched Group 5 Balls 1000X . . . . .	A-40
47	First Layer Etch Group 5 Balls 1000X . . . . .	A-40
48	Magnification of Figure 47 Group 5 Balls 3000X . . . . .	A-40
49	Specimen 1 Unetched Bearing Surfaces Damaged by The Machining Process 1000X . . . . .	A-41
49a	Specimen 1 One Layer Etch Bearing Surfaces Damaged by The Machining Process 1000X . . . . .	A-41
50	Specimen 2 Unetched Bearing Surfaces Damaged by The Machining Process 1000X . . . . .	A-42
50a	Specimen 2 One Layer Etch Bearing Surfaces Damaged by The Machining Process 1000X . . . . .	A-42
51	Specimen 3 Unetched Bearing Surfaces Damaged by The Machining Process 1000X . . . . .	A-43
51a	Specimen 3 One Layer Etch Bearing Surfaces Damaged by The Machining Process 1000X . . . . .	A-43
52	Specimen 4 Unetched Bearing Surfaces Damaged by The Machining Process 1000X . . . . .	A-44
52a	Specimen 4 One Layer Etch Bearing Surfaces Damaged by The Machining Process 1000X . . . . .	A-44
53	Specimen 5 Unetched Bearing Surfaces Damaged by The Machining Process 1000X . . . . .	A-45
53a	Specimen 5 One Layer Etch Bearing Surfaces Damaged by The Machining Process 1000X . . . . .	A-45
54	Specimen 6 Unetched Bearing Surfaces Damaged by The Machining Process 1000X . . . . .	A-46
54a	Specimen 6 One Layer Etch Bearing Surfaces Damaged by The Machining Process 500X . . . . .	A-46
54b	Magnification of Figure 6a 1000X . . . . .	A-46
55	Roller In As Received Condition Bearing Surfaces Damaged by The Machining Process 3000X . . . . .	A-47
56	Ball In As Received Condition Bearing Surfaces Damaged by The Machining Process 3000X . . . . .	A-47
56a	Ball After First Layer Etch Bearing Surfaces Damaged by The Machining Process 3000X . . . . .	A-47

**LIST OF ILLUSTRATIONS (cont)**

<b>Figure</b>	<b>Title</b>	<b>Page</b>
57	Bearing Surface Damaged by The Machining Process . . . . .	A-48
58	Bearing Surface Damaged by The Machining Process . . . . .	A-48
59	Bearing Surface Damaged by The Machining Process . . . . .	A-49
60	Bearing Surface Damaged by The Machining Process . . . . .	A-49
61	Bearing Surface Damaged by The Machining Process . . . . .	A-49
62	Ball - Williams Research Corp. Condition: Unetched 3000X . . . . .	A-50
63	Ball - Williams Research Corp. Condition: One Layer Etch 3000X . . . . .	A-50
64	Inner Race - Williams Research Corp. Condition: Unetched 3000X . . . . .	A-50
65	Inner Race - Williams Research Corp. Condition: One Layer Etch 3000X . . . . .	A-50
66	Bearing Surface Damaged by The Machining Process 200X . . . . .	A-51
67	Bearing Surface Damaged by The Machining Process 3000X . . . . .	A-51
68	Refractory Hard Metal Coating Applied on Steel and Cemented Tungsten Carbide R-3 Balls by The CVD Process . . . . .	A-52
69	Refractory Hard Metal Coating Applied on Steel and Cemented Tungsten Carbide R-3 Balls by The CVD Process . . . . .	A-52
70	Refractory Hard Metal Coating Applied on Steel and Cemented Tungsten Carbide R-3 Balls by The CVD Process . . . . .	A-52
71	Refractory Hard Metal Coating Applied on Steel and Cemented Tungsten Carbide R-3 Balls by The CVD Process . . . . .	A-52

**LIST OF ILLUSTRATIONS (cont)**

<b>Figure</b>	<b>Title</b>	<b>Page</b>
72	Rockwell Hardness and Chemical Analysis of CrC-TiC Refractory Hard Metal Coated Steel Balls . . . . .	A-53
73	Rockwell Hardness and Chemical Analysis of CrC-TiC Refractory Hard Metal Coated Steel Balls .. . . . .	A-53
74	Ball Geometry . . . . .	A-54
75	CrC-TiC Coated Steel Ball Unetched - Group 6 1000X . . . . .	A-55
76	CrC-TiC Coated Steel Ball Layer Etch - 5 Minutes Notice No Impurities Along Grain Boundary - Group 6 1000X . . . . .	A-55
77	TiC Coating on Sintered Tungsten Carbide - Group 7 1000X . . . . .	A-56
78	TiC Coating on Sintered Tungsten Carbide - Group 8 1000X . . . . .	A-56
79	TiC Coating on Sintered Tungsten Carbide - Group 8 1000X . . . . .	A-57
80	TiC Coating on Sintered Tungsten Carbide - Group 8 - Etched 1000X . . . . .	A-57
81	TiC Coating on Sintered Tungsten Carbide - Group 9 1000X . . . . .	A-58
82	TiC Coating on Sintered Tungsten Carbide - Group 9 - Etched 1000X . . . . .	A-58
83	Schematic - High Speed Bearing Tester . . . . .	A-59
84	Testing Sequence of Bearings with Coated Balls. . A-60	
85	High Speed Testing Results of Uncoated R-3 52100 Steel Bearing . . . . .	A-61
86	High Speed Testing Results of 52100 Steel Bearing with 440C Steel Backs . . . . .	A-61
87	High Speed Test Results of Bearing with TiC Coated Cemented Tungsten Carbide Balls . . . . .	A-66
88	High Speed Test Results of Bearing with TiC Coated Cemented Tungsten Carbide Balls . . . . .	A-67

LIST OF ILLUSTRATIONS (cont)

Figure	Title	Page
89	High Speed Test Results of Bearing with TiC Coated Cemented Tungsten Carbide Balls . . . . .	A-68
90	Bearing 36 Ball Track 3000X . . . . .	A-69
91	Bearing 36 Near Ball Track 3000X . . . . .	A-69
92	Transition Zone Near Ball Track 1000X . . . . .	A-69
93	Transition Zone Near Ball Track 3000X . . . . .	A-69
94	In Ball Track 500X . . . . .	A-70
95	In Ball Track 1000X . . . . .	A-70
96	In Ball Track 3000X . . . . .	A-70

DEVELOPMENT OF SOLID LUBRICATED GYRO BEARINGS  
SEMI-ANNUAL STATUS REPORT NO. 13

This report summarizes Litton's work on the DARPA/Hughes Litton contract over the period from September 1st 1979 through January 31st 1980.

1. BACKGROUND

Wear is the destructive mechanism responsible for the inconsistencies in ball bearing life and reliability no matter if applied to instrument, turbine or other bearings, fabricated from presently available bearing steels. Wear resistance is not an inherent mechanical property but must be considered to be part of a tribological system.

The various system parameters of a bearing which influence wear rate are the following:

- a. Design Requirements
- b. Operating Conditions
- c. Material Properties

In recent years the empirical development of solid lubrication has begun to yield to a more fundamental approach based on the great advantages it offers in comparison to liquid lubrication. By introducing solid lubrication we leave the elegant elasto-hydrodynamic bearing and, depending on the type of solid lubricant used, enter the transition from mixed hydrodynamic to boundary lubrication. In the past the concept of the surface was generally treated with casual familiarity. The science of surface technology was delayed. Although surface topography was given considerable attention, the study of surface metallurgy is relatively new. Differences in the surfaces of bearings can originate in the mill product such as bar, rod and wire and the

machining of components. When severe enough these conditions will effect life and reliability in liquid lubricated ball bearings and lead to bearing failure. The significance is that the problems of liquid lubricated instrument ball bearing surface conditions is not relegated to this type of bearing alone but is also unacceptable for solid lubrication. In reality the carbide phase and impurities in bearing steels act as asperities. These hard particles remove material by plowing into the softer surface of the part being worn. The amount of carbides and carbide precipitation differs markedly in components of bearings because they are not made from the same heat; are subjected to different amounts of deformation to form bar-stock. Differences in heat treatment and finish machining operations further increase the inconsistency in carbide precipitation among bearing components. The finish-machining process therefore can hardly be controlled, leading to Beilby-Smear and excessive carbide precipitation. Friction and wear increase temperatures leading further to the destruction of the lubrication system.

In view of the above, boundary lubrication with solid lubricants requires that all second phases and impurities must be removed and a one-phase surface condition provided. The utilization of single phase Refractory Hard Metal coatings on steels has therefore gained great practical importance. Graded refractory hard metal coatings can now be applied in a sequence of inter-layers by the CVD process which, at the same time, permits regaining the base metal properties by heat treatment during the coating process in the CVD reactor. The coating interlayers applied develop, by diffusion, a graded wear resistant solid solution which exceeds in hardness, purity and ductility any other coating system.

Such a coating provides the one-phase surface condition which is necessary for solid lubrication to meet boundary lubrication requirements. The much disputed question whether thick coatings, in comparison to thin-film hard metal coatings, bear the load directly and do not transmit it to the substrate has been answered with the development of the graded refractory hard metal coating.

The following tasks were investigated:

- a. Surface Analysis of Bearing Surfaces Machined by Manufacturers in this country and abroad.
- b. Metallurgical Characterization of Refractory Hard Metal Coatings and High-Speed and Life Testing of CrC-TiC coated 440C Steel and TiC coated Cemented Tungsten Carbide Balls in Instrument Ball Bearings with uncoated 52100 Steel Races.
- c. Evaluation of Baseline Properties of Solid Lubricated Ball Bearings, TiC coated by Cold Sputtering.
- d. Program for the Characterization of the Westinghouse Lubricant WSe<sub>2</sub>-Ga + In for the development of advanced, similar, Solid Lubricants which can be applied by Sputter Deposition Processing.

## 2. CONCLUSIONS

A. A study of the machined surface on bearings of five major bearing manufacturers of this country and abroad revealed that the surface integrity requirements of the machined surface on bearings are disregarded or not well understood. All machined surfaces investigated were either damaged, deformed and covered with Beilby-Smear, responsible for the inconsistencies in life and reliability of bearings.

To meet todays stringent requirements of bearings for military systems a machining development program should be conducted to introduce the surface integrity approach in the bearing manufacturing industry.

B. One-phase solid solution refractory hard metal coatings applied by the CVD process should be introduced and applied on bearings operating under stringent requirements. Coatings such as the CrC-TiC refractory metal carbide improve life and reliability of the bearing and don't spall when applied by the CVD process. This process provides a graded coating by interdiffusion of the carbide layers, providing outstanding hardness and wear resistance. This coating process provides a refractory hard metal solid solution of satisfactory ductility, practically free of interstitials which can act as asperities and damage the bearing surface when applied by other process methods. None of the bearings with CrC-TiC and TiC coated balls tested failed during testing and are running at high loads.

C. A program is required for the development of solid lubricants of the Westinghouse type which can be applied by the sputtering process.

D. To overcome existing steel problems which tend to segregate and distort the bearing component by necessary heat treatments, the introduction of powder metallurgy for the production of

bearing components will be required. This will prevent early fatigue failure and reduce stress development caused by segregations of the alloying elements present in mill products produced by standard production methods. This will be required, especially for larger bearing parts, and support the application of refractory hard metal coatings for the improvement of wear resistance, life and reliability, of bearings.

E. Titanium carbide coatings for the improvement of wear resistance of bearing-components cannot be applied by the cold sputtering process. Coatings crack and peel off during storage before any testing can be conducted.

### 3. SURFACE ANALYSIS OF BEARING SURFACES MACHINED BY MANUFACTURERS IN THIS COUNTRY AND ABROAD

#### A. INTRODUCTION

The quality of a machined surface is becoming more and more important to satisfy the increasing demands of sophisticated bearing performance, their longevity and reliability for military and other commercial aerospace applications subjected to more severe conditions of stress, temperature and hostile environments. Bearing size is being reduced in response to the goal of reduced weight so that the surface condition of a bearing has an ever-increasing influence on its performance. Modern machining methods, both conventional and those which are electrically assisted, have been developed to more efficiently process the high strength bearing alloys which have evolved in recent years. The high performance bearing materials have generally become inherently more difficult to machine. Considering the nature of bearing materials requiring improved capabilities, the difficulty in machining and finishing these materials, and the sensitivity of component surfaces inherent in many operational modes to which bearings are subjected. The need for paying careful attention to the surfaces of finished bearings has been brought critically into focus. It has been recognized for a long time that grinding alters bearing surfaces and the surface layers which develop are responsible for bearing failure. In surface grinding, gentle conditions are those which keep the wheel sharp, while abusive conditions are those which promote wheel dulling. In grinding, there are four important parameters which affect gentle or abusive grinding. They are: wheel grade, wheel speed, down feed, and grinding fluid.

The surface integrity cut serves as a stress relieving cut, for removing small defects, refines the rough machining pattern and provides correct dimensional requirements. Beilby-Smear develops

when tools are dull and rub on the surface. It consists of an amorphous material containing machining fluids and lubricants and fatigues during bearing performance. The fatigued particles enter the lubricant film which increases wear and develops new defects to add to the larger defects left by the roughing pass. These lead to a reduction in bearing performance and finally bearing failure by surface fatigue.

When machining any component, it is necessary to satisfy the surface integrity requirements. Surface integrity is defined as the inherent or enhanced condition of a surface produced in a machining operation.

Although the surface integrity approach has been adopted for the production of components for critical applications in the aerospace industry to prevent their early failure, this approach has never been used by the bearing manufacturer, permitting unacceptable inconsistencies in bearing life and reliability and early bearing failure.

In the following, examples will be cited demonstrating the incapability of well known bearing manufacturers in this country and abroad to provide machined bearings which satisfy surface integrity requirements such as the absence of metallurgical alterations, excessive stresses, Beilby-Layer and other defects, to provide longevity and reliability which meet increasing military demands.

B. EVALUATION OF THE SURFACE INTEGRITY OF INSTRUMENT BEARING RACES AND BALLS MACHINED BY MANUFACTURER A.

Information on samples submitted.

A/ 52100 steel races:

N°1: IR FR2ZZTG4

- honing .
- polishing with diamond paste SF3

N°2: IR FR2ZZTG4

- honing
- polishing with aluminum oxide 1  $\mu\text{m}$  mixed in ESSO UNIVIS P12 oil

N°3: IR SP6727

- no honing
- 1st polishing with diamond paste SF 12
- 2nd polishing, suspension of diamond JKS 3  $\mu\text{m}$

B/ 440 C steel races:

N°4: IR WSP4619

- honing
- polishing: 30 s with aluminum oxide 0.04  $\mu\text{m}$  mixed in HONILO 171 oil  
30 s with dry aluminum oxide 0.04  $\mu\text{m}$

N°5: IR WX10

- honing
- polishing with aluminum oxide 1  $\mu\text{m}$  mixed in ESSO UNIVIS P12 oil

N°6: IR WX10

- honing
- polishing with diamond paste SF3

C/ 52100 steel balls:

Balls grades 3 and 10, manufacturing process not revealed.

#### Evaluation of Surface Finished 52100 Steel Races (Manufacturer A)

Excessive segregated steel was used for races No. 1 and 2, surface finished with polishing methods No. 1 and 2. This is shown in electronmicrographs Figures 23 and 25, illustrating the well known ghostline pattern typical of segregated 52100 steel.

Cluster development of carbides between ghostlines is visible. This type of structure tends to lead to bearing failure by plowing into the opposing component surface, especially when of the standard microstructure of 52100 steel in which small amounts of carbides are uniformly distributed in the martensitic matrix.

The finished unetched surfaces shown in Figures 22 and 24 appear to be acceptable. However, smoothness does not indicate a good surface when segregations and excessive carbide precipitations are present as shown after the first layer etch in Figures 23 and 25. Beilby-Layer did not develop. Because of the presence of segregations an evaluation of polishing methods No. 1 and 2 is not possible.

Polishing method No. 3 produced an acceptable surface finish on Race No. 3 shown in the unetched condition in Figure 26. Beilby-Layer is visible on the surface after the first layer etch as illustrated in Figure 27. After the second layer etch Beilby-Layer is no longer present, as shown in Figure 28. However, a slight amount of excessive carbide precipitation is visible, indicating that the surface temperature during polishing reached the precipitation temperature of the carbides. Beilby-Layer development and excessive carbide precipitation seem to develop when the finishing process is extended over a too long time permitting temperature development in the surface.

#### Evaluation of Surface Finished 440C Steel Races (Manufacturer A)

The unetched surface of Race 4, finished by polishing method No. 4 illustrated in Figure 29, shows an unacceptable surface

finish with deep scratches, carbide pullout and other polishing defects. After the first layer etch a smooth surface covered with Beilby-Layer, covering the carbides which appear as dark inclusions, is visible. This is shown in Figure 30. Figure 31 demonstrates the surface condition of the same specimen after the second layer etch. Beilby-Layer has been partly removed. In the martensitic matrix carbides and Beilby-Smear are visible. This surface will not provide reliable performance for instrument ball bearings.

The surface finish of Race No. 5 finish polished with Method No. 5 is shown in the unetched condition in Figure 32 and in the layer etched condition in Figure No. 33. Deep scratches and carbide pullout are visible in the unetched microstructure of Figure 32 and excessive carbide precipitation in the microstructure of Figure No. 33. The first layer etch indicates that finishing Method No. 5 does not provide the surface finish required for the good performance of instrument ball bearings.

The surface condition of Race No. 6 surface finished with Method No. 6 is shown in the unetched condition in Figure No. 34 and in the layer etched condition in Figure No. 35. Figure No. 36 is a magnification of Figure No. 35.

The surface finish of Race No. 6 in Figure 34 appears to be smeared, also indicating surface defects caused by the finish polishing process. The surface of Race No. 6 in Figure 36 illustrates excessive carbide precipitation. Along the edge of the carbides remnants of Beilby-Smear are left. This surface condition is not acceptable for instrument ball bearings when reliable performance of a bearing is expected.

Surface Condition of Balls Grades 3 and 10 Fabricated of 52100 Steel (Manufacturer A)

Figures 37 through 39 illustrate the surface condition of a Grade 3 ball unetched in Figure 37, after the first layer etch in Figure 38 and the second layer etch in Figure 39. In the unetched

condition the surface appears smooth and acceptable. However after the first layer etch, microsegregations covered with a thin layer of Beilby-Smear, especially over the ghostline pattern. In addition to this, excessive carbide precipitation is visible.

After the second layer etch Beilby-Smear has been removed. However, microsegregations and additional excessive carbide precipitation is visible in the microstructure of the surface. The microstructure of the Grade 3 balls is unacceptable for instrument ball bearings.

The microstructure of the surface of the Grade 10 ball is shown in the unetched condition in Figure 40 and after the first layer etch in Figure 41. Figure 42 is a magnification of Figure 41. The microstructure in the surface does not present the normal microstructure of 52100 steel. However, the Grade 10 balls are acceptable because only limited excessive carbide precipitation is present.

C. EVALUATION OF THE SURFACE INTEGRITY OF INSTRUMENT BEARING  
BALLS MACHINED BY MANUFACTURER B

Two groups of 440C balls for the R-3 instrument ball bearing were submitted. Figures 43 through 45 present the surface microstructure of balls of Group I. The unetched surface in Figure 43 shows porosity in the surface indicating a porous layer of Beilby-Smear. Figure 44 illustrates a ball surface after the first layer etch illustrating the presence of Beilby-Layer which developed during excessive process finishing operations. The surface condition of the same ball is shown in Figure 45. Beilby-Smear has been removed. The excessive finishing operation also left a damaged microstructure in the surface of the ball.

Figures 46 through 48 illustrate the microstructure of a 440 C ball of Group V. The unetched surface shown in Figure 46 appears smooth and defect free. Beilby-Smear is not present, as shown after the first layer etch of the ball shown in Figure 47 and at higher magnification in Figure 48. However, an unacceptable amount of carbide precipitation is present which leads to the destruction of bearing surfaces during bearing operations by carbide pull out caused by the loss of strength of the martensitic matrix by excessive carbide development. The surface condition of both ball groups does not meet surface integrity requirements.

D. EVALUATION OF THE SURFACE INTEGRITY OF TURBINE BEARINGS,  
RACES, BALLS AND ROLLERS MACHINED BY MANUFACTURER C

Figures 49 through 54 illustrate the unetched surface of the six race samples submitted for evaluation. All surfaces are similar in appearance at the high magnification used. They are covered with Beilby-Smear which developed during the finishing pass. The layer covers also the deep scratches left in the surface by the last roughing pass. The finishing pass, also called the surface integrity cut, should not be used to remove deep scratches or deep defects of the roughing pass.

The surface integrity requirements are not met by the finishing pass used for the six experimental samples because of Beilby-Smear development.

Figures 49a through 54a illustrate the surface condition of the race tracts after the first layer etch. They indicate the surface condition developed by the roughing pass. Remnants of Beilby-Smear are left in the surface of all samples, in addition the roughing tool did not cut but was tearing, as indicated by deep scratches covered with secondary smear and pull out of the secondary carbides. The surface is too rough and lends itself to Beilby-Smear development. This condition can be corrected when sharp tools are used and the chip removal rate of the last roughing pass is corrected to meet the surface requirements of the finishing pass or surface integrity cut.

The surface of rollers is illustrated in Figure 55, for the balls in the unetched condition in Figure 56 and Figure 56a after the first layer etch. Beilby-Smear could not be removed by production etching the rollers. The lapping procedure used for the balls developed a thick Beilby-Smear and is shown after the first layer etch in Figure 56a.

Manufacturers tend to extend the finishing pass for bearings because the Beilby-Smear provides a shiny smooth surface and covers defects when machining processes are not properly conducted; or, for economical reasons rough grinding steps are reduced and leave a too-rough surface which cannot be properly finished by the finish grinding pass.

Surface integrity requirements were not met by this manufacturer because of the presence of deep scratches and Beilby-Layer which lead to the destruction of bearing surfaces by surface fatigue.

E. RESULTS OF THE SURFACE INTEGRITY EVALUATION OF AN M50 STEEL CYLINDRICAL ROLLER BEARING OUTER RING BY FINISHING PORTIONS OF THE STANDARD MACHINED RING BY A VARIETY OF POLISHING METHODS.

Of special interest were 4 surface finishing methods Manufacturer D used to improve the surface finish of a standard machined outer race surface.

The finishing methods were the following:

- a. As ground.
- b. As ground and etched.
- c. Ground and emery polished.
- d. Ground and diamond polished.
- e. Ground, emery polished and Nital etched.

Of great disadvantage was that portions of the outer race surface were surface finished by the above shown methods. This prevented a distinct separation of the finishing methods used. The standard machined surface on which the finishing methods were investigated was too rough and heavily surface damaged. Because of this the damaged surface was only partly affected by the finishing methods used. This is shown in Figures 57 through 61. All electron micrographs show the damaged and torn structure of the finish grinding pass used, and adjacent to it bands of the finish polishing pass consisting of Beilby-Smear. The outer race ring presents one of the worst machined surfaces ever observed on a turbine bearing.

F. EVALUATION OF THE SURFACE INTEGRITY OF A WILLIAMS RESEARCH CORPORATION TURBINE BEARING (M50-STEEL) BAR DEN PART NO. M1906GX14, MACHINED BY MANUFACTURER E.

Figure 62 illustrates the finish machined ball surface in the unetched condition while Figure 63 illustrates the machined surface of the ball after the first layer etch.

Figure 64 illustrates the finish machined surface of the inner race of the bearing in the unetched condition while Figure 65 illustrates the machined surface of the inner race after the first layer etch.

Although the microstructure of ball and race surfaces indicate slight deformation of the martensitic structure, surface integrity requirements were met by the machining process used as is indicated by the absence of surface defects and Beilby-Smear.

The same manufacturer was under contract to machine several hundred flat specimens with a surface finish as required for gyro bearings. Surface integrity requirements were not achieved, as shown in Figure 66 illustrating a flat specimen in the unetched condition and Figure 67 the surface structure of a flat specimen after the first layer etch. The layer etched surface in Figure 67 illustrates Beilby-Smear along the numerous scratches developed by the finish machining process used to finish the surface of the flat specimens.

4. METALLURGICAL CHARACTERIZATION AND PRELIMINARY HIGH SPEED AND LIFE TESTING OF CrC-TiC COATED 440C STEEL and TiC COATED CEMENTED TUNGSTEN CARBIDE BALLS IN BALL BEARINGS WITH UNCOATED 52100 STEEL RACES.

The Swiss laboratory LSRH coated, for the program, 440C steel balls with the CrC-TiC coating and cemented tungsten-carbide balls with the TiC coating for tests in R-3 instrument ball bearings with uncoated 52100 steel races. The refractory hard metal coatings were applied by the CVD Process. A thorough metallurgical investigation of the coated balls was conducted by investigating the diffusion-bond at the interface coating-substrate for cracks in the coating, its hardness and chemical composition over the cross section of the coating, ball geometry and surface finish of the machined coated balls.

Figures 68 through 71 illustrate cross sectioned coated balls, machined after coating.

Figure 68 presenting the CrC-TiC coated steel ball indicates that no second phase at the interface developed. However, the TiC coated cemented tungsten-carbide balls show eta phase development at the interface which can be observed in Figures 69 through 71. Eta phase development, kept to a minimum thickness, did not develop embrittlement at the interface.

The coating on all balls was properly diffused at the substrate-coating interface, no defects or cracks can be observed.

Figure 72

Illustrates the determination of Knoop Hardness over the cross section of a coating in the as coated condition. Brown collar on the surface of the coating is gold.

Note that the hardness of the coating exceeds that of TiC which is 3000-3200 Knoop at 25g. load. Hardness gradually decreased in the diffused CrC-TiC coating to the interface coating substrate,



caused by the intermittent application of CrC and TiC by Chemical Vapor Deposition on the steel. This approach permits adhesion by diffusion into the substrate, and ductility and toughness by complex solid solution development. The coating does not spall, chip or crack and can be machined to final dimensions.

Figure 73

Illustrates analysis of the coating by Auger electron spectrographic analysis conducted for the first time over a cross section of a coating. Coating is 5 micrometers thick. The analysis of the coating illustrates the gradual decrease of CrC to the surface and that of TiC from the surface to the interface of the coating. This provides its non spalling and non cracking capabilities.

A. BALL GEOMETRY

Figure 74 presents the geometry of the balls. Roundness was within one millions of an inch, a remarkable accuracy when considering that these balls were machined in production lots.

Surface Integrity of Machined Hard Metal Coated Balls

Figures 75-76 illustrate the surface of a CrC-TiC coated 440C steel ball as received and as layer etched in Villela etch for 5 minutes. A very weak, hardly visible grain boundary network appeared after layer etching, shown in Figure 76. No inclusions or impurities along grain-boundaries and in the grain structure were observed. The surfaces of all balls (unetched and etched) appeared clean smooth defect free and without scratches. The surface finish appeared to be one microinch.

Figures 77 through 82

Figures 77 through 82 illustrate the surface conditions of the titanium carbide coated tungsten carbide balls. These balls were of the same high quality in the unetched and layer etched



condition as the CrC-TiC coated steel balls. Figures 77-78 illustrate the Group 7, Figures 79-80 the Group 8 and Figures 81-82 the Group 9 balls.

Hard Metal coated bearing balls don't present a surface integrity problem and because of their high hardness can easily be machined without Beilby-Smear development.

B. HIGH SPEED AND LIFE TEST RESULTS OF R-3 INSTRUMENT BALL BEARINGS WITH HARD METAL COATED BALLS AND UNCOATED RACES

High Speed Testing

Figure 83 illustrates a schematic drawing of the Litton High Speed Tester used for the testing of gyro bearings on this program.

The tests so far conducted were planned to start with benign conditions and increase stress progressively to find out just how tough the various improved components are.

Bearing tests were started using liquid lubrication, standard 52100 races and conventional porous phenolic retainers. This permitted us to evaluate the ability of the coatings to withstand the high cycle rate compressive stresses developed in the hertzian contacts of ball bearings. Secondly, it permitted evaluation in conditions otherwise identical to gyro bearing tests, for which a large data base exists.

Since the coated balls were received only a few months ago, time was too short for a complete evaluation. Coated races are scheduled to be received in the near future after which they will be similarly tested in combinations.

Each of the coated-ball tests was first run at the standard two pound load. In each case they ran exceptionally well and the loads were increased progressively. Behavior, torque levels and stability were judged very good and loads which are very high for gyro bearings were introduced quite early. Figure 84 shows the run time/load profile.

Subsequent to the first 24 hours running, the first bearing (TiC coated) was inspected, while the second was on test, and found to be in excellent condition, confirming the test data. It was put back on test and loads increased ultimately to ten pounds for a few hours.

High speed test results are shown in Figures 85 through 89.

Figure 85 illustrates those for a standard uncoated 52100 steel ball bearing.

Figure 86 those for a bearing with uncoated 440C steel balls and 52100 races.

Figure 87 those for a bearing with CrC-TiC coated 440C steel balls and 52100 steel races.

Figure 88 those for a bearing with TiC coated cemented tungsten-carbide balls and 52100 steel races.

Figure 89 is a bearing with TiC coated cemented tungsten-carbide balls with 52100 steel races.

After testing, all coated-ball bearings were disassembled and inspected and were found to be in nearly perfect condition. Only the faintest ghost of a wear-track could be seen in the tracks; no detectable indication of running could be seen on the balls.

The uncoated 440C and 52100 balls fared less well, exhibiting distinct, but not serious, wear bands in both races and balls. The prognosis is for much earlier failure than for the coated-ball combinations.

#### C. LIFE TESTING

Three life tests are in progress and will shortly exceed a testing time of 1000 hours. They are conducted with bearing spindles and gyro motors in gyro housings. The bearings on spindles used consist of CrC-TiC coated steel balls in 52100 steel races and TiC coated, cemented carbide balls in 52100 steel races. Test runs are conducted at a 6 pound load, 22500 RPM. Bearings are liquid lubricated. The life tests continue to run with no detectable inconsistencies.

At the present time solid lubricant hard metal coated bearings are being prepared for testing.

The successful test results with hard metal coated balls indicate that the objective of the program, the introduction of "Solid Lubrication" when hard metal coated bearing components are used, can be achieved.

5. BASELINE PROPERTY STUDY OF INSTRUMENT BALL BEARINGS COATED WITH TITANIUM CARBIDE IN COMBINATION WITH AN OVERLAY OF THE LAYER-LATTICE MOLYBDENUM DISULFIDE BY APPLYING THE DUPLEX COATING BY COLD SPUTTERING

Baseline properties were established with instrument ball bearing components cold sputtered with the duplex coating system, Titanium carbide-Molybdenum disulfide. This program was conducted to prove that the same coating system when applied by CVD (chemical vapor deposition) provides far superior bonding properties when the TiC is diffused into the bearing surface than when applied by cold sputtering which provides only adhesive properties.

Instrument ball bearings were coated with the above coating system by applying the Titanium Carbide in an advanced, powerful magnetron-system now commonly used for the application of cold sputtered coatings. Although the coating system provides satisfactory adhesion on beryllium alloy substrates for gas bearings it does not provide diffusion bonded coatings on steel surfaces for ball bearings, which have to perform under much higher loads.

The good adhesion of TiC on instrument-beryllium can be attributed to the high oxygen content of the substrate material. The energy of adhesion is proposed to be closely related to the change in free energy of oxide formation. Thus, the film adhesion is high in those cases where the transition region of suitable oxides and suboxides of the film or the substrate at the interface exists. Any load increase exceeding the load strength of the oxide film can lead to coating failure.

It is now well understood that utmost adhesion can be achieved on oxidized surfaces such as the instrument beryllium components for gas bearings. However, the high strength of coatings required at the interface coating-substrate for ball bearings operating under higher loads can only be achieved by a diffusion coating

process which requires oxide free surfaces for the application of hard metal coatings.

Increasing the impingement force of atom ions by excessive voltage to the magnatron gun for cold sputtering will only lead to stress development and high surface temperatures producing excessive carbide precipitation in the surface of the substrate. Both stress development and carbide precipitation lead to spalling of the applied coating during environmental condition changes and operation of the bearing. This is shown in Figures 91 through 97. Peeling of cold-sputtered coatings occurred before testing of bearings.

Figure 90

Figure 90 illustrates the unetched coated race track of an inner race of 52100 steel. It is probable that the deep scratches visible in the surface are cracks in the TiC thin film.

Figure 91

Figure 91 illustrates the microstructure near the coated race track. Excessive carbide precipitation and Beilby-Smear are visible. This structure indicates a highly stressed surface.

Figure 92

Figure 92 illustrates the transition zone between the TiC coated race track and uncoated area of the inner race surface. Remnants of the peeled coating are visible in the transition zone.

Figure 93

Figure 93 is a magnification of figure 92 illustrating Beilby-Smear and excessive carbide precipitates in a highly stressed surface.

Figure 94

Figure 94 shows the coated ball track of the inner race. The coating peeled in the direction of the machining which acted as stress raiser. Excessive carbide precipitation and Beilby-Smear are visible in the substrate surface where the coating peeled off. It is possible that heat development during the sputtering process contributed to excessive carbide precipitation.

Figures 95 and 96

Figures 95 and 96 illustrate the microstructure of the coating demonstrating the presence of excessive porosity. These structural defects leave the coating in a high stressed condition.

It is recommended to discontinue this program.



6. PHASE III DEVELOPMENT PROGRAM: CHARACTERIZATION OF THE WESTINGHOUSE SOLID LUBRICANT WSe<sub>2</sub>-Ga+In FOR THE DEVELOPMENT OF ADVANCED SOLID LUBRICANTS FOR INSTRUMENT AND TURBINE BEARINGS

A Phase III task will be conducted to characterize the Westinghouse solid lubricant WSe<sub>2</sub>-Ga+In in order that needed improvements in reproducibility and processing by sputtering, as a deposition process, may be achieved.

We will attempt to identify crystal structure, phases and transformations which occur at various temperatures and pressures the material undergoes in an operating bearing environment. The program will provide information for improving the transition chalcogenides by modification with diverse elements forming amalgam compounds. Ga and In additions have imparted remarkable lubricative properties to WSe<sub>2</sub>. This lubricant is oxidation resistant in oxidizing atmospheres up to 1400°F and self healing. It is anticipated that it's self healing characteristics and lubrication capabilities depend on the development of a thin film which develops in the surface of the lubricant. Special emphasis will be placed on the identification of composition and structure of the surface film.

The characterization of the Westinghouse lubricant is a necessity for the development of compositions which can be applied by sputtering as a deposition process.

Phase III Tasks

Task A FV 1980

Tables X and XI outline the test plan which will be conducted on as-received and on heat-treated specimens of the Westinghouse type WSe<sub>2</sub> lubricant. The identification of phases and of the thin film which provides self-healing, self-lubricating and

oxidation resistance to the lubricant is an objective. Determination of the lubricant phases will be conducted for the conditions shown, including heat treatment in both vacuum and air, in Table X. Test will be performed by Electron Microscopy, AUGER-ESCA a structural analysis by x-ray.

Task B FY 1980

Samples prepared as in Task A will be tested at temperatures and pressures simulating high-temperature bearing operating conditions. Pressures and temperatures will be produced in a diamond high-pressure cell sited at NRL, Arlington, Virginia. Temperatures to 1000°F and pressures of 250,000 psi will be applied to the samples listed in Table XI while x-ray diffractograms are made for the study of phase changes.

The attached Tables illustrate the approach to be taken for the characterization of the Westinghouse lubricant.

TABLE X. PHASE III TASK A  
Determination of Phases in  $\text{WSe}_2 + \text{Ga} +$  In Lubricant by Electronmicroscopy,  
Auger-Esca and x-ray Analysis

Type of Specimen	Weight Changes Before and After Heat Treatment	Thickness of Surface Film in Micro-inches	Scanning - Electron Microscopy Identification of Phases	Auger - Esca Profiling Analysis of Surface Film	x-ray Structural Analysis
No. 1 as received	"	"	"	"	"
No. 2 18 hrs. $450^{\circ}\text{F}$ heat treated in air	"	"	"	"	"
No. 3 8 hrs. $650^{\circ}\text{F}$ heat treated in air	"	"	"	"	"
No. 4 8 hrs. $1050^{\circ}\text{F}$ heat treated in air	"	"	"	"	"
No. 5 8 hrs. $650^{\circ}\text{F}$ heat treated in vacuum	"	"	"	"	"
No. 6 8 hrs. $1050^{\circ}\text{F}$ heat treated in vacuum	"	"	"	"	"

TABLE XI. PHASE III TASK A  
Diamond-Anvil Pressure Cell Test Programs for Identification of Structural Changes in Westinghouse Lubricant

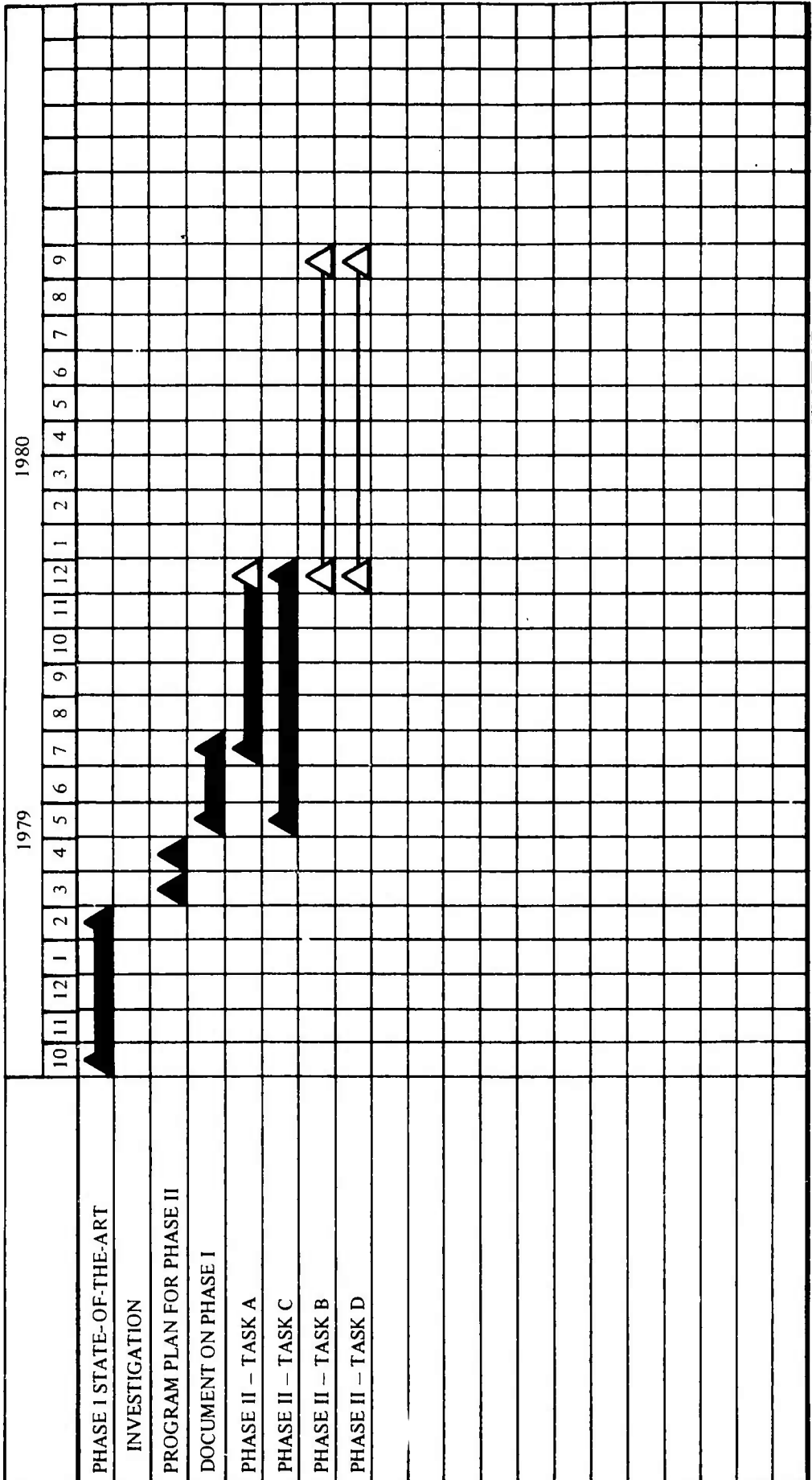
Type of Specimen	Temp.	Pressure	Temp.	Pressure	Temp.	Pressure	Temp.	Pressure	Temp.	Pressure	Temp.	Pressure
No. 1 as received	rvvm °F 150,000 psi	250°F 150,000 psi	450°F 250,000 psi	150,000 psi	650°F 250,000 psi	150,000 psi	850°F 250,000 psi	150,000 psi	1050°F 250,000 psi	150,000 psi	1050°F 250,000 psi	150,000 psi
No. 2 10 hrs. - 450°F heat treated in air	"	"	"	"	"	"	"	"	"	"	"	"
No. 3 8 hrs. - 650°F heat treated in air	"	"	"	"	"	"	"	"	"	"	"	"
No. 4 8 hrs. - 1050°F heat treated in air	"	"	"	"	"	"	"	"	"	"	"	"
No. 5 8 hrs. - 650°F heat treated in vacuum	"	"	"	"	"	"	"	"	"	"	"	"
No. 6 8 hrs. - 1050°F heat treated in vacuum	"	"	"	"	"	"	"	"	"	"	"	"



**TITLE** DEVELOPMENT OF SOLID LUBRICATED GYRO BEARINGS  
CUSTOMER CONTRACT NO. 04-493-DARPA-AFML-HUGHES.

**DIRECTORATE** INSTRUMENT ENGINEERING

PRIME CONTRACT NO. F33615-78-C5197  
CUSTOMER CONTRACT NO. 04-493431-F55



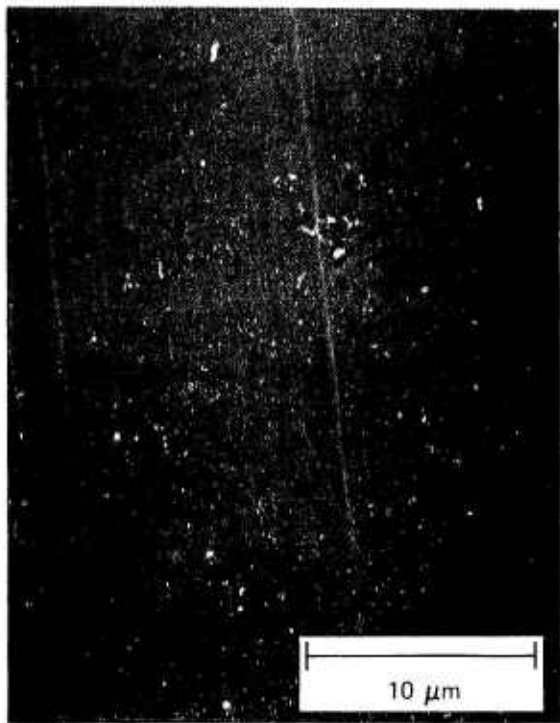


Figure 22. Race 1 Unetched 3000X

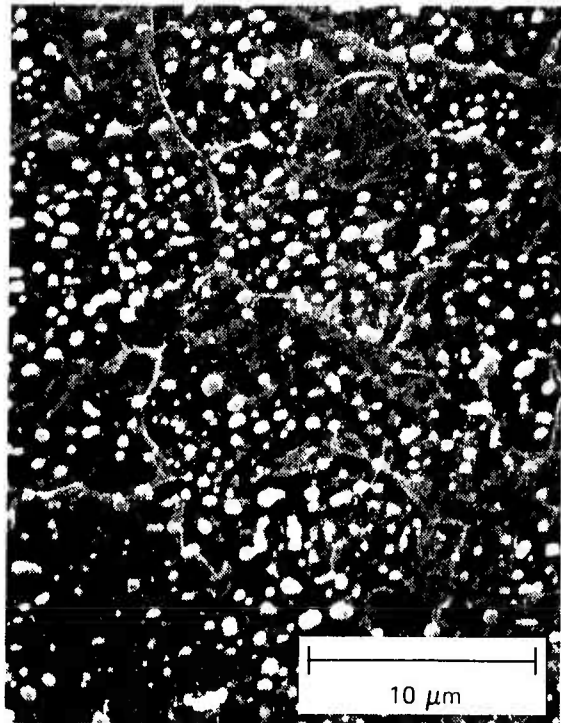


Figure 23. Race 1 Layer Etched 3000X

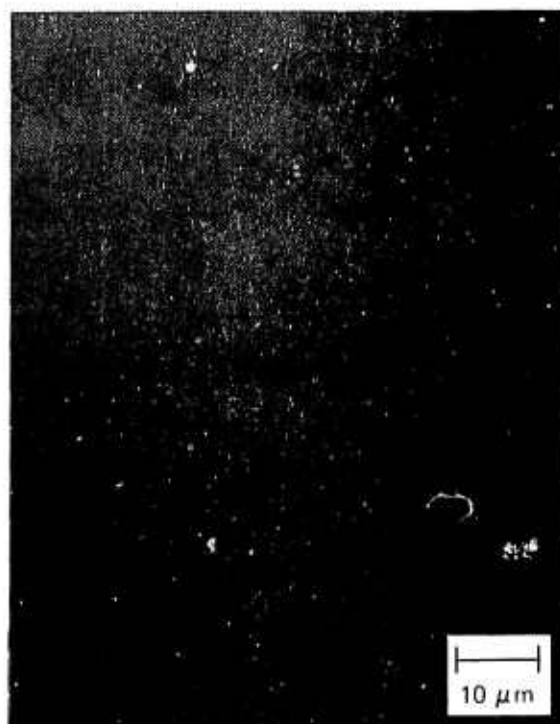


Figure 24. Race 2 Unetched 1000X

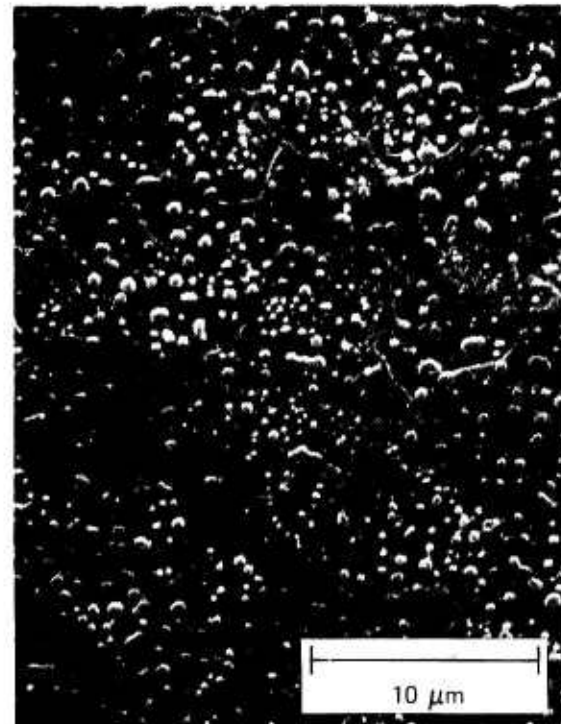


Figure 25. Race 2 Layer Etched 3000X

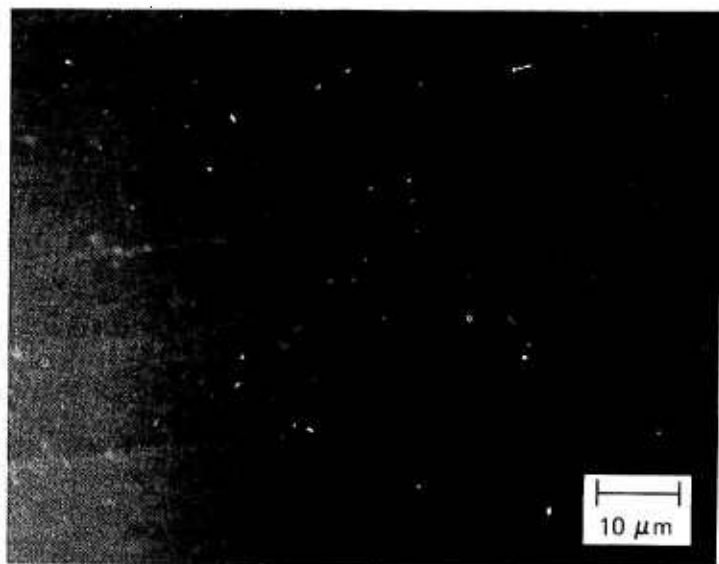


Figure 26. Unetched Race No. 3                  1000X

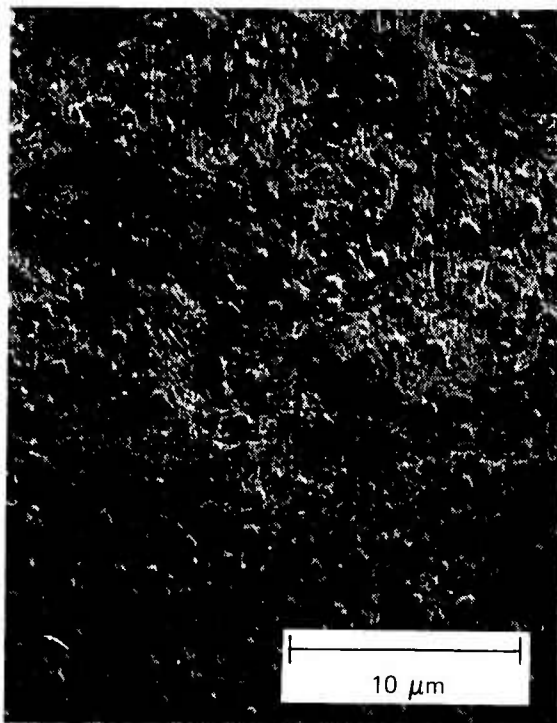


Figure 27. Layer Etched                  3000X  
Race No. 3



Figure 28. Second Layer Etch          3000X  
Race No. 3

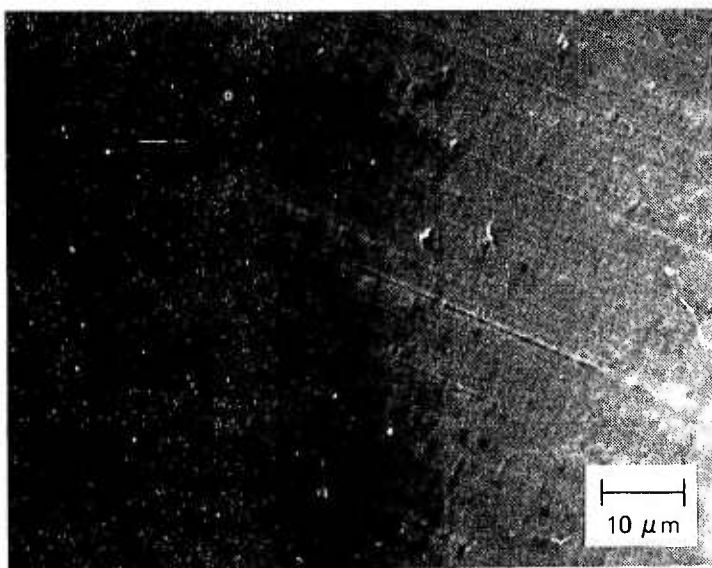


Figure 29. Unetched Race No. 4      1000X

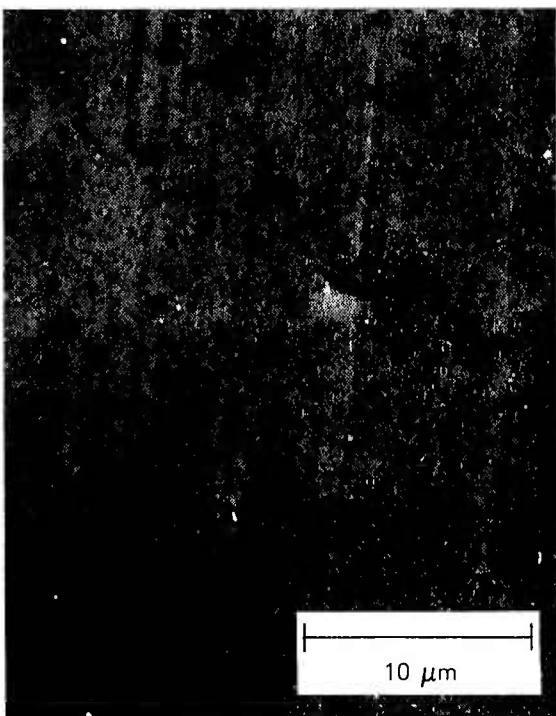


Figure 30. First Layer Etch      3000X  
Race No. 4



Figure 31. Second Layer Etch 3000X  
Race No. 4

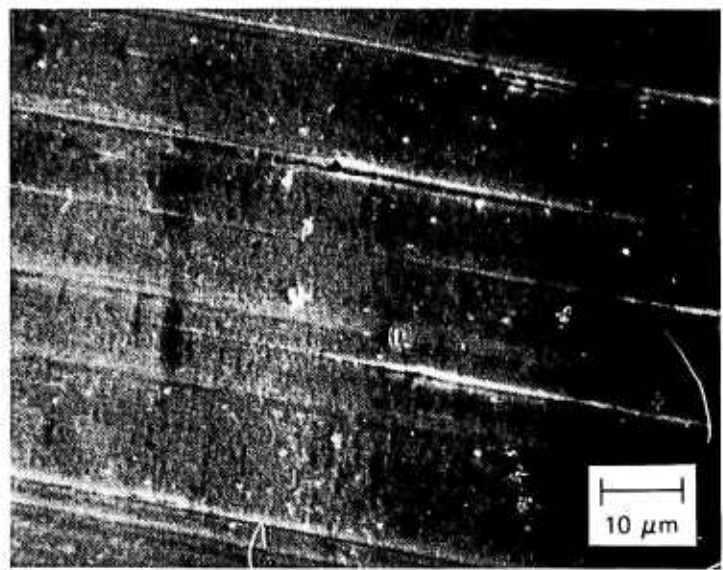


Figure 32. Unetched Race No. 5                    1000X

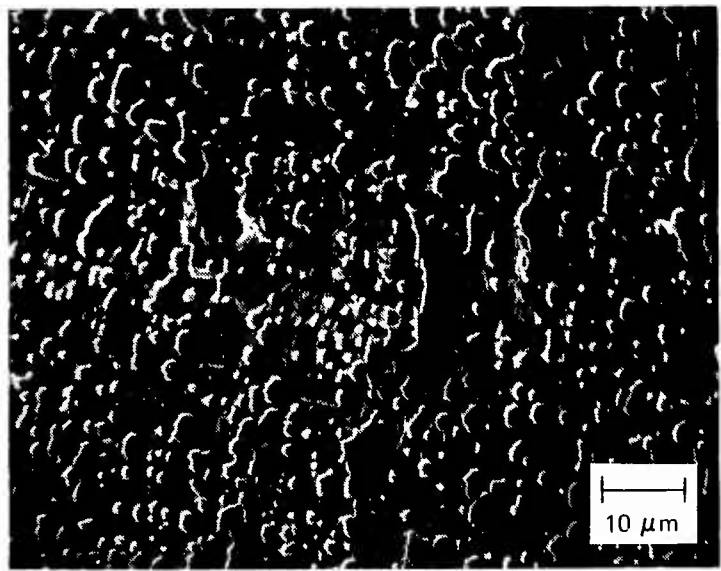


Figure 33. First Layer Etch                    1000X  
Race No. 5

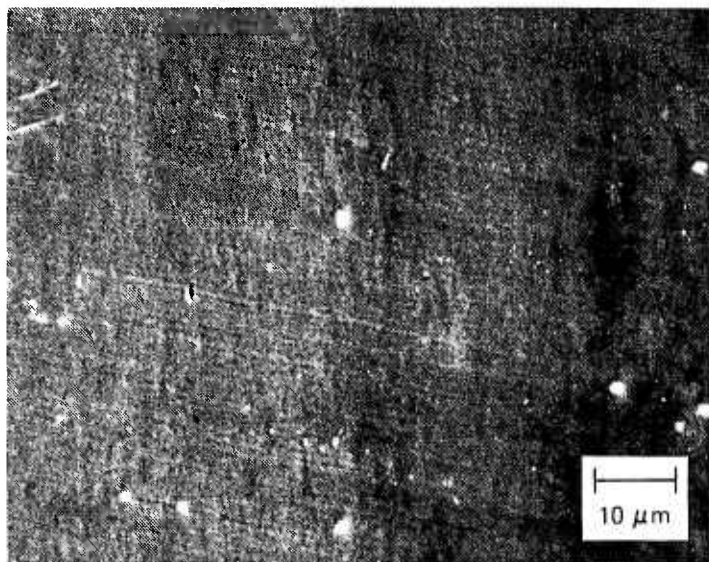


Figure 34. Race No. 6 Unetched 3000X

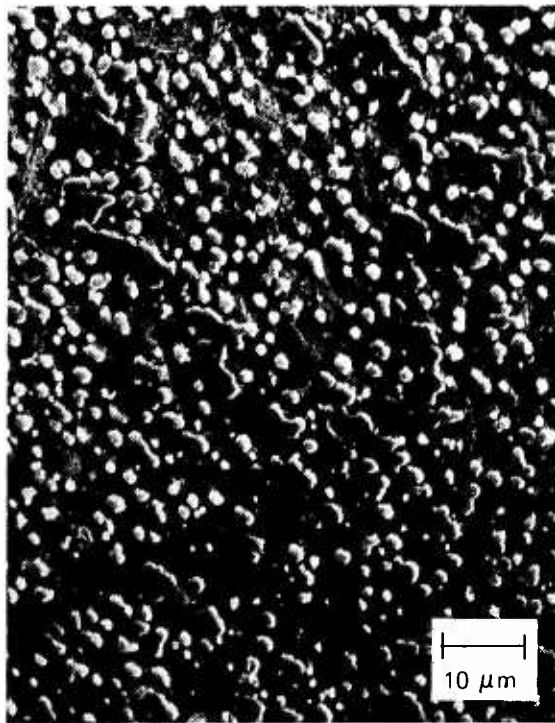


Figure 35. Race No. 6  
First Layer Etch 1000X



Figure 36. Race No. 6  
Magnification of 35 –  
Notice Micro-Cracks 3000X

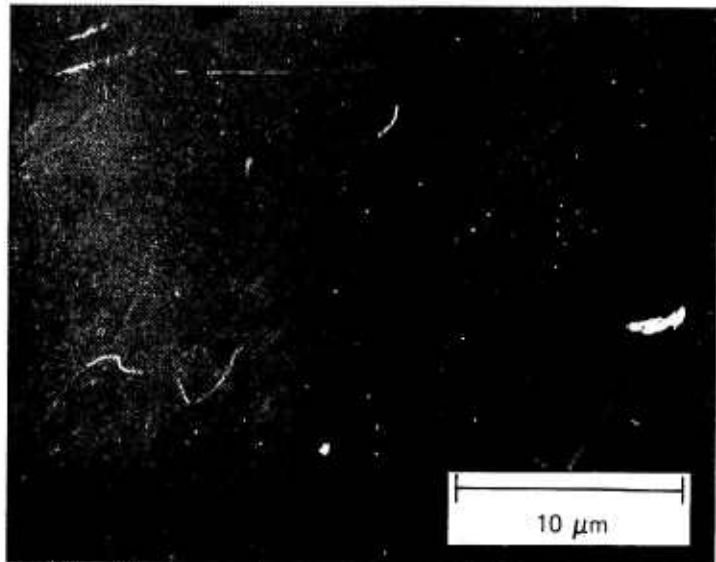


Figure 37. Grade 3 Ball 3000X

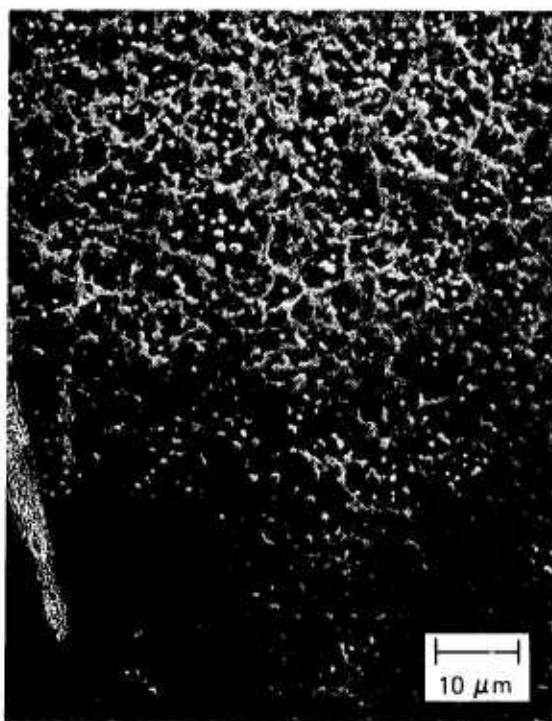


Figure 38. Grade 3 Ball  
First Layer Etch 1000X

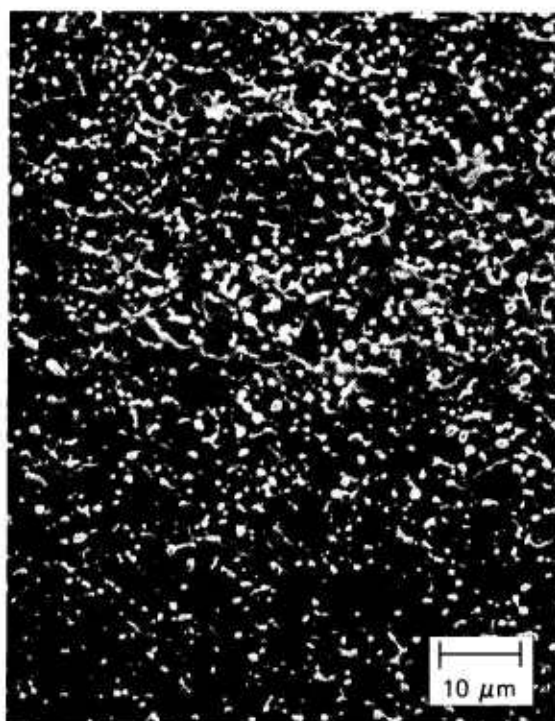


Figure 39. Grade 3 Ball  
Second Layer Etch 1000X

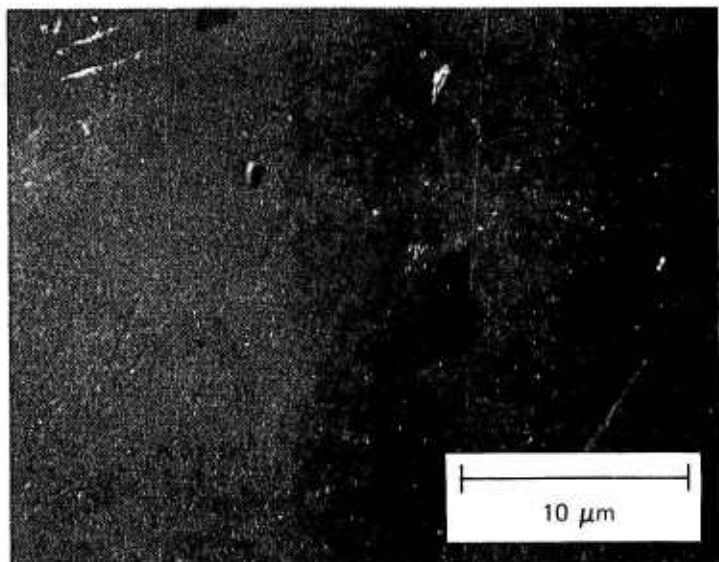


Figure 37. Grade 3 Ball

3000X

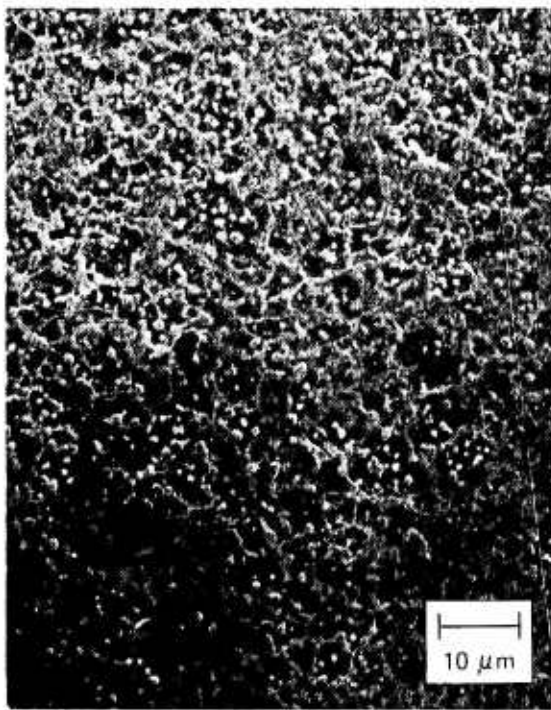


Figure 38. Grade 4 Ball  
First Layer Etch

1000X

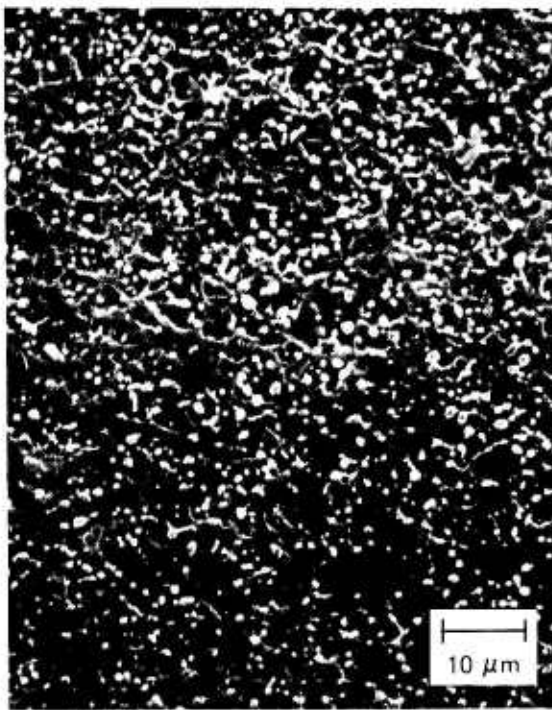


Figure 39. Grade 3 Ball  
Second Layer Etch

1000X

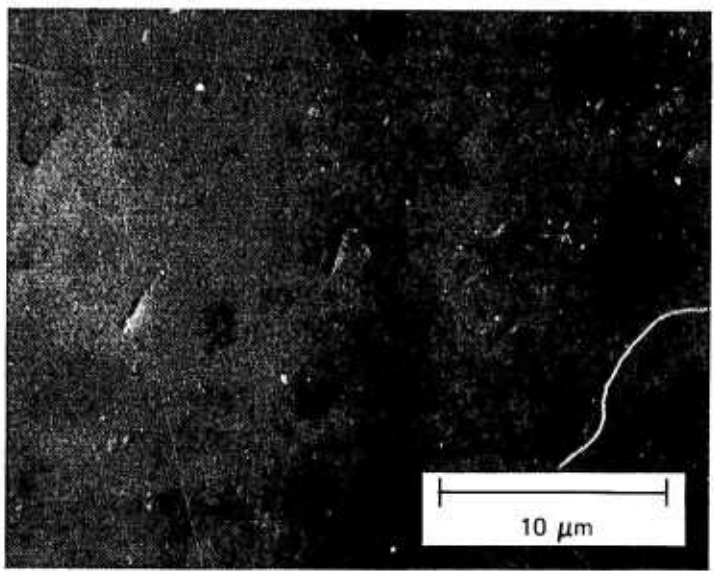


Figure 40. Grade 10 Ball

3000X

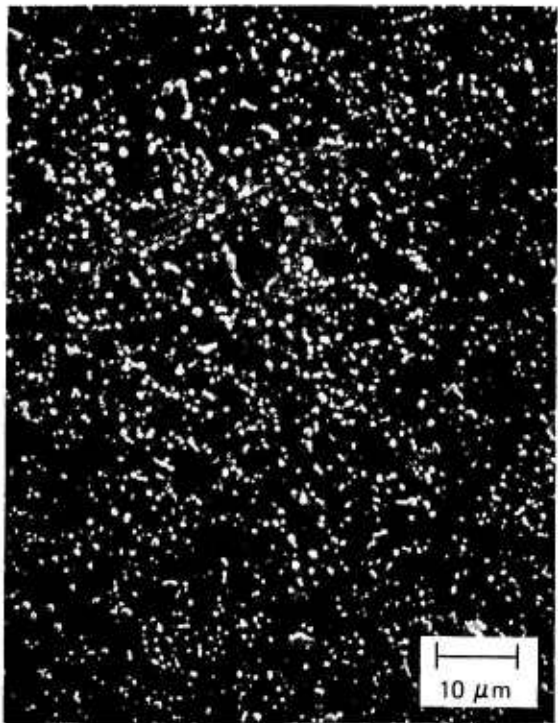


Figure 41. Grade 10 Ball  
First Layer Etch      1000X

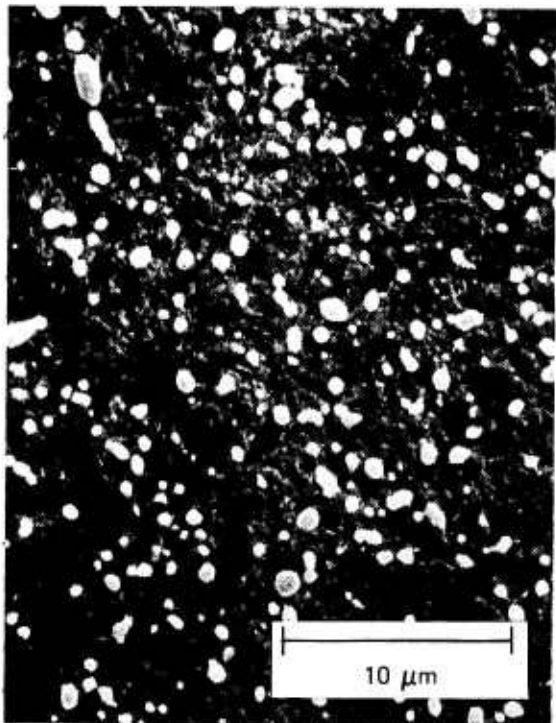


Figure 42. Grade 10 Ball      3000X  
Magnification of Figure 41



Figure 43. Unetched  
Manufactured 2  
Group 1 Balls  
1000X

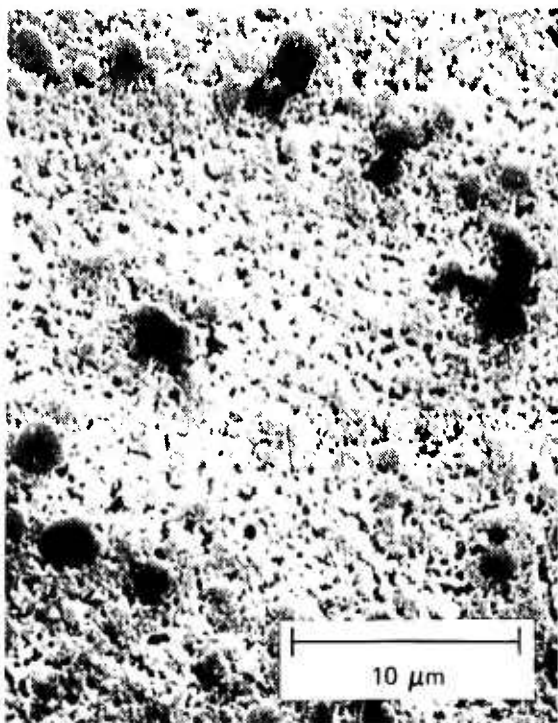


Figure 44. First Layer Etch  
3000X

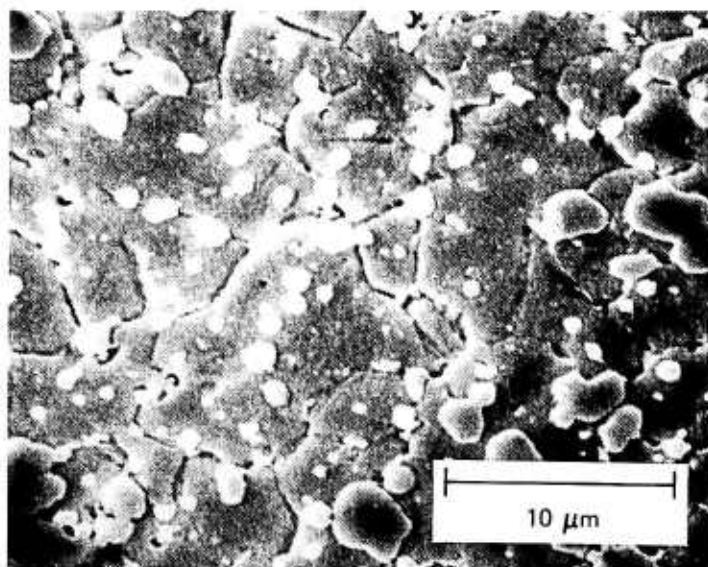


Figure 45. Second Layer Etch  
Group 1 Balls  
3000X

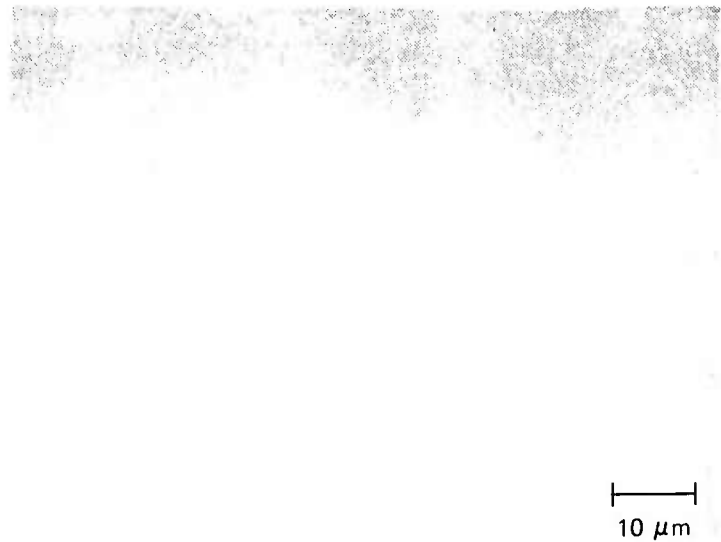


Figure 46. Unetched Group 5 Balls      1000X

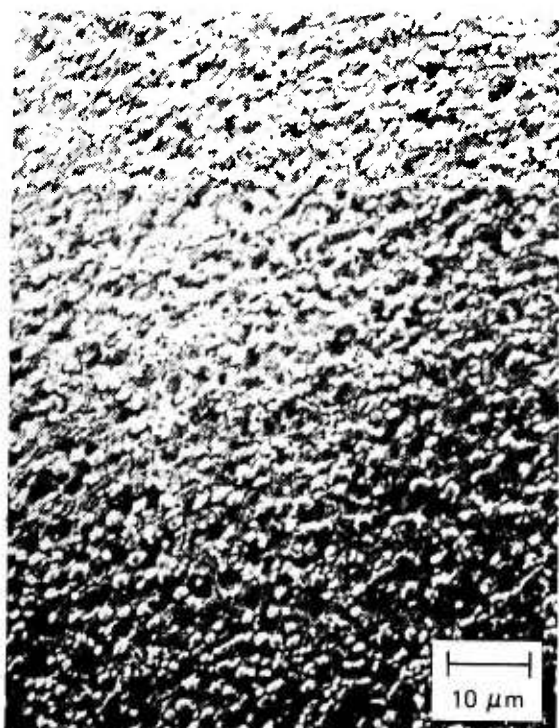


Figure 47. First Layer Etch      1000X  
Group 5 Balls



Figure 48. Magnification of      3000X  
Figure 47      Group 5 Balls

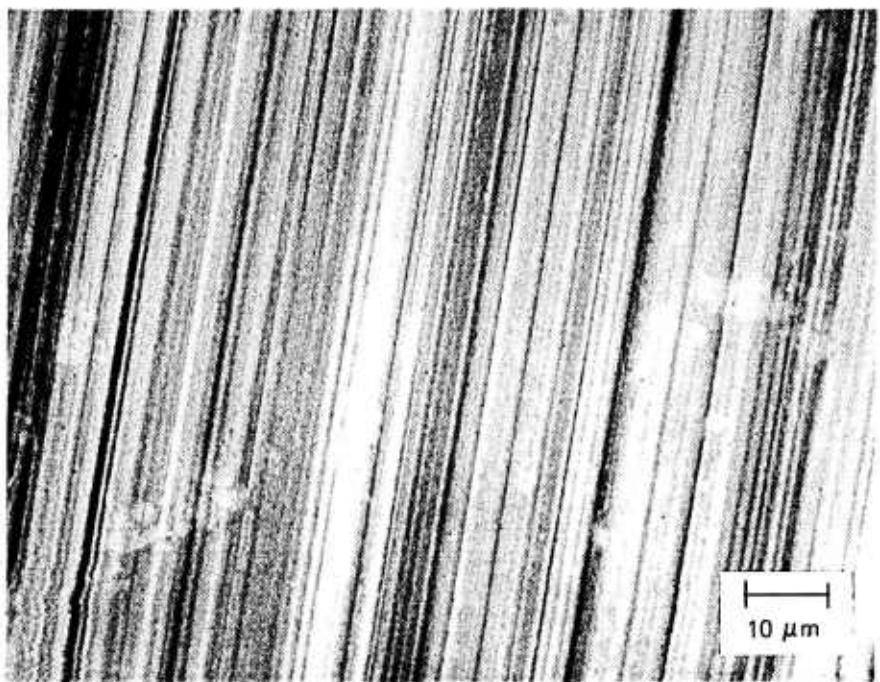


Figure 49. Specimen 1 Unetched Bearing Surfaces Damaged by  
The Machining Process 1000X

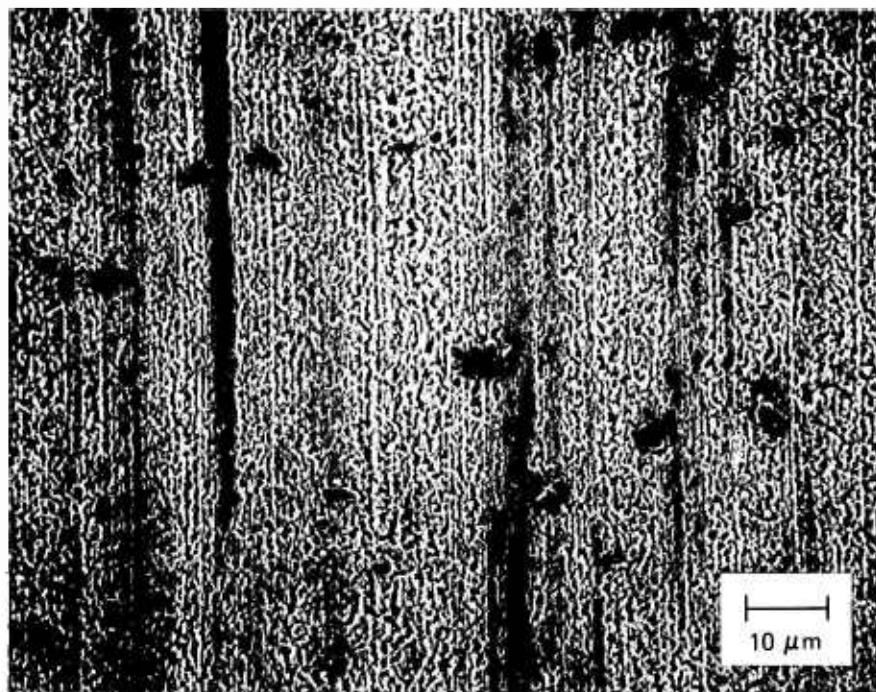


Figure 49a. Specimen 1 One Layer Etch Bearing Surfaces Damaged  
by The Machining Process 1000X

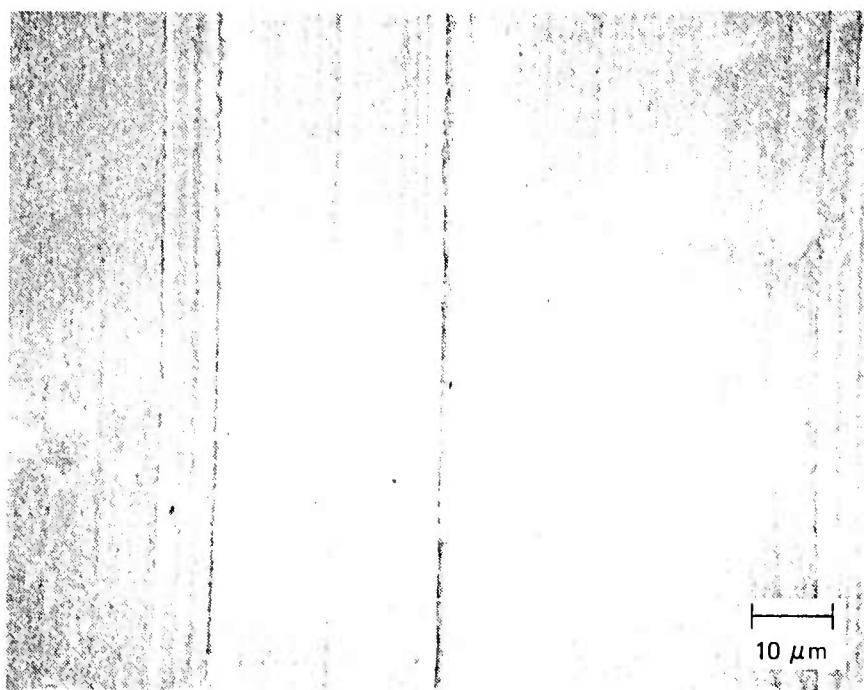


Figure 50. Specimen 2 Unetched Bearing Surfaces Damaged by  
The Machining Process 1000X

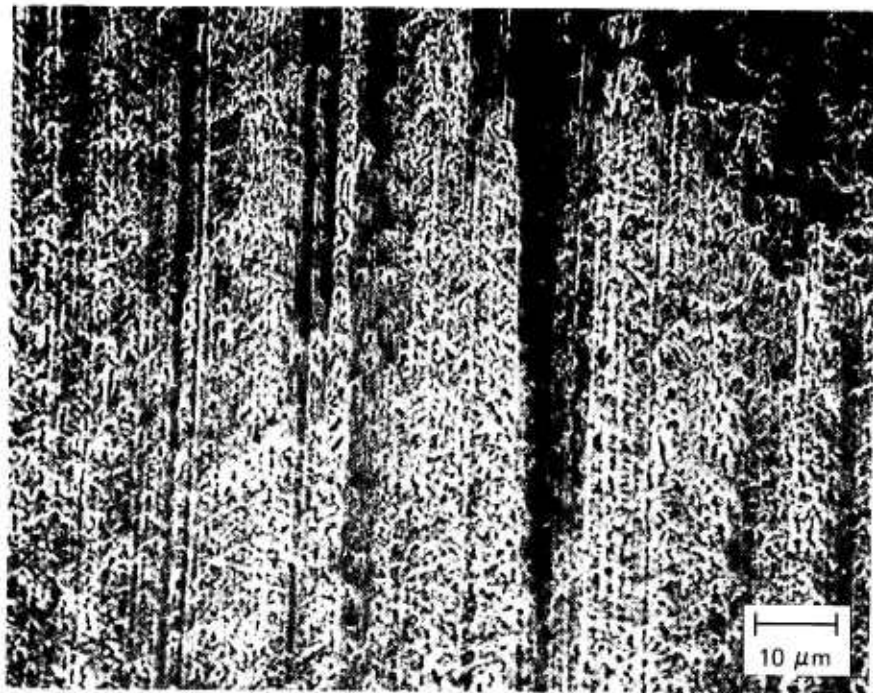


Figure 50a. Specimen 2 One Layer Etch Bearing Surfaces Damaged  
by The Machining Process 1000X

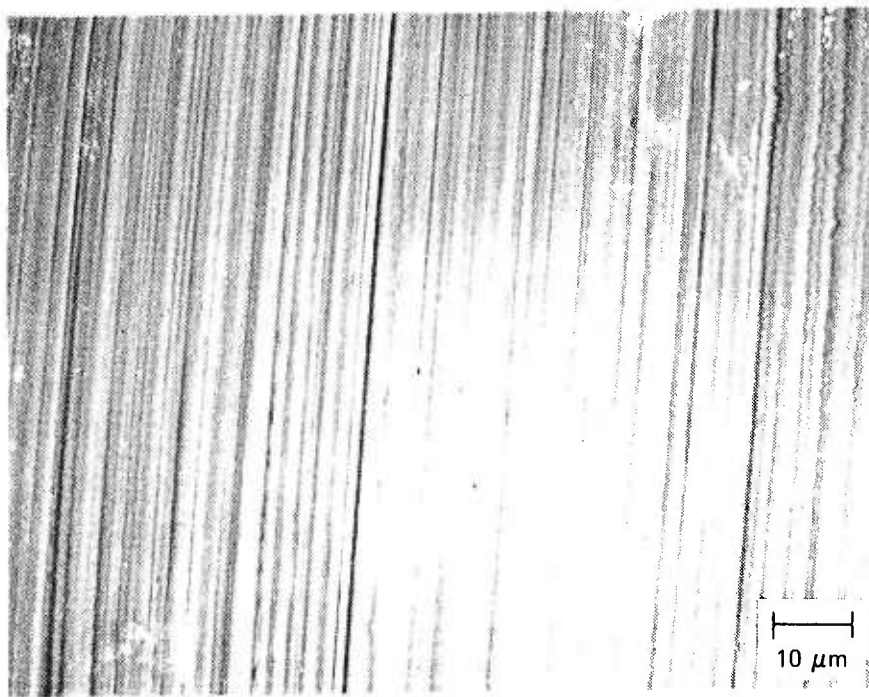


Figure 51. Specimen 3 Unetched Bearing Surfaces Damaged by  
The Machining Process 1000X

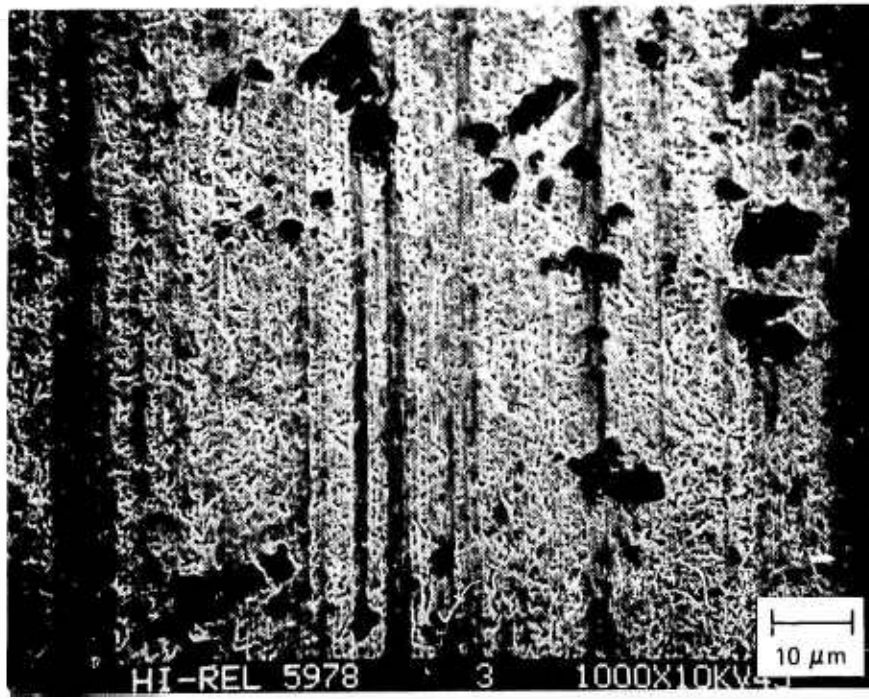


Figure 51a. Specimen 3 One Layer Etch Bearing Surfaces Damaged  
by The Machining Process 1000X

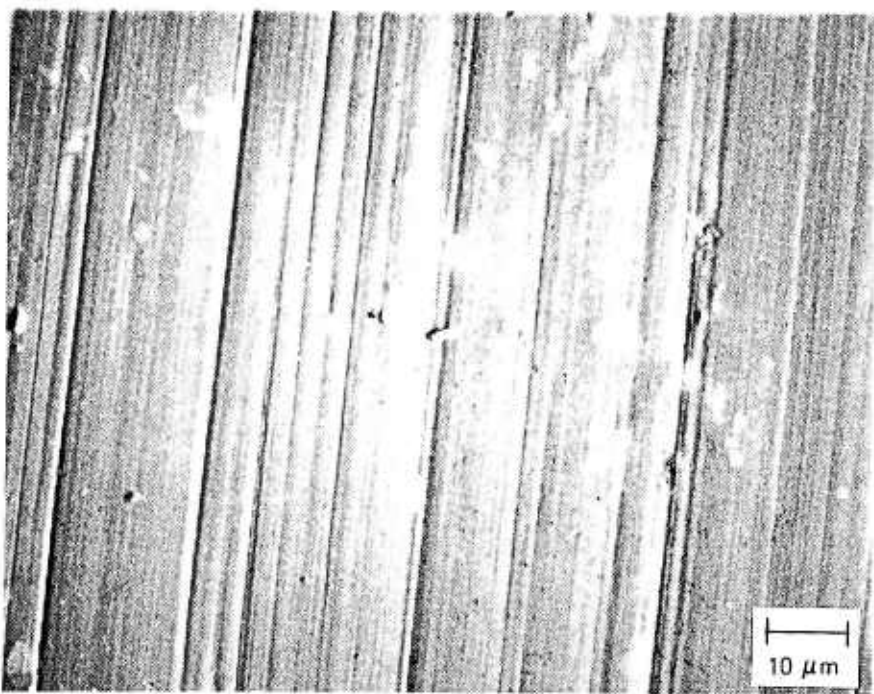


Figure 52. Specimen 4 Unetched Bearing Surfaces Damaged by  
The Machining Process 1000X

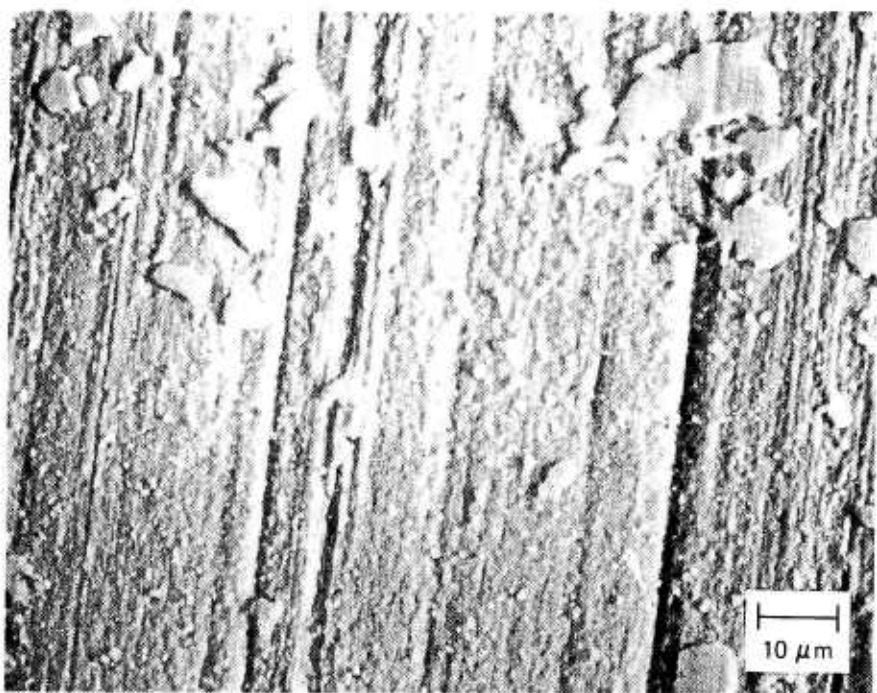


Figure 52a. Specimen 4 One Layer Etch Bearing Surfaces Damaged  
by the Machining Process 1000X

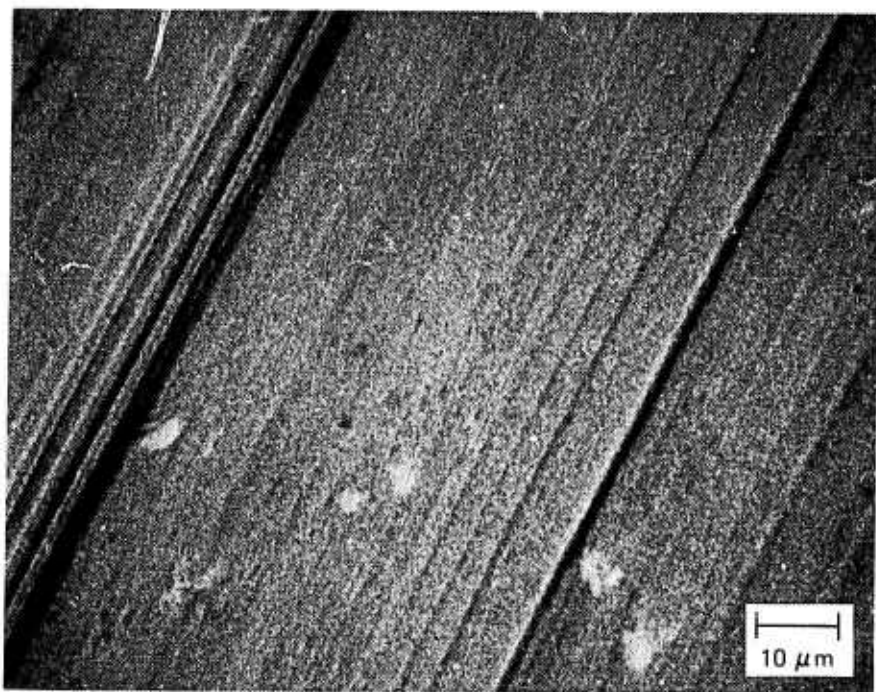


Figure 53. Specimen 5 Unetched Bearing Surfaces Damaged by  
The Machining Process      1000X

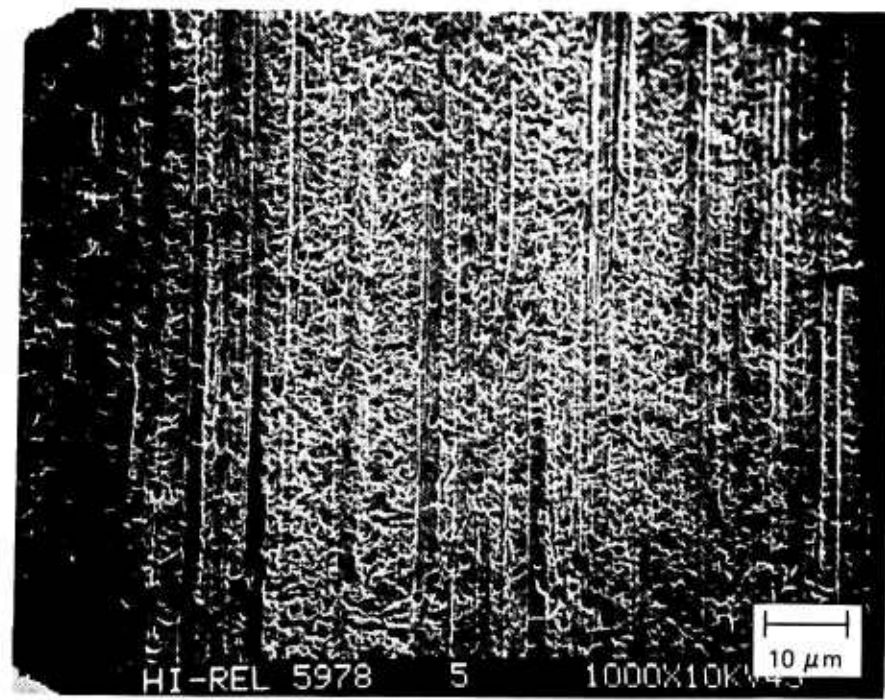


Figure 53a. Specimen 5 One Layer Etch Bearing Surfaces Damaged  
by The Machining Process      1000X

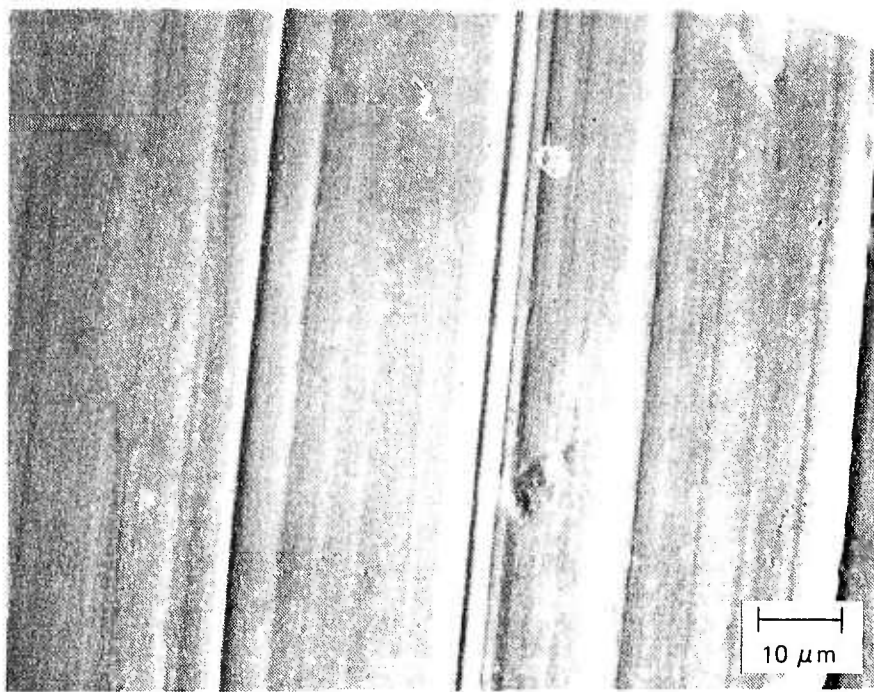


Figure 54. Specimen 6 Unetched Bearing Surfaces Damaged by  
The Machining Process 1000X



Figure 54a. Specimen 6 One Layer Etch Bearing Surfaces  
Damaged by The Machining Process 500X

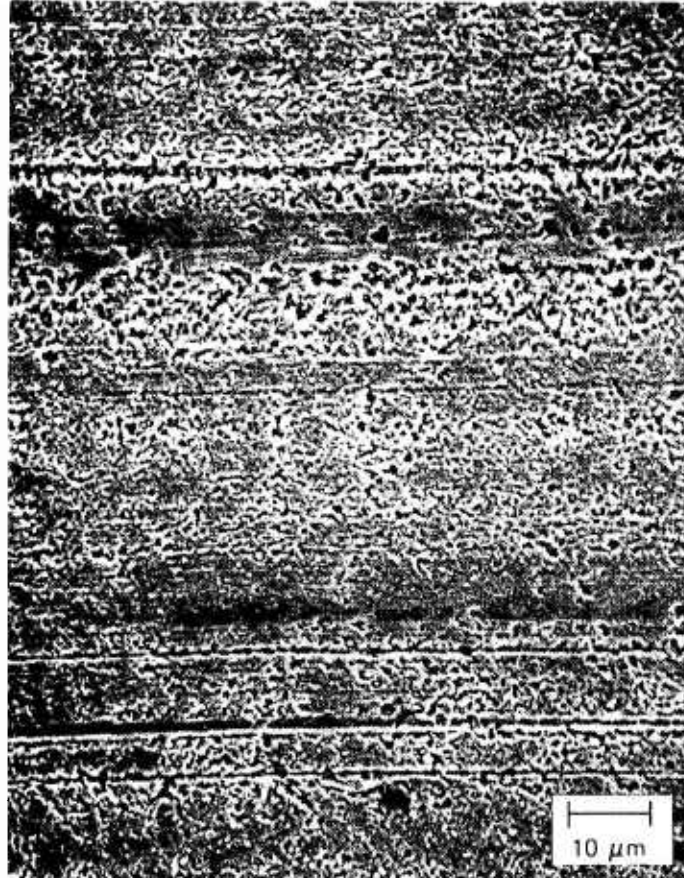


Figure 54b. Magnification of Figure 6a. 1000X

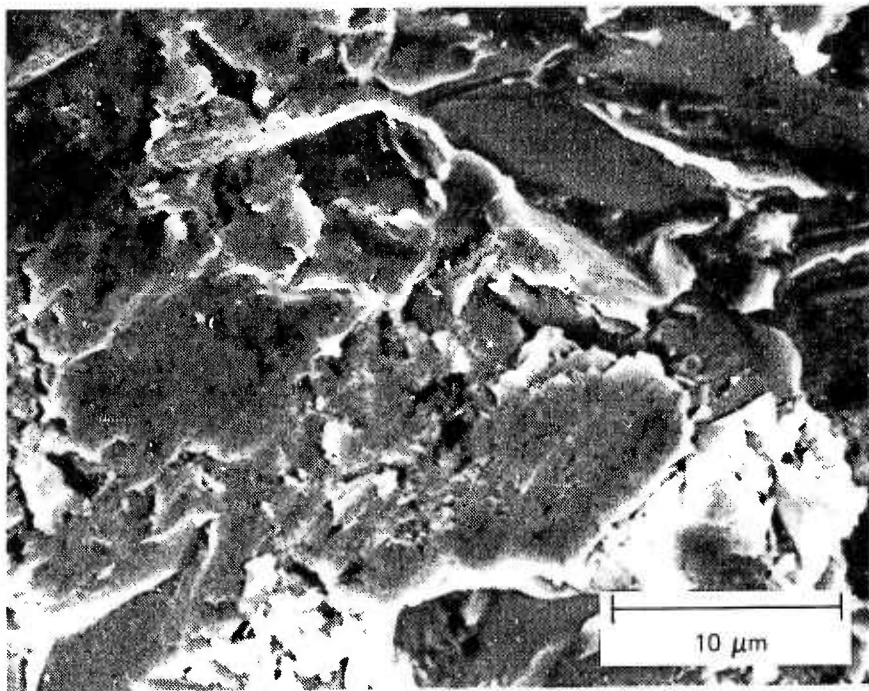


Figure 55. Roller In As Received Condition Bearing Surfaces  
Damaged by the Machining Process 3000X



Figure 56. Ball In As Received Condition Bearing Surfaces  
Damaged by The Machining Process 3000X

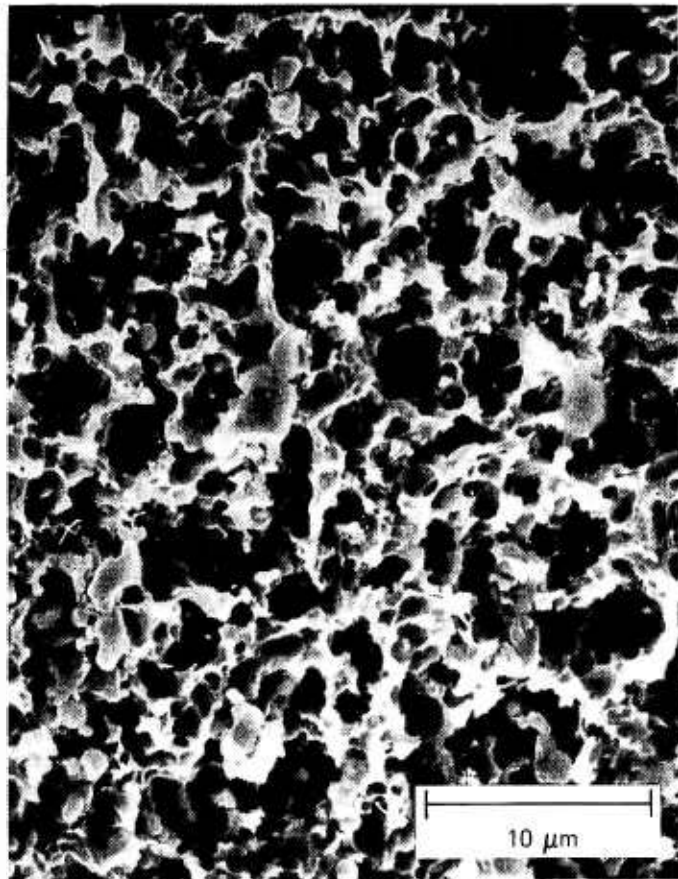


Figure 56a. Ball After First Layer Etch Bearing Surfaces  
Damaged by The Machining Process 3000X

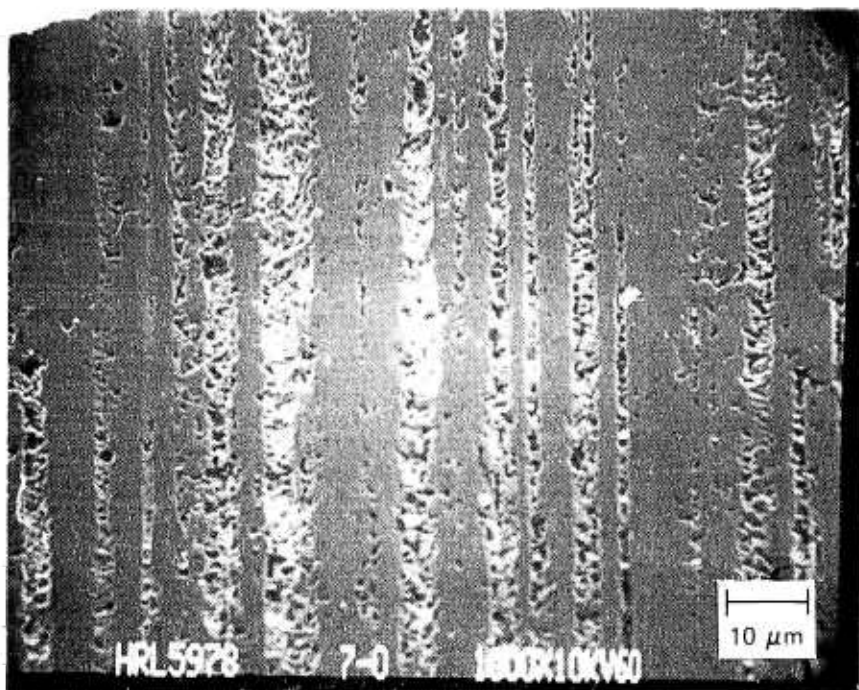


Figure 57. Bearing Surface Damaged by The Machining Process

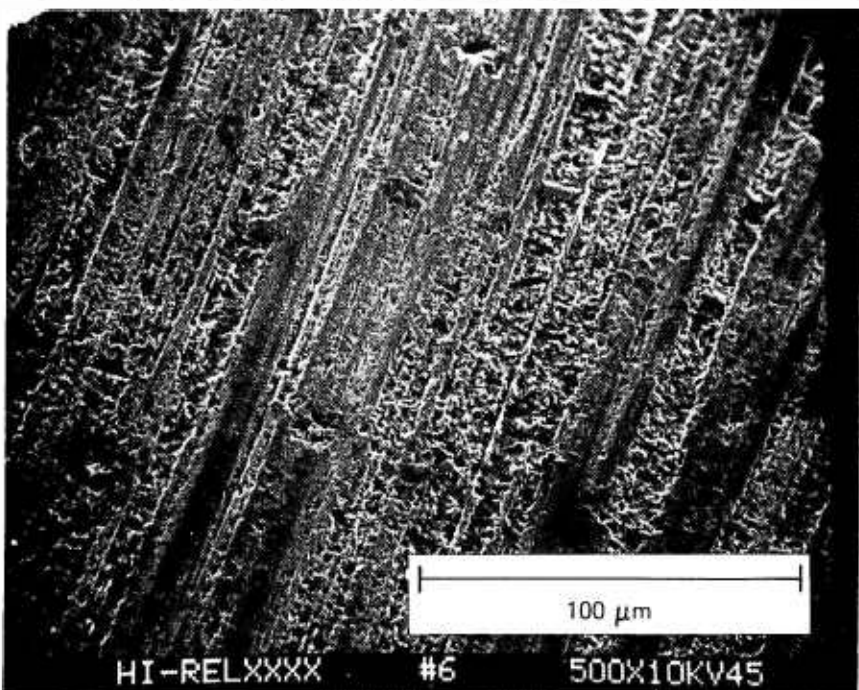


Figure 58. Bearing Surface Damaged by The Machining Process

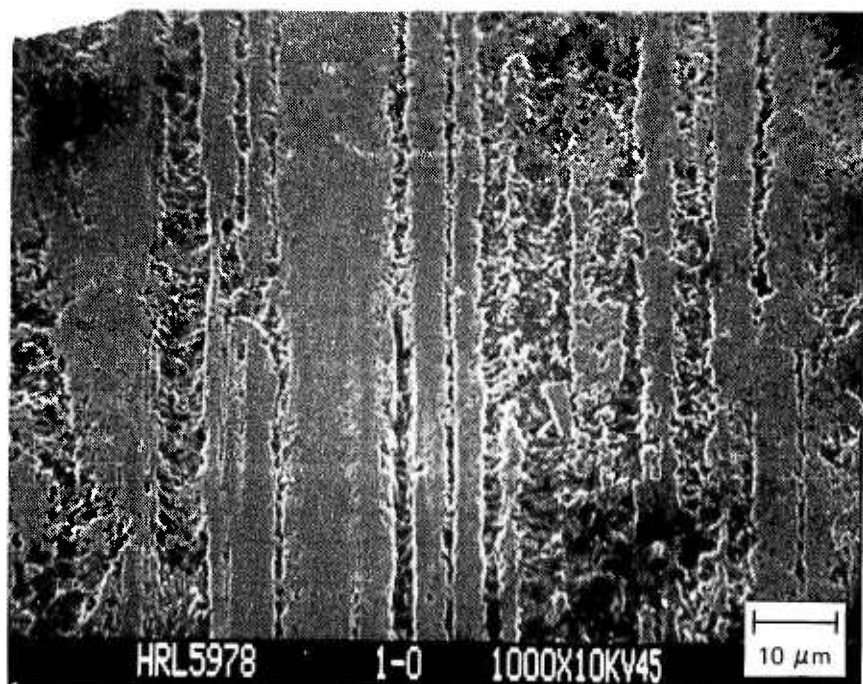


Figure 59. Bearing Surface Damaged by The Machining Process



Figure 60. Bearing Surface Damaged by The Machining Process

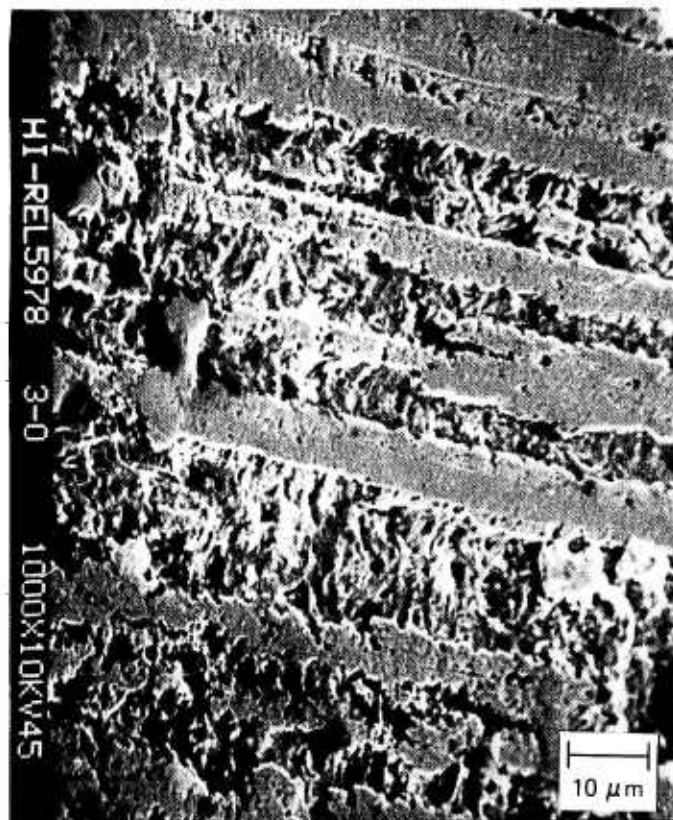


Figure 61. Bearing Surface Damaged by The Machining Process

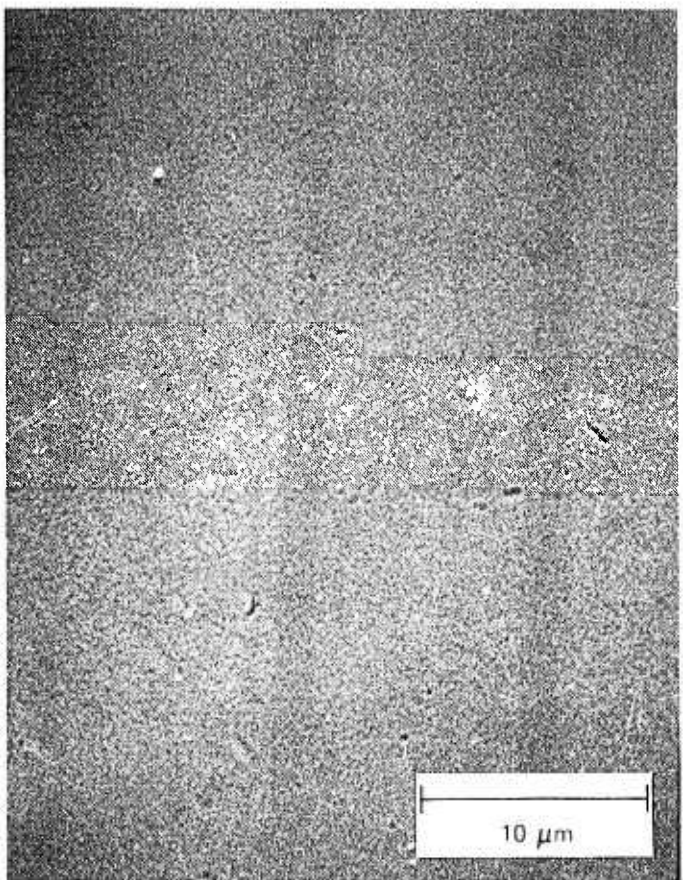


Figure 62. Ball - Williams Research Corp. 3000X  
Condition: Unetched

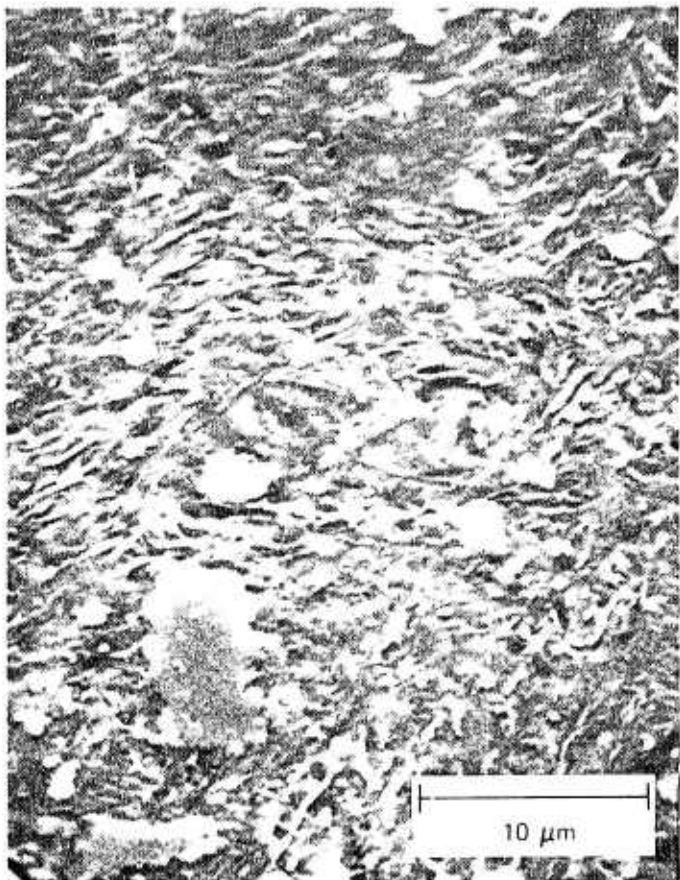


Figure 63. Ball - Williams Research Corp. 3000X  
Condition: One Layer Etch

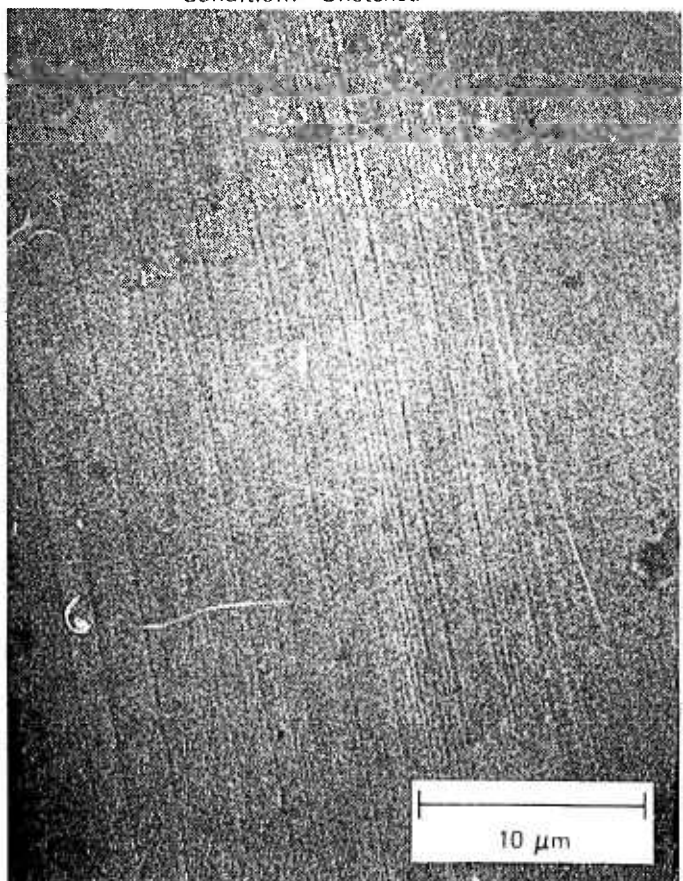


Figure 64. Inner Race - Williams Research Corp. 3000X  
Condition: Unetched

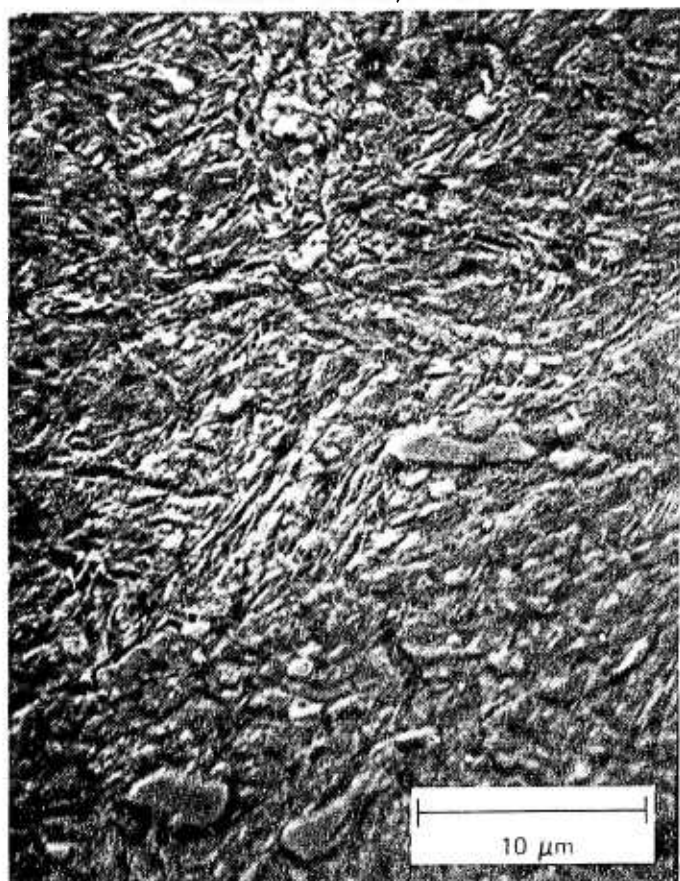


Figure 65. Inner Race - Williams Research Corp. 3000X  
Condition: One Layer Etch

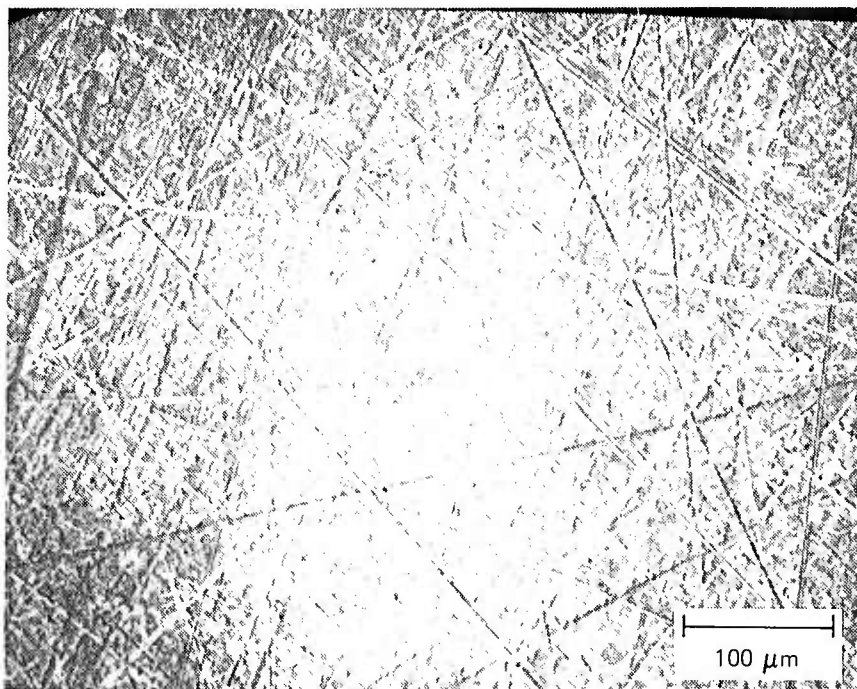


Figure 66. Bearing Surface Damaged by The Machining Process 200X

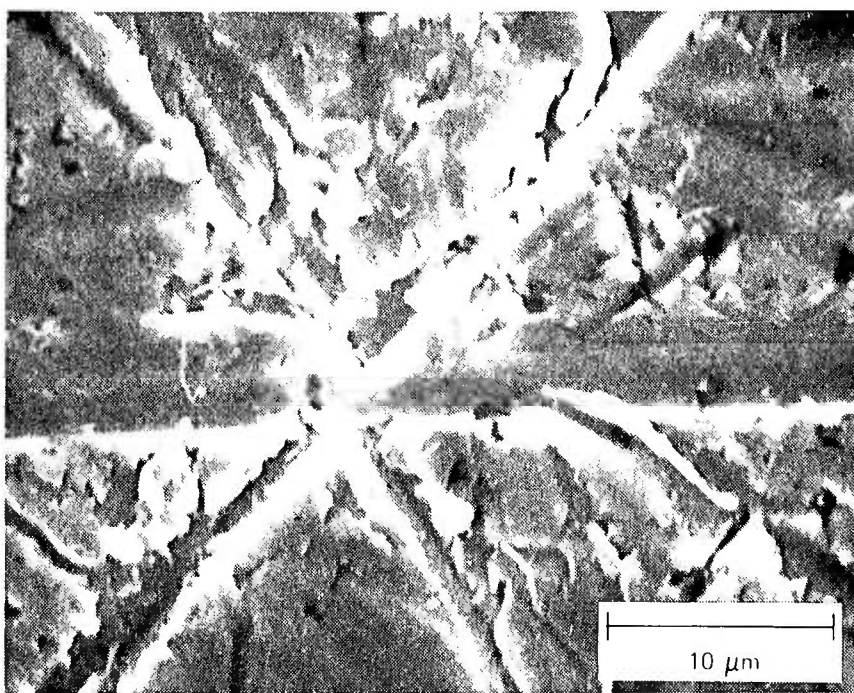


Figure 67. Bearing Surface Damaged by The Machining Process 3000X



Figure 68. CrC-TiC Coating on 400C-R3 Ball – Group 6 1650X



Figure 69. TiC Coating on R3 Cemented Carbide Ball – Group 7 1600X



Figure 70. TiC Coating on Cemented Carbide Ball – Group 8 1600X

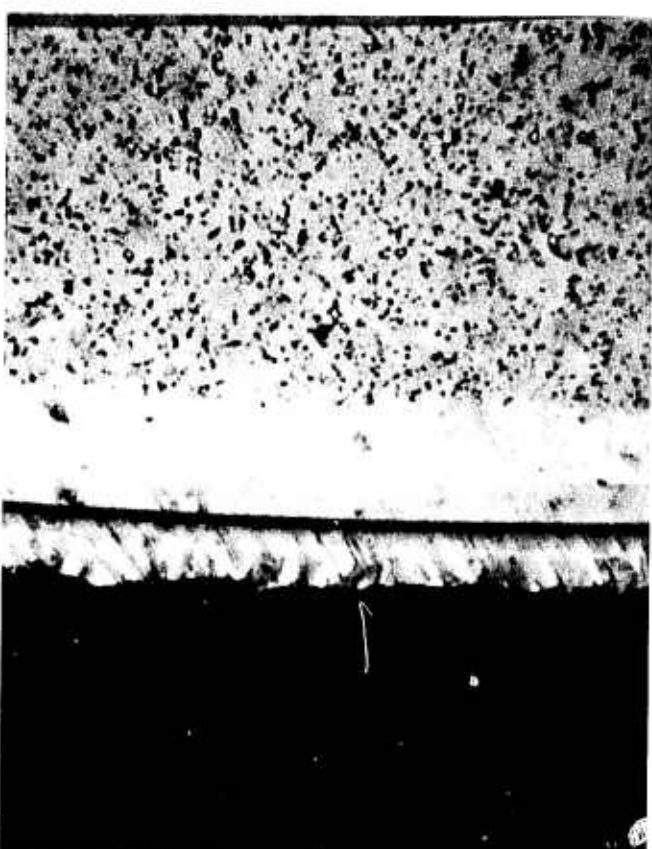


Figure 71. TiC Coating on R3 Cemented Carbide Ball – Group 9 1600X



Figure 72. Dimensions of Diagonal of Diamond Penetration 25 GM Load Micro-Hardness Test

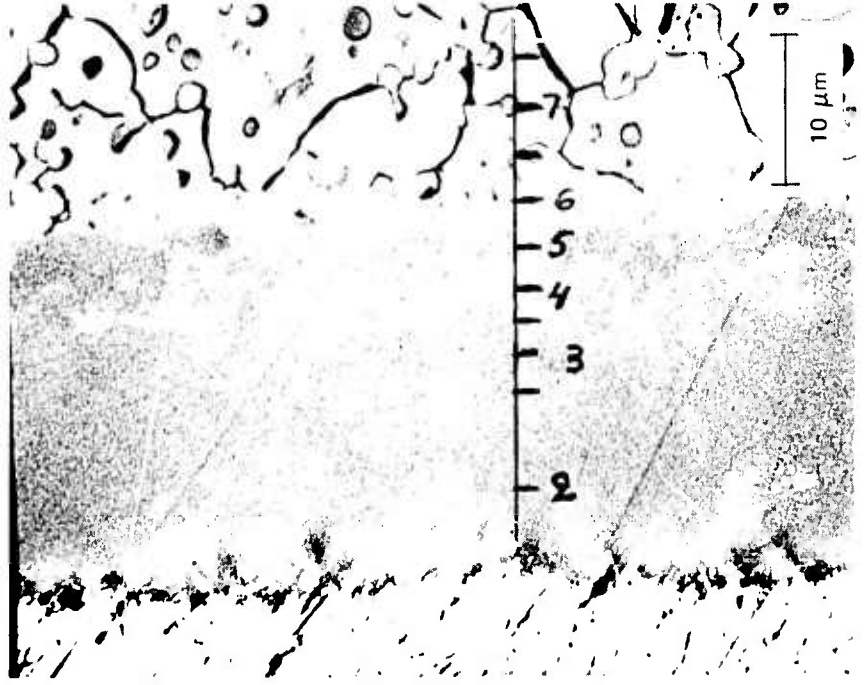
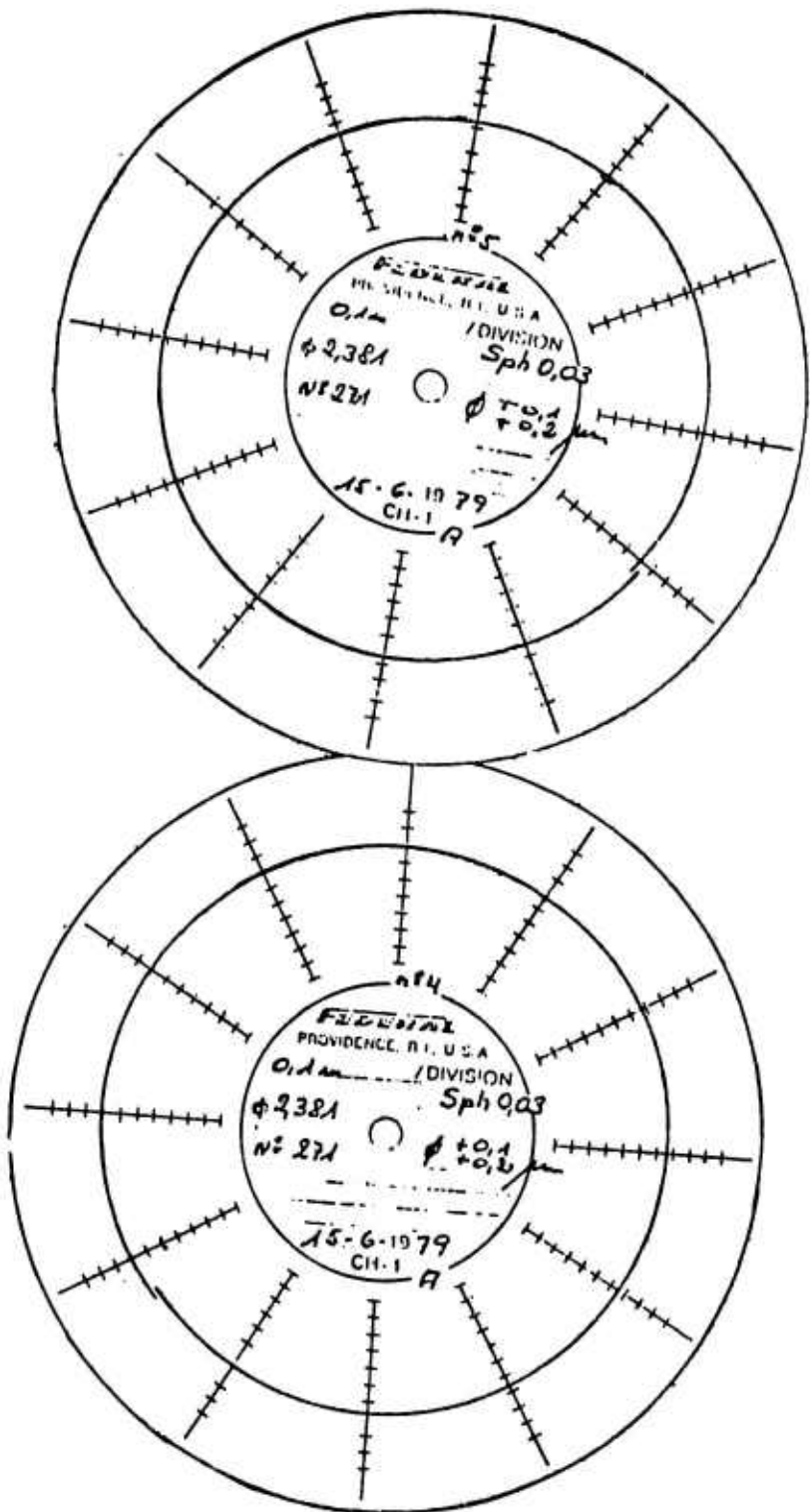


Figure 73. Composition of Coating Across Cross-Section of Coating as Shown Below in Atomic Percentage

INCHES	$\mu$	CONVERSION FACTOR	KNOOP HARDNESS
1 .44	8.9 $\mu$	179.6	4490
2 .45	9.1 $\mu$	171.8	4295
3 .47	9.6 $\mu$	154.4	3860
4 .534	10.8 $\mu$	122.0	3050
5 .505	10.2 $\mu$	136.8	3420
6 .63	12.8 $\mu$	86.85	2171
7 .65	13.2 $\mu$	61.66	2042
8 .80	16.3 $\mu$	53.55	1339
9 .79	16.1 $\mu$	54.89	1372
10 .92	18.7 $\mu$	40.69	1017
11 .93	18.9 $\mu$	39.83	996
12 .96	19.5 $\mu$	37.42	935



P.O. No: 04 - 498319 - F55  
Item 16  
 AISI 440C Steel balls  
 C-TiC coated  
 $\phi 2.381$

Figure 74. Ball Geometry

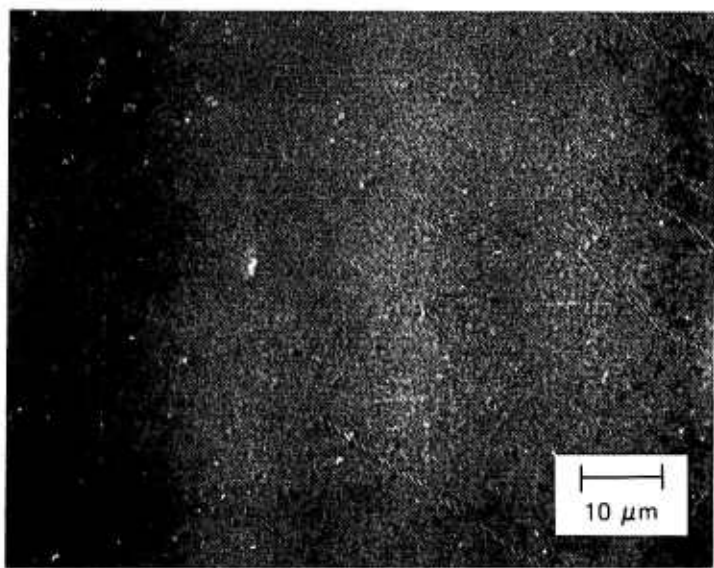


Figure 75. CrC-TiC Coated Steel Ball      1000X  
Unetched – Group 6

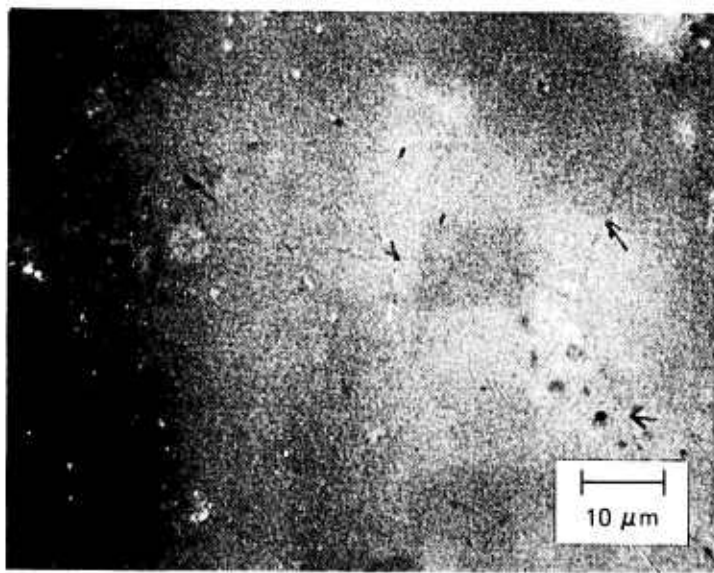


Figure 76. CrC-TiC Coated Steel Ball      1000X  
Layer Etch – 5 Minutes  
Notice No Impurities Along Grain  
Boundary – Group 6

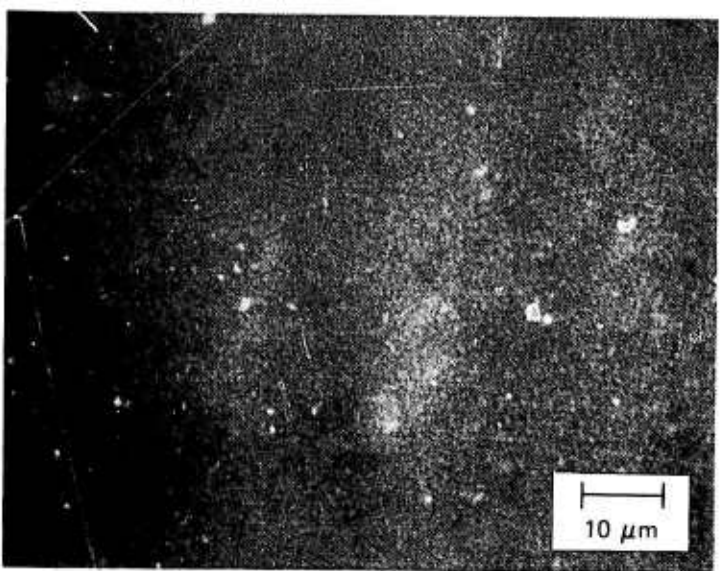


Figure 77. TiC Coating on Sintered  
Tungsten Carbide – Group 7      1000X

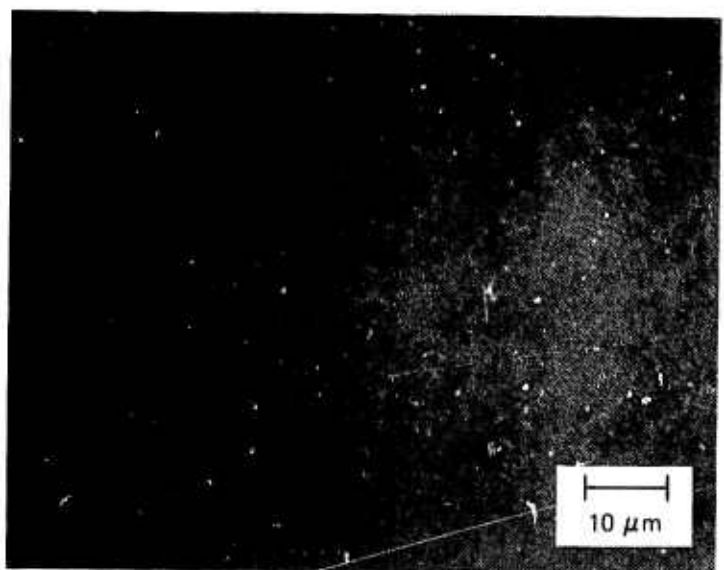


Figure 78. TiC Coating on Sintered  
Tungsten Carbide – Group 8      1000X

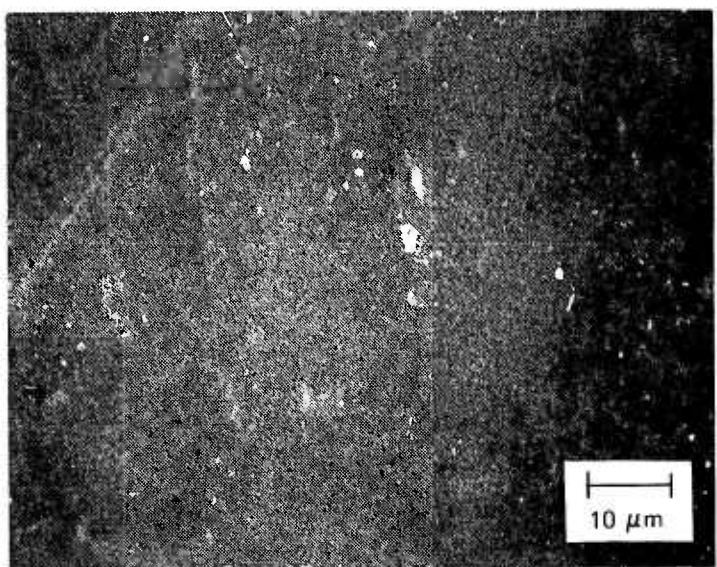


Figure 79. TiC Coating on Sintered  
Tungsten Carbide — Group 8      1000X

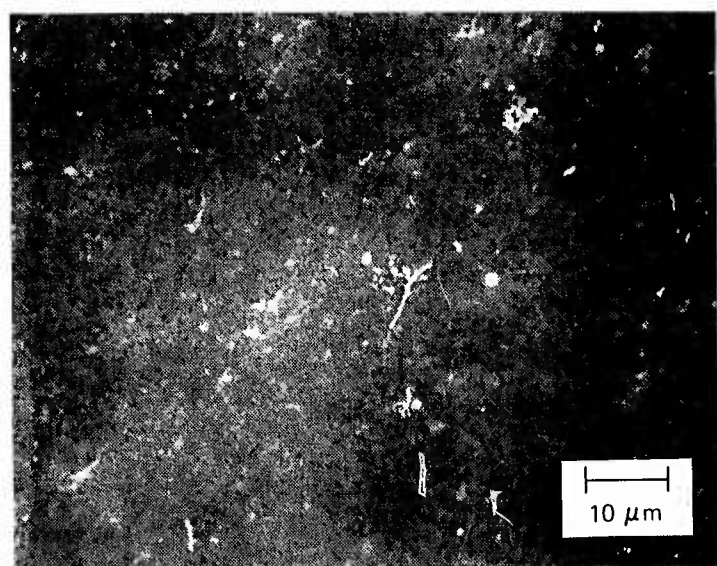


Figure 80. TiC Coating on Sintered  
Tungsten Carbide — Group 8 — Etched      1000X

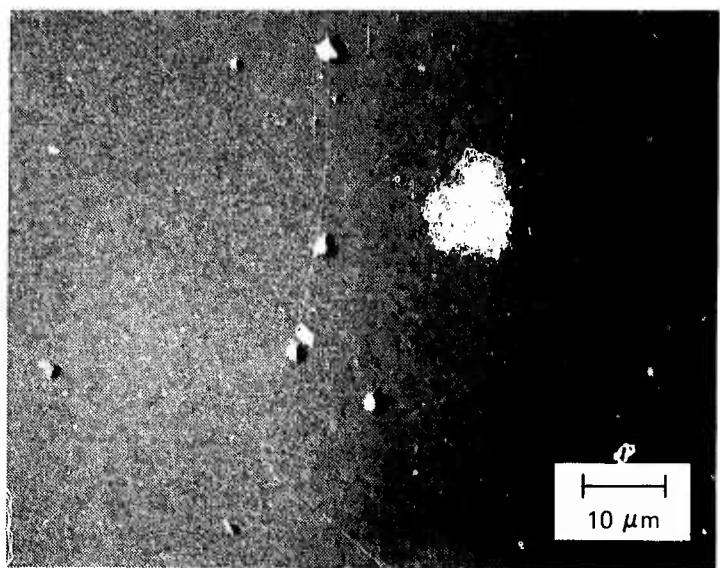


Figure 81. TiC Coating on Sintered  
Tungsten Carbide — Group 9      1000X

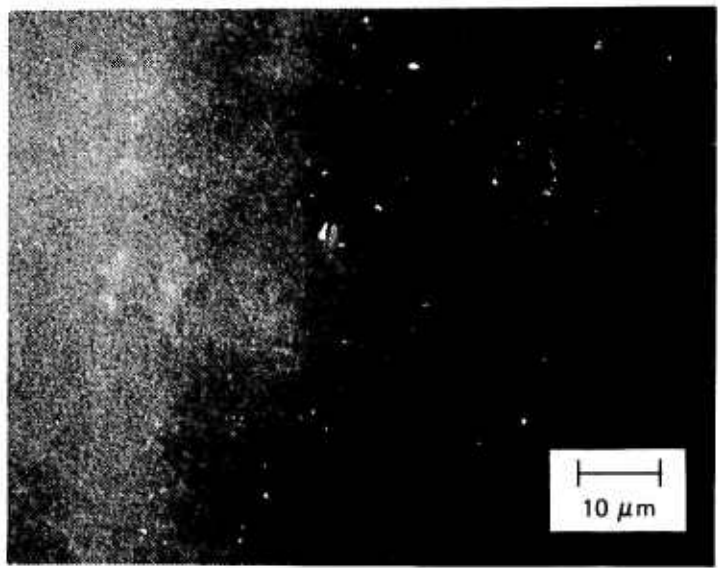


Figure 82. TiC Coating on Sintered  
Tungsten Carbide — Group 9 — Etched      1000X

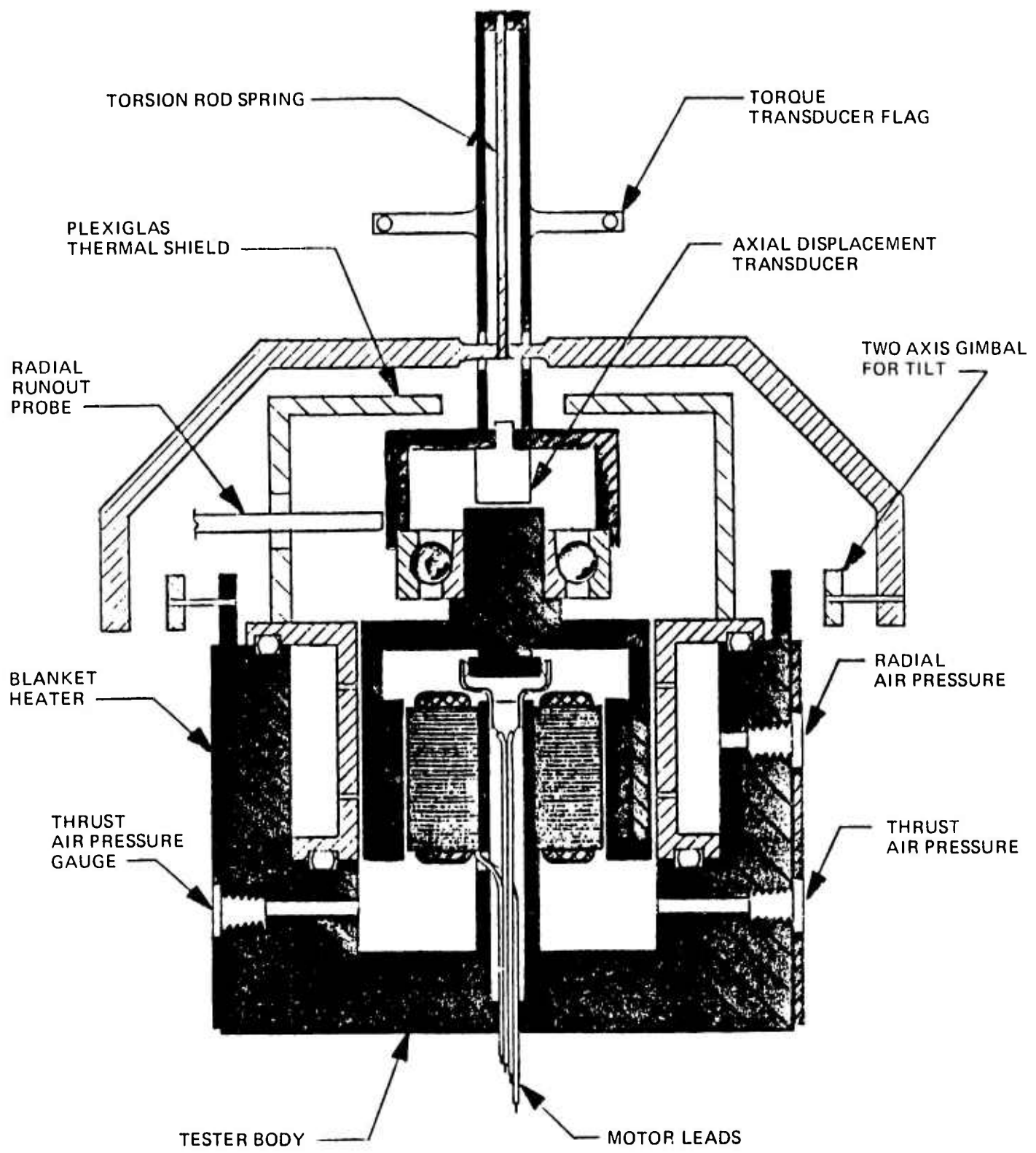


Figure 83. Schematic – High Speed Bearing Tester

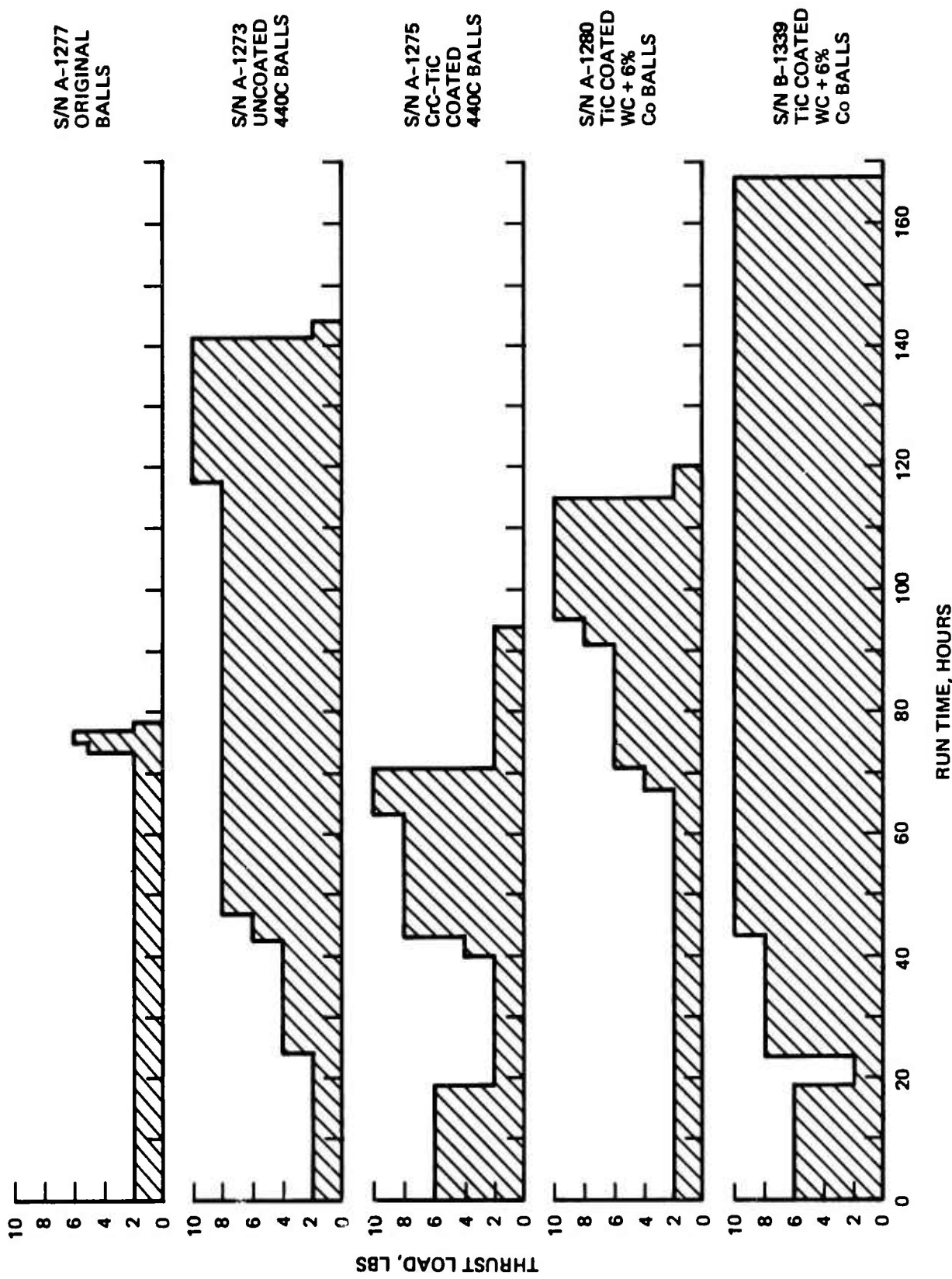


Figure 84. Testing Sequence of Bearings with Coated Balls

TEST TYPE: Coated Bearings

BRG SIZE: R-3

NO. OF BALLS: 8

OIL TYPE: SRG-160

BRG MFR: Barden

RET. MAT'L: Paper-phenolic

OIL RETENTION (%): 7.4

LITTON P/N: BX448-13

RET. MFR: Barden

CENTRIFUGED AT (G's): 900

BRG LOT: 2-20-79

RET. LOT: 5-31-79

TYPE: (IRR) ORR

BRG (OR) S/N: A 1277

RET. S/N: 101

ACID ETCH: NO (YES)

C.A. (DEGREES): 20.5

FLATS: 2

OTHER: Original balls 52100

NUMBER OF RUNS: 6

		RUN 1	RUN 2	RUN 3	RUN 4	RUN 5	RUN 6
COND.	DATE	11-15-79	11-16-79	11-17-79	11-19-79	11-19-79	11-19-79
	THRUST LOAD (LBS)	2.0	2.0	2.0	5.0	6.0	2.0
	BEARING SPEED (HZ)	375	375	375	375	375	375
CUM HOURS	METAL PARTS: PRE-RUN (HRS)	0	0.2	6.2	73.1	75.7	76.6
	METAL PARTS: POST-RUN (HRS)	0.2	6.2	73.1	75.7	76.6	77.5
	RETAINER: PRE-RUN (HRS)	0	0.2	6.2	73.1	75.7	76.6
	RETAINER: POST-RUN (HRS)	0.2	6.2	73.1	75.7	76.6	77.5
HIGH SPEED DATA	AXIAL HASH ( $\mu$ IN)	-	0.8	2.0	0.6	0.80	1.0
	TORQUE HASH (GM-CM)	-	0.5	0.44	0.45	0.36	0.50
	1/2 AMPLITUDE TORQUE (GM-CM)	-	0.38	0.40	0.90	-	-
	CW AXIAL DISP ( $\mu$ IN)	-	14	9	11	-	-
	TEMP ( $^{\circ}$ F)	-	167	166	164	-	-
	1/2 AMPLITUDE TORQUE (GM-CM)	-	0.40	0.40	0.80	-	-
	CCW AXIAL DISP ( $\mu$ IN)	18	-	-	-	14	13
	TEMP ( $^{\circ}$ F)	-	-	-	-	162	162
	EHD OIL FILM THICKNESS ( $\mu$ IN)	3.0	2.2	1.3	2.0	2.0	2.1
LOW SPEED DATA	RADIAL RUN-OUT ( $\mu$ IN)	35	18	-	-	-	180
	AXIAL RUN-OUT ( $\mu$ IN)	7.0	6	-	-	-	4.0
	TORQUE HASH (GM-CM)	1.1	0.45	-	-	-	0.8
	1/2 AMPLITUDE TORQUE (GM-CM)	0.45	0.35	-	-	-	0.45
SLOPE	AXIAL (mV)	120	140	130	75	-	120
	RADIAL (mV)	180	120	120	60	-	65
	TORQUE (mV)	200	250	280	360	-	320
SWEET ANALYZER	FREQ (HZ)	mV	FREQ (HZ)	mV			
	280	0	843	0			
	375 (1N)	10.0	1125	1.8			
	420	2.2	1876	2.1			
	647	0	2590	0			
	750 ('N)	10.0	3750	0.4			
PARTS CONDITION	INNER RACE	0	4				
	OUTER RACE	0	4				
	RETAINER	0	2				
	BALLS	0	2				

VISUAL QUANT.	CAGE SPEED (HZ)
	BRG SPEED (HZ)
VISUAL QUAL.	DYNAMIC SPEED RATIO
	TORSIONAL MOTION
VISUAL QUAL.	RADIAL MOTION
	OUT-OF-PLANE MOTION
VISUAL QUAL.	FOCCECTRICITY
	BALL STABILITY

Figure 85. High Speed Testing Results of Uncoated R-3 52100 Steel Bearing

TEST TYPE: Coated Bearings  
PPG SIZE: 6-3

**BRG SIZE:** R-3

BRG MFR: Barden

LITTON P/N: 972251-13

BRG LOT: 2-32-73

BRG (DR) S/N: A-1277

C.A. (DEGREES): 20.5

NUMBER OF PINS: 9

NO. OF BALLS: 8

RET. MAT'L: Paper=appendic.

REPT MEB: A 1-

RET. LOT: 5-31-79

R&T: 201: J-31  
BET: 6/4/1986

R.D. 5, P.M.  
FLATS - 2

OIL TYPE: SRG-160

OIL RETENTION (%): 9.2

CENTRIFUGED AT (G's): 900

TYPE:  IRR  ORR

ACID ETCH: NO  YES

OTHER: Original balls

NUMBER OF RUNS: 8		RUN 1	RUN 2	RUN 3	RUN 4	RUN 5	RUN 6
COND.	DATE	12-11-79	12-12-79	12-12-79	12-13-79	12-14-79	12-17-79
CUM HOURS	THRUST LOAD (LBS)	2.0	4.0	6.0	8.0	10.0	10.0
	BEARING SPEED (HZ)	375	375	375	375	375	375
HIGH SPEED DATA	METAL PARTS: PRE-RUN (HRS)	77.5	95.7	100.6	119.7	125.5	144.0
	METAL PARTS: POST-RUN (HRS)	95.7	100.6	119.7	125.5	144.0	219.6
	RETAINER: PRE-RUN (HRS)	77.5	95.7	100.6	119.7	125.5	144.0
	RETAINER: POST-RUN (HRS)	95.7	100.6	119.7	125.5	144.0	219.6
LOW SPEED DATA	AXIAL HASH ( $\mu$ IN)	0.8	1.0	4.4	1.7	0.5	0.6
	TORQUE HASH (GM-CM)	0.22	0.24	0.16	0.16	0.16	0.14
	1/2 AMPLITUDE TORQUE (GM-CM)	0.35	0.70	1.30	1.50	1.90	2.00
	CW AXIAL DISP ( $\mu$ IN)	18	18	23	26	28	28
	TEMP ( $^{\circ}$ F)	153	153	150	149	150	150
	1/2 AMPLITUDE TORQUE (GM-CM)	0.40	0.65	1.20	1.50	2.10	2.10
	CCW AXIAL DISP ( $\mu$ IN)	25	18	22	24	-	26
	TEMP ( $^{\circ}$ F)	153	151	150	150	149	150
SCOPE	EHD OIL FILM THICKNESS ( $\mu$ IN)	3.70	3.32	4.21	4.70	5.26	5.08
	RADIAL RUN-OUT ( $\mu$ IN)	150	-	-	-	-	-
	AXIAL RUN-OUT ( $\mu$ IN)	12	-	-	-	-	-
SWEEP ANALYZER	TORQUE HASH (GM-CM)	0.6	-	-	-	-	-
	1/2 AMPLITUDE TORQUE (GM-CM)	0.4	-	-	-	-	-
PARTS CONDITION	AXIAL (mV)	60	70	70	80	75	110
	RADIAL (mV)	50	110	70	110	75	140
	TORQUE (mV)	700	540	650	550	820	580
	FREQ (HZ)	mV	FREQ (HZ)	mV			
	280	1.4	843	0	CAGE SPEED (HZ)		
	375 (1N)	5.2	1125	2.8			
VISUAL QUANT.	420	2.8	1876	0			
	647	2.0	2590	0	BRG SPEED (HZ)		
	750 (2N)	2.8	3750	0			
	FREQUENCY TEST		DYNAMIC SPEED RATIO				
PARTS CONDITION	INNER RACE				TORSIONAL MOTION		
	OUTER RACE						
	RETAINER						
	BALLS				RADIAL MOTION		
VISUAL QUAL.					OUT-OF-PLANE MOTION		
VISUAL QUAL.					ECCENTRICITY		
VISUAL QUAL.					BALL STABILITY		

Figure 85. High Speed Testing Results of Uncoated R-3 52100 Steel Bearing (cont)

## TEST TYPE:

BRG SIZE:

NO. OF BALLS:

OIL TYPE:

BRG MFR:

RET. MAT'L:

OIL RETENTION (%):

LITTON P/N:

RET. MFR:

CENTRIFUGED AT (G's):

BRG LOT:

RET. LOT:

TYPE: IRR ORR

BRG (OR) S/N: A-1277

RBT. S/N:

ACID ETCH: NO YES

C.A. (DEGREES):

FLATS:

OTHER:

NUMBER OF RUNS:

		RUN 1	RUN 2	RUN 3	RUN 4	RUN 5	RUN 6
COND.	DATE	12-17-79	12-18-79				
	THRUST LOAD (LBS)	2.0	10.0				
	BEARING SPEED (HZ)	375	375				
CUM HOURS	METAL PARTS: PRE-RUN (HRS)	219.6	244.4				
	METAL PARTS: POST-RUN (HRS)	244.4	263.3				
	RETAINER: PRE-RUN (HRS)	219.6	244.4				
	RETAINER: POST-RUN (HRS)	244.4	263.3				
HIGH SPEED DATA	AXIAL HASH ( $\mu$ IN)	0.6	0.5				
	TORQUE HASH (GM-CM)	0.23	0.17				
	1/2 AMPLITUDE TORQUE (GM-CM)	0.33	2.05				
	CW AXIAL DISP ( $\mu$ IN)	22	28				
	TEMP ( $^{\circ}$ F)	150	151				
	1/2 AMPLITUDE TORQUE (GM-CM)	0.20	2.10				
	CCW AXIAL DISP ( $\mu$ IN)	21	26				
	TEMP ( $^{\circ}$ F)	150	151				
	EHD OIL FILM THICKNESS ( $\mu$ IN)	3.70	5.08				
LOW SPEED DATA	RADIAL RUN-OUT ( $\mu$ IN)	-	.55				
	AXIAL RUN-OUT ( $\mu$ IN)	-	12				
	TORQUE HASH (GM-CM)	-	2.6				
	1/2 AMPLITUDE TORQUE (GM-CM)	-	0.45				
SCOPE	AXIAL (mV)	70	80				
	RADIAL (mV)	65	110				
	TORQUE (mV)	750	750				
SWEET ANALYZER	FREQ (HZ)	mV	FREQ (HZ)	mV			
	280		843				
	375 (1N)		1125				
	420		1876				
	647		2590				
	750 (2N)		3750				
PARTS CONDITION	INNER RACE		POLE-HIST				
	OUTER RACE						
	RETAINER						
	BALLS						
	VISUAL QUAL.	VISUAL QUANT.	CAGE SPEED (HZ)				
			BRG SPEED (HZ)				
			DYNAMIC SPEED RATIO				
			TORSIONAL MOTION				
			RADIAL MOTION				
			OUT-OF-PLANE MOTION				
			ECCENTRICITY				
			BALL STABILITY				

PAGE 2 OF 2

Figure 85. High Speed Testing Results of Uncoated R-3 52100 Steel Bearing (cont)

TEST TYPE: Coated Bearings

BRG SIZE: R-3

BRG MFR: Barden

LITTON P/N: 9772251-13

BRG LOT: 2-20-79

BRG (OR) S/N: A-1273

C.A. (DEGREES): 23.6

NUMBER OF RUNS: 7

NO. OF BALLS: 8

RET. MAT'L: Paper-phenolic

RET. MFR: Barden

RET. LOT: 5-31-79

RET. S/N: 110

FLATS: 2

OIL TYPE: JRG-160

OIL RETENTION (%): 7.1

CENTRIFUGED AT (G's): 903

TYPE:  IRR  ORR

ACID ETCH: NO  YES

ITEM NO. 1. OTHER: Uncoated 440C BALLS.

COND.	DATE	RUN 1	RUN 2	RUN 3	RUN 4	RUN 5	RUN 6
	THRUST LOAD (LBS)	2.0	4.0	6.0	8.0	8.0	10
	BEARING SPEED (HZ)	375	375	375	375	375	375
CUM HOURS	METAL PARTS: PRE-RUN (HRS)	0	23.5	42.2	46.2	48.3	117.3
	METAL PARTS: POST-RUN (HRS)	23.5	42.2	46.2	48.3	117.3	140.3
	RETAINER: PRE-RUN (HRS)	0	23.5	42.2	46.2	48.3	117.3
	RETAINER: POST-RUN (HRS)	23.5	42.2	46.2	48.3	117.3	140.3
HIGH SPEED DATA	AXIAL HASH ( $\mu$ IN)	1.20	0.8	0.7	1.20	0.9	1.40
	TORQUE HASH (GM-CM)	0.31	0.2	0.19	0.15	0.16	0.24
	1/2 AMPLITUDE TORQUE (GM-CM)	0.38	0.73	1.13	1.70	1.50	2.10
	CW AXIAL DISP ( $\mu$ IN)	20	14	16	-	17	16
	TEMP (°F)	153	155	154	153	154	151
	1/2 AMPLITUDE TORQUE (GM-CM)	0.48	0.70	1.10	1.70	1.70	2.10
	CCW AXIAL DISP ( $\mu$ IN)	22	14	14	-	17	18
	TEMP (°F)	153	152	154	154	152	151
LOW SPEED DATA	EHD OIL FILM THICKNESS ( $\mu$ IN)	3.9	2.9	3.2	-	3.7	3.7
	RADIAL RUN-OUT ( $\mu$ IN)	40	-	-	-	-	-
	AXIAL RUN-OUT ( $\mu$ IN)	6	-	-	-	-	-
	TORQUE HASH (GM-CM)	.45	-	-	-	-	-
SCOPE	1/2 AMPLITUDE TORQUE (GM-CM)	.40	-	-	-	-	-
	AXIAL (mV)	90	90	100	100	90	100
	RADIAL (mV)	50	50	60	55	60	60
	TORQUE (mV)	780	800	775	800	800	800
SWEEP ANALYZER	FREQ (HZ)	mV	FREQ (HZ)	mV	VISUAL QUANT.	CAGE SPEED (HZ)	
	280	16	843	0		BRG SPEED (HZ)	
	375 (1N)	5.0	1125	5.8		DYNAMIC SPEED RATIO	
	420	4.0	1876	9.0		TORSIONAL MOTION	
	647	3.4	2590	0		RADIAL MOTION	
	750 (2N)	8.6	3750	2.6		OUT-OF-PLANE MOTION	
PARTS CONDITION	PRE-TEST	POST-TEST	PRE-TEST	POST-TEST	VISUAL QUANT.	LOCENTRICITY	
	INNER RACE	0	3	3		BALL STABILITY	
	OUTER RACE	0	3	3			
	RETAINER	0	5	1			
	BALLS	0	1	1			

VISUAL QUANT.	CAGE SPEED (HZ)
	BRG SPEED (HZ)
	DYNAMIC SPEED RATIO
	TORSIONAL MOTION
	RADIAL MOTION
	OUT-OF-PLANE MOTION
	LOCENTRICITY
	BALL STABILITY

Figure 86. High Speed Testing Results of 52100 Steel Bearing with 440C Steel Backs

## TEST TYPE:

BRG SIZE:

NO. OF BALLS:

OIL TYPE:

BRG MFR:

RET. MAT'L:

OIL RETENTION (%):

LITTON P/N:

RET. MFR:

CENTRIFUGED AT (G's):

BRG LOT:

RET. LOT:

TYPE: IRR ORR

BRG (OR) S/N: A-1273

RET. S/N:

ACID ETCH: NO YES

C.A. (DEGREES):

FLATS:

OTHER:

NUMBER OF RUNS:

RUN 1    RUN 2    RUN 3    RUN 4    RUN 5    RUN 6

COND.	DATE		12-11-79				
	THRUST LOAD (LBS)		2.0				
	BEARING SPEED (HZ)		375				
CUM HOURS	METAL PARTS: PRE-RUN (HRS)		140.3				
	METAL PARTS: POST-RUN (HRS)		143.5				
	RETAINER: PRE-RUN (HRS)		140.3				
	RETAINER: POST-RUN (HRS)		143.5				
HIGH SPEED DATA	AXIAL HASH ( $\mu$ IN)		0.80				
	TORQUE HASH (GM-CM)		0.26				
	1/2 AMPLITUDE TORQUE (GM-CM)		0.38				
	CW AXIAL DISP ( $\mu$ IN)		17				
	TEMP ( $^{\circ}$ F)		150				
	1/2 AMPLITUDE TORQUE (GM-CM)		0.35				
	CCW AXIAL DISP ( $\mu$ IN)		19				
	TEMP ( $^{\circ}$ F)		150				
LOW SPEED DATA	EHD OIL FILM THICKNESS ( $\mu$ IN)		3.2				
	RADIAL RUN-OUT ( $\mu$ IN)		60				
	AXIAL RUN-OUT ( $\mu$ IN)		8				
	TORQUE HASH (GM-CM)		1.6				
	1/2 AMPLITUDE TORQUE (GM-CM)		0.3				
SCOPE	AXIAL (mV)		90				
	RADIAL (mV)		60				
	TORQUE (mV)		650				
SWEEP ANALYZER	FREQ (HZ)	mV	FREQ (HZ)	mV	VISUAL QUANT.	CAGE SPEED (HZ)	
	280		843		BRG SPEED (HZ)		
	375 (1N)		1125		DYNAMIC SPEED RATIO		
	420		1876		TORSIONAL MOTION		
	647		2590		RADIAL MOTION		
	750 (2N)		3750		OUT-OF-PLANE MOTION		
PARTS CONDITION	PRE-TEST		POST-TEST		VISUAL QUAL.	ROTATION	
	INNER RACE						
	OUTER RACE						
	RETAINER						
	BALLS						

VISUAL QUANT.	CAGE SPEED (HZ)
BRG SPEED (HZ)	
DYNAMIC SPEED RATIO	
TORSIONAL MOTION	
RADIAL MOTION	
OUT-OF-PLANE MOTION	
ROTATION	
ECENTRICITY	
BALL STABILITY	

PAGE 2 OF 2

Figure 86. High Speed Testing Results of 52100 Steel Bearing with 440C Steel Backs (cont)

TEST TYPE: Coated Bearing

BRG SIZE: R-3

BRG MFR: Barden

LITTON P/N: 972251-13

BRG LOT: 2-20-77

BRG (OR) S/N: A-1275

C.A. (DEGREES): 22.7

NUMBER OF RUNS: 6

NO. OF BALLS: 8

RET. MAT'L: Paper-phenolic

RBT. MFR: Barden

RET. LOT: 5-31-77

RET. S/N: 117

FLATS: 2

OIL TYPE: SRG-160

OIL RETENTION (%): 6.9

CENTRIFUGED AT (G's): 900

TYPE: (IRR) ORR

ACID ETCH: NO (YES)

ITEM NO. 6. OTHER: TiC coated balls

COND.		RUN 1	RUN 2	RUN 3	RUN 4	RUN 5	RUN 6
CUM HOURS	DATE	11-26-77	11-27-77	11-28-77	11-28-77	11-29-77	11-29-77
	THRUST LOAD (LBS)	6.0	2.0	4.0	8.0	10.0	2.0
	BEARING SPEED (HZ)	375	375	375	375	375	375
	METAL PARTS: PRE-RUN (HRS)	0	18.5	39.6	43.0	63.9	70.3
	METAL PARTS: POST-RUN (HRS)	18.5	39.6	43.0	63.9	70.3	93.3
	RETAINER: PRE-RUN (HRS)	0	18.5	39.6	43.0	63.9	70.3
	RETAINER: POST-RUN (HRS)	18.5	39.6	43.0	63.9	70.3	93.3
HIGH SPEED DATA	AXIAL HASH ( $\mu$ IN)	2.8	1.0	0.8	1.4	1.4	0.6
	TORQUE HASH (GM-CM)	0.36	0.37	0.31	0.33	0.23	0.32
	1/2 AMPLITUDE TORQUE (GM-CM)	1.45	0.63	0.95	1.8	2.40	0.65
	CW AXIAL DISP ( $\mu$ IN)	27	22	20	24	2.8	22
	TEMP (°F)	163	149	149	154	152	151
	1/2 AMPLITUDE TORQUE (GM-CM)	1.38	0.58	1.00	1.85	2.40	0.70
	CCW AXIAL DISP ( $\mu$ IN)	26	27	22	-	22	24
	TEMP (°F)	162	150	150	-	152	154
	EHD OIL FILM THICKNESS ( $\mu$ IN)	5.6	4.6	4.3	5.1	5.3	4.3
LOW SPEED DATA	RADIAL RUN-OUT ( $\mu$ IN)	90	-	-	-	-	180
	AXIAL RUN-OUT ( $\mu$ IN)	6	-	-	-	-	10
	TORQUE HASH (GM-CM)	.40	-	-	-	-	1.0
	1/2 AMPLITUDE TORQUE (GM-CM)	.25	-	-	-	-	0.30
SCOPE	AXIAL (mV)	180	125	200	200	190	100
	RADIAL (mV)	100	120	110	55	55	50
	TORQUE (mV)	850	900	1100	460	550	520
SWEEP ANALYZER	FREQ (HZ)	mV	FREQ (HZ)	mV	VISUAL QUANT.	CAGE SPEED (HZ)	
	280	48	843	0		BRG SPEED (HZ)	
	375 (1N)	3.4	1125	3.0		DYNAMIC SPEED RATIO	
	420	0	1876	5.6		TORSIONAL MOTION	
	647	5.6	2590	0		RADIAL MOTION	
	750 (?N)	6.0	3750	4.4		OUT-OF-PLANE MOTION	
PARTS CONDITION	PRE-TEST	POST-TEST	VISUAL QUAL.	ECCENTRICITY			
	INNER RACE	0		BALL STABILITY			
	OUTER RACE	0					
	RETAINER	0					
	BALLS	0					

PAGE 1 of 1

Figure 87. High Speed Test Results of Bearing with TiC Coated Cemented Tungsten Carbide Balls

TEST TYPE: Coated Bearing

BKG SIZE: 8-3

BRG MFR: Barden

LITTON P/N: 972251-13

BRG LOT: 7-23-79

BRG (OR) S/N: A-1283

C.A. (DEGREES): 23.7

NUMBER OF RUNS: 6

NO. OF BALLS: 8

RET. MAT'L: Paper - phenolic

RET. MFR: Barden

RET. LOT: 5-31-73

RET. S/N: 113

FLATS: 2

OIL TYPE: SFG-140

OIL RETENTION (%): 7.0

CENTRIFUGED AT (G's): 930

TYPE:  IRR  ORR

ACID ETCH: NO YES  
OTHER: WC + 6% Co mill w/T: C

NUMBER OF RUNS: 6

NUMBER OF RUNS: 6		RUN 1	RUN 2	RUN 3	RUN 4	RUN 5	RUN 6
COND.	DATE	11-30-79	12-3-79	12-3-79	12-4-79	12-4-79	12-5-79
	THRUST LOAD (LBS)	2.0	4.0	6.0	8.0	10.0	2.0
	BEARING SPEED (HZ)	375	375	375	375	375	375
CUM HOURS	METAL PARTS: PRE-RUN (HRS)	0	67.5	71.5	90.9	94.7	115.1
	METAL PARTS: POST-RUN (HRS)	67.5	71.5	90.9	94.7	115.1	120.1
	RETAINER: PRE-RUN (HRS)	0	67.5	71.5	90.9	94.7	115.1
	RETAINER: POST-RUN (HRS)	67.5	71.5	90.9	94.7	115.1	120.1
HIGH SPEED DATA	AXIAL HASH ( $\mu$ IN)	0.5	0.5	0.6	0.5	0.5	0.5
	TORQUE HASH (GM-CM)	0.36	0.30	0.29	0.23	0.24	0.25
	1/2 AMPLITUDE TORQUE (GM-CM)	0.35	0.70	1.10	1.50	1.95	0.35
	CW AXIAL DISP ( $\mu$ IN)	40	26	22	20	19	40
	TEMP ( $^{\circ}$ F)	155	155	155	155	156	160
	1/2 AMPLITUDE TORQUE (GM-CM)	.35	0.68	1.10	1.50	2.03	0.40
	CCW AXIAL DISP ( $\mu$ IN)	44	26	22	20	20	40
	TEMP ( $^{\circ}$ F)	155	153	153	154	154	155
LOW SPEED DATA	EHD OIL FILM THICKNESS ( $\mu$ IN)	8.5	5.5	4.7	4.3	4.2	8.1
	RADIAL RUN-OUT ( $\mu$ IN)	40	-	-	-	-	60
	AXIAL RUN-OUT ( $\mu$ IN)	6	-	-	-	-	6
	TORQUE HASH (GM-CM)	0.35	-	-	-	-	0.30
SCOPE	1/2 AMPLITUDE TORQUE (GM-CM)	0.2	-	-	-	-	0.18
	AXIAL (mV)	80	80	70	80	70	70
	RADIAL (mV)	110	125	55	125	55	60
SWEEP ANALYZER	TORQUE (mV)	880	900	800	950	850	750
	FREQ (HZ)	mV	FREQ (HZ)	mV	VISUAL QUANT.		
	280	0	843	0			
	375 (1N)	7.8	1125	2.6			
	420	2.2	1876	5.3			
PARTS CONDITION	647	0	2590	0	VISUAL QUAL.		
	750 (2N)	5.4	3750	2.8			
INNER RACE		O	2-				
OUTER RACE		O	-				
RETAINER		O	-				
BALLS		O	-				
CO-CENTRICITY		-	-				
BALL STABILITY		-	-				

Figure 88. High Speed Test Results of Bearing with TiC Coated Cemented Tungsten Carbide Balls

TEST TYPE: Coated Beany

BRG SIZE: R-3

BRG MFR: Borden

LITTON P/N: 972251-14

BRG LOT: 2-20-79

BRG (OR) S/N: B 1339

C.A. (DEGREES):

NUMBER OF RUNS: 6

NO. OF BALLS: 8

RET. MAT'L: Paper-phenolic

RET. MFR:

RET. LOT: 5-31-79

RET. S/N: 116

FLATS:

ITEM NO. 8'

OIL TYPE: SRG-160

OIL RETENTION (%): 7.1

CENTRIFUGED AT (G's): 900

TYPE: IRR ORR

ACID ETCH: NO YES

OTHER: TiC coated WC+6%<sup>Co</sup> mill.

COND.	DATE	RUN 1	RUN 2	RUN 3	RUN 4	RUN 5	RUN 6
	THRUST LOAD (LBS)	2.0	6.0	2.0	8.0	10.0	10
	BEARING SPEED (HZ)	375	375	375	375	375	375
CUM HOURS	METAL PARTS: PRE-RUN (HRS)	0	0.3	18.8	23.5	43.1	161.2
	METAL PARTS: POST-RUN (HRS)	0.3	18.8	23.5	43.1	161.2	167.6
	RETAINER: PRE-RUN (HRS)	0	0.3	18.8	23.5	43.1	161.2
	RETAINER: POST-RUN (HRS)	0.3	18.8	23.5	43.1	161.2	167.6
HIGH SPEED DATA	AXIAL HASH ( $\mu$ IN)	-	0.80	1.2	1.8	2.0	4.0
	TORQUE HASH (GM-CM)	0.31	0.40	0.32	0.40	0.31	0.44
	1/2 AMPLITUDE TORQUE (GM-CM)	-	1.2	0.5	1.7	2.3	1.8
	CW AXIAL DISP ( $\mu$ IN)	-	19	28	17	16	18
	TEMP (°F)	-	165	167	163	163	168
	1/2 AMPLITUDE TORQUE (GM-CM)	-	1.25	0.5	1.7	2.2	2.0
	CCW AXIAL DISP ( $\mu$ IN)	-	19	28	17	23	22
	TEMP (°F)	-	165	167	162	163	162
	EHD OIL FILM THICKNESS ( $\mu$ IN)	-					
LOW SPEED DATA	RADIAL RUN-OUT ( $\mu$ IN)	190	-	-	-	-	100
	AXIAL RUN-OUT ( $\mu$ IN)	10	-	-	-	-	5
	TORQUE HASH (GM-CM)	1.5	-	-	-	-	0.9
	1/2 AMPLITUDE TORQUE (GM-CM)	0.35	-	-	-	-	1.6
SCOPE	AXIAL (mV)	80	75	110	100	75	70
	RADIAL (mV)	45	65	45	45	40	50
	TORQUE (mV)	180	220	200	650	800	320
SWEEP ANALYZER	FREQ (HZ)	mV	FREQ (HZ)	mV	VISUAL QUANT.	CAGE SPEED (HZ)	
	280	0	843	0		BRG SPEED (HZ)	
	375 (1N)	6.5	1125	3.2		DYNAMIC SPEED RATIO	
	420	1.4	1876	3.2		TORSIONAL MOTION	
	647	0	2590	1.2		RADIAL MOTION	
	750 (?N)	9.0	3750	0		OUT-OF-PLANE MOTION	
PARTS CONDITION	INNER TEST	OUTER TEST	VISUAL QUAL.	CENTRICITY	BALL STABILITY		
	INNER RACE	?					
	OUTER RACE	?					
	RETAINER	?					
	BALLS	?					

PAGE 1 OF 1

Figure 89. High Speed Test Results of Bearing with TiC Coated Cemented Tungsten Carbide Balls



Figure 90. Bearing 36      3000X  
Ball Track

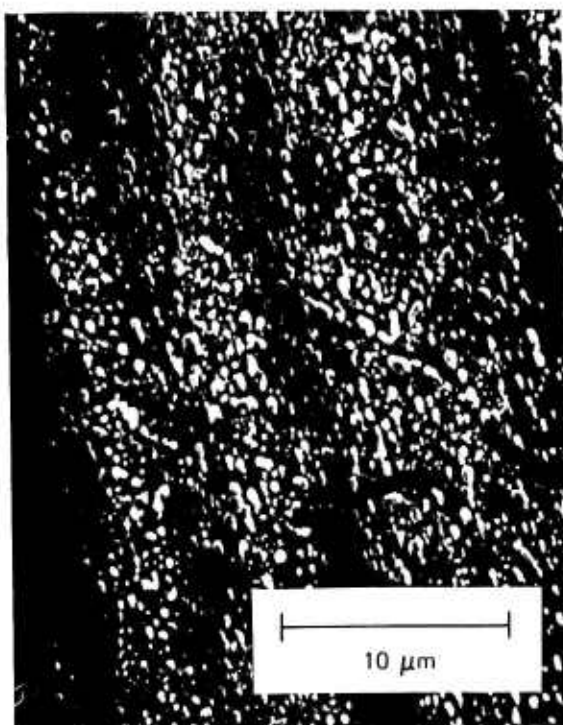


Figure 91. Bearing 36 Near      3000X  
Ball Track

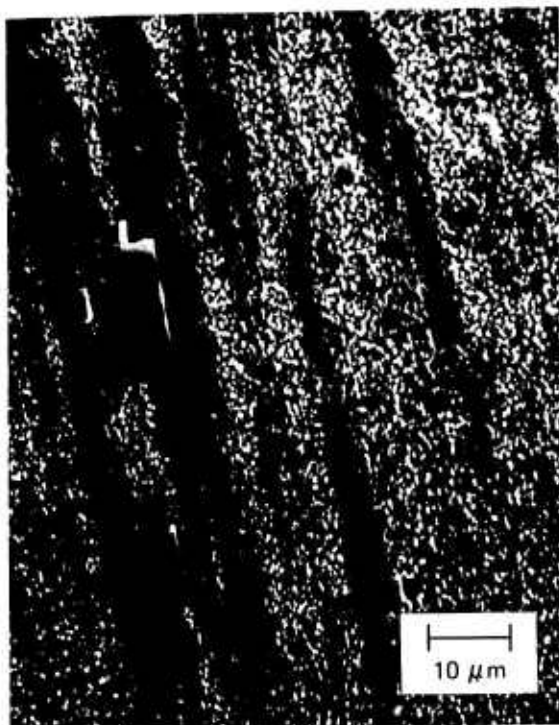


Figure 92. Transition Zone      1000X  
Near Ball Track



Figure 93. Transition Zone      3000X  
Near Ball Track

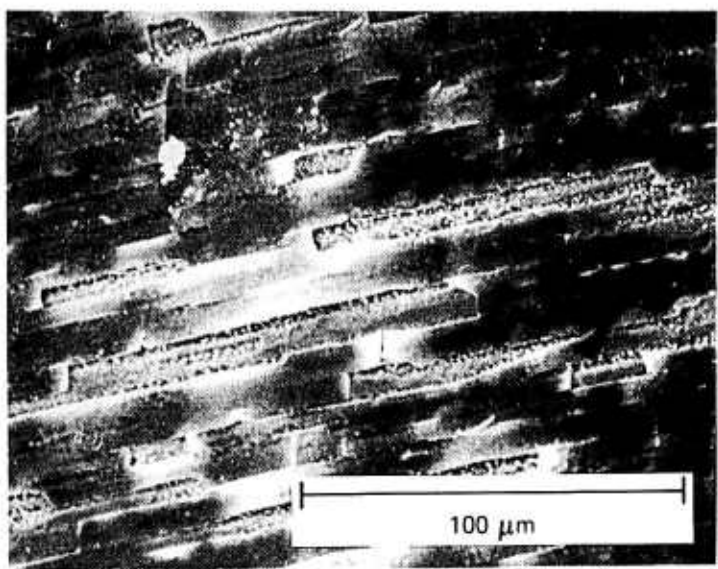


Figure 94. In Ball Track

500X

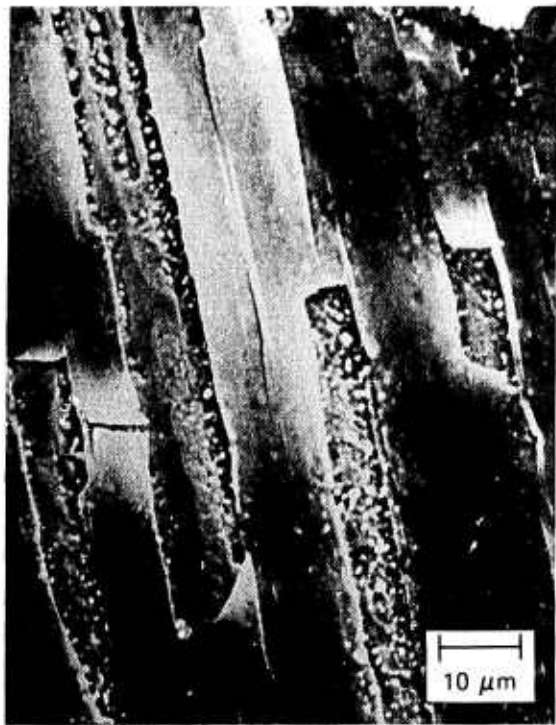


Figure 95. In Ball Track

1000X



Figure 96. In Ball Track

3000X

APPENDIX B

WEGLEIN, R. D. TO GARDOS, M. N.,  
"ACOUSTIC MICROSCOPY OF GYRO BEARING BALLS",  
Hughes Technical Internal Correspondence 7621. 30/162,  
4 January 1980.

# HUGHES AIRCRAFT COMPANY

## TECHNICAL INTERNAL CORRESPONDENCE

TO: M. N. Gardos

DATE: 4 January 1980  
REF: 7621.30/162

SUBJECT: Acoustic Microscopy of Gyro Bearing Balls FROM: R. D. Weglein

BLDG. 6 MAIL STA.D129  
EXT. 4454

---

ABSTRACT:

Acoustic micrographs of 52100 stainless steel bearing balls have been made using a reflection acoustic microscope, operating near 400 MHz. The surface layers in both the spherical bearing surface and polished planar section were characterized by using the acoustic material signature technique. Rayleigh wave velocities on these surfaces and the acoustic absorption were measured in a nondestructive way and the results are reported herein. The spherical surface combines the imaging and characterization modes to produce a two-dimensional map of the elastic properties. This nondestructive mapping may provide a simple, rapid NDE technique for the quality control of fully machined bearing balls and raceways.

## ACOUSTIC MICROSCOPY OF GYRO BEARING BALLS

R. D. Weglein

Hughes Research Laboratories  
(on loan to Technology Support Division)

### INTRODUCTION

One of the main objectives of the present DARPA/Hughes Solid Lubricated Rolling Element Bearing Program is to identify ideal bearing substrates for solid lubricants. Conventionally machined bearing balls and races are usually in a surface-damaged condition caused by poor machining practices. This damage consists, among others, of imperfections in the physical metallurgy and chemistry of the raceway and ball surfaces. Improper pressure or duration of grinding or lapping and the concommittant temperature increase causes preferential precipitation of carbides near the bearing surfaces, covered by a soft smear layer originating from the decarburized martensitic matrix.

The present technique for identifying the damage consists of a costly and time consuming combination of layer etch and SEM photomicrographic procedure. The acoustic microscope appears to be a likely, fast and convenient substrate NDE technique to examine bearing balls and races, provided the needed information could be obtained.

Acoustic microscopy has recently been applied to the elastic characterization of materials<sup>(1)</sup> and to the thickness measurement of thin films used in semiconductor device fabrication<sup>(2)</sup>. The acoustic microscope offers great promise in the early detection of defective materials and devices during the fabrication process.

This is largely because the procedure is nondestructive as well as noncontaminating. Without exception, the predicted and demonstrated results have to date been concerned with planar samples, yielding acoustic images as well as acoustic material signatures (AMS)<sup>(1)</sup>.

The acoustic examination of bearing balls represents a significant departure from the prior work in that heretofore, curved surfaces have not been imaged. In this memorandum, acoustic micrographs of portions of 52100 stainless steel gyro bearing balls are presented. The spherical surface combines the imaging and characterization modes of the acoustic microscope in a unique manner. It is suggested that quantitative evaluation of the elastic properties of spherical surface layers may be possible with the aid of this new technique.

#### EXPERIMENT

Gyro bearing balls were sectioned to provide a comparison between results on both planar and spherical surfaces. The balls were of 52100 stainless steel, R-3 (3/32 in. dia., nominal) sample lot 9-21-73, OR 584, IR 250, received from Mr. W. Baginski of Litton Guidance and Control Systems, Woodland Hills, CA. Acoustic material signatures (AMS)<sup>(1)</sup> and raster-scanned acoustic images were obtained in the experimental acoustic microscope that had previously been developed with DARPA/NBS support\*. In the AMS mode, Rayleigh waves are launched and detected coherently. The bearing ball sections were cemented to a fused quartz plate using a low temperature wax, a convenient technique that was previously developed for general diagnostic inspection and is now the standard procedure in the acoustic microscope. A scanning electron micrograph of the mounted sections is shown in Figure 1. The ball

---

\* DARDA/NBS Contract No. 5-35898

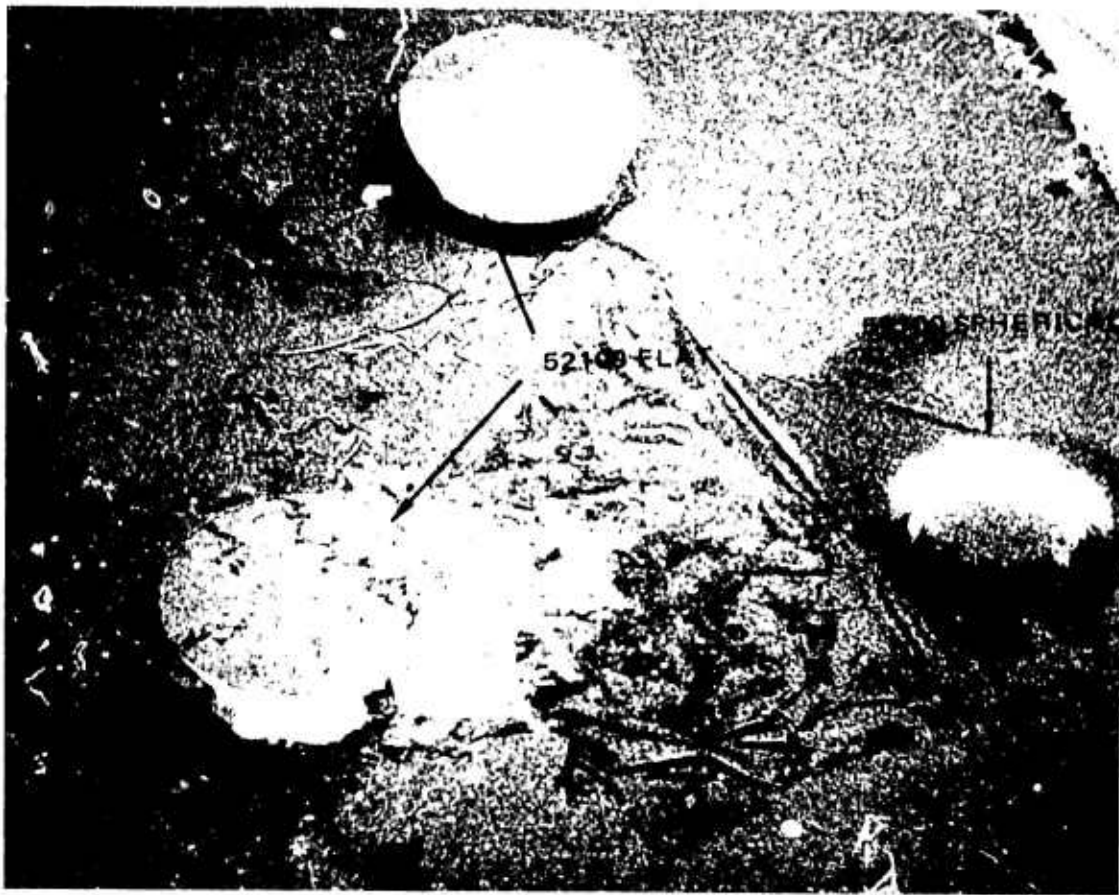


Figure 1. Bearing Ball sections mounted for diagnostic inspection in the acoustic microscope

section with its planar face up exposes a Hughes-polished 52100 stainless steel surface. The section denoted by the arrow is mounted with the spherical surface pointing up, and, therefore, presents a conventionally lapped bearing ball surface for diagnostic inspection. The arrow points to the apex of the sphere where the measurements were made.

Acoustic material signatures (AMS) for these two cases are shown in Figure 2. The solid curve represents the measurement on the planar (Hughes-polished) surface, while the dashed curve is for the spherical bearing surface. The AMS curves are the transducer output power variation with object translation along the lens axis  $z$ . The periodic nature of the signature has been previously explained<sup>(1)</sup>. It is the result of interference between

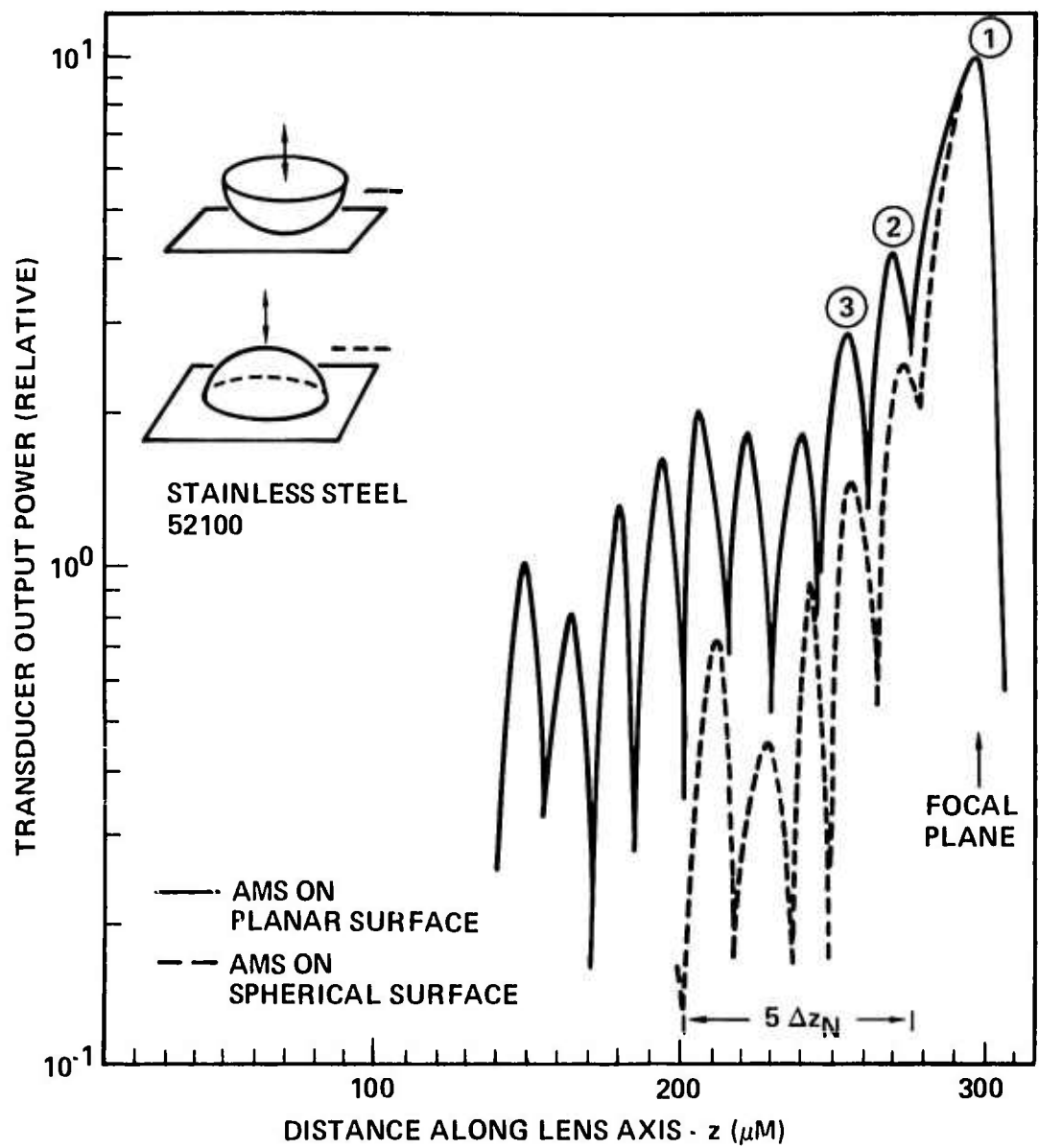


Figure 2. Acoustic Material Signatures on planar and spherical surface

two component waves that are reflected from the substrate (bearing) into the coupling liquid (deionized water,  $v = 1.5 \text{ mm}/\mu\text{sec}$ ) and are vectorially summed in the piezoelectric transducer. From the physical model that was developed to explain the acoustic material

signature the AMS period  $\Delta z_N$  is proportional to the square of the mean Rayleigh velocity in the plane of the substrate material. The measured period averaged over all periods in the figure yields the Rayleigh velocity  $v_R$  directly as given by Equation 1:

$$v_R = (v_\ell \cdot f \cdot \Delta z_N)^{\frac{1}{2}} \quad (1)$$

$$= 23.56 (\Delta z_N)^{\frac{1}{2}}$$

where the frequency of 370 MHz has been assumed, and  $v_\ell$  is the velocity in water. Measured and derived results from Figure 2 are listed in Table 1. For completeness and comparison, the published Rayleigh velocity for 347 stainless steel has been included. The listed value was calculated from the published shear velocity and

TABLE 1

Measured Rayleigh Velocities on 52100 Stainless Steel Gyro Bearing Ball

Surface	Type	$\Delta z_N$	$\bar{v}_R$
		( $\mu\text{m}$ )	$\text{mm}/\mu\text{sec}$
Planar	Ground & polished 52100 at Hughes	14.6	2.85
Spherical	52100 Conventional lapping by ball manufacturer	13.2	2.71
Planar	347 stainless steel		2.88*

\*  $v_R = \frac{0.87 + 1.12\sigma}{1 + \sigma} v_{sh}; c_{347} = 0.20; v_{sh} = 3.10 \text{ mm}/\mu\text{sec}$

$\Delta z_N$  - AMS Period  
 $\bar{v}_R$  - Mean Rayleigh Velocity  
 $v_{sh}$  - Shear velocity  
 $\sigma$  - Poisson Ratio

Poisson ratio<sup>(3)</sup> using an approximate functional relationship also shown in Table 1.<sup>(4)</sup>

An acoustic image of the spherical bearing surface, taken with the acoustic microscope, is shown in Figure 3a. This raster-scanned micrograph was taken with the apex of the spherical bearing surface at approximately 40  $\mu\text{m}$  inside the acoustic focal plane (see Figure 3b) at a magnification of 100X. The nominal focal distance of this acoustic lens was previously determined to be 450  $\mu\text{m}$ . The image covers an area approximately 600  $\mu\text{m}$  in diameter, as Figure 3b indicates. The same approximate area, imaged in a scanning electron microscope, is seen in Figure 3c. A number of common surface features, such as surface indentations and debris, are clearly seen in both acoustic and SEM micrographs. The excellent image resolution of the SEM is evident.

Superposed on this surface detail is a series of bright and dark circular regions, visible only in the acoustic micrograph. These nearly concentric rings, denoted by (1), (2) and (3) in Figure 3b, correspond to the similarly-numbered peaks of the spherical surface AMS shown previously in Figure 2. The outer ring represents the annular surface approximately in the focal plane, while the inner two bright fields, (2) and (3), represent elastic information at 23  $\mu\text{m}$  and 40  $\mu\text{m}$  respectively, in front of the focal plane. This image, therefore, constitutes a regional map of the acoustic material signature of the bearing ball. Just as the null spacing in the AMS of Figure 2 yields Rayleigh velocity information at one point on the surface, so does the radial spacing of the dark rings in Figure 3 yield the Rayleigh velocity in the two-dimensional plane. The particular number of rings shown here is quite arbitrary. The number may be increased to a maximum that corresponds to the number of periods shown in Figure 2, merely by further translation of the bearing surface toward the acoustic lens.

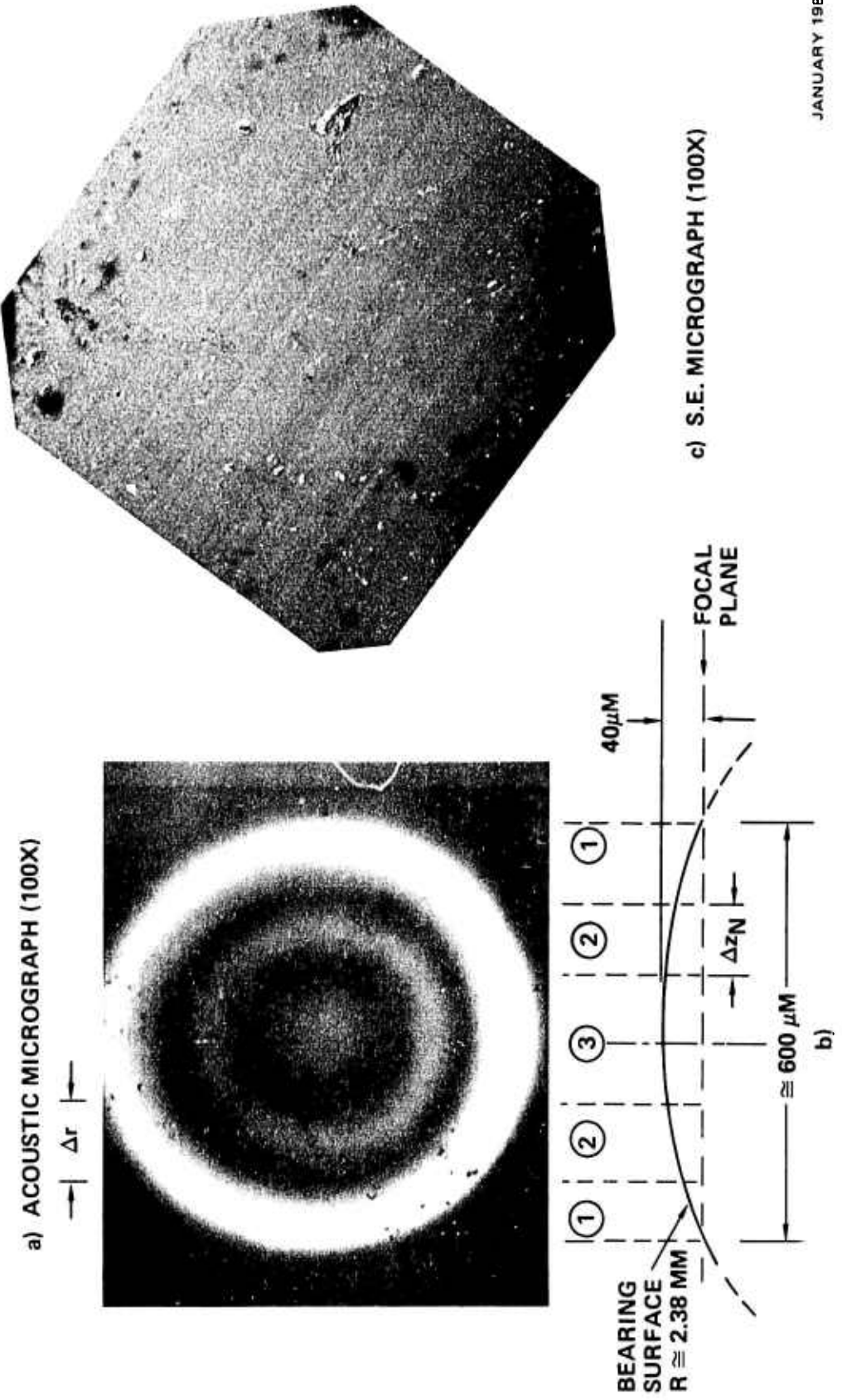


Figure 3. Acoustic image of Gyro Bearing Ball surface

## DISCUSSION

Material characterization in a curved surface region of a gyro bearing ball has been experimentally investigated with the reflection acoustic microscope. No such work has been reported in the open literature to date. The new information takes on the form of a local acoustic material signature, measured in a circular area approximately 150  $\mu\text{m}$  in diameter, and in a two-dimensional map that yields Rayleigh velocity information directly. Because the information is new, some interpretations of these initial results is warranted.

A comparison of the measured AMS curves of Figure 2 shows some differences in amplitude variation and in the period  $\Delta z_N$ . The AMS of the spherical surface is seen from Figure 2 to decrease somewhat faster than the planar surface AMS, as the distance from the focal plane increases. Although no prior information exists on acoustic characterization of curved surfaces, this measured behavior is consistent with the ray model of the AMS<sup>(5)</sup>. One would expect increased divergence of the acoustic beam as it is reflected from the convex surface, thus reducing the acoustic power intercepted by the piezoelectric transducer of finite diameter. Therefore, the amplitude differences of the two curves of Figure 2 may be attributed to the acoustic beam divergence effect on the spherical reflecting surface. Greater curvature would most likely increase the effect.

Further, the measured Rayleigh velocities, from Table 1, differ by approximately 5 percent between the planar and spherical surfaces. This difference cannot be attributed to Rayleigh wave propagation on curved and planar surfaces. Analysis<sup>(6)</sup> has shown that in the case of propagation on a convex cylindrical surface, the curved surface velocity is larger, and that the ratio of Rayleigh velocities on curved and planar surfaces decreases monotonically from a maximum

of about 1.3 and approaches unity asymptotically as the surface radius to wavelength ratio  $R/\lambda_R$  exceeds 100. In the present case,  $R/\lambda_R > 10^3$ , thus rendering the curvature effect negligible.

The materials in the two surfaces, on the other hand, may be different. The planar surface has been machined during sectioning and metallographic polishing with an aqueous .03  $\mu\text{m}$  alumina powder slurry. The introduced surface damage and general condition is not known at this time. Even though the spherical surface layer of the gyro bearing was not disturbed by any sectioning, its thickness and constituency is still not characterized beyond what has been described by W. A. Baginski in connection with Figure 63 of this referenced document<sup>(7)</sup>. That figure, containing a cross section of a 52100 steel bearing gyro ball, similar to that studied in the present report, shows a surface layer approximately 35  $\mu\text{m}$  thick "...containing excessive carbide precipitation that developed during the grinding process due to an overheated surface...". In an attempt to relate the reduced Rayleigh velocity on the spherical bearing surface to material parameters, one would have to postulate a corresponding reduction of  $(c/\rho)$ , where  $c$  is an equivalent stiffness coefficient for Rayleigh waves and  $\rho$  is the material density in the layer. Such an interpretation is premature because of the lack of detailed layer characterization. However, the observed velocity reduction in the bearing surface would be consistent with a postulated "softer" bearing layer that resulted from decarburization of the martensitic matrix (i.e., commensurate with precipitation of the harder carbide grains).

Acoustic absorption estimates may also be derived nondestructively from the AMS curves. Information of this type may be useful in comparing materials as to visco-elastic as well as scattering properties of the matrix material containing grain distributions. An upper limit of acoustic propagation loss may be calculated by noting the peak-to-null ratio of the AMS period, shown in Figure 2,

and the path length of the leaky Rayleigh wave in the ray model. The per wavelength acoustic absorption is given in Equation (2).

$$L_\lambda = \frac{\lambda_R}{2\Delta z \sin \theta_R} \cdot 20 \log \frac{R+1}{R-1} \quad (\text{dB}/\lambda) \quad (2)$$

where  $\Delta z$  = the axial distance from the focal plane to the position of the minimum,

$$\sin \theta_R = v_{H_2 O} / v_R$$

$R$  = peak to valley ratio at  $\Delta z$

With the aid of Equation (2) and the data in Figure 2, the 52100 stainless steel surface layer exhibits a maximum acoustic propagation loss for Rayleigh waves of 0.12 dB per wavelength at 0.375 GHz.

The literature is very sparse in acoustic absorption information in stainless steel, in particular, for Rayleigh waves, information that is simply obtained in a completely nondestructive way through the pulsed reflection acoustic microscope. The origin of this attenuation due to, for example, thermal phonons or grain boundary scattering, could be found from an extension of this work at other frequencies. The various mechanisms may be identified in this way because they exhibit classically different frequency dependence<sup>(8)</sup>.

The image of the bearing surface shown in Figure 3a and its cross-sectional sketch of Figure 3b deserve further discussion. The concentric set of bright and dark rings was earlier related to the corresponding peaks and valleys of the acoustic material signature of Figure 2. These rings and in particular, their radial spacing are believed to contain elastic information of the imaged surface region. For example, the radial separation of the dark rings along any radial direction, denoted by  $\Delta r$  in Figure 3, corresponds

to the AMS spacing  $\Delta z_N$  and is therefore a measure of the Rayleigh velocity in that direction. Any variation in  $\Delta r$  would therefore reveal a local change in stiffness, density or a combination of these. In fact, some variation in the width of the dark rings is quite evident in the left side of the imaged region. However, the assignment of a quantitative interpretation must await a full physical characterization (e.g., layer etch and SEM examination) of the surface, as was indicated earlier in connection with Reference 7.

A further comment may be made regarding the concentricity of these rings. A spherical ball is self-aligned under the acoustic beam. Therefore, the assumption of a spherical surface demands concentric regions if the elastic properties of the surface region do not vary spatially. If the acoustic material signature is known for an isotropic material, the radius of curvature of a gyro ball bearing may then be measured in an essentially noncontacting manner by this method.

Penetration of acoustic energy into the bearing surface is of some interest if non-destructive depth profiling of surface regions is desired. "Skin Depth" for Rayleigh waves is of the order of  $\lambda_R/2\pi$ , where in the present case the Rayleigh wavelength  $\lambda_R$  is 7.23  $\mu\text{m}$ . It would be expected, therefore, that the two-dimensional AMS of Figure 3a reveals the elastic parameters within a surface region approximately 1.15  $\mu\text{m}$  thick. Shallower and thicker surface regions may be similarly probed by appropriately scaling acoustic lenses that operate at higher as well as lower frequencies.

## Conclusions

Imaging of a spherically-shaped steel object has been investigated in a preliminary way using the acoustic microscope. In particular, the new imaging capability has been applied to the examination of 52100 stainless steel gyro bearing balls of 3/32 inch nominal diameter. It was shown that the acoustic microscope provides two types of complementary data that may be useful in the diagnostic inspection and materials characterization of fully-machined (i.e., lapped) bearing balls.

In the nonscanning mode, elastic parameters, such as Rayleigh velocity and acoustic absorption were locally determined nondestructively via the acoustic material signature (AMS) technique. Specifically, one measurement of the Rayleigh velocity on the spherical surface of a conventionally-lapped bearing surface and on a locally-polished planar 52100 stainless steel surface yielded 2.71 and 2.85 mm/ $\mu$ sec, respectively. An upper limit of acoustic propagation loss in the stainless steel surface of 16 dB/mm or 0.12 dB/wavelength at 0.375 GHz was obtained. Measurements of this type, when extended over a wide frequency range with appropriately-designed acoustic lenses, should reveal an elastic depth profile of the bearing surface layer, as well as the grain size distribution of carbides and other segregate embedded in the steel matrix. It was suggested that the measured 5% difference in Rayleigh velocities, given above, is attributable to the variations in the mechanical texture of the encountered surface layers and does not depend on their shape differences. Rayleigh wave penetration in the present experiment is estimated to be about 1.25  $\mu$ m.

In the raster-scanning mode, a two-dimensional regional map of the acoustic material signature was obtained. There appear to be observable variations of the surface layer elastic

properties. In the image of the bearing ball, surface features (scratches, nicks, debris) are superimposed on a set of nearly concentric bright and dark regions, that contain a spatial map of the elastic parameters in the form of Rayleigh velocities. The number of rings that are imaged depends on the distance of the spherical surface from the lens and may attain a maximum equal to the number of periods in the one-dimensional AMS.

It was suggested that the observed deviations from concentricity in the rings denote spatial variations of the Rayleigh velocities and, therefore, provide a simple, cost-effective diagnostic or pre-screening technique for fully-machined bearing balls. However, the observed effects should be verified by the physical (somewhat destructive) examination techniques previously described.

The detectability of small variations in surface layers is not known at the present time. The reproducibility of the AMS period in well-ordered crystalline materials, such as the <100> plane of silicon is between 1 and 2 percent in the present laboratory acoustic microscope. Substantial improvements in the AMS and image resolution are predicted with increased stability and sophistication in an electronic, digitally-implemented organization. The serial signal output format of the acoustic microscope, a consequence of raster scanning, lends itself uniquely to that task.

Finally, the demonstrated ability of the present acoustic microscope to image and map the elastic parameter distribution of convex spherical surface regions suggests that it may be possible to perform the same type of inspection on other curved surfaces, such as the concave cylindrical surfaces of bearing raceways.

## REFERENCES

1. R. D. Weglein, "A Model for Predicting Acoustic Material Signatures", *Appl. Phys. Lett.*, Vol. 34, No. 3, Feb. 1, 1979, pp. 179-181.
2. R. D. Weglein, "SAW Dispersion and Film Thickness Measurement by Acoustic Microscopy". *Appl. Phys. Lettr.*, Vol. 35, No. 3, Aug. 1, 1979, pp. 215-217.
3. American Institute of Physics Handbook, McGraw-Hill Co., N. Y., 3rd Edition, Chapter 3.
4. L. Bergmann, *DER ULTRASCHALL*, Hirzel Verlay, Zurich, 1949.
5. W. Parmon and H. L. Bertoni, "Ray Interpretation of the Material Signature in the Acoustic Microscope", *Electronic Letters*, Vol. 15, No. 21., Oct. 1979, pp. 684-686.
6. I. A. Victorov, "Rayleigh and Lamb Waves", Plenum Press, N. Y. 1967, Chapter I-4.
7. W. A. Baginski, "Phase 1 - A New Approach to Advance the State-of-the-Art of Liquid Lubricated Instrument Ball Bearings", Customer Contract No. 04-493431-FS-5, Prime Contract No. F33615-78-C-4196, July 1979. Appendix A to; Gardos, M. N., "Solid Lubricated Rolling Element Bearings - Semiannual Report No. 2," DARPA Order No. 3576, AFML Contract No. F33615-78-C-5196, Hughes Aircraft Company Report No. FR-79-76-1041, 15 August 1979.
8. E.P. Papadakis in "Physical Acoustics" (W.P. Mason, ed.) Vol. IV, p. 269 ACADEMIC PRESS, N.Y. 1968.

### Future Work

Based on the conclusions of this exploratory effort in which NDE of surface layers in a gyro bearing ball is performed by acoustic microscopy, the following tasks are suggested to develop the technique to its full potential. This should lead to a cost-effective NDE method applicable to the testing of fully-machined stainless steel (or possibly ceramic) bearing balls and raceways.

Task 1 An extensive measurements program should be undertaken on gyro and turbine bearing balls. Measurements on each ball should include:

- a) One-dimensional AMS
- b) Two-dimensional AMS (raster-scanned image)
- c) Physical analysis (chem-etch/AM/SEM)

Data should be acquired on bearing balls of different surface treatments ranging from the conventionally-lapped surface layer to the refractory hard metal coatings developed in Switzerland by LSRH/RMB/Saphirwerk.

Task 2 To accomplish Task 1, a rapid, stable AMS acquisition method should be developed, along with an expeditious data reduction, sorting and reporting routine.

Task 3 Develop a comparable technique for concave surfaces of bearing raceways.

Task 4 Analytically extend the AMS model to allow for phase as well as amplitude effects; e.g.,

- a) Energy loss due to non-focal condition;
- b) Spherical vs planar energy loss;
- c) Deflection effects in acoustic lens rod and liquid.

- Task 5 Develop a lens system complement for wide frequency band acoustic absorption and depth profile measurement.
- Task 6 Perform research oriented toward increasing the velocity resolution in the AMS and Imaging modes to distinguish between variations in the fabrication procedures.
- Task 7 Analytically extend the AMS model to relate velocity information more specifically to elastic parameters and, in turn, surface layer texture. As a result, direct interpretation of observation and fabrication sequence may be related.

# A model for predicting acoustic material signatures

R. D. Weglein

Hughes Research Laboratories, 3011 Malibu Canyon Road, Malibu, California 90265

(Received 25 September 1978; accepted for publication 30 November 1978)

Unique acoustic material signatures (AMS) may be obtained in the reflection acoustic microscope. The proposed model shows that they result from interference between two components reradiated into the immersion fluid at the materials critical Rayleigh angle  $\theta_R$ . The characteristic period  $\Delta z_N$  of this interference signature varies as the square of the Rayleigh wave velocity and is empirically given by  $\Delta z_N = \lambda_R / \sin \theta_R$ , where  $\lambda_R$  is the Rayleigh wavelength. Materials covering a greater than 3:1 velocity range agree well with this physical model. Substitution of the longitudinal wave velocity in the expression extends the range of measurable AMS to acoustically slower materials. A variety of applications for AMS is suggested.

PACS numbers: 43.35.Cg, 06.30.Gv, 43.35.Yb, 68.25. + j

Attempts at a satisfactory understanding of acoustic material signatures (AMS), recently obtained in reflection acoustic microscopy,<sup>1</sup> have to date met with limited success. Two approaches, an analysis based on the angular decomposition of the converging beam into a spectrum of plane waves and a "paraxial ray" approach,<sup>2</sup> have explored the material-dependent nature of these signatures. The impact of this new acoustic technique on materials characterization and surface diagnostics makes the development of a simple model quite desirable.

AMS data are obtained with the reflection acoustic microscope operating in the pulsed nonscanning mode,<sup>3</sup> by recording the transducer output voltage as a function of the translation of the material surface along the axis of the acoustic beam. The highly convergent beam of circular cross section, generated at the polished hemispherical cavity of half-angle  $\theta_{\max} = 55^\circ$  in a sapphire rod, is coupled to the material surface via a water droplet. The frequency of the sound-wave bursts is near 370 MHz.

A typical AMS is shown, for illustrative purposes, in Fig. 1, where three characteristic regions are delineated.<sup>4</sup> Only region II is of interest here, because this portion of the signature, and in particular, the periodic variation of the interference-like phenomenon, is uniquely material dependent. This period is labeled  $\Delta z_N$  and it is the prediction of its characteristic spacing between nulls with which this paper is concerned.

While analyzing signatures from a host of materials covering an acoustic velocity range of greater than 3:1, it was observed that for the examined candidates<sup>4</sup> the periodic null spacing  $\Delta z_N$  of these material signatures varied consistently as the square of the mean Rayleigh wave velocity  $\bar{v}_R$  in the plane normal to the axis of the incident acoustic beam. Figure 2 shows the variation of  $\Delta z_N$  as a function of Rayleigh wave velocity for these materials. For six of the examined materials, which are crystalline, and therefore exhibit anisotropic velocity variations as a function of azimuth angle in the plane normal to the incident acoustic beam, a weighted average Rayleigh wave velocity  $\bar{v}_R$  was computed, based on available published data.<sup>5,6</sup> In the case of one crystalline ma-

terial with large electromechanical coupling constant  $k^2$  for surface acoustic waves (*Y*-cut LiNbO<sub>3</sub>), the effect of water loading on velocity was taken into account.<sup>7</sup>

One can show that the AMS periodicity is quite accurately predicted by

$$\Delta z_N = \bar{v}_R^2 (f v_{H,O})^{-1}, \quad (1)$$

where  $f$  is the frequency and  $v_{H,O}$  is the velocity of the immersion fluid. Since the critical angle for phase matching the wave in the liquid to the Rayleigh wave in the solid is defined by  $\sin \bar{\theta}_R = v_{H,O} / \bar{v}_R$ , Eq. (1) may be restated as

$$\Delta z_N = \bar{\lambda}_R / \sin \bar{\theta}_R, \quad (2)$$

where  $\bar{\lambda}_R$  is the mean Rayleigh wavelength. Equation (2) is shown by the solid curve in Fig. 2. The characteristic null spacing is also linearly dependent on frequency and on the velocity of the immersion fluid.

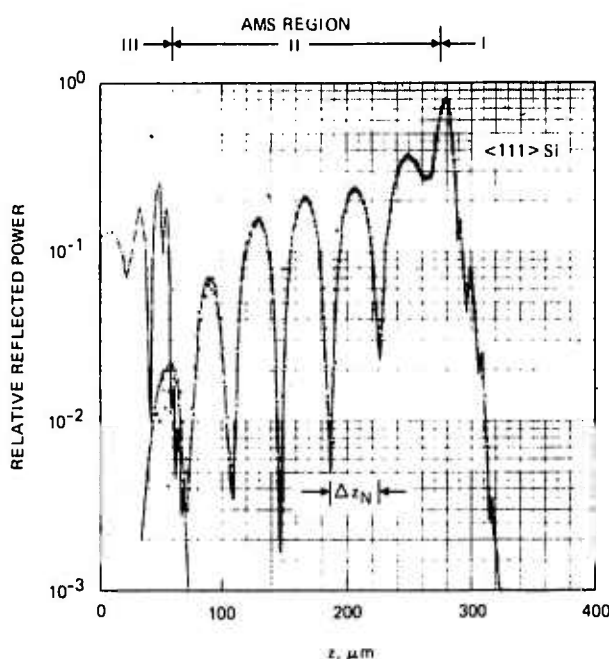


FIG. 1. Typical acoustic material signature (AMS); example is <111> silicon.

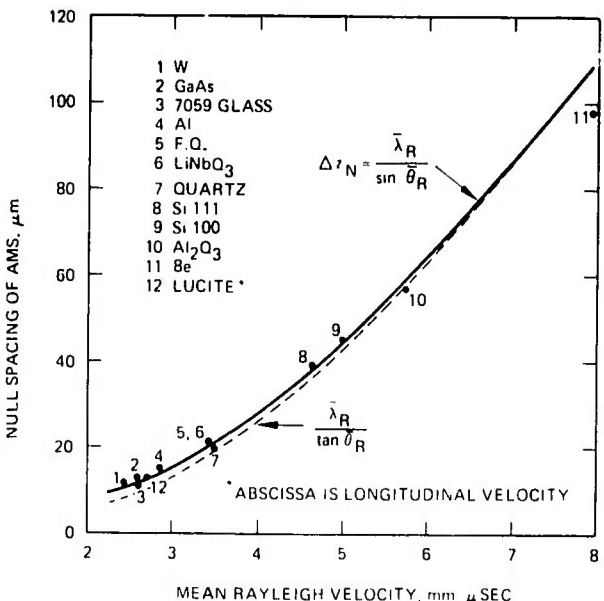


FIG. 2. Periodicity of acoustic material signature.

The physical mechanism proposed here (Fig. 3) is a cylindrically symmetric extension of the planar model that has explained the observed lateral shift of a broad incident acoustic beam through excitation of a leaky Rayleigh wave at the liquid-solid interface.<sup>6</sup> The AMS (region II of Fig. 1) in the present model is the result of interference between two components radiating into the liquid at the critical Rayleigh angle  $\theta_R$ . One component is specularly reflected from the solid, and its sign is labeled according to Ref. 8. The second component undergoes a lateral shift before reradiating at  $\theta_R$ . The amount of shift is proportional to the axial translation  $\delta z$  of the solid surface from the focal plane toward the lens, as is shown in Fig. 3. Except for the lateral phase shift, the two components in this model have, to first order, identical propagation delays. The delay common to both component waves includes refraction at the liquid-solid interface of the hemispherical acoustic lens as well as subsequent diffraction and propagation through the lens material (sapphire) to the vectorial summing point at the piezoelectric transducer (not shown), positioned parallel to the substrate plane. The differential phase delay between the two components is due to the lateral (radial) shift  $r$ , shown in Fig. 3. In this physical picture, the two components that are intercepted by the transducer are of approximately equal magnitude and phase opposition, and separated by an amount  $r = \delta z \tan \bar{\theta}_R$ , shown as the lateral displacement in Fig. 3, as the solid surface is axially translated toward the lens. The rate of separation occurs at the mean Rayleigh wave velocity  $v_R$  in the plane of the solid surface. Therefore, the additional phase lag of the shifted wave relative to the specularly reflected one is given by

$$\phi = 2\pi(\delta z/\lambda_R) \tan \bar{\theta}_R. \quad (3)$$

The transducer output voltage will, therefore, vary as

$$V_{\text{out}} = V_0 \sin(\pi \delta z \tan \bar{\theta}_R) / \lambda_R, \quad (4)$$

will interference nulls spaced at intervals given by

$$\Delta z_N = \bar{\lambda}_R / \tan \bar{\theta}_R, \quad (5)$$

shown by the dashed curve in Fig. 2. Although for large values of Rayleigh velocities (small  $\theta_R$ ), Eq. (5) agrees well with the experimental results, Eq. (2) represents a consistently better fit for all the measured materials. Neglecting the materials at the extremes of the velocity range that were experimentally explored, the mean deviation from Eq. (2) is 3.1% with an rms deviation of 1.4%. Both tungsten (W) and beryllium (Be), which were assumed to be isotropic, may be partially crystalline, resulting in some variation of  $\bar{v}_R$  from the published isotropic values.

It appears that Rayleigh wave phenomena are exclusively involved in forming the observed material signatures. It is interesting to note that<sup>8</sup> the effective angular range  $\delta \bar{\theta}_R$  near the Rayleigh angle is quite small ( $\delta \bar{\theta}_R < \pm 0.5^\circ$ ), and therefore the radial thickness of the active conical beam shell, assumed in the model, is usually less than  $\lambda_R$ . Similarly, the radial beam shift, assumed to be proportional to the axial translation, is also small ( $0 < r < 5\lambda_R$ ), compared to the corresponding shift ( $> 20\lambda_R$ ) encountered in the planar cases.<sup>8,9</sup> The large effect that constitutes the AMS may be the result of the combined coherent addition of the annular acoustic flux of mean radius  $r$  in the incident beam of circular cross section.

The highly convergent beam used in the acoustic microscope includes critical angles for total internal reflection of both longitudinal and shear waves in the substrate as well as Rayleigh critical angles. Yet these waves do not appear to influence the AMS in a significant manner. The excitation of leaky surface-skimming bulk waves<sup>10</sup> is in most cases restricted and quite small. The inefficient excitation of shear and longitudinal waves and correspondingly low amplitudes of the laterally shifted beams has been reported.<sup>11</sup> Unlike Rayleigh waves, the energy distribution of surface-skimming bulk waves is not confined to the solid surface, thus substantially reducing the intensity and consequently the periodic surface particle excursion that provides coupling to the liquid. The efficiency of surface-skimming bulk-wave ex-

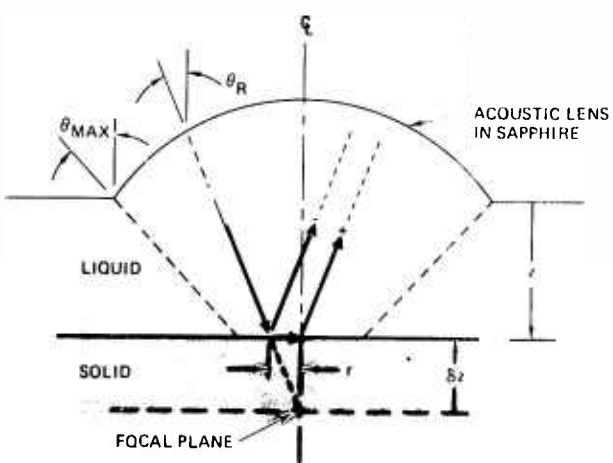


FIG. 3. Reflection at liquid-solid interface near the Rayleigh angle.

citation is further reduced in most of the examined materials because of the usually large acoustic impedance mismatch at the liquid-solid interface that permits little energy to be transmitted into the solid.

An interesting exception to these restrictions is the case of Lucite (material 12) shown in Fig. 2. The  $\Delta z_N$  of Lucite is consistent with the proposed model [Eqs. (1) or (2)], provided the compressional rather than the Rayleigh wave velocity of Lucite is used ( $v_c = 2.68 \text{ mm}/\mu\text{sec}$ ,  $v_R = 1.04 \text{ mm}/\mu\text{sec}$ ). The latter velocity is sufficiently slow to preclude phase matching to the incident acoustic beam ( $\sin\theta_R = v_{H_2O}/v_R > 1$ ). In such cases, a leaky surface-skimming compressional wave is believed to be excited in the solid and behave in an analogous manner to the leaky Rayleigh wave in forming the interference phenomena. The fact that the observed AMS for Lucite has substantial magnitude and thus permits quite accurate determination of  $\Delta z_N$  may be attributed to: (a) the absence of strong Rayleigh wave interaction, (b) low acoustic reflection coefficient at the water-Lucite interface, and (c) a large Poisson ratio ( $\sigma = 0.4$ ) rendering the material elastically very deformable. Under these conditions, a longitudinal wave propagating parallel and in close proximity to the liquid-solid interface in Lucite produces a propagating transverse surface deformation that interacts with the liquid to form the observed AMS. Other low-velocity materials are currently being investigated.

In this paper, a simple physical model accounted for the formation of acoustic material signatures in the acoustic microscope. Rayleigh wave phenomena, adapted from the analytical treatment,<sup>7</sup> and observed behavior<sup>8</sup> of planar beams incident at a liquid-solid interface was used to explain the formation of the interference phenomena in the spherically symmetric case of the acoustic microscope. The derived period of the AMS, that varies directly as the square of the mean Rayleigh wave velocity and inversely with frequency and the immersion liquid velocity, is in excellent agreement with materials covering a greater than 3 : 1 velocity range. In the case of one low-velocity plastic material, the observed AMS was found to be consistent with the excitation of a leaky surface-skimming compressional wave.

The apparent discrepancy between Eq. (5) (model) and the observed null spacing [Eq. (1) and (2)] may be attributed to the extreme simplicity of the proposed physical mechanism that is solely based on the relative shift between two component waves that are reradiated into the immersion liquid and vectorially summed (intercepted) at the piezoelec-

tric transducer. In spite of this simplicity that provides new physical insight, the results are in excellent agreement with experiment over the entire range of practically encountered material velocities.

The exclusive use of Rayleigh waves in accounting for the observed behavior, coupled with the narrow active angular range near the Rayleigh angle,<sup>9</sup> suggests that the highly convergent solid acoustic beam used in these experiments may not be the most efficient means of producing the AMS.

The large velocity range over which the proposed model appears to hold suggests that the AMS technique may be used to predict the elastic behavior of unknown material surfaces and the thickness-dependent parameters of layered structures. As an example, it should be possible to measure readily the velocity dispersion of surface acoustic waves in layered nonpiezoelectric composites. The linear frequency dependence of the AMS period implies that the technique may be scaled for diagnostic purposes to any desired material depth and layer thickness.

The extension of the AMS model to account for the unequal magnitude of the two reradiated components should permit the indirect measurement of acoustic absorption in material surfaces.

This research was partially funded by the Advanced Research Projects Agency Order 2397 through the National Bureau of Standards Semiconductor Technology Program Contract 5-35898.

- <sup>1</sup>R.D. Weglein and R.G. Wilson, Electron. Lett. **14**, 352-355 (1978).
- <sup>2</sup>A. Atalar, C.F. Quate, and H.K. Wickramasinghe, Appl. Phys. Lett. **31**, 791-793 (1977).
- <sup>3</sup>R.D. Weglein and R.G. Wilson, Appl. Phys. Lett. **31**, 793-796 (1977).
- <sup>4</sup>R.G. Wilson and R.D. Weglein, 1st International Symposium on Ultrasonic Materials Characterization, Program and Abstracts. (National Bureau of Standards, Gaithersburg, Md., 1978), p. 83.
- <sup>5</sup>A.J. Slobodnik, Jr., E.D. Conway, and R.F. Delmonico, AFCRL-TR-73-0597, 1973 (unpublished).
- <sup>6</sup>American Institute of Physics Handbook, (McGraw-Hill, New York, 1957), Chap. 3.
- <sup>7</sup>J.J. Campbell and W.R. Jones, IEEE Trans. Sonics Ultrason. SU-17, 71-76 (1970).
- <sup>8</sup>H.L. Bertoni and T. Tamir, Appl. Phys. **2**, 157-172 (1973).
- <sup>9</sup>M.A. Breazeale, L. Adler, and G.W. Scott, J. Appl. Phys. **48**, 530-537 (1977).
- <sup>10</sup>M. Lewis, 1977 Ultrasonic Symposium Proceedings, Catalogue No. 77CH1264-ISU, pp. 744-752 (unpublished).
- <sup>11</sup>W.E. Neubauer, J. Appl. Phys. **44**, 48-55 (1973).

## SAW dispersion and film-thickness measurement by acoustic microscopy

R. D. Weglein

*Hughes Research Laboratories, 3011 Malibu Canyon Road, Malibu, California 90265*

(Received 9 April 1979; accepted for publication 23 May 1979)

The reflection acoustic microscope has been used to measure SAW velocity dispersion and to indirectly measure the film thickness in a layered composite consisting of Au on a Si substrate. A quantitative thickness determination was made via the acoustic material signature technique, that is nondestructive and noncontacting. A theoretical prediction of SAW dispersion is in excellent agreement with these measurements.

PACS numbers: 43.35.Ns, 43.35.Cg, 43.35.Yb, 68.60. + q

The determination of the SAW (surface acoustic wave) velocity dependence on frequency (dispersion) in layered nonpiezoelectric structures has to date been primarily a

theoretical undertaking.<sup>1,2</sup> The knowledge of SAW dispersions is required for the optimum design of planar acoustoelectric spectrum analyzer<sup>3</sup> and to a lesser extent in disper-

sive SAW filters. Experimental determination is in most cases difficult, if not impossible, because of the problem of broadband excitation and the detection of surface acoustic waves on nonpiezoelectric layered media. At lower frequencies, wedge couplers<sup>4,5</sup> have been used for the generation of surface waves. At microwave frequencies, dispersion measurements are made via sputter-deposited ZnO transducers<sup>6</sup> where the required broad bandwidth is generally difficult to obtain.

The acoustic material signature (AMS) technique<sup>7,8</sup> uses the reflection acoustic microscope without a lateral scan. A focused acoustic beam strikes the surface of the sample, originally adjusted to lie in the focal plane. If that surface is now gradually moved toward the acoustic lens, periodic minima are observed in the reflected power. The spacing of these minima is a direct measure of the SAW velocity. Thus the AMS provides a simple nondestructive technique for the experimental determination of SAW dispersion in nonpiezoelectric as well as in piezoelectric layered media. In particular, the measurement of SAW dispersion in a Au-film Si-substrate system is described in this paper. The results compare favorably with theoretical predictions that are based on bulk values of the layer's elastic constants.

The AMS technique was applied to the measurement of velocity dispersion of Rayleigh (SAW) waves in a layered composite, consisting of a Au film of thickness  $h$  deposited on a <100>-oriented substrate of Si. Although believed to be applicable to layered composites in general, the choice of this particular material combination was based on the large velocity difference between the constituents materials. From considerations of the energy distribution in film and substrate one would expect that the SAW velocity would initially decrease from the mean value ( $\bar{v}_R = 4.68 \text{ mm}/\mu\text{sec}$ ) of the unclad silicon in direct proportion to the thickness of the Au film ( $v_R = 1.13 \text{ mm}/\mu\text{sec}$ ), measured in units of the SAW wavelength  $\lambda$ . Thus, under the assumption that  $v_R = f(h/\lambda)$ , the dispersion may be measured either by frequency dependence in a layered composite at constant  $h$ , or at a single frequency by altering the film thickness. The latter method proved more advantageous because of the wide thickness range of Au films that could easily and quickly be deposited on a single silicon substrate.

The acoustic material signature AMS exhibits a period  $\Delta z_N$  that is characteristic of the material involved and varies as the square of the mean Rayleigh velocity  $\bar{v}_R$  in the plane normal to the incident beam. In particular, the period  $\Delta z_N$  is given by<sup>8</sup>

$$\Delta z_N = \bar{v}_R^2 (f v_L)^{-1} \quad (1)$$

where  $v_L$  is the velocity of the immersion fluid and  $f$  is the acoustic frequency.

The AMS period  $\Delta z_N$  was measured for Au films ranging in thickness from 800 Å to in excess of 3000 Å.<sup>7</sup> At the operating frequency of 370 MHz, the SAW velocity is obtained from  $\Delta z_N$  with the aid of Eq. (1),

$$\bar{v}_R = 23.56 (\Delta z_N)^{1/2} \quad (\text{mm}/\mu\text{sec}), \quad (2)$$

where  $\bar{v}_R$  is measured in  $\text{mm}/\mu\text{sec}$  and  $z_N$  in mm. The velocities for four film thicknesses ( $0.08 \mu\text{m}$ ,  $0.14 \mu\text{m}$ ,  $0.20 \mu\text{m}$ ,

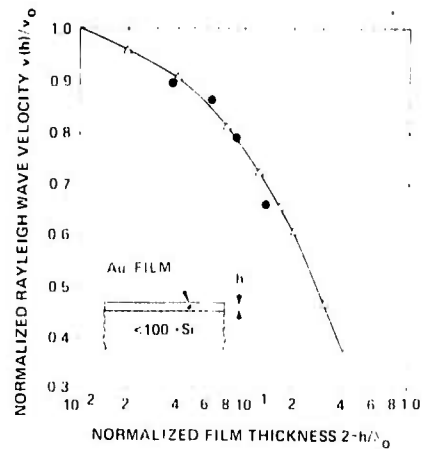


FIG. 1. SAW velocity dependence on frequency and film thickness. (○) measured by AMS technique; (Δ) computed from LAYERS program (Ref. 1).

and  $0.30 \mu\text{m}$ ) are shown (circles) in Fig. 1 as a function of the normalized film thickness  $2\pi h / \lambda_0$ . Here,  $v_0$  and  $\lambda_0$  refer to the SAW velocity and corresponding SAW wavelength on the bare silicon substrate. It is seen that the qualitatively predicted velocity decrease with increasing film thickness (or frequency) is, in fact, realized. The large velocity reducing effect ( $\approx 10\%$ ) of even a very thin Au films (800 Å or  $0.006\lambda_0$ ) is particularly noteworthy in that it suggests a sensitive technique for film-thickness measurement and monitoring to which the AMS may be applied.

A computer calculation of the SAW velocity dispersion of a Au film on silicon has been included in Fig. 1. The program, originally developed for the general design of a wide variety of dispersive SAW devices based on layered composites,<sup>1</sup> has recently been used to predict SAW dispersion in a layered composite containing thin-film materials appropriate to a planar Si-based Bragg cell.<sup>6</sup> The dispersion curve, shown in Fig. 1 (triangles), though it is based on bulk elastic values of Au, exhibits nevertheless quite close agreement to the AMS-measured velocity variation with normalized film thickness. It is quite conceivable that the minute differences between the measured points and the computed curve may at least in part be due to the bulk values assumed for the Au film, that was in fact quite thin.

Because SAW dispersion is a function of the parameter  $2\pi h / \lambda_0$ , the velocity of a given composite depends on frequency as well as on film thickness. Therefore, if the SAW dispersion is known from analysis, as is the case here, an absolute film-thickness measurement is obtained. Since the technique is, in principle, fast, nondestructive, and essentially noncontacting, except through a minute quantity of deionized water, it may lend itself advantageously to the process control of layer fabrication employed in advanced integrated circuits. At our acoustic microscope's present status and operating frequency range it should be possible to detect readily Au films on Si as thin as 160 Å. Correspondingly smaller film thickness should be measurable at higher microwave frequencies. Based on the scaling indicated by Eq. (1), a 3-GHz acoustic microscope<sup>9</sup> should be capable of measuring the thickness of an Au film approximately 20 Å thick. The

measurement of other metal and dielectric layers used in integrated circuits, such as Al,  $\text{SiO}_2$ ,  $\text{Si}_3\text{N}_4$ , may be made in a similar way. It should be noted, however, that the ability to resolve the velocity and, in turn, the thickness for these layer materials will decrease from that shown for Au on Si in direct proportion to the velocity difference of materials used in the film and the substrate forming the integrated circuit.

The velocity of surface acoustic waves in a dispersive nonpiezoelectric layered structure consisting of various thicknesses of Au films on silicon has been experimentally obtained for the first time. The measurement was made via the acoustic material signature AMS technique in a reflection acoustic microscope at 370 MHz. A theoretical computation of the SAW dispersion that assumed bulk material constants in the layer agreed well with the experiment. Since the dispersion is a known function of the film-thickness-to-wavelength ratio, the measurement represents effectively a technique for determining the absolute film thickness. Because these measurements represent the first such determination, their accuracy has as yet not been established. However, the repeatability of a typical AMS and period  $\Delta z_N$  on the bare silicon substrate has been found to be somewhat better than 2%.

The demonstrated measurement technique is directly applicable to arbitrary material combinations and a large layer thickness range merely by frequency scaling. Because of the nondestructive nature of the technique, on-chip pro-

cess monitoring in integrated-circuit fabrication appears feasible. Further, the required area for obtaining an AMS (typically a circular area of diameter  $\approx 150 \mu\text{m}$  at 370 MHz) decrease linearly with the wavelength. Therefore, the method presented here may be viewed as a potential nondestructive presorting technique for on-line monitoring and process control of integrated-circuit chips subsequent to fabrication but prior to electrical evaluation.

The author gratefully acknowledges the collaboration of W.R. Smith, who computed the SAW dispersion curve in Fig. 1. Helpful comments on reviewing the manuscript were contributed by O.W. Otto and C.J. Swigert.

<sup>1</sup>W.R. Smith, M.T. Wauk, H.M. Gerard, and R.L. Zimmerman, *Proc. 1972 Ultrasonic Symposium*, IEE Cat. No. 72CH0708-8-SU (IEEE, New York, 1972), pp. 367-369.

<sup>2</sup>G.W. Farnell and E.A. Adler, *Physical Acoustics* (Academic, New York, 1972), Vol. 9.

<sup>3</sup>S.K. Yao, R.R. August, and D.B. Anderson, in *Proc. 1977 Ultrasonic Symposium*, IEEE Cat. No. 77CH1264-1 SU (IEEE, New York, 1977).

<sup>4</sup>I.A. Victorov, *Rayleigh and Lamb Waves* (Plenum, New York, 1967), pp. 7-25.

<sup>5</sup>H.I. Berthoni and T. Tamir, *IEEE Trans. Sonics Ultrason.* **SU-22**, 415-420 (1975).

<sup>6</sup>F.S. Hickerell, *Proc. IEEE* **64**, 631-635 (1976).

<sup>7</sup>R.G. Wilson and R.D. Weglein, *1st International Symposium on Ultrasonic Materials Characterization. Program and Abstracts* (National Bureau of Standards, Gaithersburg, Md., 1978), p. 83.

<sup>8</sup>R.D. Weglein, *Appl. Phys. Lett.* **34**, 179-181 (1979).

<sup>9</sup>V. Jipson and C.F. Quate, *Appl. Phys. Lett.* **32**, 789-791 (1978).

APPENDIX C

DEMEO, D. A. TO GARDOS, M. N., "DIAMOND TURNING",  
Hughes Interdepartmental Correspondence 7621.30/169,  
18 January 1980



## **INTERDEPARTMENTAL CORRESPONDENCE**



TO: M. N. Gardos  
ORG: 76-21-10  
SUBJECT: Diamond Turning

cc: R. H. Johnson  
R. Y. Scapple  
B. J. Tilley  
A. J. Tuckerman

DATE: 18 January 1980  
REF: 7621.30/169

FROM: D. A. Demeo  
ORG: 76-21-30

BLDG. 6 MAIL STA. D129  
LOC. CC EXT. 4381

Precision machining, or diamond turning, is a term used to name a process which is capable of producing machined surfaces sufficiently smooth and flat to be usable as infrared optics without further polishing and other treatment. The process is similar to conventional machining but has much more stringent requirements on the equipment and tooling, environment, and the process itself.

The desired property of a diamond machined surface, as opposed to a ground or polished surface, is that surface and subsurface damage is greatly reduced and contamination from polishing compounds and removed material is eliminated. The machining operation neatly cuts away material with minimal surface damage and without the welding and tearing effects which can be encountered with metal tools. Reflectivities of gold, silver, and copper diamond turned optics have been within 0.5% of those of state-of-the-art vacuum deposited metals. Mirrors with low scattering have been made, and laser damage thresholds as high as 80% of theoretical have been observed for diamond turned mirrors.

The equipment used in precision machining is similar to a conventional lathe or mill, but with much tighter tolerances. High cutting speeds are used, with air bearing spindles and slides for precise control of part and tool motions, oil showers for temperature control of the parts and machine itself, and, most importantly, a diamond tool for cutting. The equipment is usually located in areas with strict controls on temperature, humidity, airborne particulates, and other environmental factors which might affect either the surface quality or figure of the cut.

Similarly, the materials machined must be controlled. The beryllium oxide present in hot pressed beryllium causes a high rate of diamond tool wear. Machinists have seen aluminum oxide inclusions in 6061-T6 aluminum alloy; these were not cut, but were pushed aside by the diamond tool. In order to obtain machinable surfaces, platings such as electroless nickel have been employed. While having their own processing problems, such platings should be free of stringers and other inclusions found in commercially available bar or rod stock.

Precision machining has been principally applied to optical components, where extreme requirements of flatness or figure accuracy exist. Many hours are often necessary to grind and polish mirrors or lenses to the required accuracy and smoothness with conventional techniques. Coincident with this time factor is a cost factor; the ability to machine an optical surface would reduce these factors substantially.

The materials which respond favorably to diamond tooling cover a wide range: plastics, aluminum, copper, electroless nickel, germanium, and glass have all been successfully machined by this technique. In general, the softer face centered cubic (fcc) crystals machine well, meaning with a specular finish of optical quality. Some fcc materials, such as platinum, high purity iron, and nickel have been machined with diamond tool bits, but the desired optical properties of the surfaces have not been produced.

Steel machining has been attempted, but high diamond tool wear attributed to graphitization was the result. It was hypothesized that the carbon diffused into iron under the local stresses at the cutting edge. However, I have not seen full documentation of such attempts, just a report of failure. A careful attempt at such machining is necessary to confirm such results, along with metallurgical examination of the material. Carbide inclusions in the steel used may have caused the results seen.

With only the reported failure of the diamond turning of steels, it would be presumptuous to propose diamond turned bearings. However, it is quite possible that someone will develop a technique for diamond machining steels. There are other possibilities for precision machining, such as on regions built up through plating. Electroless nickel can be machined; I have seen no reports of attempts on chromium, but this element might possibly provide a good surface. A bridge needs to be built between the diamond turning people, who are principally optics people, and the tribological community, which appears to have similar needs in some areas.



D. A. Demeo

DAD:jsh

Why not  
try it?

APPENDIX D

RAMALINGAM, S. AND WINER, W. O.,  
"REACTIVE SPUTTERING OF TiN AND SOLID LUBRICANTS AND  
SHEAR STRENGTH TESTING OF SOLID LUBRICANTS,"  
Progress Report No. 1, Hughes P. O. 04-406163-FS5,  
Georgia Institute of Technology,  
Atlanta, Georgia,  
16 January 1980.

MIKE GARDOS

(213) 391-0711  
EX 4532

GEORGIA INSTITUTE OF TECHNOLOGY  
ATLANTA, GEORGIA 30332

SCHOOL OF  
MECHANICAL ENGINEERING

January 16, 1980

Mr. M. N. Gardos  
Program Manager, Technology Support  
Hughes Aircraft Company, M.S. D-133  
Culver City, Calif. 90230

Subject: Progress Report No. 1. "Reactive Sputtering of TiN and Solid Lubricants and Shear Strength Testing of Solid Lubricants".

Dear Mr. Gardos:

The activity at Georgia Tech in support of this program, at the present time, is principally concerned with reactive sputtering of TiN films on bearing elements. Work connected with the coating and evaluation of solid lubricant films awaits the arrival of Ga/In/WSe material for target fabrication.

In the time period to January 15, 1980, some preliminary phases of the work have been carried out. They are:

1. Coating of traction test specimens and bearing balls.

Traction discs, bearing inner race traction test specimens and bearing balls received for TiN coating from Hughes have been sputter coated with TiN and sent back to Hughes for additional solid lubricant coating prior to traction tests.

The traction discs and inner races were coated with a rotary jig at a cathode-to-specimen distance of 7 cm at a pressure slightly less than 133 mPa. Commercial purity titanium target was reactively sputtered with argon and nitrogen flow to synthesize and deposit TiN. The coating conditions used were identified in a earlier phase (see 3 below) of reactive sputtering process development.

The traction discs and inner races were not masked during coating to obtain a normal flux of sputtering species.

Bearing balls, held in a perforated steel basket, were coated under stationary conditions. Apart from this the coating conditions were identical to those used for traction specimens.

Specimens coated were ultrasonically cleaned in xylene and acetone prior to vapor degreasing in tricholoroethylene. They were then washed in acetone and dried with a blast of nitrogen. Specimens loaded into the coating system were pumped to 0.66 mPa prior to sputter cleaning at 2.6 Pa (3 kV; 50 ma). Temperature rise during the 15 minute sputter cleaning was not monitored and from prior experience estimated at between 200C to 250C.

2. Fixture development for ball coating.

To obtain uniform coating, a fixture which presents the entire surface of a sphere to the coating flux is needed. Kinematically this requires uniformly (statistically) random ball motion during coating. This can be obtained by rolling the ball by equal amounts around two instantaneously orthogonal axes.

A ball rocked in a basket around the horizontal axis will roll around that axis. By constraining it to travel at 45° to the rocking axis during its rolling, rotation around two mutually orthogonal axes can be obtained. A stainless steel basket capable of providing this motion was constructed and rocked with a 10 rpm motor to obtain the desired motion. Visually uniform coatings have been produced with this fixture on commercial 1/4 inch diameter bearing balls. The required angular excursion during ball coating is 5°.

By interposing a thick mask (1/4" thick) with a pattern of close packed holes (1/8" in diameter) between the target and the basket, the angular range of flux arriving at the basket can be restricted to  $\pm 14^\circ$  around the normal. This mask and the rocking will allow coating with incident flux deviating from the normal by  $\pm 19^\circ$ . Smaller angle variation can be obtained both by decreasing the hole size or mask thickness.

Ideal close packing will permit a maximum mask transparency of 78.54%. Realistically 33% mask transparency can be obtained with ease which will raise coating time by a factor of three.

It is planned to build such a masking fixture. Radiant heating of the basket will permit coating at temperatures to 500C. With this system substantially normal coating flux can be obtained to coat at desired elevated temperatures. This work is about to be started.

3. Reactive sputtering process development for triboelement coating and preliminary test results.

Hardened steel balls, 1 1/4" in dia. were coated with a thin film of TiN using a disc magnetron system. Reactive sputter coating was carried out at a cathode current of 0.75 amp. (with a 5 cm target) using a commercial purity titanium target. Golden yellow and bronze colored TiN films were produced.

X-ray diffraction analysis carried out on a test coupon with Cu-K radiation yielded dominant TiN peaks within  $1/2^\circ$  of ASTM powder file values. Taper sectioned thin films were found to be optically dense. Measured film microhardnesses were found to be approximately  $1900 \text{ kgf/mm}^2$  (Knoop indentor; 25 g load;  $15^\circ$  taper section).

The coated steel balls were tested in an EHD test rig which subjects the surface to both sliding and rolling contacts. The rig is constructed with a main contact, which can be observed continuously, and three support contacts. The support contacts are all sliding while the main contact, which can be rolling or sliding, was rolling in these tests. The opposing surfaces for all contacts were flat sapphires and all contact tracks are independent. The Hertz pressure at the rolling contact was about 1.343 GPa while at the sliding contacts it was about 0.992 GPa. The rolling contact velocities were about 1 m/s for both surfaces while the ball surface velocity for the sliding contacts was about 0.8 to 0.9 m/s. The lubricant was an unformulated low viscosity mineral oil which we have called .1 in several publications (24 cst at 37C and 3.7 cst at 98C). All contacts were fully flooded. The bath temperature was measured but not controlled. It started at about 24C and reached an equilibrium of about 51C in 15 to 20 minutes. Both the ball and sapphire surfaces were very smooth ( $\leq 1 \mu$  in RMS) and for all contacts under all operating conditions the EHD film thickness was from 4 to 11 times the composite surface roughness. Hence asperity interaction was essentially nonexistent.

Although the contact tractions and temperatures were not measured, it is known from previous measurements that the traction (or friction) coefficient at the sliding contacts will be about 0.06 while that at the rolling contact will be less than 10 percent of this value. The maximum ball surface temperature rise in the sliding contacts will be about 48C while in the rolling contact it will be less than 5 to 8C.

In summary, none of the contacts experienced solid surface interaction, they all experienced similar Hertz pressures and normal stress cycling. The two major differences in conditions were that the sliding contacts experienced higher shear stresses (about 55 MPa versus less than 5.5 MPa) and higher transient peak surface temperatures (about 48C versus 5.5C above bath temperature). Under these conditions the coating at the sliding contacts was removed after 30,000 cycles while the coating at the rolling contact was still intact when the test was terminated after  $10^6$  cycles. Several less successful previous

attempts suggest that to survive these conditions the film must be thin (typically much less than one micro-meter).

January 1980

Very truly yours,

May  
Sputtering  
S. Ramalingam  
Professor

Subbiah (Colled Ram)

Phone 404-894-3238

Ward  
Ward O. Winer  
Professor

894-3270  
Home 404-252-9321

School of Mechanical Engineering  
Georgia Institute of Technology  
Atlanta, Georgia 30332

Scott Bair Research Engineer  
could also be contacted

Must get rid of inclusions for Adhesion  
of TiN

## APPENDIX E

JAMISON, W. E., "SOLID LUBRICANT RESEARCH,"  
Semi-annual Report, Hughes P.O. 04-406148-FS5,  
Tribomatics Development Corporation,  
Evergreen, Colorado,  
15 January 1980.

SEMI-ANNUAL REPORT

on

SOLID LUBRICANT RESEARCH

to

HUGHES AIRCRAFT COMPANY

January 15, 1980

Tribo Materials Development Corporation  
29946 Monroe Drive, Evergreen, CO 80439

FOREWORD

This report covers work accomplished by TMD between the initiation of the project on October 16, 1979 and December 31, 1979, on Contract Number F33615-78-C-5196.

The research was conducted by Dr. Warren E. Jamison, acting as principal investigator and TMD Project Director. Technical direction was provided by Mr. M. N. Garuos, Program Manager for Hughes.

## 1. PROJECT OBJECTIVES AND ORGANIZATION

The overall objective of the research being reported herein is to develop new solid lubricant materials with superior performance capabilities. The desired material is a solid which is capable of being incorporated into a self-lubricating composite and/or of being deposited by spattering or ion implantation onto bearing surfaces, and which is thermally, oxidatively and hydrolytically stable to at least 1500°F. The prototype for this material is molybdenum disulfide, a crystalline solid with layered structure and inherent lubricating properties.

The materials development aspects of this project are based on a theory developed by Dr. Jamison (1,2) which states that the structural stability and lubricating effectiveness of transition metal dichalcogenides are controlled by the free electron concentration within the material. This electron concentration can be adjusted by at least two mechanisms: addition of extra electron donor atoms to the structure and substitutional alloying of atoms with different valences. It should be pointed out, however, that the successful outcome of this research does not depend on verification of the validity of Jamison's theory - it has already been demonstrated that the techniques proposed to modify the electron contraction do, in fact, alter the structure of the materials and improve the lubricating performance.

Improvement of lubricating properties is inadequate if the resultant materials are unstable in the environment where they are to be used. Therefore, the first task in this project was to review the published literature on thermodynamic stability of the candidate lubricant materials. Other tasks in the project are concerned with synthesizing the materials, constructing special apparatus and equipment to measure properties, and measurement

of lubricating performance and other properties. These tasks will be discussed below in separate sections of this report.

## 2. THERMODYNAMIC ANALYSIS AND MATERIALS STABILITY

The materials being studied in this research are the disulfides and diselenides of the transition metals of groups IV, V and VI of the periodic table. These materials adopt layered crystal structures of the type shown in Figure 1. Two basic variations exist in the crystal structures. Group IV metals usually adopt structures with octahedrally coordinated chalcogen atoms around the metal to form trigonal antiprisms (TAP). Group six metals are trigonal prismatic (TP) coordinated. It was shown by Jamison (3) that only trigonal prismatic structures with crystal lattice ratios of  $c/na > 1.92$  were intrinsic lubricants. Also, it was shown that materials with TAP structures could be reorganized to TP structures by proper adjustments of electron concentration and that these materials become good lubricants if  $c/na > 1.92$ . Table 1 summarizes the structure and properties of these materials.

One of the methods being studied in this research to develop lubricants with improved properties is to dope some of the materials in Table 1 with other species to increase the  $c/na$  parameter. Considerable work has been done in recent years to define the structure and properties of transition metal chalcogenides which have been intercalated with alkali atoms. These studies have been accomplished in an effort to develop cathode materials for new battery systems.

## TABLE 1

Structure and Properties of  
Candidate Lubricant Materials

<u>Material</u>	<u>Metal Group</u>	<u>Crystal Structure</u>	<u>c/na</u>	<u>Lube Properties</u>	<u>Intercalate Atoms which give c/na &gt; 1.90</u>
TiS <sub>2</sub>	IV	TAP	1.672	Poor	Na, K, Rb, Cs
TiSe <sub>2</sub>	IV	TAP	1.698		Na, K
ZrS <sub>2</sub>	IV	TAP	1.592		Na, K, Rb, Cs
ZrSe <sub>2</sub>	IV	TAP	1.631		K
HfS <sub>2</sub>	IV	TAP	1.611		
HfSe <sub>2</sub>	IV	TAP	1.646		
V <sub>2</sub> S <sub>2</sub>	V	(unstable)		-	Na
VSe <sub>2</sub>	V	TAP	1.821	Poor	Na
NbS <sub>2</sub>	V	TP	1.796		Li, Cu, Ag, Tl
NbSe <sub>2</sub>	V	TP	1.817		Li, Cu, Ag, Tl
TaS <sub>2</sub>	V	TAP/TP	1.803		Li, Cu, Zn, Ce, Na, K, Ag, Tl
TaSe <sub>2</sub>	V	TAP/TP	1.847		Li, Na, K, Tl
CrS <sub>2</sub>	VI	(unstable)		-	Na, Cu, Ag, Tl
CrGe <sub>2</sub>	VI	(unstable)		-	Na, Cu, Ag, Tl
MoS <sub>2</sub>	VI	TP	1.946	Good	Li, Na, K, Rb, Cs
MoSe <sub>2</sub>	VI	TP	1.970	Good	
WS <sub>2</sub>	VI	TP	1.956	Good	Li, Na, L, Rb, Cs
WSe <sub>2</sub>	VI	TP	1.970	Good	

Intercalation consists of inserting atoms in between the layers of sulfur atoms shown in Figure 1, to form compounds with a chemical formula of  $A_xM\bar{X}_2$ . In this formula, A represents the intercalated species, M is the transition Metal, X is the chalcogen atom and x is the relative amount of the intercalated species. In the alkali intercalated species,  $0 < x < 1$  and the alkali atoms are randomly distributed in the voids between the sulfur atoms.

The battery development has different objectives from the lubricant materials development, and the intercalation requirements are somewhat different. In both cases, a large free energy of intercalation is desired; to stabilize the structure for lubrication and to store energy for batteries. For electrochemical applications a high mobility of the intercalate is desired for ease in charge transfer. In lubrication, diffusion is unimportant, although a critical factor is the expansion of the lattice in the c direction. To meet potential battery needs, the intercalation research has been concentrated on lithium intercalated into  $TiS_2$ . Titanium disulfide is a desirable host material because of its low cost and light weight. These factors are desirable for lubricant applications too. However, intercalation of lithium atoms into  $TiS_2$  generally does not expand the lattice sufficiently for lubrication applications. Table 1 lists intercalant atoms for the candidate lubricants which have been reported in the literature to expand the lattices to give  $c/na > 1.90$ , the estimated minimum for good lubrication. In general, lithium will intercalate into all structures, but does not give a large enough lattice expansion to yield  $c/na > 1.90$  except in those materials already close to this value.

In assessing the stability of intercalated chalcogenides, several factors need to be considered. First, Whittingham (4)

has stated that unequivocally, the alkali metal atoms contribute free electrons to the structure upon intercalation and that they generally occupy the octahedral voids in the van der Waals gap between the sulfur layers. In the Group IV and V transition metal dichalcogenides, in which the electron concentration is too low to stabilize the  $\text{MoS}_2$  structure, intercalation of alkali metals can stabilize this structure. In addition, both  $\text{CrS}_2$  and  $\text{VS}_2$  do not exist because the electron concentration is too low. However, intercalation of electron donors into the structures can stabilize them at the stoichiometric  $\text{MX}_2$  composition. Also, intercalation of alkali metal atoms into chalcogenides already possessing the  $\text{MoS}_2$  structure does not occur easily and does not always produce a lattice expansion.

Most of the dichalcogenides listed in Table 1 can exist as metal-rich compounds;  $\text{M}_{1+y}\text{X}_2$ . The extra metal atoms occupy spaces in the van der Waals gap, in competition with the intercalate atoms. Whittingham (4) has shown that  $\text{Ti}_{1.1}\text{S}_2$  has a lattice expansion of about 4% over that of  $\text{TiS}_2$ . He also states that the excess Ti atoms inhibit subsequent intercalation of lithium atoms. Niobium and Tantalum chalcogenides are also known to produce lattice expansions by incorporating excess metal atoms into the van der Waals gap.

Whereas intercalated alkali atoms reside in octahedral holes in the van der Waals gap, there are some data which show that the extra metal atoms occupy other sites, giving evidence of two different kinds of bonding. Although little data exist, it appears that non-alkali metal atoms, such as Au, Ag, Cu & Zn, can be intercalated into the dichalcogenides with results similar to that of the alkali metals. However, these atoms occupy tetrahedral voids, similar to the extra host metal atoms

and unlike the alkali metal atoms. These latter intercalates are more likely to promote the  $\text{MoS}_2$  type structure, but do not expand the lattice as much as the alkali metal atoms. Table 2 shows the effect of intercalating a variety of metal atoms into  $\text{TaS}_2$

TABLE 2  
Intercalates in A<sub>x</sub> TaS<sub>2</sub> (from ref 5)

Intercalate	<u>x<sub>max</sub></u>	<u>T<sub>f</sub> (°C)</u>	<u>c/n/a</u>
Cu	2/3	1025	1.97
Zn	1/2	425	1.90
Cd	1	300	1.80
Hg	1	200	1.80
Al	1/3	200	1.88
Ga	1	450	1.72
In	1	450	1.76
Ge	1/3	550	2.06
Sn	1	850	1.77
Pb	1	600	1.77
Bi	2/3	800	1.75

Very few thermodynamic data are available for the intercalation reactions. Although  $\text{Li}_x\text{TiS}_2$  is not a viable candidate for lubrication studies, it has been investigated for battery applications and serves as a thermodynamic model. The following reactions show that although  $\text{Li}_x\text{TiS}_2$  is stable relative to

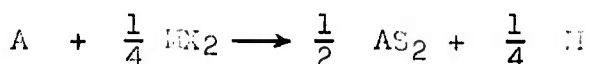
disproportionation, it is not stable to oxidation by oxygen or water.

Ti	+	2S	→	TiS <sub>2</sub>	Δ G =	-396	kJ/mol
Ti	+	O <sub>2</sub>	→	TiO <sub>2</sub>	"	-889	"
TiS <sub>2</sub>	+	O <sub>2</sub>	→	TiO <sub>2</sub> +2S	"	-493	"
TiS <sub>2</sub>	+	3O <sub>2</sub>	→	TiO <sub>2</sub> 2SO <sub>2</sub>	"	-109	"
TiS <sub>2</sub>	+	SO <sub>2</sub>	→	TiO <sub>2</sub> +3S	"	-193	"

The free energies of typical lithium intercalation reactions are:

Li <sub>x</sub> TiS <sub>2</sub>	ΔG =	-206	kJ/mol
Li <sub>x</sub> NbSc <sub>2</sub>	"	-200	"
Li <sub>x</sub> TiSc <sub>2</sub>	"	-186	"
Li <sub>x</sub> VSe <sub>2</sub>	"	-222	"

The intercalation reactions must be more energetically favorable than the displacement reaction



if the intercalation is to be accomplished. Table 3 lists energies of formation and of the displacement reactions with A = lithium.

TABLE 3

Energies of Formation and of  
Lithium Displacement Reactions (kJ/mol)

<u>Material</u>	<u>- <math>\Delta G_f</math></u>	<u>- <math>\Delta G_{disp}</math></u>
HfS <sub>2</sub>	573	75
ZrS <sub>2</sub>	562	78
TiS <sub>2</sub>	396	120
NbS <sub>2</sub>	346	132
TaS <sub>2</sub>	345	132
MoS <sub>2</sub>	268	152
WS <sub>2</sub>	236	160

Since the lithium intercalation energies are  $\sim 200$  kJ/mol, it appears that intercalation with lithium can proceed with materials above MoS<sub>2</sub>. No thermodynamic data have been found for intercalation of non-alkali metals into the candidate hosts. However, the intercalation temperatures listed in Table 2 give an indication of stability; the higher the intercalation temperature, the more stable the compound.

### 3. SAMPLE PREPARATION

Until more thermodynamic data can be obtained and stability limits calculated for the candidates, qualitative data such as those in Table 2 are being used to prepare initial samples in this research. Table 2 shows that Cu and Ge will produce the greatest lattice expansion in TaS<sub>2</sub>. However, Ge does not appear to have the optimum stability. Aluminum has a high intercalation

temperature, but does not yield satisfactory lattice expansion. These three elements are being used as intercalates in  $TaS_2$  and  $TiS_2$  to study sample preparation techniques and lubricating properties. Initial preparations were made in which powders of the elements were reacted in evacuated quartz tubes. Many of the samples exploded in the furnace and new preparations are being reacted at lower temperatures for longer periods of time..

#### 4. CONTACT POTENTIAL STUDIES

Contact potential measurements have been selected as a method of characterizing the electronic state of the candidate materials. The apparatus has been designed and all major components acquired. Since the surface state of the material may be modified by absorbed gases, the measurements will be made in ultrahigh vacuum. The apparatus shown in Figure 2 can be used to measure the contact potential of six specimens on each pump-down.

#### 5. LUBRICATING PROPERTIES MEASUREMENTS

A tester is being built to measure the friction and wear properties of both powders and compacts of candidate materials prepared in this study. The apparatus is configured like a Timken tester, in which either the lubricant compact or a steel block submersed in lubricant powder is loaded against a rotating tapered roller cup, as shown in Figure 3. The variable speed

drive motor and strain gauge friction apparatus have been acquired. Assembly will proceed when machined parts have been received.

Respectfully submitted,

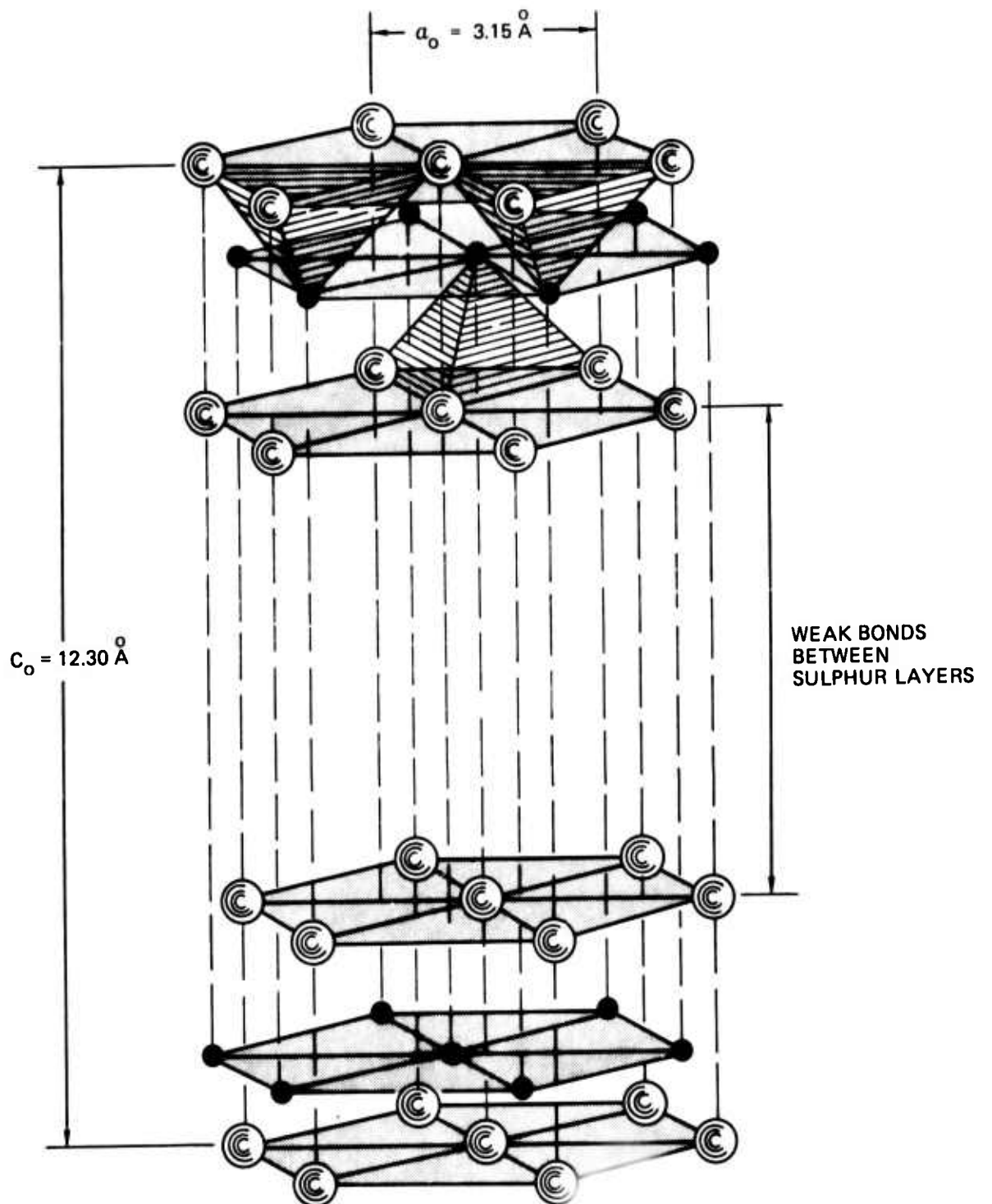
*Warren C. Jamison /mlm*

Warren E. Jamison,  
President  
Tribol Materials Development Corp.

WEJ/mlm

REFERENCES

1. Jamison, W.E., "Structure and Bonding Effects on the Lubricating Properties of Crystalline Solids", ASLE Trans., 15, 295-303 (1972).
2. Jamison, W.E., "Electronic Effects on the Lubricating Properties of Molybdenum Disulfide and Related Materials", ASLE Proceedings - 2nd International Conference on Solid Lubrication, Denver, August 1978, ASLE Special Publication 6, 1-8 (1978).
3. Jamison, W.E., and Cosgrove, S.L., "Friction Characteristics of Transition Metal Disulfides and Diselenides" ASLE Trans., 14, 62-72 (1971).
4. Whittingham, M.S., "Chemistry of Intercalation Compounds: Metal Guests in Chalcogenide Hosts", Prog. Solid State Chem., 12, 41-99 (1978).
5. DiSalvo, F.J., Hall,Jr., G.M., Schwartz, L.H., Voorhoeve,J.J., and Waszczak, J.V., "Metal Intercalation Compounds of TaS<sub>2</sub>: Preparation and Properties", J. Chem. Phys., 59, 1922-9 (1973).



CRYSTAL STRUCTURE OF  $\text{MoS}_2$

● Mo

○ S

Figure 1

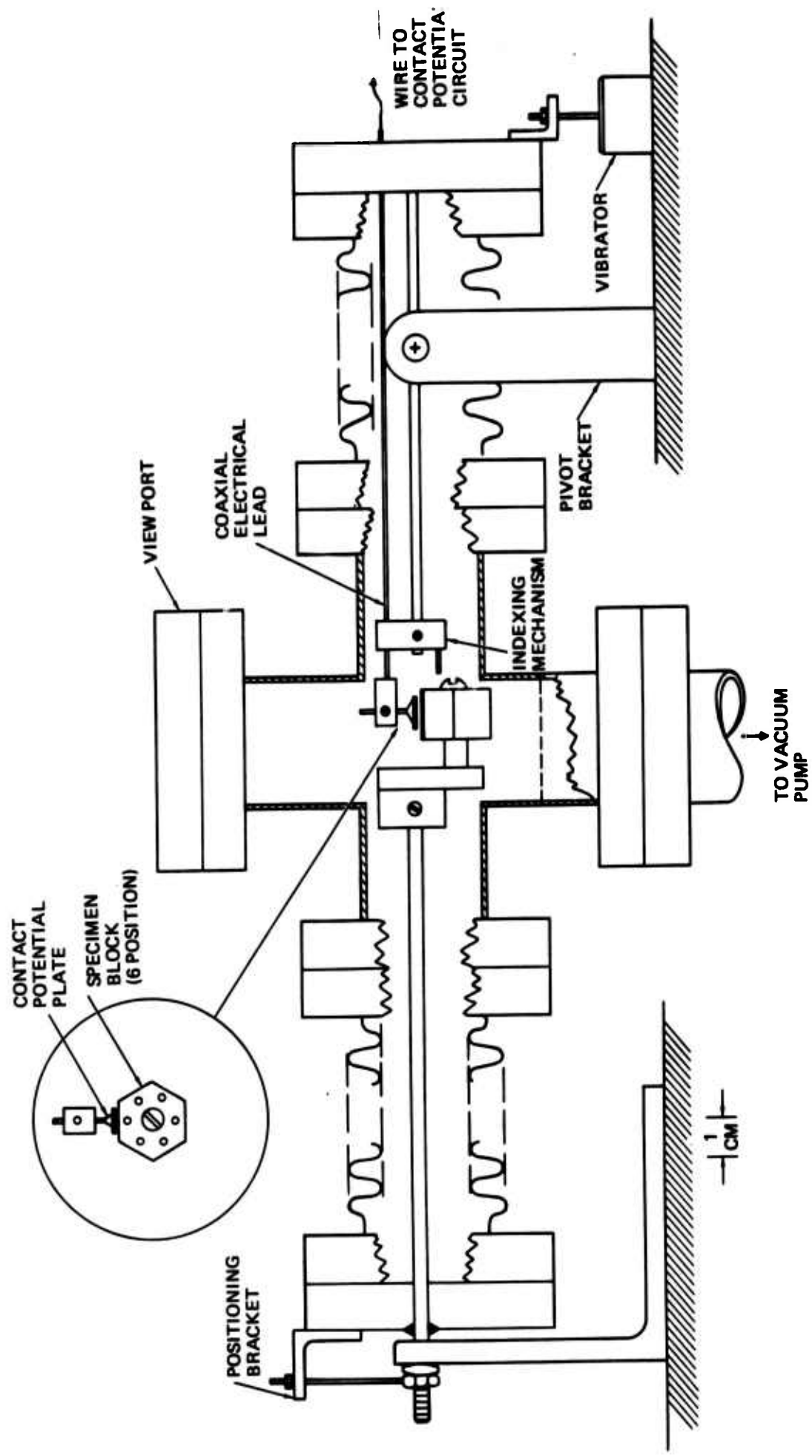
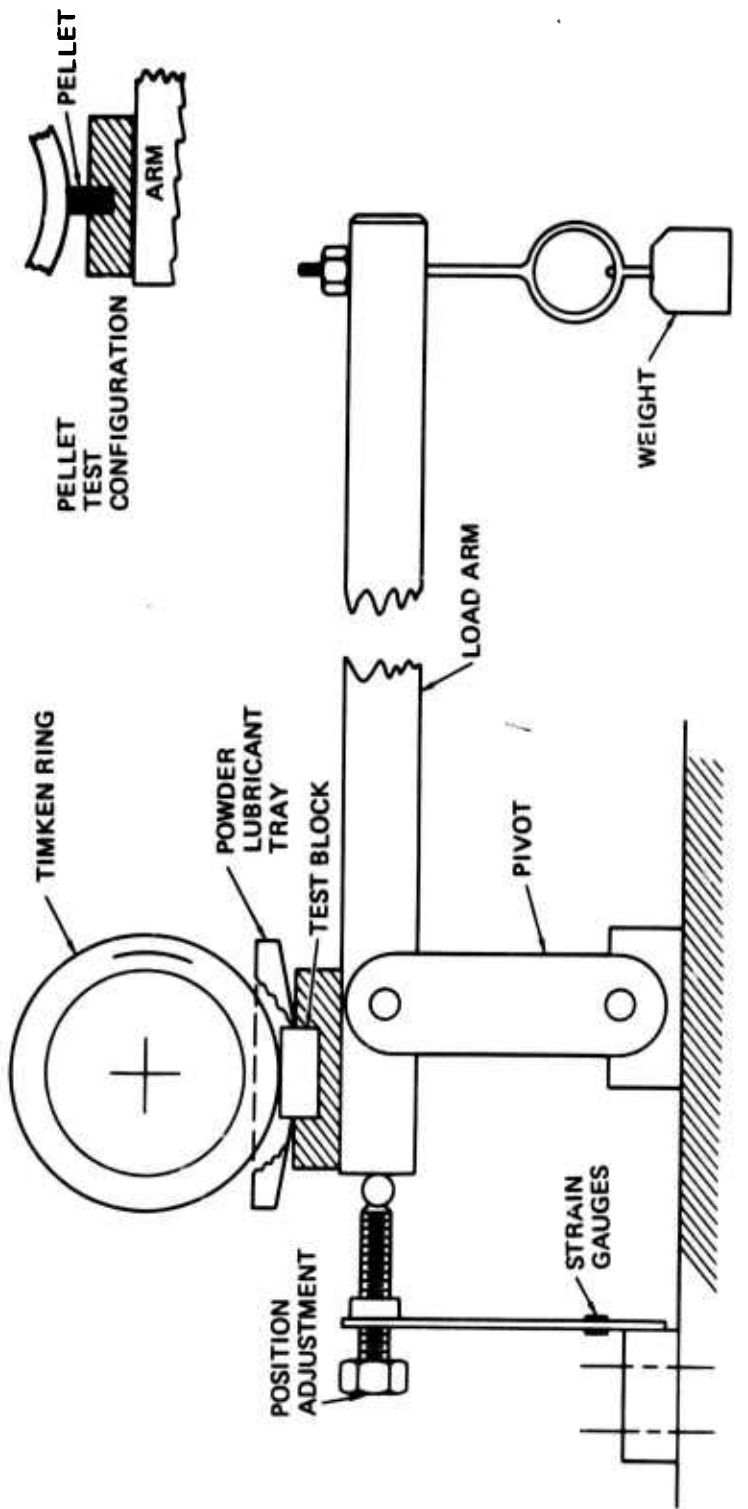


Figure 2. Contact Potential Apparatus



1/10/80

Figure 3. Atmospheric Test Rig

APPENDIX F

PIETROKOWSKY, P. TO GARDOS, M. N.,  
"CHARACTERIZATION OF THE WESTINGHOUSE COMPACT",  
Hughes Technical Internal Correspondence 7621.31/57,  
1 February 1980.

# HUGHES AIRCRAFT COMPANY

## TECHNICAL INTERNAL CORRESPONDENCE

TO: M. N. Gardos  
(76-21-10)

cc: See Distribution

DATE: 1 February 1980  
REF: 7621.31/57

SUBJECT: Characterization of the  
Westinghouse Compact

FROM: P. Pietrokowsky  
(76-21-33)

BLDG. 6 MAIL STA. D-133  
EXT. 6663

---

**ABSTRACT:**

This report describes the results of a recent effort to characterize a solid lubricant composite designated as "Westinghouse compact". A commercial grade of tungsten diselenide obtained from BEMOL, Inc. of Newton, Massachusetts, was also examined for purposes of comparison. A precision, Hagg-modified, Guinier x-ray powder diffraction camera was used to obtain data.

Analysis of x-ray diffraction data from the commercial grade of tungsten diselenide indicates that it is a crystalline hexagonal phase, see Figure 1. Results of (unrefined) lattice parameter calculations are in excellent agreement with the most reliable data reported in the literature. Structure calculations for this material reveal that selenium and tungsten atoms reside in equally populated hexagonal nets which alternate in the sequence: -Se-Se-W-Se-Se-W-. The distance between layers, or net of atoms, has been calculated and it has also been determined that selenium and tungsten are coordinated in a trigonal prism.

Analysis of x-ray diffraction data from the Westinghouse material indicates the presence of at least three constituents, see Figure 2. There is a constituent of crystal structure similar to tungsten diselenide. However, there are significant differences: the distances between layers are greater than observed in the BEMOL material and there is evidence to indicate chemical and/or crystallographic disorder of atoms in the direction of the six-fold symmetry axis. X-ray data indicates that the Westinghouse compact also contains very small particles of body-centered cubic, metallic tungsten. Additionally, the material exhibits x-ray diffraction maxima which are in reasonable agreement with data reported in the literature for gallium selenide.

Scanning electron microscope (SEM) photographs confirm the morphology of tungsten diselenide in the sample of BEMOL material, provide additional evidence for the existence of very small particles in the Westinghouse material and establish the morphology of gallium selenide. Finally, as a result of our analysis, it is possible to explain anomalous x-ray diffraction results for tungsten diselenide published by Russian investigators.

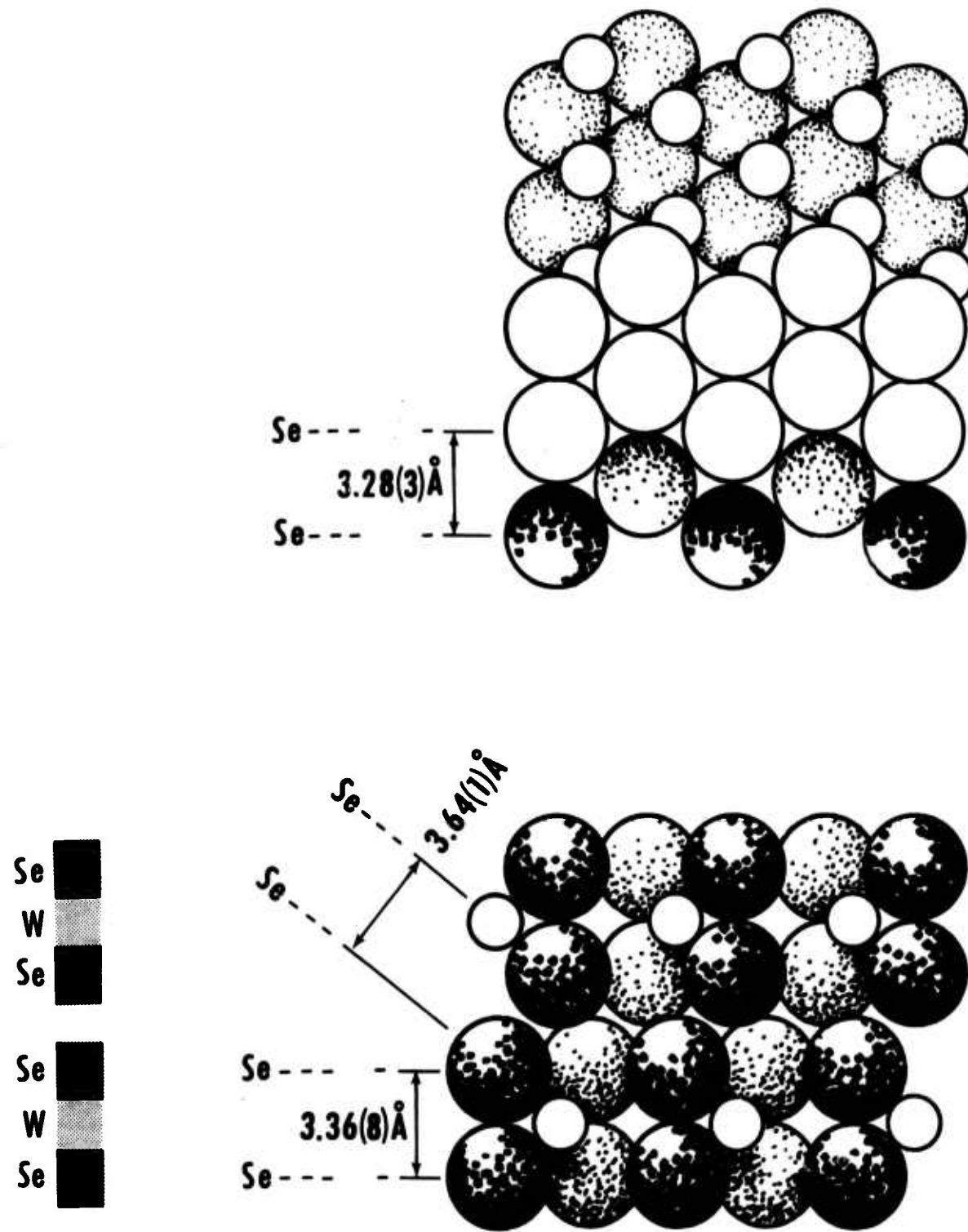
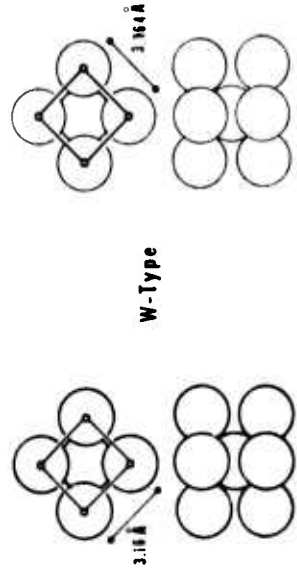


Figure 1. Crystal structure of hexagonal tungsten diselenide.

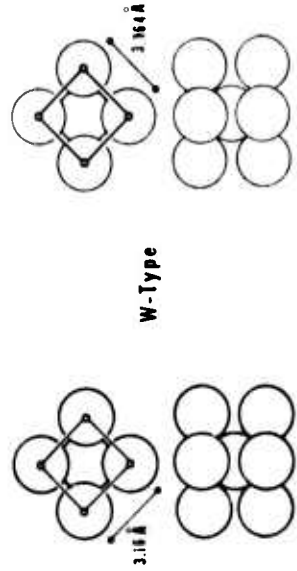
WESTINGHOUSE  
COMPACT

## REFERENCE MATERIALS



**Fig. 20**

## REFERENCE MATERIALS



W-Type

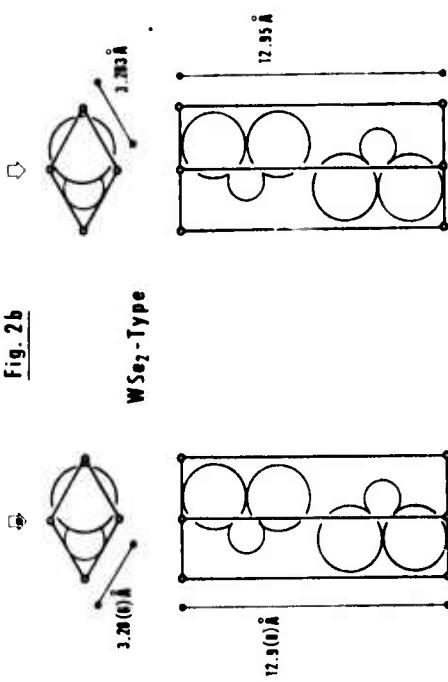
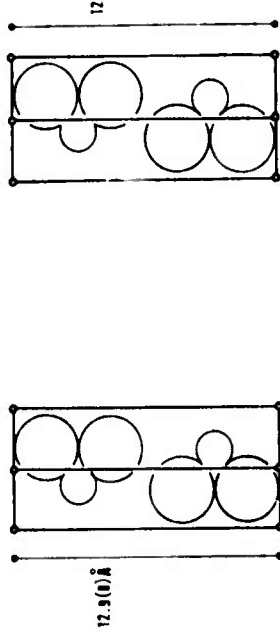


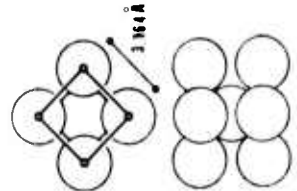
Fig. 2b

W587-LV88



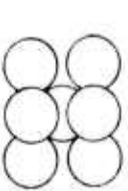
1.3838

1



1

Gas - 1 types



Gas - 1 types

Fig. 26

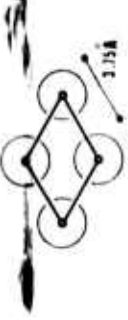
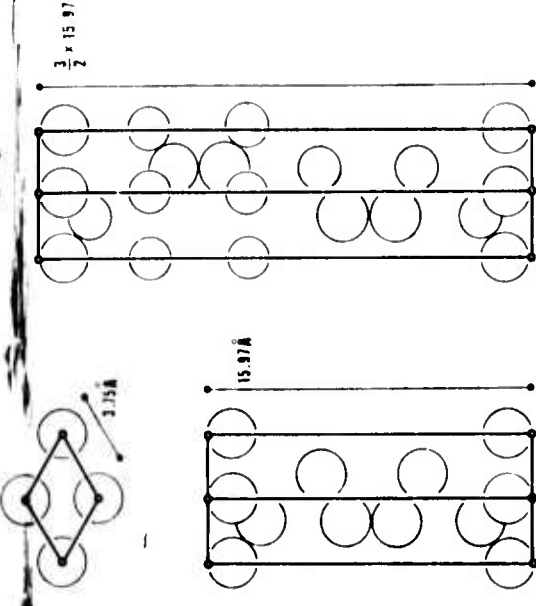


Fig. 26

10



10

material and selected reference materials.

## CONTENTS

ABSTRACT . . . . .	F-1
INTRODUCTION . . . . .	F-11
General . . . . .	F-11
Equipment Selection . . . . .	F-11
Materials Review . . . . .	F-11
DESCRIPTION OF WORK . . . . .	F-13
X-ray Diffraction Experiments . . . . .	
and Intensity Calculations . . . . .	F-13
Materials Preparation . . . . .	F-14
CONCLUSIONS . . . . .	F-16
Westinghouse Compact Material . . . . .	F-16
Morphology of Solid Lubricant Materials . . . . .	F-18
PROPOSED FUTURE WORK . . . . .	F-21
List of Figures in Text . . . . .	F-9
List of References . . . . .	F-23
APPENDICES . . . . .	
Appendix A. A DESCRIPTION OF THE PRECISION GUINIER X-RAY POWDER DIFFRACTION CAMERA . . . . .	F-25
Appendix B. X-RAY POWDER DIFFRACTION DATA OBTAINED FROM THE PRECISION GUINIER CAMERA AND A DIFFRACTOMETER . . .	F-39

CONTENTS (con't)

Appendix C. INTENSITY CALCULATIONS FOR TUNGSTEN AND TUNGSTEN DISELENIDE .....	F-53
Appendix D. SURFACE METALLOGRAPHY AND ENERGY DISPERITIVE X-RAY FLUORESCENCE ANALYSIS DATA .....	F-57

## LISTS OF ILLUSTRATION

### Figure

- |   |   |      |
|---|---|------|
| 1 | Crystal structure of hexagonal tungsten diselenide. ....  | F-3  |
| 2 | Constituents in Westinghouse compact material and selected reference materials. ....  | F-5  |
| 3 | Structural descriptions of phases in the gallium-indium-selenium ternary system. Model compounds, open circles. Cubic structures (squares), hexagonal structures (hexagons), graphite-like structures (hexagons with bars), rhombohedral structures (triangles), orthorhombic structures (rectangles), and monoclinic structures (parallelograms). .... | F-15 |
| 4 | Morphology of tungsten diselenide. Relationships between the crystalline lattice and the reciprocal lattice. Relationships between the hexagonal c-axis and shear strain. ....  | F-19 |
| 5 | Diffractometer recording of tungsten diselenide as reported by Kiparisov and co-workers, Ref. (3). ....   | F-19 |

## INTRODUCTION

### General

The purpose of this engineering investigation was to characterize an as-received solid lubricant composite material identified as "Westinghouse compact." The unique properties of similar solid lubricating materials for high temperature application in an ambient of air were described over one decade ago by American engineers (1, 2) and more recently by Russian investigators (3). Materials known to be used in the formulation of these composites include tungsten diselenide, and a gallium-indium alloy. The role of these materials and their interactions during synthesis, fabrication, and bearing component life cycle are not well understood. There is a lack of information as to the atomic crystallography and defect structure of the formulation materials. In addition, complex non-equilibrium solid state reactions take place during reduction and oxidation cycles. Previous attempts to characterize these materials have been hampered by limitations inherent in the analytical equipment used to obtain data.

### Equipment Selection

A precision, high-resolution Guinier x-ray powder diffraction camera was selected to obtain data from the Westinghouse compact material. The choice of this particular equipment was determined by physical requirements of the material and x-ray testing. Low background signal-to-noise ratio is a feature of the Guinier x-ray diffraction camera. Characteristic wavelength selection, from the x-ray source, can be accomplished and is important because fluorescence due to tungsten atoms does increase the background level and obscure weak diffraction lines. Focusing of diffracted x-rays by the Guinier camera results in narrow diffraction lines and thereby increases the detectability of weak lines. Measurement of the positions of x-ray diffraction lines can be accomplished with considerable precision even when the lines are broadened.

### Materials Review

The literature reveals that there is a lack of agreement as to the values of the lattice parameters of tungsten diselenide and a quantitative determination of

atomic positions in this alloy has not been accomplished. Clemser and co-workers (4), indexed an x-ray powder diffraction photograph of tungsten diselenide and calculated the lattice constants. They concluded that tungsten diselenide was isomorphous with tungsten disulfide and molybaenum disulfide on the basis of qualitative arguments. Atomic positions were not determined. Lattice parameters of tungsten diselenide were independently determined by Brixner from data obtained with a Philips 114.6 mm diameter x-ray powder diffraction camera and reported in two publications (5, 6). Although Brixner used the same component materials and specimen preparation techniques in both investigations, the reported values of lattice parameters are not the same in both publications. Moreover, if one assumes that the reported accuracy of these measurements represent the standard deviation, the lack of agreement in basal plane measurements is within one standard deviation and in the perpendicular direction it exceeds three standard deviations. The literature contains no information as to the homogeneity (composition) range of tungsten diselenide nor has there been consideration of defect structures. The existence of tungsten triselenide has been reported (4). Solid solubility of the terminal phases in this binary phase diagram has not been determined.

Selenium reacts with both gallium and indium. Schubert and co-workers (7) reported a hexagonal phase of gallium-rich GaSe and a rhombohedral phase of selenium-rich GaSe. These results were confirmed by the x-ray diffraction results of a subsequent study by Jellinek and Hahn (8). Later, Suzuki and Mori (9) investigated the gallium-selenium phase diagram and reported a hexagonal gallium selenide phase of stoichiometric composition, GaSe. They reported lattice parameters, but did not make a quantitative determination of the crystal structure of hexagonal gallium selenide. Rhombohedral gallium selenide was not reported. Gallium sesquiselenide has been reported by several research groups (9, 10, 11). A homogeneity range for  $\text{Ga}_2\text{Se}_3$  has been reported by Russian workers (12).

Indium-selenium phase relationships were investigated by Schubert and co-workers (13). A rhombohedral form of indium selenide was reported. Lattice parameter measurements indicate that rhombohedral InSe could be isomorphous with the previously mentioned selenium-rich GaSe. Several

crystallographic modifications of indium sesquiselenide have been found. Alpha-In<sub>2</sub>Se<sub>3</sub> has been reported (14, 15, 16) and a high temperature, beta-In<sub>2</sub>Se<sub>3</sub> has been observed (16).

A recent investigation of the gallium-indium phase diagram reports that metastable phases can be retained at atmospheric pressure (17). Previous investigations of this equilibrium binary system have indicated the presence of eutectic reaction.

## DESCRIPTION OF WORK

### X-Ray Diffraction Experiments and Intensity Calculations

The precision Guinier x-ray powder diffraction camera, described in Appendix A, was used to obtain a diffraction photograph of the Westinghouse compact material. A reproduction of this equipment is shown in Figure B-1 of Appendix B. Strategy for measurement of these x-ray diffraction lines was improvised because the latter are broadened and not resolved into characteristic components (CuK $\alpha_1$  and CuK $\alpha_2$ ). In this case, the raw data does not offer a "favorable situation" for analysis. Nevertheless, it is an excellent test of the capabilities of the precision Guinier camera. Diffraction lines from the Westinghouse compact material were tentatively indexed using the data in Table B-1 of Appendix B. Materials identified were: (1) a phase of the tungsten diselenide-type crystal structure; (2) a body-centered cubic phase, with lattice parameter close to that of metallic tungsten; and (3) a phase with similarities in x-ray diffraction pattern to hexagonal gallium selenide. The precision Guinier camera was also used to prepare x-ray diffraction photographs of commercial grade of tungsten diselenide obtained from BEMOL, Inc., and a hydrogen-reduced tungsten powder. See Appendix B, Figure B-2 and B-3. The x-ray diffraction photograph of metallic tungsten contains few diffraction lines. The reproduction in Figure B-3 is completely labeled. The latter may be compared with Figure A-1, which depicts the diffraction geometry. The image of the incident radiation is difficult to see in these reproductions because if the x-ray film is overexposed, these fiducial marks cannot be located to an accuracy of 0.02 mm. The beam trap shutter mechanism in the Guinier

camera is used to create a latent image of the fiducial marks prior to the recording of diffraction maxima from the specimen.

During this investigation, it was noticed that there were significant differences between the x-ray diffraction spectrum of tungsten diselenide obtained with the Guinier camera and the diffractometer data published by Kiparisov and co-workers (3). Therefore, x-ray diffractometer recordings of both the Westinghouse compact material and the commercial grade of tungsten diselenide were made, see Appendix B. Intensity calculations for the Guinier camera data were initiated. Objectives of these calculations were to resolve differences observed in the x-ray diffraction data for tungsten diselenide, and to detect and identify overlapping x-ray spectra in the Westinghouse compact material. Intensity calculations are discussed in Appendix C.

#### Materials Preparation

Several alloys in the gallium-indium-selenium system were prepared in order to verify and/or clarify metallurgical phase equilibria reported in the literature, and corroborate data from the precision Guinier x-ray powder diffraction camera. High purity starting materials were weighed to the nearest five milligrams and sealed in evacuated quartz ampoules. Standard metallurgical laboratory equipment was used to melt these materials and prepare alloys of nominal composition: (1) 60Ga40Se, (2) 25Ga25In50Se, and (3) 50In-50Se. The first alloy was prepared because there is a definite lack of agreement amongst previous investigators. The third alloy was made to verify the existing literature and search for structural similarities to the corresponding gallium-selenium alloy. The ternary alloy was prepared to explore the homogeneity range of crystal structures along the gallium-selenide/indium-selenide tie line. These alloy compositions, as well as previously-reported relevant phases, are shown in Figure 3. Scanning electron microscope (SEM) photographs and energy dispersive mode detection of fluorescent x-rays (EDAX) for these alloys, the Westinghouse compact, and the commerical grade of tungsten diselenide are presented in Appendix D.

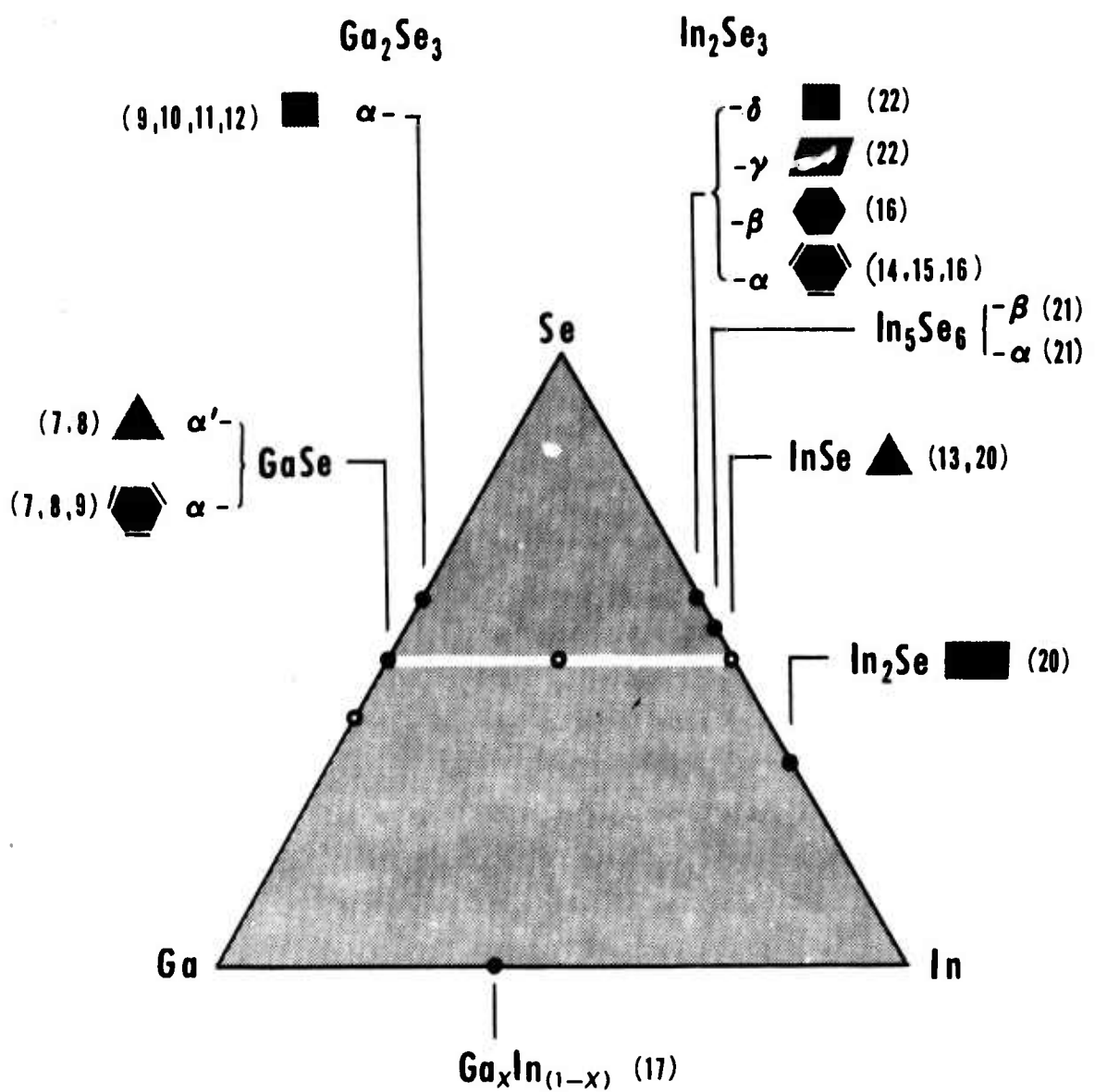


Figure 3. Structural description of phases in the gallium-indium-selenium ternary system.  
 Model compounds, open circles. Cubic structures (squares), hexagonal  
 structures (hexagons), graphite-like structures (hexagons with bars),  
 rhombohedral structures (triangles), orthorhombic structures (rectangles),  
 and monoclinic structures (parallelograms).

## CONCLUSIONS

### Westinghouse Compact Material

The Westinghouse compact material contains at least three different constituents. Tentative indexing of x-ray powder diffraction photographs made with a precision Guinier camera provides a crystallographic description of these materials. The possibility that x-ray spectra from different crystallographic species overlap does give rise to a measure of uncertainty. However, the calculated relative x-ray intensities provide additional confidence for the analysis. The largest source of uncertainty in the accuracy of our lattice parameter measurements is due to the fact that the precision Guinier camera requires calibration. On the basis of previous experience, the order of magnitude of this correction is known. Therefore, the lattice parameter calculations are reported conservatively. A summary of these results appears in the illustrations of Figure 2 and the following text:

1. Metallic tungsten is present in the Westinghouse compact. X-ray spectra indicate the presence of a body-centered cubic phase. Relative intensity calculations for diffraction lines due to tungsten are in agreement with the experimental data. Lattice parameter calculations for the tungsten microconstituent are in agreement with the literature. At this stage of the analysis we do not know if gallium and/or indium have alloyed with metallic tungsten. The metallic radii of gallium and tungsten atoms are favorable to the formation of solid solutions. On the other hand, the metallic radii of indium and tungsten atoms are not favorable to the formation of solid solutions. Tungsten in the Westinghouse compact is present as very small particles. All x-ray diffraction lines for this microconstituent are broadened, see Figure B-1. The latter can be compared with the x-ray diffraction pattern from a 325 mesh tungsten powder, see Figure B-3. Differences in x-ray diffraction line breadth can be attributed to particle size and/or alloying effects. Alloying effects have not been identified as being of major importance. Corroborative evidence for small tungsten particles in Westinghouse compact material appears in Figures D-6 and D-7.

2. A tungsten diselenide-type constituent is present in the Westinghouse compact material. X-ray diffraction data indicates that there are significant differences between the commercial grade of tungsten diselenide obtained from BEMOL, Inc. and the related hexagonal phase in the Westinghouse compact. A comparison of calculated lattice parameters shows that there is very little change in distances within the hexagonal close-packed layers of selenium atoms and tungsten atoms. The distances between layers of atoms in these materials is probably different. Lattice parameter calculations indicate a slight expansion along the axial direction for tungsten diselenide-type phase found in the Westinghouse compact. Another difference in these isostructural materials is the line breadth of x-ray diffraction patterns, compare Figures B-1 and B-2. In the former, x-ray diffraction lines corresponding to  $(00.l)$  indices appear to vary in line breadth; in the latter this phenomenon does not appear. Systematic variation in the line breadth of x-ray reflections of the  $(00.l)$  type can be attributed to structural disorder and/or chemical variations. Selenium atoms attain closest packing with a layer or sheet. Selenium-to-selenium packing is less dense in other directions, see Figure 1. Therefore it would not be surprising if the selenium in tungsten diselenide adjusted to externally-induced perturbations by rearrangement to an atomic configuration akin to the spiral chain crystal structure elemental selenium. It is also significant that all basal plane reflections for the tungsten diselenide-type phase in the Westinghouse compact do not exhibit anomalous x-ray line broadening: see  $(10.0)$ ,  $(11.0)$  and  $(20.0)$  reflections in Figure B-1. This observation would lead to the conclusion that the projection of atomic coordinates in the basal plane is ordered. Whereas the project of atomic coordinates along the axial (perpendicular) direction could be disordered.

3. At least one more constituent is present in this compact material. There is reasonable correspondence between x-ray diffraction lines assigned to the gallium indium selenide phase (Ga, In)Se, Figure B-1, and the three strongest x-ray diffraction lines reported in the literature for hexagonal GaSe, Reference (9). The measured (00.2) and (00.4) reflections are in excellent agreement and, if assigned to a GaSe-type phase, would indicate an increase in axial length of the unit cell. The random substitution of indium atoms for gallium atoms in the gallium selenide lattice is reasonable and would explain this observation. A diffraction maximum from the basal plane (11.0) was very diffuse. In fact, it was observed as a band. Therefore, little can be said about unit cell dimensions in the basal plane other than that they are in the same ballpark, see Figure 2.

#### Morphology of Solid Lubricant Materials

Structural analysis of these materials leads to a consideration of crystal morphology and the manner in which it influences the properties of solid lubricants. The morphology of crystals, excluding the classes of cubic symmetry, resembles the reciprocal lattice of the structure rather than crystal lattice, see Figure 4. Tungsten diselenide crystals have an axial ratio ( $c/a$ ) greater than unity. Therefore, primary crystals of tungsten diselenide should grow as plates. Basal planes (faces) of hexagonal symmetry and prism planes (faces) are clearly visible in Figures D-1 and D-2. Plate-like crystals have a tendency to pack in a preferential direction, see Figures D-13 and D-14. In the case of tungsten diselenide, this leads to a preferred orientation of the unique (c) axis of the crystals and a favorable relationship between the direction of shear strain and (cleavage) planes of weak, selenium-to-selenium bonds, see Figure 4. Plates of tungsten diselenide can attain a very high degree of preferred orientation. Data published by Russian investigators, Figure 3a of Reference 3, is excellent evidence for this phenomenon, also see Figure 5 of this text. In this case, tungsten diselenide crystals have packed in a manner which makes them diffract x-rays as (essentially) a single crystal with random order in the basal plane. The diffractometer recording published by Kiparisov and co-workers shows a (10.3)

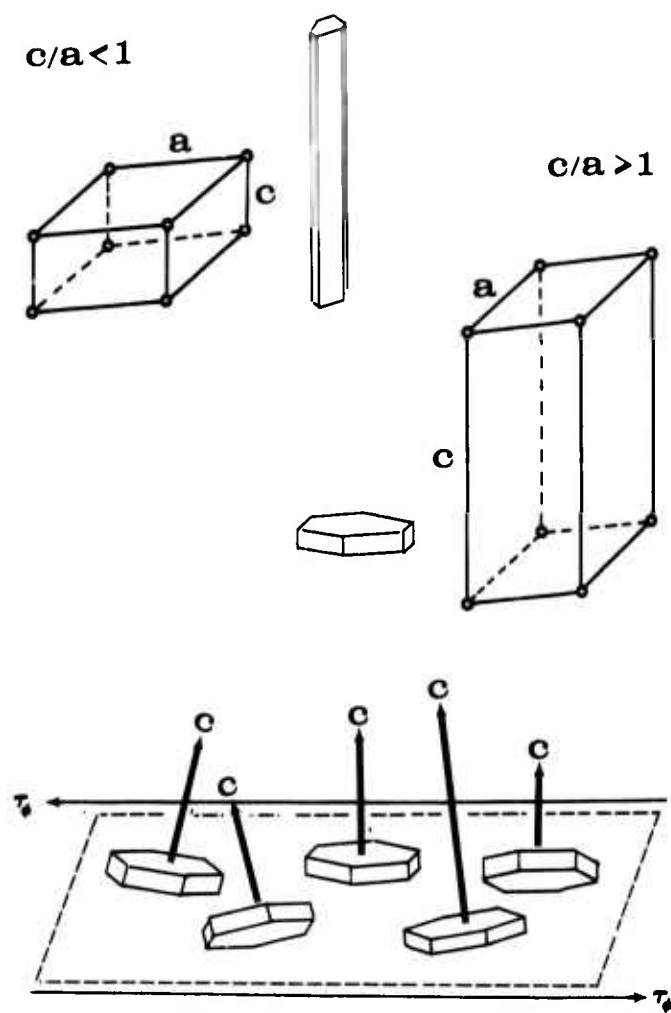


Figure 4. Morphology of tungsten diselenide. Relationships between the crystalline lattice and the reciprocal lattice. Relationships between the hexagonal c-axis and shear strain.

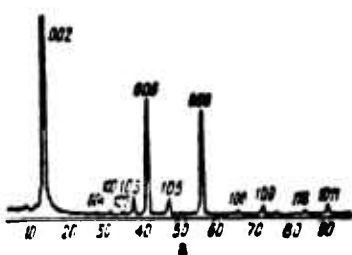


Figure 5. Diffractometer recording of tungsten diselenide reported by Kiparisov and coworkers, Ref. (3).

reflection which is less than one-tenth intensity of the (00.2), the reflection of maximum intensity. Calculations indicate that both reflections should be of approximately equal intensity, see Figure C-1. X-ray powder diffraction photographs made with the precision Guinier camera confirm these calculations, see Figure B-2, and demonstrate the excellent sampling which is attained with this instrument. Diffractometer recordings made during this engineering study also show evidence of preferred orientation, Figures B-4 and B-5. Other investigators have reported similar effects in the study of powders of isomorphous molybdenum ditelluride, Reference (19).

#### Solid Lubricant Matrix Phases

Tungsten diselenide-type crystals in the Westinghouse compact reside in a matrix of metallurgical phases. These matrix constituents contribute to the mechanical and tribo-oxidative properties of this material. Structural considerations, based on atomic architecture and local fields, are important from the experimental point of view because it is possible to relate chemical bonding to microscopic tribo-physical properties. X-ray diffraction experiments and the more recently developed extended x-ray absorption fine structure analysis (EXAFS) are complementary experimental techniques which provide this information.

Chemical bonding in tungsten diselenide is quite different than in the matrix phases. The extent of these differences is not known at the present time. An overview of structural aspects of the technology can be obtained from consideration of constituents in the Westinghouse compact, published phase equilibria and crystal structures, and model compounds prepared in this study, see Figures 2 and 3. Atoms in these materials are represented by the "hard sphere" approximation and shown to scale in Figure 2. In tungsten diselenide, tungsten (charge IV) is the smallest atom in the crystal structure, Figure 2b. When reduced to the matrix phase of metallic tungsten (charge 0), the atomic radius increases as is expected, Figure 2a. Selenium atoms in tungsten diselenide from d-s-p bonds and our calculated radius for selenium (charge II) is reasonable. In matrix phases, Figure 2c, available information indicates that selenium may be present in combination with gallium and/or indium and therefore we expect differences in chemical bonding and atomic structure.

The proposed crystal structures for GaSe indicate atomic double layer configurations: -Ga-Ga-Se-Se-Ga-Ga. The proposed rhombohedral modification, to far right in Figure 2c, requires greater differences in atomic radii and on this basis one would expect corresponding differences in chemical bonding. Despite similarities in crystal structure, only the hexagonal form of GaSe, to far left in Figure 2c, is reported to be a "graphite-like" structure. The possibility of a gallium-indium-selenium ternary phase of rhombohedral symmetry is apparent from the morphology of a model compound prepared in this study, see Figure D-21. Rhombohedral crystal symmetry may be possible across the entire tie line depicted in Figure 3, although other variables — pressure, temperature, and structural defects — may have considerable influence.

#### PROPOSED FUTURE WORK

Future work is proposed in significant areas of tribo technology which include the improvement of solid lubricants with demonstrated engineering properties in oxidizing atmospheres, a search-survey experimental investigation for solid lubricant materials with extended operational temperature range, and development of ultra-precision x-ray diffraction equipment for this specific field of technology:

1. Continuation of the instant analysis of phase equilibria and structure in Ga/In/WSe<sub>2</sub> materials. Emphasis on the role of microconstituents and the improvement of tribo-oxidative and physical properties by selective alloying techniques. Application of solid state spectroscopy to determine productive atomic engineering approaches.
2. Investigation of structural materials suitable for solid lubrication at high temperature in oxidizing atmospheres. Identification, modification, and selection of double-layer materials with structural attributes for advanced solid lubrication applications.

3. Development of an ultra-precision Guinier powder diffraction camera for solid lubricant technology. Improvement in monochromation of radiation, intensity, and resolution. Utilization of film-reading techniques and computer data processing to implement "stripping techniques" for complex x-ray diffraction patterns and thereby provide phase separation analysis.

Approved



J. W. Peters, Head  
Chemical Physics Section



P. Pietrokowski

## REFERENCES

1. D. J. Boes; "Unique Solid Lubricating Materials for High Temperature-Air Applications": ASLE Transactions, 1967, vol. 10, pp. 19-27.
2. D. J. Boes and B. Chamberlain; "Chemical Interactions Involved in the Formation of Oxidation - Resistant Solid Lubricant Composites": ASLE Transactions, 1968, vol. 11, pp. 131-139.
3. S. S. Kiparisov, G. A. Shvetsova, T. A. Lobova, L. M. Sergeeva, A. Z. Pimenova and G. A. Volodina; "Structure and Properties of a Self-Lubricating Material Based on Tungsten Diselenide": Poroshkovaya Metalurgiya, 1978, vol. 185, No. 5, pp. 88-91.
4. O. Glemser, H. Saver and P. Konig; "Über Wolframsulfide und Wolfram-selenide": Zeit. für Anorganische Chemie, 1948, vol. 257, pp. 241-246.
5. L.H. Brixner; "Preparation and Properties of the Single Crystalline AB<sub>2</sub>-Type Selenides and Tellurides of Niobium, Tantalum, Molybdenum and Tungsten": J. Inorg. Nucl. Chem., 1962, vol. 24, pp 257-263.
6. L. H. Brixner; "X-ray Study and Thermoelectric Properties of the W<sub>x</sub>-Ta<sub>1-x</sub>Se<sub>2</sub> System": J. of the Electrochemical Society, 1963, vol. 110, pp. 289-293.
7. K. Schubert, E. Dörre and M. Kluge; "Zur Kristallchemie der B-Metalle, III. Kristallstruktur von GaSe und InTe": Zeit. für Metallkunde, 1955, vol. 46, pp. 216-224.
8. F. Jellinek and H. Hahn, Z. Naturforsch. 16b, (1961) 713-715.
9. H. Suzuki and R. Mori; "Phase Study on Binary System Ga-Se": Japanese J. of Applied Physics, 1974, vol. 13, pp. 417-422.
10. W. Klemm and H. U. Vogel; "Über die Chalkogenide von Gallium and Indium Indium": Zeit für Anorg. und Alleg. Chemie, 1934, vol. 219, pp. 45-64.
11. N. Goryunova and V. Grigoreva, Soviet Phys. - Technical Physics., 1 (1956) 2094-2098.
12. L. S. Palatnik, E. K. Belova and A. A. Kozma, Soviet Physics, "Doklady", 9 (1965) pp. 1014-1017.
13. K. Schubert, E. Dörre and E. Günzel; "Kristallchemische Ergebnisse an Phasen aus B-Elementen": Die Naturwissenschaften, 1954, vol. 41, p. 448.
14. H. Hahn and G. Frank; "Zur Kristallstruktur des In<sub>2</sub>Se<sub>3</sub>": Die Naturwissenschaften, 1957, vol. 44, pp. 533-534.

REFERENCE (con't)

15. H. Miyazawa and S. Sugaike, "Phase Transitions of  $In_2 Se_3$ ": J. Phys., Soc. Japan, 12 (1957) p. 312.
16. K. Osamura, Y. Murakami and Y. Tomue; "Crystal Structures of Alpha and Beta-Indium Selenide,  $In_2 Se_3$ ": J. Phys. Soc. Japan, 1966, vol. 21, pg. 1848.
17. S. Delcroix, A. Defrain, and I. Epelboin, "Sur les Diagrammes D'Alliages Du Gallium I ou II Avec L'Etain, le Zinc ou L'Indium" J. Phys. et Radium, 24 (1963) pp. 17-20.
18. "Crystal Data — Determinative Tables", American Crystallographic Association, ACA Monograph No. 5.
19. D. Puotinen and R. E. Newnham, "The Crystal Structure of  $MoTe_2$ ", Aeta. Cryst. 14 (1961) pp. 691-692.
20. K. Schubert, E. Dörre and E. Günzel, "Kristallchemische Ergebnisse an Phasen aus B-Elementen" Die Naturwissenschaften, 41 (1954) p. 448.
21. G. K. Slavnova, N. P. Luzhnaya and Z. S. Medvedeva, "Equilibrium Diagram of the Indium-Selenium System", Russian Journal of Inorganic Chemistry (Translation) 8 (1963) pp. 622-624.
22. G. K. Slavnova, N. P. Luzhnaya and Z. S. Medvedeva, "Equilibrium Diagram of the Indium-Selenium System", Russian Journal of Inorganic Chemistry (Translation) 8 (1963) pp. 78-81.

## APPENDIX A

### A DESCRIPTION OF THE PRECISION GUINIER X-RAY POWDER DIFFRACTION CAMERA

A precision Guinier x-ray powder diffraction camera was selected for this effort. The novel features and advantages of this instrument can be understood from a description of the geometry shown in Figure A-1. Divergent white (broadband) radiation from a copper target x-ray tube impinges on a curved quartz crystal monochromator that has a narrow passband. The latter includes the strong components of characteristic wavelength,  $\text{CuK}\alpha_1$  and  $\text{CuK}\alpha_2$ . It is this design feature which provides a favorable signal-to-noise ratio, or low background. The bent quartz crystal is designed to focus each of the characteristic x-ray wavelengths. Points of focus are determined experimentally. The x-ray camera is a circular cylinder (sector) disposed in a manner which brings the periphery of the camera into coincidence with the focused incident radiation. A strip of double emulsion x-ray film is placed in the camera and retained in a circular geometry. Therefore we can use the images of the focused incident beams as fiducial marks. This property of the Guinier camera is of great importance, especially when the powder sample yields broadened, diffuse diffraction maxima, as is the case for Westinghouse compact material. If the powder specimen is placed on the periphery of the x-ray camera, or an imaginary extension thereof, diffracted x-rays will be focused on the inner emulsion of the photographic film. At small diffraction angles, both components of the characteristic radiation are focused to the same part of the film. This feature of the Guinier camera permits the detection of very weak diffraction lines that are seldom observed with other experimental techniques. At larger diffraction angles, the components of characteristic radiation are split, as shown in Figure A-1. The linear resolution of the incident  $\text{CuK}\alpha_1$  and  $\text{CuK}\alpha_2$  radiation at the film plane is 0.06 mm. A set of slits can be used to remove most of the  $\text{CuK}\alpha_2$  radiation if greater purity is required.

Realization of the focusing principle devised by A. Guinier requires precise instrumentation to achieve all benefits offered by this powder diffraction technique. The equipment used in this work is shown in Figure A-2. The pre-

cision Guinier x-ray diffraction camera is mounted in a water-cooled chamber which can be evacuated. The camera is operated in vacua to reduce the scattering of x-rays by air. Circulating water provides thermal control of the camera. Heat generated by the specimen drive motor within the evacuated chamber is removed by an independent water flow circuit. The x-ray source (tube) is independent of the evacuated chamber which contains both the camera and the monochromator crystal. This design feature makes monochromator focusing insensitive to variations which take place in the x-ray tube and permits exposure times of hundreds of hours without broadening or degradation of the photographic image. These components can be seen in operating position in Figure A-3. The camera is not a complete cylinder, see Figure A-4. The x-ray film is placed on the periphery of the camera and is retained in position by a spring-loaded device, see Figure A-5. This illustration shows the manually-operated incident beam trap which is used to produce a fiducial mark on the x-ray film. The camera assembly has three spherical instrumentation mounts which fit into symmetrically displaced v-grooves. This kinematic design provides for accurate positioning of the camera after film loading operations, Figure A-6. The entire camera and v-groove mounting assembly can be adjusted in the x-y plane by use of the mechanism shown in Figure A-7. The powder specimen holder shown in the previous illustration can be removed, exposing the fourth set of horizontal and vertical divergence slits, Figure A-8. Retaining springs, which keep the powder specimen holder against a reference surface, can be seen in this illustration.

X-ray diffraction films made with the Guinier camera are measured at low optical magnification with a specially designed comparator, see Figures A-9 and A-10. The comparator measurement scale has been calibrated to an accuracy of one micron, at every ten millimeters, against Standard Invar Meter Bar No. 91. The optics of the low power traveling microscope contains a reticule with both horizontal and vertical reference marks. Measurements of the location of x-ray diffraction (maxima) lines are accurate to 0.02 mm. The precision of these measurements is sufficient to permit an indexing of diffraction maxima which leads to agreement of the fifth place in  $\sin^2\theta$ . The accuracy of these measurements depends on camera design considerations, care taken in camera fabrication and

usage, and the use of calibration substances. Correction for the shrinkage of each x-ray powder diffraction film is obtained by comparator measurements of an accurate scale printed on each film, prior to x-ray exposure, with the equipment shown in Figure A-11. The latter contains a replica of a scribed glass scale manufactured and registered by Carl Zeiss.

## APPENDIX A

### A DESCRIPTION OF THE PRECISION GUINIER X-RAY POWDER DIFFRACTION CAMERA

#### LIST OF FIGURES

Figure		Page
A-1	Geometrical focusing of x-rays by a curved crystal monochromator and disposition of the Guinier powder x-ray diffraction camera: camera (C), film (F), quartz monochromator crystal (M), powder sample (P), sets of horizontal and vertical divergence-limiting slits ( $S_1, S_2, S_3, S_4$ ), and x-ray tube target (T) . . . . .	F-33
A-2	Precision Guinier x-ray powder diffraction camera on adjustable table mount; x-ray tube and tube mount with three degrees of mechanical adjustment; evacuated chamber (E), adjustable table mount for camera chamber (TM), x-ray diffraction tube (SRT), and x-ray diffraction tube mount (XRTM) . . . . .	F-34
A-3	Precision Guinier x-ray powder diffraction camera and x-ray source: evacuated chamber (E), water circulating system for evacuated chamber ( $CW_1$ ), water circulating system for specimen holder drive motor ( $CW_2$ ), x-ray tube (XRT), and x-ray diffraction tube mount with three degrees of mechanical adjustment (XRTM) . . . . .	F-34
A-4	Precision Guinier camera film holder and powder specimen holders: Guinier camera film holder assembly (C), manually-operated beam trap lever (BTL), light shutter (LS), and powder specimen holders (PH) . . . . .	F-35
A-5	Precision Guinier camera film holder assembly and powder specimen holders: reference surface for x-ray film (RF), retaining spring for film (RS), beam trap (BT), light tight enclosure (LT), and powder specimen holders (PH) . . . . .	F-35
A-6	Precision Guinier camera - view of open water-cooled chamber and x-ray tube: camera assembly (C), specimen drive motor (DM), monochromator crystal and slit assembly (MS) . . . . .	F-36

FIGURES (Continued)

Figure		Page
A-7	Precision Guinier camera - view from open water-cooled chamber toward x-ray tube: camera mount (CM), x-y plane adjustments (XY), and set of divergence-limiting slits (S <sub>3</sub> ) . . . . .	F-36
A-8	Precision Guinier camera - view from open water-cooled chamber toward x-ray tube: set of divergence-limiting slits (S <sub>4</sub> ) and retaining springs (RP) for powder specimen holder . . . . .	F-37
A-9	Comparator and x-ray diffraction film reader: spring-loaded film retainers (FS), grips for manual (rapid) traversing (G), vernier adjustment control bar (VB), low power optical microscope (X), and light glare suppression shield (SS) . . . . .	F-37
A-10	Comparator and x-ray diffraction film reader - closeup: x-ray diffraction film (F) in position and illuminated with source of diffuse light . . . . .	F-38
A-11	Exposure timer and printer equipment for placing image of accurate Zeiss scale on x-ray films . . . . .	F-38

APPENDIX A  
A DESCRIPTION OF THE PRECISION GUINIER  
X-RAY POWDER DIFFRACTION  
CAMERA

**LIST OF SYMBOLS USED IN ILLUSTRATIONS**

Appendix A contains a graphical description of the focusing principle utilized in the precision Guinier x-ray powder diffraction camera, photographs of the instrument with associated x-ray source, and ancillary equipment. Components and parts in this instrumentation have been designated by a set of alphabetic symbols which are used consistently throughout all illustrations.

SYMBOLS	DESCRIPTION	FIGURES
BT	X-ray film camera beam trap	A-5
BTL	X-ray film camera beam trap lever	A-4
C	X-ray film camera assembly	A-1, A-4, A-6
CM	X-ray diffraction camera film-holder mount	A-7
CW <sub>1</sub>	Cooling water circulating system for evacuated chamber	A-3
CW <sub>2</sub>	Cooling water circulating system for specimen holder drive motor	A-3
DM	Specimen drive motor	A-6
E	Evacuated chamber for x-ray film camera and slit/monochromator assembly	A-2, A-3
F	X-ray film	A-1, A-10
FS	Comparator spring-located film retaining chips	A-9
G	Comparator rapid traverse grips	A-9
LS	Camera film holder assembly light shutter	A-4
LT	X-ray camera light-tight enclosure	A-5
M	Monochromator crystal	A-1
MS	Monochromator crystal and slit assembly	A-6
P	Powder sample	A-1
PH	Powder specimen holder	A-4, A-5
RF	Reference surface for x-ray film	A-5

List of Symbols Cont'd.

SYMBOLS	DESCRIPTION	FIGURES
RP	Retaining springs for powder specimen holder	A-8
RS	Retaining springs for x-ray film	A-5
S	Sets of horizontal and vertical divergence-limiting slits	A-1,A-7,A-8
SS	Comparator light glare suppression shield	A-9
T	X-ray tube (anode) target	A-1
TM	Adjustable table mount for camera chamber	A-2
VB	Comparator vernier adjustment control bar	A-9
X	Comparator low power optical microscope	A-9
XRT	X-ray diffraction tube	A-2,A-3
XRTM	X-ray diffraction tube mount	A-2,A-3
XY	X-Y plane adjustments for camera assembly mounting bracket	A-7

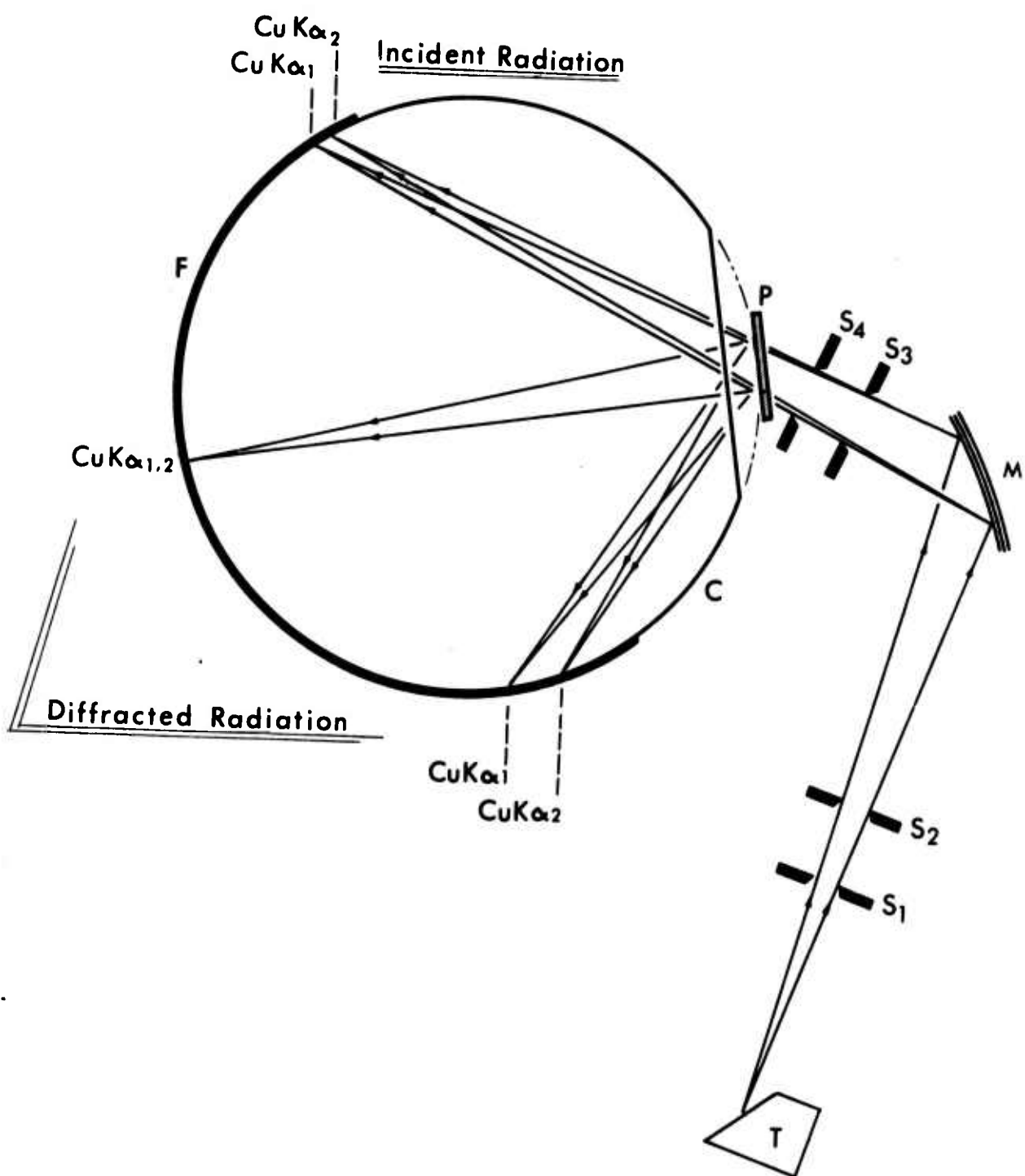


Figure A-1. Geometrical focusing of x-rays by a curved crystal monochromator and disposition of the Guinier powder x-ray diffraction camera: camera (C), film (F), quartz monochromator crystal (M), powder sample (P), sets of horizontal and vertical divergence-limiting slits ( $S_1$ ,  $S_2$ ,  $S_3$ ,  $S_4$ ), and x-ray tube target (T).

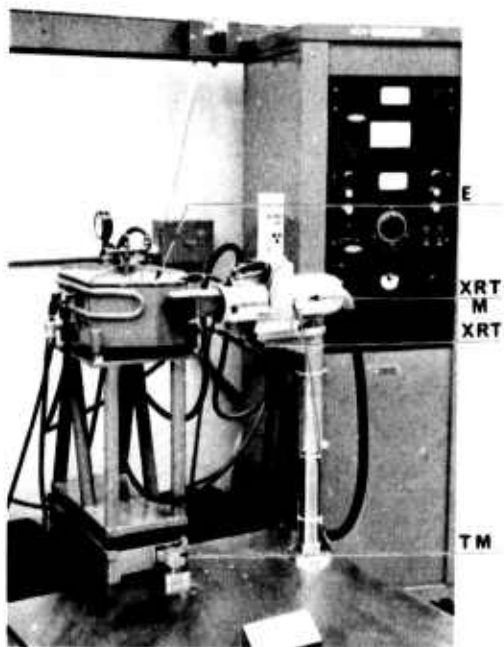


Figure A-2. Precision Guinier x-ray powder diffraction camera on adjustable table mount; x-ray tube and tube mount with three degrees of mechanical adjustment: evacuated chamber (E), adjustable table mount for camera chamber (TM), x-ray diffraction tube (SRT), and x-ray diffraction tube mount (XRTM).

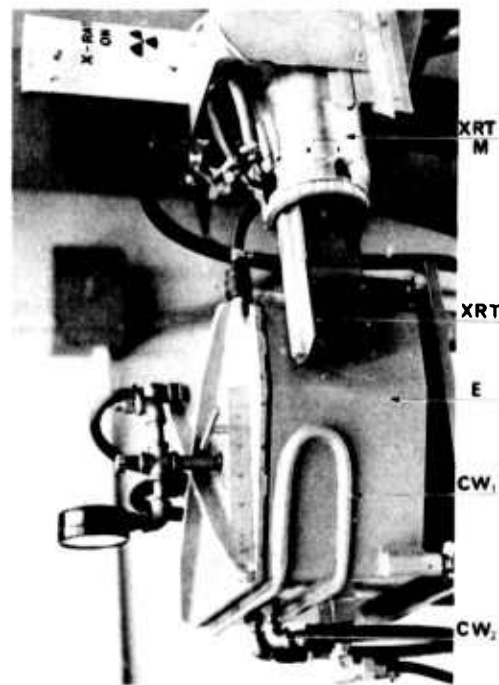


Figure A-3. Precision Guinier x-ray powder diffraction camera and x-ray source: evacuated chamber (E), water circulating system for evacuated chamber (CW<sub>1</sub>), water circulating system for specimen holder drive motor (CW<sub>2</sub>), x-ray tube (XRT), and x-ray diffraction tube mount with three degrees of mechanical adjustment (XRTM).



Figure A-4. Precision Guinier camera film holder and powder specimen holders:  
Guinier camera film holder assembly (C), manually-operated beam trap  
level (BTL), light shutter (LS), and powder specimen holders (PH).

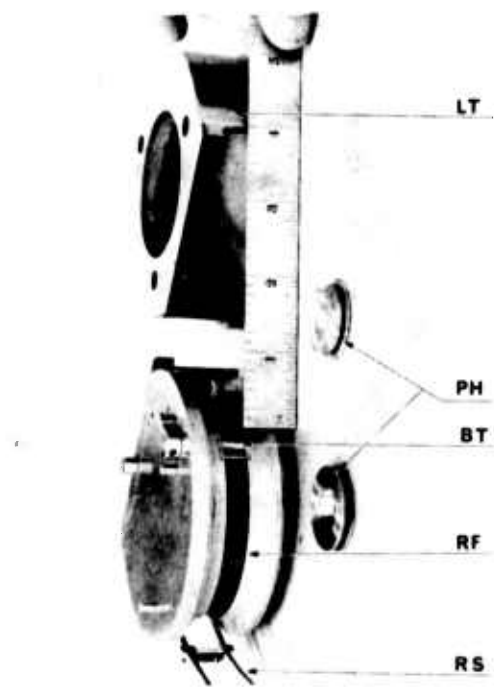


Figure A-5. Precision Guinier camera film holder assembly and powder specimen  
holders: reference surface for x-ray film (RF), retaining spring for film (RS),  
beam trap (BT), light tight enclosure (LT), and powder specimen  
holders (PH).

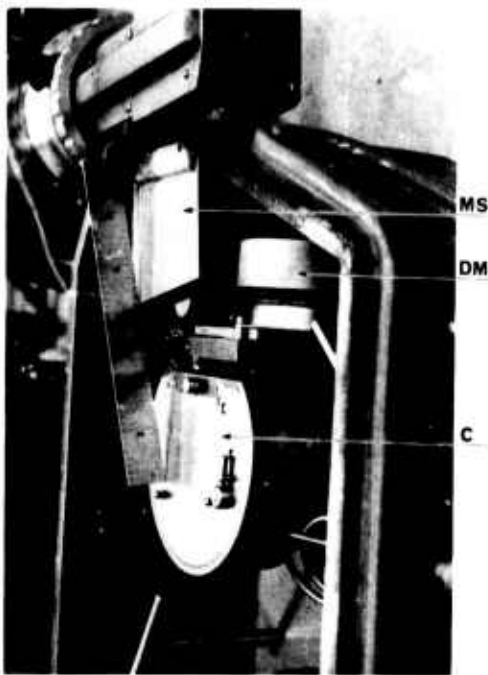


Figure A-6. Precision Guinier camera - view of open water-cooled chamber and x-ray tube: camera assembly (C), specimen drive motor (DM), monochromator crystal and slit assembly (MS).

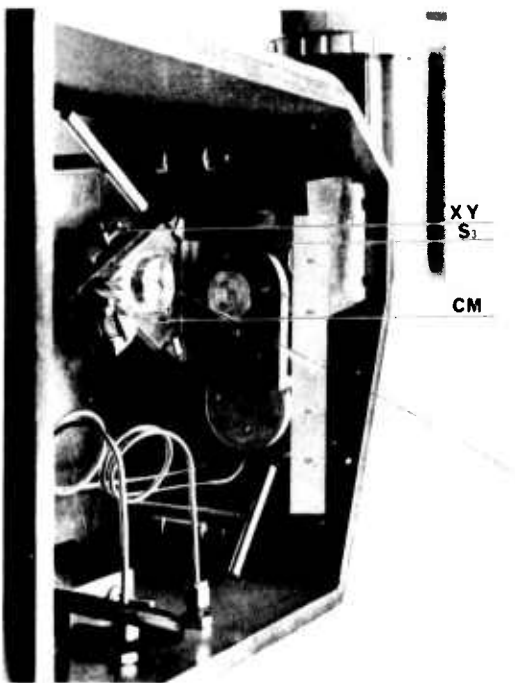


Figure A-7. Precision Guinier camera - view from open water-cooled chamber toward x-ray tube: camera mount (CM), x-y plane adjustments (XY), and set of divergence-limiting slits (S<sub>3</sub>).

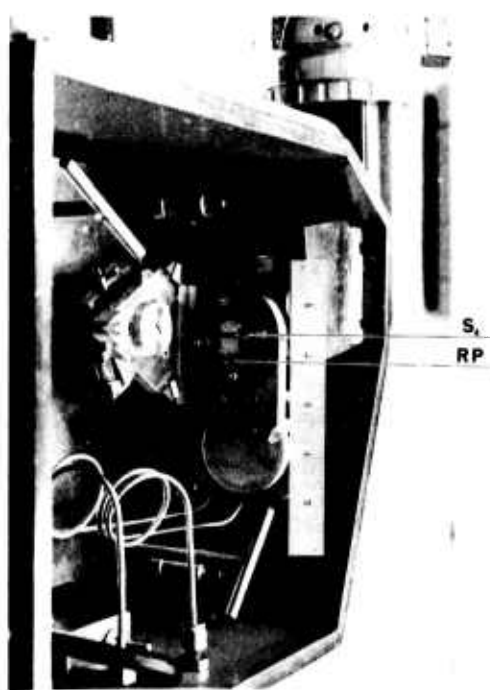


Figure A-8. Precision Guinier camera - view from open water-cooled chamber toward x-ray tube: set of divergence-limiting slits ( $S_4$ ) and retaining springs (RP) for powder specimen holder.

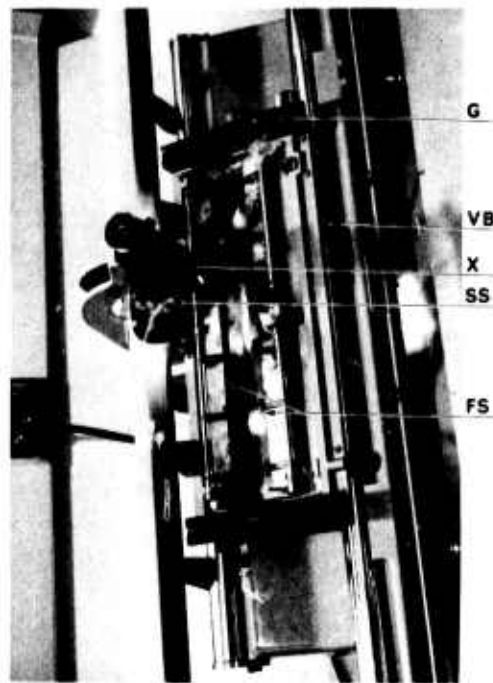


Figure A-9. Comparator and x-ray diffraction film reader: spring-loaded film retainers (FS), grips for manual (rapid) traversing (G), vernier adjustment control bar (VB), low power optical microscope (X), and light glare suppression shield (SS).

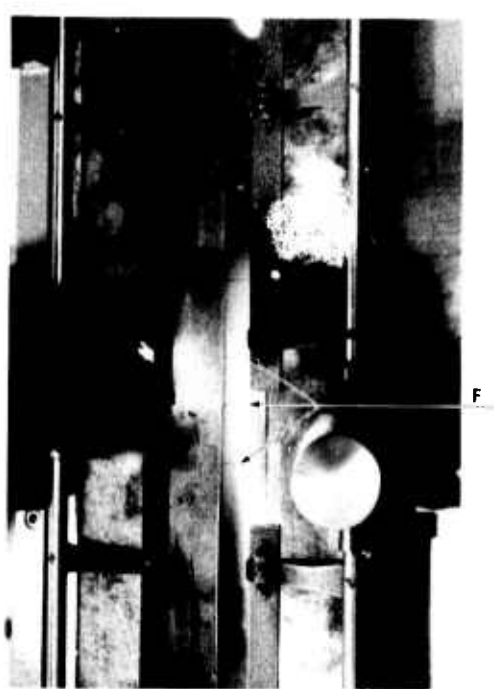


Figure A-10. Comparator and x-ray diffraction film reader - closeup: x-ray diffraction film (F) in position and illuminated with source of diffuse light.

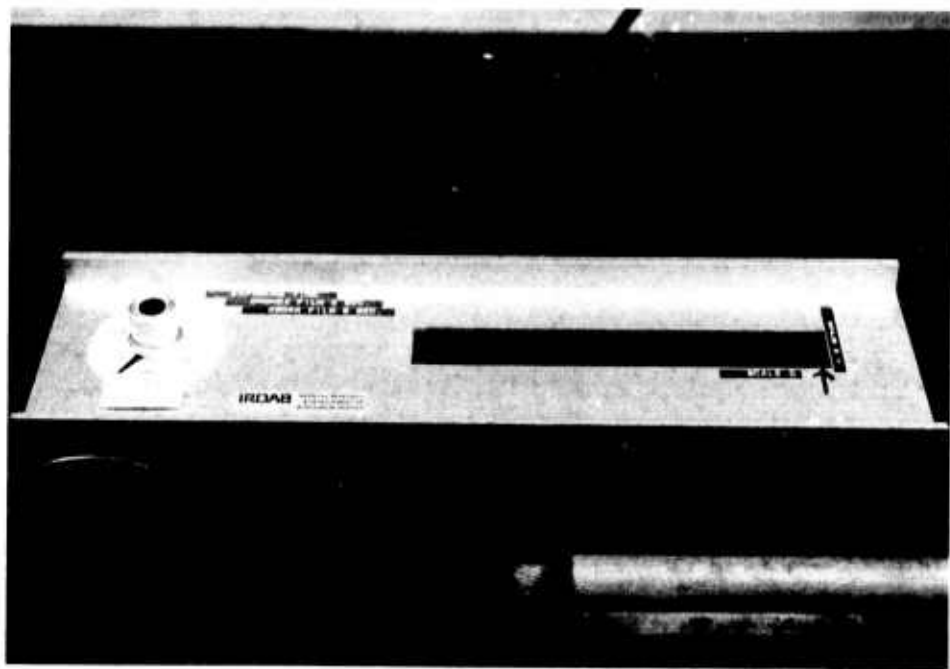


Figure A-11. Exposure timer and printer equipment for placing image of accurate Zeiss scale on x-ray films.

## APPENDIX B

### PRECISION GUINIER X-RAY POWDER DIFFRACTION PHOTOGRAPHS, DIFFRACTOMETER RECORDINGS, AND INDEXED DATA.

A strategy for measurement of lines on diffraction photographs of Westinghouse compact material was devised. The latter was necessary because of x-ray diffraction line broadening. Resolved copper characteristic doublets were not observed. The comparator, Figures A-9 and A-10, provides both horizontal and vertical fiducial marks for measurements. After preliminary measurements, the following line-reading procedure was used. Whenever possible, three measurements of each x-ray diffraction line were made with the vertical fiducial mark: (1) at the low-angle side of the diffraction maxima, (2) at the high-angle side of the diffraction maxima, and (3) at the center of darkening of the film-as visually estimated. Data obtained in this manner is given in Table B-1. Conventional line measurement techniques were used to obtain data from x-ray diffraction photographs of tungsten diselenide and metallic tungsten. Data for these materials appear in Tables B-2 and B-3.

Data was indexed by comparison of observed and calculated values of  $\sin^2 \theta$ . Statistical treatment of the data has not been performed because the Guinier camera has not been calibrated recently. Therefore, all lattice parameters reported in this work are derived from constants which appear in analytical expressions for calculated values of  $\sin^2 \theta$ . These expressions are as follows:

Figure B-1

Tungsten diselenide-type phase,

$$\sin^2 = 0.07366(h^2 + hk + k^2) + 0.003528(l)^2$$

Tungsten phase,

$$\sin^2 \theta = 0.05949 (h^2 + k^2 + l^2).$$

Gallium/indium selenide-type phase,

$$\sin^2 \theta = 0.0590 (h^2 + hk + k^2) + 0.002293 (l^2)$$

Figure B-2

Commercial grade of tungsten diselenide,

$$\sin^2 \theta = 0.07340 (h^2 + hk + k^2) + 0.003530 (l^2)$$

Figure B-3

Metallic tungsten powder,

$$\sin^2 \theta = 0.05927 (h^2 + k^2 + l^2).$$

## LIST OF ILLUSTRATIONS

### Figure

- B-1 Precision Guinier x-ray powder diffraction film of Westinghouse compact material. Characteristic copper x-radiation.
- B-2 Precision Guinier x-ray powder diffraction film of a commercial grade of tungsten diselenide obtained from BEMOL, Inc. Characteristic copper x-radiation.
- B-3 Precision Guinier x-ray powder diffraction film of tungsten powder. Characteristic copper radiation.
- B-4 Copy of x-ray diffractometer recording of Westinghouse compact material. Characteristic copper radiation.
- B-5 Copy of x-ray diffractometer recording of commercial grade of tungsten diselenide obtained from BEMOL, Inc. Characteristic copper radiation.

## LIST OF TABLES

Table	Page
B-1	Westinghouse Compact Material X-ray Powder Diffraction Data.
B-2	Commercial-Grade Tungsten Diselenide X-ray Powder Diffraction Data.
B-3	Tungsten X-ray Powder Diffraction Data.

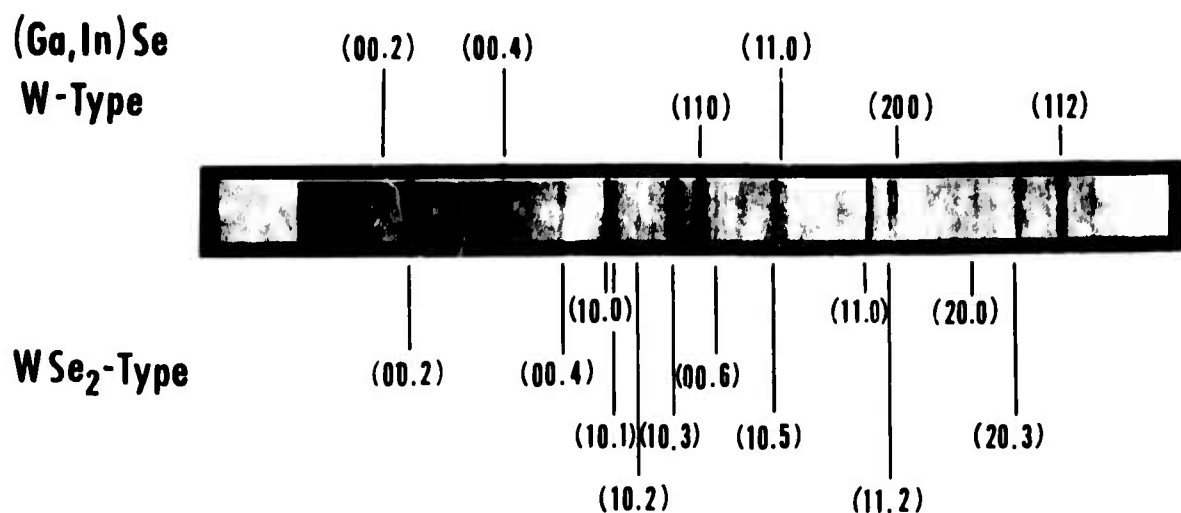


**Figure B-1.** Precision Guinier x-ray powder diffraction film of Westinghouse compact material. Characteristic copper x-radiation.

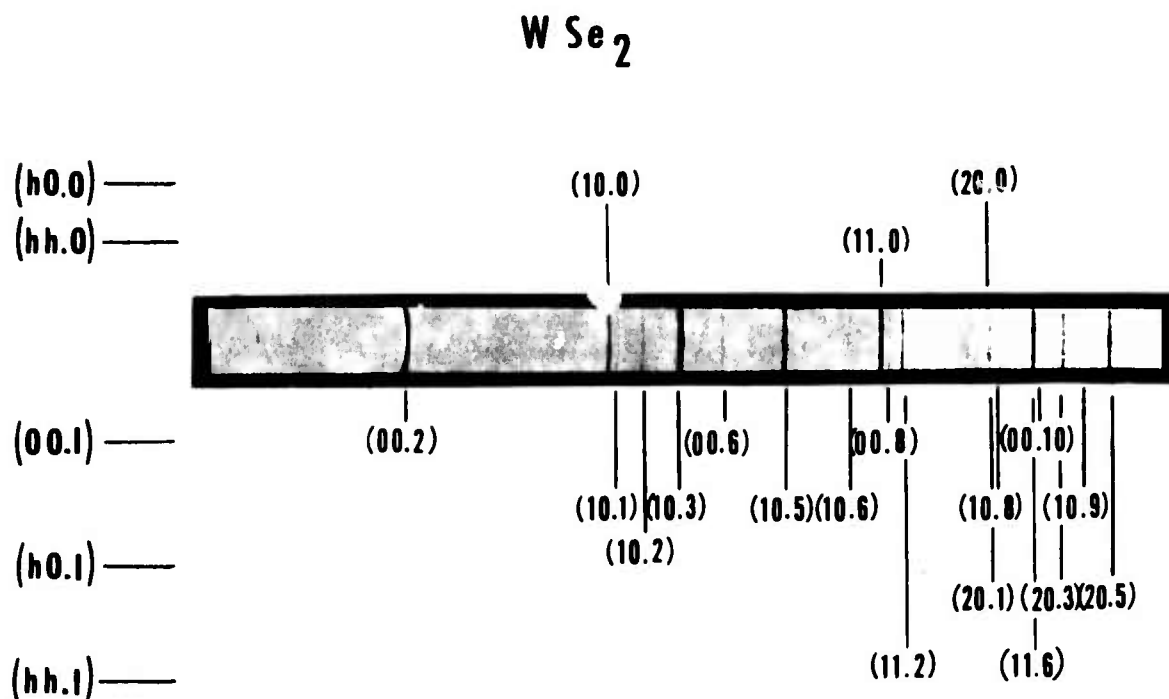


**Figure B-2.** Precision Guinier x-ray powder diffraction film of a commercial grade of tungsten diselenide obtained from BEMOL, Inc.  
Characteristic copper x-radiation.

## Tungsten

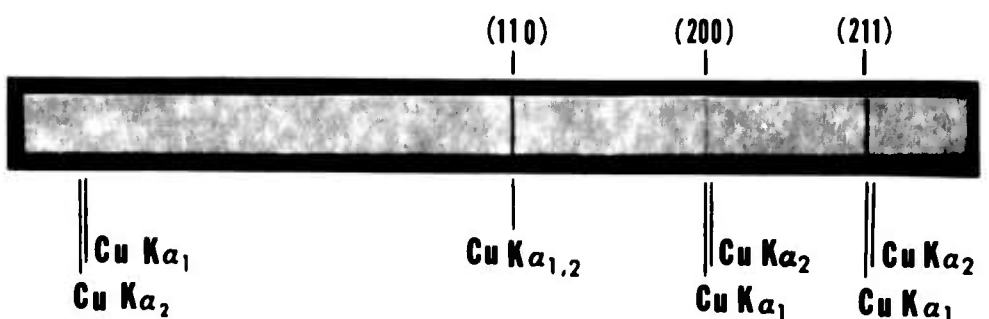


Figure B-3. Precision Guinier x-ray powder diffraction film of tungsten powder.  
Characteristic copper x-radiation.

FIG  
B-4

F-45

1 af 8

100

85

80

20/8

(25)

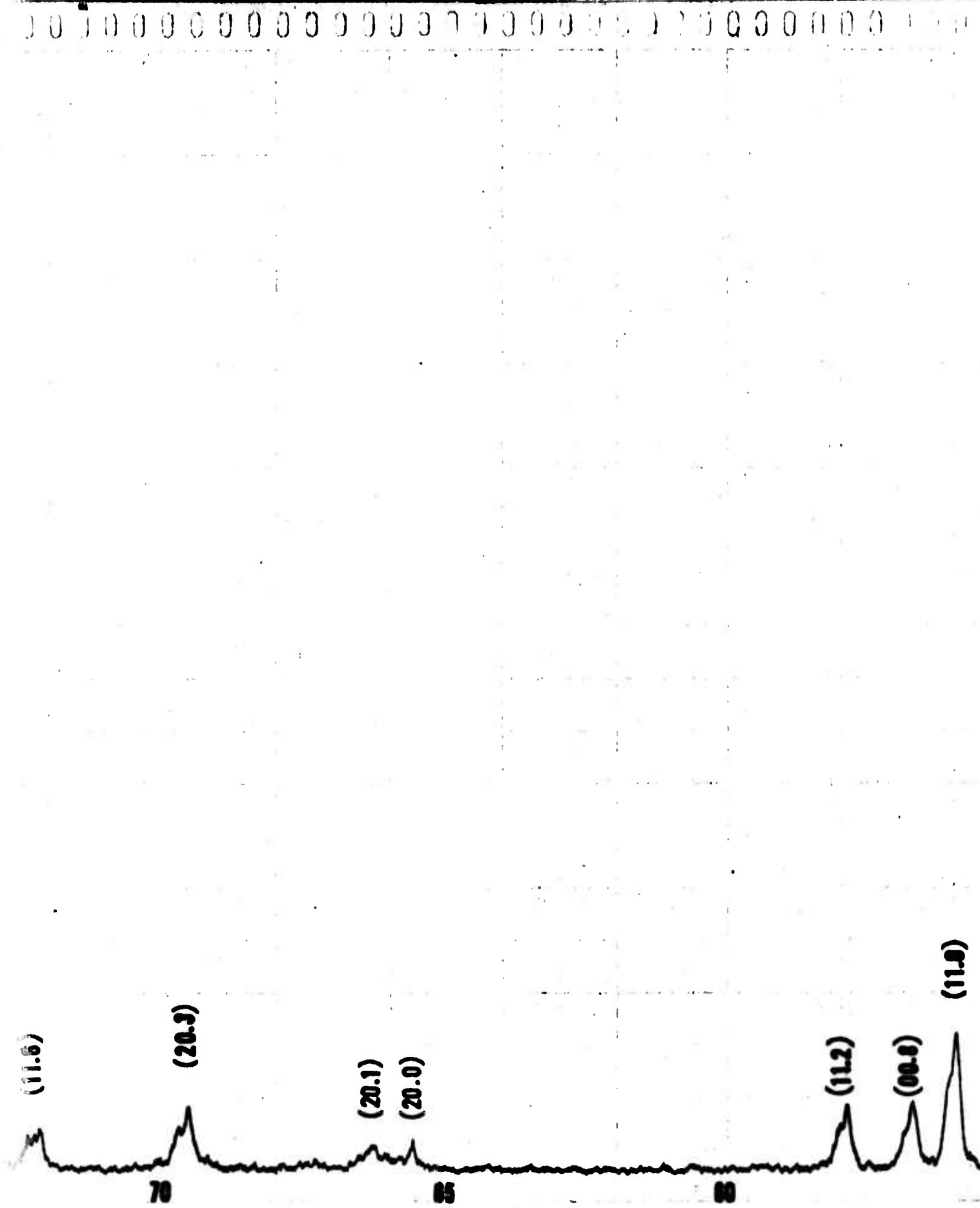
三

85

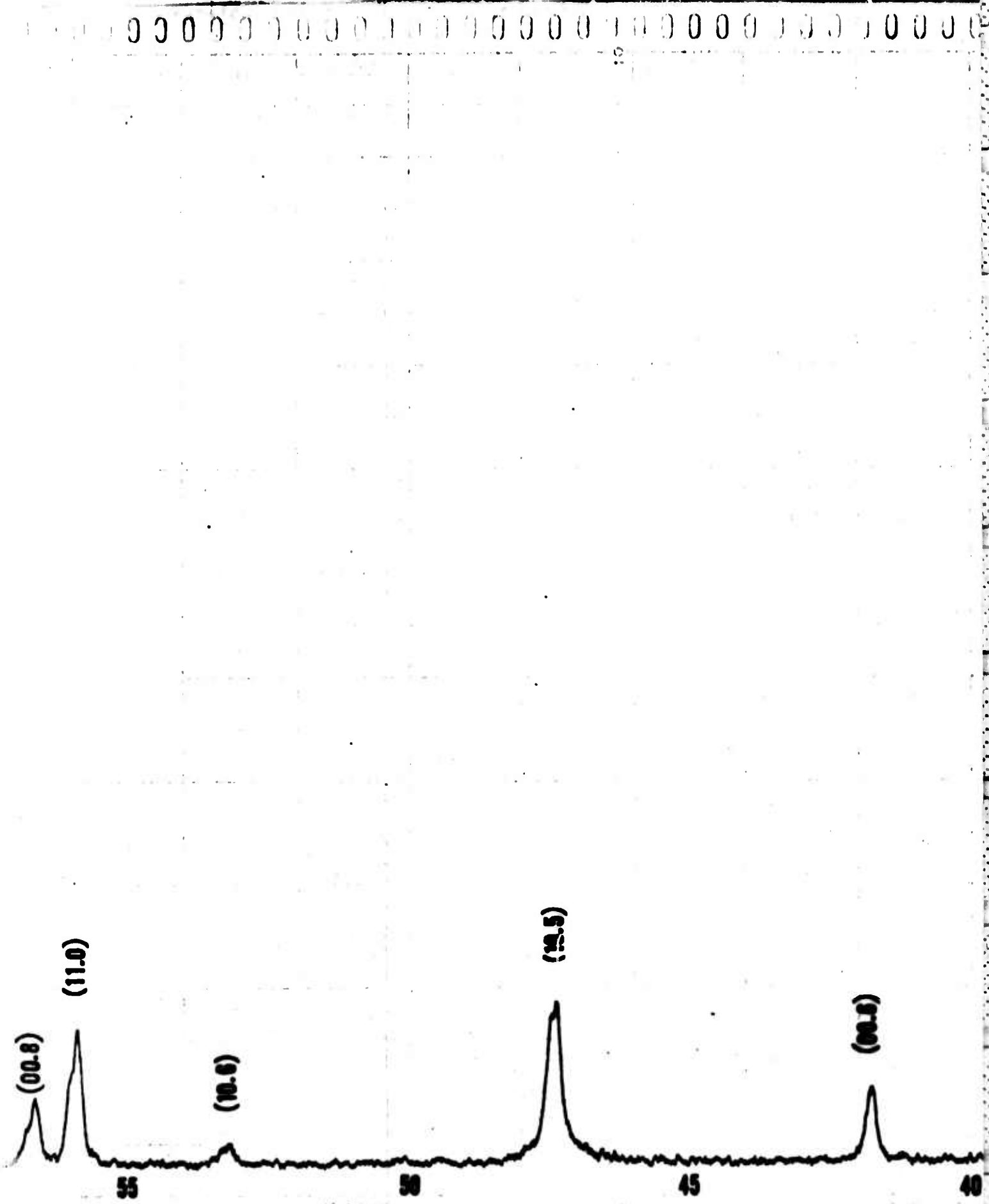
80

75

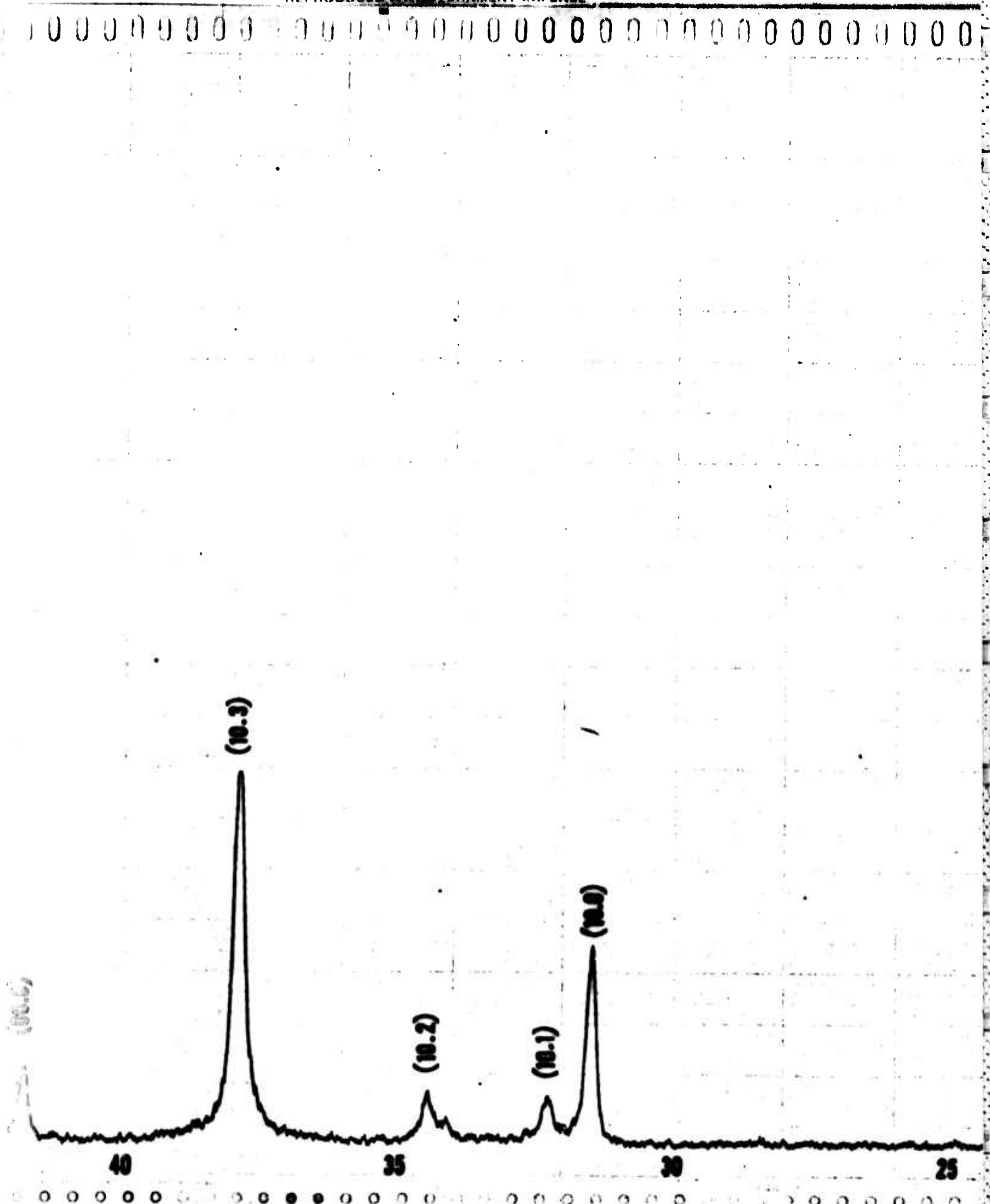
3af 8



4af 8



5 of 8



6 of 8

2

25

20

15

10

748

**Figure B-4**

F-45

**Figure 8-4.** X-ray diffractometer recording. Commercial grade of tungsten diselenide from BEMOL, Inc. As received.  
 Filtered copper radiation. Diffractometer Mg.  
 D62-279. Diffraction angle range: 5° to 90°.  
 Full scale deflection is 1000 counts.

FIG  
B-5

10f

7

PREVIOUS PAGE  
IS BLANK

F-47

85

Zaf

7

THIS DOC

Reproduced from  
best available copy.

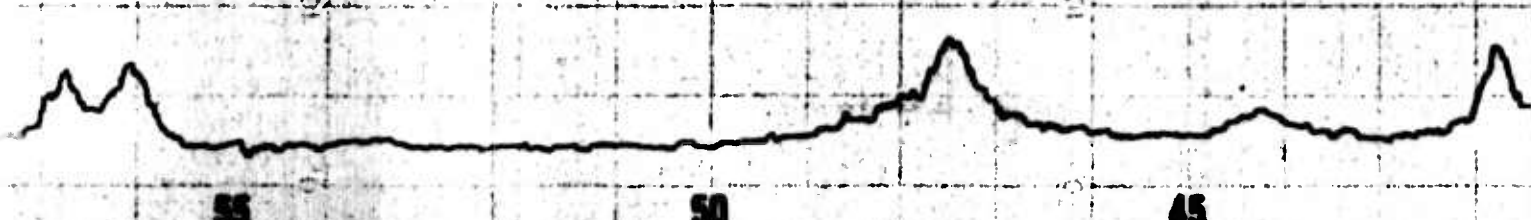
309 7

70

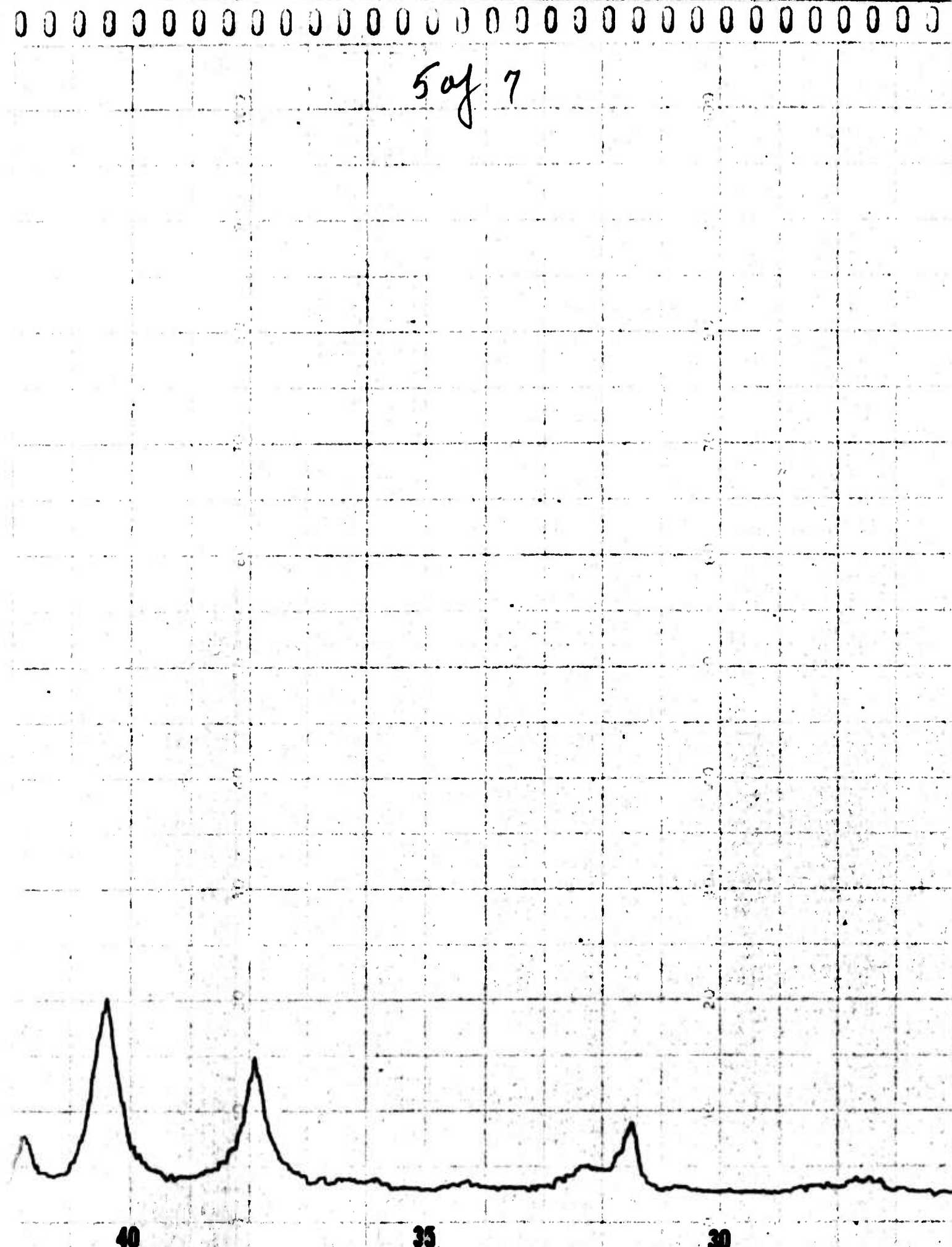
65

3

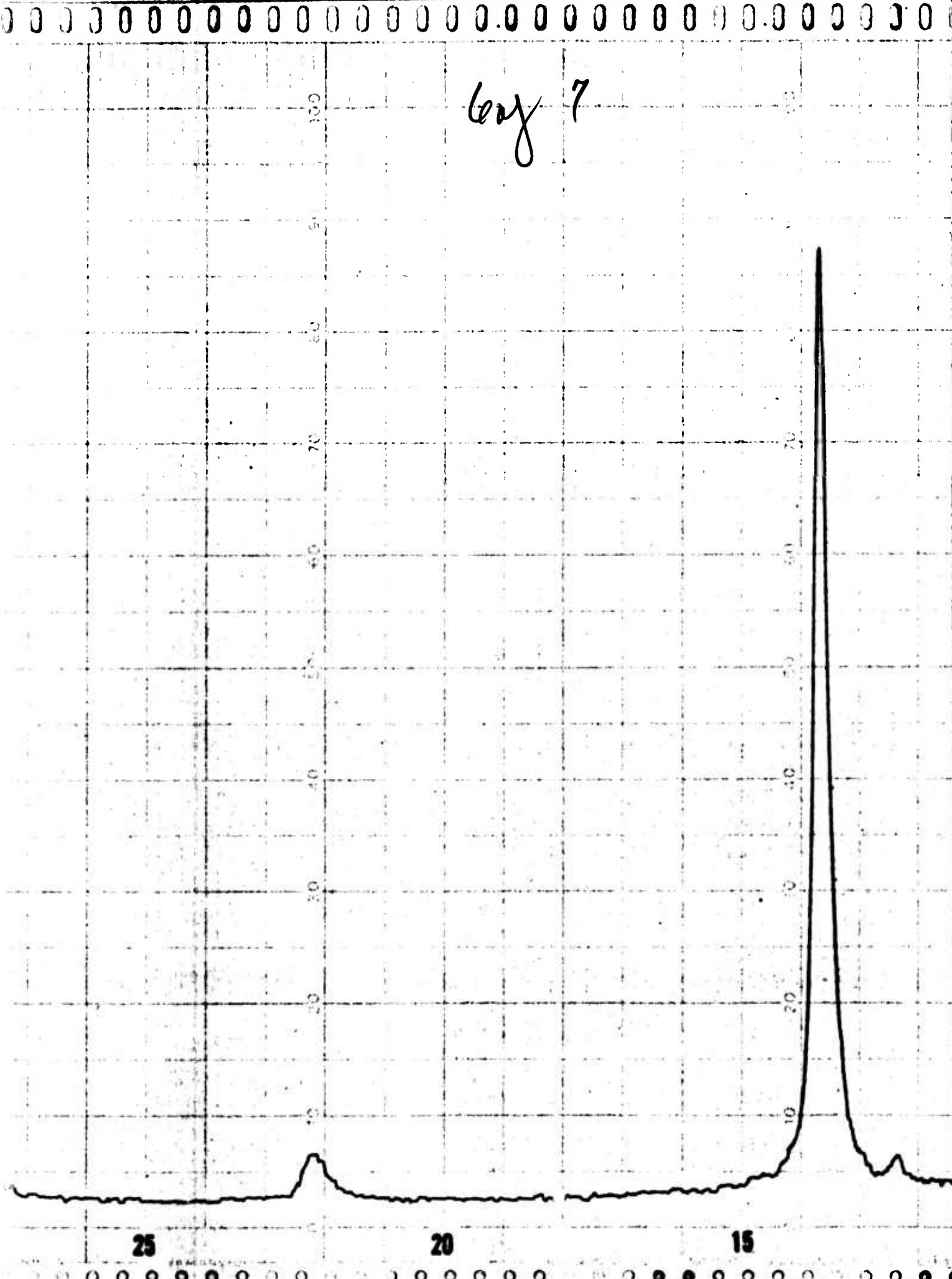
4af 7



5 of 7



6ay 7



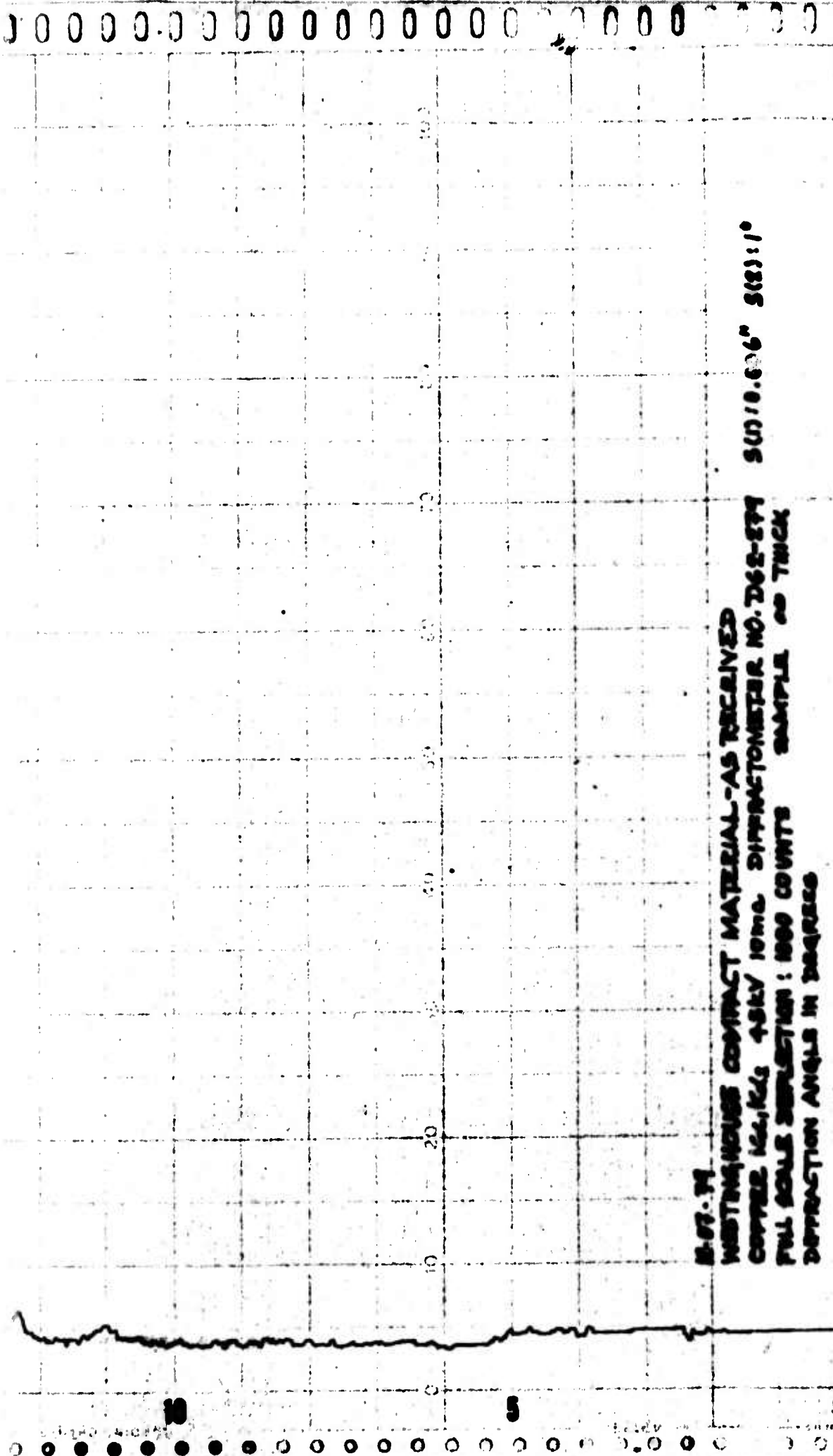


Figure B-5

Figure B-5. X-ray diffractometer recording. Westinghouse compact material. As received. Filtered copper radiation. Diffractometer No. D62-279. Diffraction angle range: 50 to 100°. Full scale deflection is 1000 counts.

F-47

Table B-1. Westinghouse Compact Material X-ray Powder Diffraction Data.

<u>Diffraction Line*</u>	<u>Radiation</u>	<u>d (Å)</u>	<u><math>\sin^2 \theta_{\text{obs}}</math></u>	<u>Tentative Indexing</u>	
1 W	$\alpha_1, 2$	8.098	0.00906	(00.2)	Ga/In/Se
		6.632	0.01351		
2 VS	$\alpha_1, 2$	6.562	0.01380	(00.2)	WSe <sub>2</sub> -type
		6.480	0.01415		
		4.059	0.03606		
3 M	$\alpha_1, 2$	4.031	0.03658	(00.4)	Ga/In/Se
		4.010	0.03695		
		3.300	0.05456		
4 W	$\alpha_1, 2$	3.262	0.05586	(00.4)	WSe <sub>2</sub> -type
		3.243	0.05649		
5 VS	$\alpha_1, 2$	2.484	0.07326	(10.0)	WSe <sub>2</sub> -type
6 M	$\alpha_1, 2$	2.783	0.07674	(10.1)	WSe <sub>2</sub> -type
7 W	$\alpha_1, 2$	2.611	0.08718	(10.2)	WSe <sub>2</sub> -type
		2.535	0.09244		
8 W	$\alpha_1, 2$	2.511	0.09426		
		2.492	0.09572		
		2.387	0.10430		
9 S	$\alpha_1, 2$	2.379	0.10499	(10.3)	WSe <sub>2</sub> -type
		2.374	0.10545		
		2.250	0.11735		
10 VS	$\alpha_1, 2$	2.237	0.11871	(110)	W
		2.226	0.11992		
11 WM	$\alpha_1, 2$	2.166	0.12663	(00.6)	WSe <sub>2</sub> -type
		2.066	0.13922		
12 W	$\alpha_1, 2$	2.055	0.14069		
		2.046	0.14191		

\*Observed intensity symbols: VS = very strong, S = strong,  
MS = medium strong, M = medium, W = weak, VW = very weak.

Table B-1. (continued)

<u>Diffraction Line</u>	<u>Radiation</u>	<u>d (Å)</u>	<u><math>\sin^2 \theta_{\text{obs}}</math></u>	<u>Tentative Indexing</u>	
13 S	$\alpha_1, 2$	1.920	0.16127	(10.5)	WSe <sub>2</sub> -type
		1.907	0.16347		
14 M	$\alpha_1, 2$	-	-	(11.0)	Ga/In/Se
		1.762	0.19132		
15 VW	$\alpha_1, 2$				
		1.645	0.21967		
16 VS	$\alpha_1, 2$	1.643	0.22008	(11.0)	WSe <sub>2</sub> -type
		1.642	0.22049		
17 W	$\alpha_1, 2$	1.625	0.22515	(00.8)	WSe <sub>2</sub> -type
18 MS	$\alpha_1, 2$	1.593	0.23426	(11.2)	WSe <sub>2</sub> -type
		1.584	0.23691		
19 M	$\alpha_1, 2$	1.580	0.23796	(200)	W
		1.577	0.23892		
20 M	$\alpha_1, 2$	1.422	0.29399	(20.0)	WSe <sub>2</sub> -type
		1.352	0.32494		
21 S	$\alpha_1, 2$	1.350	0.32599	(20.3)	WSe <sub>2</sub> -type
		1.350	0.32622		
22 W	$\alpha_1, 2$	1.308	0.34728	(11.6)	WSe <sub>2</sub> -type
		1.292	0.35584		
23 VS	$\alpha_1, 2$	1.289	0.35775	(112)	W
		1.287	0.35870		
24 W	$\alpha_1, 2$	1.246	0.38263	(20.5)	WSe <sub>2</sub> -type

Table B-2. Commercial-Grade Tungsten  
Diselenide X-ray Powder  
Diffraction Data.

<u>Diffraction Line</u>	<u>Radiation</u>	<u><math>\sin^2 \theta_{\text{obs}}</math></u>	<u>Indices</u>
1	$\alpha$ 1, 2	0.01414	(00.2)
2	$\alpha$ 1, 2	0.07352	(10.0)
3	$\alpha$ 1, 2	0.07706	(10.1)
4	$\alpha$ 1, 2	0.08766	(10.2)
5	$\alpha$ 1, 2	0.10534	(10.3)
6	$\alpha$ 1, 2	0.12730	(00.6)
7	$\alpha$ 1, 2	0.16192	(10.5)
8	$\alpha$ 1, 2	0.20082	(10.6)
9	$\alpha$ 1, 2	0.22056	(11.0)
10	$\alpha$ 1	0.22592	(00.8)
11	$\alpha$ 1	0.23432	(11.2)
12	$\alpha$ 1	0.29360	(20.0)
13	$\alpha$ 1	0.29713	(20.1)
14	$\alpha$ 1	0.29932	(10.8)
15	$\alpha$ 1	0.30772	(20.2)
16	$\alpha$ 1	0.32537	(20.3)
17	$\alpha$ 1	0.34728	(11.6)
18	$\alpha$ 1	0.35300	(00.10)
19	$\alpha$ 1	0.35933	(10.9)
20	$\alpha$ 1	0.38185	(20.5)

Table B-3. Tungsten X-ray Powder Diffraction Data

<u>Diffraction Line</u>	<u>Radiation</u>	<u><math>\sin^2 \theta_{\text{obs}}</math></u>	<u>Indices</u>
1	$\alpha$ 1, 2	0.11880	(110)
2	$\alpha$ 1	0.23762	(200)
3	$\alpha$ 1	0.35637	(211)

APPENDIX C  
INTENSITY CALCULATIONS FOR TUNGSTEN  
AND TUNGSTEN DISelenide

Relative x-ray intensities were calculated with well-known analytical expressions for Lorentz and polarization factors, crystal plane multiplicity, a geometrical factor for the Guinier camera, and the structure factor. Atomic scattering factors were corrected for anomalous dispersion due to characteristic copper x-radiation. Temperature factors were not included in the analysis.

The trial structure used for tungsten diselenide is derived from the isomorphous disulphide of molybdenum. An ideal positional parameter for the Group VIb atoms was used:  $z$  equal to 0.625. Results of the calculations are presented in Table C-1. Agreement is reasonable and there is no indication of preferred-orientation effects due to our sample preparation techniques. Refinement was accomplished by calculation of relative intensities for a selected group of reflections over the  $z$ -parameter interval from 0.610 to 0.640, see Figure C-1. A reasonably good fit to the data appears at 0.620. Statistical treatment of data from this commercial material is not warranted until a more complete chemical characterization is available. Available data indicates that structural differences may occur in samples of tungsten diselenide used by different investigators.

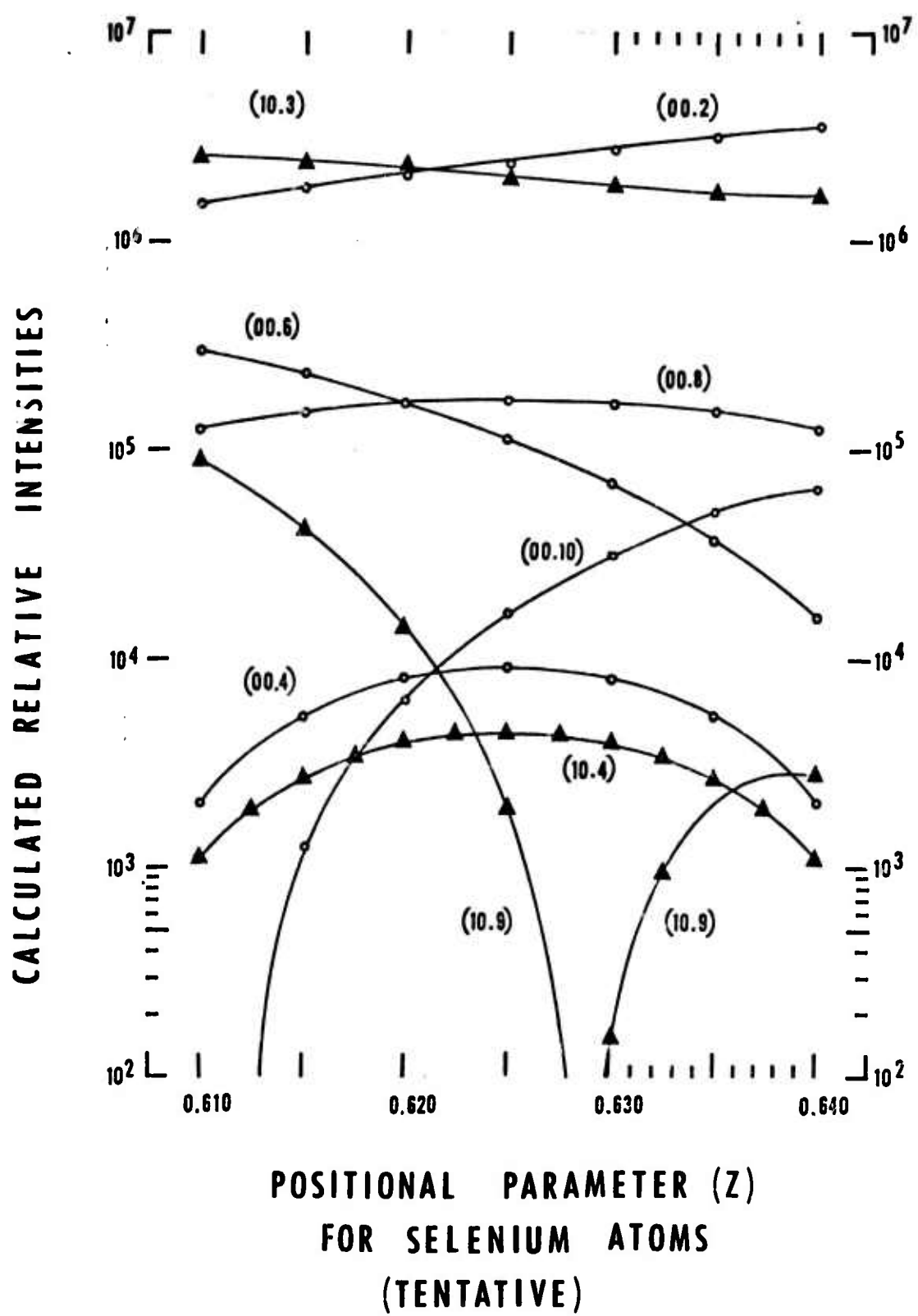


Figure C-1. Calculated relative intensities for selected x-ray reflections from the tungsten diselenide crystal structure.

Table C-1. Calculated relative intensities for tungsten diselenide: molybdenite crystal structure, positional parameter for selenium atoms is 0.625.

<u>X-ray Reflections</u>	<u>X-ray Relative Intensities</u>			
	<u>Observed*</u>	<u>Calculated</u>		
00.2	VS	3.51	06	
00.4	N	8.06	03	
10.0	VS	1.05	06	
10.1	MS	2.33	05	
10.2	MS	4.78	05	
10.3	VS	2.87	06	
00.6	M	1.91	05	
10.4	N	5.02	03	
10.5	VS	1.62	06	
10.6	W	1.59	05	
00.8	M	2.86	05	
11.0	VS	8.56	05	
11.2	S	4.63	05	
10.7	N	5.75	05	
11.4	N	1.00	04	
10.8	N	3.02	05	
20.0	M	1.51	05	
20.1	VW	4.64	04	
20.2	VW	8.33	04	
20.3	VS	5.44	05	
00.10	VVW	4.69	05	
11.6	S	2.81	05	
10.9	VVW	1.25	03	

\*Observed intensity symbols: VS = very strong, S = strong, MS = medium strong, M = medium, W = weak, VW = very weak, VVW = barely detectable, and N = not observed.

Table C-2. Calculated relative intensities for body-centered cubic tungsten.

<u>X-ray Reflections</u>	<u>X-ray Relative Intensities</u>		
	<u>Observed</u> <sup>*</sup>	<u>Calculated</u>	
110	VS	1.02	06
200	M	0.16	06
112	VS	0.44	06

\* Observed intensity symbols: VS = very strong, and M = medium

## APPENDIX D

### SURFACE METALLOGRAPHY AND ENERGY DISPERITIVE X-RAY FLUORESCENCE ANALYSIS DATA

#### LIST OF FIGURES

<u>Figure</u>		<u>Page</u>
D-1	SEM photograph of a commercial grade of tungsten diselenide. Hexagonal plates of tungsten diselenide and a randomly-oriented unidentified phase on the surface of the tungsten diselenide. 1000X . . . . .	F-61
D-2	SEM photograph of an area selected from the field of view shown in Figure D-1. 5000X . . . . .	F-61
D-3	SEM photograph of a commercial grade of tungsten diselenide. Hexagonal plates of tungsten diselenide with a randomly-oriented unidentified surface phase, and unidentified material with fibrous texture. 900X . . . . .	F-62
D-4	SEM photograph of an area selected from the field of view shown in Figure D-3. 4500X. . . . .	F-62
D-5	Typical SEM EDAX-mode data for the commercial grade of tungsten diselenide shown in Figures D-1 through D-4: detection of selenium and tungsten. . . . .	F-63
D-6	SEM photograph of Westinghouse compact material. The largest particles are probably tungsten diselenide and the smaller particles a mixture of metallic tungsten and residual phases. 900X . . . . .	F-63
D-7	SEM photograph of an area selected from the field of view shown in Figure D-6. 4500X . . . . .	F-64
D-8	Typical SEM EDAX-mode data for the Westinghouse compact material shown in Figures D-6 and D-7: detection of gallium, indium, selenium and tungsten . . . . .	F-64
D-9	SEM photograph of the furnace-cooled 60Ga40Se alloy. Constituents present are: (a) gallium selenide with defined morphology, (b) ribbons and/or whiskers of gallium selenide, and (c) globular particles of gallium metal. 450X. . . . .	F-65
D-10	SEM photograph of an area selected from the field of view shown in Figure D-9. 1800X . . . . .	F-65

FIGURES (Continued)

<u>Figure</u>		<u>Page</u>
D-11	SEM photograph of the furnace-cooled 60Fa40Se alloy. The constituent present is gallium selenide. 960X. . . . .	F-66
D-12	SEM photograph of an area selected from the field of view shown in Figure D-11. The morphology of massive (bulk) gallium selenide. 480X. . . . .	F-66
D-13	SEM photograph of the furcace-cooled 60Fa40Se alloy. Plates of gallium selenide can be seen in the center of the field of view. Globular particles of metallic gallium appear in the matrix. 200X . . . . .	F-67
D-14	SEM photograph of the furnace-cooled 60Ga40Se alloy. Plates of gallium selenide. 960X . . . . .	F-67
D-15	SEM EDAX-mode data obtained from the furnace-cooled 60Ga40Se alloy. Results are typical of data from massive bulk material, plates, and ribbons and/or whickers: detection of gallium and selenium . . . . .	F-68
D-16	SEM EDAX-mode obtained from the furnace-cooled 60Ga40Se alloy. Results are typical of analysis from the globular particles: detection of gallium . . . . .	F-68
D-17	SEM photograph of the furnace-cooled 25Ga25In50Se alloy. Primary crystals and matrix formed by residual liquid during solidification. 20X . . . . .	F-69
D-18	SEM photograph of an area selected from the field of view shown in Figure D-17. 100X . . . . .	F-69
D-19	SEM EDAX-mode data obtained from the furnace-cooled 25Ga25In50Se alloy. Results are typical of mixtures of primary crystals and matrix: detection of gallium, indium and selenium . . . . .	F-70
D-20	SEM photograph of alloy vapor deposited on the wall of the quartz ampoule during preparation of the 25Ga25In50Se alloy. Nodules have highly reflective surfaces. 180X . . . . .	F-70
D-21	SEM photograph of an area selected from the field of view shown in Figure D-20. Morphology of ternary alloy plates. 900X . . . . .	F-71
D-22	SEM EDAX-mode data from the ternary alloy shown in Figures D-20 and D-21: detection of gallium, indium and selenium . . . . .	F-71

FIGURES (Continued)

Figure		Page
D-23	SEM photograph of the furnace-cooled 50In50Se alloy. Primary crystals in bulk material. 20X . . . . .	F- 72
D-24	SEM photograph of an area selected from the field of view shown in Figure D-23. Primary crystals. 200X . . . . .	F- 72
D-25	SEM photograph of the furnace-cooled 50In50Se alloy. Primary crystals in bulk materials. 52X . . . . .	F- 73
D-26	SEM photograph of an area selected from the field of view shown in Figure D-25. Morphology of primary crystals. 520X . . . . .	F- 73
D-27	SEM photograph of an area selected from the field of view shown in Figure D-26. Morphology of primary crystals. 2100X . . . . .	F- 74
D-28	SEM EDAX-mode data from bulk of furnace-cooled 50In50Se alloy: detection of indium and selenium . . . . .	F- 74

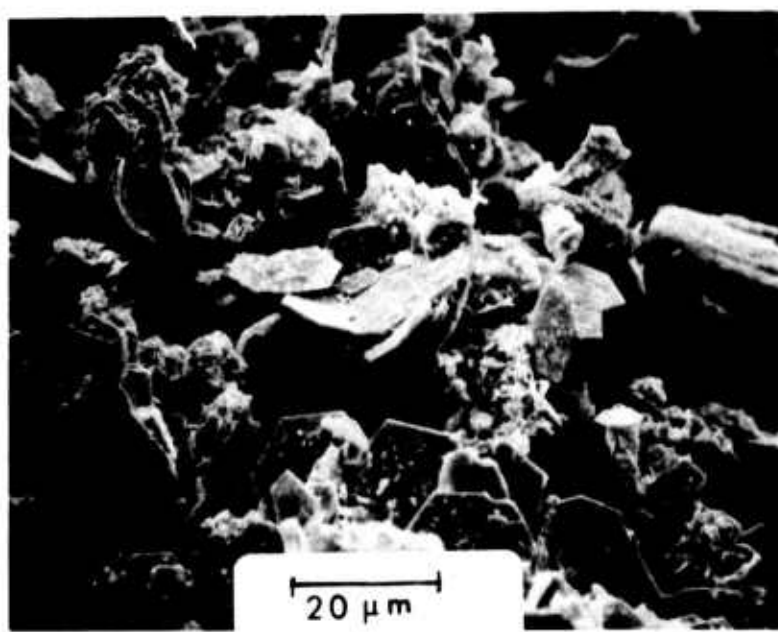


Figure D-1. SEM photograph of a commercial grade of tungsten diselenide. Hexagonal plates of tungsten diselenide and a randomly-oriented unidentified phase on the surface of the tungsten diselenide. 1000X.

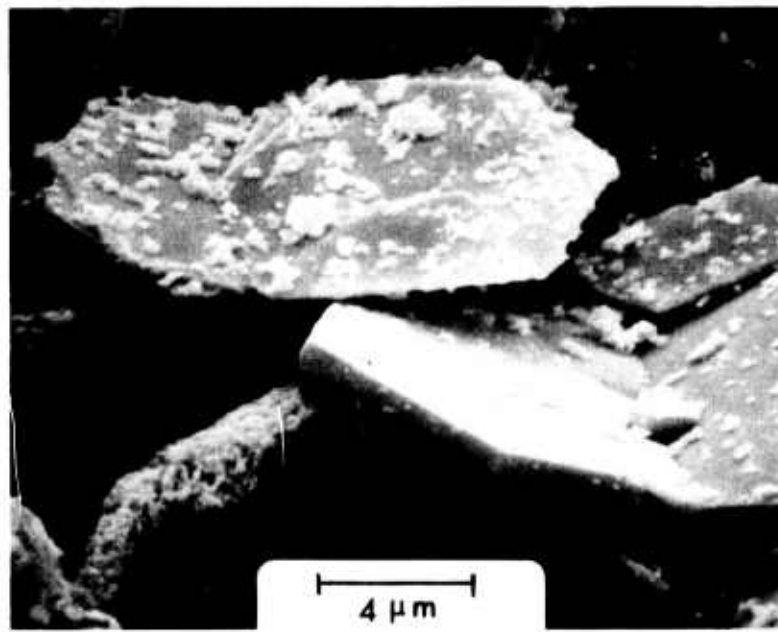


Figure D-2. SEM photograph of an area selected from the field of view shown in Figure D-1. 5000X.

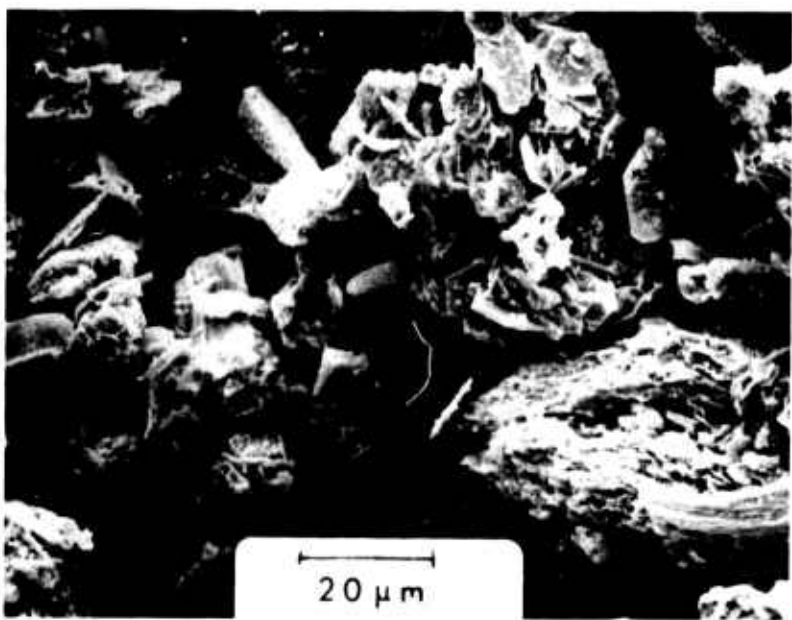


Figure D-3. SEM photograph of a commercial grade of tungsten diselenide. Hexagonal plates of tungsten diselenide with a randomly-oriented unidentified surface phase, and unidentified material with fiberous texture. 900X.

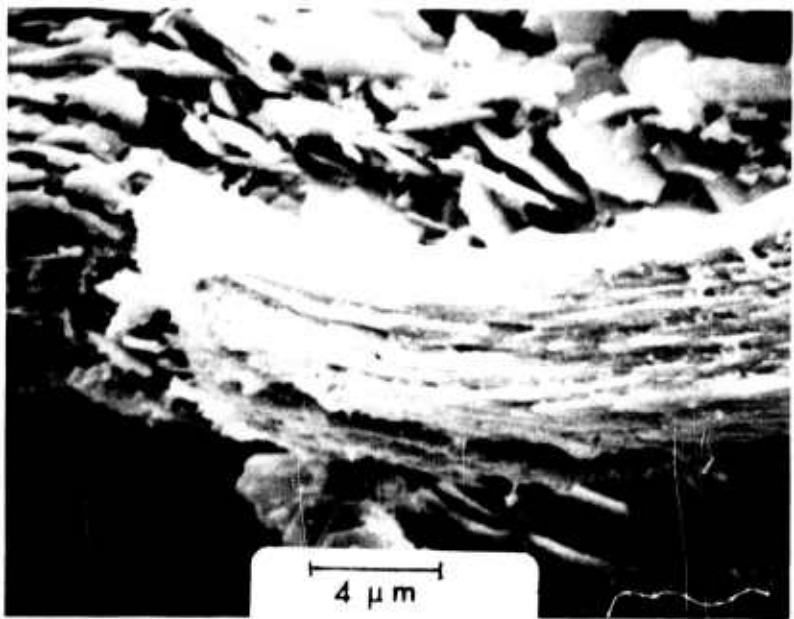


Figure D-4. SEM photograph of an area selected from the field of view shown in Figure D-3. 4500X.

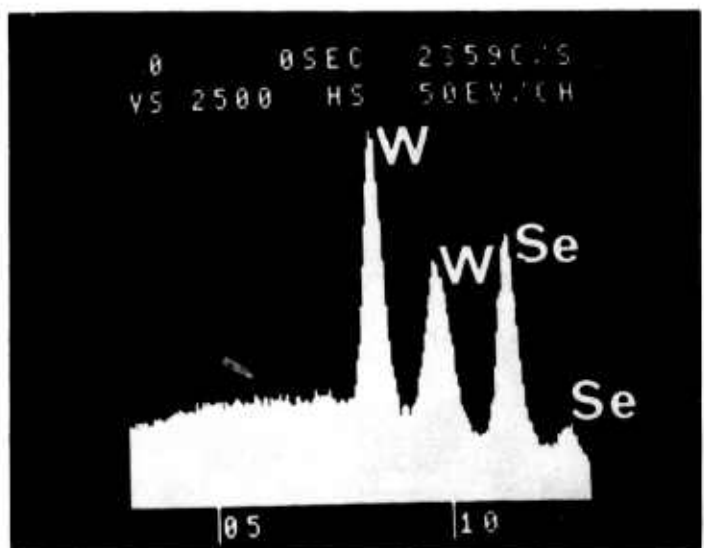


Figure D-5. Typical SEM EDAX-mode data for the commercial grade of tungsten diselenide shown in Figures D-2 through D-4: detection of selenium and tungsten.

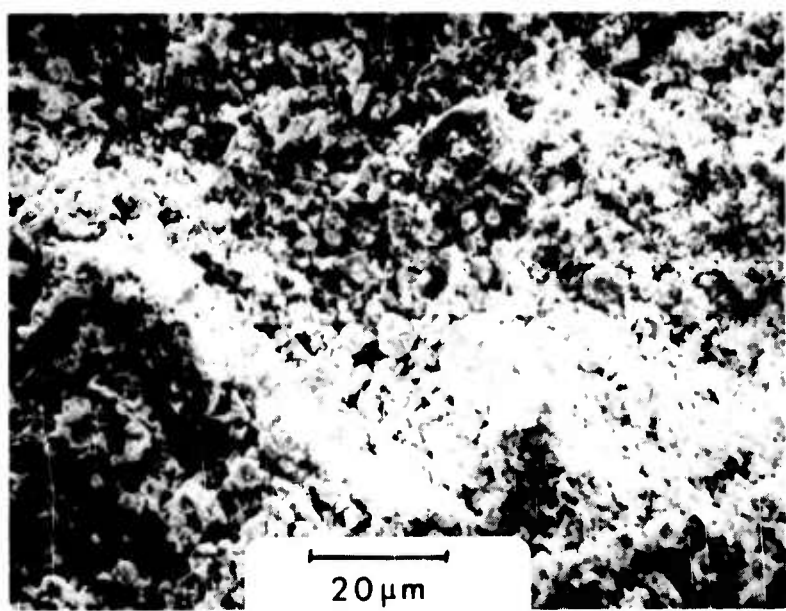


Figure D-6. SEM photograph of Westinghouse compact material. The largest particles are probably tungsten diselenide and the smaller particles a mixture of metallic tungsten and residual phases. 900X.

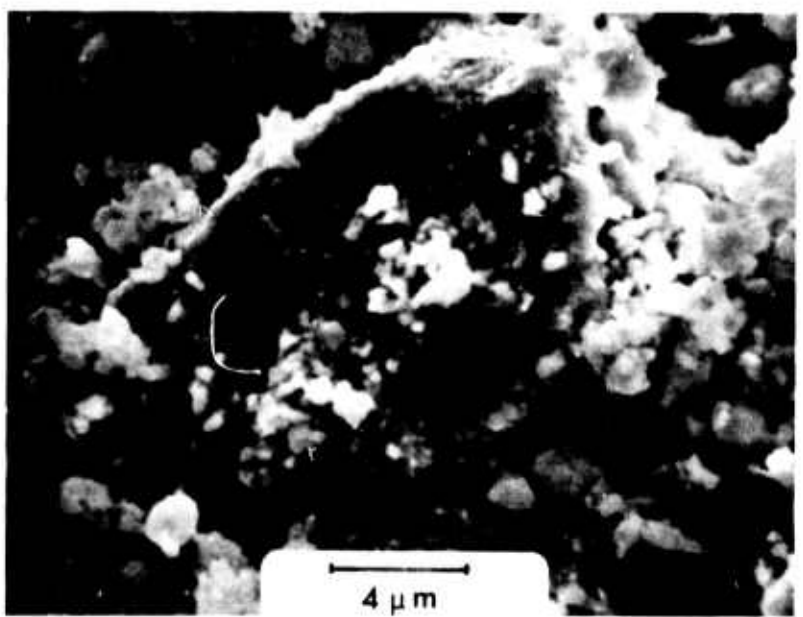


Figure D-7. SEM photograph of an area selected from the field of view shown in Figure D-6. 4500X.

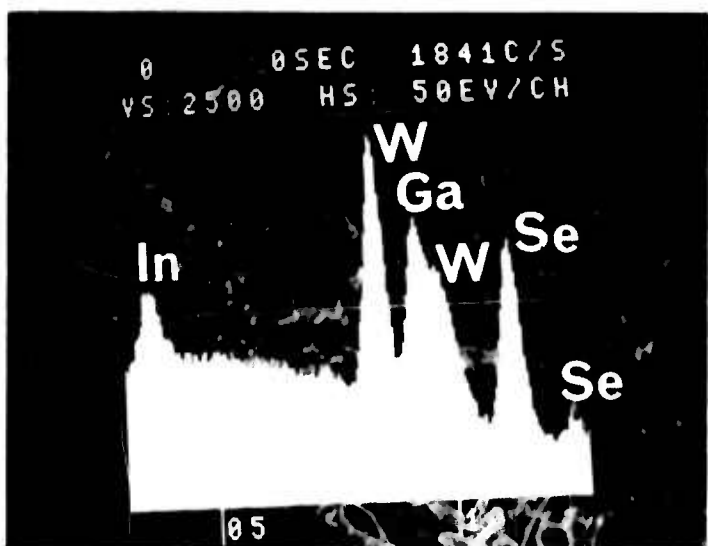


Figure D-8. Typical SEM EDAX-mode data for the Westinghouse compact material shown in Figures D-6 through D-7: detection of gallium, indium, selenium and tungsten.

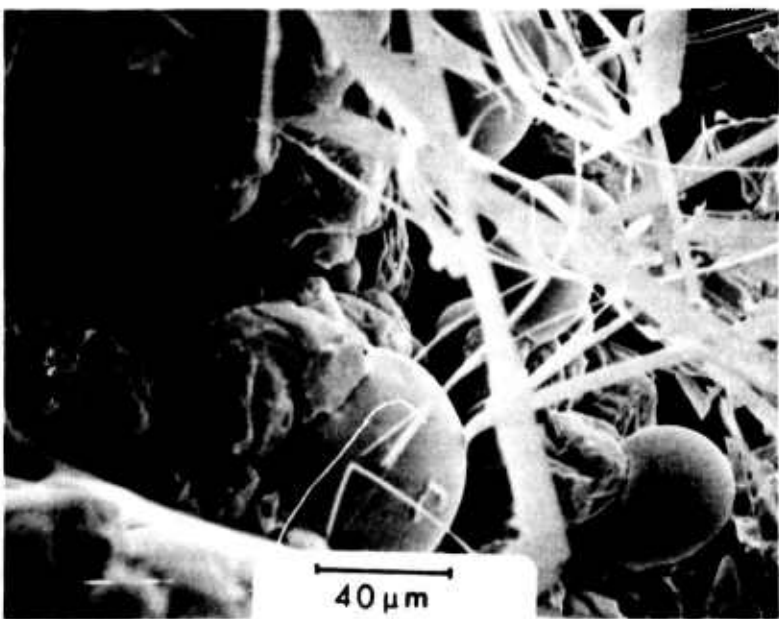


Figure D 9. SEM photograph of the furnace-cooled 60Ga40Se alloy. Constituents present are: (a) gallium selenide with defined morphology, (b) ribbons and/or whiskers of gallium selenide, and (c) globular particles of gallium metal. 450X.

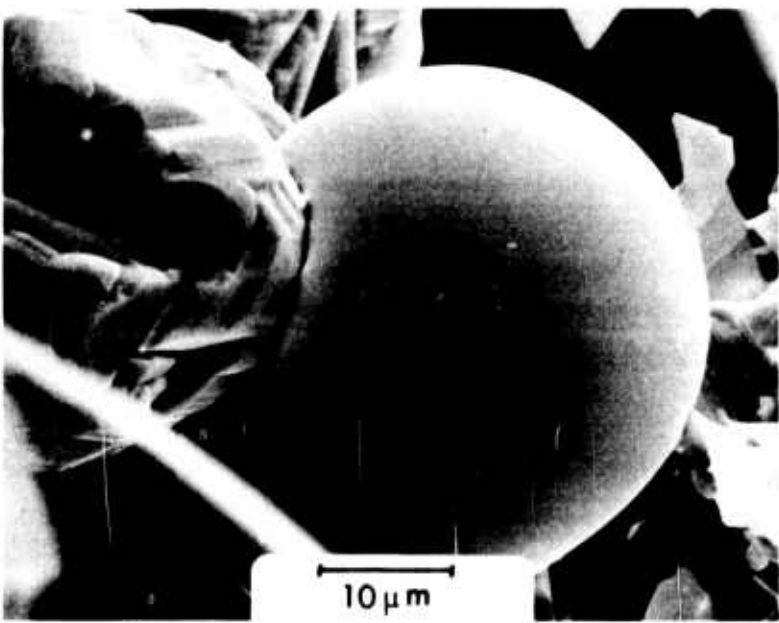


Figure D-10. SEM photograph of an area selected from the field of view shown in Figure D-9. 1800X.

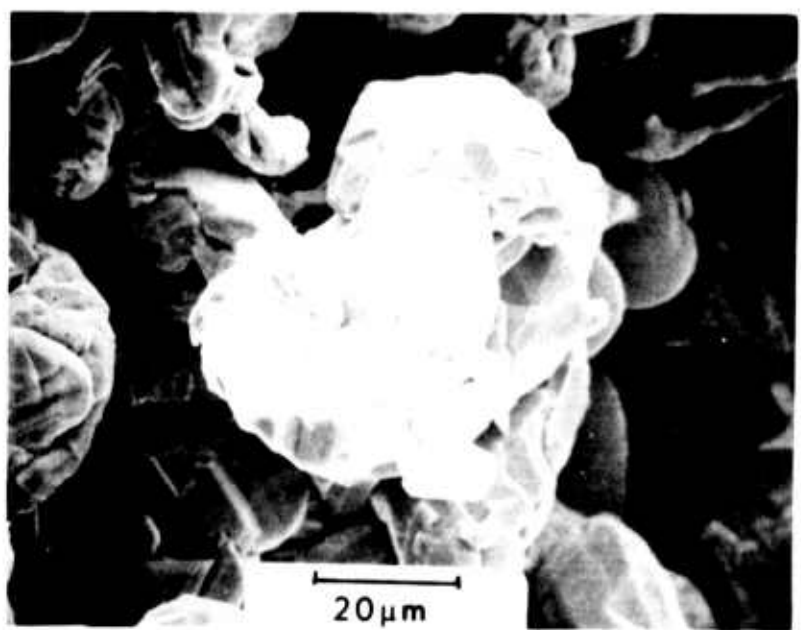


Figure D-11. SEM photograph of the furnace-cooled 60Ga40Se alloy. The constituent present is gallium selenide. 960X.

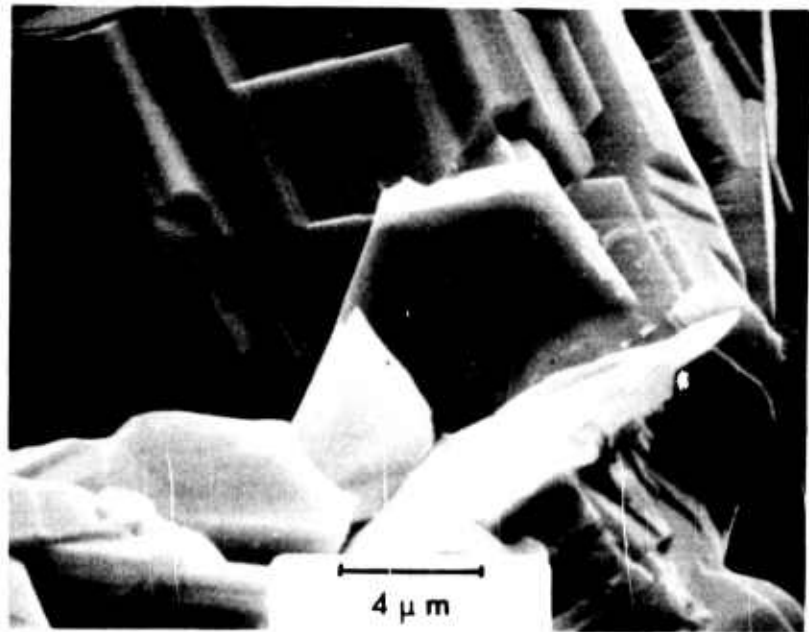


Figure D-12. SEM photograph of an area selected from the field of view shown in Figure D-11. The morphology of massive (bulk) gallium selenide. 4800X.

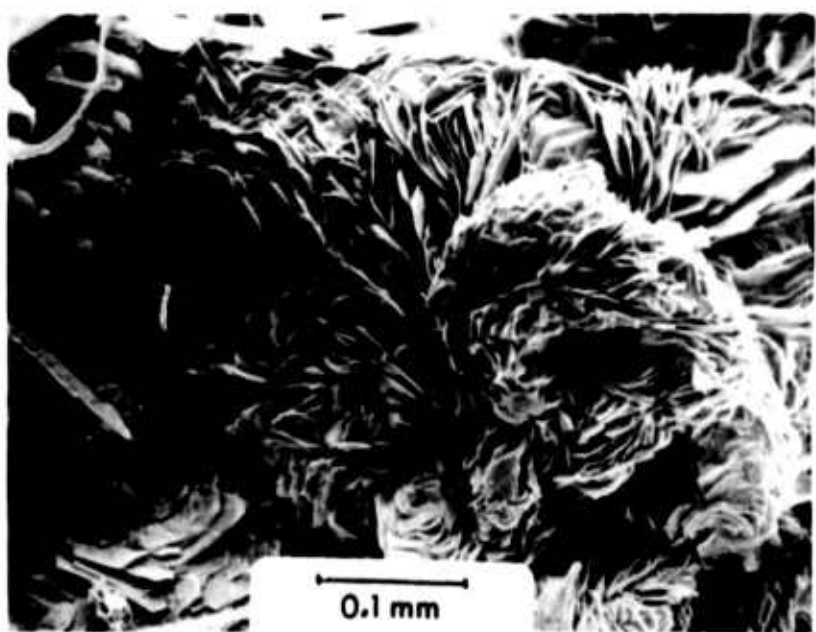


Figure D-13. SEM photograph of the furnace-cooled 60Ga40Se alloy. Plates of gallium selenide can be seen in the center of the field of view. Globular particles of metallic gallium appear in the matrix. 200X.

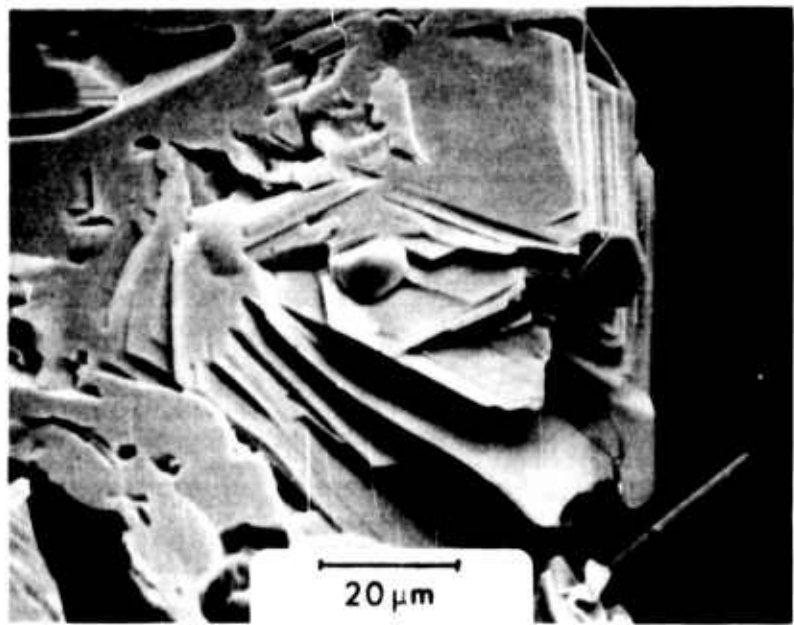


Figure D-14. SEM photograph of the furnace-cooled 60Ga40Se alloy. Plates of gallium selenide. 960X.

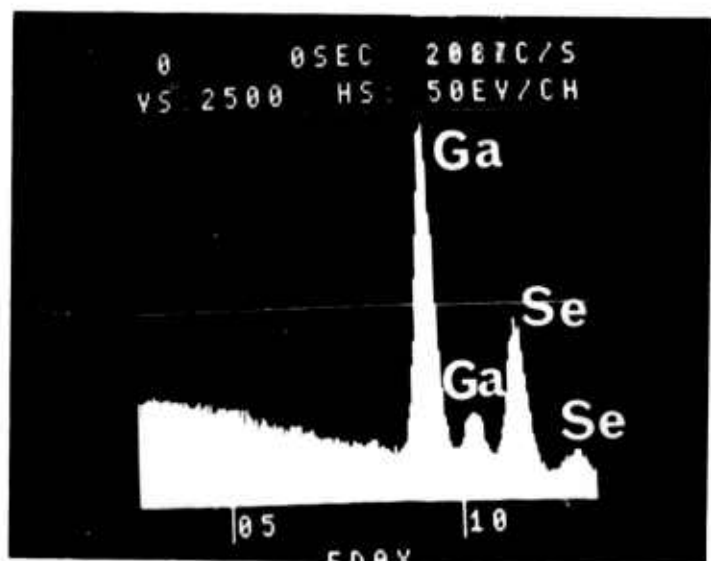


Figure D-15. SEM EDAX-mode data obtained from the furnace-cooled 60Ga40Se alloy. Results are typical of data from massive bulk material, plates, and ribbons and/or whiskers: detection of gallium and selenium.

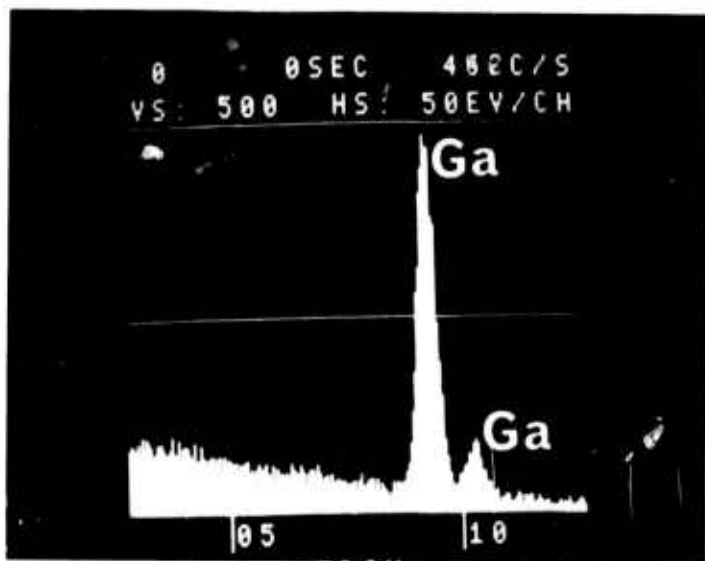


Figure D-16. SEM EDAX-mode data obtained from the furnace-cooled 60Ga40Se alloy. Results are typical of analysis from the globular particles: detection of gallium.

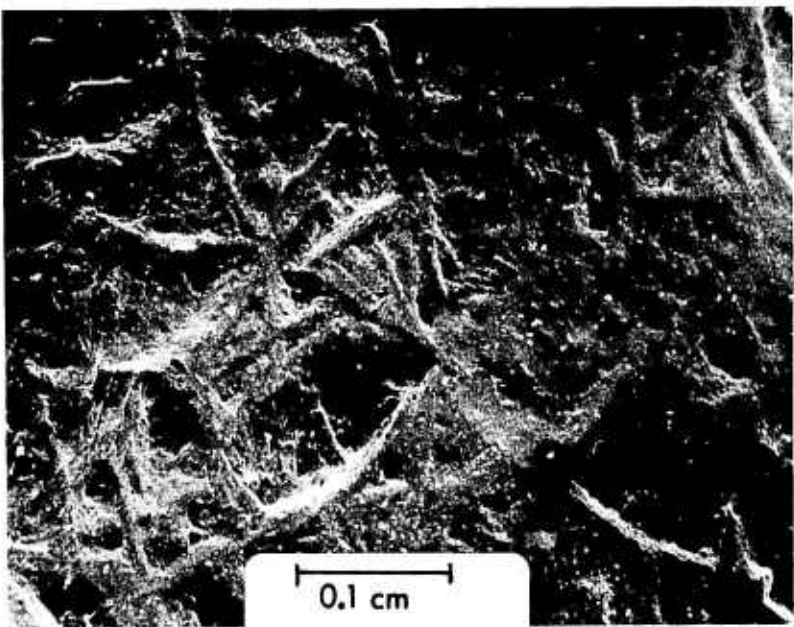


Figure D-17. SEM photograph of the furnace-cooled 25Ga25In50Se alloy. Primary crystals and matrix formed by residual liquid during solidification. 20X.

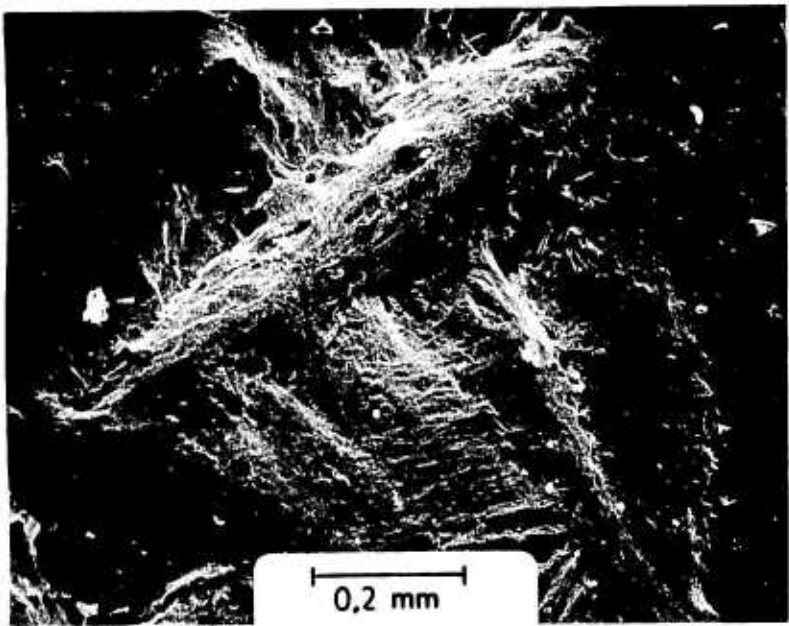


Figure D-18. SEM photograph of an area selected from the field of view shown in Figure D-17. 100X.

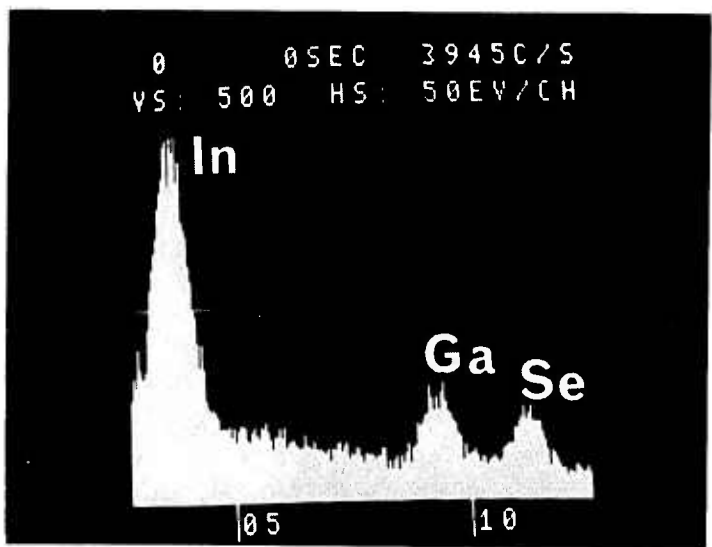


Figure D-19. SEM EDAX-mode data obtained from the furnace-cooled 25Ga25In50Se alloy. Results are typical of mixtures of primary crystals and matrix: detection of gallium, indium and selenium.

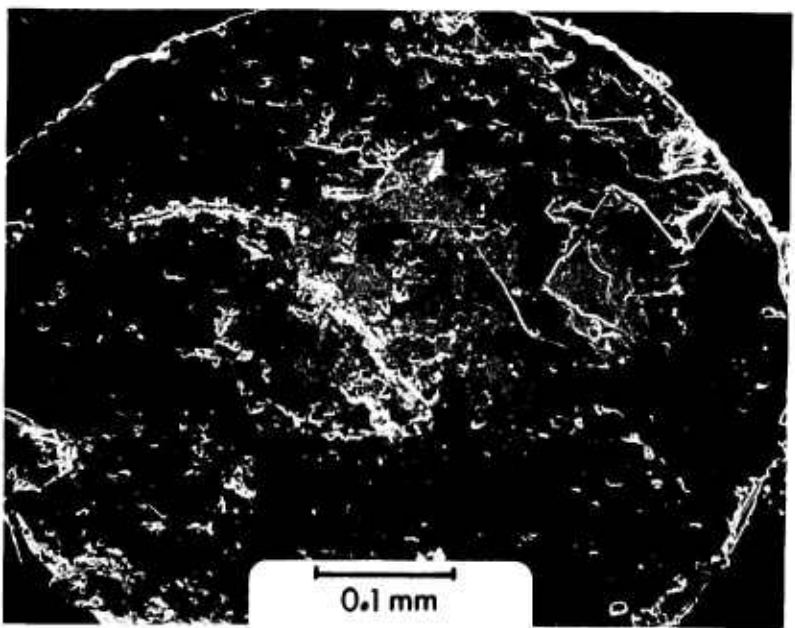


Figure D-20. SEM photograph of alloy vapor deposited on the wall of the quartz ampoule during preparation of the 25Ga25In50Se alloy. Nodules have highly reflective surfaces. 180X.

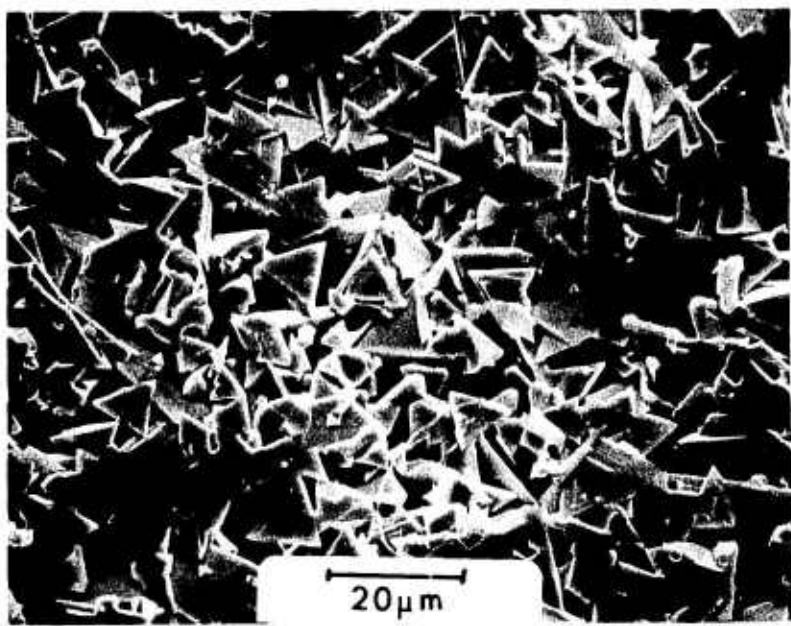


Figure D-21. SEM photograph of an area selected from the field of view shown in Figure D-20. Morphology of ternary alloy plates. 900X.

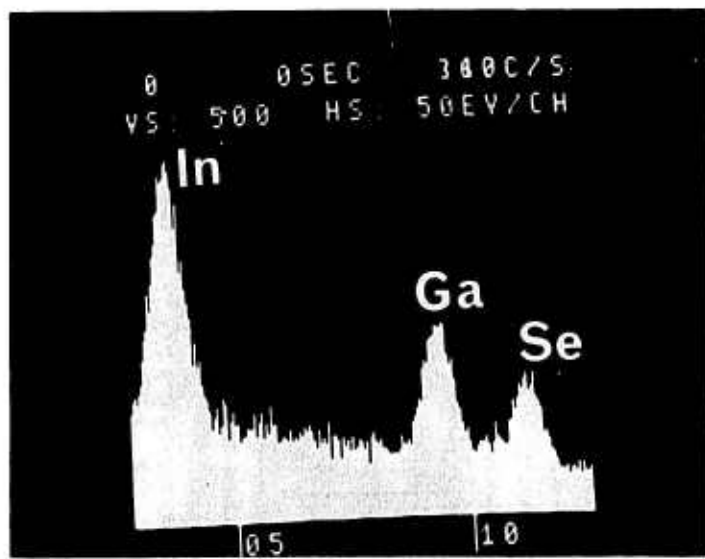


Figure D-22. SEM EDAX-mode data from the ternary alloy shown in Figures D-20 through D-21: detection of gallium, indium and selenium.

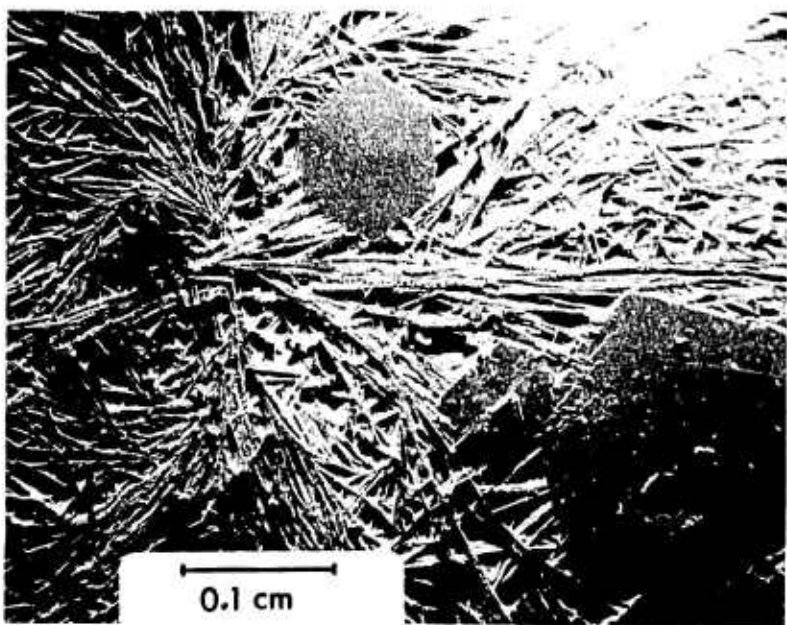


Figure D-23. SEM photograph of the furnace-cooled 50In50Se alloy. Primary crystals in bulk material. 20X.

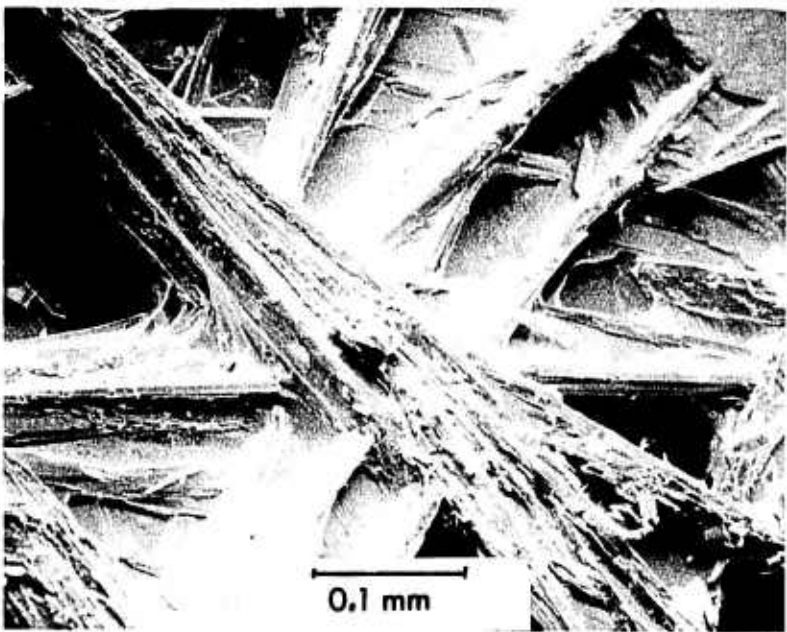


Figure D-24. SEM photograph of an area selected from the field of view shown in Figure D-23. Primary crystals. 200X.

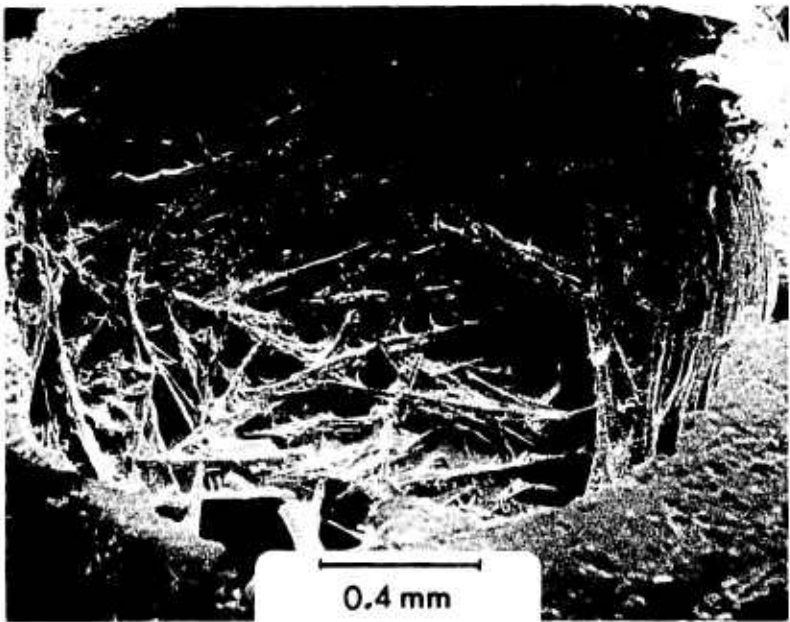


Figure D-25. SEM photograph of the furnace-cooled 50In50Se alloy. Primary crystals in bulk material. 52X.

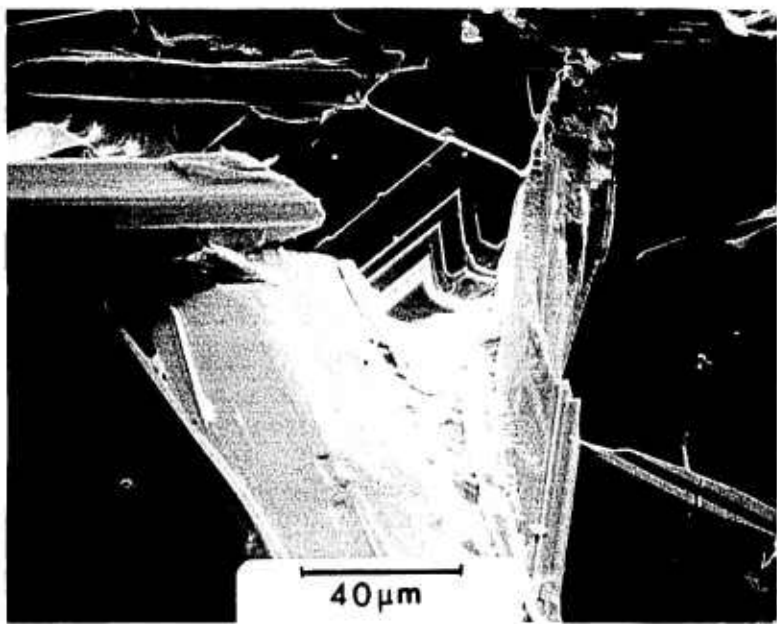


Figure D-26. SEM photograph of an area selected from the field of view shown in Figure D-25. Morphology of primary crystals. 520X.

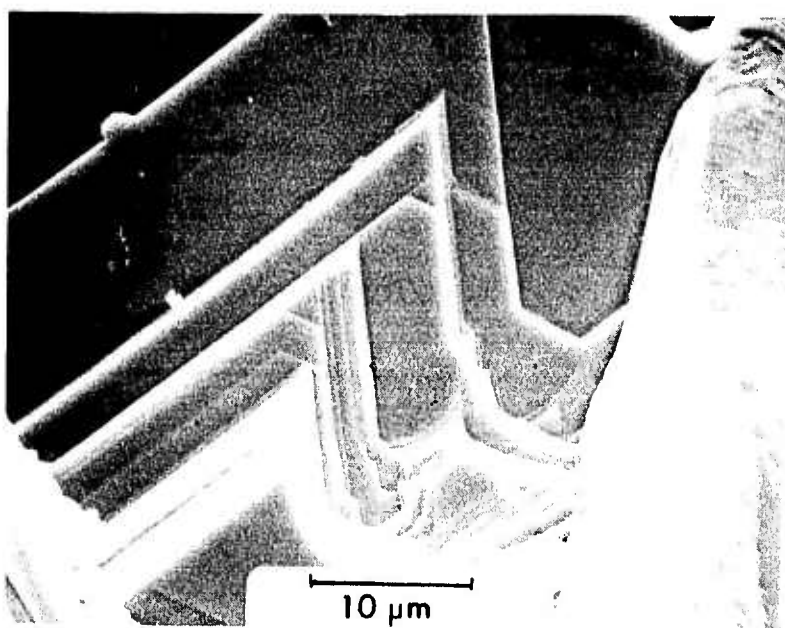


Figure D-27. SEM photograph of an area selected from the field of view shown in Figure D-26. Morphology of primary crystals. 2100X.

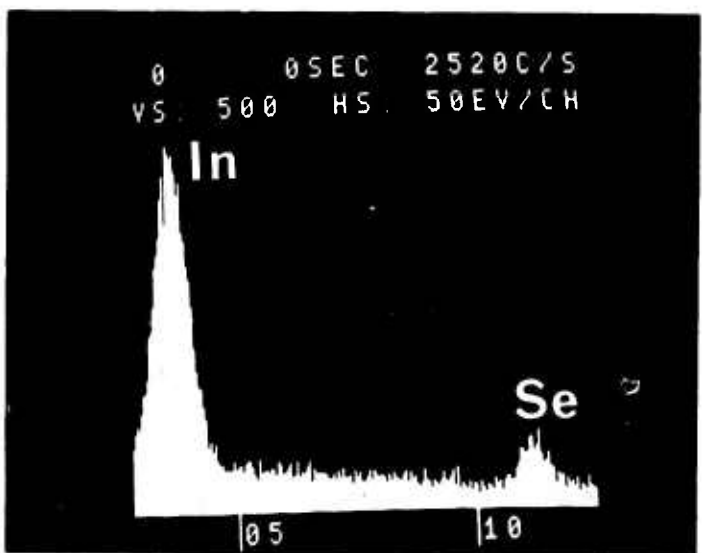


Figure D-28. SEM EDAX-mode data from bulk of furnace-cooled 50In50Se alloy: detection of indium and selenium.

## APPENDIX G

CHRISTY, R. I. TO GARDOS, M. N.,  
"SOLID LUBRICANT SPUTTERING PROGRESS AND  
PLANS FOR DARPA/HUGHES S. L. R. E. B. PROGRAM,"  
Hughes Interdepartmental Correspondence 4142.20/721,  
January 22, 1980.



TO: M. N. Gardos CC: F. A. Glassow DATE: January 22, 1980  
ORG: H. R. Ludwig REF. 4142.20/721  
W. L. Townsend  
  
SUBJECT: Solid Lubricant Sputtering FROM: R. I. Christy  
Progress and Plans for DARPA/  
Hughes S.L.R.E.B. Program ORG.  
  
BLDG. 366 MAIL STA. V320  
LOC. SC EXT. 84369

#### • Sputtered MoS<sub>2</sub> Parameter Study Results

An initial previously reported<sup>1</sup> study of sputtering parameter effects on MoS<sub>2</sub> wear life was extended to include new parameters. The previous work investigated chamber pressure, target distance, target power, and sputter etch duration on the substrate. The more recent work explored substrate geometry with respect to the target, substrate bias, sliding vs. rolling wear life, and air vs. N<sub>2</sub> atmosphere wear life. The recent results are shown in Figures 1 to 5.

A general comparison of various coatings is shown in Fig. 1, demonstrating the improvements in the sputtered MoS<sub>2</sub>. It is interesting to note that the improved RF sputtered MoS<sub>2</sub> at 16,000 Å outperformed a bonded solid Lubeco 905 coating that was ten times thicker. Each data point is an average of three tests, for figures 1 to 5. In Figure 2, both sliding and rolling wear specimens were tested in both air and nitrogen. In both cases, there is a dramatic decrease in wear life in air, indicating nitrogen purging is necessary for improved life during air operation. A sliding wear test for the bonded Lubeco 905 coating was also done for comparison, as shown in Fig. 3. Again there was a significant reduction in wear life in air, but not as dramatic as for the sputtered coatings. An additional test with an initial 1/2 hr. purge prior to rotation was done to evaluate the case of a purge prior to operation where a purge could not be continued during operation, and this resulted in a small increase in wear life over the air data in Fig. 3.

Various substrate bias potentials were evaluated as shown in Fig. 4. In all cases, grounding the substrate resulted in improved wear life. Negative bias significantly reduces wear life. In the floating case, the substrate is undoubtedly negative each half cycle due to an induced rf voltage. Other workers have reported that negative bias results in molybdenum rich coatings, and future work here will verify this.

The most dramatic effect on wear life thus far has been substrate position as shown in fig. 5. There is a significant reduction in wear life for substrates positioned perpendicular to the target during coating. More work will be done to determine other geometry effects, and to analyze the mechanisms causing these large differences in wear life.

- Recent Coating Progress

Balls, rings, and retainers for three R-3 size gyro bearings have been RF sputtered with  $\text{MoS}_2$  for evaluation. A number of flat and spherical sliding friction specimens, (some TiN coated) were RF sputtered with  $\text{MoS}_2$  for friction testing.

- Future Plans for  $\text{MoS}_2$  Parameter Study

The initial work done relating  $\text{MoS}_2$  coating parameters to wear life used the pragmatic approach of comparing wear life directly to coating parameters, without considering the mechanisms causing the changes in coating life. All wear testing was done initially on sliding wear test samples. Because of the large variations in wear life that were measured, it is now important to understand the mechanisms in order to assure optimum coatings in the future. It is also important to verify that the optimum coating for sliding contact is also optimum for the rolling contact case. Therefore, all future investigations will include both sliding and rolling wear samples, along with test samples for both  $\text{MoS}_2$  structure and stoichiometry. A number of previous tests will be repeated with grounded substrates. The parameters listed below will be investigated as a function of sliding and rolling wear life, coating structure, and stoichiometry, and with substrates grounded.

1. Substrate position parallel or perpendicular to target.
2. Motion parallel to target in and out of flux.
3. Motion approaching and leaving target.
4. Circular motion in and out of flux.
5. Chamber pressure 10 microns, 20 microns, 30 microns
6. Target distance 1 inch, 2 inches, 3 inches
7. Sputter etch voltage 1000 volts, 2000 volts, 3500 volts
8. Sputter etch duration 0 min., 5 min., 15 min.
9. Wattage on 10" dia. target 500 watts, 1000 watts, 1500 watts

Initially, only one variable will be evaluated for each test. After initial results are tabulated, combinations of more than one variable will be selected for further evaluation. As time permits, portions of the above matrix may be repeated with a newly acquired magnetron sputtering target. The optimum coatings will be applied to test bearings, and other specimens according to program requirements.

/tss

R. I. Christy

- ① RF Sputtered  $\text{MoS}_2$  Parameter Effects on Wear Life. R.I. Christy and H.R. Ludwig. Thin Solid Films Vol. 64, No. 2 pp 223-229.

# COATING METHODS COMPARED

HUGHES

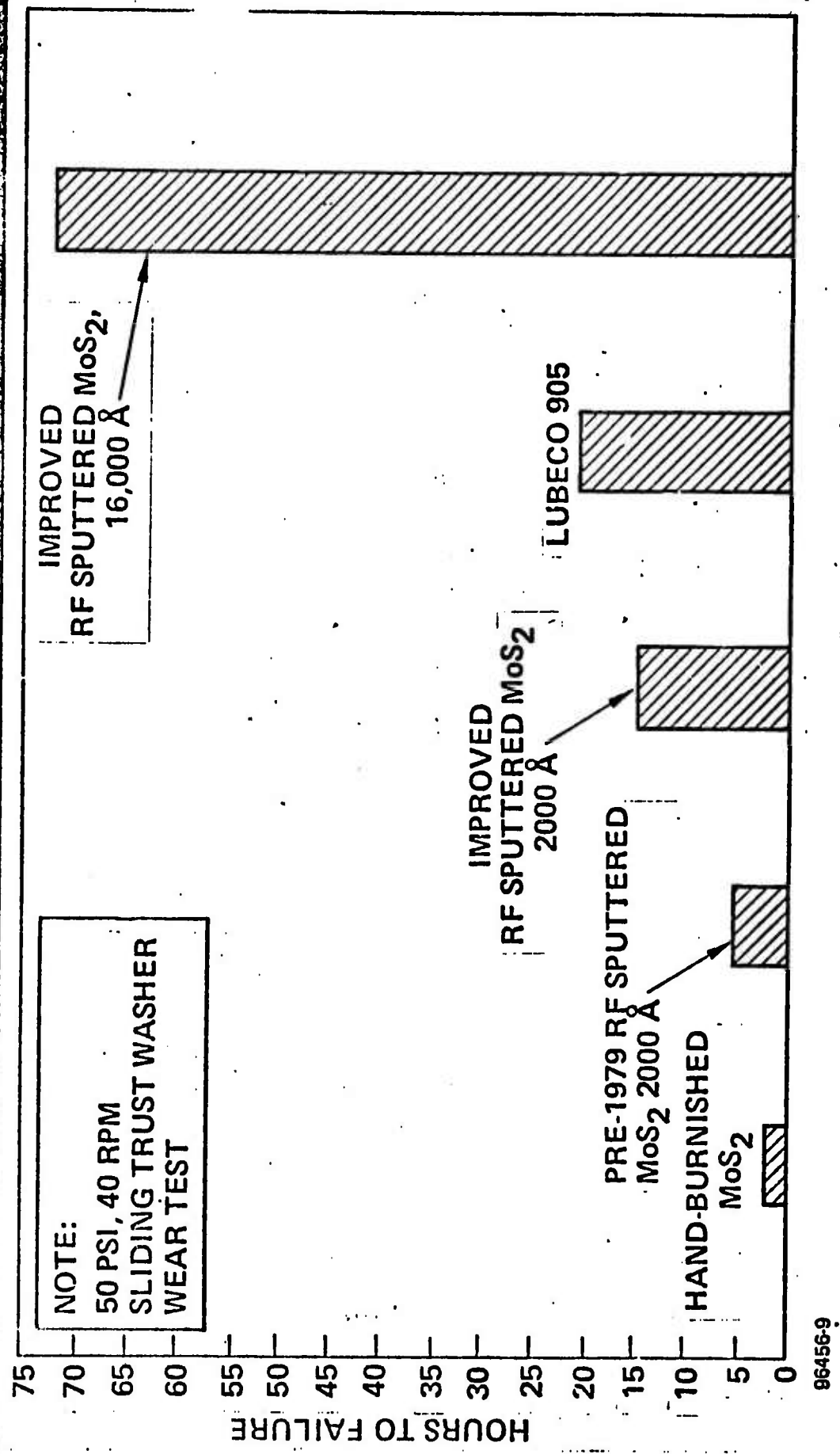


FIGURE 1

**RF SPUTTERED MoS<sub>2</sub> AIR VS N<sub>2</sub> PERFORMANCE  
(2000 Å MoS<sub>2</sub>)**

**HUGHES**

**SLIDING WASHER  
50 PSI (10 LB LOAD), 40 RPM**

**ROLLING THRUST BEARING  
100 LB LOAD, 700 RPM**

**12**

**10**

**8**

**6**

**4**

**2**

**0**

**HOOURS TO FAILURE**

**G-4**

**96456-3**

**N<sub>2</sub>**

**AIR**

**N<sub>2</sub>**

**AIR**

**FIGURE 2**

# LUBE<sup>CO</sup> 905 AIR VS N<sub>2</sub> PERFORMANCE

HUGHES

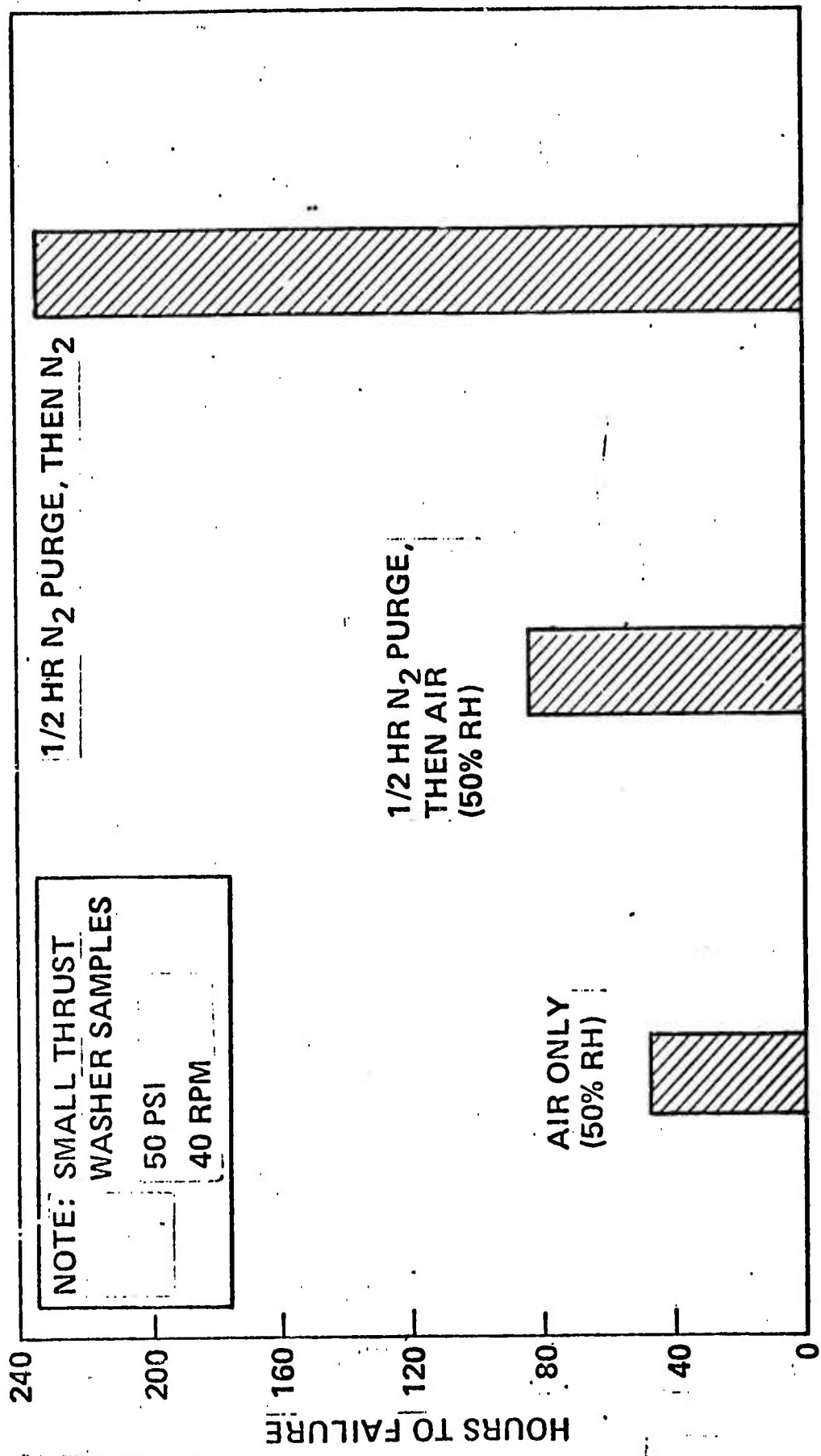


FIGURE 3

HUGHES

RF SPUTTERED  
 $\text{MoS}_2$  GROUNDED  
VS  
FLOATING  
BIAS PERFORMANCE

THRUST WASHER SLIDING SAMPLES

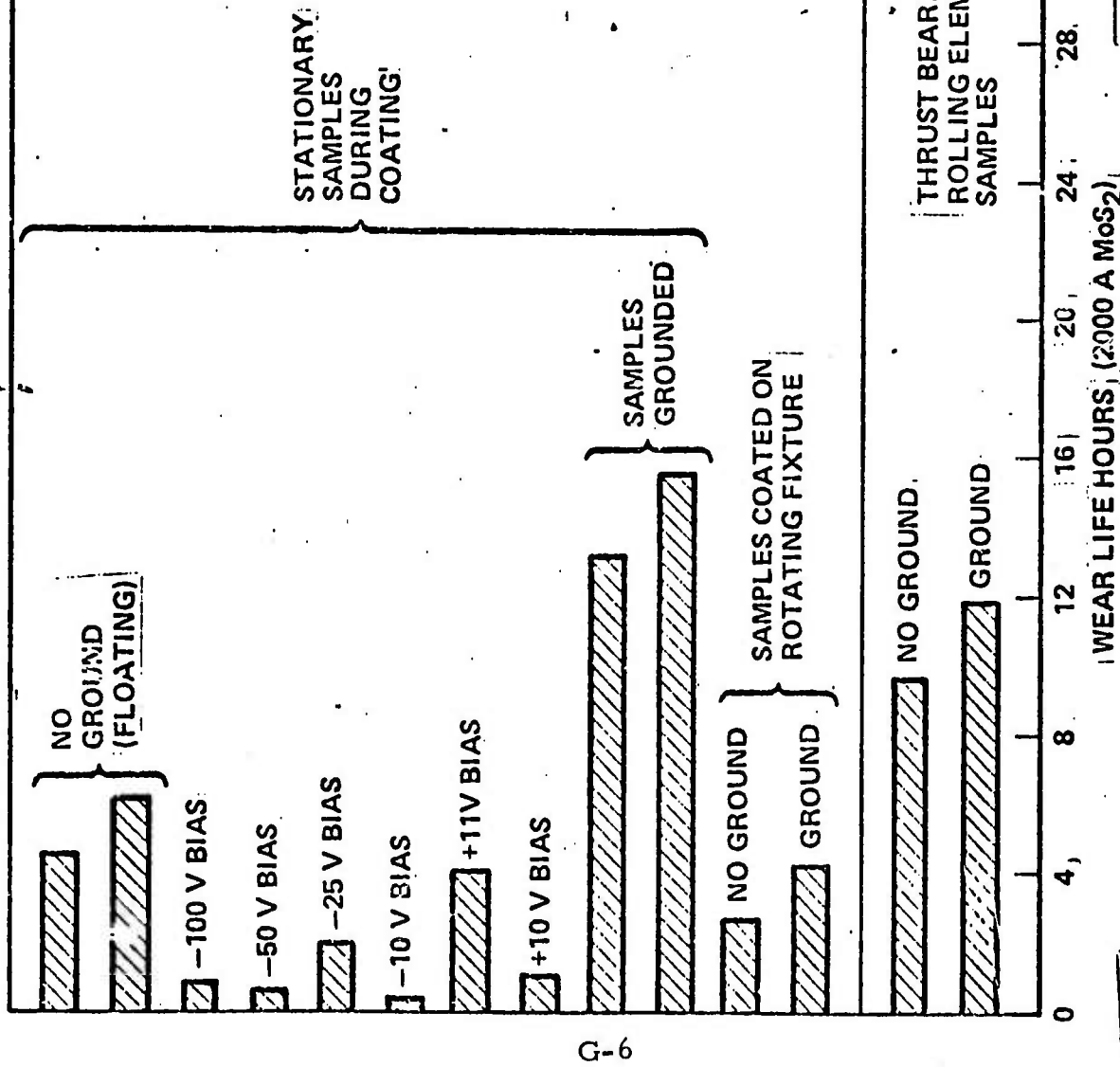


FIGURE 4

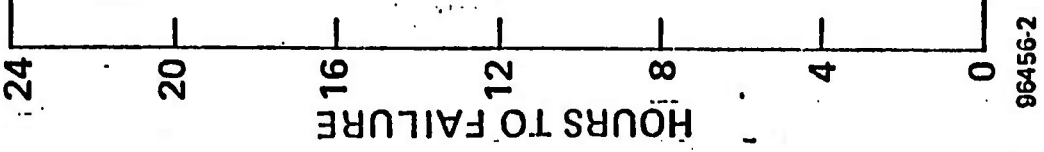
96456-4

# RF SPUTTERED MoS<sub>2</sub> PERFORMANCE VS SAMPLE POSITIONING

HUGHES

24

NOTE: 20000 Å MoS<sub>2</sub>  
SLIDING SAMPLE  
50 PSI  
40 RPM



G-7

96456-2

FIGURE 5

## APPENDIX H

GARDOS, M. N., "THEORY AND PRACTICE OF SELF-LUBRICATED,  
OSCILLATORY BEARING OPERATION FOR HIGH VACUUM  
APPLICATIONS - PART I; SELECTION OF THE SELF-  
LUBRICATING COMPOSITE RETAINER MATERIAL,"  
paper accepted for presentation and publication at the  
ASME-ASLE Int. Conf.; Aug. 18-21, 1980,  
St. Francis Hotel, San Francisco, California

Theory and Practice of Self - Lubricated, Oscillatory  
Bearing Operation for High Vacuum Applications -  
Part I; Selection of the Self-Lubricating  
Composite Retainer Material

M. N. Gardos (ASLE)  
Hughes Aircraft Company, Culver City, CA.

Paper to be presented at the ASME - ASLE International Conference,  
August 18-21, 1980, St. Francis Hotel, San Francisco, CA.

## ABSTRACT

A seven year, interdisciplinary effort was recently completed successfully in developing self-lubricated bearings capable of continuous oscillatory motion for the equivalent of 5+ years in high vacuum, while maintaining arc second alignment accuracy of precision gimbal pointing mechanisms.

This paper, the first of a two-part series, describes the selection method for the PTFE-based, polymeric self-lubricating composite, which was eventually used as the lubricative retainer. The method consisted of statistical matrices of oscillatory sliding and rolling element friction and wear tests completed with commercially available and special test apparatus. Regression analysis of the data led to parametric wear equations. These wear equations, revealing quantitative wear behavior differences between two seemingly similar composites, coupled with extensive analysis of the worn bearing surfaces helped uncover the fundamental causes of these differences and clarify the parametric influences on wear and friction. The resulting ability to predict composite wear accurately as non-linear functions of load, speed and time and as a function of atmosphere offers the first promising, semiempirical approach to accelerated testing of self-lubricated bearings, as indicated by the bearing test results of the second paper of this series.

## INTRODUCTION

Solid lubrication of moving mechanical assemblies (MMA-s) for space application is often preferred in place of liquid lubrication, especially when contamination of nearby spacecraft optical and thermal control surfaces by condensation or migration is anticipated. Weight and cost savings provided by solid lubricants are also taken into account, since labyrinth sealing, barrier coat application, careful retainer or oil reservoir saturation with the oil and other weight or labor intensive techniques are eliminated.

Solid lubrication encompasses a number of methods, procedures and lubricant types. A particular selection may be satisfactory for a specific MMA, but marginal or unacceptable with another. The lubricants themselves may be separated into two general groups: (a) non-replenishable films, mainly applied as thin, sacrificial layers ranging from angstrom thicknesses to as much as  $5.1 \times 10^{-5}$  m(0.002 in), and (b) replenishable films, formed by a film transfer process from a self-lubricating composite to a metallic bearing surface. The latter technique itself can be further divided into two parts: films formed by (a) the single transfer mechanism, where only a composite/metal bearing pair (e.g., a metal pin/composite bushing or a metal spherical bearing/composite bearing liner combination) is involved in forming a friction and wear reducing film on the surfaces of the metallic member of the pair, and (b) the double transfer mechanism, where the single-transferred, low shear strength composite film from the metallic bearing part is further transferred to a second, bare metallic bearing component which is integral within the system (e.g., from the ball of a self-lubricated ball bearing to the races or from a lubricative composite idler gear to the rest of the metallic members of a gear train).

One can, of course, conceive a combination of such applications, such as single/double transfer onto previously solid lubricated (e.g., burnished or sputtered) metallic surfaces.

In an effort to design a solid lubricated bearing system for use in long life (5 + years), ultra-precision gimbal pointing mechanisms, the double transfer mechanism of a self-lubricating composite bearing retainer was selected. The desirable self-replenishing mechanism illustrating an ideal ball/self-lubricating composite retainer ball pocket interaction during bearing operation would be represented by minimal (but adequate) transfer of the composite by the rubbing action of the ball. This composite wear action should form and maintain an evenly thin, solid lubricant film, which prevents metallic wear of the balls and the races.

If the retainer wear is excessive due to high ball-to-ball pocket loads, high speeds and long durations of operation with a high wear rate composite, the progressively thicker transfer film will have a torque-increasing blocking effect first, followed by eventual destruction of the retainer. On the other hand, high Hertzian stresses combined with a limited load carrying capacity or incomplete nature of the transfer film can induce excessive ball and race wear, manifesting in metallic debris generation, high torque, torque noise or possible loss of preload.

With the ever-increasing life requirements for space vehicles, component life-testing is rapidly becoming prohibitive in terms of lead time and cost. Accelerated testing of self-lubricated bearings, however, cannot even be approached unless the above described basic friction and wear mechanisms are understood.

In this first paper of two-part series, a sequence of retainer material selection and metallic bearing surface pretreatment is described, which led not only to the selection of a candidate retainer material but to some fundamental understanding of polymeric composite friction and wear also. This selection process involved wear and friction testing of the two likeliest reinforced PTFE/MoS<sub>2</sub> composite candidates under single transfer conditions, along with formulation and check of parametric wear equations and similar examination of the better of the two materials under double-transfer conditions. The work was done using commercially available and specially designed test equipment, both in inert gas and in vacuum test atmospheres.

The second paper of this series will describe the bearing specimens and test equipment, the bearing life test results and analyses, as well as the correlation between the results and the wear equations presented herein.

## TEST PHILOSOPHY, EQUIPMENT AND PROCEDURES

### Philosophy

The study described in this paper (Part I) was started in the summer of 1972. At that time, composite wear and the mechanism of transfer film formation (especially in vacuum) were little-researched phenomena. The principle was used because "it worked" under certain, empirically established conditions, mainly with polytetrafluoroethylene (PTFE) - MoS<sub>2</sub> composites reinforced with fiberglass (References 1 through 7), or with powder-metallurgically prepared, self-lubricating compacts (References 8 and 9).

The first attempt to investigate the film transfer phenomenon as the function of composite type under pseudo-rolling element bearing conditions was done by Jones and Gardos (Reference 10). These and all previous data indicated that glass-reinforced PTFE - MoS<sub>2</sub> composites had the best chance of providing long term, trouble-free operation for the following reasons:

1. The most experience was accumulated with these materials (References 1, 2, 4, 5, and 7).
2. Reinforced PTFE-MoS<sub>2</sub> composites exhibited the smallest differences in friction between air and vacuum, promising the greatest ease in handling test operations in air or an inert gas atmosphere and correlating test data with those of the actual performance (Reference 6).
3. Satisfactory transfer film formation occurred with these composites (Reference 10).
4. Experimental materials tend to exhibit erratic performance due to extensive batch-to-batch variations. Also, sudden non-availability could have seriously injured the program. Therefore, only commercial, off-the-shelf materials with established track records had to be used. In the early '70-s, reinforced PTFE composites represented the most reliable species of this lubricant type for a variety of applications.

Furthermore, additional research (Reference 11) confirmed previous contentions (References 5 and 9) that excessive wear of the retainer may be the most prevalent failure mode. It appeared that accelerated testing of transfer lubricated bearings could be presumed equivalent to induced, excess wear of the retainer. It was also shown that retainer wear is the function of maximum ball excursion, stemming from ball speed variations (Reference 12) and the resultant ball to ball pocket loading.

Based on the above information and other past Hughes experience, two commercially available, self-lubricating composites were selected for further scrutiny:

Composite A - 80% PTFE, 20% chopped glass fibers + 5% MoS<sub>2</sub>

Composite B - 60% PTFE, 40% fiberglass + 3% MoS<sub>2</sub>

Due to the proprietary nature of these materials, no other compositional data could be obtained from the manufacturer.

In view of all of the collected information, the following test plan was devised and completed:

Step 1: The wear behavior differences (if any) between Composites A and B were quantized under single transfer conditions by using Rhee's parametric wear equation method (Reference 13), where the equation is in the form of  $\Delta W = K F^a V^b t^c$  ( $\Delta W$  = composite weight loss;  $K$  = wear factor;  $F$  = normal load;  $V$  = sliding velocity;  $t$  = time of sliding and  $a$ ,  $b$ ,  $c$  = experimentally determined parameters). The value of this approach was confirmed by Mecklenburg (Reference 14), who has done similar work with self-lubricating compacts of the type described in Reference 8. The Hughes developed LFW-1 oscillatory procedure (Reference 15) of a conforming composite block sliding against a steel ring in an argon atmosphere was used to develop a test matrix, where the data were subjected to regression analysis in determining  $K$ ,  $a$ ,  $b$  and  $c$  of equations similar to the type proposed by Rhee.

Step 2: The validity and extrapolating ability of the wear equations were checked by performing vacuum friction tests with an equipment approximating the ball/ball pocket mini-contact in vacuum better than the LFW-1 test machine can. Since this vacuum tester differs entirely from that of the LFW-1 in terms of design, loads, speeds and environment (see Reference 6), this step lended itself to the realistic comparison of the predicted macro-contact wear in argon versus actual mini-contact composite wear in vacuum.

Step 3: A unique ball bearing simulator test tool was designed and constructed capable of measuring the wear of the best of the two composites under double transfer conditions, both in argon and in vacuum. Another statistically designed test matrix, coupled with regression analysis of the data led to another wear equation similar to that of Rhee's. This new equation revealed differences in the parametric effects of composite wear between single and double transfer conditions and established the usability of the final composite candidate under accelerated bearing test-like conditions.

#### Single Transfer Mode Test Equipment and Procedure (Argon)

The LFW-1 friction and wear tester was selected for the single transfer wear equation work because of the well-established repeatability of several test procedures (References 16, 17, and 18). Of particular importance are the low-load oscillating LFW-1 tests of self-lubricating composites originally developed by Hughes technologists (Reference 15).

The general operating principle of the LFW-1 is illustrated in Figure 1. In the present case a conforming, self-lubricating composite block is loaded normally against an oscillating Timken outer race by a compound load lever system. The friction force is sensed at a tangent by a transducer. The load and speed parameters as well as the randomized test pattern are given in Table 1. All other pertinent parameters for this test phases are described below.

- Block Materials . . . . . Composite A and B, as machined;
- Ring Material . . . . . 440C steel, R<sub>c</sub> 58-63, 2-4 rms (the gimbal bearing alloy);
- Ring Treatment . . . . . PHASE I = bare steel and Composite A or B block run-in for 3 hours at highest load/speed (see Table 1)  
PHASE II = MoS<sub>2</sub> powder (per MIL-M-7866) burnish in technical grade argon; no run-in;
- Ring Oscillation Angle. . . 90 degrees;
- Block Weight Loss Measurement . . . . . Each test after 2, 4, 7 and 23 hours, to the nearest 0.01 mg;
- Temperature . . . . . Ambient, periodically measured;

- Test Specimen Environment . . . . . 0.71 m<sup>3</sup> (25 ft<sup>3</sup>) per hour argon purge (the technical grade argon per MIL-A-18455 was sufficiently pure due to the non-hermetically sealed nature of the LFW-1 environmental chamber).

Deformation of the blocks (flaring and loss of precise area contact) due to the long-term oscillation stresses under the test loads was mitigated by a specially-designed, rectangular, stainless steel retaining collar. A small hole, drilled through the collar and into the middle of each block, permitted the insertion of a thin thermocouple into the composite block, approximately 3 mm away from the wear surfaces. This thermocouple measured the bulk temperature of the composite block during sliding to  $\pm 1\text{C}$  ( $\pm 2\text{F}$ ).

During the first test phase (Phase I) the composites were sliding against bare 440C steel. The test data and the examination of the used mating surfaces indicated, however, unexpectedly poor wear performance on the part of Composite A.

While the wear of Composite B appeared orderly and predictable, the unusual behavior of Composite A seemed to stem from its initially abrasive properties. Run-in abrasiveness was tentatively attributed to abrasive filler/metallic surface interaction, whereby the comparatively large diameter glass fiber particles (~10  $\mu\text{m}$  wide, up to 80  $\mu\text{m}$  long) in Composite A removed or damaged portions of the mating metallic surface. Such action resulted in gradually increasing surface damage, continually degrading both the composite and the metallic interfaces and preventing orderly transfer film formation and composite wear.

The purpose of the second phase (Phase II) study was to investigate any protection MoS<sub>2</sub>-burnishing might offer to the 440C surfaces during the wear-in period. All of the experiments of Phase I were repeated with new composite blocks, incorporating the following changes in the testing procedure:

1. Instead of assuming transfer film formation by run-in under an arbitrarily selected load, for an arbitrarily selected time period, all steel test ring surfaces were hand burnished with MoS<sub>2</sub> powder (per MIL-M-7866) in an argon atmosphere, using solvent extracted cotton swabs.

2. Each material and load combination of the eighteen LFW-1 tests was provided a separate ring surface, i.e., no ring contact area saw more than three tests (at a given load, at three different speeds). Note that during Phase I all nine tests of each composite were conducted against a single ring segment.
3. A constant voltage transformer was inserted between the wall current and the test machine to alleviate line voltage changes, which previously caused some minor but measurable variations in the pre-set LFW-1 oscillating speeds. Selected new and worn surfaces of both composites were examined by energy dispersion X-ray spectrometry (EDX) and scanning electron microscopy (SEM).

Load, speed and time factor regression analyses of the weight loss data from both phases were performed for the three levels of load, three levels of oscillating speed and four levels of time, with both composites. The previously mentioned line voltage change induced variations in oscillating velocity were found minor by an analysis of variance, showing no significant interactions with any of the independent variables.

However, the influence of all independent variables on wear was significant with the sliding velocity being the most significant at a level of 0.01.

Wear equations were then formulated for both materials, both in a simple and the advanced form, where the former is expressed as one version of the widely used Archard equation:

$$\Delta W = K P V t \quad (1)$$

$\Delta W$  = weight loss, g;

K = wear coefficient;

P = unit load, g . cm<sup>-2</sup>;

V = sliding velocity, cm . sec<sup>-1</sup>;

t = test duration, sec.

The advanced relationships were formulated, as previously suggested by Rhee:

$$\Delta W = K' P^a V^b t^c, \quad (2)$$

where  $\Delta W$ ,  $K'$ ,  $P$ ,  $V$  and  $t$  are as described previously and, likewise, the exponents  $a$ ,  $b$  and  $c$  are constants, experimentally determined for each material.

#### Single Transfer Mode Test Equipment and Procedure (Vacuum)

In order to check the validity and general usefulness of the above equations, vacuum wear data generated by an available friction and wear tester were compared with those extrapolated by the equations developed through wear in argon.

The Hughes vacuum friction tester is a specially designed apparatus capable of testing bonded solid lubricants and self-lubricating composites in a small displacement oscillating mode and low unit loads. This test machine was originally designed for the tribological examination of potentiometer contacts operating in ultrahigh ( $< 1 \times 10^{-8}$  torr) vacuum (Reference 19). A minor redesign enabled the testing of self-lubricating composites in vacuum (Reference 6).

The current design (see Figure 2) retained the original concept presented in References 6 and 19 while incorporating an increase in the composite contact size and weight over an order of magnitude, without changing the unit loads significantly. This enabled the measurement of wear not only from the size of the developed wear scar, but by accurate microbalance weighings of the composite contacts as well. The other pertinent test parameters are described below:

- Contacts (Forward and Rear) . . . . . Composite A and B as machined; nominal weight of forward contact = 0.2 g; rear contact = 0.8 g;
- Wire Specimens . . . . . 440C steel,  $R_c$  58-63, 2-4 rms (the gimbal bearing alloy); 0.254 cm = 0.1 in dia.;
- Wire Treatment . . . . . PHASE I = bare steel and Composite A or B block run-in equivalent to LFW-1 run-in, in distance.  
PHASE II =  $\text{MoS}_2$  powder (per MIL-M-7866) burnish in technical grade argon; no run-in;

- Oscillating Speed . . . . .  $60 \text{ cpm} = 1.02 \text{ cm} \cdot \text{sec}^{-1} = 2.0 \text{ ft} \cdot \text{min}^{-1}$  (average);
- Oscillatory Displacement . .  $1/2 \text{ cycle} = 0.508 \text{ cm} = 0.2 \text{ in.};$
- Upper Specimen Weight . . . 48 g;
- Test Duration . . . . . 3 to 4 days per test.

The unit loads between the steel wires (3 ea. new wire per test) and the composite contacts are calculated from the contact wear scars, the angle of each contact, the dead weight of the upper specimen (contact) holder and the load distribution of the upper specimen design. The weight loss of the contacts was determined by weighing on an ultramicrobalance to the nearest 0.001 mg before and after test. After each vacuum test the contact surfaces and the wire specimens were photographed at high magnification, and the unit loads were calculated accordingly.

During Phase I, the unit loads on the composite contacts were calculated based on the projected area of the final wear scars, constituting a first order approximation only. Actually, the wear scars gradually develop during the respective tests, starting out with the initial Hertzian indentation widths.

Since no analytical expressions have been derived yet in defining the growth of the cylinder-to-plane wear scars of the wire/composite contact specimen pairs, a second approximation was introduced for Phase II by incorporating a  $(q_o + q_f)/2$  unit load average in some of the calculations. The symbols  $q_o$  and  $q_f$  signify the initial Hertzian contact stresses calculated by well-established formulae dealing with a cylinder to plane contact configuration (Reference 20) and the final, measured unit load, based on the wear scar projections determined after the tests.

In the present "mini-contact" situation, care had to be taken in selecting the correct Young moduli ( $E$ ), Poisson's ratios  $\nu$  and, therefore, the elastic constants for Composites A and B. The above parameters of reinforced composites are measured with fairly large specimens to preclude localized effects. Here however, under the low load/small contact area situation, the localized effects would dominate and material homogeneity/filler orientation would be magnified in influencing the  $E$  and  $\nu$  values. For this reason, the "apparent" Young's moduli and Poisson's ratios of Composite A and B were approximated by taking the arithmetic averages of those reported for the respective composites and those for pure PTFE.

## Double Transfer Mode Test Equipment and Procedure (Argon)

After determining the facts that (a) the wear rate of Composite B was significantly higher than that of Composite A and that the former was, therefore, believed unsuitable for long term use in self-lubricated gimbal bearings and (b) the simple and advanced empirical wear equations did show acceptable validity in the single transfer mode even under extrapolated conditions, it remained to be seen whether the behavior of the remaining candidate (Composite A) was similarly acceptable in the double transfer, oscillatory mode. Sliding behavior here was quantized by a wear equation similar to that previously presented in Eq. (2). Wear data were generated by a unique ball bearing simulator (Reference 21) and the data were transformed into a wear equation somewhat less complete than that previously suggested by this writer in Reference 21:

$$\Delta V = K'' P_H^\alpha V^\beta t^\gamma \quad [3]$$

where

$K''$  = wear coefficient;

$\Delta V$  = wear volume loss,  $\text{cm}^3$ ;

$P_H$  = ball/race mean Hertzian stress,  $\text{g}(\text{force}) \cdot \text{cm}^{-2}$ ;

$V$  = ball/composite sliding speed,  $\text{cm} \cdot \text{sec}^{-1}$ ;

$t$  = test duration, sec.;

$\alpha, \beta, \gamma$  = exponents determined by regression analysis.

As shown in the schematic of the ball bearing simulator previously described in Reference 21 (also see Figure 3 herein), the ball/composite button (i.e., simulated ball/retainer ball pocket) load is variable. Here, this load was held to 100 g, because a previous computer program predicted

this value to be the most likely average transient load arising from the ball speed variations and from typical misalignment tolerances characteristic of the gimbal bearing designs. Ideally, of course, a test matrix should have included three levels of ball/composite loads also. As it is, the abbreviated Composite A matrix consisted of one test at each of three given bearing stresses and three average oscillating speeds quite comparable to those of the LFW-1, for a total of nine tests (see Table 2). The Composite A buttons were fabricated from used LFW-1 blocks previously utilized in developing the single transfer wear equations given in Table 3. However, the periodic button wear measurements here were conducted differently: they were performed after certain, predetermined sliding distances regardless of the speeds involved.

The test equipment and the general test procedures were adequately described in Reference 21. The additional pertinent test parameters are described below:

- Ball and Race  
Diameter . . . . .      440C ( $R_c$  58-63), 2-4 rms surface finish;
  - Ball and Race  
Diameter . . . . .      1.59 cm = 0.625 in. and 4.45 cm = 1.75 in., respectively;
  - Ball Pretreatment . . . . .      MoS<sub>2</sub> powder (per MIL-M-7866) burnishing
  - Race Pretreatment. . . . .      MoS<sub>2</sub> powder (per MIL-M-7866) burnishing, followed by a special Composite A stick-burnishing process to provide a pre-established, rub-on transfer film;
  - Total Included Drive  
Race Oscillation Angle . . . . .      129 degrees per cycle;
  - Total Surface Travel  
per Cycle . . . . .      4.993 cm = 1.966 in.;
  - Total Surface Travel  
per Test . . . . .      Approximately  $5.24 \times 10^5$  cm =  $2.063 \times 10^5$  in. =  $1.719 \times 10^4$  ft.;
  - Wear Measurements after  
Predetermined Distances.. . . . .       $1.747 \times 10^5$  cm,  $3.490 \times 10^5$  cm,  $5.240 \times 10^5$  cm.

- Temperature . . . . .      Ambient;
- Test Specimen Environment    Argon (per MIL-A-18455).

#### Double Transfer Mode Test Equipment and Procedure (Vacuum)

Since the ball bearing simulator is unique, the only possibility of checking the validity of the double transfer wear equation of Composite A was by placing carefully aligned test specimen combinations and the main support structure of the test machine into a specially constructed vacuum chamber. The drive and load feed-throughs permitted the completion of two selected load-speed combinations similar to those of the matrix tests previously performed in an argon atmosphere.

The following test parameters were employed:

- Atmosphere . . . . .       $4.0 \times 10^{-6}$  Pa ( $\sim 3 \times 10^{-8}$  torr);
- Hertzian Stress . . . . .    689.48 MPa (100 ksi);
- Composite A/Ball Load . . 100 g (0.221 lbs);
- Composite A/Ball Speed. .  
Test No. 1 =  $0.97 \text{ cm} \cdot \text{sec}^{-1}$   
 $(1.90 \text{ ft} \cdot \text{min}^{-1})$   
Test No. 2 =  $5.84 \text{ cm} \cdot \text{sec}^{-1}$   
 $(11.5 \text{ ft} \cdot \text{min}^{-1})$ ;
- Total Test Duration . . . .  
Test No. 1 = 30 days;  
Test No. 2 = 5 days.

All other test parameters were as described previously.

The transfer of Composite A and the composite button wear scars were examined by SEM and optical microscopy, as well as by profilometry. The experimentally determined wear volumes (for general methodology see Reference 21) were converted to weight loss by multiplying  $\Delta V$  with the density of Composite A ( $2.32 \text{ g} \cdot \text{cm}^{-3}$ ) to yield  $\Delta W$ .

#### DATA AND DISCUSSION

##### Single Transfer

The simple and advanced LFW-1 wear rate relationships are presented in Table 3. The examination of these equations, especially with respect to the P, V, t exponents, the relative magnitude of Archard K and

Rhee K' factors as well as the respective correlation coefficients indicate the following:

1. Burnishing the 440C surfaces with MoS<sub>2</sub> not only reduced the wear of Composite A by over a factor of two, but significantly improved the statistical validity of the wear data.
2. MoS<sub>2</sub> burnishing had little effect on the wear of Composite B. Strict interpretation of the somewhat greater wear on burnishing is not warranted: the slight differences in the Archard K values are attributed to the experimental error limits of the statistical design and LFW-1 machine itself.
3. The wear of Composite B is inherently greater by about a factor of two than that of Composite A. The wear of the former can be predicted with greater accuracy, however, due probably to a much more orderly wear process.
4. Comparison of the P, V, and t exponents of the Composite A and B advanced equations reveal important differences in wear behavior. At first, caution was exercised not to overinterpret the significance of the magnitude of these exponents. Later, especially after the examination of the new and used sliding LFW-1 block surfaces, a pattern was found emerging. This pattern was the first indication of materials parameters (e.g., reinforcement type, amount and distribution) which can influence composite wear behavior. In particular, the thin fiberglass strands in Composite B are less than 1  $\mu\text{m}$  in diameter, while the chopped glass fibers in the other are over an order of magnitude larger. The well-worn surfaces of both composites running against MoS<sub>2</sub> burnished steel surfaces in Figure 4 reveal this and the resultant dichotomy in wear behavior, attributed to the characteristic reinforcement morphology. The lower wear and lower sensitivity to load of Composite A (P1.29 versus P1.44 see Table 3) may be attributed to the preferential accumulation of the wear-flattened, relatively large glass fibers reinforcing the worn composite's surface. This preferential accumulation of fibers on Composite A is confirmed by the EDX spectra in Figure 5. The thin and brittle fiber ends on the Composite B surface also fragment, but the broken tips are incapable of the same preferential accumulation and are unable to provide the same load-carrying support. On the contrary, these small fragments turn into mobile abrasive particles, ploughing into the soft PTFE-MoS<sub>2</sub> matrix. The influence of surface morphology on the velocity exponents is even greater: note that the effect of velocity was found to be the most significant during regression analysis. The larger diameter glass fiber reinforced PTFE appears to be more vulnerable to repeated cyclic shear stress under load ( $V^{2.42}$  versus  $V^{0.39}$ , see Table 3), presumably due to large variations in preferential accumulation of components on the wear surface, polymer/fiber adhesion, thermal conductivity and glass wear behavior effects.

5. The influence of  $\text{MoS}_2$  burnishing the steel surface is profound in governing the wear behavior of Composite A. It was observed that the appearance of the as-machined Composite A and B blocks under high SEM magnifications shows little difference, due to a thin PTFE oversmear that apparently forms during block grinding. This thin "camouflage" quickly disappears on sliding, exposing the ends and edges of the relatively large chopped glass fibers in Composite A. The protruding sharp and hard edges act as an abrasive phase in sandpaper, when rubbing against the bare 440C surface. In contrast, the freshly machined Composite A surface sliding against the  $\text{MoS}_2$  - burnished steel undergoes a more orderly reinforcement wear process. The residual  $\text{MoS}_2$  film, however thin or uneven it is (as burnished films normally are), appears to protect the metal from abrasive damage until a more or less satisfactory wear and flattened alignment of the glass particles occur. The additional, beneficial effects of burnishing, especially in the case of Composite A show themselves indirectly in Figure 6, where load and speed are correlated with Phase I and II block temperature and friction. In line with the above findings, no Composite A transfer film could be detected on the single ring segment in PHASE I (continuous abrasive removal). The Phase II Composite A film, as well as those of Composite B in both phases were patchy but microscopically complete under moderate ( $\sim 20X$ ) magnifications.
6. Since the Archard relationships of Composite B, derived from Phase I and II data are in close agreement, one would expect the same from the Rhee-type relationships. While the respective  $K'$  factors and the  $P$ ,  $t$  exponents are comparable, the  $V_b$  terms are significantly different. On the other hand, cross-plotting the Phase I equation with Phase II data and vice versa indicated well-fitted correlations in each case about the lines of equal values. For this reason, all Phase I and Phase II data were subjected to regression analysis to observe any changes in  $K'$  and velocity exponent magnitudes. As shown by the BI-IIR(s) equation (dealing with Composite B, derived from Phase I and II data, of the Rhee (advanced) type, single transfer mode), the resulting  $K'$  factor and exponents are nearly arithmetic averages of the "parent" equations BIR(s) and BIIR(s). These data point to a need for some care in the interpretation of the physical meaning of the exponents. Among other possible causes, this idiosyncrasy is attributed mainly to the lack of velocity sensitivity of the softer, less surface-reinforced Composite B. Only additional equation development with other PTFE composites reinforced with varied rheologies of solid-fillers or with high modulus polymers (no solid fillers) can shed more light on this supposition.

The  $K$  factors of the Archard equations are more systems than materials parameters, unless their universality can be shown by practical means (see forthcoming discussion). This is also true, although to a lesser extent, with

the K' and K'' factors of the Rhee-type relationships, the magnitude of which are heavily affected by the numerical value and total factorial influence of the respective P, V and t exponents.

In spite of the anticipated limitations, the extrapolative ability of the wear equations listed in Table 3 is surprisingly powerful, as applied to vacuum friction contact wear prognosis. As indicated by the data shown in Table 4, composite wear in vacuum is predictable within a factor of two or better, especially by the Rhee-type relationships. In light of the accuracy of current wear prediction methods, this data fit is considered unusually good.

Since the wear scar measurements (see typical contact wear scars in Figure 7 generally depicting unit loads ranging from 2 to  $9 \times 10^3 \text{ g} \cdot \text{cm}^{-2}$ ) as well as the other experimental measurements were subject to some error, these errors could have fortuitously cancelled each other to yield the close correlations presented here. In light of the consistently good results, the probability of cancellation is small. Nevertheless, to investigate the most likely source of error, i.e., inaccuracies in wear prediction stemming from using final unit stresses and not some integrated unit load value from  $q_0$  to  $q_f$ , further correlations were made in Table 5.

The data in Table 5 indicate that wear scar development is probably so rapid and the estimation of fundamental values such as modulus and Poisson's ratio for a complex composite's microcontact is so full of pitfalls that the utilization of the final wear scar unit loads represents a justifiably close approximation. More recent work by Mecklenburg with a pin (sphere)-on-disc tester (Reference 22) did indeed show the rapid development of wear scar on the pin, causing an almost immediate drop in the unit load, approaching some asymptotic value. A similarly rapid composite contact wear scar development with a (steel) cylinder-to-composite plane combination of the vacuum friction tester is not unexpected.

#### Double Transfer

Regression analysis of the ball bearing simulator data (argon) yielded the following equation:

$$\Delta V = \frac{\Delta W}{2.32} = 3.41 \times 10^{-17} P_H^{0.88} V^{0.71} t^{1.0} \quad [\text{AIIR(d)}]$$

This type of  $K''$  conversion from wear volume to wear weight inherently assumes that the double transfer wear of Composite A is homogeneous with no preferential change in composite surface or transfer film composition as the load/speed/time-influenced wear process progresses. This is, at best, only approximately true, because we now know that significant changes take place (i.e., there if preferential accumulation of constituents) on the composite wear surface.

Note that due to the paucity of data, no correlation coefficient is presented here. However, as shown in Table 6, the equation predicts the measured (volume loss) values within about a factor of two to three, or better. Since these data are the first of their kind, no comparison with previous standards can be given with respect to the degree of satisfactory data fit. However, as shown in Reference 21, the 100 gram ball/composite load and the resulting projected wear scar areas (on the order of 3 to  $5 \times 10^{-3} \text{ cm}^2$ ) placed the unit loads within a reasonable extrapolating distance of the LFW-1 wear equation load range. It is extremely gratifying to find that the wear coefficients of the AIIR(s) ( $K' = 4.85 \times 10^{-17}$ ) and the AIIR(d) [ $K'' = (2.32)(3.41 \times 10^{-17}) = 7.91 \times 10^{-17}$ ] equations are very close, indicating an orderly, believably correlatable wear process between the single and double transfer mode of Composite A.

Examination of the ball and test race surfaces indicated the presence of highly compacted, extremely adherent transfer films. The unique rheology of the double transfer films manifested itself in reducing the time exponent of  $c = 1.29$  [Equation AIIR(s)], associated with a less complete and predictable single transfer film to  $\gamma = 1.00$  [see Equation AIIR(d)]. Note that Rhee (Reference 13) attributed the time exponent's unit value of his equations to an orderly formation of transfer films. The corresponding changes in the velocity exponents cannot be explained at this time.

Generally, higher Hertzian stresses between the ball and the races and lower speeds resulted in the thickest transfer films. It is likely that at any given bearing load and number of cycles, a higher oscillating speed resulted in composite wear more in the form of macro, rather than micro debris.

After completion of the two ball bearing simulator vacuum tests, the respective wear scars were examined and the microscopic and profilometric estimates of the wear scar depths were found to agree within 30 to 40 percent. The somewhat irregular shape of wear scars deviating from the theoretical did, however, complicate the measurements. The experimental weight losses of the low and high speed tests were  $9.2 \times 10^{-5}$  g and  $5.5 \times 10^{-5}$  g respectively. The equivalent values predicted by Equation AIIR(d) are  $3.6 \times 10^{-5}$  g and  $6.0 \times 10^{-5}$  g, again showing good agreement between  $W_m$  and  $W_p$ .

Note that the profilometric traces did give some indication of higher wear at the lower speed. This phenomenon however, in light of only two tests, is not considered statistically significant.

#### Advantages and Limitations of Empirical Wear Equations

The wear coefficients  $K$ ,  $K'$  and  $K''$  are not materials constants. They represent systems properties where each coefficient inherently contains effects, such as transfer film and substrate materials, surface roughness condition and treatments, surface (flash) and environmental temperature, friction couple geometry and operating conditions. The advantages of  $K'$  and  $K''$  over  $K$  lie in removing the load, speed and time effects from  $K$ .  $P$ ,  $V$  and  $t$  are, however, engineering and not fundamental independent variables.

Ideally, the wear of polymers and all-polymeric composites should be predictable on the basis of viscoelasticity fundamentals and energy expenditures alone. Unfortunately, efforts along these lines are meager, painting an even more dismal picture for an "equation-of-state" that can provide precise wear prognosis of solid filler-reinforced, self-lubricating composites.

In lieu of such fundamentals, the practicing technologist must turn to empirical wear equations. The experimental design must, however, adhere to the most rigorous yet practicable methods of tribological systems analysis (see Czichos' recent book in Reference 23) to produce usable formulas. It is demonstrated here that the Rhee-type equation is useful if the above cited cautions are observed. Essentially, regression analytical wear equations

development of polymeric composites must adhere to the following general rules:

1. The test temperature range must not contain temperatures where the wear of polymers drastically changes due to primary and secondary phase transitions in the polymer. Changes such as pyrolysis on the wear surface (due to higher than ambient temperatures through flash temperature superposition) can be accounted for, as previously demonstrated by Liu and Rhee (Reference 24). In spite of the most careful test machine parameter design, specimen machining and other care, incorrect temperature range selection will manifest itself in wide scatter of wear data and very low correlation coefficients of the regression analysis.
2. Extending the above rule, degradation should occur at the composite/alloy interface and not within the composite nor within the mating bearing material's bulk. For example, thermal degradation of the polymer/reinforcing fiber interface that leads to weakening of the composite will result in a time- and load-dependent, scattered increase in wear, not attributable to an interface wear phenomenon alone. This writer has recently shown this assumption valid through high temperature ( $316^{\circ}\text{C} = 600^{\circ}\text{F}$ ) wear equation work at load/speed combinations up to  $27.58 \text{ MPa}/76 \text{ cm} \cdot \text{sec}^{-1}$  ( $4000 \text{ psi}/150 \text{ ft} \cdot \text{min}^{-1} = 600,000 \text{ PV}$ ), using 3D carbon fiber weave reinforced, lubricative additives containing, polyimide-based self-lubricating composites (Reference 25). These and other large but otherwise unexplainable changes in wear behavior on the composite surface will contribute to poor statistical validity of the test data.

The utility of the wear equations presented in this paper as predictive tools for self-lubricated, rolling element bearing behavior depends a great deal on understanding the precise mechanism of ball/ball pocket and ball/race interactions. As shown in the Part II paper of this series, understanding of those mechanisms, combined with the appropriate wear equation(s) can provide a reasonable, semiempirical method of bearing test acceleration. The same is true for the accelerated testing of plain bearing combinations, with the appropriate modifications.

## CONCLUSIONS

An extensive study of empirical wear equation development was successfully completed showing that the wear of glass fiber reinforced MoS<sub>2</sub> containing PTFE self-lubricating composites in vacuum can be predicted within about a factor of two to three by wear equations developed in argon. This indicates close similarities in the respective wear processes and reduces the complexity and cost of wear equation development methods for the PTFE-based self-lubricating composites. The most useful equation format between the Archard and the Rhee-type equations is shown to be the latter, in the general form of  $\Delta W = K' P^a V^b t^c$ .

These wear equations, describing both pin and bushing-like (single transfer) and ball pocket-to-ball and to race (double transfer) rolling element bearing-like behavior are deemed useful for accelerated testing of self-lubricated plain and ball bearings provided that the systems interactions of the respective mechanisms are definable and correlatable with composite wear and transfer film formation. The degree of usefulness in the present case is discussed in the Part II paper of this series.

There are indications that filler geometry parameters and preferential, topographic changes on the worn composite surfaces, along with the resultant wear and film formation tend to manifest themselves in reasonably predictable numerical differences of the P, V and t exponents. This unique characteristic of the Rhee-type equation may also offer the first avenue to tailorability of self-lubricating composites for specific applications. Additional data are unquestionably needed to lend more credence to this hypothesis.

## ACKNOWLEDGMENTS

The author is deeply indebted to Messrs. J. Gardner, N. R. Kramer, H. S. Noji, K. Price and M. Weber of Hughes Aircraft Company for their support during the course of this work. The help of Mr. S. Feuerstein and Dr. G. W. Stupian of the Aerospace Corporation is also much appreciated for performing the ball bearing simulator vacuum tests and releasing the data. The permission of Hughes Aircraft Company for publishing this paper is hereby gratefully acknowledged.

## LIST OF REFERENCES

1. Evans, H.E. et al., "Evaluation of Dry Film Lubricating Materials for Spacecraft Application," Proc. 6th Ann. Structures and Materials Conf., April 1965.
2. Mabie, H.H., "The Effects of Dry and Fluid Lubrication on Instrument Ball Bearing Torques at High Speed," Lub. Eng., 21, 242 (1965).
3. Young, W.C. and Clauss, F.J., "Lubrication for Spacecraft Applications," Lub. Eng., 22, 219 (1966).
4. Johnson, R. L. and Buckley, D.H., "Lubricants and Mechanical Components of Lubrication Systems for Space Environment," Lub. Eng., 22, 408 (1966).
5. Smith, G.R. and Vest, C.E., "Lubrication of Spacecraft Mechanism Using the Transfer Film Technique," Lub. Eng., 27, 12 (1971).
6. Jones, J.R. and Gardos, M.N., "Friction and Wear Characteristics of Lubricative Composites in Air and in Vacuum," Lub. Eng., 27, 47 (1971).
7. NASA Space Vehicle Design Criteria (Structures), "Lubrication, Friction and Wear," NASA SP-8063, June 1971.
8. Hubbell, R.D. et al., "Development of Solid Lubricant Compacts for use in Ball Bearing Separators," Lub. Eng., 25, 31 (1969).
9. Boes, D.J. et al., "The Solid Lubrication of Ball Bearings Under High Speed - High Load Conditions from -225 to +1000F," Lub. Eng., 27, 150 (1971).
10. Jones, J.R. and Gardos, M.N., "Transfer Film Formation by Lubricative Composites," Proc. 2nd Int. Conf. on Solid Lubrication, 24-27 August 1971, Denver, Colorado, ASLE SP-3, pp. 185-197.
11. Vest, C.E., "Evaluation of Several Additional Dry Lubricants for Space Applications," Lub. Eng., 30, 246 (1974).
12. Barish, T., "Ball Speed Variation in Ball Bearings and its Effect on Cage Design," Lub. Eng., 25, 110 (1969).
13. Rhee, S.K., "Wear Equation for Polymers Sliding Against Metal Surfaces," Wear, 16, 431 (1970).
14. Mecklenburg, K.R., "Wear Rate Relationships for Three Lubricant Compact Materials," AFML-TR-7--123, July 1971.

15. Jones, J. R., "Low-load Oscillating Tests of Bonded Solid Lubricants and Composites," Lub. Eng., 24, 464 (1968).
16. ASTM Method D2714-68, "Calibration and Operation of the Alpha Model LFW-1 Friction and Wear Testing Machine."
17. Bahun, C. J. and Jones, J. R., "Influence of Load, Speed and Coating Thickness on the Wear Life of a Bonded Solid Lubricant," Lub. Eng., 25, 351 (1969).
18. DiSapio, A. and Lindsey, I., "Some Effects Oscillatory Motion on Bonded Solid Lubricants," Lub. Eng., 26, 412 (1970).
19. Jones, J. R., "Friction and Wear of Potentiometer Contacts in Vacuum," Wear, 11, 355 (1968).
20. Carrol, J. G., "Contact Stresses in Lubricant Testers," Lub. Eng., 24, 8 (1968).
21. Gardos, M. N. and Preston, D. F., "A Ball Bearing Simulator - A Tool for Accelerated Testing of Self-Lubricated Bearings," ASLE Trans., 20, 133 (1977).
22. Mecklenburg, K. R., "The Effect of Wear on the Compressive Stress in the Sphere-on-Plane Configuration," ASLE Trans., 17, 149 (1974).
23. Czichos, H., "TRIBOLOGY - A Systems Approach to the Science and Technology of Friction, Lubrication and Wear," Elsevier, Amsterdam, 1978.
24. Liu, T. and Rhee, S. K., "High Temperature Wear of Asbestos - Reinforced Friction Materials," Wear, 37, 291 (1976).
25. Gardos, M. N. and Castillo, A. A., "Self-Lubricating Bearing Materials - Part I: Development of a High Load, High Temperature, Self-Lubricating Composite," AFML-TR-4091, Part I, Hughes Aircraft Company, Culver City, California, August 1979.

TABLE 1. LFW-1 WEAR RATE RELATIONSHIP STUDY,  
ARGON TEST ATMOSPHERE (PHASES I AND II)

Test No.	Composite	Unit Load <sup>(2)</sup>		Speed Setting <sup>(1)</sup>		
		g(force).cm <sup>-2</sup>	psi	cpm	cm.sec <sup>-1</sup> <sup>(3)</sup>	ft.min <sup>-1</sup> <sup>(3)</sup>
1	B	4.2184 x 10 <sup>4</sup>	600	70	6.43	12.66
2	A	4.2184 x 10 <sup>4</sup>	600	70	6.43	12.66
3	B	2.8123 x 10 <sup>4</sup>	400	95	8.73	17.18
4	B	4.2184 x 10 <sup>4</sup>	600	50	4.59	9.04
5	A	5.6246 x 10 <sup>4</sup>	800	95	8.73	17.18
6	B	5.6246 x 10 <sup>4</sup>	800	50	4.59	9.04
7	A	5.6246 x 10 <sup>4</sup>	800	50	4.59	9.04
8	A	4.2184 x 10 <sup>4</sup>	600	95	8.73	17.18
9	A	4.2184 x 10 <sup>4</sup>	600	50	4.59	9.04
10	A	2.8123 x 10 <sup>4</sup>	400	95	8.73	17.18
11	B	5.6246 x 10 <sup>4</sup>	800	95	8.73	17.18
12	B	2.8123 x 10 <sup>4</sup>	400	50	4.59	9.04
13	A	2.8123 x 10 <sup>4</sup>	400	50	4.59	9.04
14	A	2.8123 x 10 <sup>4</sup>	400	70	6.43	12.66
15	B	5.6246 x 10 <sup>4</sup>	800	70	6.43	12.66
16	B	4.2184 x 10 <sup>4</sup>	600	95	8.73	17.18
17	B	2.8123 x 10 <sup>4</sup>	400	70	6.43	12.66
18	A	5.6246 x 10 <sup>4</sup>	800	70	6.43	12.66

(1) The actual (observed) speeds were slightly different.

(2) 1000 psi = 7.0307 x 10<sup>4</sup> g(force).cm<sup>-2</sup> = 6.8948 MPa.

(3) Average value, based on sinusoidal motion.

TABLE 2. BALL BEARING SIMULATOR OSCILLATORY TEST  
MATRIX (BALL/COMPOSITE LOAD = 100g = 0.221 lbs)

Test No.	Ball/Race Mean Hertzian Contact Stress <sup>(1)</sup>		Ball/Race and Ball/Composite Speed Setting		
	g(force)·cm <sup>-2</sup>	Kpsi	cpm	cm·sec <sup>-1</sup> <sup>(2)</sup>	ft·min <sup>-1</sup> <sup>(2)</sup>
1	$3.5154 \times 10^6$	50	110	9.15	18.03
2	$3.5154 \times 10^6$	50	200	16.62	37.74
3	$10.5461 \times 10^6$	150	20	1.66	3.27
4	$7.0307 \times 10^6$	100	20	1.66	3.27
5	$10.5461 \times 10^6$	150	200	16.62	37.74
6	$3.5154 \times 10^6$	50	20	1.66	3.27
7	$7.0307 \times 10^6$	100	110	9.15	18.03
8	$10.5461 \times 10^6$	150	110	9.15	18.03
9	$7.0307 \times 10^6$	100	200	16.62	37.74

(1) 10,000 psi =  $7.0307 \times 10^5$  g(force) cm<sup>-2</sup> = 68.948 MPa.  
(2) Average value, based on sinusoidal motion.

TABLE 3. WEAR EQUATIONS FOR THE SINGLE TRANSFER MODE

Composite	Phase	Equation Type	$W$ grams = Equation	Equation I.D. No.	Correlation Coefficient
<b>A</b>	I	Archard (1)	$5.87 \times 10^{-13} PVt$	AI A(s)	0.66
	Rhee (2)	Not obtainable*		—	—
	II	Archard (1)	$2.24 \times 10^{-13} PVt$	AIIA(s)	0.87
	Rhee (2)	$4.85 \times 10^{-17} P^1.29 V^2.42 t^1.27$	AIIR(s)	0.93	
	I	Archard (1)	$4.82 \times 10^{-13} PVt$	BIA(s)	0.98
	Rhee (2)	$4.52 \times 10^{-13} P^1.41 V^0.93 t^0.80$	BIR(s)	0.98	
<b>R</b>	II	Archard (1)	$5.44 \times 10^{-13} PVt$	BIIA(s)	0.92
	Rhee (2)	$1.40 \times 10^{-12} P^1.44 V^0.39 t^0.74$	BIIR(s)	0.93	
	I & II Rhee (2)	$7.26 \times 10^{-13} P^1.43 V^0.69 t^0.77$	BI-II R(s)	0.95	

\*Six out of the nine weighings after 2 hours showed negative weight loss (i.e., weight gain), preventing regression analytical work.

TABLE 4. APPLICABILITY OF THE SINGLE TRANSFER WEAR EQUATIONS TO COMPOSITES SLIDING IN ULTRA-HIGH VACUUM VS. BARE AND MoS<sub>2</sub> - BURNISHED 440C STEEL (PHASES I AND II).

Composite Type	Contact	Equation <sup>(1)</sup>	$\frac{\text{Wear} \text{ (predicted)} [W_p]}{\text{Wear} \text{ (measured)} [W_m]}$
A	Forward	AIA(s)	0.61
		— (2)	— (2)
		AIIA(s)	16.7
		AIIR(s)	1.3
	Rear	AIA(s)	0.63
		— (2)	— (2)
		AIIA(s)	3.8
		AIIR(s)	0.3
B	Forward	BIA(s)	2.3
		BIR(s)	0.5
		BIIA(s)	2.3
		BIIR(s)	1.1
		BI-IIR(s)	0.8 <sup>(3)</sup> /0.7 <sup>(4)</sup>
	Rear	BIA(s)	2.0
		BIR(s)	0.5
		BIIA(s)	0.7
		BIIR(s)	0.6
		BI-IIR(s)	0.9 <sup>(3)</sup> /0.4 <sup>(4)</sup>

(1) See Table 3.

(2) Equation not obtainable.

(3) PHASE I data.

(4) PHASE II data.

TABLE 5. EFFECT OF THE ESTIMATED UNIT LOAD ON THE PREDICTABILITY  
OF COMPOSITE WEAR (PHASES I AND II).

Composite Forward Contact	Equation (1)	Initial (2) Stress, $q_o$ ( $\text{g} \cdot \text{cm}^{-2}$ )	Final (3) Stress, $q_f$ ( $\text{g} \cdot \text{cm}^{-2}$ )	Wear(predicted) [ $W_p$ ]	
				Wear(measured) [ $W_m$ ]	Based on $q_o + q_f$
A	AIA(s)	$3.1305 \times 10^4$	$1.834 \times 10^3$	2.3	20.8
	- (4)	- (4)	- (4)	- (4)	- (4)
B	AIIA(s)	$3.9623 \times 10^4$	$2.213 \times 10^3$	16.7	157.8
	AIIR(s)	$4.7499 \times 10^4$	$2.376 \times 10^3$	1.3	25.4
C	BIA(s)	$3.1280 \times 10^4$	$2.303 \times 10^3$	2.3	24.2
	BIR(s)	-	-	0.5	16.4
D	BIIA(s)	-	-	2.3	16.8
	BIIR(s)	-	-	1.1	19.2

- (1) See Table 3.
- (2) Calculated by formulas and assumptions described in text.
- (3) Calculated by final, projected wear scar.
- (4) Equation not obtainable.

TABLE 6. COMPARISON OF PREDICTED AND MEASURED WEAR VOLUMES [EQUATION AIIR(d)](1)

Test No.	After Incremental Rolling Distances (2)	Composite A Specimen Wear Volume Loss ( $\Delta V$ , $\text{cm}^3$ )		$\frac{W_p}{W_m}$
		Predicted ( $W_p$ )	Measured ( $W_m$ )	
1	1st	$2.9 \times 10^{-6}$	$2.0 \times 10^{-6}$	1.45
	2nd	$6.0 \times 10^{-6}$	$5.4 \times 10^{-6}$	1.11
	3rd	$0.2 \times 10^{-6}$	$6.5 \times 10^{-6}$	1.42
2	1st	$2.4 \times 10^{-6}$	$5.1 \times 10^{-6}$	0.47
	2nd	$4.9 \times 10^{-6}$	$5.1 \times 10^{-6}$	0.96
	3rd	$7.5 \times 10^{-6}$	$7.9 \times 10^{-6}$	0.95
3	1st	$1.35 \times 10^{-5}$	$5.4 \times 10^{-6}$	2.50
	2nd	$2.80 \times 10^{-5}$	$1.10 \times 10^{-5}$	2.54
	3rd	$4.29 \times 10^{-5}$	$1.301 \times 10^{-4}$	0.53
4	1st	$9.5 \times 10^{-6}$	$1.31 \times 10^{-5}$	0.73
	2nd	$1.96 \times 10^{-5}$	$1.52 \times 10^{-5}$	1.29
	3rd	$3.00 \times 10^{-5}$	$9.34 \times 10^{-5}$	0.32
5	1st	$6.2 \times 10^{-6}$	$5.5 \times 10^{-6}$	1.13
	2nd	$1.29 \times 10^{-5}$	$6.2 \times 10^{-6}$	2.08
	3rd	$1.97 \times 10^{-5}$	$1.14 \times 10^{-5}$	1.73
6	1st	$5.2 \times 10^{-6}$	$6.2 \times 10^{-6}$	0.84
	2nd	$1.07 \times 10^{-5}$	$9.0 \times 10^{-6}$	1.19
	3rd	$1.63 \times 10^{-5}$	$1.36 \times 10^{-5}$	1.20
7	1st	$5.3 \times 10^{-6}$	$2.3 \times 10^{-6}$	2.30
	2nd	$1.10 \times 10^{-5}$	$5.8 \times 10^{-6}$	1.90
	3rd	$1.69 \times 10^{-5}$	$7.1 \times 10^{-6}$	2.38
8	1st	$7.6 \times 10^{-6}$	$1.65 \times 10^{-5}$	0.46
	2nd	$1.58 \times 10^{-5}$	$1.93 \times 10^{-5}$	0.82
	3rd	$2.41 \times 10^{-5}$	$6.55 \times 10^{-5}$	0.37
9	1st	$4.4 \times 10^{-6}$	$1.15 \times 10^{-5}$	0.38
	2nd	$9.0 \times 10^{-6}$	$1.32 \times 10^{-5}$	0.68
	3rd	$1.38 \times 10^{-5}$	$1.42 \times 10^{-5}$	0.97

(1) See Table 2 for test matrix parameters.

(2) 1st =  $1.747 \times 10^5$  cm; 2nd =  $3.490 \times 10^5$  cm; 3rd =  $5.240 \times 10^5$  cm.

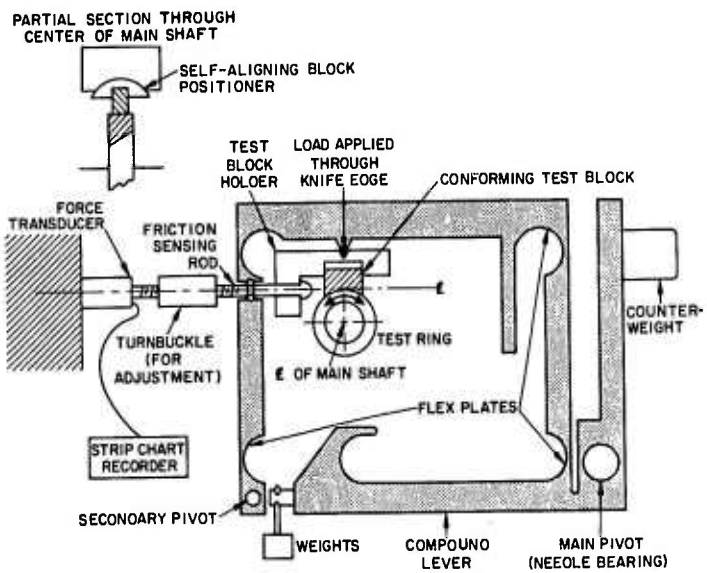


Figure 1. Schematic representation of the LFW-1 machine.

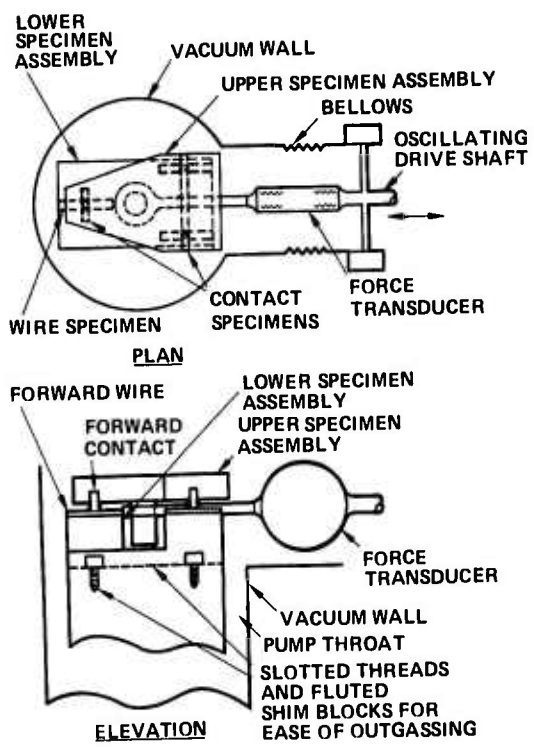


Figure 2. Schematic representation of the Hughes vacuum friction and wear tester.

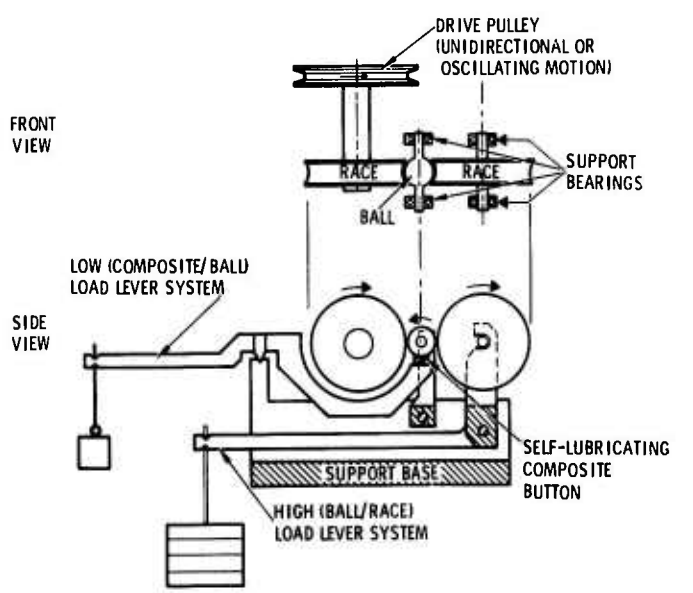


Figure 3. Detailed schematic of the Hughes bearing simulator apparatus.

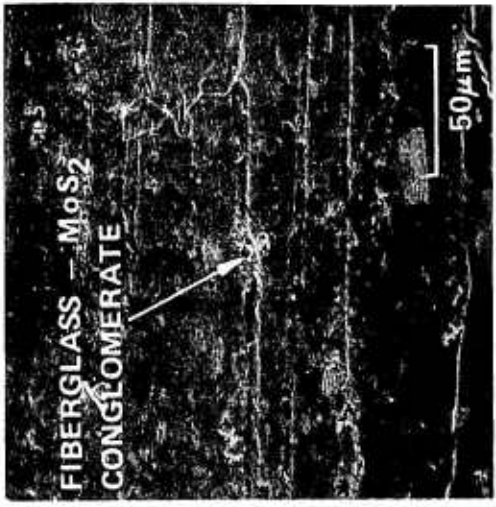
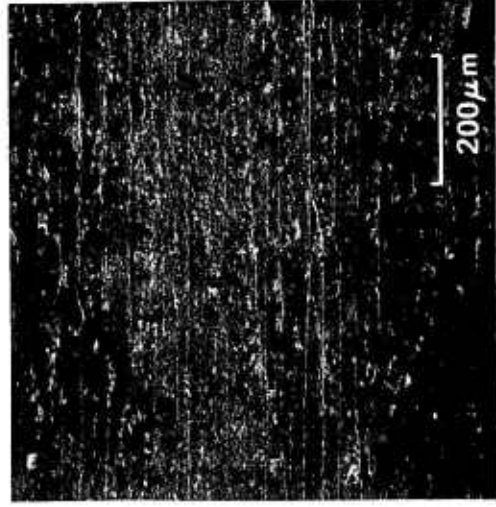
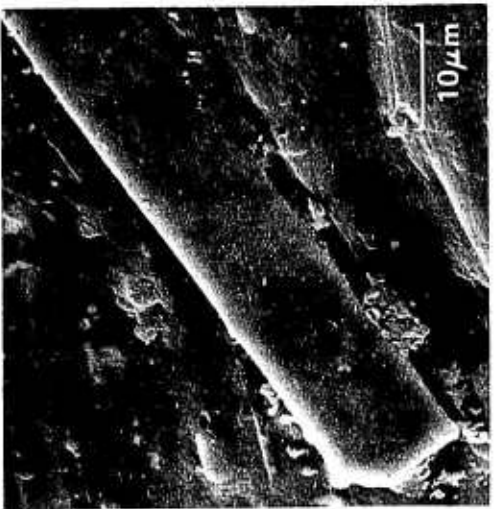
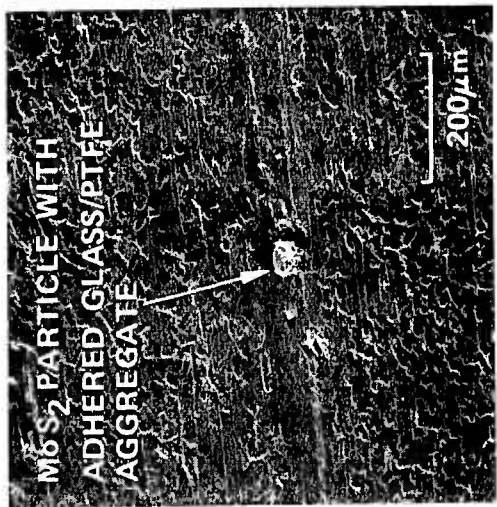


Figure 4. Well-worn composite surfaces against MoS<sub>2</sub>-burnished 440C steel; (a, b and c)  
Composite A at 100X, 400X and 1600X magnification; (d, e and f)  
Composite B at 100X, 400X and 1600X magnification.

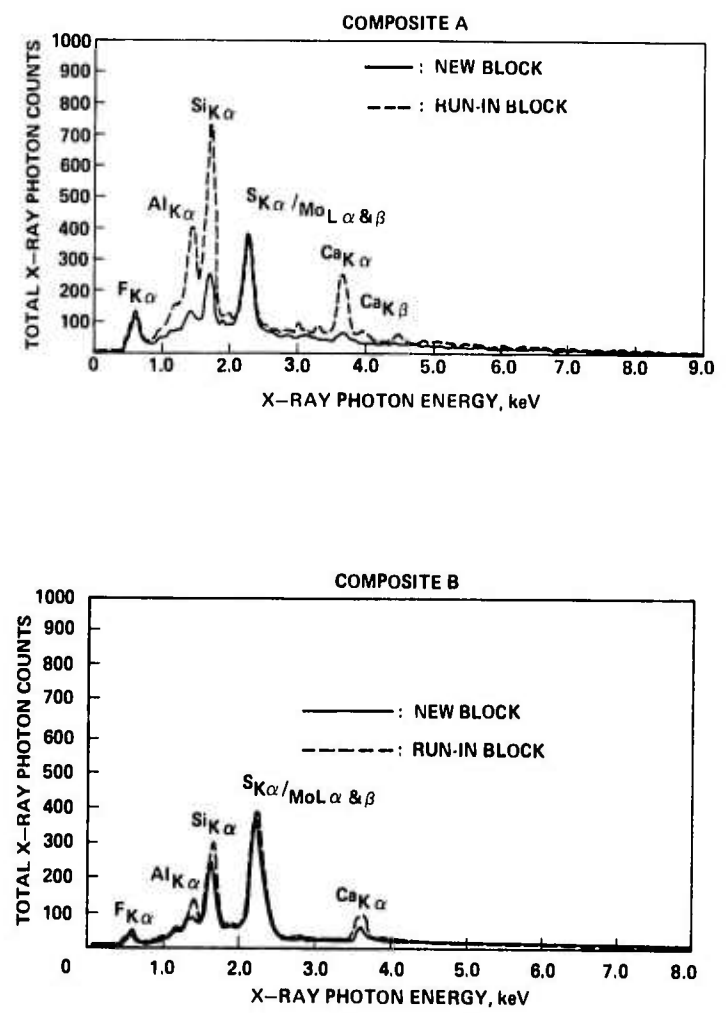


Figure 5. EDX spectra of composite surfaces  
(also see Figure 4); Phase II.

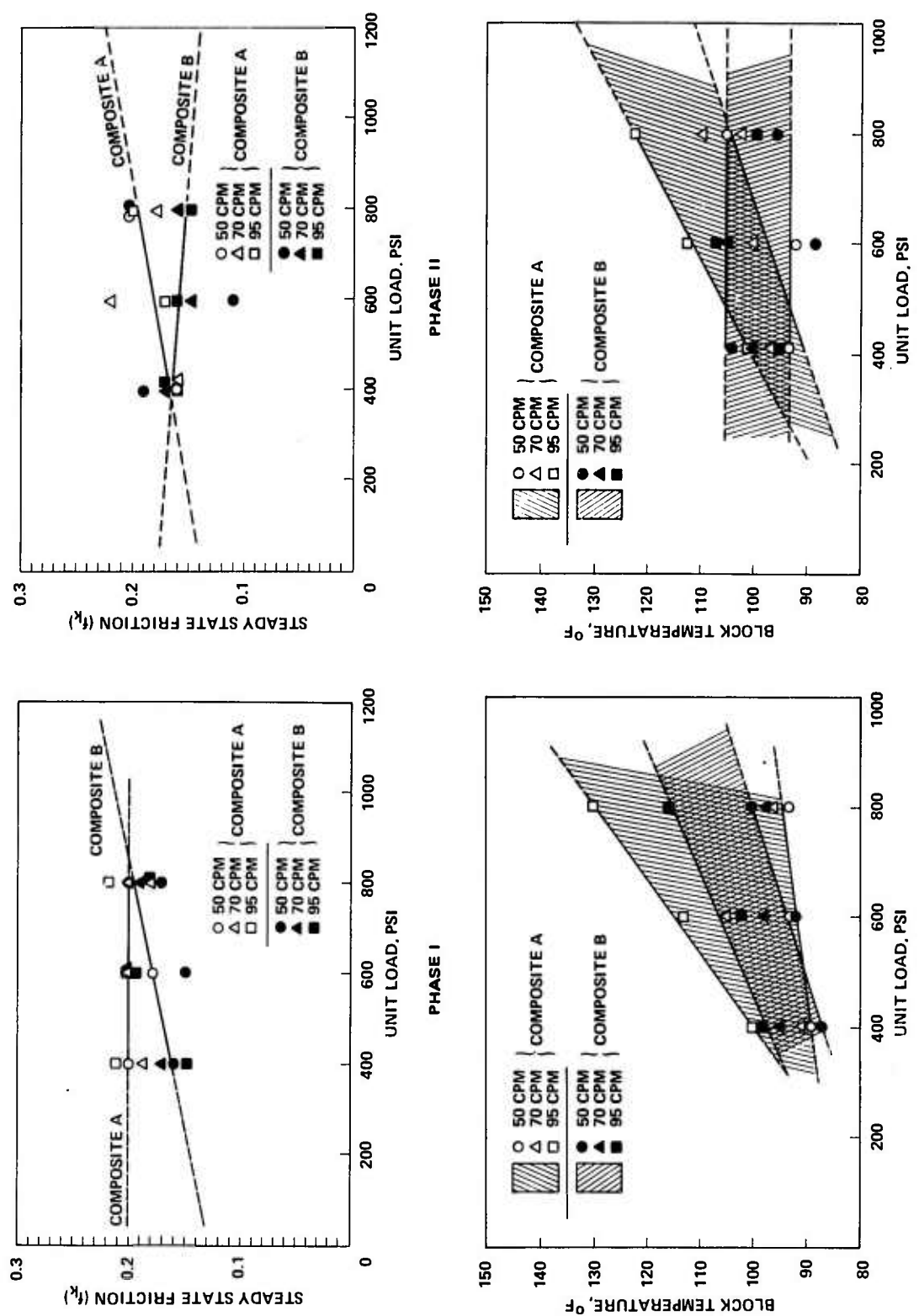


Figure 6. Effect of MoS<sub>2</sub> burnishing on the load/speed/friction/temperature interactions of composite/steel surfaces.

**COMPOSITE A**



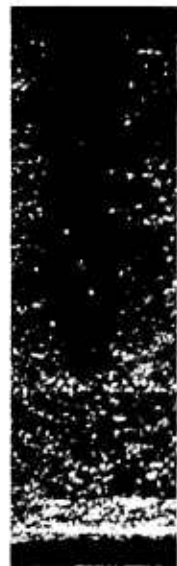
**COMPOSITE B**



0.5 mm



**FORWARD CONTACT**



**REAR CONTACT**

**REAR CONTACT**

Figure 7. Appearance of contact wear scars at  
35X magnification; Phase II.

## LIST OF TABLES

1. LFW-1 Wear Rate Relationship Study, Argon Test Atmosphere (Phases I and II).
2. Ball Bearing Simulator Oscillatory Test Matrix (Ball/Composite Load = 100g = 0.221 lbs.).
3. Wear Equations for the Single Transfer Mode.
4. Applicability of the Single Transfer Wear Equations to Composites Sliding in Ultrahigh Vacuum vs. Bare and MoS<sub>2</sub>-Burnished 440C Steel (Phases I and II).
5. Effect of the Estimated Unit Load on the Predictability of Composite Wear (Phases I and II).
6. Comparison of Predicted and Measured Wear Volumes [Equation AIIR(d)].

## LIST OF ILLUSTRATIONS

### Figure

1. Schematic representation of the LFW-1 machine.
2. Schematic representation of the Hughes vacuum friction and wear tester.
3. Detailed schematic of the Hughes bearing simulator apparatus.
4. Well worn composite surfaces against MoS<sub>2</sub>-burnished 440C steel:  
(a, b, and c) Composite A at 100X, 400X, and 1600X SEM magnification; (d, e and f) Composite B at 100X, 400X and 1600X SEM magnification.
5. EDX spectra of composite surfaces (also see Figure 4); Phase II.
6. Effect of MoS<sub>2</sub> burnishing on the load/speed/friction/temperature interactions of composite/steel surfaces.
7. Appearance of contact wear scars at 35X magnification; Phase II.

## APPENDIX I

MEEKS, C. R., "THEORY AND PRACTICE OF SELF-LUBRICATED,  
OSCILLATORY BEARING OPERATION FOR HIGH VACUUM  
APPLICATIONS - PART II; ACCELERATED LIFE TESTS  
AND ANALYSIS OF BEARINGS,"  
paper accepted for presentation and publication at the  
ASME-ASLE Int. Conf., ; Aug. 18-21, 1980,  
St. Francis Hotel, San Francisco, California.

THEORY AND PRACTICE OF SELF-LUBRICATED,  
OSCILLATORY BEARINGS FOR  
HIGH VACUUM APPLICATIONS

Part II - Accelerated Life Tests and Analysis of Bearings

Crawford R. Meeks  
Hughes Aircraft Company, Culver City, CA

Paper accepted for presentation at the ASME-ASLE International Conference,  
August 18-21, 1980, Saint Francis Hotel, San Francisco, CA.

## CONTENTS

THEORY AND PRACTICE OF SELF-LUBRICATED, OSCILLATORY BEARINGS FOR HIGH VACUUM APPLICATIONS . . . . .	I-1
Abstract . . . . .	I-1
Introduction . . . . .	I-2
Accelerated Testing . . . . .	I-3
Ball Separator Wear . . . . .	I-3
Ball and Race Wear . . . . .	I-5
Experiment . . . . .	I-6
Experimental Results and Analysis . . . . .	I-7
Friction Torque . . . . .	I-7
Ball and Raceway Wear . . . . .	I-8
Ball Separator Pocket Wear . . . . .	I-9
Raceway Wear . . . . .	I-12
Conclusions . . . . .	I-13
Acknowledgments . . . . .	I-15
References . . . . .	I-16
APPENDIX ANALYSIS OF BEARING TORQUE DUE TO SEPARATOR FORCES . . . . .	I-17

## LIST OF ILLUSTRATIONS

Figure		Page
1	Typical Test Apparatus.....	I-21
2	Bearing Friction Torque Performance.....	I-21
3	Photomicrographs of Bearing Raceway and Lubricant Film .....	I-23
4	Ball Pocket Wear Scars .....	I-24
5	Ball Pocket Wear Scar Traces .....	I-25
6	Measurement Method for Ball Pocket Wear Scar .....	I-26
7	Ball Pocket Wear vs Ball Travel .....	I-26
8	Raceway Wear Zone .....	I-27
9	Stylus Surface Analyzer Traces of Race Wear Track ..	I-27
10	Wear Volume Model Based on Circular Development of Secant .....	I-28
11	Bearing Raceway Wear vs Ball Travel.....	I-28

## LIST OF TABLES

Table		Page
1	Bearing Life Test Matrix .....	I-19
2	Test Bearing Design Parameters .....	I-20

## THEORY AND PRACTICE OF SELF-LUBRICATED, OSCILLATORY BEARINGS FOR HIGH VACUUM APPLICATIONS

### Part II - Accelerated Life Tests and Analysis of Bearings

#### ABSTRACT

A seven year, interdisciplinary effort was recently completed to develop self-lubricating bearings capable of continuous oscillatory motion for 5+ years in high vacuum while maintaining arc second alignment accuracy of precision gimbal pointing mechanisms.

This paper, the second in a two-part series, describes a series of accelerated vacuum life tests, designed to monitor and map the performance characteristics of the dry lubricated bearings throughout their lifetime of service by continuous monitoring of friction torque and periodic evaluation of the effects of temperature cycling and radial temperature gradients. Operating stresses were accurately controlled by initial preloading and through accurate control of radial thermal gradients. Operating loads and stresses were optimized by theoretical analysis and bearing wear and performance were compared with theoretical predictions.

Twenty-two (22) bearing specimens were tested for periods up to 15,000 hours in high vacuum and operated successfully for up to  $31 \times 10^9$  degrees of oscillatory travel.

Friction, wear and bearing torque test data, combined with optical-scanning electron microscopic and x-ray energy dispersive spectroscopic examination of the test bearing components, were used to develop a theoretical model of wear behavior. The ultimate life capability of this system was estimated using the theoretical model and extrapolation of empirically determined wear rates.

## INTRODUCTION

Dry lubrication offers certain advantages over fluid lubrication for spacecraft gimbal bearings. Dry lubricated bearings can be stored for years without "re-oiling" before use. Outgassing and deposition of oil films on optical surfaces are also eliminated. Mechanism designs can be simplified because oil reservoirs, anti-migration barrier films, and labyrinth seals are not required. Previous studies (References 1, 2 and 4) have also indicated that accelerated life tests of dry lubricated wear systems can be correlated more accurately with real time system performance than accelerated tests of fluid lubricated bearings.

The design-to-operation time period for most modern machinery is too short to permit real time life testing to establish life and reliability of bearing systems. Consequently, the capability for quickly obtaining life performance results by accelerated life testing is a significant advantage of dry lubricated bearings over fluid lubricated systems which are much more difficult to evaluate by accelerated testing.

The previous work (Part I of this two part series) evaluated candidate ball, raceway and separator transfer materials combinations in sliding block and bearing simulator test machines. However, the very complex kinematics of ball bearings cannot be simulated accurately by such tests and ultimately the performance capability of bearing/lubricant systems must be evaluated in actual ball bearing tests. The objectives of this life test program were to 1) obtain an accurate measure of gimbal bearing performance, 2) determine the degree of correlation between materials wear tests and full scale bearing tests and 3) obtain the maximum amount of information on bearing wear parameters by a test matrix covering a range of ball rolling velocities, test time periods and Hertzian contact stresses.

Because preloaded duplex bearing pairs are sensitive to installation fits, thermal variations, and mechanical properties of mounted shaft and housing components, the test apparatus was designed to simulate an actual spacecraft gimbal (Reference 5) in every significant characteristic. Bearing fits, preload clamping, shaft and housing materials were identical to the intended gimbal system. Additionally, a combination active/passive thermal

control system consisting of radiators and electric heaters provided control of bearing ball to raceway loading by controlled radial thermal expansion of shafts and housings.

#### ACCELERATED TESTING

Acceleration of a bearing test by operating at higher than design speed poses certain theoretical questions as to the correlation of test results and actual system real time performance.

By an examination of bearing physics, and possible failure modes, a reasonably valid means for accelerating dry lubricated bearing tests might be established. Running a dry lubricated bearing at speeds higher than design will result in more stress cycles of the balls and races per unit time and more total travel of the moving parts. High speed testing also results in high <sup>er</sup> sliding velocities between the separator and balls and races. The increase in stress cycles and total travel of balls and ball separator surfaces achieves the desired end of accelerating testing of the bearing for fatigue failure. Previous work in fatigue life testing of materials has shown that high cyclic rates of stress application can be used to simulate lower cyclic rates of load application with a high degree of correlation. The total travel achieved by accelerated testing will give information on wear behavior provided the wear per unit travel is reasonably close to the wear rate at design speeds.

This effort was aimed at developing bearings for a 5 year life system in a one to two year period and a 6:1 acceleration factor was chosen as a goal.

#### Ball Separator Wear

Cardos, in Part I of this paper series, developed a model of glass reinforced teflon/MoS<sub>2</sub> ball separator wear as a function of sliding velocity:

$$\Delta V = K'' P_{II}^{\alpha} V^{\beta} t^{\gamma} \quad (1)$$

where:

$\Delta V$  = wear volume loss,  $\text{cm}^3$

$K''$  = wear coefficient

$P_H$  = ball, race mean Hertzian stress,  $\text{g (force)} \cdot \text{cm}^{-2}$

$V$  = ball/composite sliding velocity,  $\text{cm} \cdot \text{sec}^{-1}$

$t$  = time, second

$\alpha, \beta, \gamma$  = empirically determined constants

Using Gardos parameters with a 100 gram load (an estimate of typical ball to ball pocket loads) and values of  $\alpha = 0.88$ ;  $\beta = 0.71$ ; and  $\gamma = 1.0$ , if the velocity were increased to 6 times the design speed, then a 3.5 times increase in the ball separator wear rate might be expected; i.e.,

$$\left(\frac{6}{1}\right)^{0.71} = 3.5$$

Snediker using a ball bearing simulator described in Reference 3 found by experiments (see Acknowledgements) on wear rate of the glass reinforced "Teflon" PTFE/MoS<sub>2</sub> ball separator that separator wear increases with speed by about 20 percent at six times the actual operating velocity.

Snediker's and Gardos' results are somewhat different and one can only speculate that the difference is probably due to the difference in test apparatus. (Gardos single ball bearing simulator machine and Snediker's slider tests are, of course, both significant departures from a ball bearing with cylindrical shaped separator pockets.) At any rate, Snediker's and Gardos' work show that it is safe to conclude that the ball separator, when operated at speeds higher than the design speed, will wear at a rate (volume/unit travel) somewhat greater than actual operational conditions. The separator wear rate appears in all cases to make more PTFE/MoS<sub>2</sub> available than actually utilized in lubricating the races and balls. Examination of these and other bearings following long term life tests shows that some of the separator material removed does not end up on the balls and wear track of the race grooves but extrudes and shifts out of the bearing as powdery debris.

The rate of deposition and actual coating of races and balls versus velocity is a complex process resulting from double transfer from separator to ball to raceways and a compacting action of the balls as they traverse the raceways. As no tests have been conducted to evaluate this phenomena and how it is affected when life tests are accelerated, we are left to estimate film buildup rates from such data as friction torque and post test bearing surface evaluations.

#### Ball and Race Wear

Ball and raceway wear rates (volume/unit travel) would probably increase slightly with a six times increase in speed because the micro-asperity heating would be greater and the impact energies of contacting asperities greater. Cunningham (Reference 2) found that dry lubricated silver slip ring brush materials using molybdenum disulfide lubricant running on solid coin silver rings have wear rates (volume wear/unit travel) that are virtually identical with variations in velocity from 7.87 cm/sec (3.1 in/sec) to 264 cm/sec (104 in/sec), a ratio of 33 to one in velocities. The baseline system ball/separat or velocity under normal operation is approximately 1.78 cm/sec (0.7 in/sec) and running at six times normal speed the velocity is about 10.7 cm/sec (4.2 in/sec) which fits reasonably within the range tested by Cunningham. Although the slip ring brush test results are obviously not directly relatable to the ball raceway wear rates, they do nonetheless serve to illustrate that dry lubricated metallic surface wear rates per unit travel tend to be relatively unchanged with increasing velocity.

From the above discussion it is reasonable to expect higher wear rates of the lubricant transfer ball separator, and approximately equivalent wear of the ball/raceway contact regions under accelerated test conditions. With this premise in mind, the gimbal accelerated bearing life tests were conducted at four different velocities (ball to raceway) so that the wear results could be evaluated to determine if the higher velocity in the accelerated test distorted the results.

## EXPERIMENT

Twenty-two bearings (11 duplex pairs) were tested in ion pumped ultra high vacuum chambers at pressures from  $10^{-6}$  to  $10^{-9}$  Torr. The tests ranged in duration from 6,000 hours to 15,000 hours. The test matrix is summarized in Table 1. The bearing bulk temperatures were varied from  $6.7^{\circ}\text{C}$  ( $44^{\circ}\text{F}$ ) to  $31.1^{\circ}\text{C}$  ( $88^{\circ}\text{F}$ ). The radial thermal gradients were very closely controlled to regulate the ball to raceway contact stresses of the duplex bearing pairs.

The test bearings were angular contact, duplex pair ball bearings ABEC 7, of 440C corrosion resistant steel with a six piece segmented ball separator of glass fibre reinforced PTFE with 5 percent MoS<sub>2</sub> ("Composition A" in the Part I paper of this series). The test bearing parameters are summarized in Table 2.

The preloads were selected to keep operating stresses low for maximum fatigue life and for optimum dry film lubricant performance. Previous experiments (personal communication with Dr. David Snediker) had shown that above 1.17 G Pa (170,000 psi) mean Hertzian contact stress the PTFE, MoS<sub>2</sub> dry film lubricant offers little wear protection, and metallic wear rates are too high for long life operation. At stresses below 551.6 M Pa (80,000 psi), ball bearings become too compliant and weight inefficient for spacecraft mechanisms.

All tests were oscillatory with bearings travelling from as little as  $\pm 8$  degrees to as much as  $\pm 250$  degrees. The oscillatory pattern was advanced around the bearing to prevent lubricant bump buildup which can occur when dry lubricant bearings oscillate over a fixed travel pattern for many cycles.

The test apparatus consists of beryllium or stainless steel vertical shafts driven by brushless DC motors. The duplex pair test bearings were mounted on the shafts and the outer race pairs were fitted into free floating housings. The floating housings were attached to piezo-electric loads cells for monitoring running friction torque. A typical test apparatus is shown in Figure 1.

Friction torque was monitored continuously as a means of failure detection and also to detect excessive lubricant film buildup which would show up as an increase in friction torque due to lubricant induced increases in the ball to raceway loading.

## EXPERIMENTAL RESULTS AND ANALYSIS

All 22 bearings in the experiments operated satisfactorily for the duration of the tests although some minor adjustments were required in the radial temperature gradients of the bearings in test Number II to avoid high running torques.

### Friction Torque

The friction torques of the four bearing test groups are plotted in Figure 2. The friction torque of most bearing pairs exhibited a characteristic torque increase during the first 500 to 1000 hours. After about 1000 hours, the friction torques declined very gradually for the remainder of the test. The one exception to this is Test II where the radial thermal control system was exercised more frequently resulting in somewhat erratic bearing torque results compared with the other tests where more steady state thermal conditions were maintained.

A hypothetical explanation is offered for the torque buildup and gradual decline. The initial increase and the long term decrease are believed to be due to two different phenomena. The initial transient increase is believed to be due to a buildup in the lubricant film thickness. The bearing races and balls are initially stick burnished with a thin film of ball separator material (PTFE and molybdenum disulfide). During the first few hundred hours, lubricant material picked up by the balls from the separator pockets deposits on the raceway faster than it is being worn away. This results in an increasing lubricant film thickness and consequently higher ball to raceway loads. The higher ball loading manifests itself as an increase in bearing rolling friction torque. At about 500 to 1000 hours the lubricant film reaches an equilibrium thickness and does not increase further. As the bearings operate over thousands of hours, another process proceeds simultaneously. The raceway wears very slowly (a few hundred micrometers over the entire life test) as illustrated by surface topography measurements described below. The gradual microscopic wear process removes a few hundred micrometers

of lubricant and metal from the raceway, increasing internal clearances and therefore reducing ball loading and rolling friction torque. Further work including precise measurements of dry film thickness changes is suggested however to further support (or refute) this hypothesis. From this hypothetical model one would conclude that for a dry lubricated ball bearing system to operate successfully, the rate of transfer lubricant from the sacrificial ball separator to the balls and raceways must be matched closely with the rate of lubricant and metallic wear loss otherwise internal clearances will change resulting in either loss of preload or increases in running torque. Because when this test series was initiated it was not known if this equilibrium lubricant film thickness state would persist, radial thermal gradient control was included in the bearing design.

As discussed above, the optimum functioning of a dry lubricated ball bearing system requires a somewhat delicate balance between the rate of lubricant transfer to the balls and raceway and lubricant loss rate or raceway wear. Various post test analyses and measurements were made to gain insight into these processes to aid in estimating the ultimate life capability of this type bearing system. The results of ball separator wear (and transfer) were compared below with theoretical predictions developed in part one of this two part paper series.

#### Ball and Raceway Wear

The balls and raceways were examined by optical microphotography, Reichart metallographs, scanning electron microscope (SEM) and electron dispersion analysis with X-rays (EDAX).

Raceway photomicrographs (see Figure 3a) show reduction in the original machining marks in the ball wear track although the machining marks are still visible. SEM photos (Figure 3b) show the lamellar platelet-like orientation of the transfer film on the raceway. The lubricant films were thin but still provided complete coverage except for a few scattered patches where the film is too thin to detect (or non-existent). EDAX analysis of the raceway films showed sulfur, silicon, and molybdenum, the materials in the ball separator transfer film and some iron and chromium presumably traces of ball and raceway wear debris.

The ball separator pockets show semi elliptical wear scars ranging from a very small thin area as shown in Figure 4b to deeper cavities with some buildup as shown in Figure 4a.

### Ball Separator Pocket Wear

The long term bearing lubricant supply must come from transfer from the ball separator pocket to the ball and the ball to raceway (double transfer). Otherwise, as the initially burnished on lubricant film is slowly worn away, the bearing raceways would become bare and susceptible to increased wear rate.

The ball separators were removed from all test specimens after the life tests and the ball pocket wear determined by a series of measurements of the wear scar. Mechanical measurements were chosen because weighing the ball separator segments before and after (which weigh about 7.0 grams) would require at least an accuracy of 0.01 milligram on a measurement of 0.6 milligram change due to wear. A microbalance with this accuracy was not available. From examination of the ball pockets, it was determined that the wear scars (see Figure 4a and 4b) come pretty close to the elliptical shape expected from ball to cylinder contact.

The wear scar depths were measured using a stylus surface analyzer ("Tallysurf" : profilometer. Typical wear scar traces are shown in Figure 5. Examination of Figure 5 shows that the wear scar indentation is very nearly parabolic in form. Therefore, by measuring the wear scar length, width and depth it should be possible to estimate the wear volumes.

Figure 6 is a view of a ball pocket showing the geometric model used in measuring the wear volume. The wear scar has approximately the shape of an elliptical paraboloid and the volume can be calculated from:

$$V = \frac{\pi}{2} a b h \quad (2)$$

where

V = wear scar volume ( $\text{cm}^3$ )

a = half length of elliptical wear scar (cm)

b = half width of elliptical wear scar (cm)

h = depth of wear scar (cm)

The results of ball separator volume wear of a number of ball pockets in tests II, III, and IV are shown in Figure 7.

Gardos in Part I of this series developed equations for predicting the wear or "transfer" rate of the ball separator material (Composite A). His equations are based on unit loading corresponding to ball to pocket loading of 100 grams only. One can easily show from kinematics that all balls in the test bearing could not simultaneously exhibit 100 gram loads on the ball separator. The friction torque power losses of the ball to separator forces must be overcome by the bearing drive torque and therefore:

$$T_f \approx \sum_0^n F_b [(1 - \mu)(R - r_b) + 1/2 (R + r_b)] \quad (3)$$

(See Appendix for derivation of equation 3.)

where

$T_f$  = friction torque due to ball separator forces (gm-cm)

$F_b$  = force of ball to separator (gm)

$\mu$  = friction coefficient of ball to separator (~ 0.08 in vacuum)

R = pitch radius of ball orbit (cm)

$r_b$  = ball radius (cm)

n = number of balls

From Equation 3, the friction torque of Type I and II bearings with all 90 balls exerting 100 gram forces on the ball separator should be of the order of  $3.5 \times 10^5$  gm cm due to the ball separator alone. Actual measured torques were typically around  $4 \times 10^3$  gm cm.

A more likely condition from the authors observations of segmented ball separator operation is that two balls in each segment would be in contact (due to ball train accordion differential travel rates, see Reference 6). The remaining balls are typically either operating in the clearance space in the ball pocket or in contact at much lower force levels than the two "controlling" balls. If one accepts this model, then only two balls per separator segment would be in loaded contact and transferring lubricant at any given time. The remaining balls would be "idling" with respect to separator contact.

Using this concept of "controlling ball pair" contact we would have 12 balls in a six segment separator bearing transferring lubricant and in the I and II Test Series this would give an equivalent duty cycle of 12/90 or 0.133 and similarly for the III and IV Test Series bearing a duty cycle of 12/54 = 0.222.

Using the duty cycle applied to the transfer time ( $t$ ) in Gardos' equation and assuming that his test condition of 100 grams ball load to be representative, the wear per separator pocket can be calculated, i. e.,

$$\Delta V = 3.41 \times 10^{-17} P_H^{0.88} V^{0.71} t^{1.0} \quad (4)$$

The calculated values are plotted in Figure 7 with the actual measured ball pocket wear. The theoretical is higher by a factor of about four for Test Series III and IV and a factor of 2 for Test Series II.

This limited correlation, while not as close as we would like, does show some degree of agreement between theoretical predictions made from sliding block tests and actual ball and separator behavior. It is very close considering the fact that Gardos tests were run simulating only one ball to pocket condition of 100 grams, and the authors analyses suggest that the ball to pocket loads are probably less than 100 grams. Clearly more work is required to be able to confidently relate materials wear/transfer test data to actual bearing operating conditions. Good data is required on:

- Ball to separator pocket forces.
- Ball to separator dynamics.
- Actual contact pressure and pressure area between balls and separator pockets.
- Traction forces of balls against separator.

While the apparent correlation in ball pocket wear here is encouraging, the validity of the two ball contact model upon which the theory is based remains to be verified or refuted by future work on ball to separator kinematics and dynamics. Sliding block tests at ball contact simulated loads other than 100 grams are also needed to compare with ball pocket wear results.

## Raceway Wear

A system was developed for approximately measuring raceway wear using stylus surface analyzer ("Tallysurf") traces of the wear track and calculation of the wear scar volume.

The surface of each bearing inside and outside raceway (see Figure 8) was mapped with a stylus surface analyzer at 90-degree intervals creating surface traces as shown in Figure 9. Numerous other surface regions were also mapped and it was found the wear track was relatively uniform around the circumference of each raceway except at high points of noncircularity in the raceway groove where locally high wear occurred. Because of the relative uniformity of wear around individual raceway grooves, a geometric approximation of the wear scar was made by treating it as a circular development of a secant as illustrated in Figure 10. The implicit assumption here is that the wear in each 90-degree quadrant is uniform and can be represented by the depth of the wear scar ( $h$ ) measured by the stylus surface analyzer.

The wear volume can be calculated from the equation:

$$V \equiv \sum_{h_o}^{h_i} \frac{1}{2} \pi D \left\{ \frac{1}{2} d \left[ \frac{1}{3} (8\sqrt{dh} - 2\sqrt{h(d-h)}) \right] + 2h\sqrt{h(d-h)} \right\} \quad (5)$$

where

- V volume of raceway wear scar ( $\text{cm}^3$ )
- D pitch diameter of ball wear track (cm)
- d ball diameter (cm)
- h depth of wear scar (cm)

Using equation (5), the wear volumes were calculated from stylus surface analyzer wear scar depth measurements at 90-degree intervals around the raceways and the results of the four groups of tests are plotted in Figure 11. The wear volume measurements were then averaged and the averages also plotted as a  $\Delta$  on Figure 11. Although there are significant

variations in individual wear scar measurement depths, the average suggest wear volume is a direct function of ball travel. The four tests represent a significant range of design parameters and test conditions. Ball orbit pitch diameters were 13.65 cm (5.375 inches) and 27.94 cm (11.0 inches). Ball to race velocity ranged from 2.02 cm/second (0.797 inch/second) to 47.75 cm/second (18.8 inches/second) and test times varied from 6000 hours to 15,000 hours.

The wear volume measurements exhibit significant scatter and a statistical significance analysis of the data was made. The one sigma deviation about the average is also plotted in Figure 11. The scatter is partly due to the fact that wear processes tend to vary from specimen to specimen (Reference 1) due to variations in surface finish, mating surface conformity, machining variations, transfer film completeness and local rheology.

This raceway wear analysis is of course a first effort. The measurement technique is subject to various errors including incomplete removal of lubricant film from the raceway and wear track, non circular shape of the wear scar (as was assumed in the wear calculations) and geometric interpolation errors in measuring the tallysurf traces. However, while the errors show a need for improved instrumentation and wear measurement techniques, the data seem to verify the theory that ball bearing raceway wear is a function of total ball to raceway travel and relatively insensitive to velocity within the test range.

## CONCLUSIONS

Tests on 22 ball bearings have demonstrated the capability for gimbal bearings lubricated with dry film lubricants and sacrificial transfer ball separators to operate for periods exceeding 15,000 hours and travels of over  $30 \times 10^9$  degrees in hard vacuum. These designs were the direct result of lubricant materials and process development in sliding block and ball bearing simulator friction and wear tests and demonstrated a reasonably good agreement between performance in the full scale bearing tests and predicted performance in the materials friction and wear tests.

Friction torque performance shows a gradual buildup of lubricant film thickness during the first few hundred to a thousand hours. The normal wear processes gradually offset the effects of lubricant buildup and as the wear process slowly decreases the ball to raceway loads, the friction torque diminishes permitting potentially long life operation.

Examination of the lubricant by SEM photomicrography shows a thin (approximately 10,000 Å) but adequate lubricating film over most of the bearing working surfaces and a definite ordering of the transfer film due to the high Hertzian stresses with the minimum force shear planes aligned along the ball rolling direction. The presence of ball separator lubricating material on the races and balls after thousands of hours of testing shows the effectiveness of the sacrificial ball separator in providing long term ball bearing raceway lubrication.

Measurements of ball separator pocket wear show acceptably low wear (transfer) rates for long life bearing operation although a significant amount of the separator material does not find its way to the wear track, but sifts out of the bearing as powdery debris. Theoretical predictions of ball separator wear rates were compared with the measured ball pocket wear (transfer) and within the limits of the assumptions made regarding ball to separator forces, acceptable agreement was found. More work is clearly suggested by this effort to more fully understand and to quantify the forces and interactions between the balls and ball separator in ball bearings.

Raceway wear measurements on these bearings which operated over a wide range of ball to raceway speeds from 2.0 cm/second to 47.6 cm/second suggest that wear is relatively independent of ball speed and simply a function of total ball travel. The measurements on raceway wear were made using Tallysurf traces and geometric calculations however, and more precise methods such as radiographic analysis using radioactive isotopes could be used to further study this hypothesis.

This work was directed toward rather ambitious goals to find correlations between full scale ball bearing tests, and materials friction and wear tests, and to evaluate the effects of testing dry lubricated ball bearings at a

variety of speeds as a means of determining feasibility of accelerated testing of dry lubricated ball bearings. While the data analysis clearly shows correlations with the theoretical predictions from sliding block friction and wear tests on separator material, a more detailed study of the kinematics of ball to separator forces and interactions is required before the bearing designer can go directly from materials performance tests to accurate estimates of new materials behavior in ball bearings.

The test results also support the hypothesis that dry lubricated bearings can be tested at high speeds to provide life test information in less than real time because wear rates were shown to be fairly uniform over a wide range of velocities. The slow steady equilibrium race wear and ball transfer processes appear to be predictable and relatively uniform over a wide range of velocities.

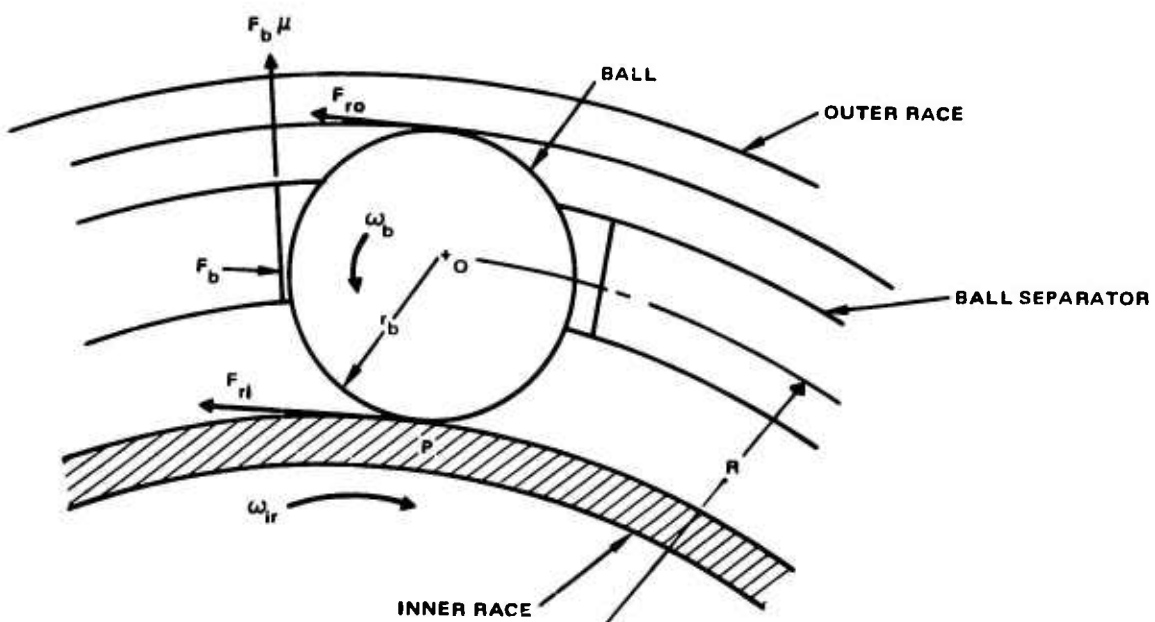
#### ACKNOWLEDGMENTS

The author expresses his appreciation to Mr. Mike Gardos of Hughes Aircraft Co. for his support and collaboration in this effort, to Dr. John Bohner of Hughes Aircraft Co. for his assistance in SEM photomicrography, to Mr. Hans Metzler for assistance in stylus surface analysis, and to Dr. Dave Snediker of Battelle Columbus Laboratories for providing unpublished test data on his dry lubricant film test work.

## REFERENCES

1. Hopkins, Vern, and Lavik, M. T., "Accelerated Testing of Solid Film Lubricants", Lubrication Engineering, Vol. 28, No. 10, p. 365, October 1962.
2. Cunningham, A.C., "Long-Life Slip Rings for Vacuum Operation", IEEE Transactions, Parts, Material and Packaging, Vol. PMP 7, No. 1, p. 48, March 1971.
3. Snediker, D. K., "An Apparatus for the Investigation of Lubricant Transfer Mechanisms in Low-Speed Oscillatory Bearings", Wear, 30, 135 (1974).
4. Meeks, C. R., "Accelerated Testing of Ball Bearings", Lubrication Engineering, Col. 28, No. 10, p. 373, October 1972.
5. Kramer, N. R., "Gimbal Bearing Design Considerations and Friction Control, Paper presented at 13th Aerospace Mechanisms Symposium, Houston, Texas, April 26-27, 1979.
6. Barish, T., "Ball Speed Variation in Ball Bearings and Its Effect on Cage Design", Lubrication Engineering, No. 25, 110 (1969).

APPENDIX  
ANALYSIS OF BEARING TORQUE DUE TO  
SEPARATOR FORCES



For static equilibrium

(a)

Summing moments about point O:

$$F_b \mu r_b - F_{ro} r_b + F_{ri} r_b = 0 \quad (b)$$

and about point p

$$F_b r_b - F_{ro} 2r_b = 0 \quad \therefore F_{ro} = 1/2 F_b \quad (c)$$

Combining (b) and (c)

$$F_{ri} = F_b (1 - \mu) \quad (d)$$

Solving for torque about bearing centerline ( $T_f$ )

$$T_f = F_{ri} (R - r_b) + F_{ro} (R + r_b)$$

or

$$T_f = F_b \left[ (1 - \mu)(R - r_b) + 1/2 (R + r_b) \right]$$

and for all balls in contact:

$$T_f = \sum_0^n F_b \left[ (1 - \mu)(R - r_b) + 1/2 (R + r_b) \right]$$

TABLE I. BEARING LIFE TEST MATRIX

Test Number	Number of Bearings	Bearing Size (cm)	Test Duration (Hours)	Total Travel (Degrees)	Ball to Raceway Velocity (cm/sec)	Calculated Average Mean Hertzian Stress (MPa)
I	2	26.67 bore 2.54 wide (10.500 in. bore) (1.000 in. wide)	8,900	$10 \times 10^8$	5.8*	758 (110,000 psi)
		26.67 bore 2.54 wide (10.500 in. bore) (1.00 in. wide)	10,000	$11 \times 10^8$	5.8*	
II	8	26.67 bore 2.54 wide (10.500 in. bore) (1.00 in. wide)	10,000	$5.6 \times 10^8$	2.0**	586 (85,000 psi)
		12.7 bore 1.90 wide (5.00 in. bore) (0.750 in. wide)	6,000	$31 \times 10^9$	23.8*** and 47.6***	
III	6	12.7 bore 1.90 wide (5.00 in. bore) (0.750 in. wide)	15,100	$31 \times 10^9$	23.8*** and 47.6***	578 (84,000 psi)
		12.7 bore 1.90 wide (5.000 in. bore) (0.750 in. wide)				
IV	6					675 (98,000 psi)

\*Note; certain portions of test were run at slower velocity (1/6) than that listed during checkout and torque measurements (less than 5% of total time).

\*\*4800 hours at 23.8 cm/sec; remaining 10,300 hours at 47.6 cm/sec.

TABLE 2. TEST BEARING DESIGN PARAMETERS

Design Parameter	Test Number			
	I	II	III	IV
Outside Diameter	(11.500 inches) 29.21 cm	(11.500 inches) 29.21 cm	(5.750 inches) 14.605 cm	(5.750 inches) 14.605 cm
Inside Diameter	(10.500 inches) 26.67 cm	(10.500 inches) 26.67 cm	(5.000 inches) 12.700 cm	(5.000 inches) 12.700 cm
Width	(1.000 inches) 2.54 cm	(1.00 inches) 2.54 cm	(0.750 inches) 1.90 cm	(0.750 inches) 1.90 cm
Type	Angular Contact, DB Duplex Pair	Angular Contact, DB Duplex Pair	Angular Contact, DB Duplex Pair	Angular Contact, DB Duplex Pair
Ball Diameter	(0.2500 inch) 0.6350 cm	(0.2500 inch) 0.6350 cm	(0.1875 inch) 0.4445 cm	(0.1875 inch) 0.4445 cm
Number of Balls/Row	90	90	54	54
Unconstrained Preload (lb)	125	125	70	70
Contact Angle (Degrees)	29	29	25	25
Ball Separator	6 piece, Chopped Glass Fibre Reinforced PTFE with 5% Molybdenum Sulfide	Same as Test I	Same as Test I	Same as Test I

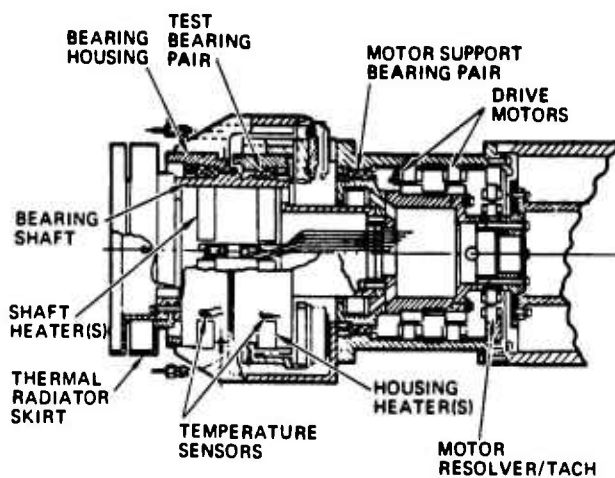
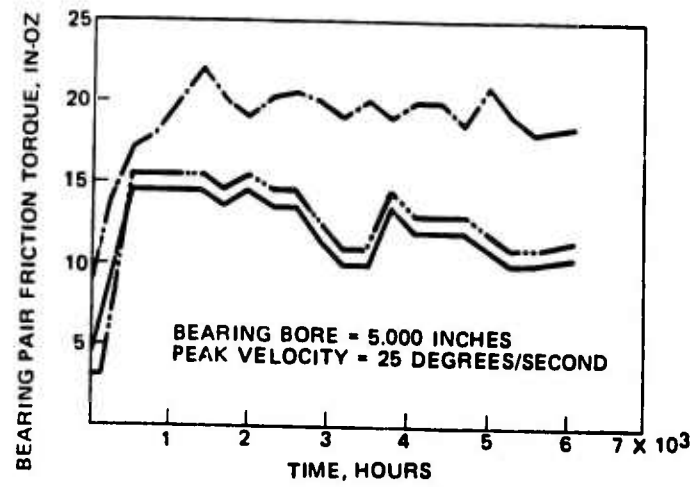
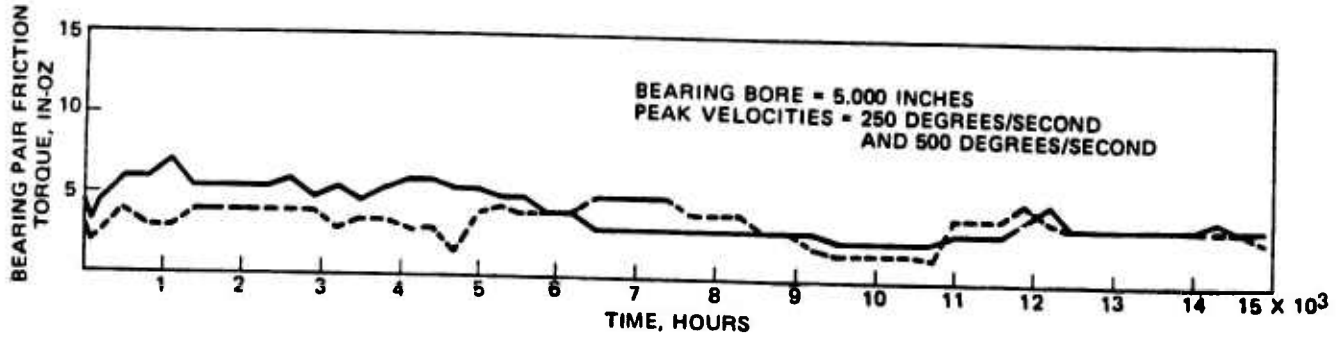


Figure 1. Typical test apparatus.

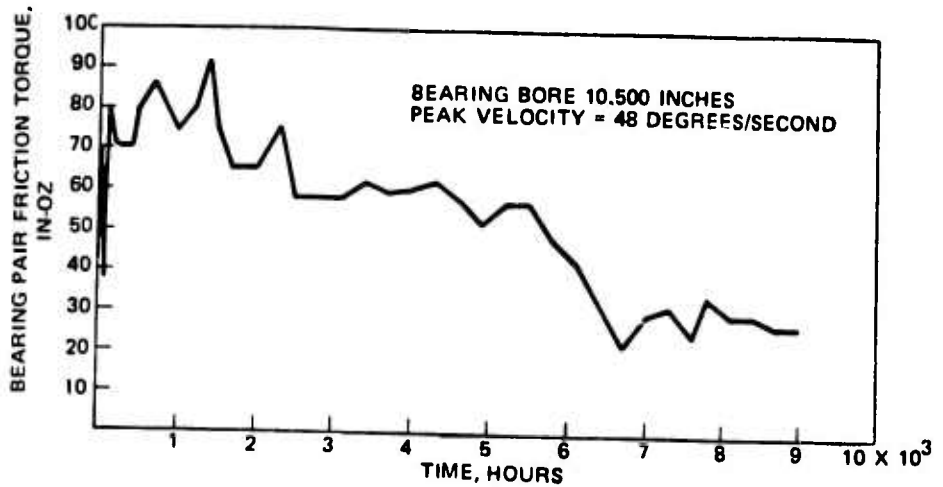


c. Friction torque vs time – Test III

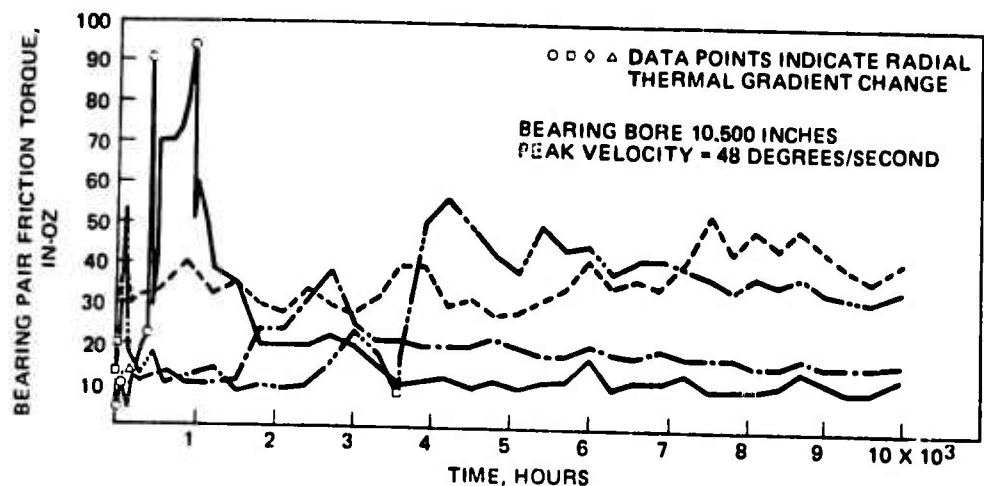


d. Friction torque vs time – Test IV

Figure 2. Bearing friction torque performance.

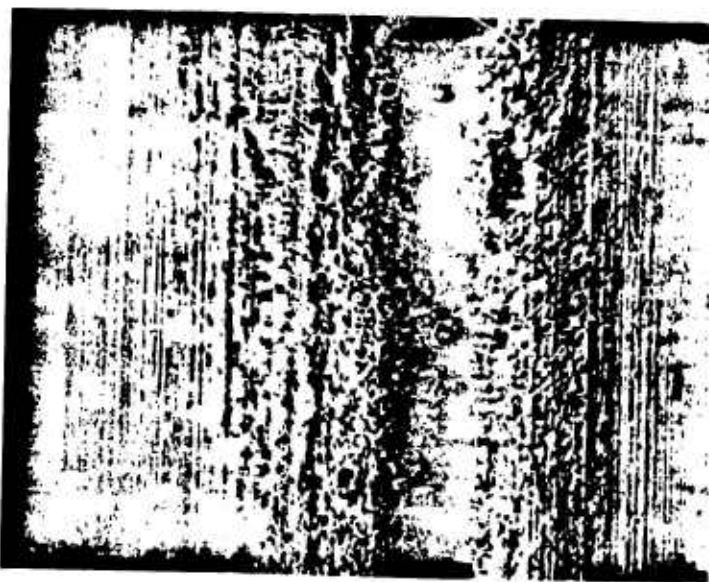


a. Friction torque vs time — Test I

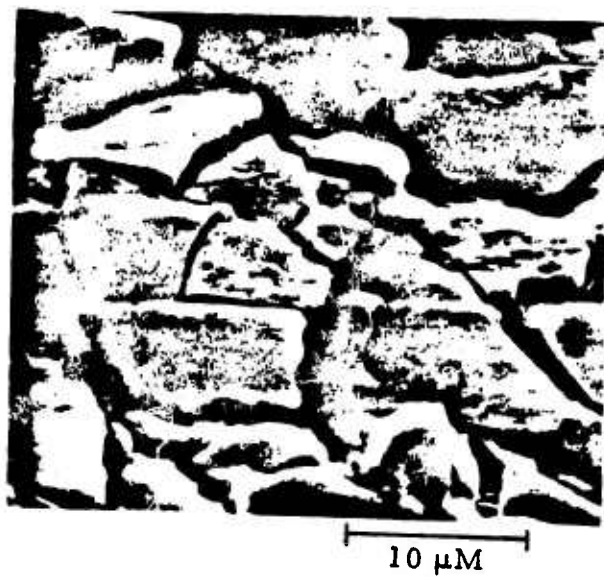


b. Friction torque vs time — Test II

Figure 2. Bearing friction torque performance.

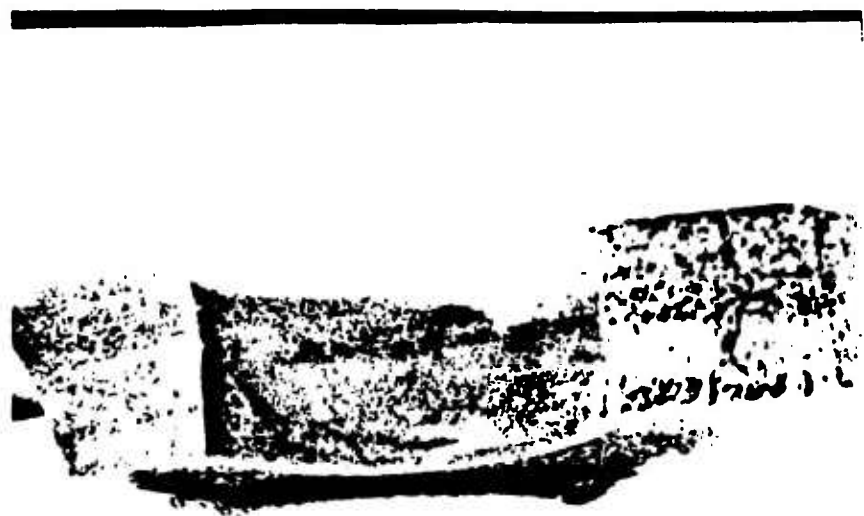


a. Photomicrograph of raceway  
wear track (100X)

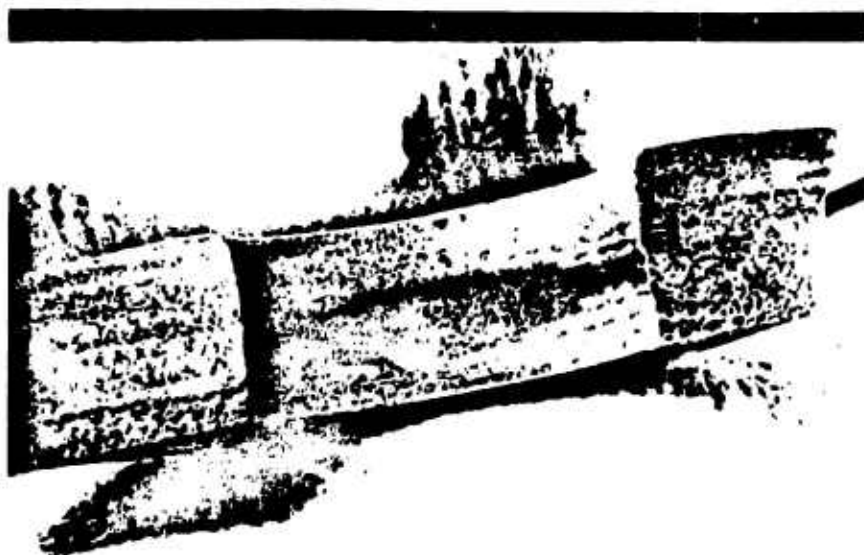


b. SEM photomicrograph of lubricant  
on raceway

Figure 3. Photomicrographs of bearing raceway  
and lubricant film.

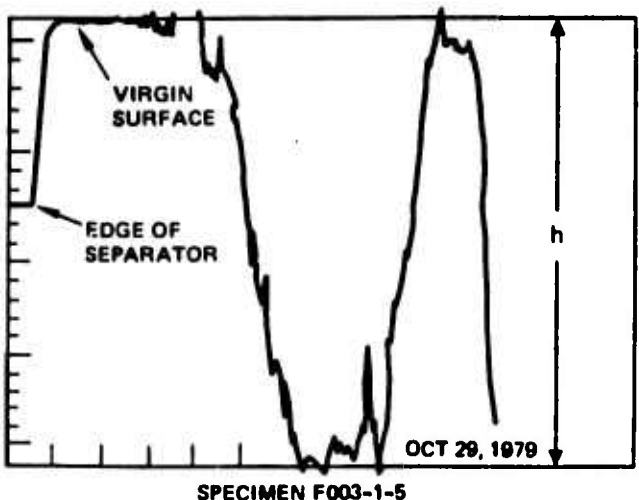


a. Low magnification (9X) photograph of a ball pocket wear scar in bearing S/N F003-1

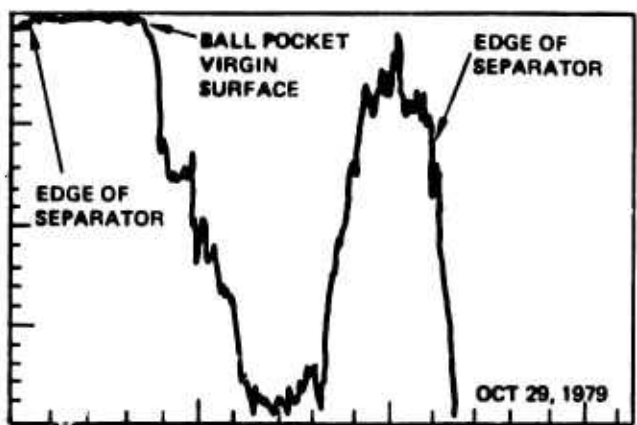


b. Low magnification (9X) photograph of a ball pocket wear scar in bearing S/N F003-2

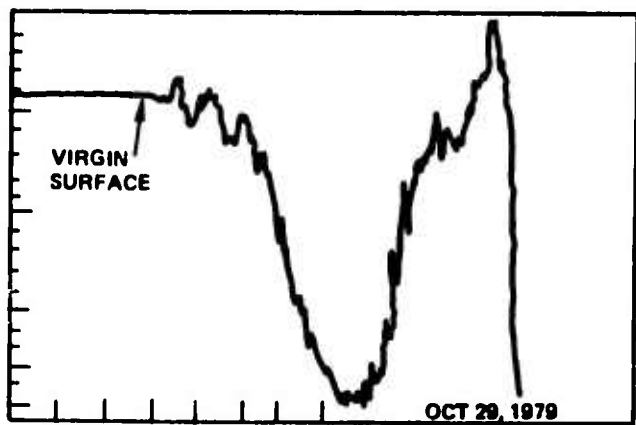
Figure 4. Ball pocket wear scars.



X → = 0.01 IN/DIVISION  
Y ↑ = 100 MICRO IN/DIVISION



SPECIMEN F009-2-6  
X → = 0.01 IN/DIVISION  
Y ↑ = 100 MICRO IN/DIVISION



SPECIMEN F006-1-3  
X → = 0.01 IN/DIVISION  
Y ↑ = 100 MICRO IN/DIVISION

Figure 5. Ball pocket wear scar traces.

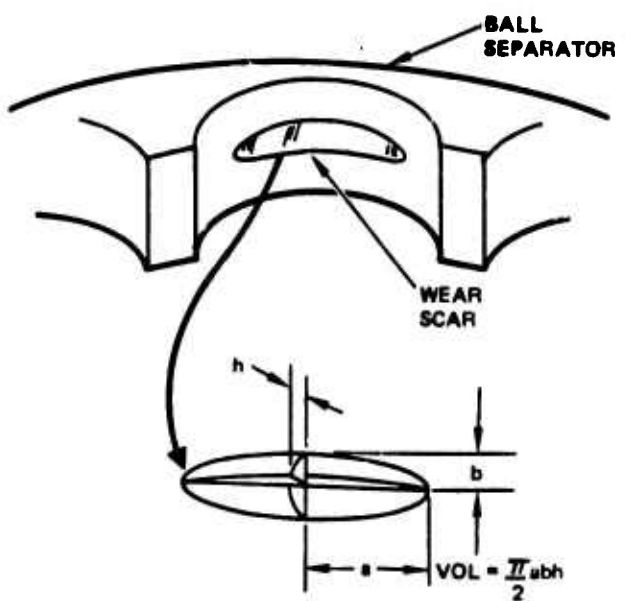


Figure 6. Measurement method for ball pocket wear scar.

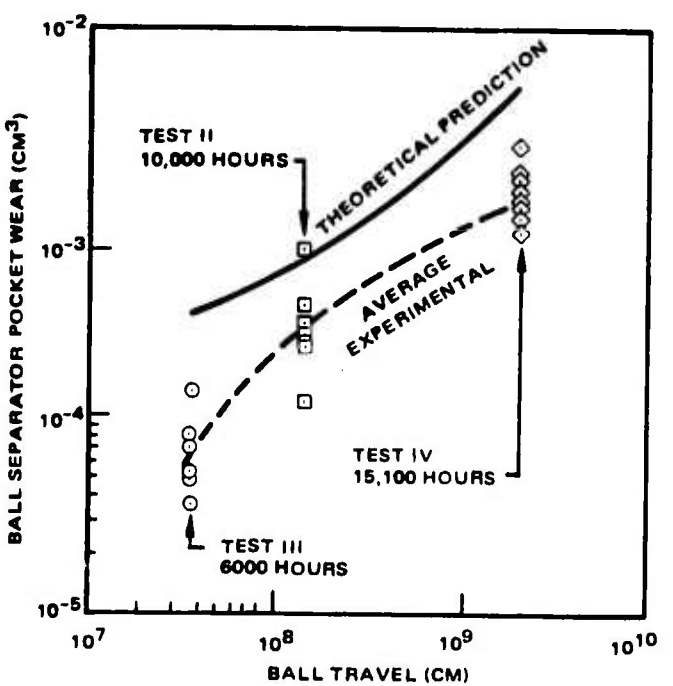


Figure 7. Ball pocket wear vs ball travel.

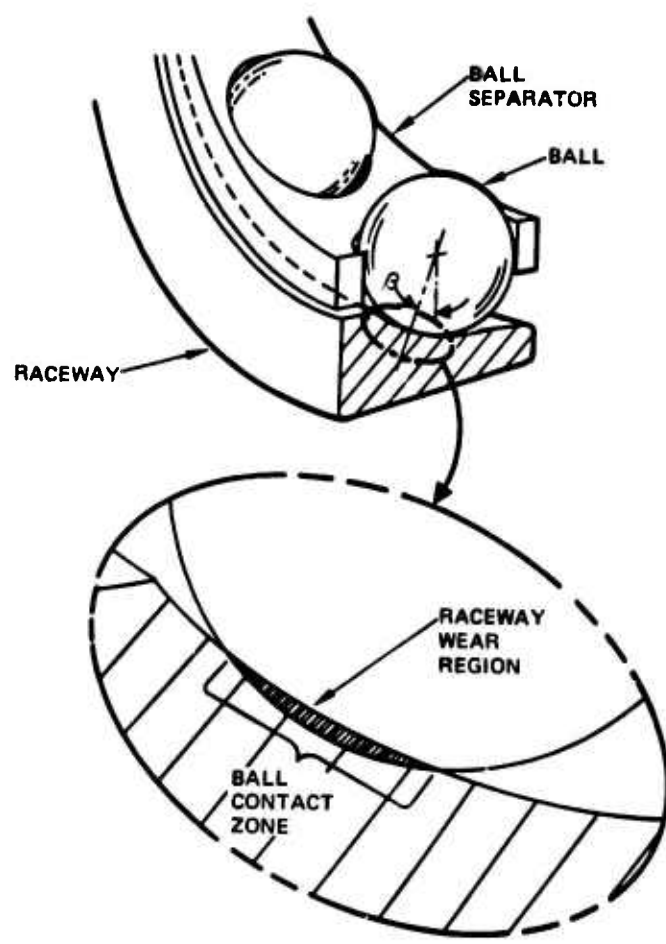


Figure 8. Raceway wear zone.

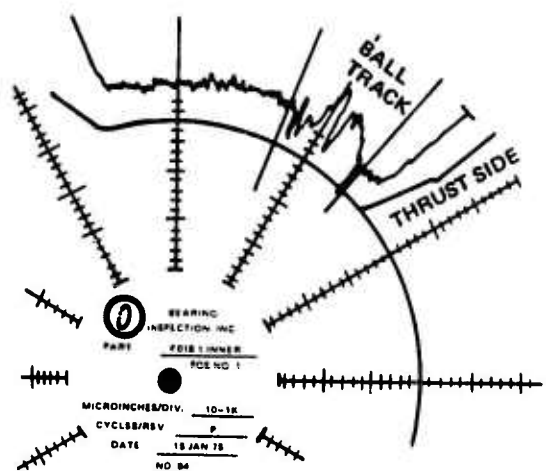
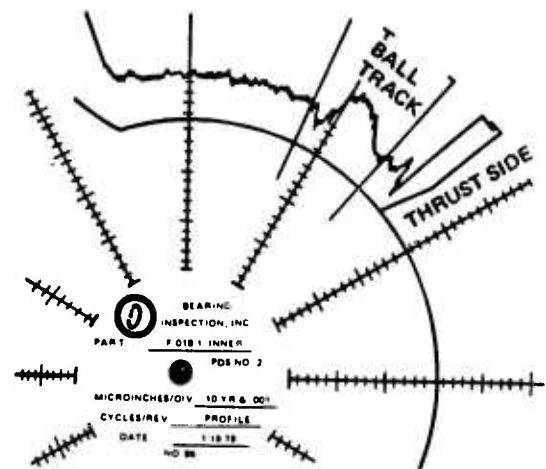


Figure 9. Stylus surface analyzer traces of race wear track.

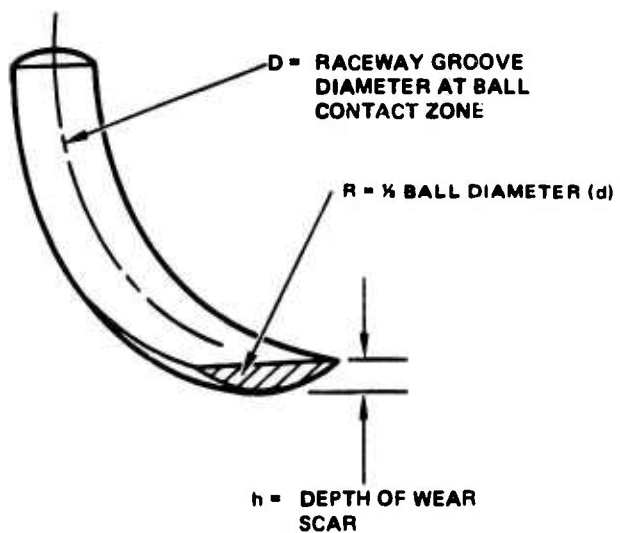


Figure 10. Wear volume model based on circular development of secant.

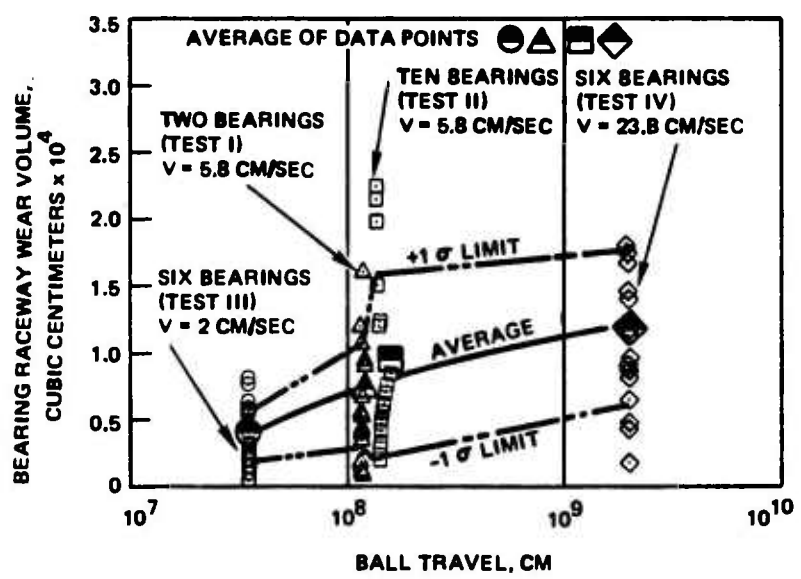


Figure 11. Bearing raceway wear vs ball travel.

**APPENDIX J**

**GUPTA, P. K. AND Eusepi, M.,  
"APPARATUS AND TECHNIQUE DEVELOPMENT  
FOR SOLID LUBRICATED BEARING,"**

Monthly Progress Report,  
Hughes P.O. 04-493436-FS5,  
Mechanical Technology, Inc.,  
Latham, New York,  
15 January 1980.

APPARATUS AND TECHNIQUE DEVELOPMENT FOR SOLID LUBRICATED BEARING

15 JANUARY 1980

SPONSORED BY:

HUGHES AIRCRAFT COMPANY PURCHASE ORDER NUMBER

04 - 493436 - F55

THROUGH

DEFENSE ADVANCED RESEARCH PROJECTS AGENCY (DoD)

DARPA ORDER NUMBER 3576

MONITORED BY AFML/MBT UNDER CONTRACT NUMBER F33615-78-C-5196

TO HUGHES AIRCRAFT COMPANY

SUBMITTED BY:

ADVANCED TECHNOLOGY DEPARTMENT

APPROVED

  
Wilbur Shapiro

Wilbur Shapiro

FORWARD

This report was prepared by Dr. Pradeep K. Gupta and Mr. Martin Eusepi under contract to Hughes Aircraft Company per Purchase Order Number 04-493436-FS5 effective starting date 1 October 1978 under the title of "Apparatus and Technique Development for Solid Lubricated Bearings." The work was administered under the technical direction of Mr. C. M. Meeks of Hughes Aircraft Company, with Mr. M. N. Gardos as Program Manager and principal investigator of the DARPA/AFWL/Hughes Solid Lubricated Rolling Element Bearing Program, DARPA Order Number 3576, AFWL Contract Number F33615-78-C-5196.

This report covers work conducted between 1 November 1979 and 31 December 1979 and is the seventh R&D Progress Report on this contract. This report will also suffice for the current semi-annual report since it contains most of the significant accomplishments during the last six months.

APPARATUS AND TECHNIQUE DEVELOPMENT FOR SOLID

LUBRICATED BEARING

Progress Report No. 7

1 November 1979 - 31 December 1979

By  
Pradeep Gupta  
Martin Eusepi

Test rig modifications for the type II bearing tests and the rotor dynamics analysis of the several possible configurations of the test stand were the primary activities during the above reporting period.

The implementation of the bearing testing for this program requires the modification of an existing test stand in order to provide both speed temperature and load capability commensurate with the programs work statement. The first step in the tester modification was the evaluation of four (4) possible rotor configurations employing rolling-element bearing for support. These concepts are illustrated in Drawings 646D003 and 004. Each configuration except concept 3 employs a two-piece rotor with concept 3 showing a one-piece rotor.

The general description of all concepts starts with the output shaft of the high speed (56,000 rpm) tester at the extreme left of each picture. Torque is transmitted through a high speed coupling to the test vehicle shaft. In concept 2, the test rotor shaft extends only past the first set of support bearings; concept 1 and 4 show the test rotor extending through both sets of support bearings, differing only in the method of attaching the remaining rotor section.

On the extreme right of each concept, an extended rotor section of a high temperature alloy which includes the mounted test bearing is shown. This rotor section acts as a heat dam, and is intended to provide at least a 400°F/in axial temperature gradient for the maximum test temperature anticipated.

Each of the concepts was reviewed prior to analysis to determine if they all were acceptable. Concept 2 was rejected because the complexity of the extra long primary tie bolt and anticipated rotor dynamics problems resulting from a rotor split between bearings. Concept 3 was rejected for two reasons; one reason was the shaft diameter between bearings was too small for good rotor stiffness, and the second reason was the anticipated difficulty in machining the entire rotor from a high temperature alloy.

Concepts 1 and 4 were analyzed for critical speed with good initial results, but both showed some rotor flexing at the first and second critical speed. It was felt that the rotor flexibility was easily remedied and the choice as to which model to use for further analysis was based on the more suitable attachment design of concept 1 which permitted a longer tie bolt to allow for an easier bolt stretch.

A full critical speed analysis was performed for concept 1 and produced the results shown on Figure 1 (curves labelled as 1). To study the effect of the tie bolt hole in the rotor, an additional analysis was performed assuming no rotor tie bolt hole. This result is plotted as concept 1a on Figure 1. The negligible difference between the two results affirmed the satisfactory tie bolt connection design at the interface between the high temperature alloy rotor section and the remainder of the rotor.

A test of rotor stiffness modification was then run assuming a journal diameter increase from 1 1/4" to 1 1/2" diameter. This change produced the results shown as 1b on Figure 1. The satisfactory critical speed map resulting from the journal diameter change permitted the rotor analysis to proceed to a rotor response and stability analysis. A review of the results to date and the experience MTI has gained over many years of high speed rotor design led to a conclusion that a ball bearing rotor support is not best suited for this application for the following reasons:

1. No damping of any consequence can be expected from the ball bearings to assist in controlling rotor response when traversing critical speeds

2. The operating DN of the bearings will exceed  $2 \times 10^6$  which would severely limit bearing life and performance

MTI has had excellent performance from pivoted shoe hydrodynamic oil bearings in their line of commercial high speed compressors. The advantages this bearing type affords is:

1. Control of bearing stiffness through geometric adjustments
2. A high level of system damping

The introduction of oil lubricated pad-type bearings may eliminate rotor response problems anticipated for the ball bearing design. MTI drawing 646E01 illustrates the initial layout of the test rotor employing the hydrodynamic oil lubricated journal and thrust bearings. This layout also shows the infrared heater in place around the test bearing and the tentative bearing housing design.

This design will be analyzed for rotor stability, unbalance response, and thermal behavior prior to any final design function.

The test specimens for the friction experiments have been received and the testing is now scheduled to start on or about February 1, 1980.

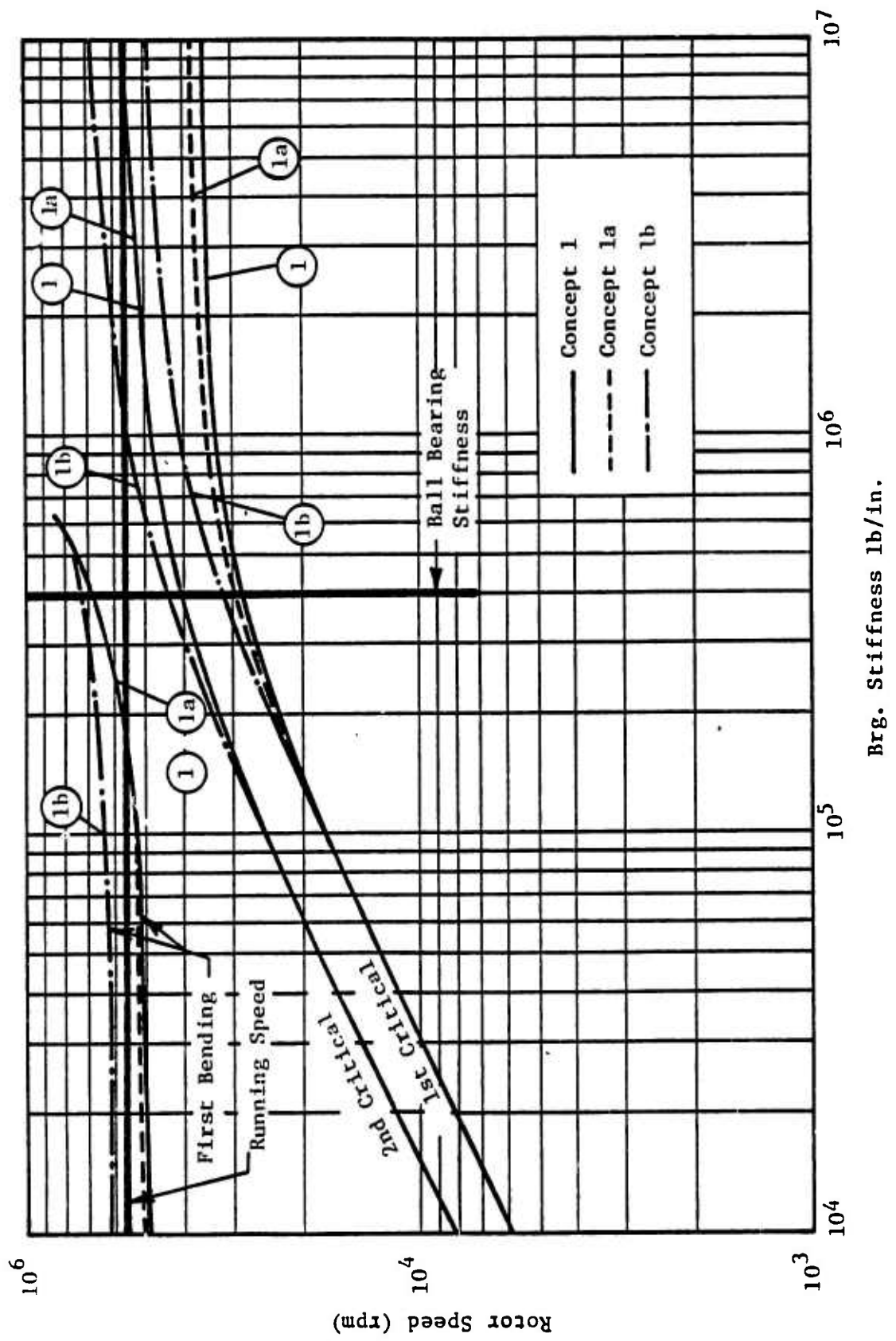


Fig. 1 Critical Speed Map for Hughes Hot Bearing Test Rig (Concept 1)

APPARATUS AND TECHNIQUE DEVELOPMENT FOR SOLID LUBRICATED BEARINGS  
 MICHIGAN AIR CRAFT COMPANY  
 (PO #04-493436-FS5)

Milestones	1978												1979												1980												Comments
	A	S	O	N	D	J	F	M	A	M	J	J	A	S	O	N	D	J	F	M	A	M	J	J	A	S	O										
PHASE I: COMPUTER MODELING																																					
Preliminary Runs on DREB																																					
DREB Modifications																																					
Pretest Runs on DREB																																					
Evaluation of Experimental Data																																					
Parametric Study																																					
PHASE II: DYNAMIC BEARING TESTS																																					
Test Rig Modifications																																					
Baseline Development																																					
Bearing Tests																																					
REPORTS																																					
Monthly Progress Report																																					
Annual Interim Report																																					

APPARATUS AND TECHNIQUE DEVELOPMENT FOR SOLID LUBRICATED BEARINGS  
HUGHES AIRCRAFT COMPANY

(PO # PENDING)

Supplemental Program (G9-517)

Task 1: Friction and Wear Experiments

Task 2: Incorporation of Friction Models in DREB

Task	Calendar Months					
	4/79	5/79	6/79	2/80	3/80	4/80
1					*	
2						

The chart shows two tasks. Task 1 is represented by a wavy line starting in May 79 and ending in January 80, with an asterisk at the end of the line. Task 2 is represented by a short horizontal line starting in March 80 and ending in April 80.

## APPENDIX K

BOHNER, J.J. TO GARDOS, M.N.,  
"INITIAL INVESTIGATION INTO THE CHEMICAL  
COMPATIBILITY AT HIGH TEMPERATURES  
BETWEEN CERAMICS AND SOLID LUBRICANTS",  
Hughes Technical Internal Correspondence  
7621.14/47, 22 January 1980.

# HUGHES AIRCRAFT COMPANY

## TECHNICAL INTERNAL CORRESPONDENCE

TO: M. N. Gardos cc: See Distribution DATE: 22 January 1980  
(76-21-10) REF: 7621.14/47

SUBJECT: Initial Investigation into the Chemical  
Compatibility at High Temperatures  
between Ceramics and Solid Lubricants FROM: J. J. Bohner  
(76-21-14)

BLDG. 20 MAIL STA. D-133  
EXT. 3796

---

### ABSTRACT:

In an effort to explore the oxidation resistance and chemical compatibility of ceramics coated with potential high temperature solid lubricants, a small theoretical and experimental program has been initiated utilizing hot-pressed silicon nitride ( $\text{Si}_3\text{N}_4$ ) as a baseline ceramic.  $\text{Si}_3\text{N}_4$  was selected because of its probable use in early rolling element bearings. Consequently,  $\text{Si}_3\text{N}_4$  test coupons will be exposed to 1500°F circulating air after being coated with various solid lubricants. Included will be such solid lubricants as chalcogenides, fluorides, the Westinghouse Ga/In/WSe<sub>2</sub> compact and, if available, intercalated dichalcogenides developed by Dr. Warren Jamison under a separate task of the DARPA/Hughes program.

Preliminary reviews of the literature to date show a strong dependence of oxidation rate on the type of sintering aid used in the hot pressing of silicon nitride as well as general purity of  $\text{Si}_3\text{N}_4$  itself. In view of these observations, and in mind of the oxidation mechanism in  $\text{Si}_3\text{N}_4$  (diffusion controlled), there is a potential for the presence of solid lubricants or their oxidation products to alter the oxidative reaction rate of silicon nitride.

## I. INTRODUCTION

Advanced cruise missile engine designs being developed will require bearings capable of tolerating temperatures up to or beyond 815°C (1500°F). Such designs require the use of ceramic bearings and can be simplified by replacing complicated liquid lubricant systems with solid lubricants. It is the objective of this study to determine what effects, if any, the presence of solid lubricants will cause when used at elevated temperature on typical ceramic bearing surfaces. To achieve the desired level of understanding, this study is divided into three tasks:

- Review of industry and literature sources for information regarding high temperature physical and chemical properties of prospective ceramics and solid lubricants.
- Static, high temperature, air circulating oven-type exposure tests of bare and hard coated coupons with and without solid lubricants.
- Analysis of coupon response including examination of the bulk ceramic, the bulk-hardcoat interface (if any), the hardcoat itself (if any), the hardcoat or bulk/solid lubricant interface (if any) and finally the residual solid lubricant.

## II. PROGRESS TO DATE

### A. Ceramic Vendor Survey

The survey of ceramic suppliers and bearing manufacturers indicated that the first attempts at bearing fabrication will use hot-pressed silicon nitride. This material is available from a variety of suppliers and is generally processed with the addition of small percentages of other ceramics. These additional ceramics act as sintering or densification aids and upon complete densification are usually found as a second phase at the silicon nitride grain boundaries. The most commonly used sintering aids are MgO and Y<sub>2</sub>O<sub>3</sub>. As well as improving densification these additions also affect strength and chemical properties. Two suppliers of hot-pressed silicon nitride have apparently found compounds which result in sufficient strength for use in bearing applications. Norton Company of Worcester, Massachusetts

markets Noralide NC-132, a MgO fluxed, hot-pressed silicon nitride while Saphirwerk of Switzerland obtains their hot-pressed silicon nitride bearing ball stock from Annawerk of Rodental, West Germany<sup>(1)</sup>, marketed under the trade name Annasnid d(AD-H).

Although detailed chemical composition of the Annawerk material is not yet available, the Norton Co. Research Dept. reports their typical compositions to be as shown in Table I.<sup>(2)</sup>

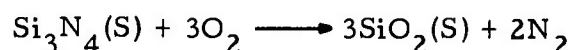
TABLE I. NORTON NORALIDE NC-132 HOT-PRESSED SILICON NITRIDE

Element	Maximum Wt. %	Typical Wt. %	Form
Mg	1.0	0.4 - 0.6	Magnesium Silicate
Fe	0.75	0.16 - 0.35	-
Al	0.5	0.18 - 0.30	-
Ca	0.05	0.006 - 0.03	-
Mn	-	0.05	-
B	-	0.003	-
W	3.0	1.5 - 2.0	Metallic W or Tungsten Silicide

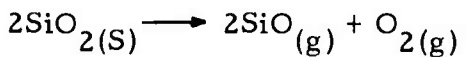
Furthermore, lineal analysis of metallographic cross sections of Norton NC-132 by Norton Co. reveals the approximate volumetric phase distributions to be 80 to 85 vol. % beta-Si<sub>3</sub>N<sub>4</sub>, 5 vol. % each of alpha-Si<sub>3</sub>N<sub>4</sub>, Si<sub>2</sub>ON<sub>2</sub> and metallic impurities such as tungsten and possibly silicon. For microstructural studies the recommended chemical etchant is either hydrofluoric acid or a mixture of hydrofluoric and nitric acids.

#### B. Oxidation Resistance of Silicon Nitride - Literature Results

A comprehensive literature survey on silicon nitride revealed that at temperatures up to at least 1500° F, hot pressed silicon nitride is oxidatively stable. Singhal<sup>(3)</sup> has examined the oxidation of Si<sub>3</sub>N<sub>4</sub> by observation of weight gain and has made kinetic calculations according to the reaction:



No detectable weight gain was observed for oxidation at  $1000^{\circ}\text{C}$  ( $1832^{\circ}\text{F}$ ) and below. The first appearance of cristobalite phase ( $\text{SiO}_2$ ) is reported at  $982^{\circ}\text{C}$ . Furthermore, the surface of oxidized  $\text{Si}_3\text{N}_4$ , the  $\text{SiO}_2$  is stable to  $1727^{\circ}\text{C}$  ( $3141^{\circ}\text{F}$ ) as long as a partial pressure of  $2. \times 10^{-1}$  atmospheres of  $\text{O}_2$  is maintained above the oxide. At lower partial pressures the oxide undergoes the reaction:



Thus should a lubricant restrict the diffusion of oxygen to the surface, the lowered partial pressure might alter the oxidation reaction and not form a protective  $\text{SiO}_2$  skin. (4)

For impure silicon nitrides such as the hot-pressed commercial grades, the sintering aids and overall chemical purity of the base material may alter the oxidation rates by as much as two orders of magnitude. Palm and Greskovich<sup>(5)</sup> experimenting with the use of 7%  $\text{BeSiN}_2$  as a sintering aid observed a 24-fold reduction in oxidation rate of their material in comparison to the Norton Noralide NC-132. The composition of their resultant material was approximately  $\text{Si}_{2.9}\text{Be}_{0.1}\text{N}_{3.8}\text{O}_{0.2}$ . The results of their study are shown in Table II.

TABLE II. WEIGHT GAIN/UNIT AREA VS. TIME IN AIR  
AT  $1045^{\circ}\text{C}$  FOR HOT-PRESSED  $\text{Si}_3\text{N}_4$  (NC-132)  
AND  $\text{Si}_3\text{N}_4$  HOT PRESSED FROM PROCESSED  
 $\text{SN}-502$   $\text{Si}_3\text{N}_4$  POWDER  
CONTAINING 7%  $\text{BeSiN}_2$

HOT PRESSED $\text{Si}_3\text{N}_4$ with 7% $\text{BeSiN}_2$		HOT PRESSED NC-132	
Time (h)	W/A ( $\text{g}/\text{m}^2$ )	Time (h)	W/A ( $\text{g}/\text{m}^2$ )
5.0	0.20	1.5	3.39
17.0	0.28	17.0	7.45
49.0	0.42	26.0	9.00
122.0	0.63	48.0	11.31
209.0	0.74	70.0	13.11
		210.0	17.40

The kinetic plot of the parabolic oxidation rate, obtained by plotting  $(w/a)^2$  vs. time for the hot-pressed  $\text{Si}_3\text{N}_4$  powder containing 7%  $\text{BeSiN}_2$  is shown in Figure 1.

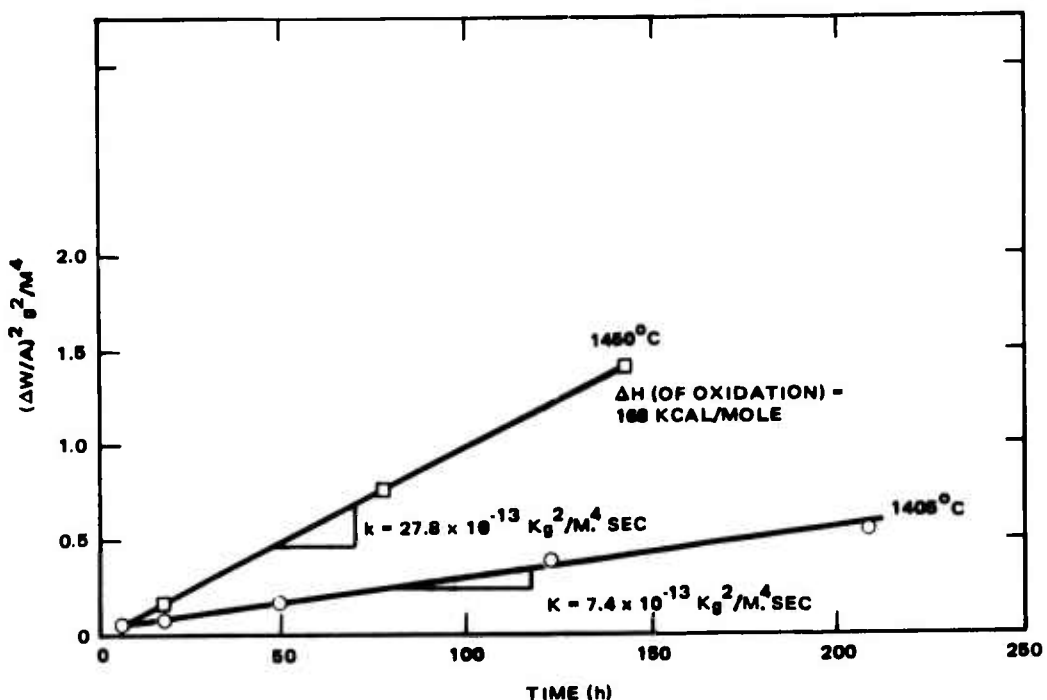


Figure 1. Oxidation kinetics of hot-pressed SN-502  $\text{Si}_3\text{N}_4$  powder containing 7%  $\text{BeSiN}_2$ ;

The parabolic rate constants at  $1405^\circ\text{C}$  ( $2561^\circ\text{F}$ ) and  $1450^\circ\text{C}$  ( $2642^\circ\text{F}$ ), calculated from the slopes of the lines in Figure 1 are  $7.4 \times 10^{-13} \text{ kg}^2/\text{m}^4 \cdot \text{sec}$ . and  $27.8 \times 10^{-13} \text{ kg}^2/\text{m}^4 \cdot \text{sec}$ , respectively.

A similar kinetic plot for oxidation of hot-pressed Noralide NC-132  $\text{Si}_3\text{N}_4$  is shown in Figure 2.

If the same computation is made for NC-132 at  $1405^\circ\text{C}$  from Figure 2 using the oxidation rate as determined through the first 25 hours of the test and extrapolated in time as indicated by the dashed line, a value of  $7.78 \times 10^{-10} \text{ kg}^2/\text{m}^4 \cdot \text{sec}$  is obtained. These results indicate the oxidation rate for the hot-pressed,  $\text{BeSiN}_2$  doped  $\text{Si}_3\text{N}_4$  is more than 3 orders of magnitude lower than NC-132 at the same temperature. However, the nonlinearity found in the oxidation rate of the NC-132 for oxidation times more than 25 hours does suggest that the difference in oxidation rates at  $1405^\circ\text{C}$  between the two

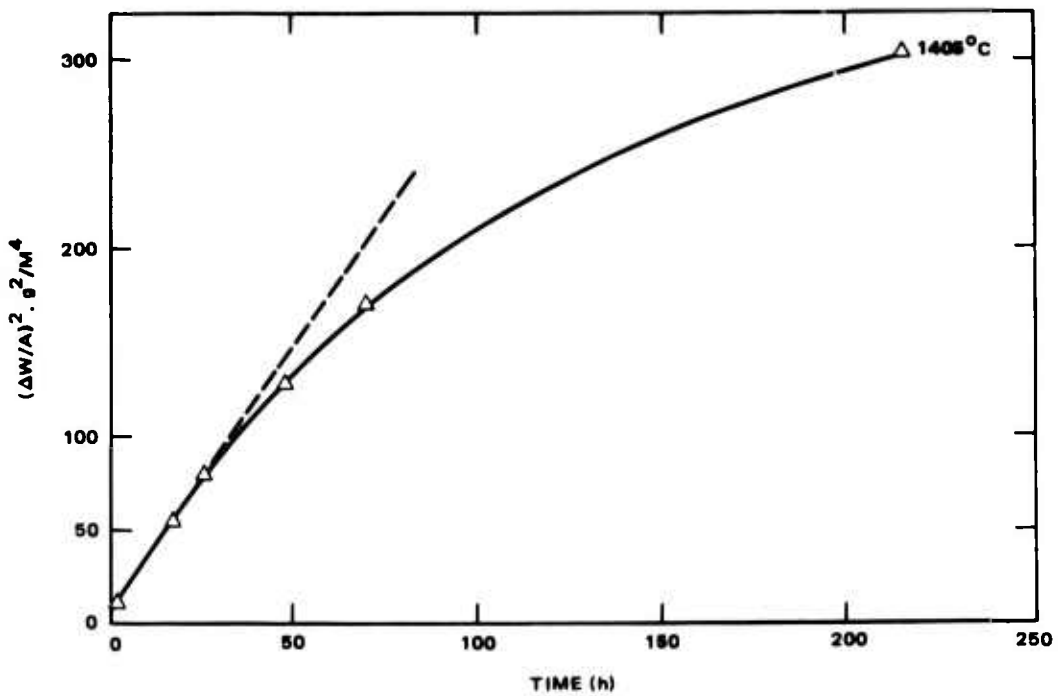


Figure 2. Oxidation kinetics of hot-pressed NC-132  $\text{Si}_3\text{N}_4$ .

materials for a specified time period beyond 25 hours would be a little lower than the 1000-fold value determined for the linear portions of the two rate processes.

The activation energy of the oxidation rate process for the  $\text{BeSiN}_2$ -doped  $\text{Si}_3\text{N}_4$  was calculated from the two curves shown in Figure 1. This value was determined to be about 165 Kcal/mole. It is more than twice the value reported for the oxidation of Si to crystalline  $\text{SiO}_2$  in which process the rate controlling process is expected to be either the rate of diffusion of O through the  $\text{SiO}_2$  to react with Si at the  $\text{Si}/\text{SiO}_2$  interface or the rate of diffusion of Si through the  $\text{SiO}_2$  to react with  $\text{O}_2$  at the  $\text{SiO}_2-\text{O}_2$  interface. The activation energy of oxidation for the  $\text{BeSiN}_2$ -doped  $\text{Si}_3\text{N}_4$  is the highest found for dense  $\text{Si}_3\text{N}_4$  and suggests that the rate controlling step in the oxidation of this material is somehow related to the presence of Be and O dissolved in the  $\text{BeSi}_3\text{N}_4$  solid solution. This deduction is supported by the

fact that only  $\alpha$ -cristobalite is detected in the oxide scale by X-ray diffraction and that the impurity levels in this hot pressed material are very low.

Further reductions in the oxidation rate of silicon nitride can be achieved with the use of CVD hardcoats on silicon nitride. This has been demonstrated by Tanzilli et al<sup>(5)</sup> who demonstrated a 10-fold reduction in oxidation rate at 1450°C (2640°F) when compared with Norton NC-132 tested at 1100°C (2000°F).

### III. OXIDATION RESISTANCE OF SOLID LUBRICANTS

Among the potentially useful solid lubricants are:

- Chalcogenides
- Fluorides
- Solid Lubricant - Protective Matrix Combinations
- Self-Lubricating Compacts

#### A. Chalcogenides

Candidate solid lubricant materials include chalcogenides of the Group IV-B, V-B, VI-B and VII-B metals, in particular sulfides, selenides, and tellurides of molybdenum, tungsten, vanadium, niobium, tantalum, and rhenium. All of the chalcogenides mentioned here are stable in vacuum at 1500°F, however, the oxidative stability in air begins to degrade at temperatures in the 350° - 400°C (662° - 752°F) range, with the exception of one of the materials, rhenium selenide, which appears to be oxidation resistant to 850°C (1562°F). A possible drawback to this material is the fact that rhenium oxide,  $Re_2O_7$  is more volatile than the oxides of molybdenum, tungsten, tantalum or niobium. A study made at General Electric Company, Space Division, showed that the most promising wear resistance for the use of this solid lubricant at elevated temperatures (up to 900°F) was exhibited when glass was used among others as a binder.

#### B. Fluorides

Some consideration was given to the calcium fluoride/barium fluoride eutectic system, which has both thermal and oxidative stability to at least

1500°F. However, inconsistencies exist in the published test data and reliable, long-term lubricative performance must still be demonstrated. These alkali metal fluorides should be recognized as antiseize agents only, i.e., while all lubricants are antiseize agents, not all antiseize agents are lubricants. However, in view of the fact that silicon nitride can be etched by 40 vol. percent of hydrofluoric acid at room temperature the structural integrity of silicon nitride may be threatened by the presence of fluorides which may preferentially attack the intergranular phases, particularly at elevated temperatures.

### C. Solid Lubricant/Protective Matrix Combinations

A portion of the literature study was devoted to a study of the properties of nickel phosphide,  $\text{Ni}_3\text{P}$ , deposited as electroless nickel. The tribological properties of a combination of  $\text{Ni}_3\text{P}$  and  $\text{MoS}_2$  have been examined at ambient temperatures. The amorphous to crystalline transition of bulk electroless nickel has been reported by Grewal, Sastri and Alexander of the Gillette Co. (8) This transition took place in three distinct stages: the first stage associated with precipitation of crystalline nickel in amorphous  $\text{Ni}_3\text{P}$  at  $150^\circ\text{C}$  ( $302^\circ\text{F}$ ), the second stage associated with the crystallization of  $\text{Ni}_3\text{P}$  to spherulites at  $335^\circ\text{C}$  ( $635^\circ\text{F}$ ), and grain growth of  $\text{Ni}_3\text{P}$  at  $400^\circ\text{C}$  ( $752^\circ\text{F}$ ). These thermal changes were associated with changes in diamond pyramid hardness (DPHN) which appeared to peak out in the  $315^\circ - 482^\circ\text{C}$  ( $600^\circ - 900^\circ\text{F}$ ) region and drop off at higher temperatures.

Thus, it appears to be unwise to give credence to any extrapolation of tribological data taken on electroless nickel formulations at ambient temperature for application at elevated temperature. The as-deposited electroless nickel at ambient temperature is amorphous. The crystalline spherulitic material obtained by heat treatment will be expected to have a different behavior in a tribological application.

D. Westinghouse Compact

Discussion of this material is left to other sections of the 3rd Semiannual Progress Report.

IV. TEST PLANS FOR OXIDATION STUDIES

Silicon nitride test coupons will be exposed in an 816°C (1500°F) air circulating oven. Coupons will be periodically weighed during the test to monitor weight gain. To evaluate the effects of lubrication, some coupons will be coated with selected solid lubricants. Also, a second series of tests will be run for each baseline material (the Norton NC-132 and the Annawerk d (AD-H)) coated with silicon nitride by chemical vapor deposition. Materials have been ordered and quotes for CVD requested from General Electric (Re-entry and Environmental System Division).

V. CONCLUSIONS

The literature, and in fact industrial experience as well, show that hot-pressed silicon nitride is both strong and oxidatively stable. Evidence exists to indicate that contaminants in the protective oxide-slag surfaces may alter the oxidation rates by orders of magnitude. While most of the oxidation studies completed have been concerned with oxidative reductions of strength, little concern has been shown for the characterization of ceramic surfaces prior to and after testing. Oxidative surface pitting, or undesirable reactions with solid lubricants may not alter bulk strength values drastically but it may be severely detrimental to close tolerance, precision bearings. The study now in progress will evaluate the results of oxidation and other reactions not only in terms of chemical kinetics but in terms of hardware effects as well.

The author gratefully acknowledges the effort of Messrs. H. Leggett and P. Dokko in collecting information used in this report as well as in planning the experimental effort.

Approved for:

R.E. Kelchner, Head  
Materials Sciences Section

J.J. Bohner, Groupleader  
Seals and Lubricants Group

## REFERENCES

1. Gardos, M. N., "Solid Lubricated Rolling Element Bearings - Semiannual Status Report No. 2", DARPA Order No. 3576, AFML Contract No. F33615-78-C-5196, Hughes Aircraft Company Report No. FR-79-76-1041, 15 August 1979.
2. Lucek, J. W., "Personal Communication;" to be published in detail elsewhere; Research Department, Industrial Ceramics Division, Norton Co., 30 January 1980
3. S. C. Singhal, Journal of Materials Science 11, 500 (1976).
4. Warburton, J. B., Antill, J. E., and Hawes, W. M., "Oxidation of Thin Sheet Reaction-Sintered Silicon Nitride", Journal of The American Ceramic Society, 61, No. 1-2, pg. 67-72, January 1978.
5. Palm, J. A., Greskovich, C. D., "Silicon Nitride for Airborne Turbine Applications" General Electric Final Report, Contract N00019-77-C-0259, July 1978.
6. Tanzilli, R. A., Gebhart, J. J., and Hanson, J. O., "Chemical Vapor Deposition of Silicon Nitride", Summary Report, ONR Contract N00019-76-C-0547, General Electric Co., Report No. 77SCR2257, September 1977.
7. P. M. Magie, Lubrication Engineering, 1966, p. 262.
8. Grewal, M. S., Sastri, S. A., and B. H. Alexander, Thermo-chimica Acta, 14, 23 (1976).

**APPENDIX L**  
**PROGRAM SCHEDULE (Separate Attachment).**

**APPENDIX M**

**PERFORMANCE AND COST REPORT  
(Separate Attachment).**